

Dissertation zur Erlangung des Doktorgrades
der Fakultät für Chemie und Pharmazie
der Ludwig-Maximilians-Universität München

**Synthesis and Characterization of
New Eco-Friendly
Nitrogen-Rich Energetic Materials**

Alexander Gerald Harter

aus

Starnberg, Deutschland

2022

Erklärung

Diese Dissertation wurde im Sinne von § 7 der Promotionsordnung vom 28. November 2011 von Herrn Prof. Dr. Thomas M. Klapötke betreut.

Eidesstattliche Versicherung

Diese Dissertation wurde eigenständig und ohne unerlaubte Hilfe erarbeitet.

München, 16.11.2022

(Alexander Gerald Harter)

Dissertation eingereicht am 31.08.2022

1. Gutachter: Prof. Dr. Thomas M. Klapötke

2. Gutachter: Prof. Dr. Konstantin L. Karaghiosoff

Mündliche Prüfung am 08.11.2022

*Da steh' ich nun, ich armer Tor,
Und bin so klug als wie zuvor!
Heiße Magister, heiße Doktor gar,
Und ziehe schon an die zehen Jahr'
Herauf, herab und quer und krumm
Meine Schüler an der Nase herum –
Und sehe, daß wir nichts wissen können!
Das will mir schier das Herz verbrennen.*

- Johann Wolfgang von Goethe -

Danksagung

Zuallererst möchte ich meinem Doktorvater Hr. Prof. Dr. Thomas M. Klapötke danken. Einerseits für die tolle Möglichkeit in seinem Arbeitskreis meine Promotion über die letzten 3 Jahre hinweg anzufertigen, andererseits für die spannende Aufgabenstellung und die große Freiheit bei der Wahl der Themen und der Forschungsarbeit selbst. Das Vertrauen, welches er mir mit der Bearbeitung von Industrie Projekten entgegengebracht hat, ehrt mich, und hat mir viel Freude bereitet. Auch möchte ich mich für die Teilnahme an verschiedenen internationalen Reisen bedanken, welche trotz Covid ermöglicht wurden.

Als Zweitgutachter möchte ich Hr. Prof. Dr. Konstantin Karaghiosoff an dieser Stelle herzlichst danken. Das Wort herzlich beschreibt „Conny“ besonders gut, es fängt bei dem Wunsch geduzt zu werden an und setzt sich in den zahlreichen interessanten und netten Gesprächen über Chemie, sowie einer tollen Hilfsbereitschaft bei jeglichen Fragen und Problemen fort.

Auch möchte ich mich bei der gesamten weiteren Prüfungskommission bedanken, welche aus Prof. Dr. Andreas Kornath, Prof. Dr. Silvija Markic, Prof. Dr. Hans-Christian Böttcher und Prof. Dr. Lena Daumann besteht.

Des Weiteren möchte ich mich bei Frau Irene Scheckenbach bedanken, welche immer die beste Anlaufstelle für jegliches Bürokratie-Problem war, und eine ausgezeichnete Süßigkeiten Versorgung in den harten Büro Zeiten gegen Ende der Promotion bereitgestellt hat.

Bei Dr. Jörg Stierstorfer möchte ich mich für seine Hilfe beim Lösen von Kristallstrukturen, sowie das Korrekturlesen zahlreicher Publikationen bedanken. Auch die netten Grillabende werden trotz kleinerer Trampolinunfälle in guter Erinnerung bleiben.

Dr. Krumm danke ich für NMR bezogene Diskussionen, sowie das bereitwillige Ausleihen von NMR Fachbüchern.

Stefan Huber möchte ich für die vielen sehr unterhaltsamen Stunden beim Sensitivitäten messen danken, welche durch seine lustige Art und Geschichten besonders schnell vergangen sind.

Meinen Arbeitskollegen aus dem Labor 3.110, Jelena Reinhardt, Michael Voggenreiter, Jan Wilhelm Kremers, Veronika Fuchs und Maurus Völkl, möchte ich für die angenehme Arbeitsatmosphäre und gute Zusammenarbeit danken. Besonders die Beauty Fridays, Astro Fridays und allgemeine Prokrastinationstage haben die Promotion erst lebenswert gemacht. Im speziellen möchte ich Jelena Reinhardt für die (nicht immer schmerzfreien) kosmetischen Behandlungen danken, ohne die ich sicher schon 5 Jahre älter aussehen würde. An dieser Stelle möchte ich auch Dr. Marc Bölter danken, welcher mich durch die Betreuung meiner Bachelorarbeit auf den Geschmack von energetischen Materialien gebracht hat und mir nicht nur seinen Platz, sondern auch seine Themen, Arbeitsweise und sein Wissen vererbt hat.

Freundschaften, sowohl alten, als auch neuen, welche während der Promotion entstanden sind möchte ich auch ein paar Sätze widmen. Tobias Lenz, Maximilian Benz, Moritz Kofen, Lukas Bauer, Marcus Lommel, Jasmin Lechner und Jelena Reinhardt sind durch viele lustige Abende, Mittagessen und Trips zu guten Freunden geworden, welche ich nicht mehr missen möchte. Speziellen Dank gebührt hier noch Jasmin Lechner, welche mein fehlendes grafisches Talent mehr als wettgemacht hat und für einen Großteil der schönen Grafiken mindestens mitverantwortlich ist.

Auch bei fast allen nicht namentlich genannten Mitglieder der Gruppe möchte ich mich bedanken, ohne welche die Promotion nicht dieselbe gewesen wäre. Sie waren die hauptsächlichen sozialen Kontakte während der Pandemie und haben selbst diese zwei Jahre zu einer guten Zeit werden lassen.

Nun möchte ich noch all meinen Praktikanten danken, Ilja Velikan, Philipp Heimerl, Philipp Kövener, Sebastian Strobel und Christoph Lauer, welche durch Ihre Mühen, meine Arbeit deutlich erleichtert haben und einen großen Teil zu dieser Doktorarbeit beigetragen haben.

Der letzte und wichtigste Dank gilt meiner Familie, besonders meinen Eltern Patricia Paul-Harter und Norbert Harter. Ohne eure grenzenlose Unterstützung wäre das Alles nicht möglich gewesen. Auch möchte ich meiner Schwester Franziska Harter, sowie Christine Reithmeier und Stefan Lulay danken. Ein besonderer Dank gilt schlussendlich noch meinem Patenonkel Dr. Gerald Paul für seine nicht endende Unterstützung während dieses langen Studiums.

Table of Contents

1. Introduction	16
1.1 Historical background and Classification	16
1.2 New eco-friendly secondary explosives	20
1.3 Towards industrial application	22
1.4 Motivation and Objectives	26
1.5 References	28
2. Conclusion.....	32
3. Synthesis and Characterization of Geminal Diazido Derivatives Based on Diethyl Malonate	40
3.1 Introduction	41
3.2 Results and Discussion	43
3.2.1 Synthesis.....	43
3.2.2 Crystal Structures.....	44
3.2.3 Physicochemical Properties	48
3.2.4 Toxicity Assessment	51
3.3 Conclusion	51
3.4 Experimental Section	52
3.5 References	55
3.6 Supplementary Information	57
3.6.1 X-ray diffraction	57
3.6.2 Experimental part and general methods	63
3.6.3 Heat of formation calculation and thermal analysis	63
3.6.4 References.....	65
4. 2-Hydrazone-propandihydrazide - a versatile precursor for high-energy materials	67
4.1 Introduction	68
4.2 Results and Discussion	70
4.2.1 Synthesis.....	70
4.2.2 Crystal Structures.....	70

4.2.3	NMR and Vibrational spectroscopy	74
4.2.4	Physicochemical Properties	74
4.2.5	Toxicity Assessment	78
4.3	Conclusion	78
4.4	Experimental Section	79
4.5	References	83
4.6	Supplementary Information	85
4.6.1	X-ray diffraction	85
4.6.2	Experimental part and general methods	92
4.6.3	Heat of formation calculation and thermal analysis	102
4.6.4	References.....	103

5. Evaluation of the methylhydrazone and oxybismethylene bridging moieties based on energetic salts of bridged nitraminotriazoles.....105

5.1	Introduction	106
5.2	Results and Discussion	107
5.2.1	Synthesis.....	107
5.2.2	NMR and Vibrational spectroscopy	108
5.2.3	Physicochemical Properties	108
5.3	Conclusion	111
5.4	Experimental Section	112
5.5	References	118
5.6	Supplementary Information	120
5.6.1	NMR Spectroscopy	120
5.6.2	DTA measurements	133

6. Synthesis, Characterization and Energetic Performance of Oxalyl Diazide, Carbamoyl Azide, and N,N'-Bis(azidocarbonyl)hydrazine136

6.1	Introduction	137
6.2	Results and Discussion	138
6.2.1	Synthesis.....	138
6.2.2	Crystal Structures.....	140

6.2.3	NMR and Vibrational spectroscopy	142
6.2.4	Physicochemical Properties	143
6.3	Conclusion	145
6.4	References	146
6.5	Supplementary Information	148
6.5.1	Experimental Procedures	148
6.5.2	NMR-Spectra	152
6.5.3	IR Spectroscopy of Carbamoyl azide (2).....	160
6.5.4	X-ray Diffraction and Hirshfeld Analysis	162
6.5.5	Thermal analysis	172
6.5.6	Computation.....	173
6.5.7	References.....	176

7. Thermodynamics of organic azides: experimental vapor pressures of organic polyazido compounds measured with the transpiration method178

7.1	Introduction	179
7.2	Materials and methods	180
7.2.1	Materials.....	180
7.2.2	Transpiration Method	181
7.3	Results and discussion.....	183
7.4	Conclusion	193

List of symbols194

7.5	References	195
7.6	Supplementary Information	199
7.6.1	Purity assessment.....	199
7.6.2	Experimental results of DE-DAM.....	201
7.6.3	Comparison of literature data	204
7.6.4	HPLC-DAD parameters.....	205
7.6.5	References.....	208

8. Lithium Nitropyrazolates as Potential Red Pyrotechnic Colorants.....209

8.1	Introduction	210
-----	--------------------	-----

8.2	Results and Discussion	213
8.2.1	Synthesis.....	213
8.2.2	Crystal Structures.....	215
8.2.3	Physico-Chemical Properties	220
8.2.4	Pyrotechnic Performance	224
8.3	Conclusion	226
8.4	Experimental Section	226
8.5	References.....	231
8.6	Supplementary Information	234
8.6.1	Synthesis Optimization.....	234
8.6.2	Thermal Dehydration Studies.....	235
8.6.3	General Methods.....	240
8.6.4	IR Spectra	242
8.6.5	NMR Spectra.....	243
8.6.6	Crystallographic Data.....	247
8.6.7	DTA Plots.....	249
8.6.8	Pyrotechnic Performance	250
8.6.9	References.....	251

9. 1,5-Dimethyltetrazole as a ligand in energetic 3d⁵ to 3d¹⁰-metal coordination compounds.....253

9.1	Introduction	254
9.2	Results and Discussion	255
9.2.1	Synthesis.....	255
9.2.2	Crystal Structures.....	257
9.2.3	Infrared spectroscopy.....	265
9.2.4	Thermal behavior and sensitivities	267
9.3	Conclusion	271
9.4	Experimental Section	273
9.5	References.....	277
9.6	Supplementary Information	281
9.6.1	Overview of compounds.....	281
9.6.2	Single Crystal X-Ray Diffraction	282
9.6.3	Single Crystal X-Ray Diffraction	287
9.6.4	NMR spectroscopy of 1–3.....	288
9.6.5	General Methods.....	291

9.6.6	References.....	292
-------	-----------------	-----

10. Kinetic Predictions Concerning the Long-Term Stability of TKX-50 and Other Common Explosives Using the NETZSCH Kinetics Neo Software.....294

10.1	Introduction	295
10.2	Experimental Section	297
10.3	Results and Discussion	298
10.3.1	Theoretical Background	298
10.3.2	Method Evaluation	300
10.3.3	Activation Energy	303
10.3.4	Isothermal predictions and long-term stability	304
10.3.5	Climatic predictions	306
10.3.6	Conclusion	308
10.4	References.....	309
10.5	Supplementary Information	312
10.5.1	Method evaluation.....	312
10.5.2	Activation energy.....	320
10.5.3	Isothermal predictions and long-term stability	324
10.5.4	Climatic predictions	328
10.5.5	Verification Experiment	332

11. Solvent Replacement and Optimization of the Industrial Scale TKX-50 Synthesis..... Fehler! Textmarke nicht definiert.

11.1	Scope of the Project.....	Fehler! Textmarke nicht definiert.
11.2	Results and Discussion	Fehler! Textmarke nicht definiert.
11.2.1	Solvent replacement	Fehler! Textmarke nicht definiert.
11.2.2	Chlorination of glyoxime	Fehler! Textmarke nicht definiert.
11.2.3	TKX-50 one-pot optimization.....	Fehler! Textmarke nicht definiert.
11.2.4	TKX-50 further characterization	Fehler! Textmarke nicht definiert.
11.3	References.....	Fehler! Textmarke nicht definiert.

1. Introduction

1.1 Historical background and Classification

The history of energetic materials began around 220 BC in China, where blackpowder, a mixture of sulfur, charcoal and potassium nitrate was discovered by accident.^[1] From a scientific perspective the research of this new field of compounds started in the 13th century with Roger Bacon, followed by Berthold Schwartz in the 14th century, which investigated the properties of blackpowder.^[2] This led to the first military application of energetic materials at the end of the 13th century across Europe. During the following centuries the performance limits of blackpowder became more and more apparent, especially in the mining and tunneling sector. This created the need to develop new and more powerful energetic materials. During the 19th century several new compounds were synthesized, starting with nitroglycerine (NG), nitrocellulose (NC), and picric acid.^[3-5] Due to the rising interest in this area, these discoveries were quickly followed by the next generation of energetic materials like 2,4,6-trinitrotoluene (TNT) and pentaerythriltetranitrat (PETN).^[6-10] The next major developments were 1,3,5-trinitro-1,3,5-triazine (RDX) and 1,3,5,7-tetranitro-1,3,5,7-tetrazocine (HMX), which are the most commonly used explosives for military applications since World War II.^[11-14] During the last decades the field of energetic materials expanded to a large spectrum of compounds with different specifications like the high temperature stable 1,3,5-triamino-2,4,6-trinitrobenzene (TATB) and 1,2-bis(2,4,6-trinitrophenyl)ethylene (HNS) or the very powerful 6,8,10,12-hexanitro-2,4,6,8,10,12-hexaazaisowurtzitane (CL-20).^[15-17]

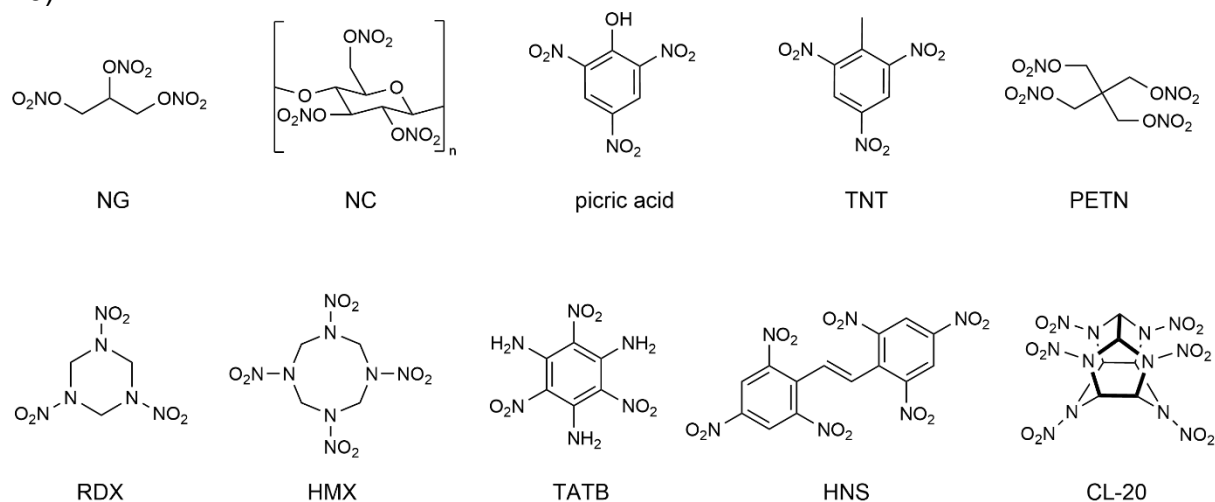


Figure 1. Lewis structures and acronyms of historically relevant energetic materials.

The focus of recent advances in the field of energetic materials has mainly shifted to nitrogen-rich heterocycles with a good oxygen balance, high heats of formations and low amounts of carbon atoms.^[18-21] Figure 1 shows the lewis structures of the above mentioned compounds.

The term “energetic materials” is described in various ways and in varying degrees of detail when looking at the literature. A very specific definition can be found in High Energy Materials by J. P. Agrawal: “An explosive is a substance which, when suitably triggered, releases a large amount of heat and pressure by way of a very rapid self - sustaining exothermic decomposition reaction. The temperature generated is in the range of 3000 – 5000 ° C and the gases produced expand 12 000 – 15 000 times than the original volume. The entire phenomenon takes place in a few microseconds, accompanied by a shock and loud noise.”^[22] The American Society for Testing and Materials (ASTM) gives a more condensed definition, which seems to be the general consensus in this matter: “An energetic material is defined as a compound or mixture of substances which contains both the fuel and the oxidizer and reacts readily with the release of energy and gas.”^[23]

Energetic materials are usually classified according to their different properties and utilization. By this method they are divided in three main categories, propellants, pyrotechnics and explosives, depicted in Figure 2.^[1] This thesis focuses mainly on the branch of secondary explosives.

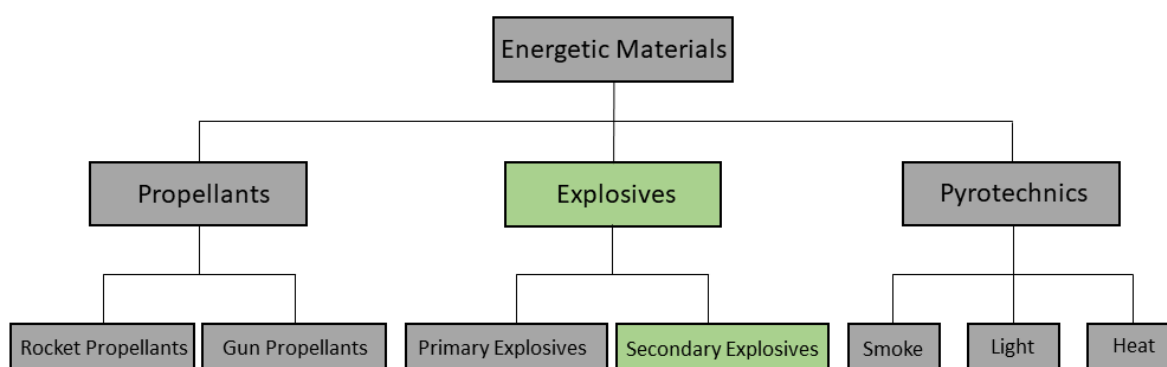


Figure 2. Classification of energetic materials. The green subsections are the main topic of this work.

Propellants generally consist of two main components, a fuel and an oxidizer and can be subdivided in gun and rocket propellants.^[1] Their main characteristic is the generation of larger amounts of hot gases upon deflagration, resulting in propulsive forces, which are able to accelerate rockets or projectiles.^[24] This propulsive force is

described by the specific impulse I_{sp} , a parameter for the effectiveness of the respective propellant system.^[24] There are three different types of gun propellants, single, double and triple base propellants, each fulfilling different requirements. Commonly used compounds are nitroguanidine, nitrocellulose and nitroglycerin, all three combined would be an example for a triple base composition.^[25] Rocket propellants can be categorized in either solid or liquid propellants. Solid propellants can once again be divided into homogenous propellants like a nitrocellulose and nitroglycerin mixture or heterogeneous propellants like a mixture of ammonium perchlorate aluminum and a binder.^[26-28] Historically, solid propellants are often based on ammonium perchlorate and therefore their main problem is the high toxicity towards organic lifeforms.^[29] In case of liquid propellants there are hypergolic and non-hypergolic mixtures. An example for the former is a mixture of nitric acid and hydrazine, for the latter just hydrazine can be used.^[30] Current research in this area focuses mainly on replacing the highly toxic ammonium perchlorate, through new compounds, which have a lower environmental impact.^[31-33]

Pyrotechnic mixtures in general react slowly and non-detonatively in comparison to other energetic materials and typically generate light, smoke, heat or noise with a wide range of applications.^[34] A pyrotechnical mixture consists of three main components, fuel, oxidizer and reducing agent.^[35] The exact composition of each mixture is highly dependent of the intended usage. While the application that comes to mind firstly is fireworks, pyrotechnics are primarily researched in regard to military use like signal flares, smoke munition or delay compositions.^[36] Current research aims to replace the commonly used toxic ingredients like perchlorates, halogens and heavy metals, which cause environmental problems and damages to living organisms.^[37] For example, strontium is used in red pyrotechnics, even though it is known to replace calcium in the bone and cause severe health issues, therefore lithium is investigated as a nontoxic alternative in those formulations.^[38]

Primary explosives differ from other energetic materials by several specific properties. They usually show a high sensitivity towards stimuli like impact (< 4 J), friction (< 10 N) and electrostatic discharge (< 20 mJ) and generally exhibit lower detonation performance including detonation velocity, pressure and temperature in comparison to secondary explosives.^[39] The most important characteristic is the fast deflagration to detonation transition (DDT). This describes the development from a

deflagration with a burn rate of about 100 m s^{-1} to a detonation at the speed of sound and above, which creates a shockwave and is able to initiate less sensitive secondary explosives.^[40] Due to those properties primary explosives are mainly used as initiators in detonators and blasting caps.^[41] The most commonly known primary explosives are lead azide, mercury fulminate and lead styphnate. Those heavy metal based compounds are used because of their low production cost and reliable performance, but once again possess the downside of high toxicity.^[42] Due to numerous studies regarding the cause of health issues of those heavy metal containing compounds, the research of finding new non-toxic primary explosives increased significantly.^[43-45] Promising new substances are metal free nitrogen-rich compounds like tetrazene (GNGT) or dipotassium 1,1'-dinitramino-5,5'-bistetrazolate (K_2DNABT), as well as compounds based on less toxic metals like copper(I) 5-nitrotetrazolate (DBX-1) or pentammin(1,5-cyclopentamethylentetrazolato- N^β)cobalt(III) perchlorate (PAC).^[46-49]

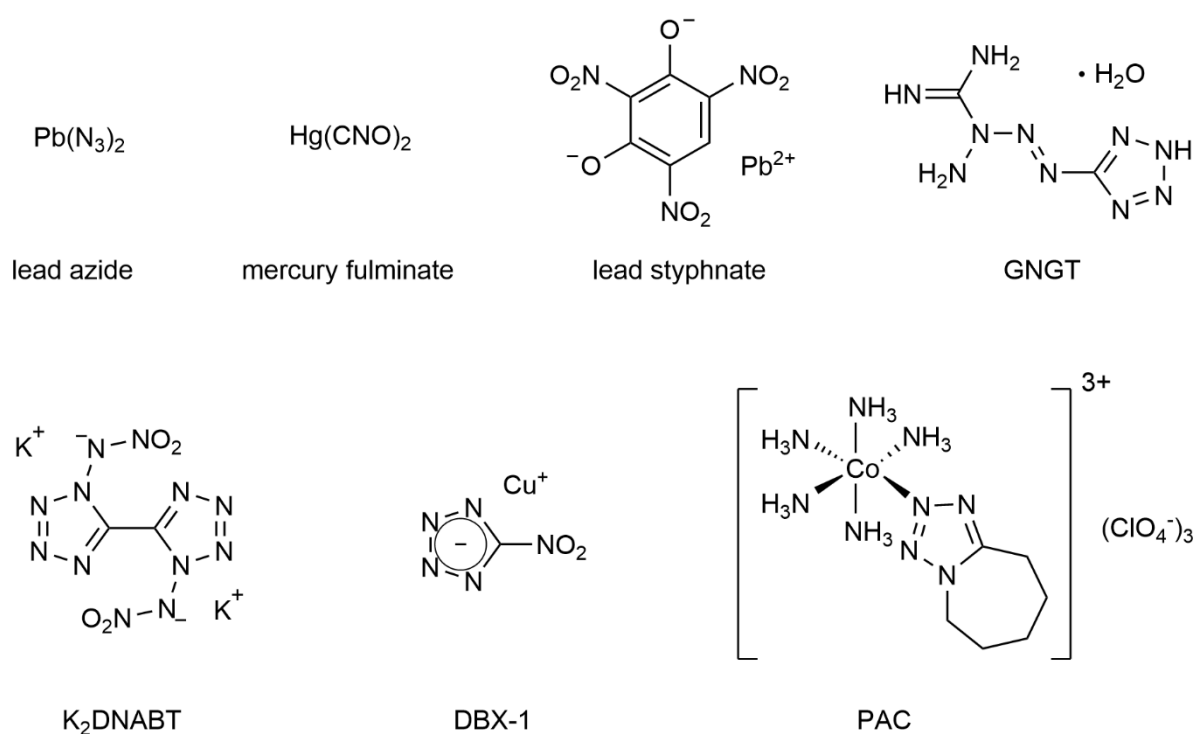


Figure 3. Selected primary explosives: lead azide, mercury fulminate, lead styphnate, tetrazene (GNGT), dipotassium 1,1'-dinitramino-5,5'-bistetrazolate (K_2DNABT), copper(I) 5-nitrotetrazolate (DBX-1) and pentammin(1,5-cyclopentamethylentetrazolato- N^β)cobalt(III) perchlorate (PAC).

Secondary explosives generally feature lower sensitivity towards external stimuli like impact ($> 4 \text{ J}$) and friction ($> 80 \text{ N}$) and higher detonation parameters in comparison to primary explosives.^[1] Therefore, secondary explosives are usually ignited by high thermal stress or the shockwave produced by detonating a primary explosive.^[50] The most important parameters describing the detonation performance are the detonation

energy ($-\Delta_E U$) detonation velocity (V_D), detonation pressure (p_{C-J}), detonation temperature (T_{C-J}) and volume of detonation gases (V_0).^[1] The most common compounds in the field of secondary explosives until today are TNT, PETN, RDX and HMX, shown in Figure 1.^[51] While these substances possess decent physiochemical properties, they are mostly used due to their cheap and simple synthesis and show significant room for improvement in terms of toxicity and detonation performance.^[52] This topic will be discussed in detail in the next chapter.

1.2 New eco-friendly secondary explosives

One of the major goals of energetic research in the field of secondary explosives is the development of a substitute for the carcinogenic and toxic hexogen (RDX).^[53] Even though RDX is a nerve poison and causes nausea, seizures, amnesia and many more severe symptoms, as well as damages to flora and fauna, it is still one of the most used energetic materials of our time.^[54] In order to find suitable replacements for the existing secondary explosives, the first thought has to be about the necessary property requirements of those new compounds, summarized in Figure 4.

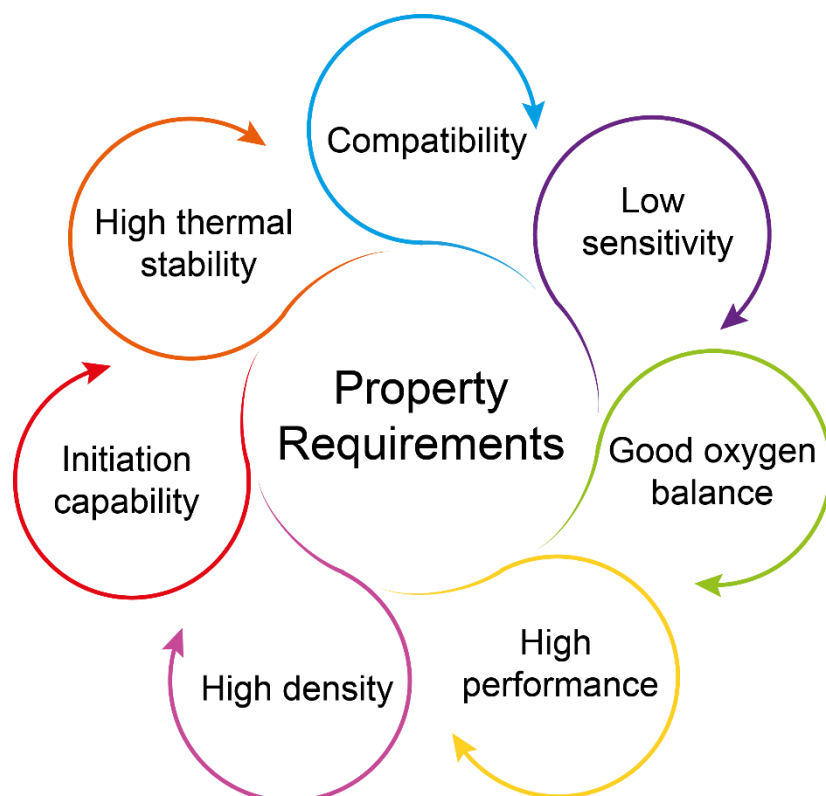


Figure 4. Requirements in regard to the properties of new secondary explosives.

The most obvious requirement is a low toxicity of the new compound and its decomposition products, combined with low solubility in water, which additionally reduces the negative environmental impact. Besides that, the new material has to

exhibit the necessary detonation properties, ideally exceeding the properties of RDX. This includes a high density, good oxygen balance, high thermal stability, high detonation velocity and pressure and low sensitivities towards all relevant external stimuli. Additionally, the new material has to be able to be initiated and be compatible with other used materials. Synthesizing a new compound, which fulfills all the mentioned requirements is a great challenge and has to be done systematically. Therefore, different methods can be used to tune the molecule in the desired direction, which are summarized in Figure 5.

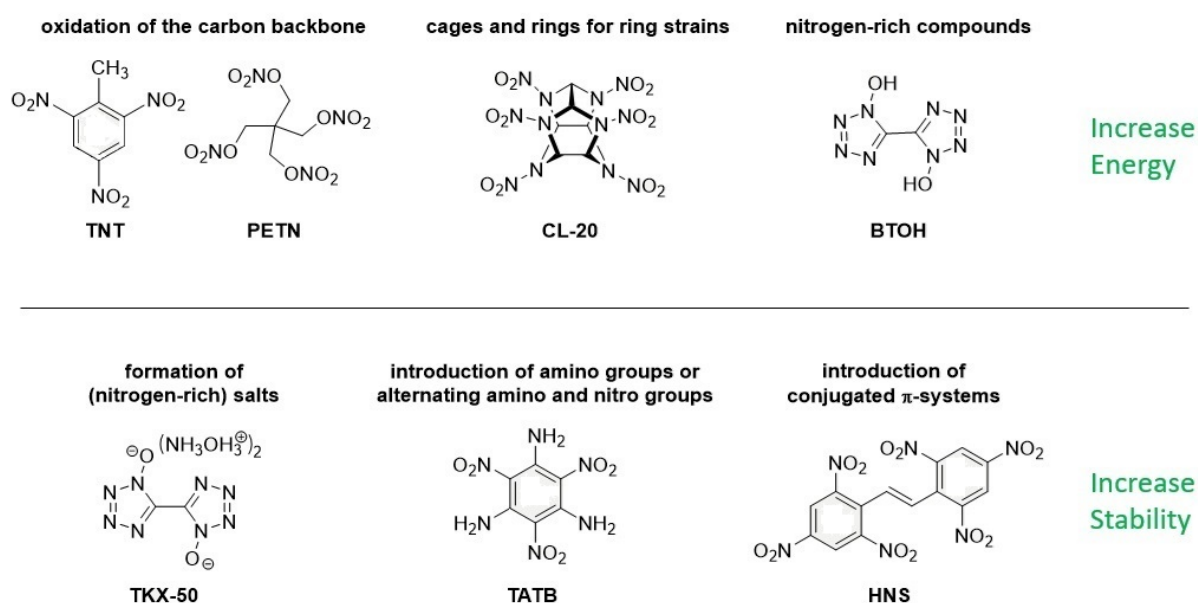


Figure 5. Strategies for tuning the properties of energetic molecules with selected examples. 2,4,6-trinitrotoluene (TNT), pentaerythrityltetranitrat (PETN), hexanitrohexaazaisowurtzitane (CL-20), 1,1'-dihydroxybistetrazole (BTOH), bishydroxylammonium 5,5'-bistetrazole-1,1'-diolate (TKX-50), 2,4,6-trinitrobenzene-1,3,5-triamine (TATB) and 1,1'-[(*E*)-Ethane-1,2-diyl]bis(2,4,6-trinitrobenzene) (HNS).

The first step is to choose the right base frame. Established compounds like RDX and TNT rely on a carbon backbone providing stability, which is then oxidized for increased energetic performance. Some of the more recent high-performing compounds like CL-20 additionally rely on the energy gained by a cage or ring strain. In order to increase their stability those compounds are often functionalized with alternating amino and nitro groups or the introduction of conjugated π -systems, as it is the case for TATB and HNS.^[22] All of those compounds show either high toxicity themselves or decompose into toxic products. In contrast, recent research focuses on compounds with a high nitrogen content like nitrogen-rich heterocycles, especially azoles and azines. These are highly promising for the purpose of new green energetic materials with high

performance values.^[55] The high amount of nitrogen atoms results in a higher heat of formations as well as mainly nontoxic and gaseous decomposition products like N₂, CO₂ and H₂O. Azoles show particularly promising features like high densities, good thermal stabilities and various possibilities for functionalization. The thermal stability for this class of compounds can even be increased by the formation of nitrogen rich salts.^[56] A prominent example in this category is TKX-50, which will be a main part of this thesis and discussed in more detail during the next chapter.

1.3 Towards industrial application

When synthesizing new energetic compounds, the ultimate goal is always the production and application in the industrial sector. Even though it is great to find a new material with good properties in terms of performance and stability, this does not mean it is suitable for industrial scale synthesis. The way from laboratory scale synthesis to industrial production is long and full of possible exclusion criteria that have to be met. Many of those criteria are correlated with the synthesis itself, which has to be cost efficient in order to be able to compete with currently used compounds and up-scalable to industrial amounts. Using cheap chemicals, having a low amount of reaction steps and obtaining high overall yields are just some of many essential factors. Additionally,

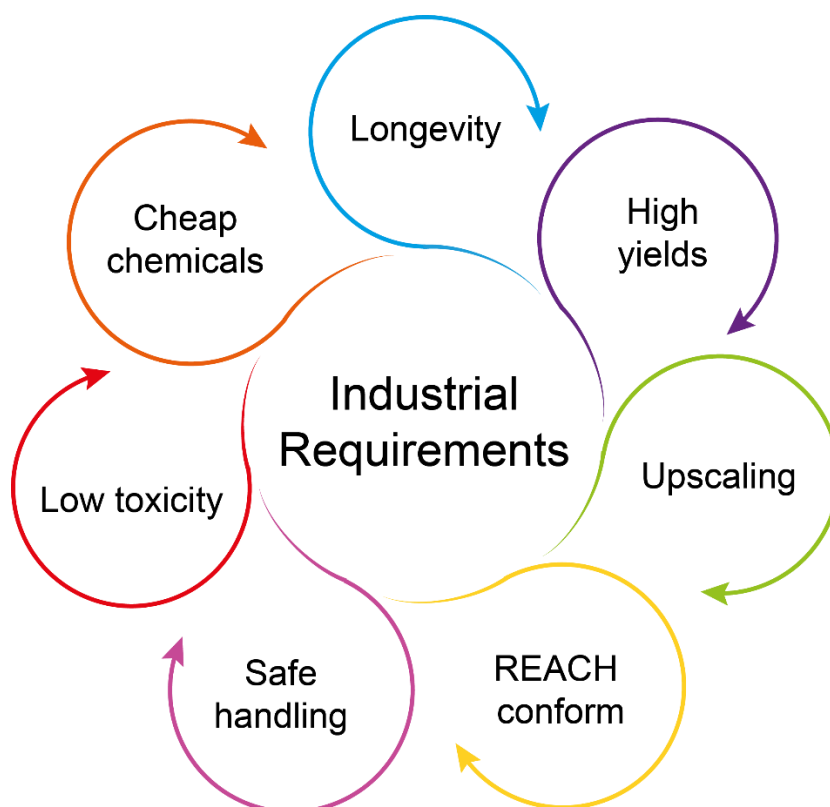
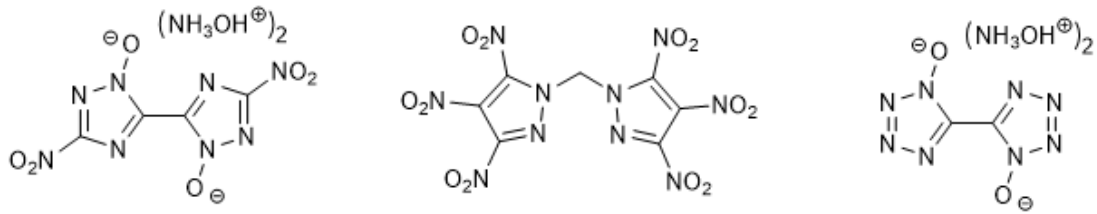


Figure 6. Requirements of new energetic materials in order to be considered for industrial scale production.

safety is a huge issue, therefore all used chemicals should be REACH conform, save to handle and exhibit low toxicity. This includes solvents and possible intermediate products. Another important parameter is the longevity of the isolated products, which directly affects storage capabilities and transportability of the energetic material. Some of the most important criteria that have to be met are summarized in Figure 6.

In the field of new secondary explosives, the group of Prof. Klapötke synthesized a number of potential RDX replacements during the last 10 years. The most promising of those compounds are MAD-X1, BTNPM and TKX-50, shown in Figure 7.^[57-59] All three compounds exceed RDX ($V_D = 8834 \text{ m s}^{-1}$) in terms of their detonation properties, show good thermal stabilities and possess high densities. MAD-X1 is an energetic salt, with a thermal stability of $217 \text{ }^\circ\text{C}$ and a calculated detonation velocity of 9195 m s^{-1} (EXPLO5). It is completely insensitive towards external stimuli with values above 40 J of impact and 360 N of friction sensitivity. The good detonation performance derives from the high density of 1.90 g m^{-3} . MAD-X1 is synthesized starting from the cheap oxalic acid, but the four-step synthesis includes the formation of a diazonium salt, which can detonate spontaneously. BTNPM consists of two methylene-bridged trinitropyrazoles and is a neutral compound. The synthesis starts from easily available *1H*-pyrazole and comprises six steps in total. Of the three candidates it has the lowest thermal stability of $205 \text{ }^\circ\text{C}$, which is still a decent value. It shows a high density of 1.93

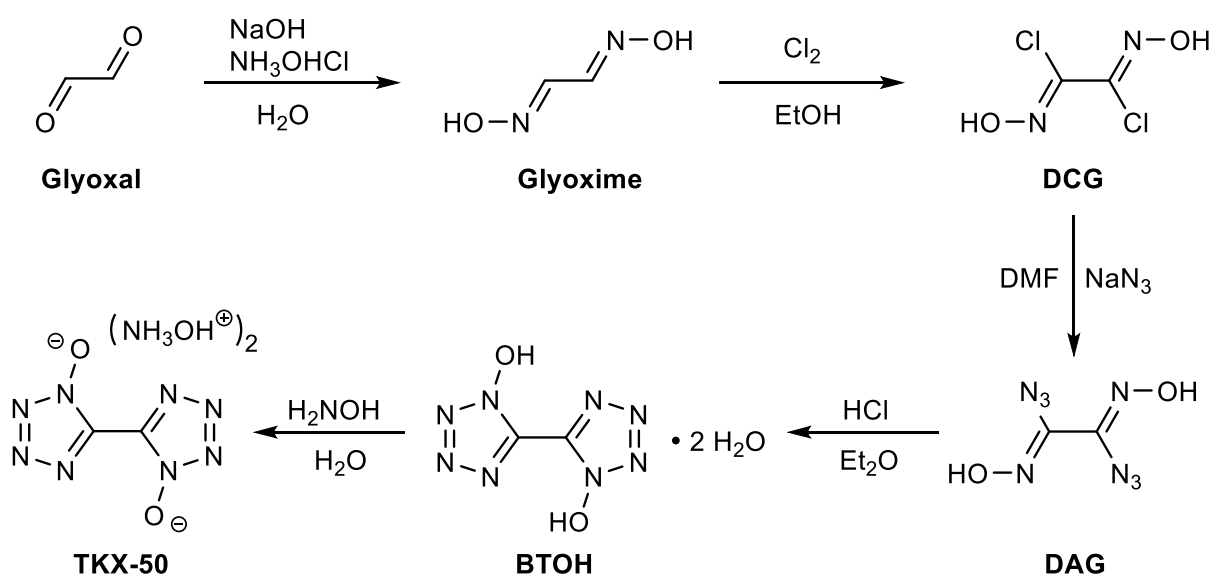


MAD-X1	BTNPM	TKX-50
1.90 g cm^{-3}	1.93 g cm^{-3}	1.88 g cm^{-3}
$217 \text{ }^\circ\text{C}$	$205 \text{ }^\circ\text{C}$	$220 \text{ }^\circ\text{C}$
9195 m s^{-1}	9304 m s^{-1}	9767 m s^{-1}
$>40 \text{ J}, >360 \text{ N}$	$4 \text{ J}, 144 \text{ N}$	$20 \text{ J}, 120 \text{ N}$

Figure 7. Structures of promising RDX replacements synthesized by Klapötke et al. with their respective values regarding density [g cm^{-3}], decomposition temperature [$^\circ\text{C}$], detonation velocity [m s^{-1}], impact [J] and friction [N] sensitivity (top to bottom).^[60]

g m^{-3} and an excellent detonation velocity of 9304 m s^{-1} . Compared to the other two candidates BTNPM is the most sensitive one. It comes up with sensitivity values of 4 J towards impact and 144 N towards friction. Nonetheless, these values are still in an acceptable range for the use as secondary explosive.

Even though the two described molecules are strong contenders for an industrial RDX replacement, the most promising compound to date is bishydroxylammonium 5,5'-bistetrazole-1,1'-diolate (TKX-50), which was discovered by Fischer *et al.* in 2012 and named after Prof. Thomas M. Klapötke in honor of his 50th birthday. This ionic molecule shows excellent properties, exceeding RDX in its detonation velocity by almost 1000 m s^{-1} with a calculated value of 9767 m s^{-1} . It possesses a high thermal stability with a decomposition temperature of $220 \text{ }^\circ\text{C}$ and high stability towards external stimuli with sensitivity values of 20 J and 120 N. This makes it safe to handle but still sensitive enough to be initiated and being used as a secondary explosive. Additionally the aquatic toxicity was determined with a luminescent marine bacterium called *Vibrio fischeri*.^[59] This measurement proved TKX-50 to be significantly less toxic than RDX and therefore be a valid green alternative. The only problematic aspect of TKX-50 is the original synthesis starting from glyoxal, which includes at least 4 steps and the isolation of dangerous intermediates like the highly sensitive diazidoglyoxime (DAG) and BTOH, shown in Scheme 1.



Scheme 1. Original synthesis of TKX-50 starting from glyoxal with all intermediate products, including glyoxime, dichloroglyoxime (DCG), diazidoglyoxime (DAG) and 1,1'-dihydroxybistetrazole (BTOH).^[59]

The original synthesis starts with an oximation of the commercially available glyoxal with hydroxylammoniumchloride in aqueous sodium hydroxide solution. Glyoxime is obtained in almost quantitative yields and is then further chlorinated using chlorine gas. The hereby synthesized DCG is reacted with sodium azide in DMF, producing DAG, which is highly sensitive towards impact and friction. BTOH is obtained by the cyclisation of DAG with gaseous hydrochloric acid and usually contains two water molecules per BTOH molecule. TKX-50 is finally afforded by the reaction of BTOH with hydroxylammonium solution.^[59]

1.4 Motivation and Objectives

In general, the goals of this thesis can be divided in two major parts. The first part focuses on the synthesis and investigation of new green energetic materials with a focus on secondary explosives and their precursors. The second part deals with the topic of long-term stability predictions of energetic materials in order to estimate storage capabilities and safety issues.

For the part focusing on synthesis and characterization of new energetic materials, especially secondary explosives and their precursors, the general approach pursues three main aspects:

- Straight forward and short synthetic routes
- “Green” compounds in terms of toxicity and decomposition products
- Powerful detonation properties, exceeding the state of the art (e.g. RDX)

Based on these prerequisites this part of the thesis starts with the investigation of a - in terms of energetic behavior - scarcely examined class of nitrogen-rich compounds, geminal diazides based on diethyl malonate. Those highly versatile molecules are promising source materials, having a relatively low molecular weight, high nitrogen content, commercially available starting materials and a high energetic potential, due to the two azido moieties. In general, an azido group adds some desirable features to the molecule. For example, it increases the heat of formation by about 260 kJ mol^{-1} and decomposes into nontoxic nitrogen gas.^[63] Using the previously described methods of salt formation, ring closing reactions, and increasing the nitrogen content and energetic character by suitable functionalization, as well as utilizing different bridging moieties, new energetic materials were investigated and extensively characterized.

The second part of the thesis covers the topic of long-term stability prediction, which is an important key figure for industrial application. While most newly synthesized energetic materials are characterized in detail regarding their physiochemical properties like thermal stability, sensitivity and detonation properties, the aspect of longevity is often neglected. The recent accident in Beirut caused by ammonium nitrate, which is not considered as a dangerous or explosive compound in general, puts long term stability in terms of storage safety in the spotlight again. Figure 8 shows



Figure 8. Harbour of Beirut before and after the accident in 2020, caused by improperly stored ammonium nitrate.

the damage caused to the storage facilities in the harbor of Beirut. Therefore, the goal of this part was to establish a fast and easy method to estimate the behavior of new energetic materials over a time span of 10 years under different temperature conditions. This includes the selection of a suitable method and software based on experimental thermogravimetric data, which can be obtained quickly. The following goal was to create a database of long-term stability predictions of selected energetic materials to provide comparability between different substances from the same class of compounds (e.g. secondary explosives).

1.5 References

- [1] T. M. Klapötke, *Chemistry of High-Energy Materials*, 4th ed., De Gruyter, Berlin, **2017**.
- [2] J. Akhavan, *The Chemistry of Explosives*, 2nd ed., Royal Society of Chemistry, Cambridge, **2011**.
- [3] W. D. Müller-Jahncke, C. Friedrich, U. Meyer, *Arzneimittelgeschichte*, 2nd ed., Wiss. Verl.-Ges, Stuttgart, **2005**.
- [4] Jochen Gartz, *Vom Griechischen Feuer zum Dynamit- eine Kulturgeschichte der Explosivstoffe*, E.S. Mittler & Sohn, Hamburg-Berlin-Bonn, **2007**.
- [5] W. Erb, *Archiv Pharm.*, **1867**, 181,123–124.
- [6] A. V. Samet, V. N. Marshalkin, K. A. Lyssenko, *Russ. Chem. Bull.*, **2009**, 58, 347–350.
- [7] L. Davis, *The Chemistry of Powder and Explosives*, Vol. 2; Wiley New York, **1943**.
- [8] J. Wilbrand, *Annalen der Chemie und Pharmacie*, **1863**, 128, 178–179.
- [9] B. Tollens, P. Wigand, *Justus Liebigs Ann. Chem.*, **1891**, 265, 316–340.
- [10] G. Bugge, *Schiess- und Sprengstoffe und die Männer die sie schufen*, Franckh'sche Verlagshandlung, Stuttgart, **1942**, 57.
- [11] A. Kumar, V. Rao, R. Sinha, A. Rao, *Propellants Explos. Pyrotech.*, **2010**, 35, 359–364.
- [12] T. Urbanski, *Chemistry and Technology of Explosives*, Vol. 4, Pergamon, Oxford, U. K., **1984**, p.202.
- [13] M. A. Cook, *The Science of High Explosives*, Reinhold, New York, **1958**.
- [14] W. E. Bachmann, J. C. Sheehan, *Journal of the American Chemical Society*, **1949**, 5, 1842–1845.
- [15] U. R. Nair, R. Sivabalan, G. M. Gore, *Combust. Explos. Shock Waves*, **2005**, 41, 121–132.
- [16] A. T. Nielsen, R. L. Atkins, W. P. Norris, *J. Org. Chem.*, **1979**, 44, 1181–1182.
- [17] P. Golding, A. M. Jayaweera-Bandara, H. Duffin, US Patent 5023386, Filed January 4, **1990**.
- [18] G. Steinhauser, T. M. Klapötke, *Angew. Chem. Int. Ed.*, **2008**, 47, 3330.

- [19] P. K. Swain, H. Singh, S. P. Tewari, *J. Mol. Liq.*, **2010**, 151, 87.
- [20] D. M. Badgujar, M. B. Talawar, S. N. Asthana, P. P. Mahulikar, *J. Hazard. Mater.*, **2008**, 151, 289–305.
- [21] J. J. Sabatini, K. D. Oyler, *Crystals*, **2016**, 6, 5.
- [22] J. P. Agrawal, *High Energy Materials: Propellants, Explosives and Pyrotechnics*, Wiley-VCH, Weinheim, **2010**.
- [23] <https://www.astm.org> (accessed 28.06.22)
- [24] N. Kubota, *Propellants and Explosives: Thermochemical Aspects of Combustion*, 3rd ed., Wiley-VCH, Weinheim, **2015**.
- [25] J. J. Sabatini, E. C. Johnson, *ACS Omega*, **2021**, 6, 18, 11813–11821.
- [26] S. K. Pradhan, V. Kedia, P. Kour, *Materials Today: Proceedings*, **2020**, 33, 5269–5272.
- [27] B. P. Mason, C. M. Roland, *Rubber Chem. and Technol.*, **2019**, 92, 1–24.
- [28] B. Sellers, K. Weeks, W. R. Alsop, *Perchlorate Environmental Problems and Solutions*, CRC, Boca Raton, FL (USA), **2007**.
- [29] D. B. Kirchner, J. C. Gaydos; M. C. Battigelli, *Textbook of Military Medicine series [Part III. Disease and the Environment]*, Office of the Surgeon General, The Borden Institute, Walter Reed Army Medical Center, Washington, DC, **1993**.
- [30] I. F. Silvera, J. W. Cole, *J. Phys.: Conf. Ser.*, **2010**, 215, 12194.
- [31] A. E. S. Nosseir, A. Cervone, A. Pasini, *Aerospace*, **2021**, 8, 20.
- [32] F. Kamal, *Applications of Ionic Liquids in Science and Technology*, IntechOpen, London, **2011**.
- [33] M. Tsay, D. Lafko, J. Zwahlen, C. William, *Development of Busek 0.5N Monopropellant Thruster*, Proceedings of the 27th Annual AIAAUSU Conference on Small Satellites, Logan, UT, USA, **2013**.
- [34] J. A. Conkling and C. Mocella, *Chemistry of Pyrotechnics Basic Principles and Theory*, Taylor Francis, **2010**.
- [35] A. A. Shidlovskiy, *Principles of pyrotechnics*, 3rd ed., Moscow, **1964**.
- [36] H. Ellern, *Military and civilian pyrotechnics*, Chemical Publishing Company, New York, **1968**.

- [37] K. Sellers et al., *Perchlorate environmental problems and solutions*, Boca Raton, FL CRC Press–Taylor & Francis, Group, **2007**.
- [38] J. Glück, T. M. Klapötke, M. Rusan, J. J. Sabatini, J. Stierstorfer, *Angew. Chem., Int. Ed.*, **2017**, *56*, 16507.
- [39] R. Matyáš, J. Pachman, *Primary Explosives*, Springer-Verlag, Berlin Heidelberg **2013**.
- [40] N. Mehta, K. Oyler, G. Cheng, A. Shah, J. Marin, K. Yee, *Z. anorg. allg. Chem.*, **2014**, *640*, 1309-1313.
- [41] B. T. Fedoroff, O. E. Sheffield, S. M. Kaye, *Encyclopedia of Explosives and Related Items.*, Picatinny Arsenal, Dover, NJ, **1960–1983**.
- [42] Brede, U., Hagel, R., Redecker, K.H., Weuter, W., *Propell. Explos. Pyrotech.*, **1996**, *21*, 113–117.
- [43] G. C. Mei, J. W. Pickett, US Patent 5417160, filed **1995**.
- [44] J. Nesveda, S. Brandejs, K. Jirašek, Patent WO 0121558, **2001**.
- [45] M. V. Huynh, M. D. Coburn, T. J. Meyer, M. Wetzer, *Proc. Natl. Acad. Sci.*, **2006**, *103*, 5409–5412.
- [46] D. Herweyer, J. L. Brusso, M. Murugesu, *New J. Chem.*, **2021**, *45*, 10150.
- [47] B. M. Rice, E. F. C. Byrd, *J. Mater. Res.*, **2006**, *21*, 2444–2452.
- [48] K. D. Oyler, *Green Primary Explosives. In Green Energetic Materials*, T. Brinck (Ed.), **2014**.
- [49] R. Deblitz, C. G. Hrib, S. Blaurock, P. G. Jones, G. Plenikowskic, F. T. Edelman, *Inorg. Chem. Front.*, **2014**, *1*, 621-640.
- [50] P. M. Dickson, J. E. Field, *Proceedings Mathematical and Physical Sciences*, **1993**, *441*, 359–375.
- [51] P. W. Cooper, *Explosives engineering*, Wiley-VCH, New York, Chichester, Weinheim, Brisbane, Singapore, Toronto, **1996**.
- [52] T. M. Klapötke, P. C. Schmid, S. Schnell, J. Stierstorfer, *Chem. Eur. J.*, **2015**, *21*, 9219–9228.
- [53] G. A. Parker, G. Reddy, M. A. Major, *Int. J. Toxicol.*, **2006**, *25*, 373–378.
- [54] H. Abadin, C. Smith, *Toxicological Profile For RDX*, U.S. Department of Health and Human Services, Public Health Service, Agency for Toxic Substances and Disease Registry, **2012**.

- [55] P. Yin, J. M. Shreeve, *Adv. Heterocycl. Chem.*, **2017**, *121*, 89–131.
- [56] H. Gao, J. M. Shreeve, *Chem. Rev.*, **2011**, *111*, 11, 7377–7436.
- [57] A. A. Dippold, T. M. Klapötke, *J. Am. Chem. Soc.*, **2013**, *135*, 26, 9931–9938.
- [58] D. Fischer, J. L. Gottfried, T. M. Klapötke, K. Karaghiosoff, J. Stierstorfer, T. G. Witkowski, *Angew. Chem. Int. Ed.*, **2016**, *55*, 16132.
- [59] N. Fischer, D. Fischer, T. M. Klapötke, D. G. Piercey, J. Stierstorfer, *J. Mater. Chem.*, **2012**, *22*, 20418-20422.
- [60] J. L. Gottfried, T. M. Klapötke, T. G. Witkowski, *Prop., Explos., Pyrotech.*, **2017**, *42*, 353.
- [61] M. F. Bölter, Dissertation thesis, LMU München, **2018**.
- [62] <https://echa.europa.eu/de/candidate-list-table>, accessed august **2022**.
- [63] M. A. Petrie, J. A. Sheehy, J. A. Boatz, G. Rasul, G. K. Surya Prakash, G. A. Olah, K. O. Christe, *J. Am. Chem. Soc.*, **1997**, *119*, 8802–8808.

2. Summary and Conclusion

The whole thesis can be divided thematically in two major parts, the content of each part and its focus are shown in Figure 1.

The first part, including chapter 3 - 9, describes the synthesis and characterization of new eco-friendly energetic materials based on nitrogen-rich moieties and heterocycles, focusing on secondary explosives and their precursors. The second part deals with long term stability predictions based on the Netsch Kinetics Neo software.

In **chapter 3** the class of geminal diazides is investigated in regard to their energetic properties. Based on diethyl malonate five new compounds were synthesized via acid base chemistry and extensively characterized, including the measurement of the respective crystal structures, density prediction, thermal behavior, hirshfeld analysis, sensitivities and energetic performance.

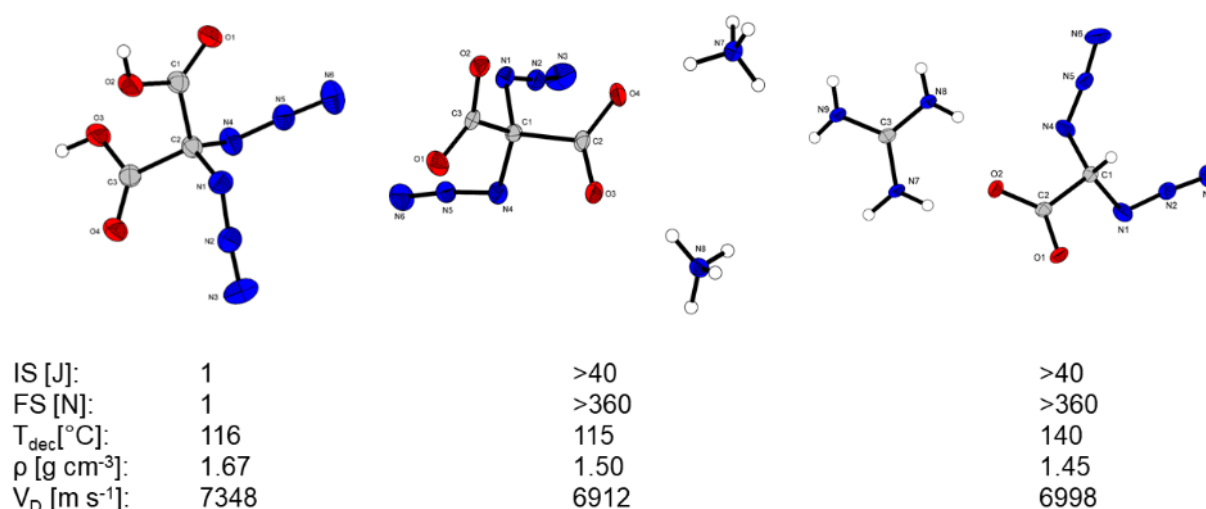
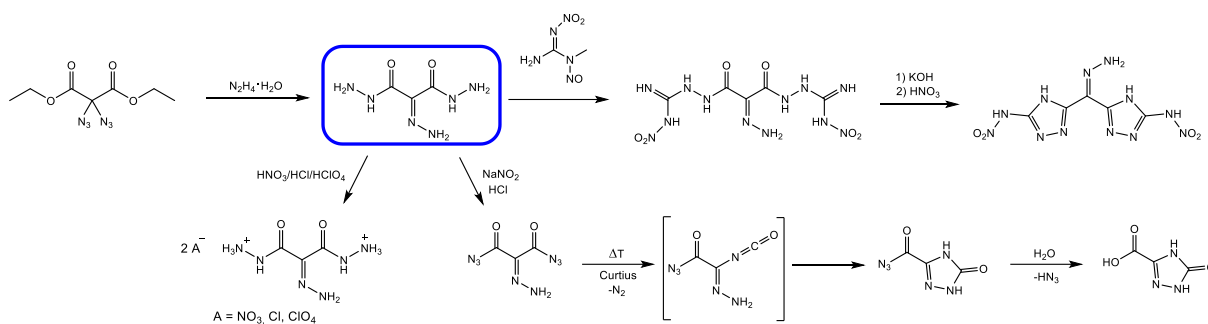


Figure 2. Crystal structures and properties of selected compounds (2,2-diazidomalonic acid (left), diammonium 2,2-diazidomalonate (mid), guanidinium 2,2-diaziidoacetate (right)).

The parent compound 2,2'-diazidomalonic acid showed extremely high sensitivities as well as low thermal stability. In contrast, the salts were relatively insensitive towards external stimuli. All compounds are non-toxic (according to aquatic toxicity measurements with the luminescent vibrio fischeri bacteria) and show energetic behaviour with detonation velocities around 7000 m s⁻¹, which is in the range of TNT. Due to the low thermal stability these compounds are of more scientific interest, due to their small size and intriguing structural features.

In **chapter 4**, originated from the geminal diazides in the previous chapter, 2-hydrazonyl-propandihydrazide was synthesized, which is a versatile, non-toxic and highly promising precursor for new energetic materials.



Scheme 1. Synthesis of various energetic materials and the new precursor 2-hydrazonyl-propandihydrazide.

Several new energetic compounds were obtained and fully characterized based on this new precursor, including its nitrate and perchlorate salts, which show excellent performance with detonation velocities of around 9000 m s^{-1} . Furthermore, by reaction with *N*-methyl-*N*-nitroso-*N*-nitroguanidine an new bridged bistriazole was synthesized, which showed promising features including good thermal stability, high density and a detonation velocity of 8654 m s^{-1} . Due to its low solubility in various solvents no crystal structure was obtained for the triazole. In addition, a Curtius rearrangement was observed by obtaining crystal structures of intermediate products, when performing a diazotation reaction on the new precursor. Due to its low toxicity and high versatility this new compound is a promising addition to the field of energetic precursors.

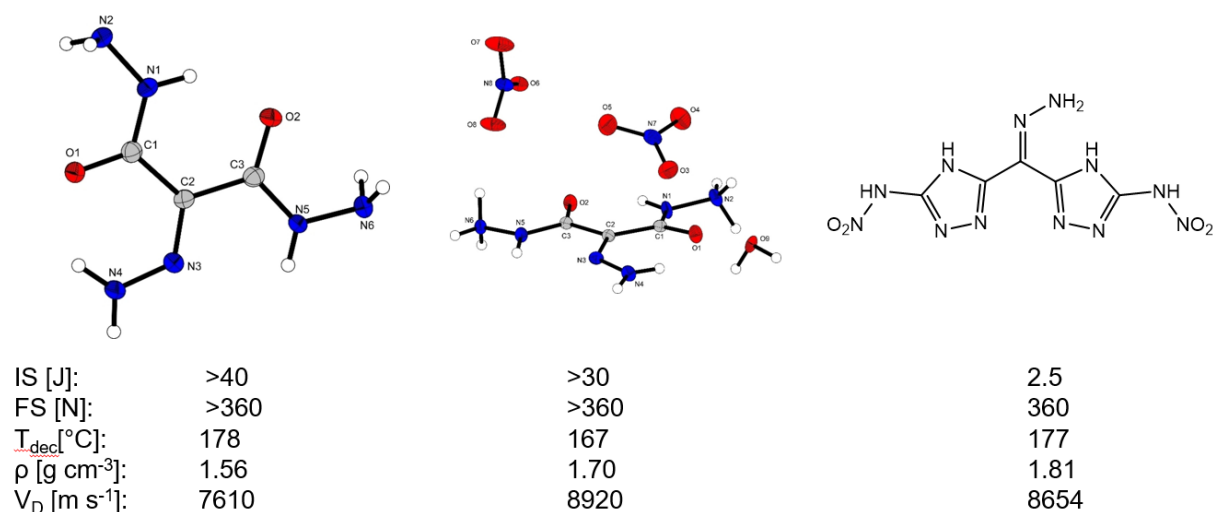


Figure 3. Crystal structures and properties of selected compounds (2-hydrazonyl-propandihydrazide (left), 2-Hydrazonyl-propandihydrazidium dinitrate · 0.25 H₂O (mid), bis(dinitramino-1*H*-1,3,4-bistriazol-5-yl) methylhydrazone (right)).

Chapter 5 describes the continued investigation of derivatives of the bridged triazole synthesized in the previous chapter, as well as the evaluation of two rarely investigated bridging moieties, the methylhydrazone and the oxybismethylene bridge. Therefore, in

addition to the respective bridged triazoles, a total of ten different energetic salts were synthesized and investigated towards their energetic properties, shown in Figure 4.

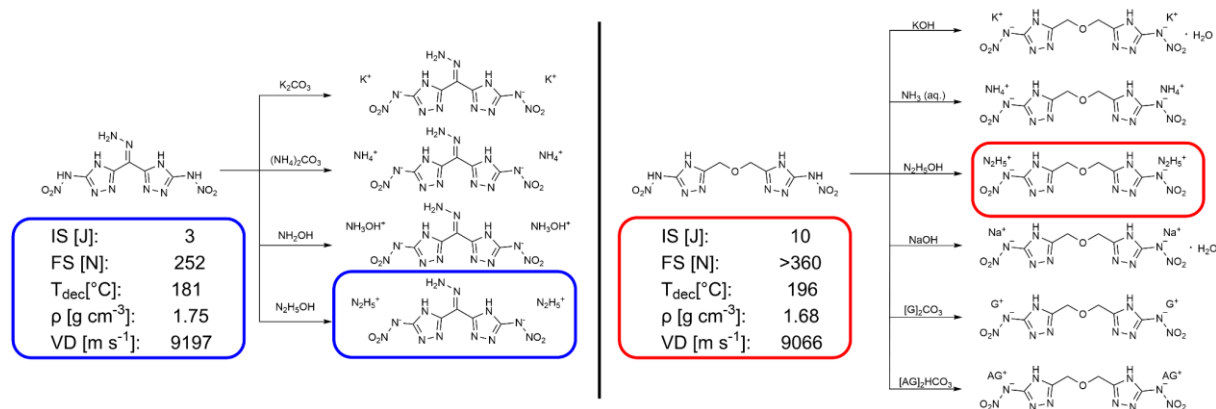


Figure 4. Synthesized energetic salts based on bis(dinitramino-1H-1,3,4-bis-triazol-5-yl) methylhydrazone (left) and bis(3-nitramino-4H-1,2,4-triazole-5-yl) oxybis(methylene) (right) and selected properties of the high performing hydrazinium salts.

Due to very low solubility in various solvents, no crystal structures were obtained up to this point. Nonetheless, the synthesized compounds show excellent energetic properties, with peak detonation velocities of over 9000 m s⁻¹ for the hydrazinium salts and decent thermal stabilities with values ranging from 170 °C to 268 °C and are therefore valid candidates for new nitrogen rich secondary explosives. When comparing both bridging moieties, the overall thermal stability is higher for the oxybismethylene bridge, additionally these compounds show lower sensitivity values regarding both impact and friction sensitivity. The compounds based on the methylhydrazone bridging moiety show the highest overall detonation performance, as well as higher combined nitrogen and oxygen contents. It also has to be mentioned, that due to the fixed double bond of the methylhydrazone, these molecules show asymmetry, which can be seen in the NMR measurements, which show twice the number of signals for the protons and carbon atoms of the triazoles.

Chapter 6 deals with the synthesis and characterization of smaller carbonyl azides like oxalyl diazide, carbamoyl azide, as well as *N,N*-bis(azidocarbonyl)hydrazine. All compounds were synthesized by diazotation of the corresponding hydrazide derivatives. As expected oxalyl diazide shows extremely high sensitivity towards external stimuli. With a detonation velocity of 8236 m s⁻¹ this compound is a very interesting and potent energetic material, which made isolation of this compound difficult but worthwhile. The other two molecules are less sensitive with decomposition temperatures of over 130 °C, which is unusually high for carbonyl azides in general. Even though, this comes with the cost of lower performance, the detonation velocities are still over 7000 m s⁻¹. Due to their high sensitivity towards impact and friction the

investigated molecules will not be used for industrial application but have a high value for scientific research.

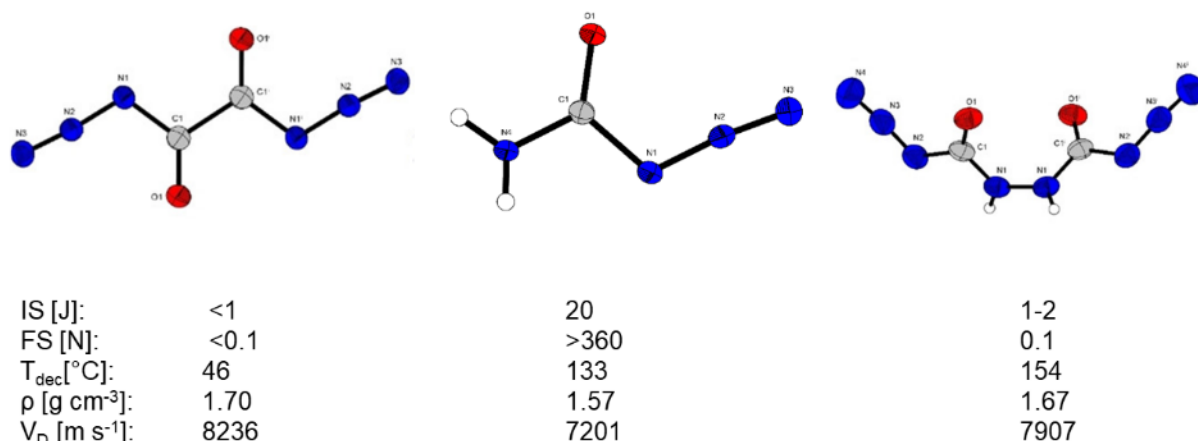


Figure 5. Crystal structures and properties of selected compounds (oxalyl diazide (left), carbamoyl azide (mid), *N,N*-bis(azidocarbonyl)hydrazine (right)).

Chapter 7 describes the determination of the vaporization behavior of the thermodynamically rarely investigated organic polyazido group. Therefore, the experimental vapor pressures of 1,3-diazidopropanol (1,3-DAP), 2,3-diazidopropanol (2,3-DAP) and 1,3-diethyl-2,2-diazidomalonate (DE-DAM) were measured using the transpiration method.

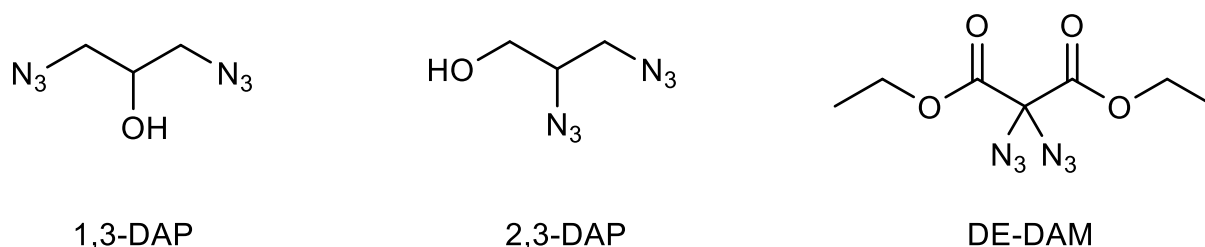


Figure 6. Molecular structures of different investigated polyazido compounds.

1,3-DAP and 2,3-DAP show very similar vaporization behaviors, with molar enthalpies of vaporization at 298.15 K of 70-75 kJ mol⁻¹. 1,3-DAP has slightly lower enthalpy values in comparison to 2,3-DAP and therefore higher absolute vapor pressure values, which can be explained through higher symmetry of the molecule leading to a lower polarity. DE-DAM exhibits both higher molar enthalpies of vaporization and lower vapor pressures. This work helps to achieve a better understanding of the vaporization behavior of organic azides and is relevant for several fields of application like security and environmental influences.

Chapter 8 investigates the lithium salts of different nitropyrazoles as potential replacements for strontium based red pyrotechnic colorants. Therefore lithium salts of 3,4-dinitro-1*H*-pyrazole, 3,5-dinitro-1*H*-pyrazole, 4-amino-3,5-dinitro-1*H*-pyrazole, 3,4,5-trinitro-1*H*-pyrazole, and 4-hydroxy-3,5-dinitro-1*H*-pyrazole were synthesized and extensively characterized by X-ray diffraction, thermoanalytical methods, and sensitivity measurements.

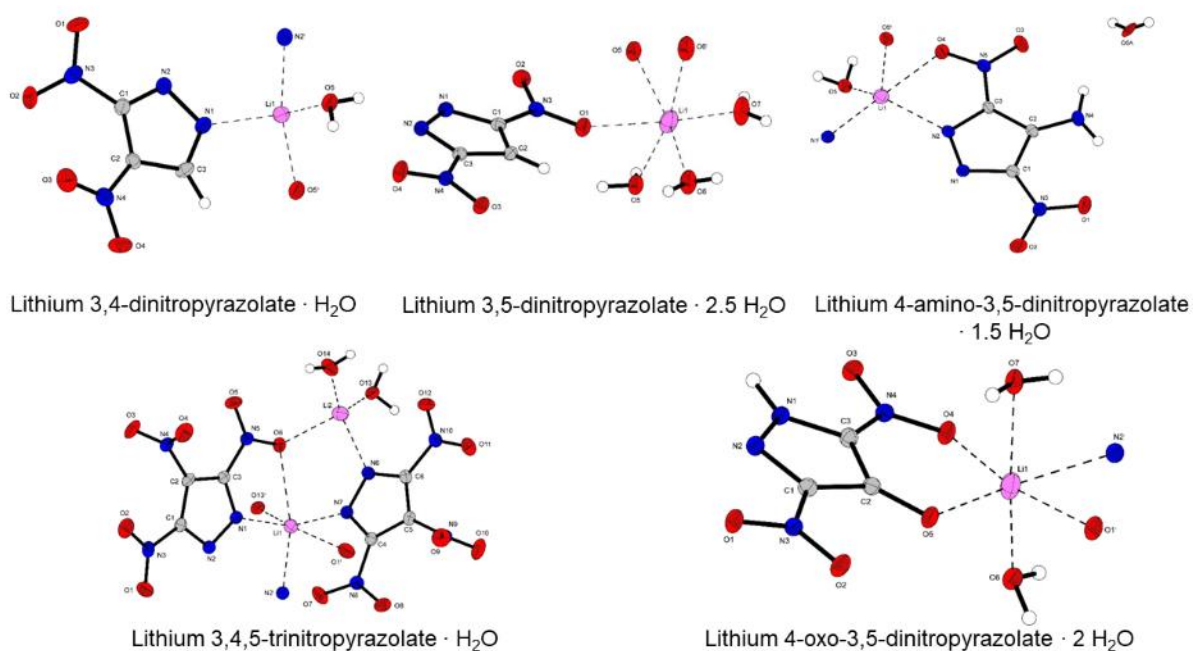


Figure 7. Crystal structures of the investigated lithium pyrazole derivatives.

Lithium 4-amino-3,5-dinitropyrazolate · 1.5 H₂O was tested in a chlorine and strontium free formulation containing ammonium nitrate, magnesium, a pyrotechnic matrix and the test substance. Although the resistance of a test formulation containing lithium 4-amino-3,5-dinitropyrazolate · 1.5 H₂O to moisture and its luminosity should be enhanced in the future, the



Figure 8. Combustion of the test formulation.

capability of this lithiated material to impart red color to a flame was demonstrated, shown in Figure 8.

Chapter 9 deals with the evaluation of 1,5-dimethyltetrazole as a ligand in energetic coordination compounds. It was synthesized by different routes and fully characterized, showing promising properties in terms of sensitivity and thermal stability, while still exhibiting a high heat of formation. Therefore 2,5-DMT was applied as a nitrogen rich ligand to coordination compounds of the $3d^5$ - $3d^{10}$ metal perchlorate salts.

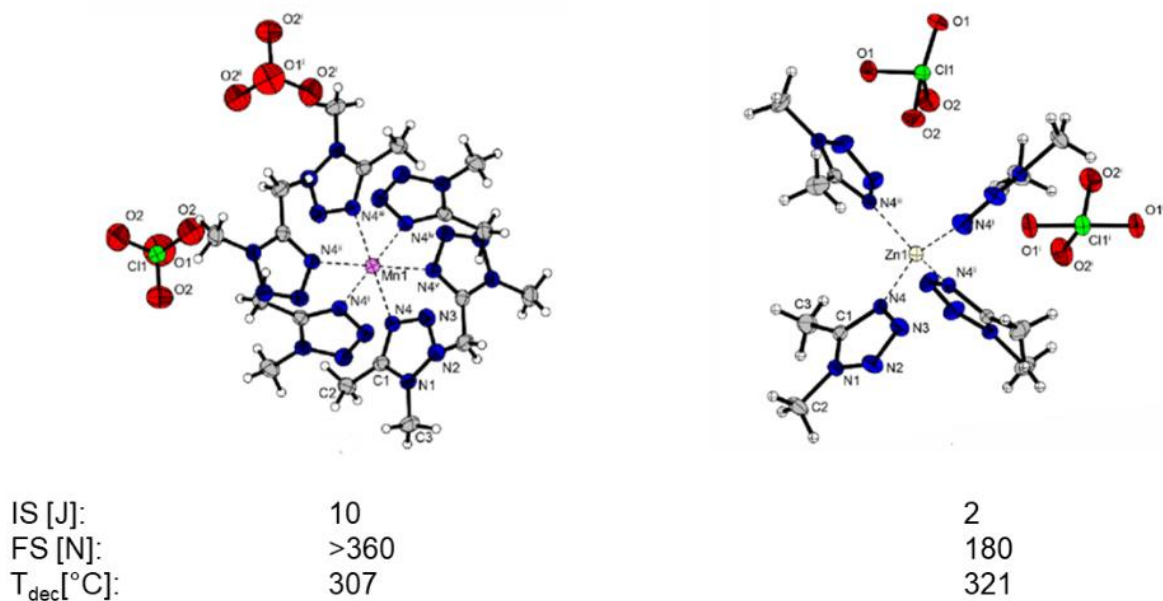


Figure 9. Crystal structures and properties of selected compounds ($[\text{Mn}(\text{DMT})_6](\text{ClO}_4)_2$ (left) and $[\text{Zn}(\text{DMT})_4](\text{ClO}_4)_2$ (right)).

All synthesized ECCs show exceptionally high thermal stabilities with decomposition temperature values ranging from 184 °C up to 321 °C. Hot plate tests of the most promising compounds showed a complete decomposition without detonation, while the hot needle tests indicated that none of the compounds can be classified as applicable primary explosives since no rapid DDT was observed, shown in Figure 10.

However, the compounds are ideal candidates for burning rate catalysts in propellant charges due to their simple and cheap syntheses and great stability.

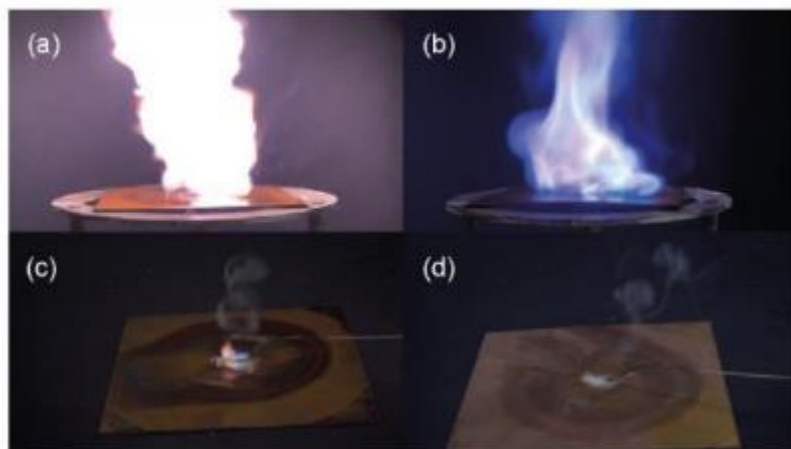


Figure 10. HP and HN tests of $[\text{Mn}(\text{DMT})_6](\text{ClO}_4)_2$ (left) and $[\text{Zn}(\text{DMT})_4](\text{ClO}_4)_2$ (right).

Chapter 10 describes the first results of a project regarding long-term stability predictions. Based on the Netsch Kinetiks Neo software a simple and fast prediction method for the long-term stability of energetic materials was developed and tested on the most commonly known representatives from the field of secondary explosives. TKX-50, RDX, HMX, CL-20 and PETN, were investigated by TGA measurements, different kinetic models, including Friedman, Ozawa-Flynn-Wall and ASTM were evaluated and the stability of each compound was predicted over 10 years at different temperatures. Additionally, the activation energies as well as prediction at specific climatic conditions were determined. The predicted data was compared with experimental values, obtained by storing samples of each compound at 100 °C over one month.

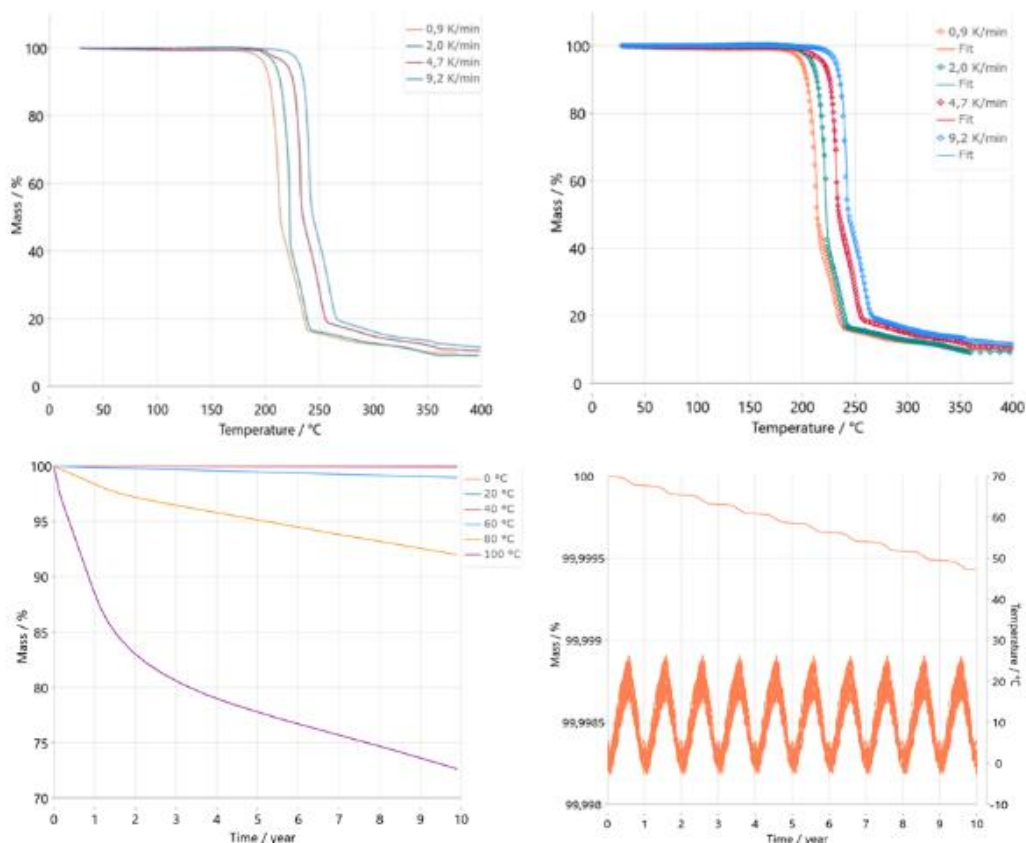


Figure 11. Long term stability predictions of TKX-50. TGA measurements at different heating rates (top left). Fit of the Friedman model (top right). Isothermal predictions over 10 years at different temperatures (bottom left). Stability predictions under climatic conditions over 10 years in Munich (bottom right).

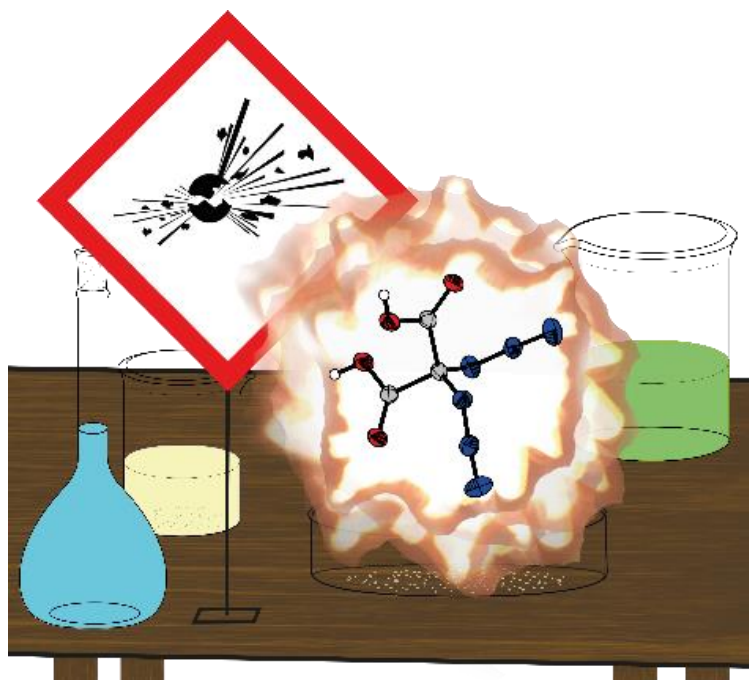
The highest long-term stability can be predicted for CL-20 and the lowest for PETN, meeting the expectations, since PETN is a nitrate ester with a high vapor pressure. TKX-50 shows excellent longevity, with a slightly better behavior than RDX. The predictions were validated by the experimental measurements, which fit the calculated data exceptionally well.

3. Synthesis and Characterization of Geminal Diazido Derivatives Based on Diethyl Malonate

Alexander G. Harter, Thomas M. Klapötke, Christian Riedelsheimer, Jörg Stierstorfer, Michael Voggenreiter

as published in European Journal of Inorganic Chemistry **2021**, 23, 2241–2247

DOI: 10.1002/ejic.202100212



Key words: organic azides, geminal diazides, structural elucidation, salt formation, toxicity assessment

Abstract: New geminal diazide derivatives based on diethyl 2,2-diazidomalonate (**1**) are presented. 2,2-Diazidomalononic acid (**2**) as well as four alkaline and nitrogen rich salts of 2,2-diazidomalonate (**3–6**) were synthesized and extensively characterized e. g. by low temperature X-ray diffraction. All compounds, which represent promising starting materials for further nitrogen-rich materials, were analyzed by ^1H and ^{13}C NMR spectroscopy, elemental analysis, differential thermal analysis (DTA) and regarding their sensitivity towards impact, friction, and electrostatic discharge according to BAM standard techniques. In addition, all synthesized compounds were evaluated regarding their energetic behavior using the EXPLO5 code and compared to TNT in order to provide a comparison to a well-known energetic material. In addition, two selected compounds were investigated towards their aquatic toxicity, using the bioluminescent bacteria *vibrio fischeri*.

3.1 Introduction

Organic azides have been well investigated during the past decades, as they are widely used in various different fields of application ranging from pharmaceutical and medical science^[1,2] over precursors for click chemistry^[3] to chemical biology^[4] and the agricultural sector^[5]. The azido moiety is also commonly found in the area of energetic materials^[6], with many materials like plasticizers, hypergolic ionic liquids and binders containing at least one functional azido group.^[7,8] Figure 1 shows a selection of commonly used organic azides in exemplary fields of application, as well as an example for the importance of geminal diazides in cyclisation reactions towards tetrazoles.^[9]

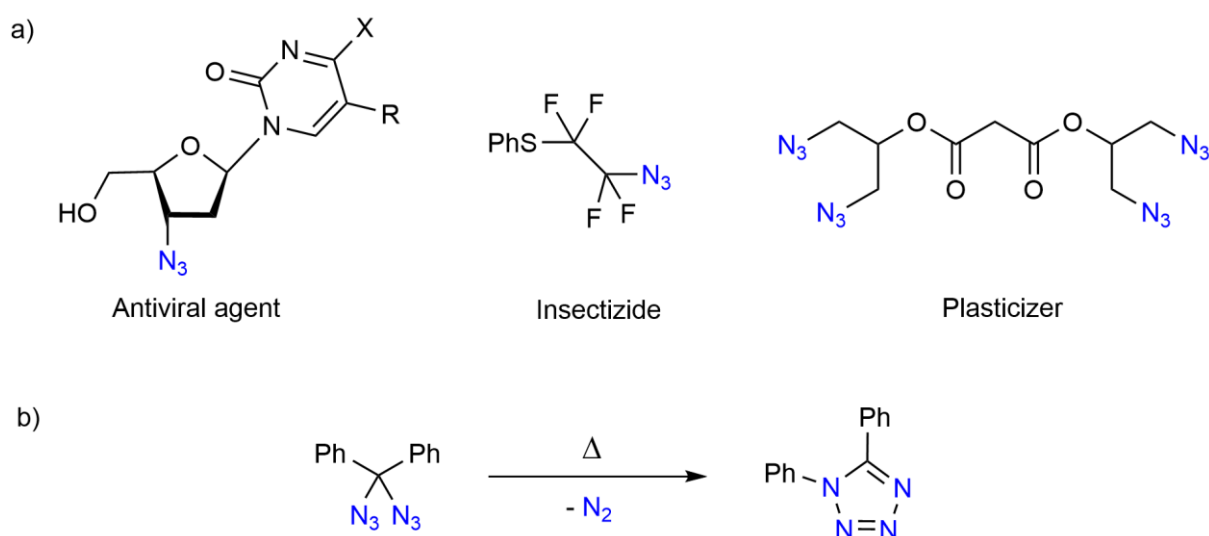


Figure 1. a) Selected applications of organic azides. b) Synthesis of a 1,5-tetrazole starting from a geminal diazide.

Some of the reasons for the attractiveness of the azido group in energetic materials are its thermodynamic properties, as it has a high positive heat of formation and adds about 260 kJ mol^{-1} of endothermic energy to a carbon-based molecule.^[10] In terms of developing more environmentally friendly and less toxic energetic materials, which has been of growing interest during the last decades, the azido group plays an important role, as it exclusively releases nitrogen gas during decomposition. However, the functionalization with azido groups is not without risks, as it is well reported, that it possibly increases the sensitivity of molecules towards external stimuli like impact and friction.^[11] Therefore, azido compounds are known for their explosive behavior, when handled without the necessary care.^[12] The subclass of geminal diazides has been discovered by *Forster et al.* in 1908, but is insufficiently investigated until today.^[13] In 2015 *Kirsch et al.* summarized the few reports on reactions involving geminal diazides, and named their potentially explosive character as a possible reason for the lack of research done regarding this topic.^[14] In the following years the spectrum of reactions evolving around the geminal diazido group was further expanded, including click chemistry^[15,16,17], fullerene addition^[18], polymerization^[19] and other new synthetic approaches^[20], summarized in figure 2, but the questions about hazards regarding its explosive behavior still remained unanswered.

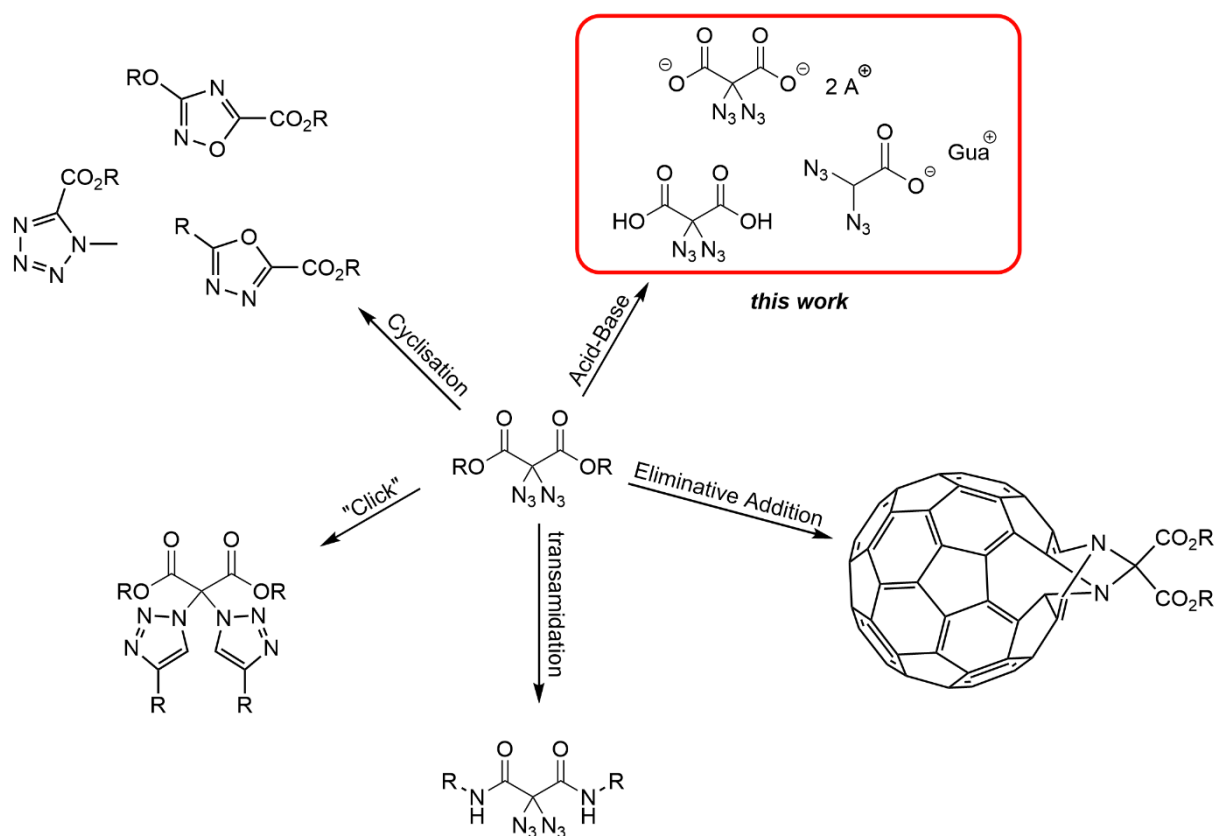


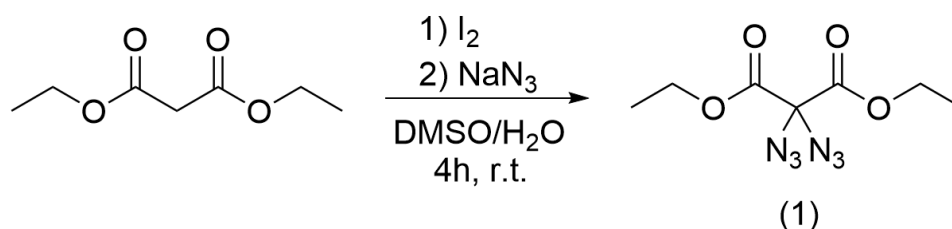
Figure 2. Extension of known reaction types starting from geminal diazide esters with acid base chemistry.

Therefore, this work focuses on the synthesis of new geminal diazido derivatives based on diethyl malonate and intensively characterizing both new and literature known geminal diazides regarding their energetic and structural properties.

3.2 Results and Discussion

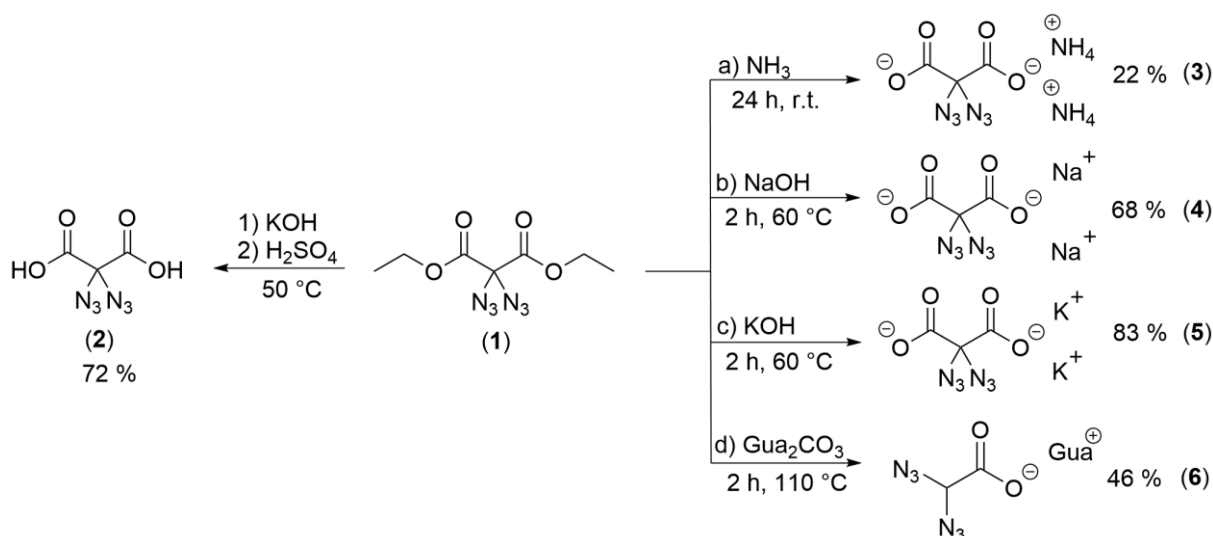
3.2.1 Synthesis

Diethyl 2,2-diazidomalonate (**1**) was synthesized according to a literature procedure, which is shown in Scheme 1.^[21] Diethyl malonate is iodized on the carbon atom between the ester groups in a slightly basic aqueous solution, followed by an iodine azide exchange, which leads to the desired geminal diazide.



Scheme 2. Synthesis of diethyl 2,2-diazidomalonate (**1**).

The synthetic route to the ionic compounds **3–6**, as well as the neutral compound **2** is depicted in scheme 2. All compounds can be formed by Brønsted acid-base chemistry. Hereby, the ethyl residue is cleaved by the basic reactants and the carboxylate-salt formation takes place. Diethyl 2,2-diazidomalonate (**1**) is mixed with water and is reacted with an equimolar amount of the respective base at slightly elevated temperatures. An exception is the guanidinium salt, which only reacts at higher



Scheme 2. Synthesis of compounds **2–6** via acid base chemistry.

temperatures. Under these conditions, CO₂ is released from **1** and compound **6** is formed. Compound **2** is formed in a similar manner, but acidified with sulfuric acid after formation of the potassium salt in order to form the dicarboxylic acid. The synthesis of 2,2-diazidomalonic acid (**2**) was described in literature, but the compound insufficiently characterized. [22]

3.2.2 Crystal Structures

Measurable crystals could be obtained for the compounds **2–6**, either directly from the reaction mixture or by recrystallization from the following solvents (**2**: diethyl ether, **3,6**: water, **4,5**: acetone)

General information on the X-ray measurements and refinements are given in the SI. Structures were deposited with the CCDC database under the following numbers (**2**: 2068210, **3**: 2068206, **4**: 2068209, **5**: 2068208, **6**: 2068207)

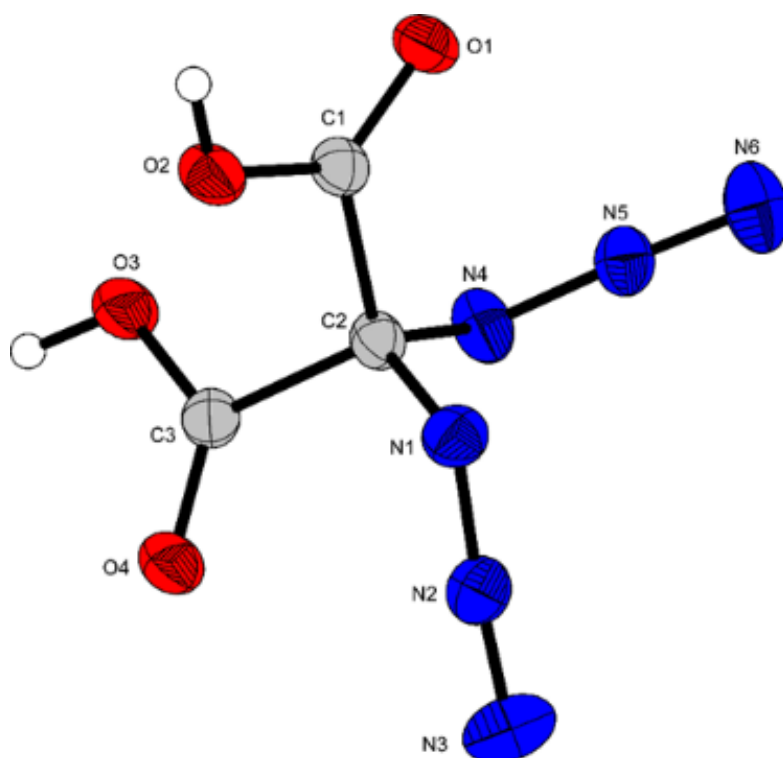


Figure 3. Molecular unit of 2,2-diazidomalonic acid (**2**). Thermal ellipsoids of non-hydrogen atoms are drawn at the 50 % probability level and hydrogen atoms are shown as small spheres of arbitrary radius.

2,2-Diazidomalonic acid (**2**) crystallizes in the orthorhombic space group $Pna2_1$ with a density of 1.705 g cm⁻³ at 173 K and four formula units per unit cell (figure 3). Due to the mutual repulsion of the functional groups, a symmetrical tetrahedral structure is expected. This is confirmed when looking at the angles around the C2 atom. In each case, the angles of the azide groups but also the carboxyl groups are nearly identical,

and correspond almost to the 109.5° of a tetrahedral conformation (C1–C2–C3 109.5° , N1–C2–C3 113.9° , N4–C2–C1 112.6° , N1–C2–N4 114.4°). Strong intermolecular hydrogen bonds can be observed between the carboxylic acid groups (O2–H2...O4, O3–H3...O1). All bond lengths comply with the expected values for C–C, C–N, C–O and N–N single and double bonds.^[23,24]

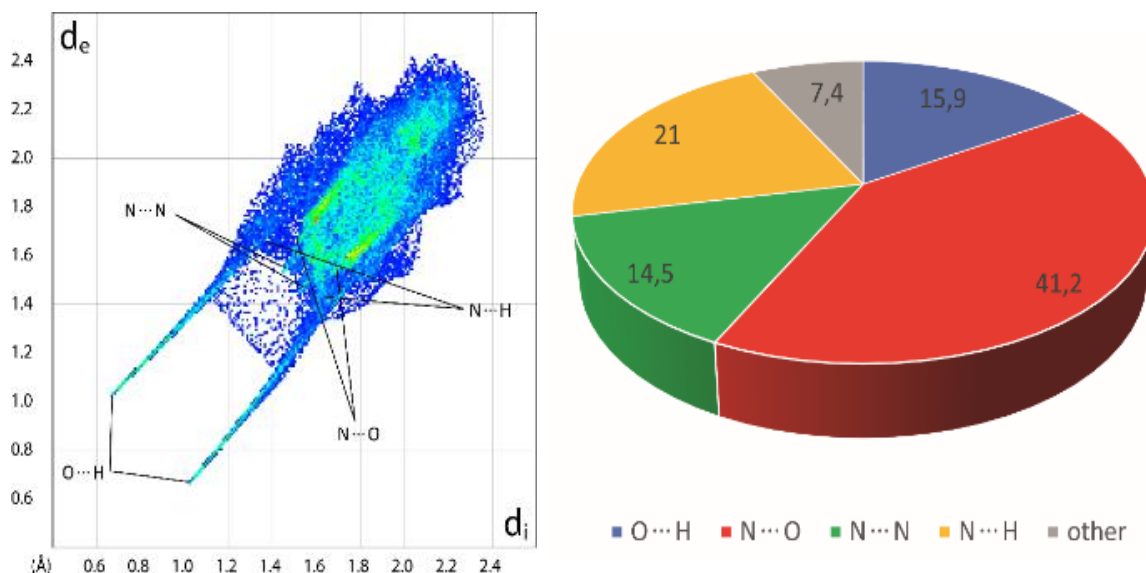


Figure 4. Two-dimensional Hirshfeld fingerprint plot of 2,2-diazidomalonic acid (**2**). Population of close contacts of **2**.

Hirshfeld analysis showed a high percentage of N...O contacts (41.2 %) which have a destabilizing effect (figure 4).^[25,26,27] A stabilizing effect is the N...H interaction (21.0 %) but the distance is large ($>3 \text{ \AA}$) and can be neglected. Further, repulsive N...N interactions (14.5 %) are found which cause strong repulsive interactions in the case of grid deformation caused by mechanical stimuli and therefore indicate a high sensitivity. Strong and stabilizing O...H interactions are found (15.9 %) having a distance of below 2 \AA .^[25,26,27] In total, the destabilizing N...N interactions are quite counterbalanced by the strong O...H interactions and the molecule should be sensitive and a low thermal stability must be assumed.

Diammonium 2,2-diazidomalonate (**3**) crystallizes in the triclinic space group *P*-1 with a density of 1.546 g cm^{-3} at 110 K (figure 5). The cell volume is $472.9(2) \text{ \AA}^3$ with two formula units per cell. The cell constants are $a = 7.0256(17) \text{ \AA}$, $b = 7.3752(13) \text{ \AA}$ and $c = 10.523(3) \text{ \AA}$. Due to the mutual repulsion of the functional groups, a symmetrical tetrahedral structure is expected. This is confirmed when looking at the angles around the C1 atom. In each case, the angles of an azide and a carboxyl group are identical, and correspond almost to the 109.5° of a tetrahedral conformation (N1–C1–N4 113.1° ,

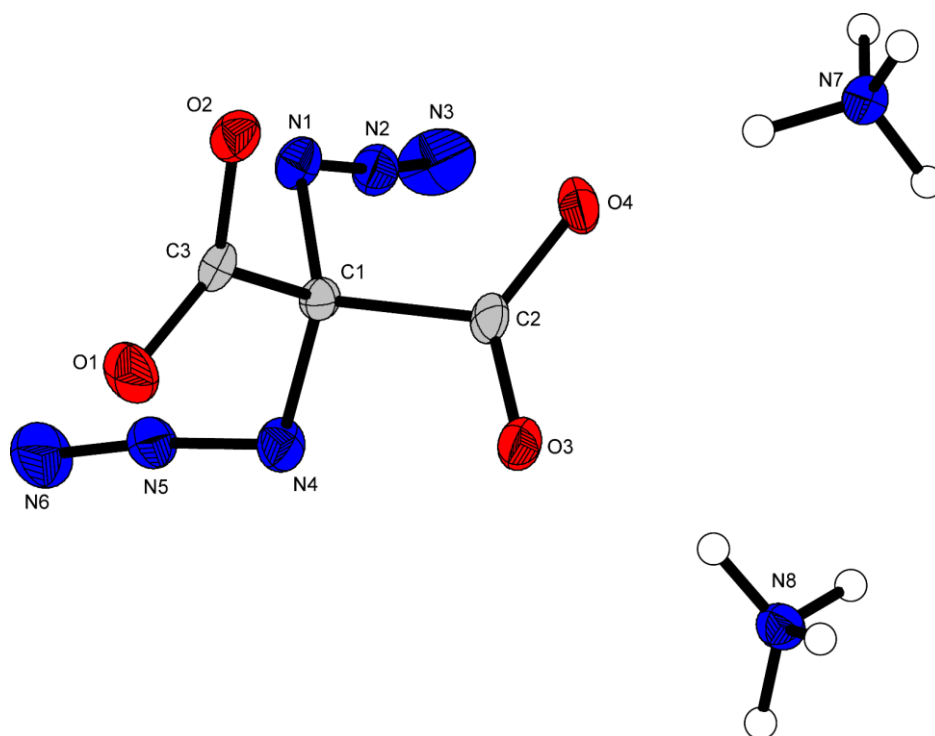


Figure 5. Molecular unit of diammonium 2,2-diazidomalonate (**3**). Thermal ellipsoids of non-hydrogen atoms are drawn at the 50 % probability level and hydrogen atoms are shown as small spheres of arbitrary radius.

N1–C1–C2 113.1°, N1–C1–C3 105.4°, N4–C1–C2 105.2°). All bond lengths comply with the expected values for C–C, C–N, C–O and N–N single and double bonds.

Compound **3** forms a layered structure consisting of one layer of the azido moieties surrounded by two layers of the ionic carboxyl and ammonium moieties, shown in figure 6. The repulsing azido groups interact with each other at a distance of 3.07 Å.

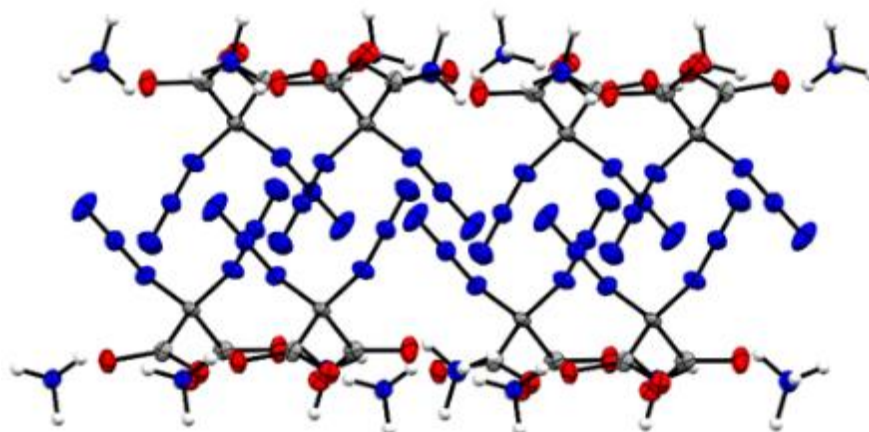


Figure 6. Layered arrangement of eight diammonium 2,2-diazidomalonate (**3**) molecules. Thermal ellipsoids of non-hydrogen atoms are drawn at the 50 % probability level and hydrogen atoms are shown as small spheres of arbitrary radius.

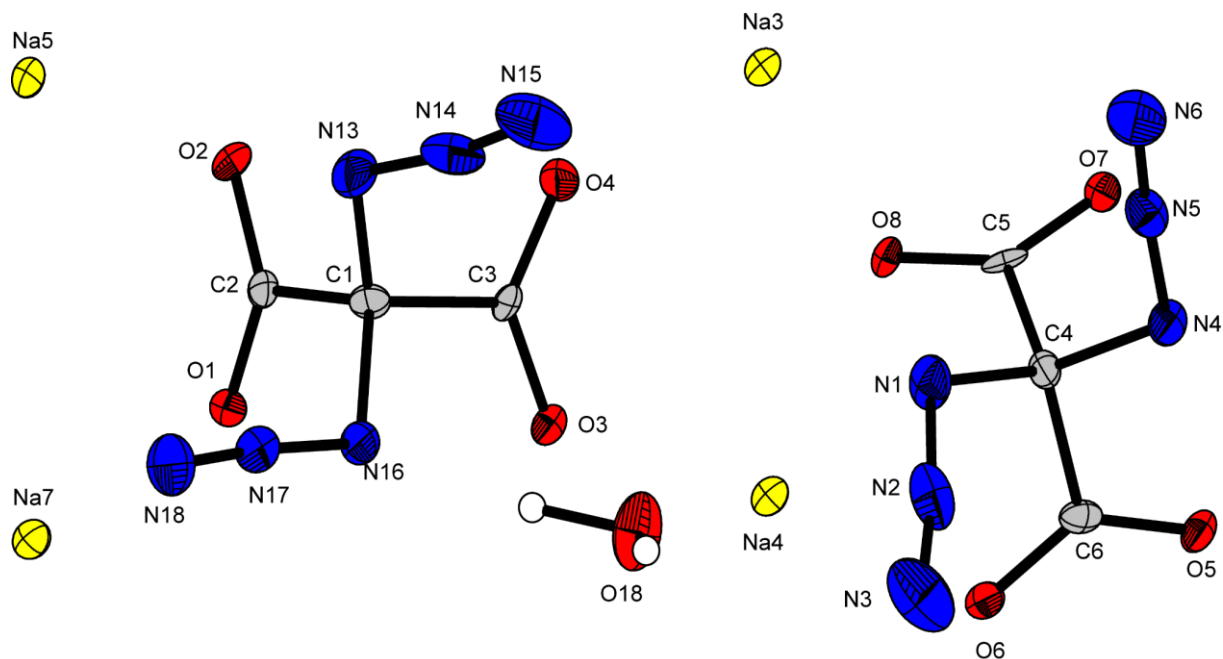


Figure 7. Molecular unit of disodium 2,2-diazidomalonate (**4**). Thermal ellipsoids of non-hydrogen atoms are drawn at the 50 % probability level and hydrogen atoms are shown as small spheres of arbitrary radius.

Disodium 2,2-diazidomalonate semihydrate (**4**) crystallizes in the monoclinic space group $P2_1/c$ with a density of 1.904 g cm^{-3} at 123 K and one water molecule per two malonate molecules (figure 7). In regard to the molecular structure, compound **4** shows a high similarity to compound **3**. It has symmetrical bond angles around the C1 atom and forms an almost tetrahedral structure (N13–C1–C2 108.3° , N13–C1–N16 112.4° , N16–C1–C2 112.0° , N16–C1–C3 106.6°). Compound **2** crystallizes with two water molecules per unit cell. All bond lengths comply with the expected values for C–C, C–N, C–O and N–N single and double bonds.

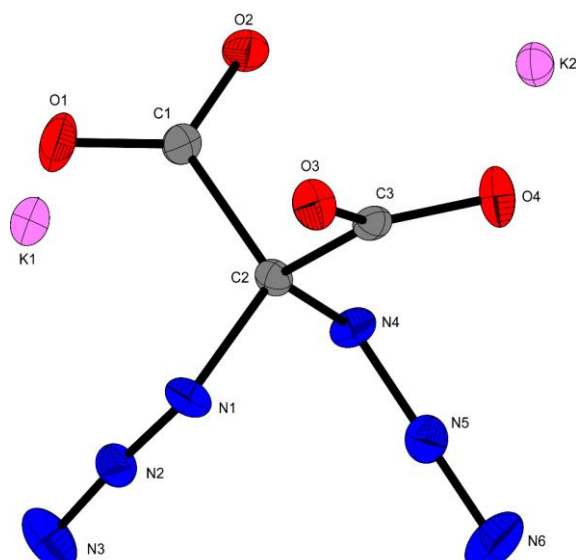


Figure 8. Molecular unit of dipotassium 2,2-diazidomalonate (**5**). Thermal ellipsoids of non-hydrogen atoms are drawn at the 50 % probability level.

Dipotassium 2,2-diazidomalonate (**5**) crystallizes in the triclinic space group $P-1$ with a density of 1.981 g cm^{-3} at 173 K (figure 8). The cell volume is $439.70(2) \text{ \AA}^3$ with two formula units per cell. The cell constants are $a = 6.8277(1) \text{ \AA}$, $b = 7.1525(2) \text{ \AA}$ and $c = 10.3164(2) \text{ \AA}$. Compound **5** shows comparable bond angles and lengths as compound **1** and **2**, forming a tetrahedral structure (N1–C2–C1 112.4° , N1–C2–C3 105.6° , N4–C2–C1 106.1° , N4–C2–C3 112.7°).

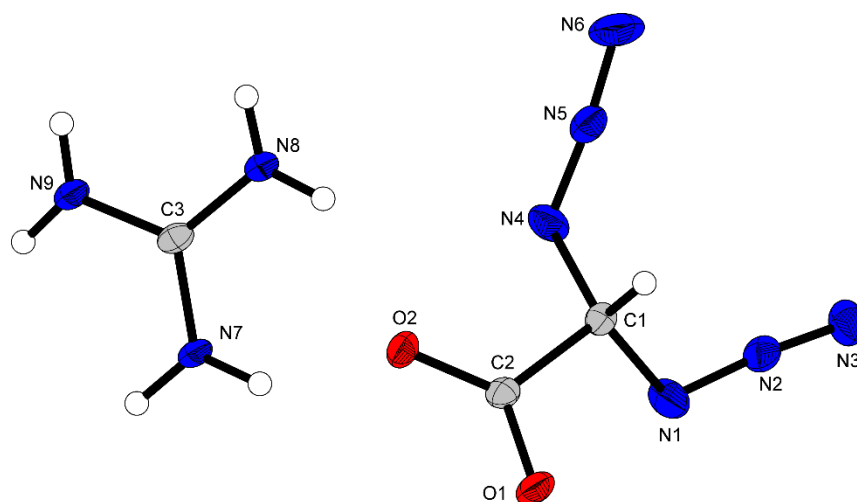


Figure 9. Molecular unit of guanidinium 2,2-diazoacetate (**6**). Thermal ellipsoids of non-hydrogen atoms are drawn at the 50 % probability level and hydrogen atoms are shown as small spheres of arbitrary radius.

Guanidinium 2,2-diazoacetate (**6**) crystallizes in the orthorhombic space group $Pna2_1$ with a density of 1.534 g cm^{-3} at 102 K (figure 9). The cell volume is $871.31(19) \text{ \AA}^3$ with four formula units per cell. The cell constants are $a = 15.725(2) \text{ \AA}$, $b = 7.6451(9) \text{ \AA}$ and $c = 7.2477(10) \text{ \AA}$. Regarding its molecular structure compound **6** corresponds surprisingly well with compound **3–5**, even though the missing carboxyl group is replaced by the much smaller hydrogen atom. This is confirmed when looking at the bond angles, which lie in the same range as the ones of previously discussed structure (N1–C1–N4 110.0° , N1–C1–C2 107.4° , N4–C1–C2 110.0° , C2–C1–H1 106.2°).

3.2.3 Physicochemical Properties

Since the focus of this work was the determination of the energetic properties of the synthesized geminal diazides, all compounds were characterized regarding their physicochemical properties. Therefore, their thermal behavior, detonation parameters and sensitivities towards impact, friction and electrostatic discharge were determined experimentally or computationally and compared to TNT, shown in Table 1. TNT was chosen as a comparable because it is a well-known energetic material, regarding the characterization and handling in an industrial scale.^[28]

The thermal behavior of all compounds was measured by differential thermal analysis. All measured compounds show rather low decomposition temperatures ranging from 105 °C to 147 °C, with compound **1** having the highest and compound **5** the lowest value. In regard to the endothermic peaks, no melting points could be observed, with compound **6** showing a water loss at 89 °C due to its hygroscopicity. In comparison to TNT all measured compounds are significantly less stable towards thermal influences. It has to be mentioned that compound **2** detonated violently upon direct heating on a metal spatula. All synthesized compounds show an exceptionally high combined nitrogen and oxygen content up to almost 80 % for compounds **2**, **3** and **6**.

The sensitivity values towards impact, friction and electrostatic discharge were determined according to the BAM standards.^[30] Compound **2** (IS = 1 J, FS = 1 N) shows the highest sensitivity towards external stimuli, followed by the potassium salt (**5**, IS = 5 J, FS = 288 N, ESD = 0.16 mJ). Both are significantly more sensitive than TNT and should therefore be handled with the appropriate care. Compound **2** exceeds the values, estimated by the Hirshfeld analysis, significantly, which is unexpected. Compound **1**, **3**, **4** and **6** are insensitive towards all external stimuli. The insensitivity for the sodium salt (**4**, IS = >40 J, FS = >360 N, ESD = 1.00 mJ) can be explained by the crystal water, which generally reduces those values. For compound **1** and **2** no values regarding electrostatic discharge sensitivities could be obtained, since those are liquids.

The detonation parameters were determined with EXPLO5 (V6.05) based on densities, obtained from the crystal structures and the heats of formation calculated with the CBS-4M method. The density of compound **1** was determined volumetrically with a Hamilton syringe. The densities of compound **2–6** show a broad range from 1.45 g cm⁻³ to 1.95 g cm⁻³. The distribution of the densities fits the expectations, with the alkaline metal salts (compound **4** and **5**) showing the highest values, followed by the malonic acid (**2**) and the nitrogen rich salts (compound **3** and **6**) at the lower end. With respect to their detonation velocities and pressures compounds **2–6** are all in the range of TNT, with detonation velocities around 7000 m s⁻¹ and detonation pressures between 14.8 GPa and 20.5 GPa. Compound **1** shows significantly lower detonation parameters with $V_D = 5509 \text{ m s}^{-1}$ and $p_{CJ} = 8.8 \text{ GPa}$, which can be explained by its relatively high carbon content. Compounds **2**, **3**, **5** and **6** exceed TNT in terms of their detonation velocity, with 2,2-diazidomalonic acid (**2**) showing the highest value of $V_D = 7348 \text{ m s}^{-1}$ and $p_{CJ} = 20.5 \text{ GPa}$.

Table 1. Physiochemical properties of compounds 1–6 and TNT.^[29]

	1	2	3	4 · 0.5 H₂O	5	6	TNT
Formula	C ₇ H ₁₀ N ₆ O ₄	C ₃ H ₂ N ₆ O ₄	C ₃ H ₈ N ₈ O ₄	C ₃ N ₆ O ₄ Na ₂	C ₃ N ₆ O ₄ K ₂	C ₃ H ₇ N ₉ O ₂	C ₇ H ₅ N ₃ O ₆
<i>FW</i> [g·mol ⁻¹]	242.20	186.09	220.15	230.05	262.27	201.15	227.13
<i>IS</i> ^[a] [J]	>40	1	>40	>40	5	>40	15
<i>FS</i> ^[b] [N]	>360	1	>360	> 360	288	>360	>360
<i>ESD</i> ^[c] [J]	–	–	0.60	1.00	0.16	0.54	0.70
<i>N+O</i> ^[d] [%]	61.12	79.55	79.97	65.18	56.44	78.58	55.52
Ω_{CO_2} ^[e] [%]	–99	–26	–43	–19	–25	–23	–74
<i>T</i> _{endo} ^[f] / <i>T</i> _{exo} ^[g] [°C]	–/147	–/116	–/115	–/126	–/105	89/140	79/306
ρ ^[h] [g·cm ⁻³]	1.20	1.67	1.50	1.86	1.95	1.45	1.63
$\Delta_f H^\circ$ ^[i] [kJ·mol ⁻¹]	–523	–563	–270	–786	–455	–555	–261
EXPLO5 V6.05							
– $\Delta_E U^\circ$ ^[j] [kJ·kg ⁻¹]	2927	3453	1226	3167	2471	1025	4399
<i>T</i> _{C-J} ^[k] [K]	2245	2966	2299	2342	1857	2494	3192
$\rho_{\text{C-J}}$ ^[l] [GPa]	8.8	20.5	16.3	14.8	19.0	16.2	18.8
<i>D</i> _{C-J} ^[m] [m·s ⁻¹]	5509	7348	6912	6589	7275	6998	6878
<i>V</i> ⁰ ^[n] [dm ³ ·kg ⁻¹]	782	741	883	449	419	874	642

[a] Impact sensitivity (BAM drophammer, method 1 of 6); [b] friction sensitivity (BAM drophammer, method 1 of 6); [c] electrostatic discharge device (OZM research); [d] combined nitrogen and oxygen content; [e] oxygen balance toward carbon dioxide ($\Omega_{\text{CO}_2} = (n\text{O} - 2x\text{C} - y\text{H}/2)(1600/\text{FW})$); [f] endothermic event (DTA, $\beta = 5^\circ\text{C}\cdot\text{min}^{-1}$); [g] temperature of decomposition (DTA, $\beta = 5^\circ\text{C}\cdot\text{min}^{-1}$); [h] density at 298 K (for **1** determined volumetrically with a Hamilton syringe 100 μL); [i] standard molar enthalpy of formation; [j] detonation energy; [k] detonation temperature; [l] detonation velocity; [m] detonation pressure; [n] volume of detonation gases at standard temperature and pressure conditions.

3.2.4 Toxicity Assessment

The ecotoxicological impact of this class of geminal diazides was determined by EC₅₀ measurements based on the bioluminescent *Vibrio fischeri* NRRL-B-11177 marine bacteria strain. Therefore, compound **2** and **3** were used as representative examples, and their EC₅₀ values measured after 15 and 30 minutes and compared to the literature known values of TNT^[31]. The EC₅₀ value refers to the concentration of a toxicant which induces a response of 50 % after a specific exposure time. In this case the EC₅₀ value is determined by inhibition of the luminescence by 50 %, when exposed to the toxicant.^[32] Based on the resulting effective concentration the measured substances were classified as nontoxic (>1.00 g L⁻¹), toxic (0.10–1.00 g L⁻¹), and very toxic (<0.10 g L⁻¹). The measured values are shown in Table 2. Compound **2** can be described as nontoxic, since its EC₅₀ value is above 1 g L⁻¹. Compound **3** is classified as toxic with values of 0.45 g L⁻¹ and 0.41 g L⁻¹ after 15 min and 30 min, respectively.

Table 2. EC₅₀ values of **2**, **3** and TNT.

EC ₅₀ (g L ⁻¹)			
Incubation	2	3	TNT
15 min	3.76	0.45	–
30 min	2.16	0.41	0.0036

3.3 Conclusion

In this work, we describe the geminal 2,2-diazidomalononic acid (**2**) as well as their twice deprotonated sodium (**3**), potassium (**4**) and ammonium (**5**) salts. The reaction of 2,2-diazidomalononic acid with guanidinium carbonate yielded guanidinium diazidoacetate. Crystal structures of all synthesized compounds were determined. The densities range from 1.45 g cm⁻³ for the guanidinium salt (**6**) to 1.95 g cm⁻³ for the potassium salt (**5**). All compounds were characterized via NMR, as well as regarding their physiochemical properties, including thermal behavior and sensitivity towards impact, friction and electrostatic discharge. Compound **2** is a highly sensitive substance with values of 1 J impact and 1 N friction and should be handle with extreme care. All other compounds are rather low or not sensitive except the potassium salt (**5**) which has an impact sensitivity of 5 J and a friction sensitivity of 288 N. In addition, all compounds were analyzed towards their detonation parameters, calculated with the EXPLO5 code. Compounds **2**, **3**, **5** and **6** exceed TNT in terms of their detonation velocity with values up to 7348 m s⁻¹ for compound **2**. Finally, selected compounds were evaluated by the luminous bacteria inhibition test in regard to their ecotoxicological impact, while it can

be assumed, that the salts are lower in toxicity than the neutral form. Potassium salt **3** is categorized as nontoxic, however the malonic acid shows toxicity towards aqueous organisms. In order to give an assessment of possible hazards, when working with geminal diazides all compounds were compared to TNT. Geminal diazides are a versatile class of compounds, which have hereby been proven to show energetic behavior.

3.4 Experimental Section

All chemicals and solvents were purchased from Sigma Aldrich and used without further purification. The general information about analytical devices including NMR, X-ray crystallography, IR, DTA, as well as information about the calculation of the energetic properties can be found in the SI.

Caution: Organic azides are potentially toxic and explosive compounds. Even though there were no hazards detected during this work, it is recommended to carry out all reactions in a small scale, while using the proper safety equipment, including ear, hand and body protection.

Diethyl 2,2-diazidomalonate (1): Diethyl 2,2-diazidomalonate (**1**) was synthesized according to literature. The pure product was obtained as a colorless oil in yields of 80 %. ¹H NMR (400 MHz, DMSO-d₆): δ (ppm) = 4.36 (q, 4H, OCH₂CH₃), 1.32 (t, 6H, CH₃); ¹³C NMR (101 MHz, DMSO-d₆): δ (ppm) = 163.5 (CO₂Et), 79.8 (C(N₃)₂), 64.9 (OCH₂CH₃), 13.9 (OCH₂CH₃); IR (ATR, rel. int.): $\tilde{\nu}$ (cm⁻¹) = 2987 (w), 2359 (w), 2340 (w), 2119 (s), 1754 (s), 1467 (w), 1447 (w), 1393 (w), 1369 (w), 1298 (m), 1226 (s), 1095 (m), 1066 (s), 1043 (s), 1016 (s), 854 (m), 822 (w), 770 (m), 739 (m), 667 (w); Elemental analysis: calcd. (%) for C₇H₁₀N₆O₄ (242.20 g mol⁻¹): C 34.71, H 4.16, N 34.70; found: C 35.28, H 3.91, N 33.87; Sensitivities: BAM impact: >40 J, BAM friction: >360 N; DTA (5 °C min⁻¹): T_{exo} = 147 °C.

2,2-Diazidomalonic acid (2): Diethyl 2,2-diazidomalonate (**1**) (500 mg, 2.06 mmol, 1.0 eq.) was mixed with 1 ml water and potassium hydroxide (500 mg, 8.26 mmol, 4 eq.) was added to the mixture. The mixture was stirred at 50 °C until there was no trace of the undissolved diethyl 2,2-diazidomalonate (**1**) visible. Afterwards an aqueous solution of 30 % sulfuric acid (2,70 g, 8.26 mmol, 4 eq.) was added to the solution. After extraction with diethyl ether (20 ml) the organic phase was dried over magnesium sulfate and left for crystallization. 2,2-Diazidomalonic acid (**2**) (275 mg, 1.48 mmol, 72 %) was obtained as colorless crystals, which are highly hygroscopic. ¹H NMR (400

MHz, CDCl₃): δ (ppm) = 8.79; ¹³C NMR (101 MHz, CDCl₃): δ (ppm) = 166.0, 79.9; IR (ATR, rel. int.): $\tilde{\nu}$ (cm⁻¹) = 2926 (w), 2102 (s), 1734 (m), 1407 (w), 1196 (s), 975 (m), 899 (m), 687 (m), 550 (m), 467 (m), 433 (m); Elemental analysis: calcd. (%) for C₇H₁₀N₆O₄ (242.20 g mol⁻¹): C 34.71, H 4.16, N 34.70; found: C 35.28, H 3.91, N 33.87; Sensitivities: BAM impact: 1 J, BAM friction: 1 N; DTA (5 °C min⁻¹): T_{exo} = 115 °C.

Diammonium 2,2-diazidomalonate (3): Diethyl 2,2-diazidomalonate (1) (1.0 g, 4.12 mmol, 1.0 eq.) was mixed with 10 ml water and ammonia (2.4 ml, 16.48 mmol, 4.0 eq.) was added to the solution. The solution was left to stir for 24 hours at room temperature after which the remaining solvent was removed in vacuo. The oil-like product was allowed to stand for crystallization and was then washed with diethyl ether, yielding a white microcrystalline solid (200 mg, 0,91 mmol, 22 %). ¹H NMR (400 MHz, DMSO-d₆): δ (ppm) = 6.90 (s, 8H); ¹³C NMR (101 MHz, DMSO-d₆): δ = 169.0, 114.4; IR (ATR, rel. int.): $\tilde{\nu}$ (cm⁻¹) = 3171 (m), 3007 (m), 2850 (m) 2263 (w), 2131 (m), 2106 (s), 1611 (s), 1425 (s), 1382 (s), 1309 (s), 1238 (w), 1209 (s), 1156 (w), 1107 (w), 1046 (w), 1026 (w), 1007 (m), 832 (w), 783 (m), 715 (s), 599 (m), 555 (m), 472 (m), 437 (w), 424 (w); Elemental analysis: calcd. (%) for C₃H₈N₈O₄ (220.07 g mol⁻¹): C 16.37, H 3.66, N 50.90; found: C 16.33, H 3.68, N 51.49; Sensitivities (grain size: 100 - 300 μ m): BAM impact: >40 J, BAM friction: >360 N, ESD: 0.608 J.; DTA (5 °C min⁻¹): T_{exo} = 115 °C.

Disodium 2,2-diazidomalonate semihydrate (4): Diethyl 2,2-diazidomalonate (1) (250 mg, 1.03 mmol, 1.0 eq.) was mixed with 5 ml water and sodium hydroxide (82.6 mg, 2.06 mmol, 2.0 eq.) was added to the solution. The solution was left to stir for 1 h at room temperature, followed by 2 h at 60 °C. The remaining solvent was concentrated in vacuo. Disodium 2,2-diazidomalonate monohydrate was obtained as a yellow powder (175 mg, 0,71 mmol, 68 %), which was recrystallized from acetone for x-ray measurements. ¹³C NMR (101 MHz, DMSO-d₆): δ (ppm) = 170.6, 108.9; IR (ATR, rel. int.): $\tilde{\nu}$ (cm⁻¹) = 3757 (w), 3662 (w), 3537 (w) 2432 (w), 2104 (s), 1667 (s), 1634 (s), 1606 (m), 1403 (m), 1315 (s), 1206 (s), 1128 (w), 1059 (w), 1041 (w), 1007 (m), 843 (w), 817 (w), 789 (s), 722 (m), 708 (m), 693 (m), 601 (w), 568 (w), 559 (w), 470 (m), 435 (w), 411 (w); Elemental analysis: calcd. (%) for C₃H₂N₆O₅Na₂ (248.07 g mol⁻¹): C 14.53, H 0.81, N 33.88; found: C 14.29, H 0.58, N 30.22; Sensitivities (grain size: 100 – 500 μ m): BAM impact: >40 J, BAM friction: >360 N, ESD: 1.0 J.; DTA (5 °C min⁻¹): T_{exo} = 126 °C.

Dipotassium 2,2-diazidomalonate (5): Diethyl 2,2-diazidomalonate (**1**) (250 mg, 1.03 mmol, 1.0 eq.) was mixed with 5 ml water and potassium hydroxide (115,8 mg, 16.48 mmol, 2.0 eq.) was added to the solution. The solution was left to stir for 1 h at room temperature, followed by 2 h at 60 °C. The remaining solvent was concentrated in vacuo. After recrystallization from acetone dipotassium 2,2-diazidomalonate was obtained as a white crystalline solid (210 mg, 0,80 mmol, 83 %). ¹³C NMR (101 MHz, CDCl₃): δ = 170.6, 107.9; IR (ATR, rel. int.): $\tilde{\nu}$ (cm⁻¹) = 3322 (w), 2432 (w), 2265 (w) 2133 (m), 2103 (s), 2047 (w), 1645 (s), 1628 (s), 1397 (m), 1379 (m), 1344 (m), 1312 (s), 1243 (s), 1214 (s), 1124 (w), 1036 (w), 1024 (w), 1003 (s), 831 (m), 809 (w), 784 (s), 737 (s), 707 (s), 597 (m), 557 (m), 472 (s), 423 (w); Elemental analysis: calcd. (%) for C₃N₆O₄K₂ (261.93 g mol⁻¹): C 13.74, N 32.04; found: C 13.20, N 30.53; Sensitivities (grain size: 500 - 1000 μm): BAM impact: 5 J, BAM friction: 288 N, ESD: 0.16 J.; DTA (5 °C min⁻¹): T_{exo} = 105 °C.

Guanidinium 2,2-diazoacetate (6): Diethyl 2,2-diazidomalonate (**1**) (250 mg, 1.03 mmol, 1.0 eq.) was mixed with 10 ml water and guanidinium carbonate (93 mg, 0.52 mmol, 0.5 eq.) was added to the solution. The solution was left to stir for 2 h at 110 °C. The remaining solvent was concentrated in vacuo. A yellow hygroscopic powder (105 mg, 0,47 mmol, 46 %) was obtained, which was recrystallized from water for x-ray measurements. ¹H NMR (400 MHz, DMSO-d₆): δ (ppm) = 7.31 (s, 6H), 4.65 (s, 1H); ¹³C NMR (101 MHz, DMSO-d₆): δ (ppm) = 169.7, 158.4, 75.5; IR (ATR, rel. int.): $\tilde{\nu}$ (cm⁻¹) = 3343 (m), 3134 (m), 2116 (m), 2042 (m), 1651 (s), 1612 (s), 1396 (m), 1321 (m), 1302 (m), 1267 (m), 1238 (m), 1062 (w), 1033 (w), 1009 (w), 986 (m), 881 (w), 788 (m), 744 (m), 526 (s), 459 (s), 407 (s); Elemental analysis: calcd. (%) for C₇H₁₄N₆O₆ (237.18 g mol⁻¹): C 15.19, H 4.67, N 53.15; found: C 14.90, H 5.01, N 66.92; Sensitivities (grain size: > 1000 μm): BAM impact: >40 J, BAM friction: >360 N, ESD: 0.54 J; DTA (5 °C min⁻¹): T_{endo} = 89 °C, T_{exo} = 140 °C.

Acknowledgements

For financial support of this work by the Ludwig-Maximilian University (LMU), the Office of Naval Research (ONR) under grant no. ONR N00014-19-1-2078 and the Strategic Environmental Research and Development Program (SERDP) under contract no. W912HQ19C0033 are gratefully acknowledged. The authors thank *Stefan Huber* for his help with the sensitivity measurement and *Jasmin Lechner* for graphical support.

3.5 References

- [1] C. Pan, A. Abdukader, J. Han, Y. Cheng, C. Zhu, *Chem. Eur. J.* **2014**, *20*, 3606.
- [2] T. S. Lin, M. S. Chen, C. McLaren, Y. S. Gao, I. Ghazzouli, W. H. Prusoff, *J. Med. Chem.* **1987**, *30*, 440.
- [3] H. A. Michaels, L. Zhu, *Chem. Asian J.* **2011**, *6*, 2825-2834.
- [4] C. I. Schilling, N. Jung, M. Biskup, U. Schepers, S. Bräse, *Chem. Soc. Rev.* **2011**, *40*, 4840-4871.
- [5] S. Voltrová, M. Muselli, J. Filgas, V. Matoušek, B. Klepetářová, P. Beier, *Org. Biomol. Chem.* **2017**, *15*, 4962.
- [6] M. Claßen, S. B. Heimsch, T. M. Klapötke, *Prop., Explos., Pyrotech.* **2019**, *44*, 1515.
- [7] D. Kumari, K. D. B. Yamajala, H. Singh, R. R. Sanghavi, N. A. Shri, K. Raju, S. Banerjee, *Propellants Explos. Pyrotech.* **2013**, *38*, 805-809.
- [8] Y. Tang, J. M. Shreeve, *Chem. Eur. J.*, **2015**, *21*, 7285-7291.
- [9] K. Holzschneider, M. L. Tong, F. Mohr, S. F. Kirsch, *Chem. Eur. J.* **2019** *25* (50), 11725-11733.
- [10] M. A. Petrie, J. A. Sheehy, J. A. Boatz, G. Rasul, G. K. Surya Prakash, G. A. Olah, K. O. Christe, *J. Am. Chem. Soc.* **1997**, *119*, 8802-8808.
- [11] O.V. Dorofeeva, O.N. Ryzhova, M.A. Suntsova, *J. Phys. Chem. A* **2013**, *117*, 6835-6845.
- [12] A. Hassner, M. Stern, H. E. Gottlieb, F. Frolow, *J. Org. Chem.* **1990**, *55*, 2304-2306.
- [13] M. O. Forster, H. E. Fierz, W. P. Joshua, *J. Chem. Soc.* **1908**, *93*, 1070-1074.
- [14] A. P. Häring, S. F. Kirsch, *Molecules* **2015**, *20*, 20042-20062.
- [15] F. Borghi, I. E. Çelik, P. Biallas, F. Mittendorf, S. F. Kirsch, *Eur. J. Org. Chem.*, **2020**, 4389-4398.
- [16] H. Erhardt, F. Mohr, S. F. Kirsch, *Chem. Commun.* **2016**, *52*, 545-548.
- [17] K. Holzschneider, F. Mohr, S. F. Kirsch, *Org. Lett.* **2018**, *20* (22), 7066-7070.
- [18] G. X. Dong; J. S. Li, T. H. Chan, *J. Chem. Soc. Chem. Commun.* **1995**, 1725-1726.
- [19] P. Biallas, J. Heider, S. F. Kirsch, *Polym. Chem.* **2019**, *10*, 60-64.

- [20] H. Erhardt, A. P. Häring, A. Kotthaus, M. Roggel, M. L. Tong, P. Biallas, M. J übermann, F. Mohr, S. F. Kirsch; *J. Org. Chem.* **2015**, *80*, 12460- 12469.
- [21] M. O. Forster, R. Müller, *J. Chem. Soc.* **1910**, *97*, 126-142.
- [22] A. F. Holleman, E. Wiberg, N. Wiberg in *Lehrbuch der anorganischen Chemie*, de Gruyter, New York, **2007**.
- [23] F. H. Allen, O. Kennard, D. G. Watson, L. Brammer, A. G. Orpen, R. Taylor, *J. Chem. Soc., Perkin Trans. 2* **1987**, 1-19.
- [24] D. E. Dosch, M. Reichel, M. Born, T. M. Klapötke and K. Karaghiosoff, *Cryst. Growth Des.* **2021**, *21*, 1, 243-248.
- [25] Y. Ma, A. Zhang, X. Xue, D. Jiang, Y. Zhu and C. Zhang, *Cryst. Growth Des.* **2014**, *14*, 6101-6114.
- [26] M. A. Spackman and D. Jayatilaka, *CrystEngComm* **2009**, *11*, 19-32.
- [27] M. Reichel, D. Dosch, T. Klapötke and K. Karaghiosoff, *J. Am. Chem. Soc.* **2019**, *141*, 19911-19916.
- [28] T. M. Klapötke in *Energetic Materials Encyclopedia*, Vol. 2 E - N, De Gruyter, Berlin, **2021**, pp. 773-968.
- [29] M. Härtel, **2017**: Studies towards the gas-phase detection of hazardous materials by vapor pressure measurements with the transpiration method in combination with vacuum outlet GC/MS. Dissertation, LMU München: Fakultät für Chemie und Pharmazie.
- [30] Test Methods According to the UN Recommendations on the Transport of Dangerous Goods, Manual of Test and Criteria, Fourth Revised Edition, United Nations Publication, New York and Geneva, **2003**, ISBN 92-1-139087 7, Sales No. E.03.VIII. 2; 13.4.2 Test 3a (ii) BAM Fallhammer.
- [31] O. Drzyzga, T. Gorontzy, A. Schmidt, *Arch. Environ. Contam. Toxicol.* **1995**, *28*, 229-235.
- [32] T. M. Klapötke, B. Krumm, C. C. Unger, *Inorg. Chem.* **2019**, *58*, 4, 2881-2887.

3.6 Supplementary Information

3.6.1 X-ray diffraction

Crystal structure data were obtained by measurements on an Oxford Xcalibur3 diffractometer with a Spellman generator (voltage 50 kV, current 40 mA) and a Kappa CCD area for data collection using Mo-K α radiation ($\lambda = 0.71073 \text{ \AA}$) or a Bruker D8 Venture TXS diffractometer equipped with a multilayer monochromator, a Photon 2 detector and a rotation-anode generator (Mo-K α radiation). The data collection was performed using the CRYSTALIS RED software.^[S1] The solution of the structure was performed by direct methods and refined by full-matrix least-squares on F2 (SHELXT)^[S2] implemented in the OLEX2^[S3] software suite. The non-hydrogen atoms were refined anisotropically and the hydrogen atoms were located and freely refined. The absorption correction was carried out by a SCALE3ABSPACK multiscan method.^[S4] The DIAMOND2 plots shown with thermal ellipsoids at the 50% probability level and hydrogen atoms are shown as small spheres of arbitrary radius. The SADABS program embedded in the Bruker APEX3 software was used for multi-scan absorption corrections in all structures.^[S5]

Table S1. Crystallographic data and structure refinement details for the prepared compounds **2-4**.

	2,2 Diazidomalonic acid (2)	Diammonium 2,2-diazidomalonate (3)	Disodium 2,2-diazidomalonate semihydrate (4)
Formula	C3 H2 N6 O4	C3 N6 O4, 2(H4 N)	C12 H4 N24 Na8 O18
FW [g mol ⁻¹]	186.11	220.17	956.31
Crystal system	orthorhombic	triclinic	monoclinic
Space group	Pna21 (No. 33)	P-1 (No. 2)	P21/c (No. 14)
Color / Habit	colourless rod	colourless block	colourless platelet
Size [mm]	0.02 x 0.03 x 0.14	0.08 x 0.10 x 0.30	0.10 x 0.18 x 0.25
a [Å]	11.1440(4)	7.0256(17)	11.6751(6)
b [Å]	5.9329(2)	7.3752(13)	12.5066(7)
c [Å]	10.9654(4)	10.523(3)	23.215(2)
α [°]		105.015(18)	90
β [°]		100.15(2)	100.154(7)
γ [°]		110.12(2)	90
V [Å ³]	724.99(4)	472.9(2)	3336.7(4)
Z	4	2	4
ρ _{calc.} [g cm ⁻³]	1.705	1.546	1.904
μ [mm ⁻¹]	0.156	0.138	0.255
F(000)	376	228	1904
λ _{MoKα} [Å]	0.71073	0.71073	0.71073
T [K]	173	110	123
θ Min-Max [°]	3.7, 26.4	2.1, 26.4	1.8, 26.4
Dataset	-13: 13 ; -7: 7 ; -13: 13	-8: 7 ; -9: 9 ; -13: 12	-14: 14 ; -15: 15 ; -29: 29
Reflections collected	13833	2952	26923
Independent refl.	1468	1885	6832
R _{int}	0.032	0.047	0.069
Observed reflections	1432	1215	3259
Parameters	126	169	566
R ₁ (obs) ^[a]	0.0220	0.0661	0.0532
wR ₂ (all data) ^[b]	0.0605	0.1360	0.1313
S ^[c]	1.07	1.05	0.99
Resd. dens [e Å ⁻³]	-0.14, 0.23	-0.32, 0.31	-0.38, 0.41
Device type	Bruker D8 Venture TXS	Xcalibur Sapphire3	Xcalibur Sapphire3
Solution	SIR-92	SIR-92	SIR-92
Refinement	SHELXL-2018	SHELXL-2018	SHELXL-2018
Absorption correction	Multi-Scan	Multi-Scan	Multi-Scan
CCDC	2068210	2068206	2068209

^[a]R₁ = Σ||F_o|-|F_c||/Σ|F_o|; ^[b]wR₂ = [Σ[w(F_o²-F_c²)²]/Σ[w(F_o)²]^{1/2}; w = [σ²(F_o²)+(xP)²+yP]⁻¹ and P=(F_o²+2F_c²)/3; ^[c]S = {Σ[w(F_o²-F_c²)²]/(n-p)}^{1/2} (n = number of reflections; p = total number of parameters).

Table S 2. Crystallographic data and structure refinement details for the prepared compounds **5** and **6**.

	Dipotassium 2,2-diazidomalonate (5)	Guanidinium 2,2-diazidoacetate (6)
Formula	C3 N6 O4, 2(K)	C2 H N6 O2, C H6 N3
FW [g mol ⁻¹]	262.29	201.18
Crystal system	Triclinic	orthorhombic
Space group	P-1 (No. 2)	Pna21 (No. 33)
Color / Habit	colourless block	colorless platelet
Size [mm]	0.11 x 0.33 x 0.49	0.12 x 0.15 x 0.20
a [Å]	6.8277(1)	15.725(2)
b [Å]	7.1525(2)	7.6451(9)
c [Å]	10.3164(2)	7.2477(10)
α [°]	103.163(2)	
β [°]	101.170(2)	
γ [°]	110.137(2)	
V [Å ³]	439.70(2)	871.31(19)
Z	2	4
ρ _{calc.} [g cm ⁻³]	1.981	1.534
μ [mm ⁻¹]	1.084	0.129
F(000)	260	416
λ _{MoKα} [Å]	0.71073	0.71073
T [K]	173	102
θ Min-Max [°]	4.2, 26.0	3.0, 25.0
Dataset	-8: 8 ; -8: 8 ; -12: 12	-18: 18 ; -8: 9 ; -8: 8
Reflections collected	6268	8310
Independent refl.	1719	1504
R _{int}	0.022	0.047
Observed reflections	1599	1365
Parameters	137	155
R ₁ (obs) ^[a]	0.0196	0.0400
wR ₂ (all data) ^[b]	0.0512	0.0814
S ^[c]	1.06	1.12
Resd. dens [e Å ⁻³]	-0.23, 0.39	-0.19, 0.19
Device type	Xcalibur Sapphire3	Bruker D8 Venture TXS
Solution	SIR-92	SIR-92
Refinement	SHELXL-2018	SHELXL-2018
Absorption correction	Multi-Scan	Multi-Scan
CCDC	2068208	2068207

^[a]R₁ = Σ||F_o|-|F_c||/Σ|F_o|; ^[b]wR₂ = {Σ[w(F_o²-F_c²)²]/Σ[w(F_o)²]}^{1/2}; w = {σ²(F_o²)+(xP)²+yP}⁻¹ and P=(F_o²+2F_c²)/3; ^[c]S = {Σ[w(F_o²-F_c²)²]/(n-p)}^{1/2} (n = number of reflections; p = total number of parameters).

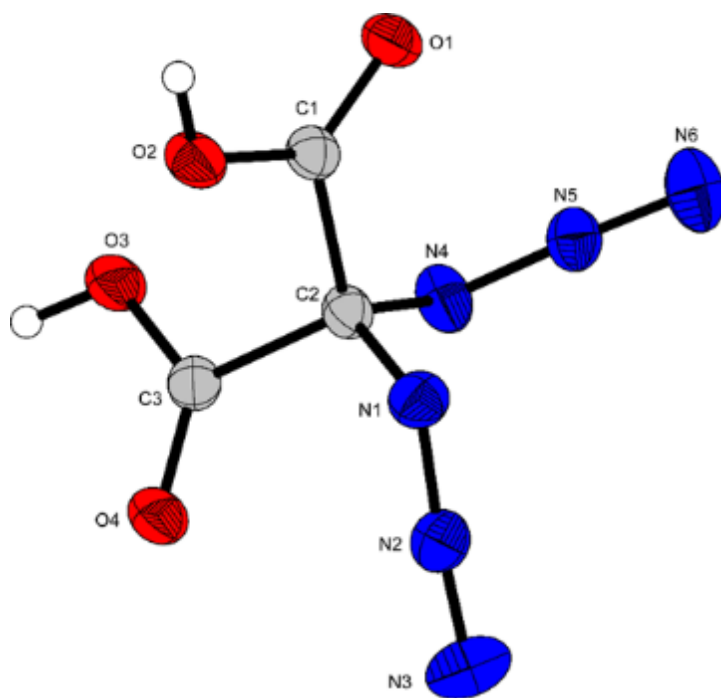


Figure S 1: X-ray structure of compound **2**; Thermal ellipsoids are drawn at the 50% probability level and hydrogen atoms are shown as small spheres of arbitrary radius.

2,2-Diazidomalonic acid (**2**) crystallizes in the orthorhombic space group $Pna2_1$ with a density of 1.705 g cm^{-3} at 173 K and four formula units per unit cell.

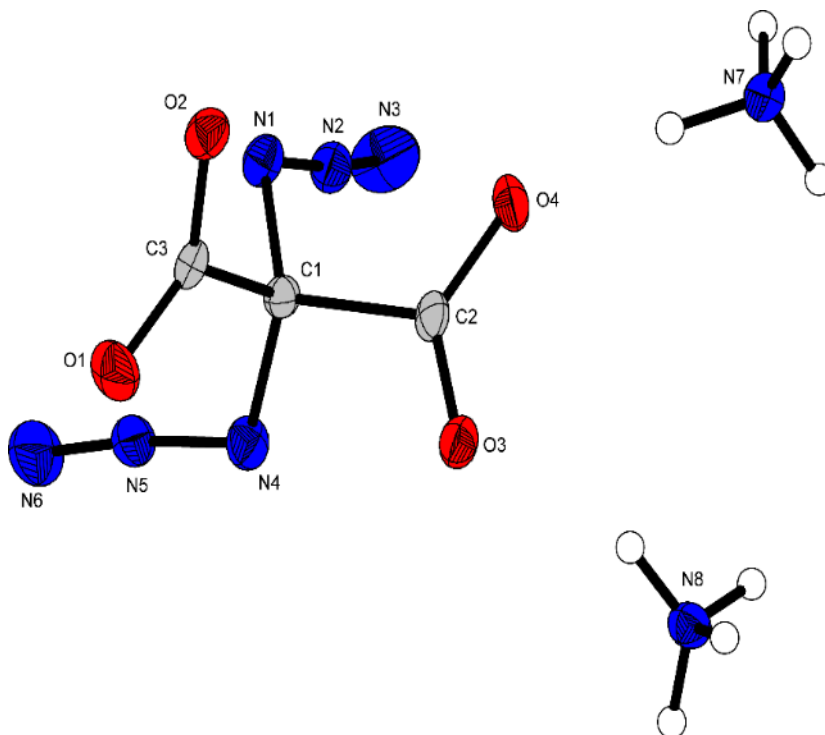


Figure S 2: X-ray structure of compound **3**; Thermal ellipsoids are drawn at the 50% probability level and hydrogen atoms are shown as small spheres of arbitrary radius.

Diammonium 2,2-diazidomalonate (**3**) crystallizes in the triclinic space group $P\bar{1}$ with a density of 1.546 g cm^{-3} at 110 K. The cell volume is $472.9(2) \text{ \AA}^3$ with two formula units per cell. The cell constants are $a = 7.0256(17) \text{ \AA}$, $b = 7.3752(13) \text{ \AA}$ and $c = 10.523(3) \text{ \AA}$.

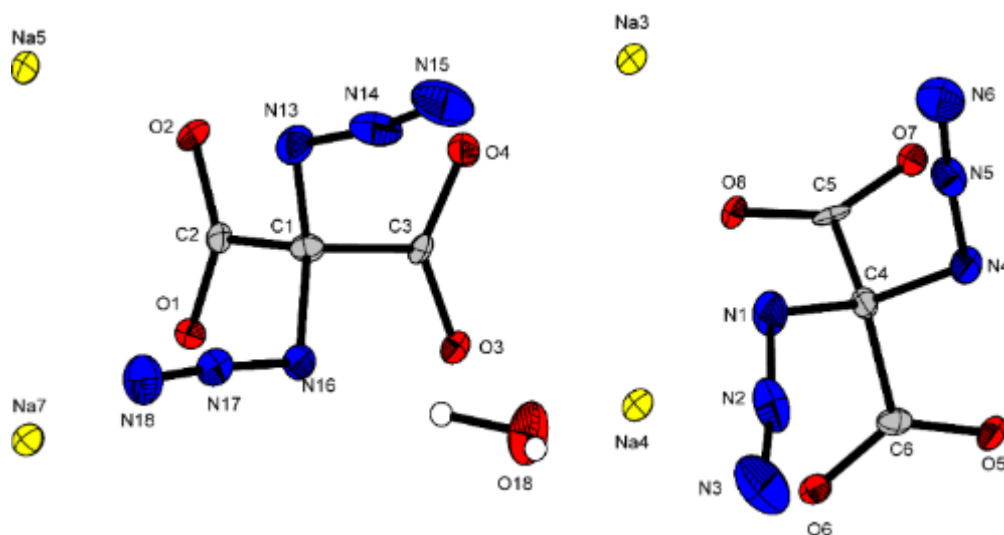


Figure S 3: X-ray structure of compound **4**; Thermal ellipsoids are drawn at the 50% probability level and hydrogen atoms are shown as small spheres of arbitrary radius.

Disodium 2,2-diazidomalonate semihydrate (**4**) crystallizes in the monoclinic space group $P2_1/c$ with a density of 1.904 g cm^{-3} at 123 K and one water molecule per two malonate molecules.

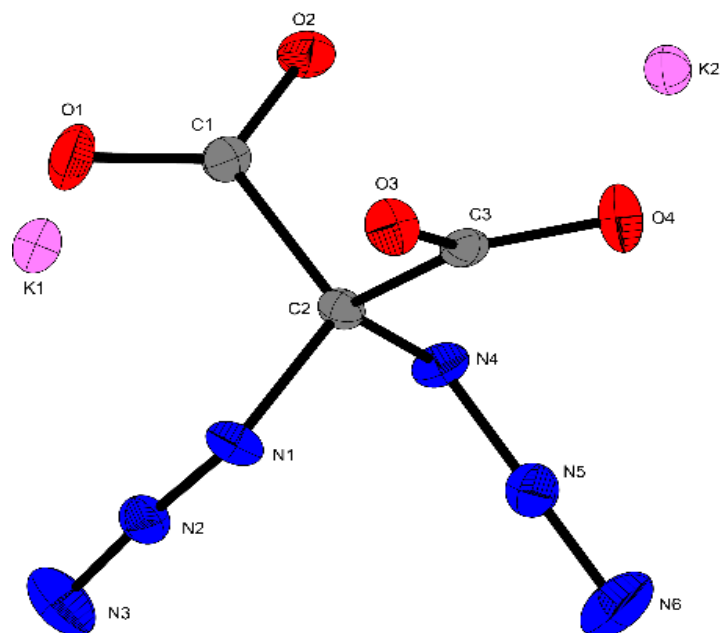


Figure S 4: X-ray structure of compound **5**; Thermal ellipsoids are drawn at the 50% probability level and hydrogen atoms are shown as small spheres of arbitrary radius.

Dipotassium 2,2-diazidomalonate (**5**) crystallizes in the triclinic space group $P\bar{1}$ with a density of 1.981 g cm^{-3} at 173 K. The cell volume is $439.70(2) \text{ \AA}^3$ with two formula units per cell. The cell constants are $a = 6.8277(1) \text{ \AA}$, $b = 7.1525(2) \text{ \AA}$ and $c = 10.3164(2) \text{ \AA}$.

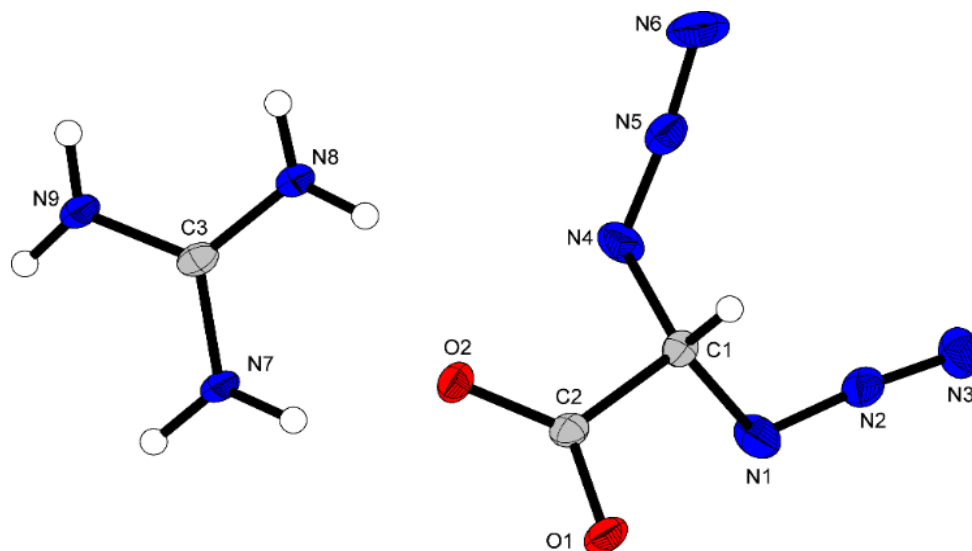


Figure S 5: X-ray structure of compound **6**; Thermal ellipsoids are drawn at the 50% probability level and hydrogen atoms are shown as small spheres of arbitrary radius.

Guanidinium 2,2-diazoacetate (**6**) crystallizes in the orthorhombic space group $Pna2_1$ with a density of 1.534 g cm^{-3} at 102 K. The cell volume is $871.31(19) \text{ \AA}^3$ with four

formula units per cell. The cell constants are $a = 15.725(2) \text{ \AA}$, $b = 7.6451(9) \text{ \AA}$ and $c = 7.2477(10) \text{ \AA}$.

3.6.2 Experimental part and general methods

Caution! Geminal Diazides are energetic materials with high sensitivities towards shock and friction. Therefore, proper security precautions (safety glass, face shield, earthed equipment and shoes, Kevlar gloves and ear plugs) have to be applied while synthesizing and handling the described compounds.

Chemicals and solvents were employed as received (Sigma-Aldrich, Acros, TCI, Spirochem AG). ^1H , ^{13}C and ^{14}N spectra were recorded using a Bruker AMX 400 instrument. The chemical shifts quoted in ppm refer to tetramethylsilane (^1H , ^{13}C) and nitromethane (^{14}N). Decompositions temperatures were determined on a Mettler Toledo DSC822e at a heating rate of $5 \text{ }^\circ\text{C min}^{-1}$ using $40 \text{ }\mu\text{L}$ aluminum crucibles and nitrogen purge gas at a flow rate of 30 mL min^{-1} . Evaluations of thermal behavior were performed using the STARe Software Version 16.20. Infrared (IR) spectra were recorded using a Perkin-Elmer Spektrum One FT-IR instrument. Raman spectra were obtained using a Bruker MultiRam FT Raman spectrometer and a neodymium-doped yttrium aluminum garnet (Nd:YAG) laser ($\lambda = 1064 \text{ nm}$, 1074 mW). Elemental analyses were performed with an Elementar Vario el by pyrolysis of the sample and subsequent analysis of formed gases (standard deviation liquids: $\pm 0.5\%$). The sensitivity data were collected using a BAM (Bundesanstalt für Materialforschung) drophammer[S6] according to STANAG 4489[S7] modified instruction[S8] and a BAM friction tester[S9] according to STANAG 4487[S10] modified instruction. The classification of the tested compounds results from the 'UN Recommendations on the Transport of Dangerous Goods'.^[S11]

3.6.3 Heat of formation calculation and thermal analysis

The atomization was used to determine the heat of formation of **1–6** using the atom energies in Table S3.

$$\Delta_f H^\circ_{(g, M, 298)} = H_{(molecule, 298)} - \sum H^\circ_{(atoms, 298)} + \sum \Delta_f H^\circ_{(atoms, 298)}$$

Table S3: CBS-4M electronic enthalpies for atoms C, H, N and O and their literature values.

	$-H^{298} / a.u.$	$\Delta_f H^\circ_{\text{gas}} [S12]$
H	0.500991	217.998
C	37.786156	716.68
N	54.522462	472.68
O	74.991202	249.18

The Gaussian16 program package was used to calculate room temperature enthalpies on the CBS-4M level of theory.^[S13] In order to obtain the energy of formation for the solid phase of **2**, the Trouton's Rule has to be applied ($\Delta H_{\text{sub}} = 188 \cdot T_m$). As compound **1** is liquid, a different factor is applied ($\Delta H_{\text{sub}} = 90 \cdot T_m$).

Table S4: Heat of formation calculation results for compounds 1–6.

<i>M</i>	$-H^{298} [a] [a.u.]$	$\Delta_f H^\circ(\text{g}, M) [b]$ [kJ mol ⁻¹]	$\Delta_f H^\circ(\text{s}) [d]$ [kJ mol ⁻¹]	Δn	$\Delta_f U(\text{s}) [e]$ [kJ kg ⁻¹]
1	900.847328	-88.8	-126.6	-10.0	-420.3
2	743.916874	-31.6	-104.7	-6.0	-482.8
3	742.780754	-95.2	-249.7	-10.0	-1021.7
4	742.780754	-115.4	-785.7	-5.0	-3361.6
5	742.780754	-95.2	-584.6	-5.0	-2181.6
6	555.044724	-117.5	-190,0	-9.0	-1055.6

[a] CBS-4M electronic enthalpy; [b] gas phase enthalpy of formation; [c] sublimation enthalpy; [d] standard solid state enthalpy of formation; [e] solid state energy of formation.

3.6.4 References

- [S1] CrysAlisPro, Oxford Diffraction Ltd. version 171.33.41, **2009**.
- [S2] G. M. Sheldrick, *Acta Cryst.*, **2015**, A71, 3–8.
- [S3] Dolomanov, O. V., Bourhis, L. J., Gildea, R. J., Howard, J. A. K. & Puschmann, H. J., *Appl. Cryst.*, **2009**, 42, 339–341.
- [S4] SCALE3 ABSPACK – An Oxford Diffraction program (1.0.4, gui: 1.0.3), Oxford Diffraction Ltd., **2005**.
- [S5] APEX3. Bruker AXS Inc., Madison, Wisconsin, USA.
- [S6] <http://www.bam.de>
- [S7] NATO Standardization Agreement (STANAG) on Explosives, *Impact Sensitivity Tests*, no. 4489, 1st ed., September 17, **1999**.
- [S8] WIWEB-Standardarbeitsanweisung 4-5.1.02, Ermittlung der Explosionsgefährlichkeit, hier der Schlagempfindlichkeit mit dem Fallhammer, November 8, **2002**.
- [S9] NATO Standardization Agreement (STANAG) on Explosives, *Friction Sensitivity Tests*, no. 4487, 1st ed., August 22, **2002**.
- [S10] WIWEB-Standardarbeitsanweisung 4-5.1.03, Ermittlung der Explosionsgefährlichkeit oder der Reibeempfindlichkeit mit dem Reibeapparat, November 8, **2002**.
- [S11] Impact: Insensitive >40 J, less sensitive ≤35 J, sensitive ≤4 J, very sensitive ≤3 J; friction: Insensitive >360 N, less sensitive=360 N, sensitive 80 N, very sensitive ≤80 N, extreme sensitive ≤10 N; According to the UN Recommendations on the Transport of Dangerous Goods (+) indicates: not safe for transport.
- [S12] M. W. Chase Jr., NIST-JANAF Thermochemical Tables, Fourth Edition, *J. Phys. Chem. Red. Data, Monograph 9*, **1998**, 1 – 1951.
- [S13] M. J. Frisch, G. W. Trucks, H. B. Schlegel, G. E. Scuseria, M. A. Robb, J. R. Cheeseman, G. Scalmani, V. Barone, G. A. Petersson, H. Nakatsuji, X. Li, M. Caricato, A. V. Marenich, J. Bloino, B. G. Janesko, R. Gomperts, B. Mennucci, H. P. Hratchian, J. V. Ortiz, A. F. Izmaylov, J. L. Sonnenberg, D. Williams-Young, F. Ding, F. Lipparini, F. Egidi, J. Goings, B. Peng, A. Petrone, T. Henderson, D. Ranasinghe, V. G. Zakrzewski, J. Gao, N. Rega, G. Zheng, W. Liang, M. Hada, M. Ehara, K. Toyota, R. Fukuda, J. Hasegawa, M. Ishida, T. Nakajima, Y. Honda, O. Kitao, H. Nakai, T. Vreven, K.

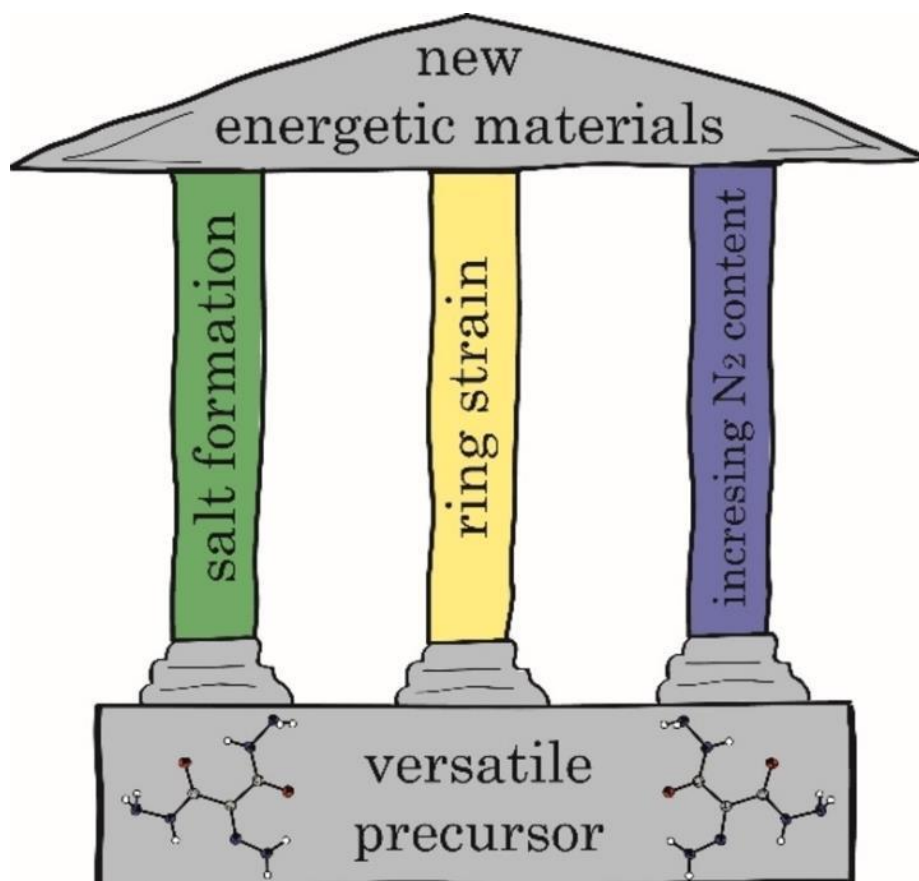
Throssell, J. A. Montgomery, Jr., J. E. Peralta, F. Ogliaro, M. J. Bearpark, J. J. Heyd, E. N. Brothers, K. N. Kudin, V. N. Staroverov, T. A. Keith, R. Kobayashi, J. Normand, K. Raghavachari, A. P. Rendell, J. C. Burant, S. S. Iyengar, J. Tomasi, M. Cossi, J. M. Millam, M. Klene, C. Adamo, R. Cammi, J. W. Ochterski, R. L. Martin, K. Morokuma, O. Farkas, J. B. Foresman, and D. J. Fox, Gaussian16 ,Gaussian, Inc., Wallingford, CT, USA, **2016**.

4. 2-Hydrazonyl-propandihydrazide - a versatile precursor for high-energy materials

Alexander G. Harter, Thomas M. Klapötke, Christian Riedelsheimer, Jörg Stierstorfer, Sebastian M. Strobel, Michael Voggenreiter

as published in European Journal of Inorganic Chemistry **2022**, 15, 1434–1948

DOI: 10.1002/ejic.202200100



Key words: precursor, energetic materials, structural elucidation, triazole, toxicity assessment

Abstract: In this work, 2-hydrazonyl-propandihydrazide (**2**), a new precursor for energetic materials based on diethyl 2,2-diazidomalonate (**1**) was investigated. Therefore, its versatility was shown by various secondary reactions, including formation of energetic salts (**3–5**), the synthesis of a nitrogen-rich bistriazole (**10**) and a highly instable diazido derivative (**6**). In addition, a *Curtius* degradation could be observed in detail. When possible, the compounds were analyzed by low temperature X-ray diffraction. All measurable compounds were analyzed by ^1H and ^{13}C NMR spectroscopy, elemental analysis, differential thermal analysis (DTA) and regarding their sensitivity towards impact and friction according to BAM standard techniques. All promising compounds were evaluated regarding their energetic behavior using the EXPLO5 code (V6.05) and compared to RDX and CL-20. In addition, compound **2** was investigated towards its aquatic toxicity, using the bioluminescent bacteria *vibrio fischeri*.

4.1 Introduction

Due to the wide spread use of energetic materials in both civilian and military applications, there is a constant need for improvement of known compounds, as well as the development of new energetic materials, exceeding their predecessors in regard to their performance, cost effectiveness and eco-friendliness.¹⁻³ Countless discoveries of the last decade have proven nitrogen rich heterocycles like oxadiazoles, triazoles and tetrazoles to be promising backbones in high-energy material (HEM) synthesis.⁴⁻⁶ Compounds based on these systems often possess the desired properties like high density and detonation performance, good thermal stabilities and low sensitivities.^{7, 8} By the formation of nitrogen rich salts these properties can be further improved.⁹ One

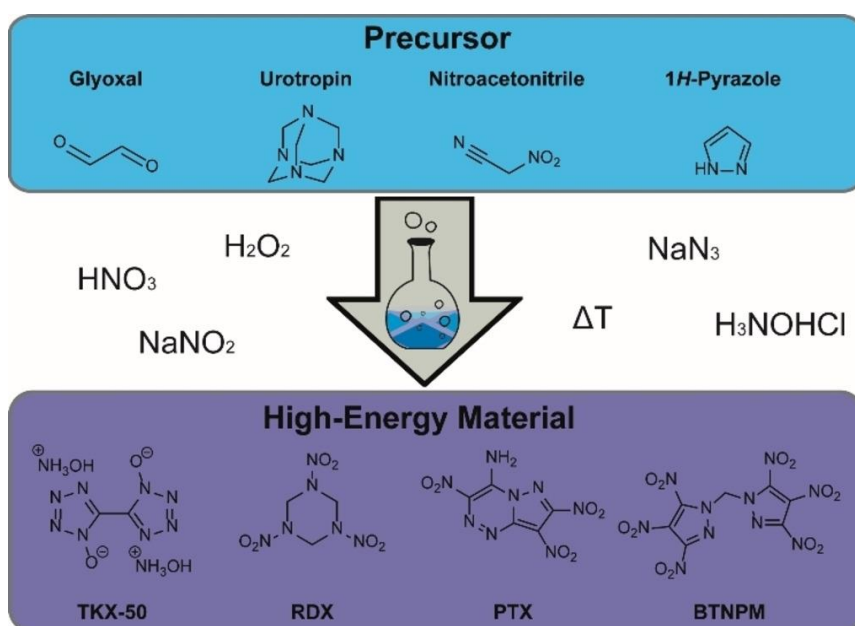


Figure 1. A selection of commonly used precursor molecules and their respective HEMs.

of the most prominent examples for this class of molecules is TKX-50, surpassing commonly used energetic materials like RDX in almost all relevant properties.¹⁰⁻¹²

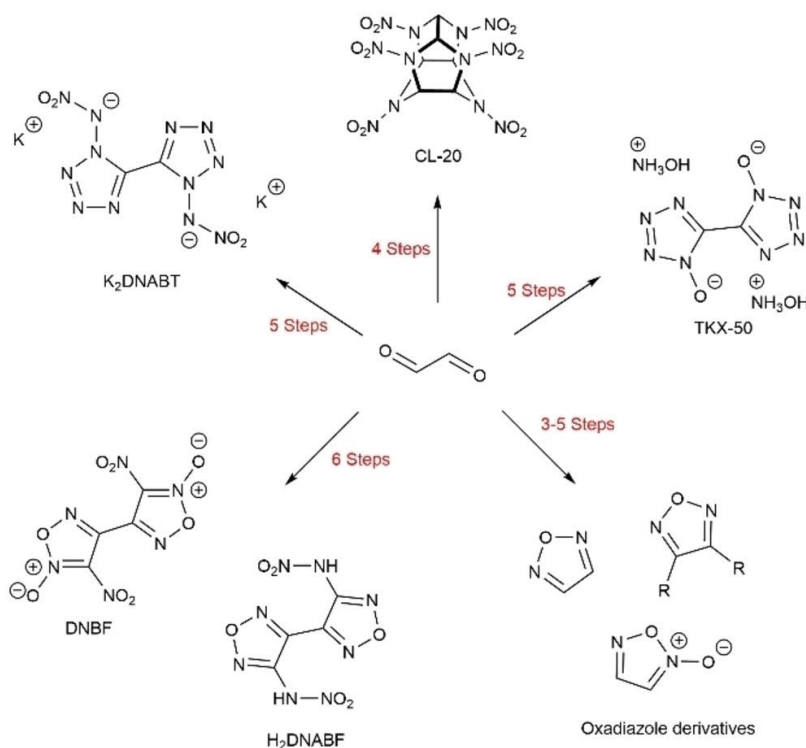


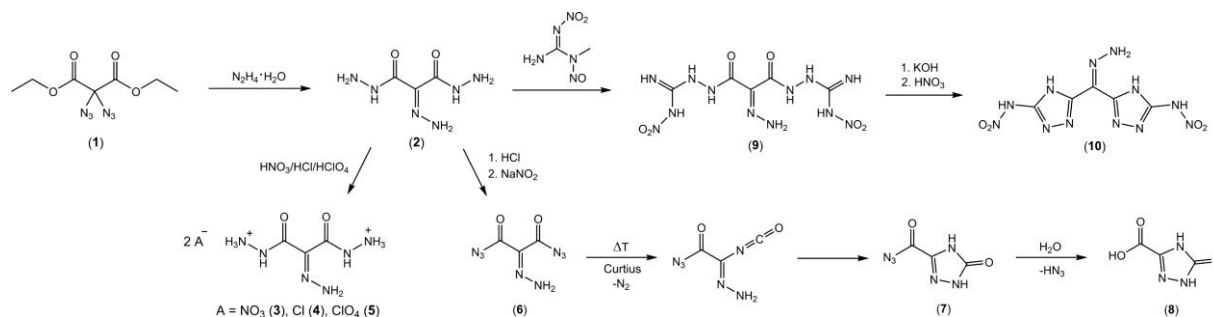
Figure 2. Glyoxal as a precursor for various energetic materials like CL-20, K_2 DNABT, TKX-50, furazane and furoxane derivatives.

It is synthesized from glyoxal, which is an excellent example for a versatile precursor in the field of HEMs. Numerous compounds including K_2 DNABT, CL-20, TKX-50, bisfuroxanes and furazanes can be prepared starting from glyoxal.¹³⁻¹⁵ Another well-known example is nitroacetonitrile, which is commonly used to synthesize annulated 1,2,4-triazines.¹⁶ Some examples for energetic precursors are summarized in Figure 1. But the way to these promising energetic compounds often consists of long synthetic routes including numerous steps and complicated reaction paths, some examples of these are shown in Figure 2. It is therefore of high importance to develop new precursor molecules, which are cheap and easy to synthesize and provide various possibilities for functionalization in order to obtain HEMs. In addition, it would be ideal if they possess low sensitivities and no toxicity. Therefore, this work focuses on the synthesis of energetic materials, based on 2-Hydrazonyl-propandihydrazide (**2**), a new energetic precursor. Those new compounds are extensively characterized in regard to their energetic and structural properties.

4.2 Results and Discussion

4.2.1 Synthesis

Diethyl 2,2-diazidomalonate (**1**) was synthesized according to literature procedure.¹⁷ 2-Hydrazonyl-propandihydrazide (**2**) was obtained by substitution of the azide groups and the ethoxy groups using an excess of hydrazinium hydroxide. Two ethanol molecules are cleaved by the nucleophilic attack of the hydrazine on the carboxyl carbon atom. The ionic compounds **3–5** are synthesized by *Brønsted* acid-base chemistry when reacting compound **2** with nitric, hydrochloric and perchloric acid, respectively. Hereby, compound **2** is protonated twice and the double salts of the 2-hydrazonemalonohydrazinium cation are formed. After diazotation of compound **2** a *Curtius* degradation starting from compound **6** can be observed. Hereby, 3-carbonylazido-1*H*-1,2,4-triazol-5-one (**7**) is formed almost instantly over the isocyanate intermediate, which reacts further to compound **8**, when exposed to ambient humidity. Additionally, compound **2** was reacted with *N*-methyl-*N*-nitroso-*N'*-nitroguanidine in order to form compound **9**, which was followed by a triazole ring closure, performed under basic conditions and subsequent acidification yielding the neutral compound **10** (Scheme 1). All compounds were fully characterized by IR and multinuclear NMR spectroscopy, mass spectrometry and differential thermal analysis. Further, selected compounds were analyzed using low-temperature single-crystal X-ray measurements.



Scheme 3. Synthesis of compound **2** as a versatile precursor for energetic compounds **3**, **4**, **5**, **9** and **10**, as well as the Curtius degradation from compound **6** to **8**.

4.2.2 Crystal Structures

Measurable crystals could be obtained for the compounds **2–5**, **7** and **8**, either directly from the reaction mixture (**7**, **8**) or by recrystallization from water (**2–5**).

General information on the X-ray measurements and refinements are given in the SI. Structures were deposited with the CCDC database under the following numbers (**2**: 2149590, **3**: 2149591, **4**: 2149592, **5**: 2149593, **7**: 2149594, **8**: 2149595).

2-Hydrazonyl-propandihydrazide (**2**) crystallizes in the monoclinic space group $P2_1/c$ with a density of 1.601 g cm^{-3} at 113 K (Figure 3). For all structures, thermal ellipsoids of non-hydrogen atoms are drawn at the 50 % probability level and hydrogen atoms are shown as small spheres of arbitrary radius. The cell volume is $664.35(9) \text{ \AA}^3$ with four formula units per cell. The molecule is highly planar, shown by the torsion angles, which are very close to 0° or 180° . ($\text{N6-N5-C3-C2 } 173.8^\circ$, $\text{N4-N3-C2-C1 } 0.3^\circ$, $\text{N2-N1-C1-C2 } 178.9^\circ$). Both, intramolecular and intermolecular hydrogen bonds can be observed. ($\text{N4-H4B} \cdots \text{O1}$, $\text{N5-H5} \cdots \text{N3}$, $\text{N1-H1} \cdots \text{O2}$, $\text{N2-H2 A} \cdots \text{O1}$, $\text{N4-H4B} \cdots \text{O2}$) The bond lengths confirm the mesomeric system, with values between single and double bonds for C1-N1 (1.333 \AA), C2-N3 (1.314 \AA), N3-N4 (1.309 \AA) and C3-N5 (1.336 \AA).^{18, 19}

2-Hydrazonyl-propandihydrazidium dinitrate $\cdot 0.25 \text{ H}_2\text{O}$ (**3**) crystallizes in the monoclinic space group $P2_1/c$ with a density of 1.743 g cm^{-3} at 107 K (Figure 4). The

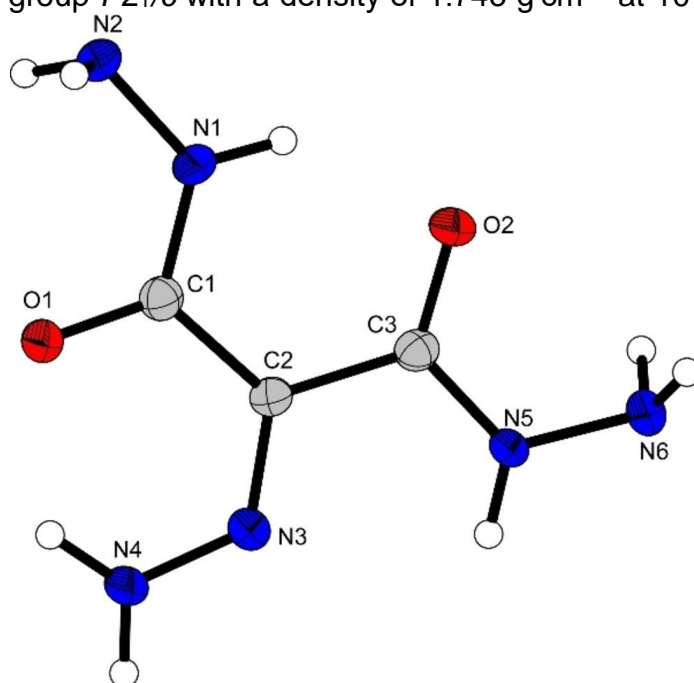


Figure 3. Molecular unit of 2-hydrazonyl-propandihydrazide (**2**).

cell volume is $1107.53(10) \text{ \AA}^3$ with one formula unit per cell. The torsion angles show a planar molecule, similar to compound **2** ($\text{N6-N5-C3-C2 } -174.9^\circ$, $\text{N4-N3-C2-C1 } 0.7^\circ$, $\text{N2-N1-C1-C2 } 176.4^\circ$). The compound crystallizes with one water per four product molecules.

Compound **4** crystallizes in the triclinic space group $P-1$ with a density of 1.657 g cm^{-3} at 100 K and two formula units per unit cell (**Figure 5**). The cell volume is $503.15(6)$

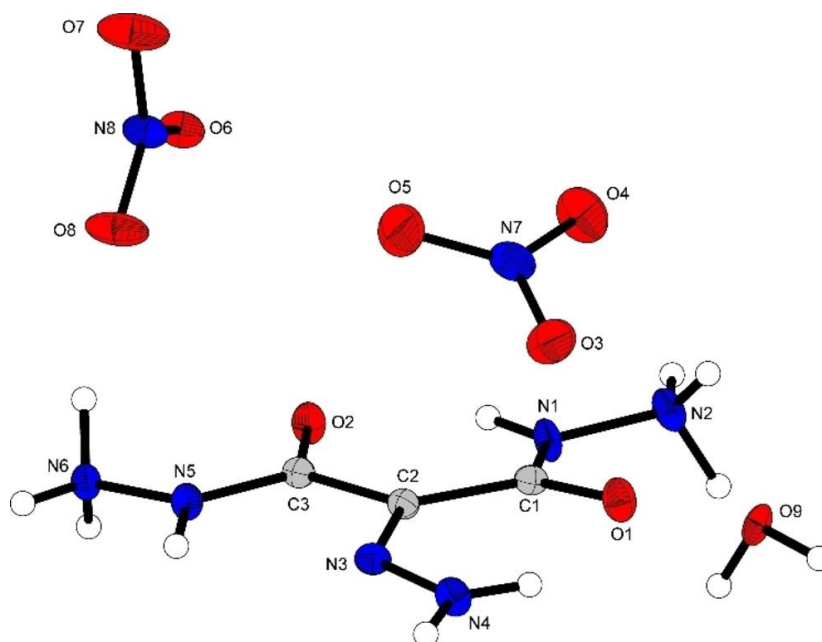


Figure 4. Molecular unit of 2-hydrazonyl-propandihyrazidium dinitrate · 0.25 H₂O (**3**).

Å³. The structure shows high similarities to the previously described compounds **2** and **3** in regard to its planarity (N6–N5–C3–C2 –172.7°, N4–N3–C2–C1 176.2°, N2–N1–C1–C2 178.3°). The crystal structure contains one water per unit cell. All bond lengths comply with the described values for compound **2**.^[18,19]

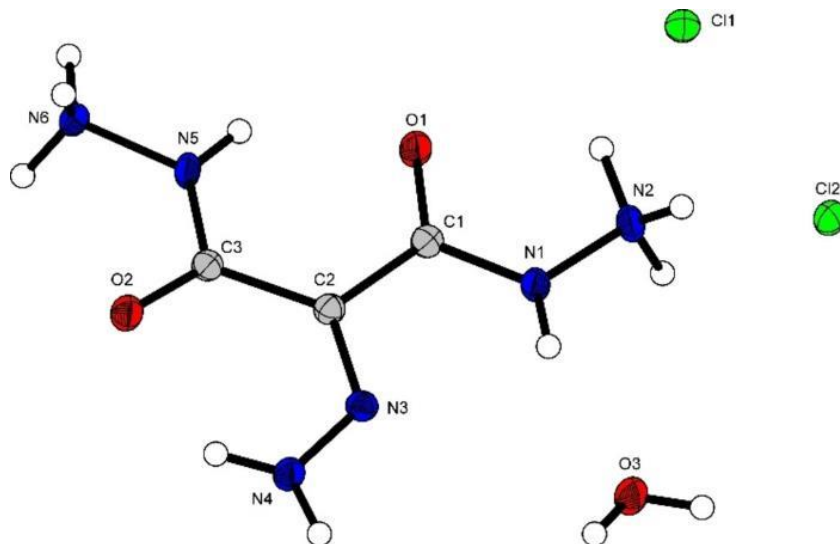


Figure 5. Molecular unit of 2-hydrazonyl-propandihyrazidium dichloride monohydrate (**4**).

Compound **5** crystallizes in the monoclinic space group $P2_1/n$ with a density of 1.991 g cm⁻³ at 105 K and four formula units per unit cell (Figure 6). The cell volume is 1264.94(13) Å³. The structure fits the expectations in regard to the torsion angles, being slightly less planar than the previous described structures (N6–N5–C3–C2 –171.0°, N4–N3–C2–C1 178.5°, N2–N1–C1–C2 –168.8°). The crystal structure

contains one water per unit cell. All bond lengths comply with the described values for compound **2**.^{18, 19}

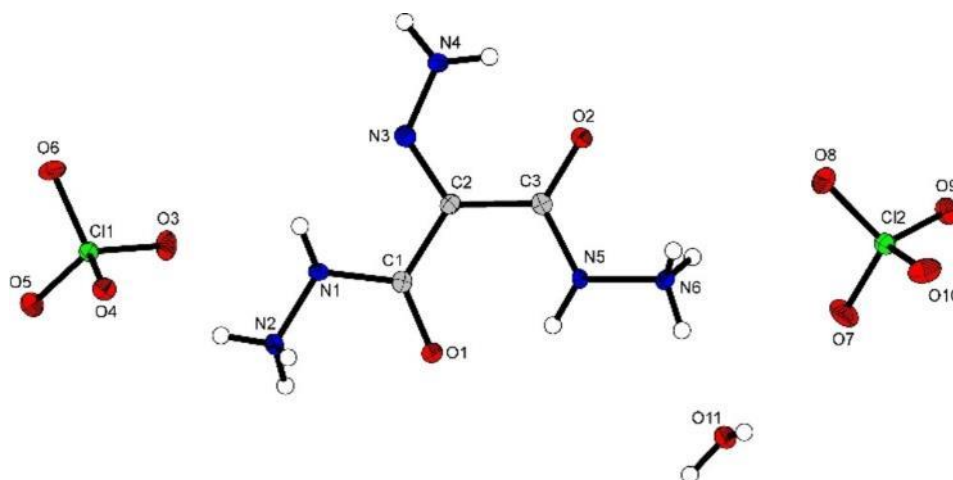


Figure 6. Molecular unit of 2-hydrazonyl-propandihydrazidium diperchlorate monohydrate (**5**).

Compound **7** crystallizes in the monoclinic space group $P2_1/c$ with a density of 1.797 g cm^{-3} at 105 K and four formula units per unit cell (figure 7). The cell volume is $569.48(17) \text{ \AA}^3$. Based on the torsion angles the structure can also be described as planar ($\text{C1-N1-N2-C2} -0.4^\circ$, $\text{N2-C2-C3-N4} 2.7^\circ$, $\text{N5-N4-C3-O2} 2.3^\circ$). All bond lengths comply with the expected values for C-C, C-N, C-O and N-N single and double bonds ($\text{C2-C3} 1.49 \text{ \AA}$, $\text{N1-N2} 1.38 \text{ \AA}$, $\text{N4-C3} 1.40 \text{ \AA}$, $\text{C1-O1} 1.25 \text{ \AA}$).^[18,19]

Compound **8** crystallizes in the monoclinic space group $P2_1/c$ with a density of 1.766

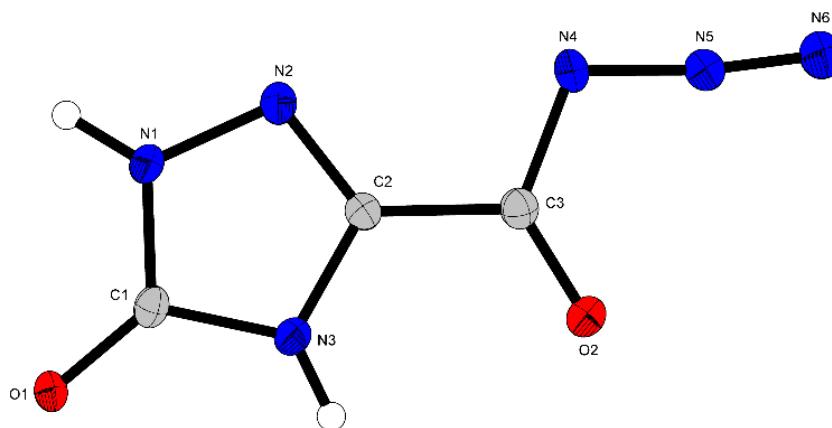


Figure 7. Molecular unit of 3-carboxylazido-1H-1,2,4-triazol-5-one (**7**).

g cm^{-3} at 102 K and four formula units per unit cell (**Figure 8**). The cell volume is $553.20(4) \text{ \AA}^3$. Similar to compound **7** the torsion angles describe a planar structure ($\text{C2-N1-C1-N2} -0.4^\circ$, $\text{N1-C2-C3-O3} 0.8^\circ$, $\text{N3-N2-C1-O1} -177.6^\circ$). The compound crystallizes with one water molecule per unit cell. All bond lengths comply with the expected values for C-C, C-N, C-O and N-N single and double bonds ($\text{C2-C3} 1.49 \text{ \AA}$, $\text{N2-N3} 1.37 \text{ \AA}$, $\text{N3-C2} 1.30 \text{ \AA}$, $\text{C1-O1} 1.25 \text{ \AA}$).^[18,19]

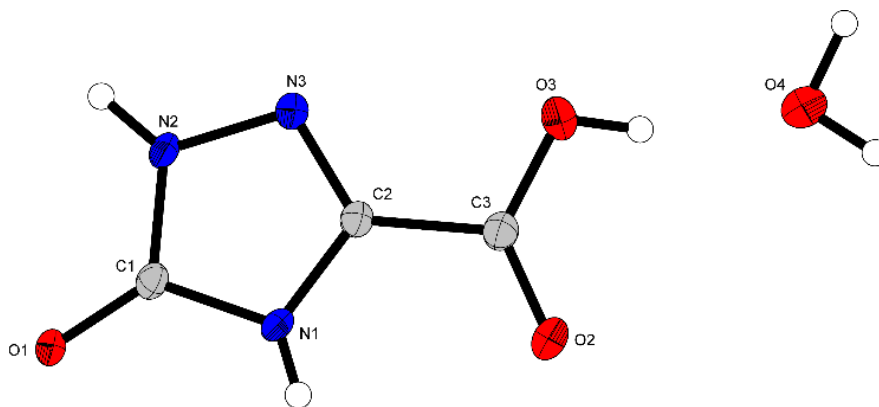


Figure 8. Molecular unit of 3-carboxyl-1*H*-1,2,4-triazol-5-one monohydrate (**8**).

4.2.3 NMR and Vibrational spectroscopy

All ^1H and ^{13}C NMR measurements were performed in DMSO-d_6 . The proton NMR of compound **2** shows five signals. This is due to the E/Z-isomerism caused by the inflexible hydrazone moiety, building intramolecular hydrogen bridges with one side of the otherwise symmetrical molecule. The two signals at 4.26 and 4.46 ppm belong to the NH_2 - groups of the hydrazides. The two signals at 8.88 and 10.20 ppm are the NH groups, which are shifted more due to a higher influence of the described effect on those protons. The same effect can be observed in the corresponding ^{13}C spectrum, which shows three signals. The two signals at 162.9 and 164.9 ppm belong to the unsymmetrically carbohydrazides and the signal at 119.0 ppm represents the hydrazone group. Compound **3**, **5** and **9** behave in a similar manner, as it would be expected. Although compound **10** also has the intermediate hydrazone group, it shows symmetric signals in the ^1H and ^{13}C spectra, which are caused by the mesomerism of the ring system. The IR spectrum of **6** was measured in chloroform, since this compound decomposes as soon as it is isolated. The hydrazone moiety can be identified by the two broad bands at 3313 and 3163 cm^{-1} , as well as the band at 1574 cm^{-1} . The band at 2129 cm^{-1} corresponds to the azide groups and the carbonyl vibration is found at 1675 cm^{-1} .^[20,21]

4.2.4 Physicochemical Properties

All energetic compounds were characterized regarding their physicochemical properties. This includes their sensitivities towards impact, friction and electrostatic discharge, the thermal behavior, heats of formation and detonation parameters. Those were determined experimentally or computationally and compared to RDX, being the state-of-the-art secondary explosive in industrial use, and CL-20, which is one of the best performing compounds in terms of detonation properties, shown in **Table 1**. The sensitivity values towards impact and friction were determined according to the BAM standards.^[22]

When looking at compound **2** and the energetic salts **3** and **5**, it was observed, that they are insensitive towards friction, with values above 360 N. In regard to the impact values only compound **3** shows a slight sensitivity of 30 J. For compound **3** and **5** the insensitivity can be explained by the crystal water, generally reducing those values. Compound **9** also shows no sensitivity towards impact and friction with values of above 40 J and 360 N. Compound **10** exhibits interesting properties, possessing a high impact sensitivity of 2.5 J, which is close to the range of primary explosives, while at the same time being almost insensitive towards friction stimuli with a value of 360 N. When compared to RDX and CL-20, all compounds are less sensitive, with the exception of compound **10** showing a higher impact sensitivity. It was attempted to measure the friction sensitivity of compound **6** directly after separating it from the reaction mixture, which resulted in positive tests at 1 N. But it has to be mentioned that the *Curtius* degradation visibly took place, as the product turned yellow during the measurement and therefore no certain values could be obtained.

The thermal properties of all compounds were determined by differential thermal analysis. None of the measured compounds show endothermic events, which could be assigned to melting points. In terms of decomposition temperatures, the range starts at a rather low value 124 °C for the perchlorate salt **5** and ends at 209 °C for compound **9**. The remaining three compounds **2**, **3** and **10** show decent decomposition temperatures slightly below 180 °C. The DTA plots of compound **2**, **9** and **10** are depicted in figure 9. With the exception of Compound **9**, all measured compounds are less stable towards thermal influences than RDX. The investigated compounds exhibit very high combined nitrogen and oxygen contents up to 84 % for compound **3**. Based on the densities, obtained by gas pycnometry or from the crystal structures the energetic properties were calculated with EXPLO5 (V6.05).^[23] The heats of formation were obtained by CBS-4M calculations. The densities of compound **2** and its salts **3** and **5** range from 1.56 g cm⁻³ to 1.94 g cm⁻³ with the neutral compound showing the lowest value, the perchlorate salt the highest value and the nitrate salt a moderate value of 1.70 g cm⁻³, which is in line with the expectations. The densities of compound **9** and **10** were determined by gas pycnometry, since no crystal structures could be obtained. Compound **9** shows a lower density of 1.73 g cm⁻³, when compared to compound **10**, which was to be expected due to the large size of the molecule. With 1.81 g cm⁻³ compound **10** is in the same density range of RDX, which is a promising starting condition for the detonation properties. When looking at the detonation velocities and pressures, the values of the measured compounds range from 7610 m·s⁻¹ and 19.3 GPa for compound **2**, up to 9082 m·s⁻¹ and 36.9 GPa for compound **5**. Therefore, compounds **3** and **5** are able to surpass RDX in terms of their detonation properties, exhibiting detonation velocities around 9000 m·s⁻¹. Compound **10** still shows decent values which are only slightly below RDX with a detonation velocity of

8654 m s⁻¹ and a pressure of 31.0 GPa. It was expected, that compounds **2** and **9** are the least well performing, since they lack structural energetic properties. This was confirmed by the calculations, with values of 7610 m s⁻¹ and 19.3 GPa for compound **2** and 8228 m s⁻¹ and 25.9 GPa for compound **9**. CL-20 surpasses all synthesized compounds in terms of thermal stability and detonation performance, which was to be expected. But due to much simpler and more cost-efficient syntheses, as well as lower sensitivities, the presented compounds are still a valuable addition to the roster of secondary explosives and prove the worth of compound **2** as an energetic precursor.

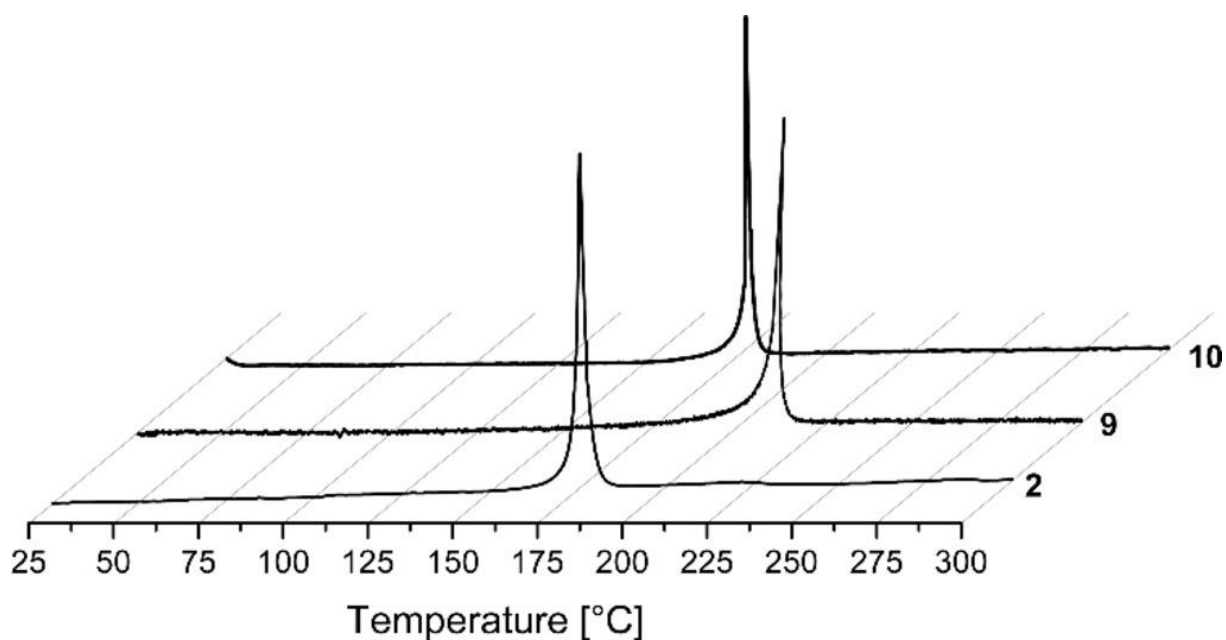


Figure 9. DTA plots of compound **2**, **9** and **10** measured with a heating rate of 5 K · min⁻¹.

Table 3. Physiochemical properties of compounds 2, 3, 5, 9, 10, RDX and CL-20^[24].

	2	3	5	9	10	RDX	CL-20
Formula	C ₃ H ₈ N ₆ O ₂	C ₃ H _{10.5} N ₈ O _{8.25}	C ₃ H ₁₂ N ₆ O ₁₁ Cl ₂	C ₅ H ₁₀ N ₁₂ O ₆	C ₅ H ₆ N ₁₂ O ₄	C ₃ H ₆ N ₆ O ₆	C ₃ H ₆ N ₆ O ₆
<i>M</i> [g·mol ⁻¹]	160.14	290.56	379.06	334.21	298.18	222.12	438.19
<i>IS</i> ^[a] [J]	>40	30	>40	>40	2.5	7.5	3
<i>FS</i> ^[b] [N]	>360	>360	>360	>360	360	120	96
<i>N+O</i> ^[c] [%]	72.46	83.89	68.60	79.01	77.83	81.06	82.17
Ω_{CO_2} ^[d] [%]	-80	-17	0	-43	-34	-22	-11
<i>T</i> _{endo} ^[e] / <i>T</i> _{exo} ^[f] [°C]	-/178	-/167	-/124	-/209	-/177	203/208	-/224
ρ ^[g] [g·cm ⁻³]	1.56	1.70	1.94	1.73	1.81	1.82	2.08
$\Delta_f H^\circ$ ^[h] [kJ·mol ⁻¹]	-21	224	-239	184	541	87	365
EXPLO5 V6.05							
$-\Delta_E U^\circ$ ^[i] [kJ·kg ⁻¹]	2851	6552	5993	4327	5137	5807	6160
<i>T</i> _{C-J} ^[j] [K]	2096	4073	4080	3023	3624	3800	4071
$\rho_{\text{C-J}}$ ^[k] [GPa]	19.3	34.2	36.9	25.9	31.0	34.0	44.5
<i>D</i> _{C-J} ^[l] [m·s ⁻¹]	7610	8920	9082	8228	8654	8882	9778
<i>V</i> ₀ ^[m] [dm ³ ·kg ⁻¹]	885	859	837	829	766	793	720

[a] Impact sensitivity (BAM drophammer, method 1 of 6); [b] friction sensitivity (BAM drophammer, method 1 of 6); [c] electrostatic discharge device (OZM research); [d] combined nitrogen and oxygen content; [e] oxygen balance toward carbon dioxide ($\Omega_{\text{CO}_2} = (n\text{O} - 2x\text{C} - y\text{H}/2)(1600/\text{FW})$); [f] endothermic event (DTA, $\beta = 5^\circ\text{C}\cdot\text{min}^{-1}$); [g] temperature of decomposition (DTA, $\beta = 5^\circ\text{C}\cdot\text{min}^{-1}$); [h] density at 298 K (for **1** determined volumetrically with a Hamilton syringe 100 μL); [i] standard molar enthalpy of formation; [j] detonation energy; [k] detonation temperature; [l] detonation velocity; [m] detonation pressure; [n] volume of detonation gases at standard temperature and pressure conditions.

4.2.5 Toxicity Assessment

In order to determine the ecotoxicological impact of the presented precursor, EC₅₀ measurements based on the bioluminescent *vibrio fischeri* NRRL-B-11177 marine bacteria strain were performed. Therefore, the EC₅₀ values of compound **2** were measured after 15 and 30 minutes and compared to the measured values of oxalyldihydrazide and glyoxal. The first one was chosen, based on the structural similarities of oxalyldihydrazide to compound **2**. While glyoxal was picked as it is one of the most common precursors in energetic synthesis. The EC₅₀ value refers to the concentration of a toxicant which induces a response of 50 % after a specific exposure time. In this case the EC₅₀ value is determined by inhibition of the luminescence by 50 %, when exposed to the toxicant.²⁵ Based on the resulting effective concentration the measured substances were classified as nontoxic (>1.00 g L⁻¹), toxic (0.10–1.00 g L⁻¹), and very toxic (<0.10 g L⁻¹).²⁶ The measured values are shown in Table 2. Compound **2** can be described as nontoxic toward aquatic organisms, since its EC₅₀ value is above 1 g L⁻¹. Oxalyldihydrazide is also categorized as nontoxic, with even higher values, which indicates a slightly increased toxicity of compound **2** due to the hydrazone moiety. Glyoxal is classified as toxic with values of 0.43 g L⁻¹ and 0.33 g L⁻¹ after 15 min and 30 min, respectively. In summary the hydrazide moiety does not seem to have a negative impact on the toxicity towards aquatic life. Therefore, compound **2** can be described as an ecofriendly precursor for energetic material synthesis.

Table 4. EC₅₀ values of **2**, oxalyldihydrazide and glyoxal.

Incubation	2	Oxalyldihydrazide	Glyoxal
15 min	4.62	19.65	0.43
30 min	2.61	12.99	0.33

4.3 Conclusion

In this work, we present 2-hydrazonyl-propandihydrazide (**2**) as a new precursor in energetic material synthesis. Therefore, the energetic salts **3** and **5**, as well as a bridged nitraminobistriazole (**10**) were synthesized deriving from compound **2** by straightforward and short methods. Additionally, a *Curtius* degradation of 2-hydrazonyl-propandihydrazide (**6**) was observed including the intermediate (**7**) and final product (**8**). Crystal structures of compounds **2–5**, **7** and **8** were determined. The densities range from 1.56 g·cm⁻³ of the precursor (**2**) to 1.94 g·cm⁻³ of the perchlorate salt (**5**). All compounds were characterized by NMR, and IR as well as regarding their physiochemical properties, including thermal behavior and sensitivity towards impact and friction. Due to its very unstable character towards various stimuli, compound **6** was only analyzed by IR spectroscopy. For compound **7**, only the crystal structure

could be obtained due to the short lifespan of this intermediate at standard conditions. The compounds investigated towards their energetic behavior show almost no friction and impact sensitivities, with the exception of compound **10** (3 J, 360 N) and compound **3** (30 J, >360 N). The compounds **2**, **3**, **5**, **9**, and **10** were investigated in regard to their detonation parameters, which were calculated with the EXPLO5 code. Compounds **3** and **5** exceed RDX in terms of all calculated values with detonation velocities of 8920 m s⁻¹ and 9082 m s⁻¹, respectively. Compounds **9** and **10** are still in the same range of RDX with values of 8228 m s⁻¹ and 8654 m s⁻¹. Finally, the new precursor was evaluated by the luminous bacteria inhibition test in order to investigate its ecotoxicological impact. It was compared to glyoxal to provide a well-known precursor as reference. 2-hydrazonyl-propandihydrazide (**2**) is categorized as nontoxic, while the measurements show a toxic classification for glyoxal towards aqueous organisms. Future work might involve upscaling, compatibility testing and additional safety evaluation.

4.4 Experimental Section

All chemicals and solvents were purchased from Sigma Aldrich and used without further purification. The general information about analytical devices including NMR, X-ray crystallography, IR, DTA, as well as information about the calculation of the energetic properties can be found in the SI. Compound (**1**) and *N*-methyl-*N*-nitroso-*N*-nitroguanidine were synthesized according to literature procedures.^[17,27]

Caution: The investigated compounds are potentially toxic and explosive. Therefore, it is recommended to carry out all reactions in a small scale, in addition to using the proper safety equipment, including ear, hand and body protection.

2-Hydrazonyl-propandihydrazide (2): Diethyl 2,2-diazidomalonate (**1**) (1.00 g, 4.13 mmol, 1.0 eq) was dissolved in water (5 mL) and hydrazine hydrate (1.2 mL, 24.77 mmol, 6.0 eq) was added. Afterwards it was stirred for 24 h at room temperature. The precipitate was filtered and washed with cold water. The filtrate was concentrated in vacuo in order to obtain an additional amount of product. Compound (**2**) was obtained as colorless solid (452 mg, 2.82 mmol, 68 %). ¹H NMR (400 MHz, DMSO-*d*₆) δ (ppm) = 10.52 (s, 2H, NH₂), 10.20 (s, 1H, NH), 8.88 (s, 1H, NH), 4.47 (s, 2H, NH₂), 4.24 (s, 2H, NH₂); ¹³C NMR (101 MHz, DMSO-*d*₆) δ (ppm) = 165.4, 163.3, 119.5; IR (ATR, rel. int.): $\tilde{\nu}$ (cm⁻¹) = 3386 (m), 3305 (m), 3195 (m), 2170 (w), 2137 (w), 2007 (w), 1992 (w), 1635 (m), 1601 (m), 1552 (m), 1488 (s), 1325 (m), 1279 (m), 1219 (m), 1137 (m),

1090 (m), 990 (m), 962 (s), 815 (m), 794 (m), 721 (s), 633 (m), 555 (s), 488 (m), 407 (s); **Elemental analysis**: calcd. (%) for $C_3H_8N_6O_2$ ($M = 160,14 \text{ g mol}^{-1}$): C 22.50, H 5.04, N 52.48; found: C 22.62, H 5.08, N 52.16; **Sensitivities** (grain size: 100 – 500 μm): BAM impact: >40 J, BAM friction: >360 N; **DTA** ($5 \text{ }^\circ\text{C min}^{-1}$): $T_{\text{exo}} = 178 \text{ }^\circ\text{C}$.

2-Hydrazonyl-propandihydrazidium dinitrate · 0.25 H₂O (3): 2-Hydrazineylidenemalonohydrazide (**2**) (250 mg, 1.56 mmol, 1.0 eq.) was mixed with nitric acid (5 ml, 65 %) and stirred at $50 \text{ }^\circ\text{C}$ for 1 h. Compound (**3**) (310 mg, 1.08 mmol, 69 %) was obtained as pale-yellow crystals. **¹H NMR** (400 MHz, DMSO-*d*₆): δ (ppm) = 11.5 – 9.0 (broad), 10.53; **¹³C NMR** (101 MHz, DMSO-*d*₆): δ (ppm) = 164.7, 161.3, 115.4; **¹⁴N NMR** (27 MHz, DMSO-*d*₆): δ (ppm) = –4, –359; **IR** (ATR, rel. int.): $\tilde{\nu}$ (cm^{-1}) = 3230 (m), 2151 (m), 2010 (w), 1997 (w), 1891 (w), 1646 (m), 1550 (m), 1495 (m), 1417 (m), 1309 (s), 1272 (s), 1186 (s), 1157 (s), 1104 (m), 1043 (m), 1010 (m), 985 (m), 824 (m), 788 (m), 688 (s), 577 (s), 491 (s), 471 (s), 436 (s), 425 (s), 410 (s), 401 (s); **Elemental analysis**: calcd. (%) for $C_3H_{10}N_8O_8 \cdot 0.25 \text{ H}_2\text{O}$ ($290.56 \text{ g mol}^{-1}$): C 12.40, H 3.64, N 38.55; found: C 12.05, H 3.40, N 38.29; **Sensitivities** (grain size: 100–300 μm): BAM impact: 30 J, BAM friction: >360 N; **DTA** ($5 \text{ }^\circ\text{C min}^{-1}$): $T_{\text{exo}} = 167 \text{ }^\circ\text{C}$.

2-Hydrazonyl-propandihydrazidium dichloride monohydrate (4): 2-Hydrazineylidenemalonohydrazide (**1**) (250 mg, 1.56 mmol, 1.0 eq.) was mixed with hydrochloric acid (5 ml, 30 %) and 5 ml water and stirred at room temperature for 1 h. Compound (**4**) (360 mg, 1.54 mmol, 99 %) was obtained as pale-yellow crystals. **¹H NMR** (400 MHz, DMSO-*d*₆): δ (ppm) = 12.0 – 9.5 (broad), 10.64, 10.56; **¹³C NMR** (101 MHz, DMSO-*d*₆): δ = 164.6, 161.2, 115.2; **IR** (ATR, rel. int.): $\tilde{\nu}$ (cm^{-1}) = 3338 (w), 3185 (w), 2758 (w), 2669 (w), 1983 (w), 1948 (w), 1670 (w), 1648 (w), 1616 (w), 1470 (m), 1335 (w), 1296 (w), 1253 (w), 1213 (w), 1175 (w), 1136 (m), 1066 (w), 1009 (w), 879 (w), 806 (w), 738 (w), 681 (w), 590 (m), 529 (m), 478 (w), 420 (m); **Elemental analysis**: calcd. (%) for $C_3H_{10}Cl_2N_6O_2 \cdot \text{H}_2\text{O}$ ($251.06 \text{ g mol}^{-1}$): C 14.35, H 4.82, N 33.47; found: C 14.40, H 4.57, N 33.65; **Sensitivities** (grain size: 100 - 300 μm): BAM impact: >40 J, BAM friction: >360 N; **DTA** ($5 \text{ }^\circ\text{C min}^{-1}$): $T_{\text{exo}} = 191 \text{ }^\circ\text{C}$.

2-Hydrazonyl-propandihydrazidium diperchlorate monohydrate (5): 2-Hydrazineylidenemalonohydrazide (**2**) (250 mg, 1.56 mmol, 1.0 eq.) was mixed with perchloric acid (0.5 ml, 60 %) and 5 ml water and stirred at room temperature for 1 h. Compound (**5**) (130 mg, 0.36 mmol, 23 %) was obtained as pale-yellow crystals. **¹H NMR** (400 MHz, DMSO-*d*₆): δ (ppm) = 10.63, 10.59, 4.98, 4.63; **¹³C NMR** (101 MHz, DMSO-*d*₆): δ (ppm) = 164.7, 161.3, 115.2; **IR** (ATR, rel. int.): $\tilde{\nu}$ (cm^{-1}) = 3543 (w), 3423

(w), 3149 (w), 1676 (w), 1580 (w), 1494 (m), 1310 (w), 1109 (m), 1041 (m), 929 (w), 807 (w), 619 (m), 585 (m), 484 (m), 417 (m); **Elemental analysis**: calcd. (%) for $C_3H_{10}N_6O_{10}Cl_2 \cdot H_2O$ (379.06 g mol⁻¹): C 9.51, H 3.19, N 22.17; found: C 9.46, H 3.00, N 21.99; **Sensitivities** (grain size: 100 – 500 μm): BAM impact: >40 J, BAM friction: >360 N; **DTA** (5 °C min⁻¹): T_{exo} = 124 °C.

2-Hydrazone-malonyldiazide (6): 2-Hydrazonyl-propandihydrazide (**2**) (500 mg, 3.12 mmol, 1.0 eq.) was dissolved in concentrated hydrochloric acid (10 ml, 32 %). Chloroform (40 mL) was added and the solution was cooled below 0 °C. Sodium nitrite (450 mg, 6.52 mmol, 2.1 eq.), dissolved in water (2 mL), was added dropwise under heavy stirring, while the temperature was kept below 0 °C. The organic phase was washed with ice water and filtered through a magnesium sulfate layer into a crystallizing bowl. The residue was left for crystallization and compound (**5**) was obtained as colorless highly hygroscopic crystals (290 mg, 1.59 mmol, 51 %). **IR** (ATR, rel. int.): $\tilde{\nu}$ (cm⁻¹) = 3312 (w), 3162 (w), 2985 (w), 2128 (w), 1978 (w), 1756 (w), 1674 (w), 1573 (w), 1467 (w), 1297 (w), 1235 (w), 1154 (w), 1046 (w), 960 (w), 854 (w), 828 (w), 753 (w), 669 (w), 588 (w), 548 (w), 470 (w), 416 (w).

3-Carbonylazido-1H-1,2,4-triazol-5-one (7):

2-Hydrazone-malonyldiazide (**6**) was stored in the freezer for 2 days at -20 °C. Colorless crystals were obtained from the stored compound, which turned out to be 3-carbonylazido-1H-1,2,4-triazol-5-one (**6**), shown by X-ray measurements.

3-Carboxyl-1H-1,2,4-triazol-5-one monohydrate (8):

2-Hydrazone-malonyldiazide (**6**) was stored in the refrigerator for 7 days at 3 °C. Yellow crystals were obtained from the stored compound, which turned out to be 3-carboxyl-1H-1,2,4-triazol-5-one (**7**), shown by x-ray measurements **¹H NMR** (400 MHz, DMSO-*d*₆): δ (ppm) = 12.54 (s, 1H), 12.43 (s, 1H); **¹³C NMR** (101 MHz, DMSO-*d*₆): δ (ppm) = 162.5, 155.8, 139.5.

2-Hydrazonyl malono-di-N-amino-nitroguanidine (9):

2-Hydrazineylidenemalonohydrazide (**2**) (725 mg, 4.53 mmol, 1.0 eq.) was dissolved in H₂O (15 ml) and N-methyl-N-nitroso-N'-nitroguanidine (1.33 g, 9.05 mmol, 2.0 eq.) dissolved in H₂O (50 ml) was added. The reaction mixture was stirred for 50 min at 95 °C. The precipitate was collected by filtration, washed with cold H₂O and cold EtOH and dried at rt to yield compound **8** (1.32 g, 3.95 mmol, 87 %) as a yellow solid. **¹H**

NMR (400 MHz, DMSO-*d*₆): δ (ppm) = 10.70, 10.40, 9.90, 9.84-9.48, 8.66, 7.99; **¹³C NMR** (101 MHz, DMSO-*d*₆): δ (ppm) = 165.5, 163.2, 161.4, 161.2, 118.5; **IR** (ATR, rel. int.): $\tilde{\nu}$ (cm⁻¹) = 3387 (vw), 3293 (vw), 3191 (w), 2971 (vw), 1739 (s), 1669 (vw), 1652 (vw), 1610 (m), 1567 (s), 1505 (m), 1476 (w), 1429 (s), 1376 (s), 1345 (s), 1261 (s), 1230 (vs), 1217 (vs), 1189 (vs), 1116 (m), 1058 (s), 954 (vw), 923 (vw), 836 (vw), 779 (vw), 739 (vw), 563 (vs), 517 (vs), 486 (vs), 473 (vs), 412 (vs); **Elemental analysis**: calcd. (%) for C₅H₁₀N₁₂O₆ (334.21 g mol⁻¹): C 17.97, H 3.02, N 50.29; found: C 18.08, H 3.04, N 50.43; **Sensitivities** (grain size: 100–500 μ m): BAM impact: >40 J, BAM friction: >360 N; **DTA** (5 °C min⁻¹): T_{exo} = 209 °C.

Bis(dinitramino-1*H*-1,3,4-bistriazol-5-yl) methylhydrazone (10): Bis(nitroguanidinyl)-2-hydrazone malonohydrazide (**9**) (3.40 g, 10.2 mmol, 1.0 eq.) was dissolved in H₂O (80 ml) and KOH (1.71 g, 30.5 mmol, 3.0 eq.) dissolved in H₂O (65 ml) was added. The reaction mixture was stirred over night at 80 °C, cooled to 50 °C and conc. HNO₃ (65 %) was added until pH = 3. The precipitate was collected by filtration, washed with cold H₂O and dried for two days at 100 °C to yield compound **10** (1.53 g, 5.13 mmol, 50 %) as a beige solid. **¹H NMR** (400 MHz, DMSO-*d*₆): δ (ppm) = 14.17 (bs, 2H, ring-NH), 10.30–9.00 (m, 4H, N-NH₂, NH); **¹³C NMR** (101 MHz, DMSO-*d*₆): δ (ppm) = 152.79, 152.11, 112.03; **MS**: m/z (ESI⁻) = 297.1 [C₅H₆N₁₂O₄]; **IR** (ATR): $\tilde{\nu}$ = 3181 (vw), 1560 (m), 1483 (w), 1401 (w), 1225 (s), 1144 (m), 1044 (m), 988 (m), 913 (m), 871 (m), 771 (s), 731 (s), 707 (s), 614 (s), 492 (vs), 419 (vs); **Elemental analysis**: calcd. (%) for C₅H₆N₁₂O₄: C 20.14, H 2.03, N 56.37 found: C 19.79, H 2.23, N 53.88; **Sensitivities** (grain size: 300–1000 μ m): BAM impact: 2.5 J, BAM friction: 360 N; **DTA** (onset, 5 °C min⁻¹): T_{exo} = 177 °C.

Acknowledgements

For financial support of this work by the Ludwig-Maximilian University (LMU), the Office of Naval Research (ONR) under grant no. ONR N00014–19–1-2078 and the Strategic Environmental Research and Development Program (SERDP) under contract no. W912HQ19C0033 are gratefully acknowledged. The authors thank Stefan Huber for his help with the sensitivity measurement and Jasmin Lechner for graphical support.

4.5 References

- [1] D. M. Badgujar, M. B. Talawar, S. N. Asthana, P. P. Mahulikar, *J. Hazard. Mat.*, **2008**, *151*, 289.
- [2] M. B. Talawar, R. Sivabalan, T. Mukundan, H. Muthurajan, A. K. Sikder, B. R. Gandhe, A. S. Rao, *J. Hazard. Mat.*, **2009**, *161*, 589.
- [3] P. F. Pagoria, G. S. Lee, A. R. Mitchell, R. D. Schmidt, *Thermochimica Acta*, **2002**, *384*, 187–204.
- [4] L. Kukuljan, K. Kranjc, *Tetrahedron Lett.*, **2019**, *60*, 207–209.
- [5] V. Thottempudi, H. Gao, and J. M. Shreeve, *J. Am. Chem. Soc.* **2011**, *133*, *16*, 6464–6471.
- [6] T. M. Klapötke, M. Leroux, P. C. Schmid, J. Stierstorfer, *Chem. Asian J.* **2016**, *11*, 844.
- [7] T. M. Klapötke, *Chemistry of High-Energy Materials*, De Gruyter, Boston, Berlin, **2019**.
- [8] Z. Xu, G. Cheng, H. Yang, X. Ju, P. Yin, J. Zhang, J. M. Shreeve, *Angew. Chem. Int. Ed.* **2017**, *56*, 5877.
- [9] C. He, G. H. Imler, D. A. Parrish, J. M. Shreeve, *J. Mater. Chem. A*, **2018**, *6*, 16833-16837.
- [10] N. Fischer, D. Fischer, T. M. Klapötke, D. G. Piercey, J. Stierstorfer, *J. Mater. Chem.*, **2012**, *22*, 20418-20422.
- [11] G. Zhao, C. He, P. Yin, G. H. Imler, D. A. Parrish, J. M. Shreeve, *J. Am. Chem. Soc.*, **2018**, *140*, 3560–3563
- [12] Y. F. Golenko, M. A. Topchiy, A. F. Asachenko, M. S. Nechaev, D. V. Pleshakov, *Chin. J. Chem.*, **2017**, *35*, 98–102
- [13] D. Fischer, T. M. Klapötke, J. Stierstorfer, *Angew. Chem. Int. Ed.*, **2014**, *53*, 8172-8175.
- [14] D. Fischer, T. M. Klapötke, J. Stierstorfer, *Eur. J. Inorg. Chem.*, **2014**: 5808-5811.
- [15] M. D. Coburn, *J. Label. Compd. Rad.*, **1985**, *22* (2), 183-187.
- [16] S. E. Creegan, D. G. Piercey, *RSC Adv.*, **2020**, *10*, 39478.
- [17] H. Erhardt, A. P. Häring, A. Kotthaus, M. Roggel, M. L. Tong, P. Biallas, M. Jübermann, F. Mohr, S. F. Kirsch, *J. Org. Chem.*, **2015**, *80* (24), 12460-12469.

- [18] A. F. Hollemann, E. Wiberg, N. Wiberg, *Lehrbuch der anorganischen Chemie*, de Gruyter: New York, **2007**.
- [19] F. H. Allen, O. Kennard, D. G. Watson, L. Brammer, A. G. Orpen, R. Taylor, *J. Chem. Soc.* **1987**, 1–19.
- [20] A. G. Harter, T. M. Klapötke, J. Stierstorfer, M. Voggenreiter, X. Zeng, *ChemPlusChem*, **2021**, 86, 870.
- [21] A. G. Harter, T. M. Klapötke, C. Riedelsheimer, J. Stierstorfer, M. Voggenreiter, *Eur. J. Inorg. Chem.* **2021**, 23, 2241.
- [22] Test Methods According to the UN Recommendations on the Transport of Dangerous Goods, Manual of Test and Criteria, Fourth Revised Edition, United Nations Publication, New York and Geneva, 2003, ISBN 92–1-139087 7, Sales No. E.03.VIII. 2; 13.4.2 Test 3a (ii) BAM Fallhammer.
- [23] M. Suceška, EXPLO5 program, Zagreb, Croatia, **2018**.
- [24] M. Härtel, **2017**: Studies towards the gas-phase detection of hazardous materials by vapor pressure measurements with the transpiration method in combination with vacuum outlet GC/MS. Dissertation, LMU München: Fakultät für Chemie und Pharmazie.
- [25] Drzyzga, O., Gorontzy, T., Schmidt, A. *et al.* Toxicity of explosives and related compounds to the luminescent bacterium *Vibrio fischeri* NRRL-B-11177. *Arch. Environ. Contam. Toxicol.* **28**, 229–235 (1995).
- [26] C. J. Cao, M. S. Johnson, M. M. Hurley, T. M. Klapötke, *J. Propuls. Energet.*, **2012**, 5, 41–51.
- [27] A. McKay, G. F. Wright, *J. Am. Chem. Soc.*, **1947**, 69, 3028–3030.

4.6 Supplementary Information

4.6.1 X-ray diffraction

Crystal structure data were obtained by measurements on an Oxford Xcalibur3 diffractometer with a Spellman generator (voltage 50 kV, current 40 mA) and a Kappa CCD area for data collection using Mo-K α radiation ($\lambda = 0.71073 \text{ \AA}$) or a Bruker D8 Venture TXS diffractometer equipped with a multilayer monochromator, a Photon 2 detector and a rotation-anode generator (Mo-K α radiation). The data collection was performed using the CRYSTALIS RED software.^[S1] The solution of the structure was performed by direct methods and refined by full-matrix least-squares on F2 (SHELXT)^[S2] implemented in the OLEX2^[S3] software suite. The non-hydrogen atoms were refined anisotropically and the hydrogen atoms were located and freely refined. The absorption correction was carried out by a SCALE3ABSPACK multiscan method.^[S4] The DIAMOND2 plots shown with thermal ellipsoids at the 50% probability level and hydrogen atoms are shown as small spheres of arbitrary radius. The SADABS program embedded in the Bruker APEX3 software was used for multi-scan absorption corrections in all structures.^[S5]

Table S3. Crystallographic data and structure refinement details for the prepared compounds **2** and **3**. Crystallographic data and structure refinement details for the prepared compounds.

	2- Hydrazonemalonohydrazide (2)	2- Hydrazonemalonohydrazinium dinitrate · 0.25 H ₂ O (3)
Formula	C ₃ H ₈ N ₆ O ₂	4(C ₃ H ₁₀ N ₆ O ₂), 8(N O ₃), H ₂ O
FW [g mol ⁻¹]	160.15	1162.77
Crystal system	monoclinic	monoclinic
Space group	P21/c (No. 14)	P21/c (No. 14)
Color / Habit	yellow plate	colorless block
Size [mm]	0.07 x 0.11 x 0.31	0.02 x 0.04 x 0.04
a [Å]	6.2858(5)	7.3700(4)
b [Å]	15.5408(11)	16.8814(9)
c [Å]	6.9831(5)	9.5319(5)
α [°]	90	90
β [°]	103.118(7)	110.949(2)
γ [°]	90	90
V [Å ³]	664.35(9)	1107.53(10)
Z	4	1
ρ _{calc.} [g cm ⁻³]	1.601	1.743
μ [mm ⁻¹]	0.134	0.168
F(000)	336	602
λ _{MoKα} [Å]	0.71073	0.71073
T [K]	113	107
θ Min-Max [°]	3.3, 26.4	2.6, 26.4
Dataset	-7: 7 ; -16: 19 ; -8: 7	-9: 9 ; -21: 21 ; -11: 11
Reflections collected	4967	18977
Independent refl.	1354	2259
R _{int}	0.039	0.041
Observed reflections	1029	1931
Parameters	132	224
R ₁ (obs) ^[a]	0.0396	0.0441
wR ₂ (all data) ^[b]	0.0916	0.1209
S ^[c]	1.02	1.08
Resd. dens [e Å ⁻³]	-0.17, 0.27	-0.39, 0.56
Device type	Xcalibur Sapphire3	Bruker D8 Venture
Solution	SIR-92	SIR-92
Refinement	SHELXL-2018	SHELXL-2018
Absorption correction	Multi-Scan	Multi-Scan
CCDC	2149590	2149591

^[a]R₁ = $\frac{\sum||F_0|-|F_c||}{\sum|F_0|}$; ^[b]wR₂ = $\frac{[\sum[w(F_0^2-F_c^2)^2]/\sum[w(F_0^2)]]^{1/2}}{[\sigma^2(F_0^2)+(xP)^2+yP]^{-1}}$ and $P=(F_0^2+2F_c^2)/3$; ^[c]S = $\{\sum[w(F_0^2-F_c^2)^2]/(n-p)\}^{1/2}$ (n = number of reflections; p = total number of parameters).

Table S 4. Crystallographic data and structure refinement details for the prepared compounds **4** and **5**.

	2-Hydrazone-malonohydrazinium dichloride monohydrate (4)	2-Hydrazone-malonohydrazinium diperchlorate monohydrate (5)
Formula	C ₃ H ₁₀ N ₆ O ₂ , 2(Cl), H ₂ O	C ₃ H ₁₀ N ₆ O ₂ , 2(Cl O ₄), H ₂ O
FW [g mol ⁻¹]	251.09	379.09
Crystal system	triclinic	monoclinic
Space group	P-1 (No. 2)	P21/n (No. 14)
Color / Habit	colorless block	colorless block
Size [mm]	0.26 x 0.29 x 0.46	0.33 x 0.44 x 0.73
a [Å]	7.1408(5)	7.5892(5)
b [Å]	8.0780(6)	9.0429(5)
c [Å]	9.1789(6)	18.7124(10)
α [°]	106.400(6)	90
β [°]	91.970(6)	99.935(6)
γ [°]	96.736(6)	90
V [Å ³]	503.15(6)	1264.94(13)
Z	2	4
ρ _{calc.} [g cm ⁻³]	1.657	1.991
μ [mm ⁻¹]	0.641	0.592
F(000)	260	776
λ _{MoKα} [Å]	0.71073	0.71073
T [K]	100	105
θ Min-Max [°]	2.3, 26.4	2.2, 26.4
Dataset	-6: 8 ; -7: 10 ; -10: 11	-9: 9 ; -5: 11 ; -23: 13
Reflections collected	3011	4478
Independent refl.	2053	2585
R _{int}	0.015	0.022
Observed reflections	1865	2159
Parameters	175	229
R ₁ (obs) ^[a]	0.0278	0.0347
wR ₂ (all data) ^[b]	0.0719	0.0873
S ^[c]	1.07	1.06
Resd. dens [e Å ⁻³]	-0.33, 0.35	-0.41, 0.41
Device type	Xcalibur Sapphire3	Xcalibur Sapphire3
Solution	SIR-92	SIR-92
Refinement	SHELXL-2018	SHELXL-2018
Absorption correction	Multi-Scan	Multi-Scan
CCDC	2149591	2149591

^[a]R₁ = $\frac{\sum ||F_o| - |F_c||}{\sum |F_o|}$; ^[b]wR₂ = $\frac{[\sum [w(F_o^2 - F_c^2)^2] / \sum [w(F_o^2)]]^{1/2}}{[\sigma^2(F_o^2) + (xP)^2 + yP]^{-1}}$ and $P = (F_o^2 + 2F_c^2) / 3$; ^[c]S = $\{\sum [w(F_o^2 - F_c^2)^2] / (n - p)\}^{1/2}$ (n = number of reflections; p = total number of parameters).

Table S 3. Crystallographic data and structure refinement details for the prepared compounds **7** and **8**.

	3-Carbonylazido-1 <i>H</i> -1,2,4-triazol-5-one (7)	3-Carboxyl-1 <i>H</i> -1,2,4-triazol-5-one monohydrate (8)
Formula	C3 H2 N6 O2	C3 H3 N3 O3, H2 O
FW [g mol ⁻¹]	154.11	147.10
Crystal system	monoclinic	monoclinic
Space group	P21/c (No. 14)	P21/c (No. 14)
Color / Habit	yellow needle	colorless block
Size [mm]	0.07 x 0.13 x 0.50	0.04 x 0.05 x 0.06
a [Å]	8.9958(18)	8.6849(4)
b [Å]	4.9646(8)	4.9774(2)
c [Å]	12.909(2)	12.8833(5)
α [°]	90	90
β [°]	98.963(16)	96.624(1)
γ [°]	90	90
V [Å ³]	569.48(17)	553.20(4)
Z	4	4
ρ _{calc.} [g cm ⁻³]	1.797	1.766
μ [mm ⁻¹]	0.153	0.164
F(000)	312	304
λ _{MoKα} [Å]	0.71073	0.71073
T [K]	105	102
θ Min-Max [°]	2.3, 26.4	3.2, 26.4
Dataset	-4: 11 ; -6: 6 ; -16: 14	-10: 10 ; -6: 6 ; -16: 16
Reflections collected	2051	8781
Independent refl.	1161	1130
R _{int}	0.024	0.030
Observed reflections	847	998
Parameters	108	108
R ₁ (obs) ^[a]	0.0431	0.0429
wR ₂ (all data) ^[b]	0.1085	0.1169
S ^[c]	1.05	1.09
Resd. dens [e Å ⁻³]	-0.22, 0.25	-0.22, 0.93
Device type	Xcalibur Sapphire3	Bruker D8 Venture
Solution	SIR-92	SIR-92
Refinement	SHELXL-2018	SHELXL-2018
Absorption correction	Multi-Scan	Multi-Scan
CCDC	2149591	2149591

^[a]R₁ = $\sum ||F_o| - |F_c|| / \sum |F_o|$; ^[b]wR₂ = $[\sum [w(F_o^2 - F_c^2)^2] / \sum [w(F_o^2)]]^{1/2}$; $w = [\sigma^2(F_o^2) + (xP)^2 + yP]^{-1}$ and $P = (F_o^2 + 2F_c^2) / 3$; ^[c]S = $\{\sum [w(F_o^2 - F_c^2)^2] / (n-p)\}^{1/2}$ (n = number of reflections; p = total number of parameters).

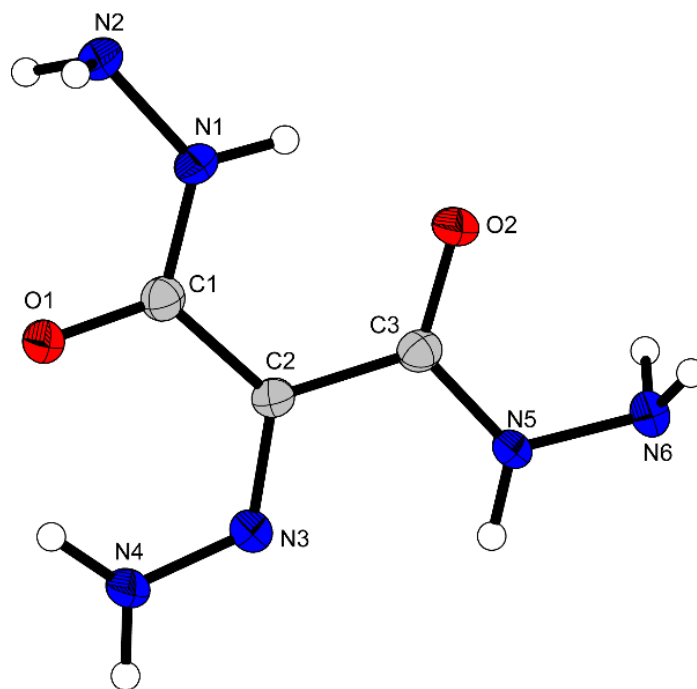


Figure S 1: X-ray structure of compound **2**; Thermal ellipsoids are drawn at the 50% probability level and hydrogen atoms are shown as small spheres of arbitrary radius.

2-Hydrazonemalonohydrazide (**2**) crystallizes in the monoclinic space group $P2_1/c$ with a density of 1.601 g/cm^3 at 113 K. The cell volume is $664.35(9) \text{ \AA}^3$ with four formula units per cell.

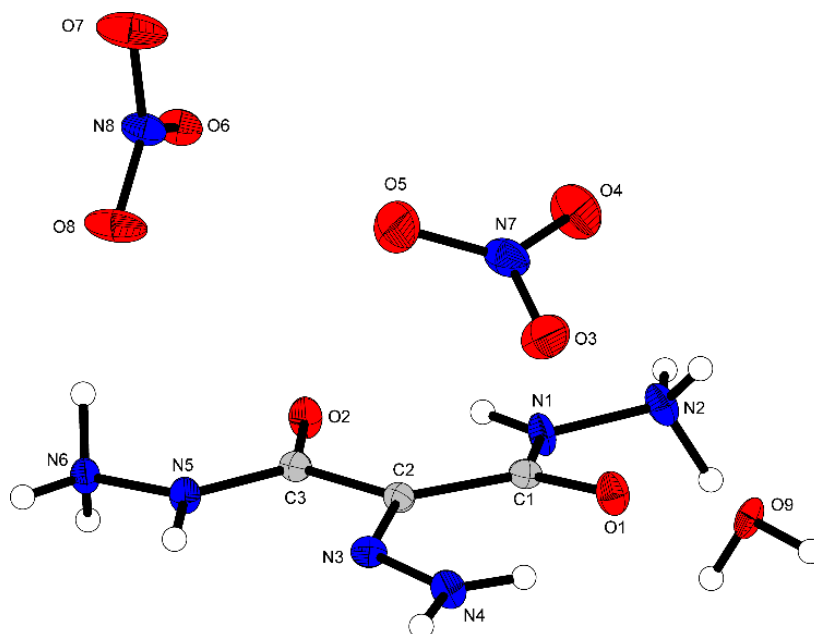


Figure S 2: X-ray structure of compound **3**; Thermal ellipsoids are drawn at the 50% probability level and hydrogen atoms are shown as small spheres of arbitrary radius.

2-Hydrazone-malonohydrazinium dinitrate · 0.25 H₂O (**3**) crystallizes in the monoclinic space group $P2_1/c$ with a density of 1.743 g/cm³ at 107 K. The cell volume is 1107.53(10) Å³ with one formula unit per cell.

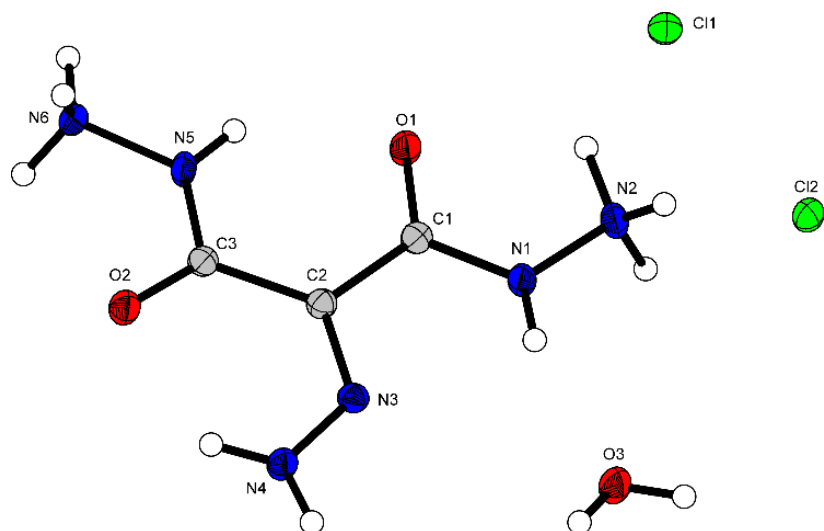


Figure S 3: X-ray structure of compound **4**; Thermal ellipsoids are drawn at the 50% probability level and hydrogen atoms are shown as small spheres of arbitrary radius.

Compound **4** crystallizes in the triclinic space group $P-1$ with a density of 1.657 g cm⁻³ at 100 K and two formula units per unit cell. The cell volume is 503.15(6) Å³ and the cell constants are $a = 7.1408(5)$ Å, $b = 8.0780(6)$ Å and $c = 9.1789(6)$ Å.

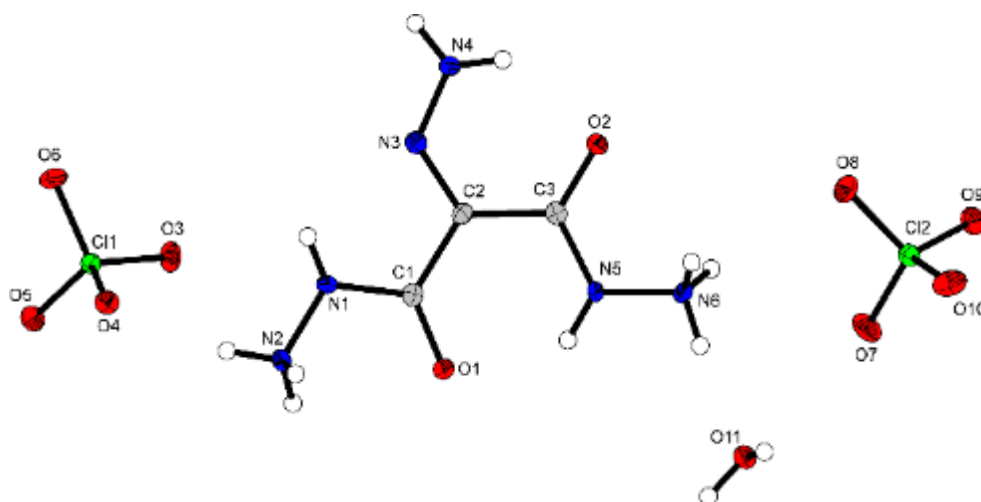


Figure S 4: X-ray structure of compound **5**; Thermal ellipsoids are drawn at the 50% probability level and hydrogen atoms are shown as small spheres of arbitrary radius.

Compound **5** crystallizes in the monoclinic space group $P2_1/n$ with a density of 1.991 g cm^{-3} at 105 K and four formula units per unit cell (figure 6). The cell volume is $1264.94(13) \text{ \AA}^3$ and the cell constants are $a = 7.5892(5) \text{ \AA}$, $b = 9.0429(5) \text{ \AA}$ and $c = 18.7124(10) \text{ \AA}$.

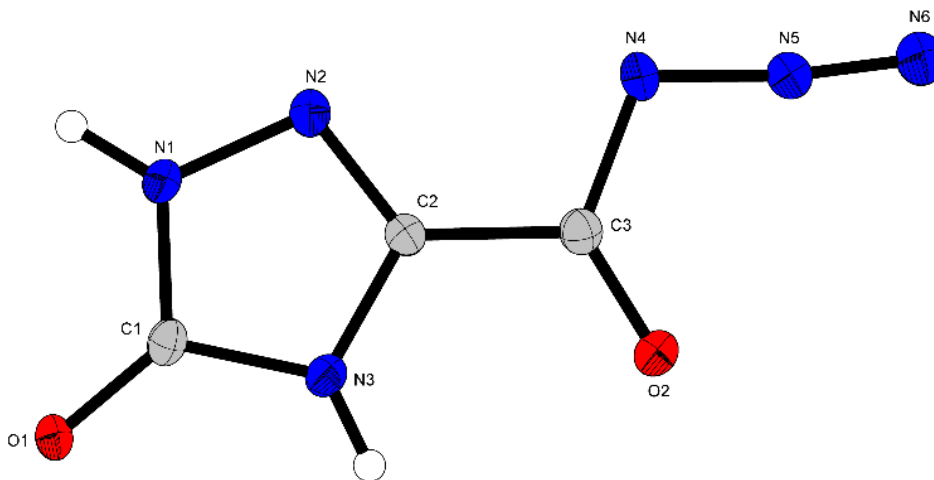
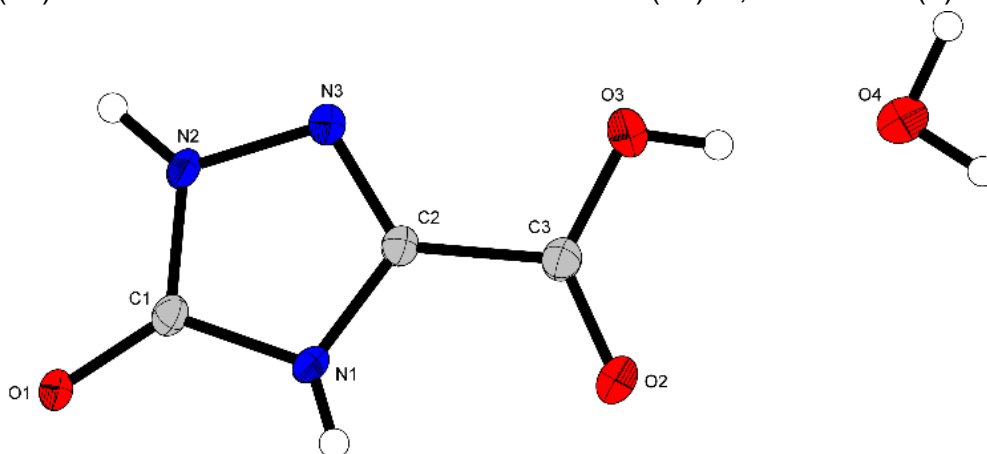


Figure S 5: X-ray structure of compound **7**; Thermal ellipsoids are drawn at the 50% probability level and hydrogen atoms are shown as small spheres of arbitrary radius.

Compound **7** crystallizes in the monoclinic space group $P2_1/c$ with a density of 1.797 g cm^{-3} at 105 K and four formula units per unit cell (figure 7). The cell volume is $569.48(17) \text{ \AA}^3$ and the cell constants are $a = 8.9958(18) \text{ \AA}$, $b = 4.9646(8) \text{ \AA}$ and $c =$



$12.909(2) \text{ \AA}$.

Figure S 5: X-ray structure of compound **8**; Thermal ellipsoids are drawn at the 50% probability level and hydrogen atoms are shown as small spheres of arbitrary radius.

Compound **8** crystallizes in the monoclinic space group $P2_1/c$ with a density of 1.766 g cm^{-3} at 102 K and four formula units per unit cell (figure 8). The cell volume is $553.20(4) \text{ \AA}^3$ and the cell constants are $a = 8.6849(4) \text{ \AA}$, $b = 4.9774(2) \text{ \AA}$ and $c = 12.8833(5) \text{ \AA}$.

4.6.2 Experimental part and general methods

Caution! Geminal diazides are energetic materials with high sensitivities towards shock and friction. Therefore, proper security precautions (safety glass, face shield, earthed equipment and shoes, Kevlar gloves and ear plugs) have to be applied while synthesizing and handling the described compounds.

Chemicals and solvents were employed as received (Sigma-Aldrich, Acros, TCI, Spirochem AG). ^1H , ^{13}C and ^{14}N spectra were recorded using a Bruker AMX 400 instrument. The chemical shifts quoted in ppm refer to tetramethylsilane (^1H , ^{13}C) and nitromethane (^{14}N). Decomposition temperatures were determined on a Mettler Toledo DSC822e at a heating rate of $5\text{ }^\circ\text{C min}^{-1}$ using $40\ \mu\text{L}$ aluminum crucibles and nitrogen purge gas at a flow rate of 30 mL min^{-1} . Evaluations of thermal behavior were performed using the STAR^e Software Version 16.20. Infrared (IR) spectra were recorded using a Perkin-Elmer Spektrum One FT-IR instrument. Raman spectra were obtained using a Bruker MultiRam FT Raman spectrometer and a neodymium-doped yttrium aluminum garnet (Nd:YAG) laser ($\lambda = 1064\text{ nm}$, 1074 mW). Elemental analyses were performed with an Elementar Vario el by pyrolysis of the sample and subsequent analysis of formed gases (standard deviation liquids: $\pm 0.5\%$). The sensitivity data were collected using a BAM (Bundesanstalt für Materialforschung) drophammer^[S6] according to STANAG 4489^[S7] modified instruction^[S8] and a BAM friction tester^[S9] according to STANAG 4487^[S10] modified instruction. The classification of the tested compounds results from the 'UN Recommendations on the Transport of Dangerous Goods'.^[S11]

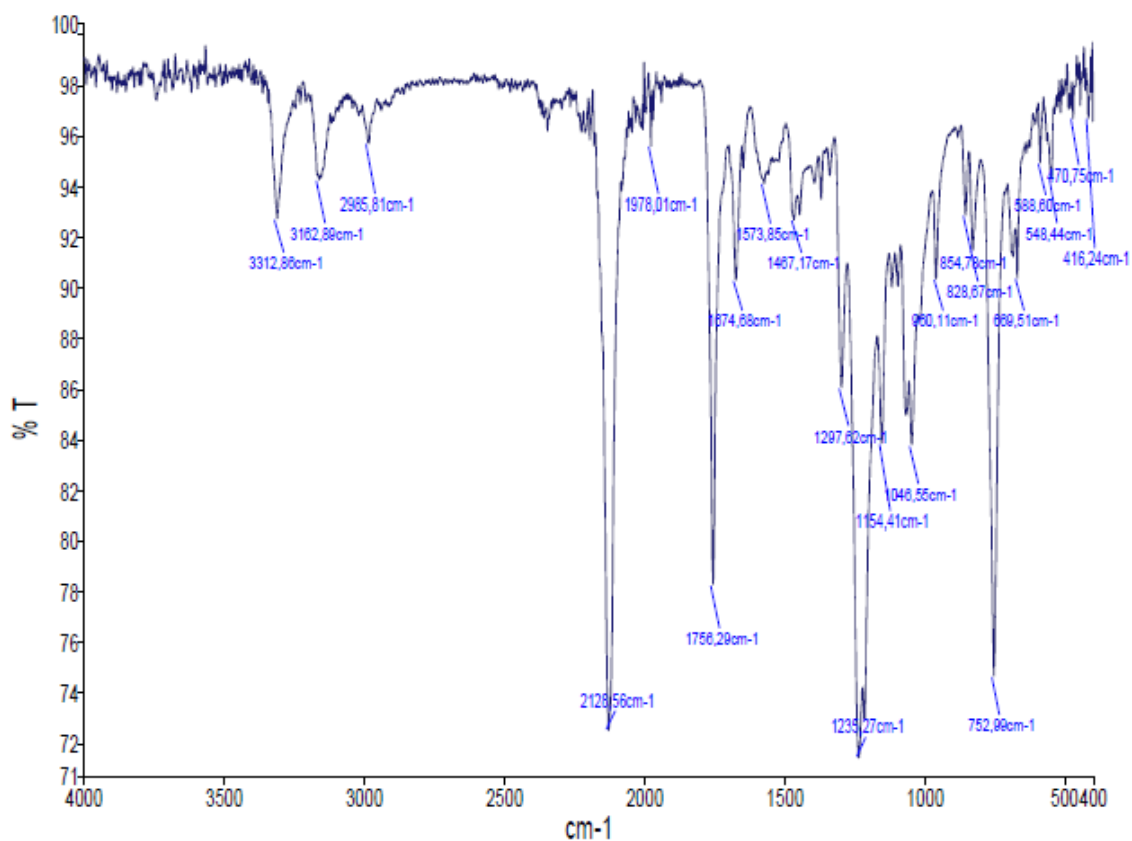


Figure S 6: IR Spektrum of compound **6** measured in chloroform.

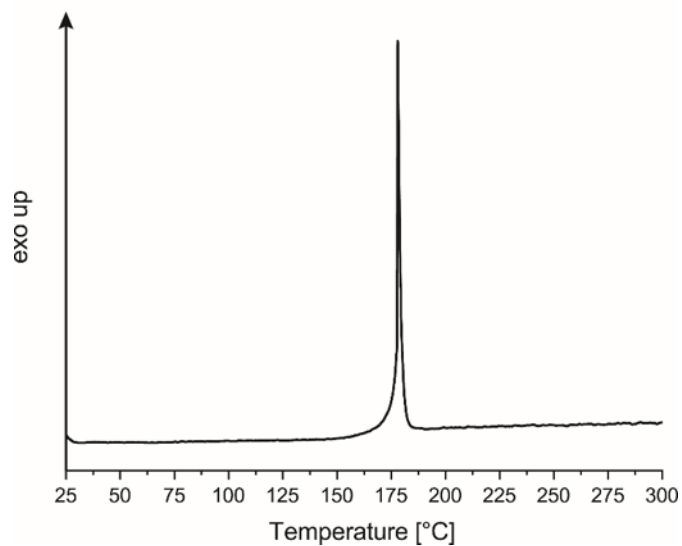


Figure S 7: DTA plot of compound **10** measured with a heating rate of 5 K·min⁻¹.

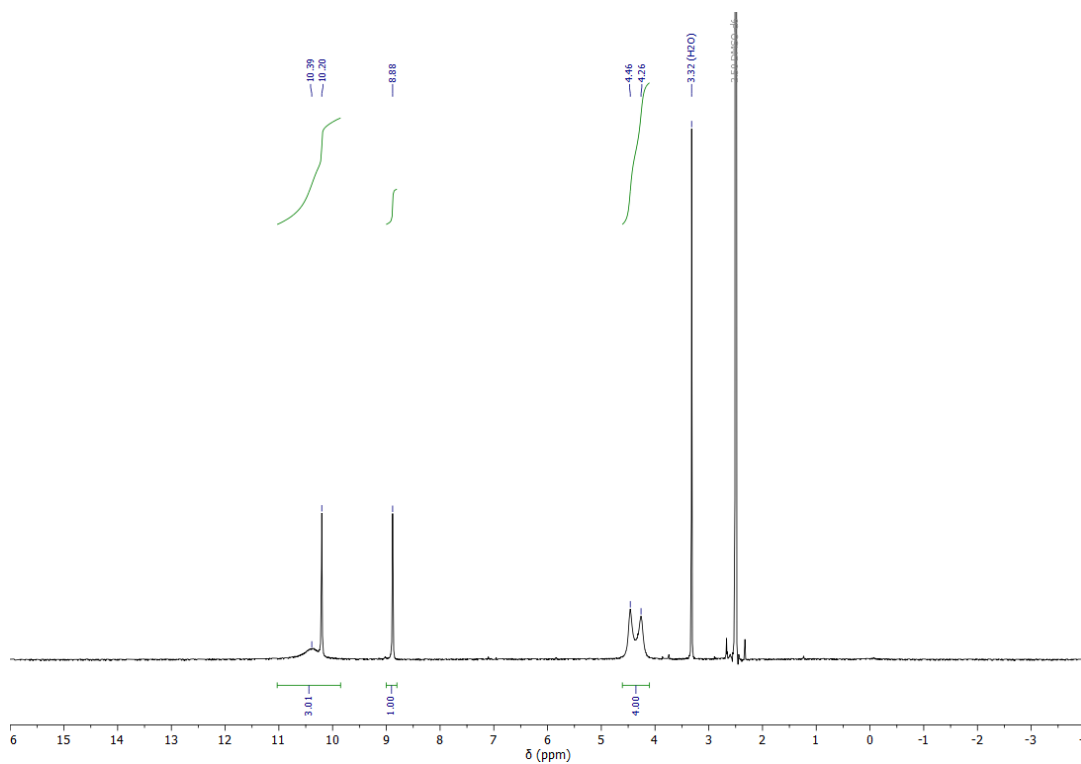


Figure S 8: ^1H NMR spectrum of compound 2 in $\text{DMSO-}d_6$.

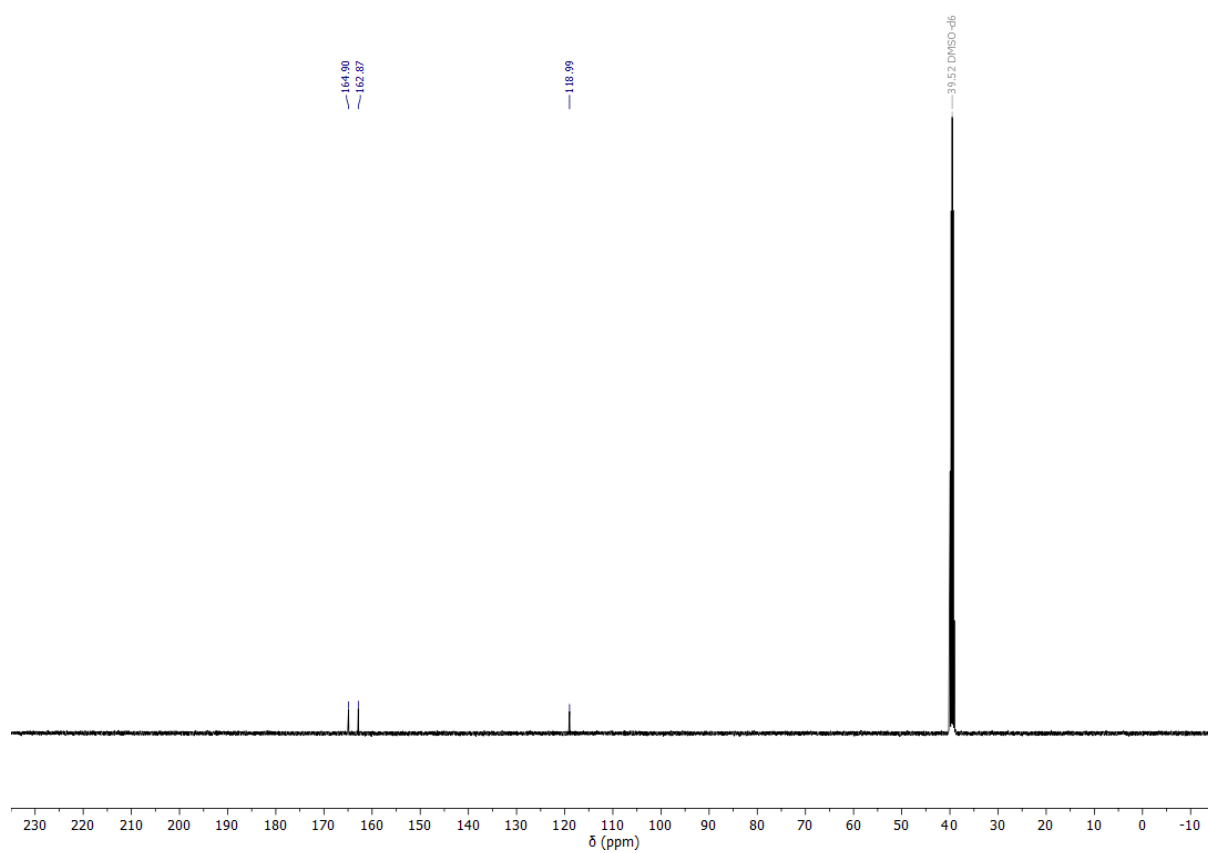


Figure S 9: ^{13}C NMR spectrum of compound 2 in $\text{DMSO-}d_6$.

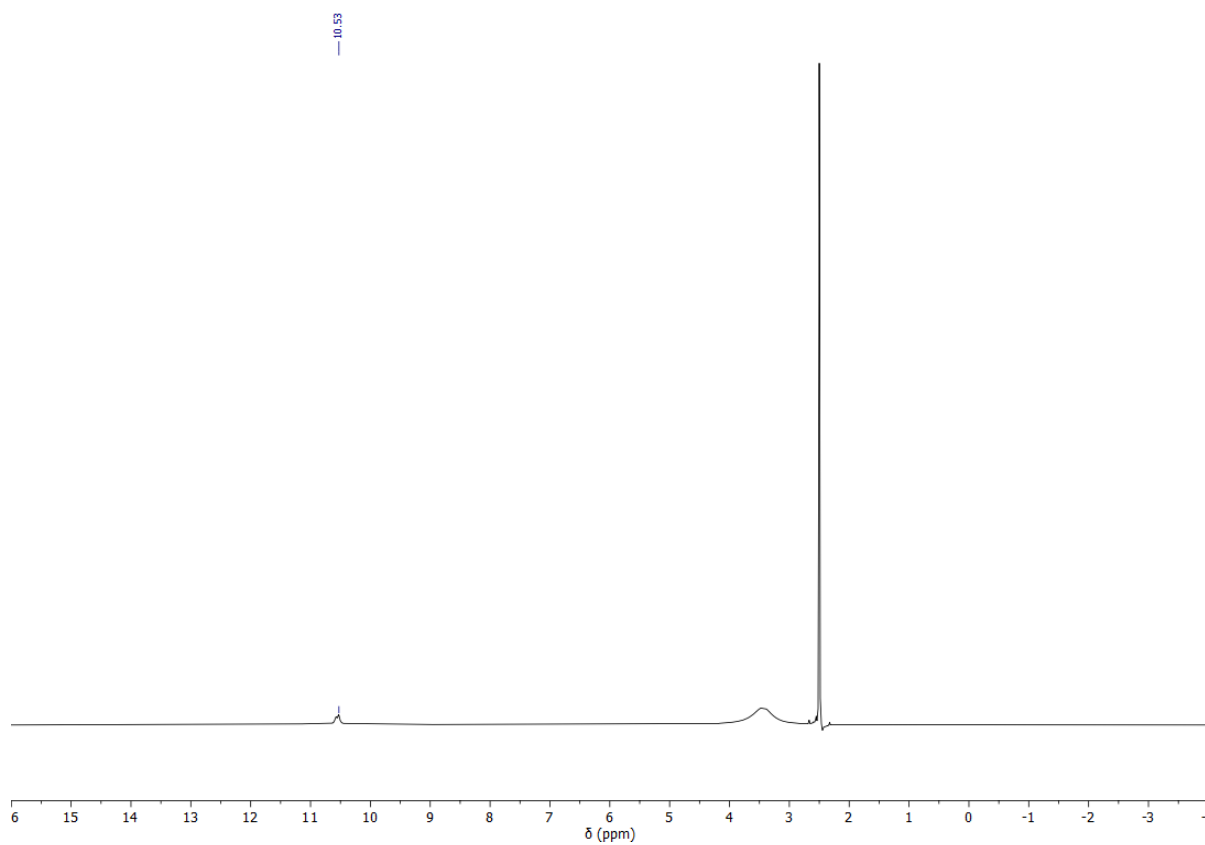


Figure S 10: ^1H NMR spectrum of compound **3** in $\text{DMSO-}d_6$.

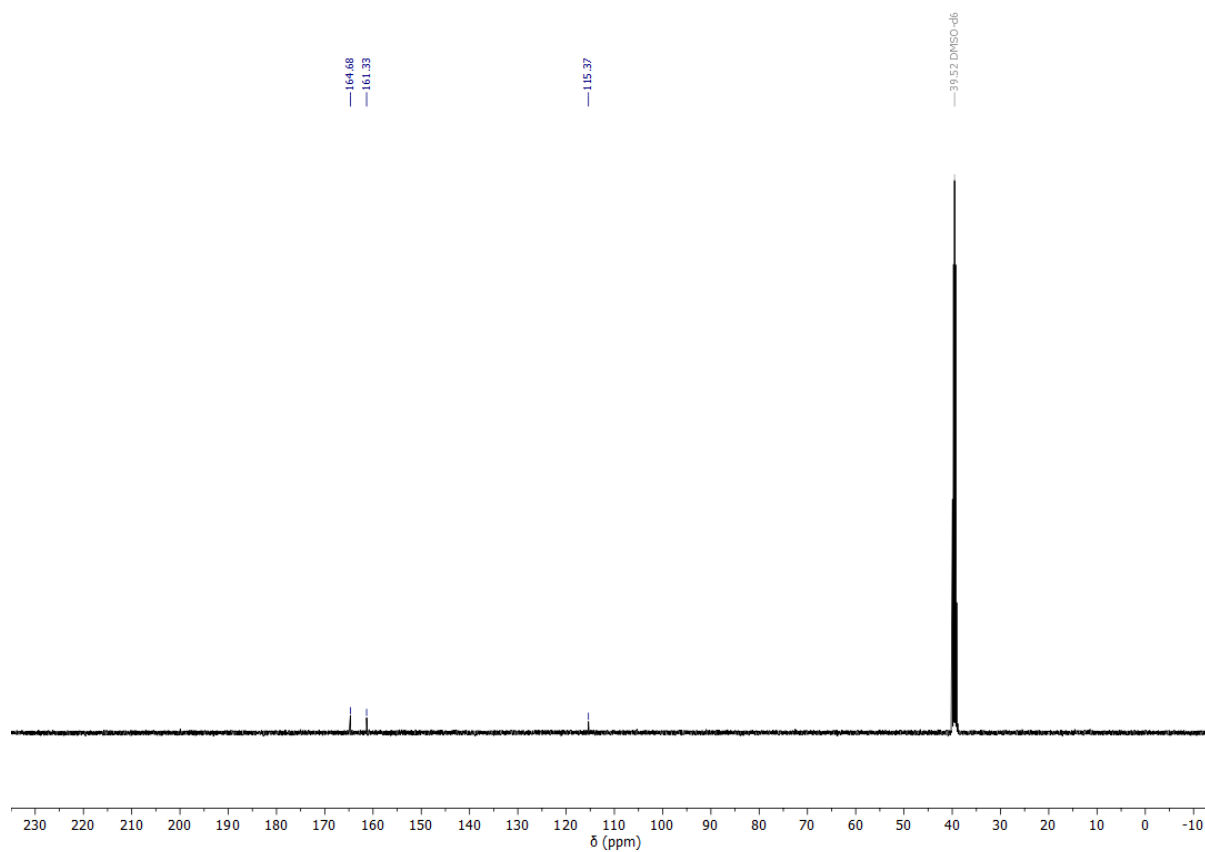


Figure S 11: ^{13}C NMR spectrum of compound **3** in $\text{DMSO-}d_6$.

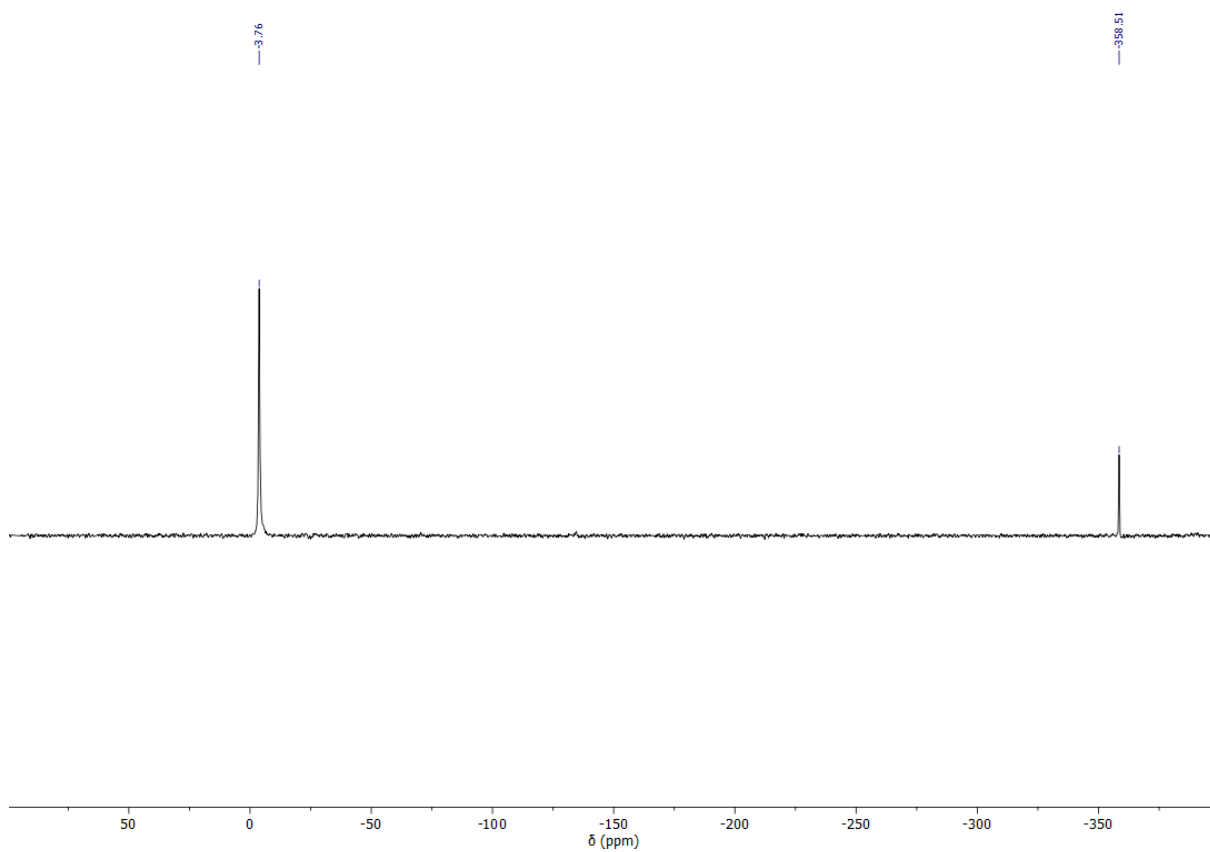


Figure S 12: ¹⁴N NMR spectrum of compound 3 in DMSO-d₆.

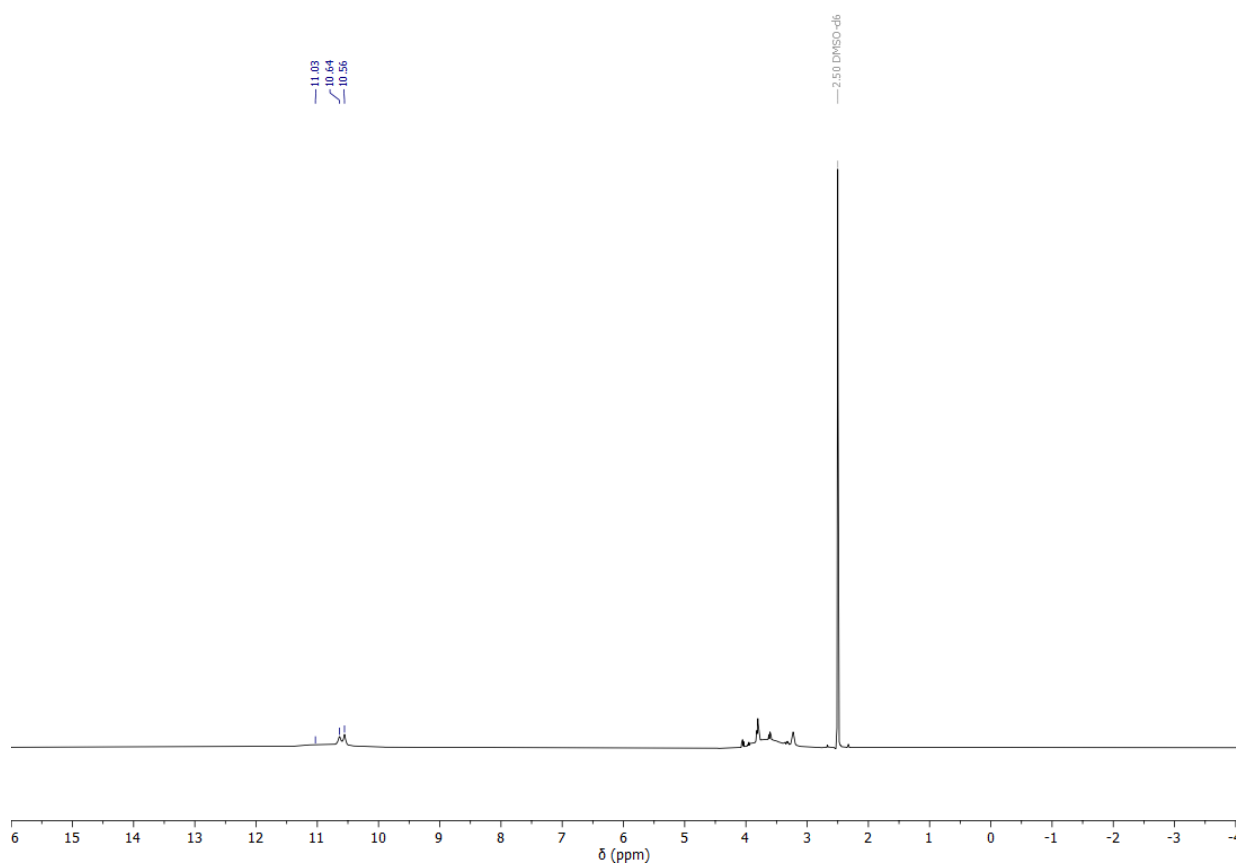


Figure S 13: ^1H NMR spectrum of compound **4** in $\text{DMSO-}d_6$.

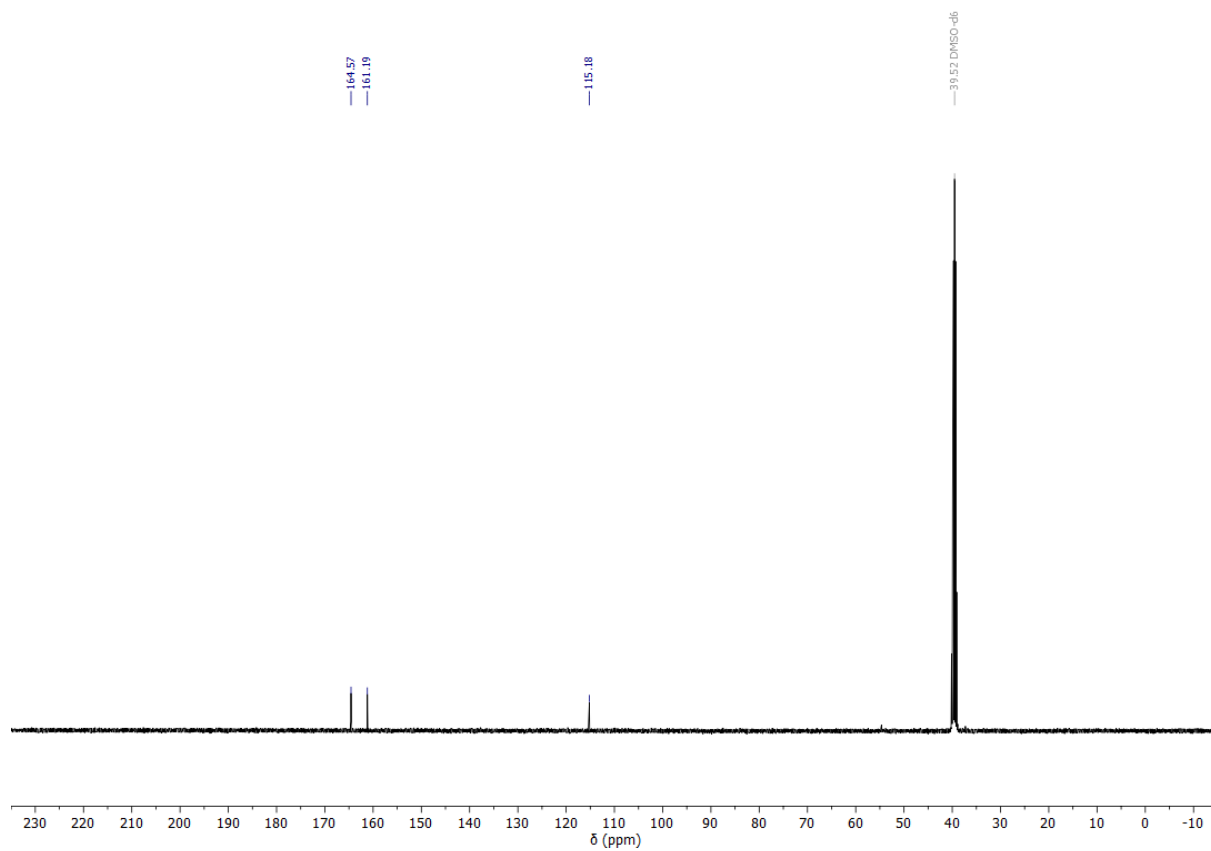


Figure S 14: ^1H NMR spectrum of compound **4** in $\text{DMSO-}d_6$.

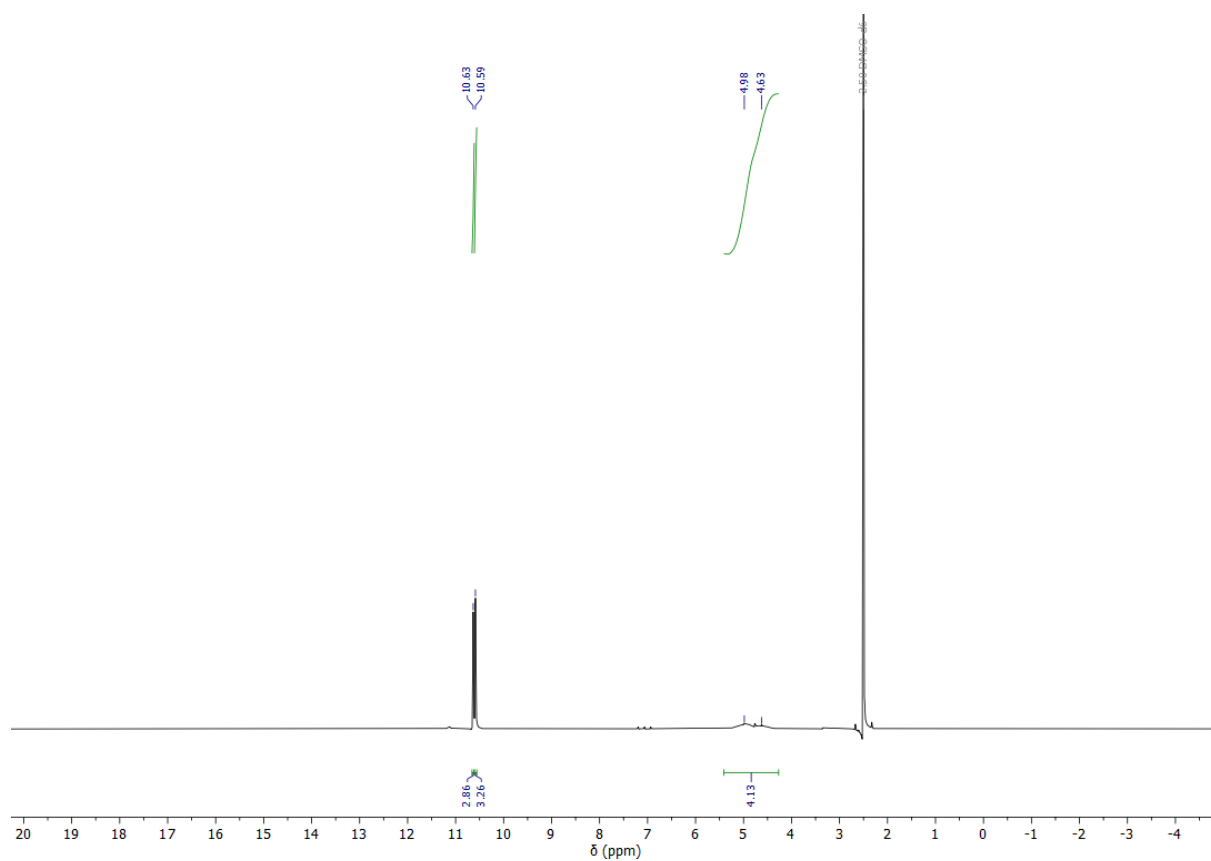


Figure S 15: ^1H NMR spectrum of compound **5** in $\text{DMSO-}d_6$.

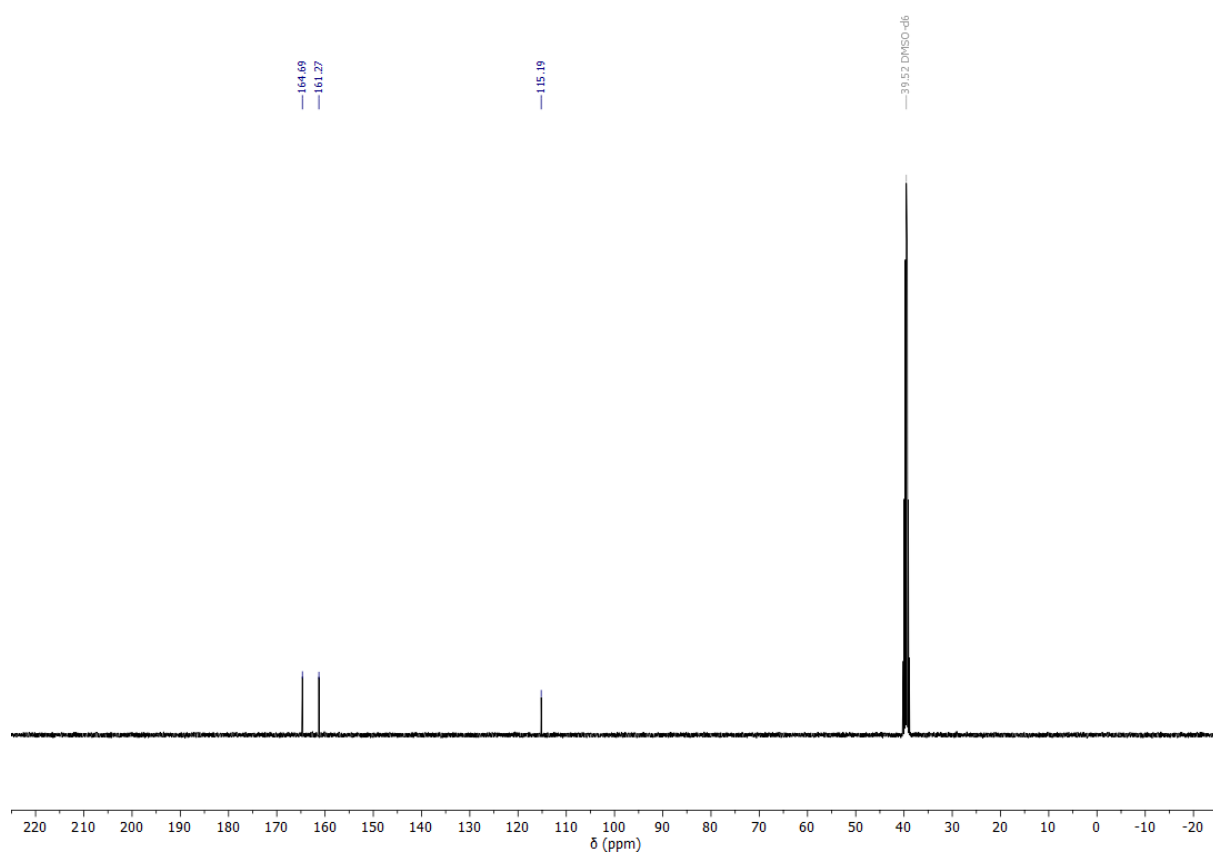


Figure S 16: ^{13}C NMR spectrum of compound **5** in $\text{DMSO-}d_6$.

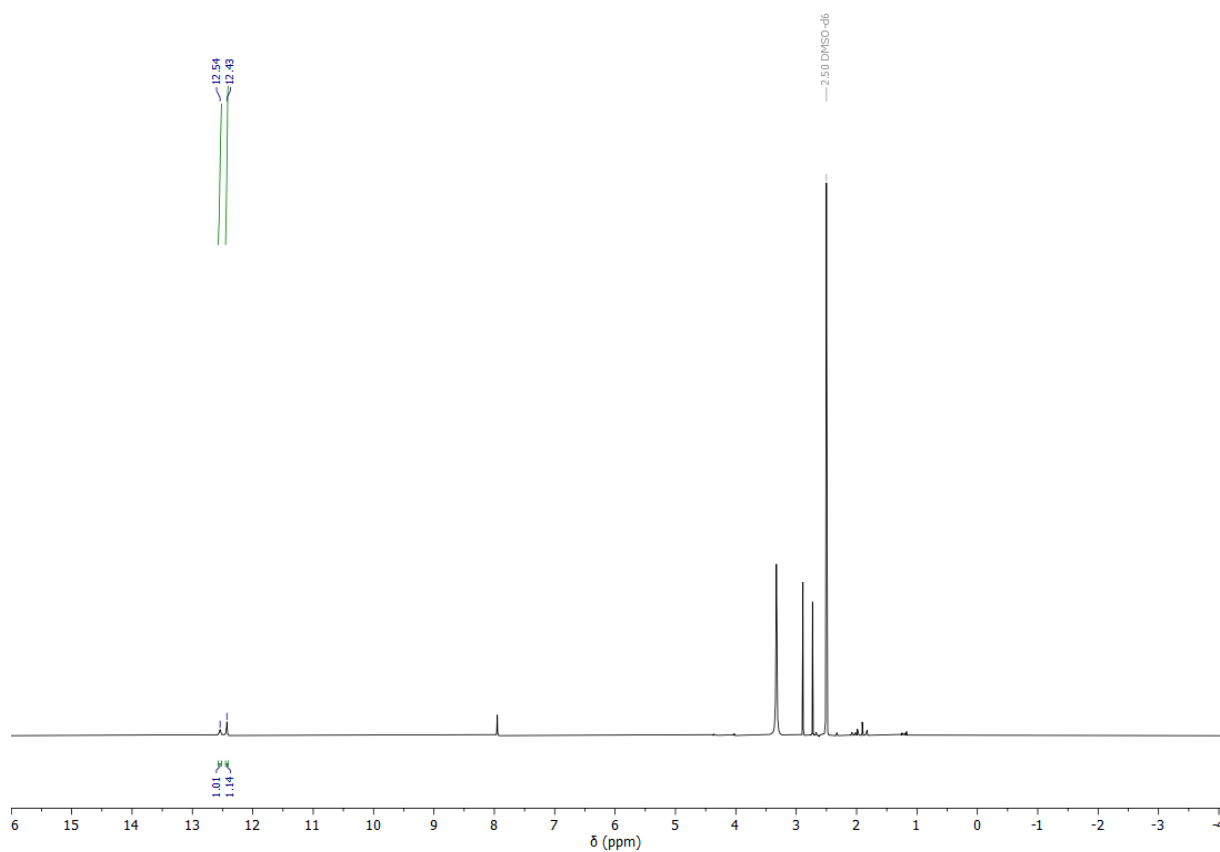


Figure S 17: ^1H NMR spectrum of compound **8** in $\text{DMSO-}d_6$.

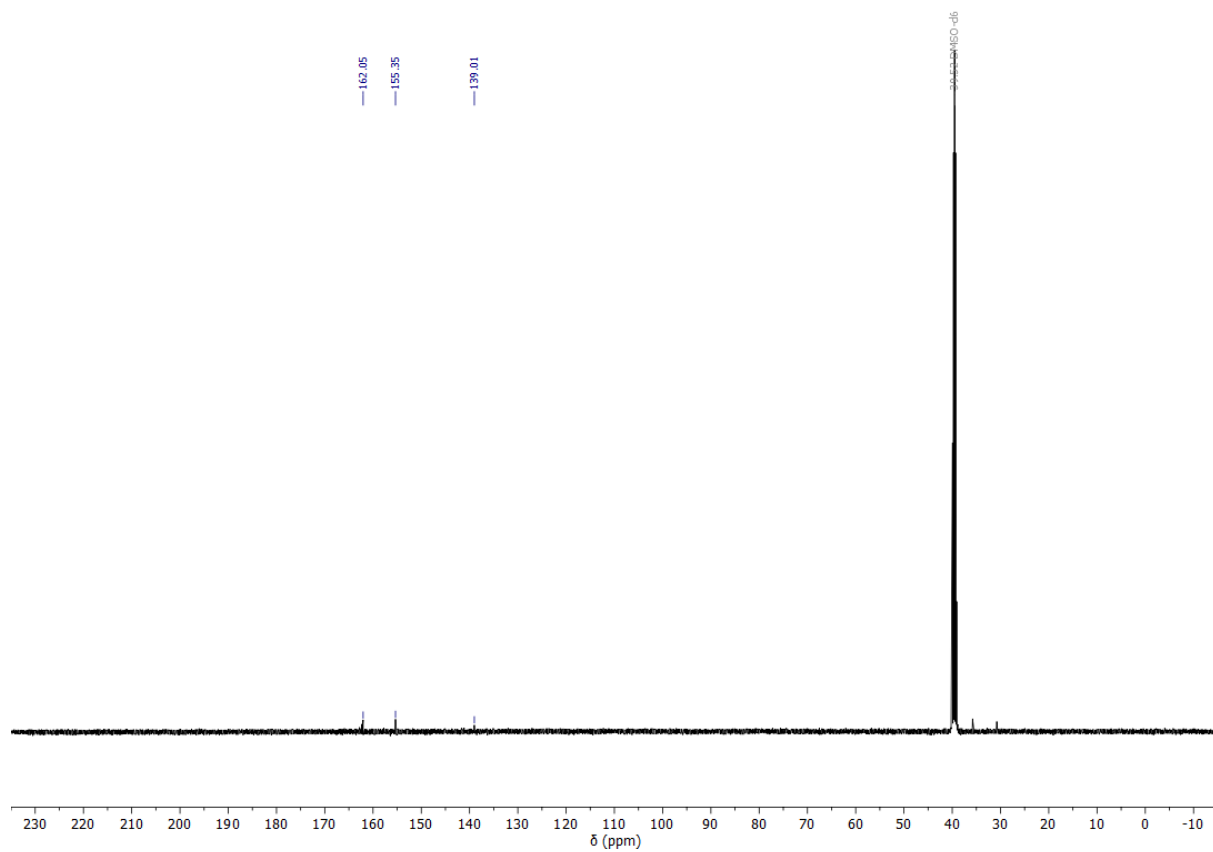


Figure S 18: ^{13}C NMR spectrum of compound **8** in $\text{DMSO-}d_6$.

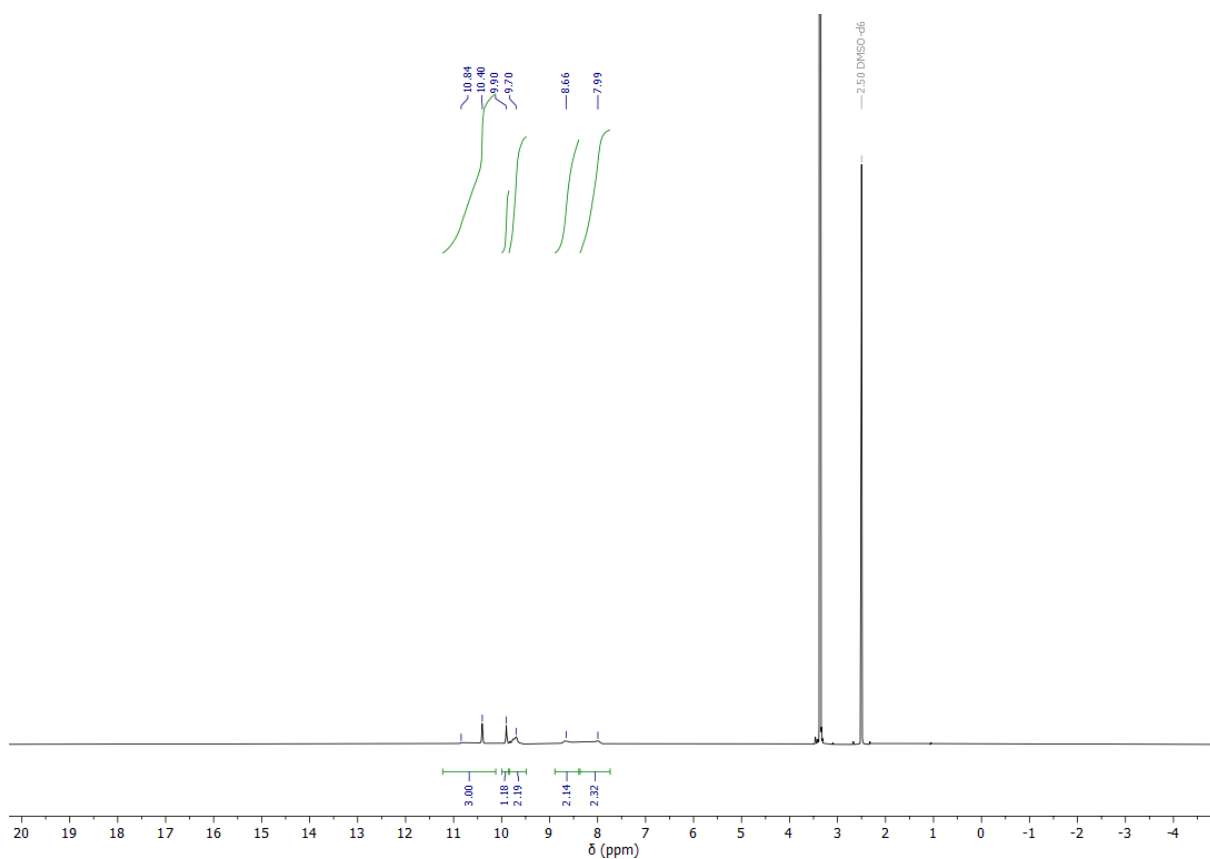


Figure S 19: ^1H NMR spectrum of compound **9** in $\text{DMSO-}d_6$.

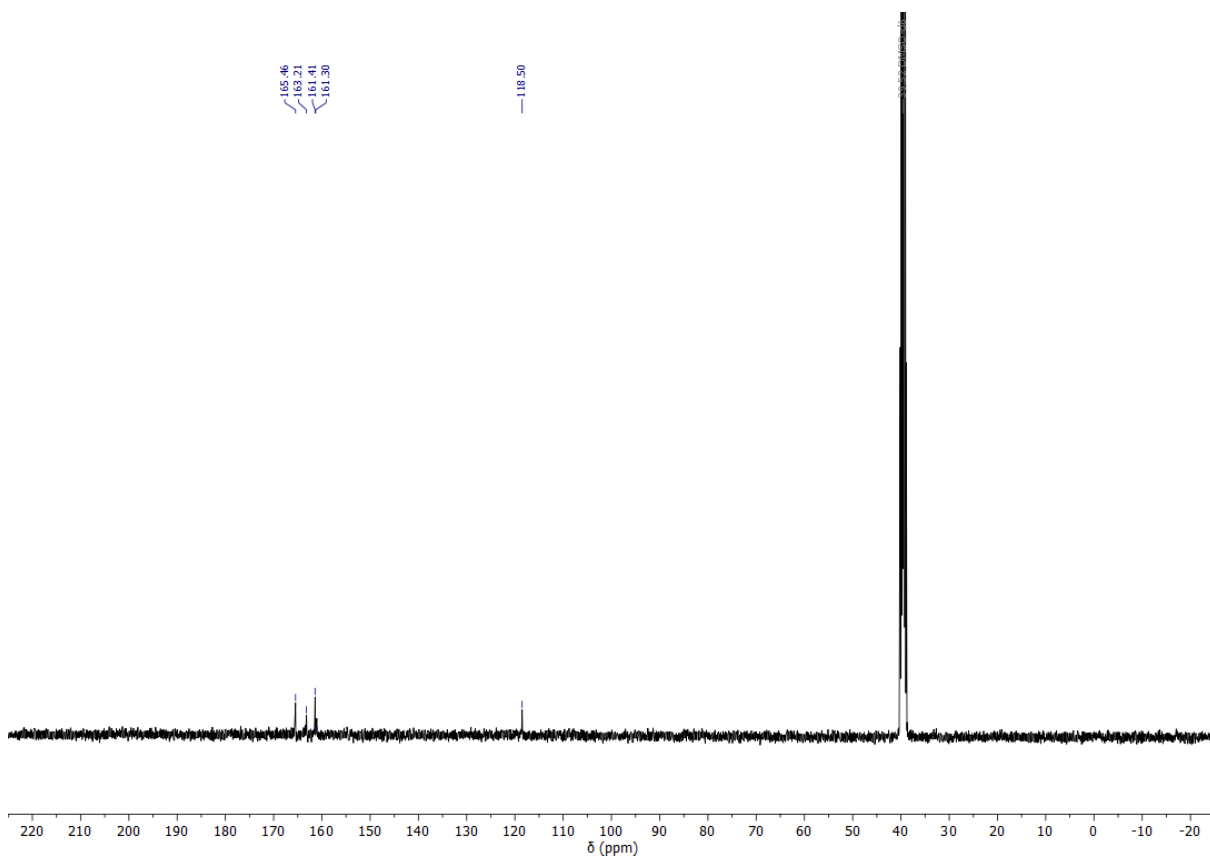


Figure S 20: ^{13}C NMR spectrum of compound **9** in $\text{DMSO-}d_6$.

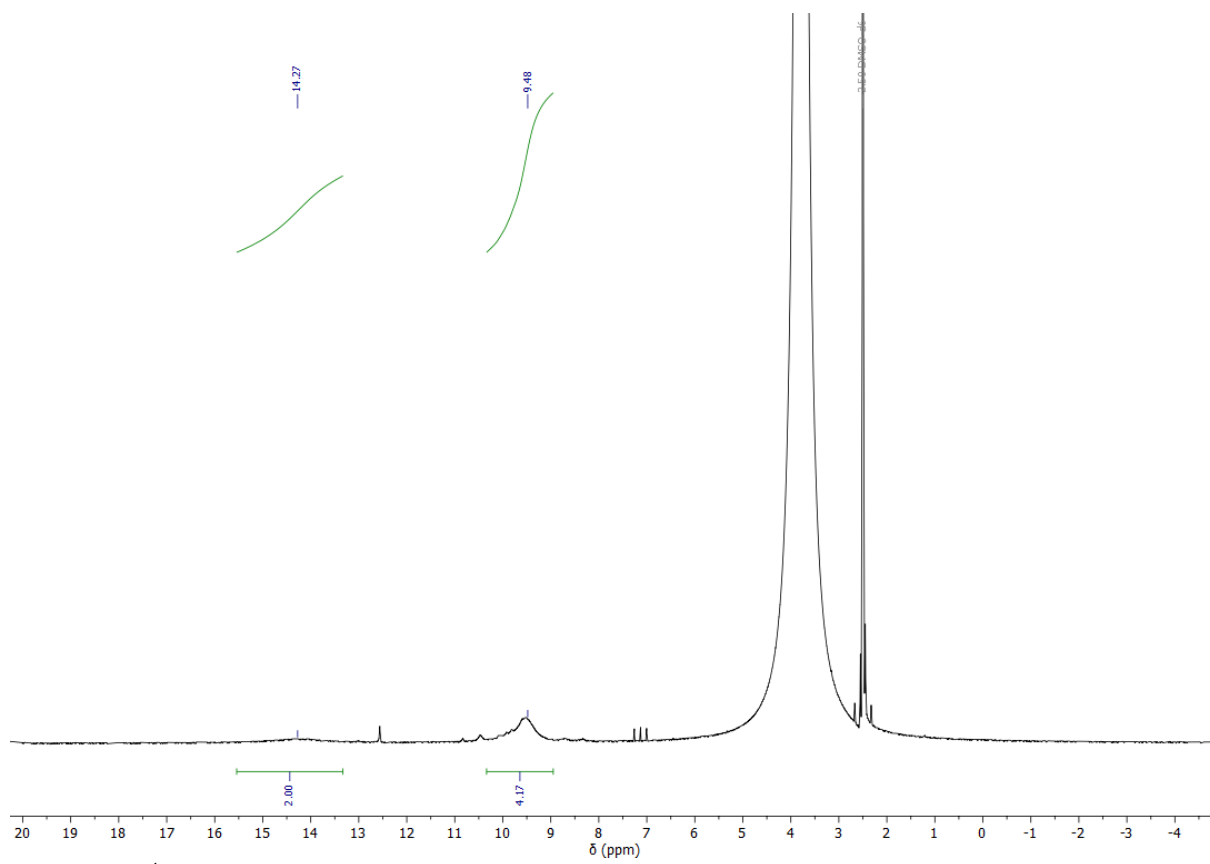


Figure S 21: ^1H NMR spectrum of compound **10** in $\text{DMSO-}d_6$.

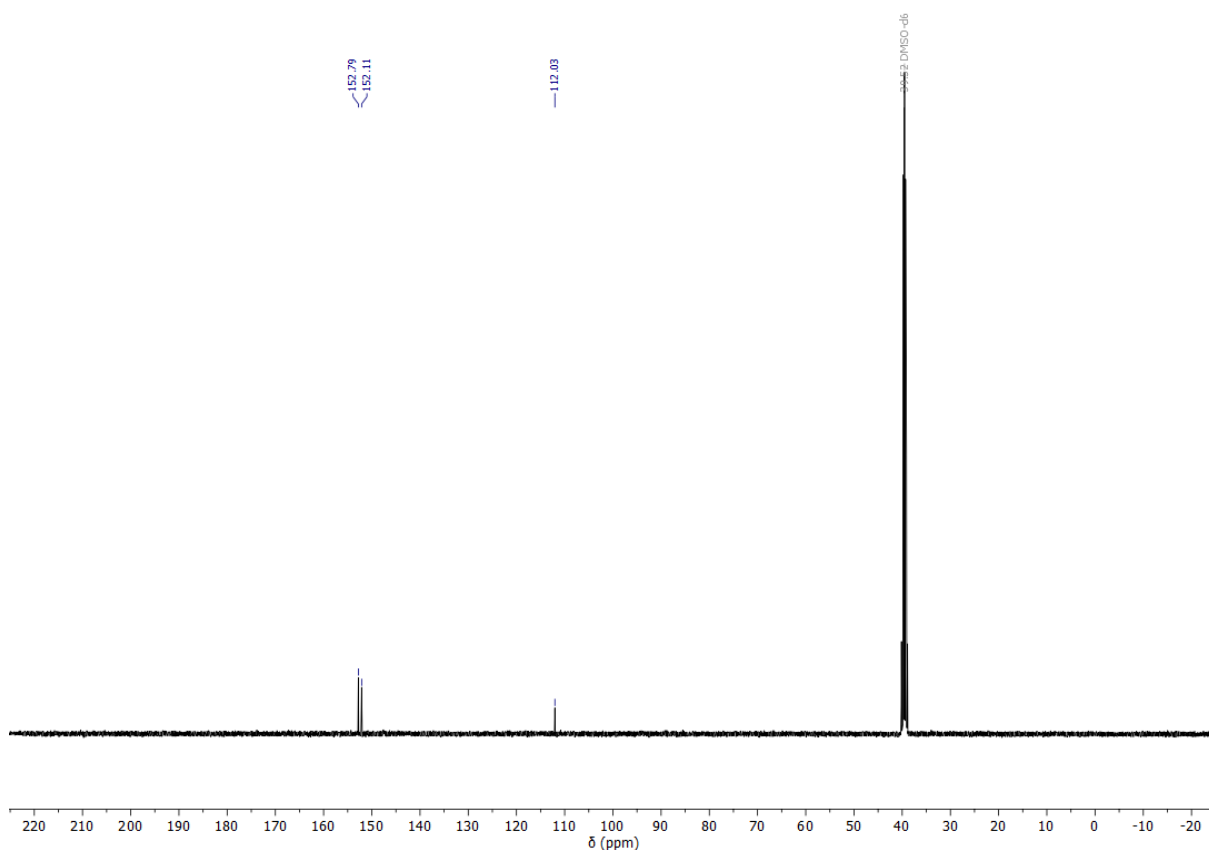


Figure S 22: ^{13}C NMR spectrum of compound **10** in $\text{DMSO-}d_6$.

4.6.3 Heat of formation calculation and thermal analysis

The atomization was used to determine the heat of formation of **1–6** using the atom energies in Table S3.

$$\Delta_f H^\circ(\text{g, M, 298}) = H(\text{molecule, 298}) - \sum H^\circ(\text{atoms, 298}) + \sum \Delta_f H^\circ(\text{atoms, 298})$$

Table S3: CBS-4M electronic enthalpies for atoms C, H, N and O and their literature values.

	$-H^{98} / a.u.$	$\Delta_f H^\circ_{\text{gas}}[\text{S12}]$
H	0.500991	217.998
C	37.786156	716.68
N	54.522462	472.68
O	74.991202	249.18

The Gaussian16 program package was used to calculate room temperature enthalpies on the CBS-4M level of theory.^[S13] In order to obtain the energy of formation for the

solid phase of **2**, the Trouton's Rule has to be applied ($\Delta H_{\text{sub}} = 188 \cdot T_m$). As compound **1** is liquid, a different factor is applied ($\Delta H_{\text{sub}} = 90 \cdot T_m$).

Table S4: Heat of formation calculation results for compounds **2–5, 7** and **8**.

<i>M</i>	$-H^{298}$ [a] [a.u.]	$\Delta_f H^\circ(\text{g, M})$ [b] [kJ mol ⁻¹]	$\Delta_f H^\circ(\text{s})$ [c] [kJ mol ⁻¹]	Δn	$\Delta_f U(\text{s})$ [e] [kJ kg ⁻¹]
2	597.21415	-59.3	-29.6	-8.0	-61.1
3	597.21415	1641.3	224.2	-13.0	896.0
5	597.21415	1641.3	-239.2	-14.0	-566.3
9	1302.977801	274.8	184.1	-14.0	654.8
10	1150.335969	625.4	540.7	-11.0	1904.9

[a] CBS-4M electronic enthalpy; [b] gas phase enthalpy of formation; [c] sublimation enthalpy; [d] standard solid state enthalpy of formation; [e] solid state energy of formation.

4.6.4 References

- [S1] CrysAlisPro, Oxford Diffraction Ltd. version 171.33.41, **2009**.
- [S2] G. M. Sheldrick, *Acta Cryst.*, **2015**, A71, 3–8.
- [S3] Dolomanov, O. V., Bourhis, L. J., Gildea, R. J., Howard, J. A. K. & Puschmann, H. J., *Appl. Cryst.*, **2009**, 42, 339–341.
- [S4] SCALE3 ABSPACK – An Oxford Diffraction program (1.0.4, gui: 1.0.3), Oxford Diffraction Ltd., **2005**.
- [S5] APEX3. Bruker AXS Inc., Madison, Wisconsin, USA.
- [S6] <http://www.bam.de>
- [S7] NATO Standardization Agreement (STANAG) on Explosives, *Impact Sensitivity Tests*, no. 4489, 1st ed., September 17, **1999**.
- [S8] WIWEB-Standardarbeitsanweisung 4-5.1.02, Ermittlung der Explosionsgefährlichkeit, hier der Schlagempfindlichkeit mit dem Fallhammer, November 8, **2002**.
- [S9] NATO Standardization Agreement (STANAG) on Explosives, *Friction Sensitivity Tests*, no. 4487, 1st ed., August 22, **2002**.

- [S10] WIWEB-Standardarbeitsanweisung 4-5.1.03, Ermittlung der Explosionsgefährlichkeit oder der Reibeempfindlichkeit mit dem Reibeapparat, November 8, **2002**.
- [S11] Impact: Insensitive >40 J, less sensitive ≤35 J, sensitive ≤4 J, very sensitive ≤3 J; friction: Insensitive >360 N, less sensitive=360 N, sensitive 80 N, very sensitive ≤80 N, extreme sensitive ≤10 N; According to the UN Recommendations on the Transport of Dangerous Goods (+) indicates: not safe for transport.
- [S12] M. W. Chase Jr., NIST-JANAF Thermochemical Tables, Fourth Edition, *J. Phys. Chem. Red. Data, Monograph 9*, **1998**, 1 – 1951.
- [S13] M. J. Frisch, G. W. Trucks, H. B. Schlegel, G. E. Scuseria, M. A. Robb, J. R. Cheeseman, G. Scalmani, V. Barone, G. A. Petersson, H. Nakatsuji, X. Li, M. Hratchian, J. V. Ortiz, A. F. Izmaylov, J. L. Sonnenberg, D. Williams-Young, F. Ding, F. Lipparini, F. Egidi, J. Goings, B. Peng, A. Petrone, T. Henderson, D. Ranasinghe, V. G. Zakrzewski, J. Gao, N. Rega, G. Zheng, W. Liang, M. Hada, M. Ehara, K. Toyota, R. Fukuda, J. Hasegawa, M. Ishida, T. Nakajima, Y. Honda, O. Kitao, H. Nakai, T. Vreven, K. Throssell, J. A. Montgomery, Jr., J. E. Peralta, F. Ogliaro, M. J. Bearpark, J. J. Heyd, E. N. Brothers, K. N. Kudin, V. N. Staroverov, T. A. Keith, R. Kobayashi, J. Normand, K. Raghavachari, A. P. Rendell, J. C. Burant, S. S. Iyengar, J. Tomasi, M. Cossi, J. M. Millam, M. Klene, C. Adamo, R. Cammi, J. W. Ochterski, R. L. Martin, K. Morokuma, O. Farkas, J. B. Foresman, and D. J. Fox, Gaussian16 ,Gaussian, Inc., Wallingford, CT, USA, **2016**.

5. Evaluation of the methylhydrazone and oxybismethylene bridging moieties based on energetic salts of bridged nitraminotriazoles

Alexander G. Harter, Thomas M. Klapötke, Christian Riedelsheimer

unpublished

5.1 Introduction

Recent advances in the field of high energetic materials have set the focus on finding less toxic and environmentally friendly compounds, in order to replace the widely used and highly toxic molecules like TNT, RDX and HMX.^[1-2] Nitrogen rich compounds based on azoles show a great potential for this purpose, since they generally offer high heat of formation, good densities and stabilities and decompose mainly into nontoxic nitrogen gas.^[3] With the goal to further improve relevant properties of azoles like pyrazoles, triazoles and tetrazoles, the class of bridged azoles became increasingly prominent during the last decade.^[4-6] These compounds are highly adjustable, by using different azoles like highly energetic but often sensitive tetrazole derivatives or the more stable but in general less energetic pyrazole derivatives.^[7-8] In addition, by using different bridging moieties specific properties can be tweaked. For example, azo bridges increase the energy and nitrogen content of the molecule but often lead to increased sensitivities in comparison to the azole itself.^[9] In contrast alkyl bridges like methylene or ethylene bridges decrease sensitivity and increase thermal stability.^[10] A selection of bridged azoles is shown in Figure 1.

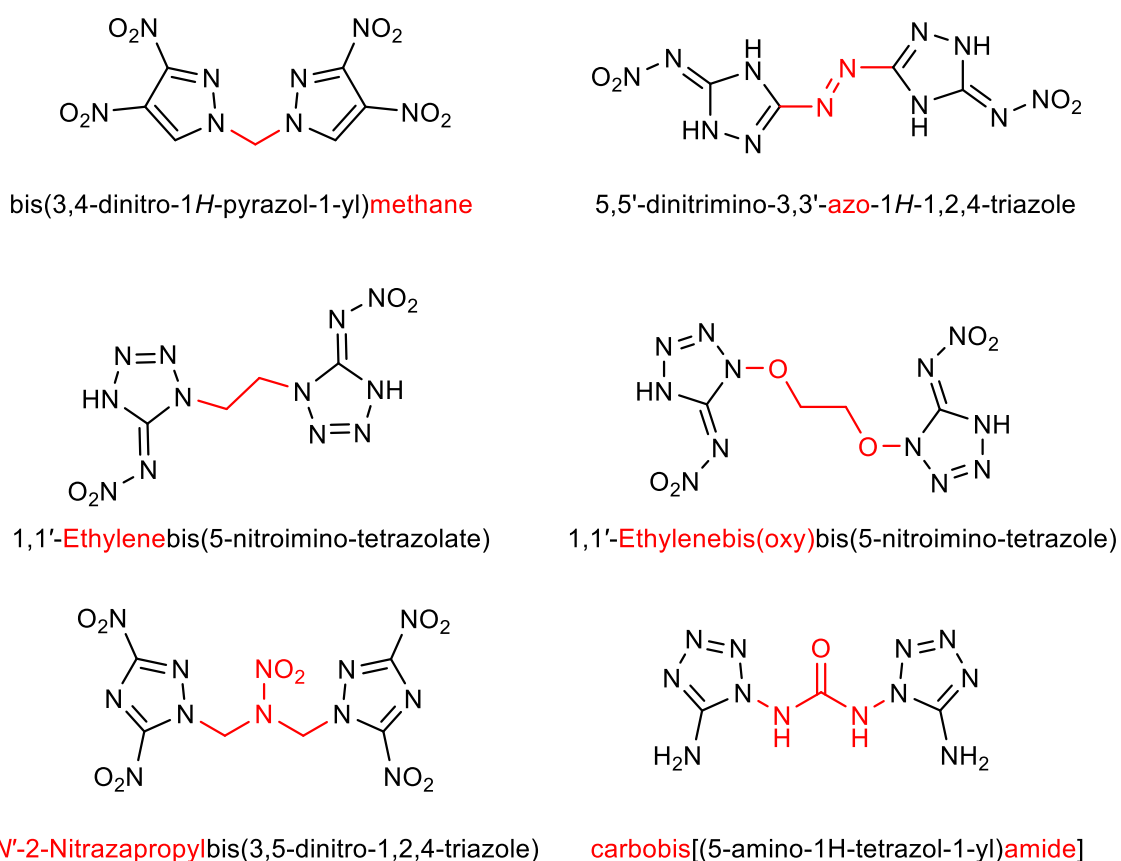


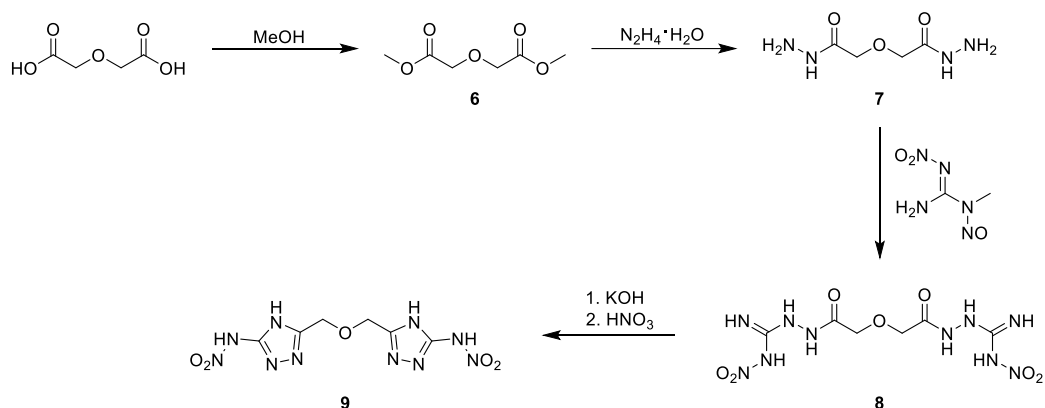
Figure 1. Selected azole derivatives with various different bridging moieties.^[11-16]

This work describes two new bridged bistriazoles, one with a methylhydrazone, the other with an oxybismethylene bridge and their respective energetic salts, and compares them in terms of energetic performance and physiochemical properties.

5.2 Results and Discussion

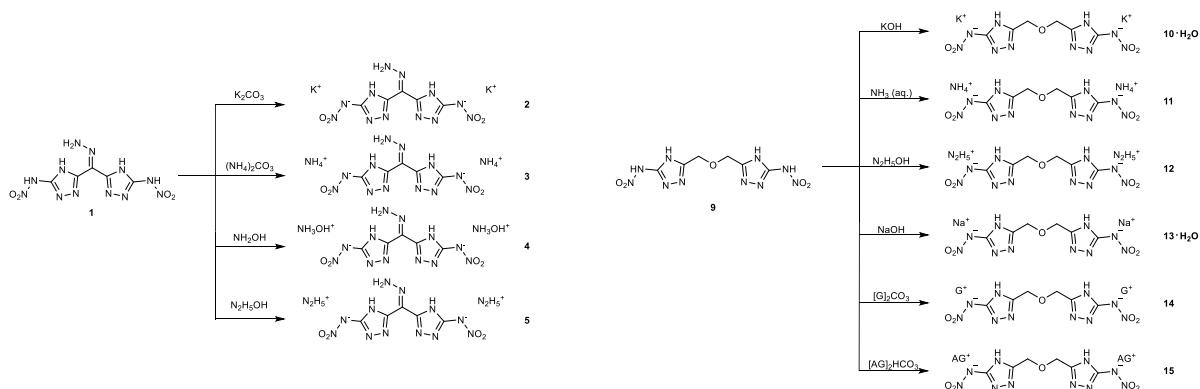
5.2.1 Synthesis

Compound **1** was synthesized according to literature by the reaction of 2-hydrazonyl-propandihydrazide with *N*-methyl-*N*-nitroso-*N'*-nitroguanidine, followed by the ring closure under basic conditions.^[17] The energetic salts **2–5** were synthesized by acid base chemistry with the respective carbonates at temperatures around 80 °C. By using equimolar amounts of the carbonates, the double salts were synthesized selectively. The synthesis towards bis(3-nitramino-4*H*-1,2,4-triazole-5-yl)oxybis(methylene) was achieved starting from diglycolic acid. First, the methyl ester was formed according to literature via thionyl chloride mediated esterification of diglycolic acid in methanol.^[18] The obtained methyl ester was refluxed with hydrazine hydrate in ethanol yielding in diglycolic dihydrazide **7** in high purity and yield.^[19] By reacting the hydrazide **7** with *N*-methyl-*N*-nitroso-*N'*-nitro-guanidine, compound **8** was obtained in moderate yield. The cyclisation towards the bis(3-nitramino-4*H*-1,2,4-triazole-5-yl) oxybis(methylene) **9** was accomplished by treating compound **8** with base followed by subsequent acidification to precipitate the bridged bis-triazole **9** in good yield and high purity (Scheme 4).



Scheme 4. Synthetic pathway towards bis(3-nitramino-4*H*-1,2,4-triazole-5-yl) oxybis(methylene) (**9**) starting from diglycolic acid.

Due to the acidic proton of the nitramino groups, salt conversions were performed with different bases, by treating the bis-triazole **9** with a minimal amount of water and adding the base and stirring until the solution cleared up. After evaporation of the solvent at 60 °C, the different salts **10–15** were obtained (Scheme 5).



Scheme 5. Salt formation overview based on bis(dinitramino-1*H*-1,3,4-bistriazol-5-yl) methylhydrazine **1** (**2–5**) and bis(3-nitramino-4*H*-1,2,4-triazole-5-yl) oxybis(methylene) **9** (**10–15**).

5.2.2 NMR and Vibrational spectroscopy

All compounds were characterized by ^1H and ^{13}C NMR spectroscopy in DMSO-d_6 .

The compounds **2–5** all possess the methylhydrazine group, as well as two nitramino triazoles. The methylhydrazine can be found between 8 and 9 ppm in the ^1H NMR spectra as singlets and in the range of 116 to 122 ppm in the ^{13}C NMR. The carbon atoms of the triazole rings show 4 signals around 150 to 156 ppm in the ^{13}C NMR spectra, this is caused due to the methylhydrazine, which has a non-rotary double bond and therefore influences one side of the molecule different than the other, making it unsymmetrical. Compounds **8–15** contain the oxybis(methylene) unit. These CH_2 groups can be found in the ^1H NMR in the range between 3.94 and 4.62 ppm as singlets. In case of the ring protons of the triazole moiety, the signals are located between 12.7 and 14.2 ppm. These compounds show also the specific signals in similar areas for the ^{13}C NMR. The signals for the CH_2 groups can be found at around 65 ppm, for the ring-carbon next to the nitramino group in the area between 147–157 ppm and for the ring carbon next to the oxybis(methylene) unit between 153 and 159 ppm.

5.2.3 Physicochemical Properties

A full characterization in regard to the physicochemical properties was conducted for all energetic compounds. This includes their sensitivities towards impact, friction and electrostatic discharge, the thermal behavior, heats of formation and detonation parameters. Those were determined experimentally if possible or computationally and compared to the state-of-the-art secondary explosive in industrial use, RDX, shown in **Fehler! Verweisquelle konnte nicht gefunden werden.** and Table 6. The sensitivity values towards impact and friction were determined with the 1 out of 6 Method according to BAM standards.^[20]

Table 5. Physiochemical properties of compounds 1–5 and RDX.^[21]

	1	2	3	4	5	RDX
Formula	C ₅ H ₆ N ₁₂ O ₄	C ₅ H ₄ N ₁₂ O ₄ K ₂	C ₅ H ₁₂ N ₁₄ O ₄	C ₅ H ₁₂ N ₁₄ O ₆	C ₅ H ₁₄ N ₁₆ O ₄	C ₃ H ₆ N ₆ O ₆
<i>M</i> [g·mol ⁻¹]	298.18	374.36	332.24	364.24	362.27	222.12
<i>IS</i> ^[a] [J]	2.5	10	2	5	3	7.5
<i>FS</i> ^[b] [N]	360	>360	252	288	252	120
<i>N+O</i> ^[c] [%]	77.83	61.99	78.28	80.19	79.53	81.06
Ω_{CO_2} ^[d] [%]	-34	-38	-58	-43	-62	-22
<i>T</i> _{endo} ^[e] / <i>T</i> _{exo} ^[f] [°C]	-/177	-/205	-/175	-/170	-/181	203/208
ρ ^[g] [g·cm ⁻³]	1.81	1.93	1.69	1.73	1.75	1.82
$\Delta_f H^\circ$ ^[h] [kJ·mol ⁻¹]	541	106	399	567	702	87
EXPLO5 V6.05						
$-\Delta_E U^\circ$ ^[i] [kJ·kg ⁻¹]	5137	3824	3958	5130	4944	5807
<i>T</i> _{C-J} ^[j] [K]	3624	2791	2714	3347	3016	3800
$\rho_{\text{C-J}}$ ^[k] [GPa]	31.0	20.2	25.2	29.1	31.4	34.0
<i>D</i> _{C-J} ^[l] [m·s ⁻¹]	8654	7271	8355	8701	9197	8882
<i>V</i> ₀ ^[m] [dm ³ ·kg ⁻¹]	766	487	866	861	887	793

[a] Impact sensitivity (BAM drophammer, method 1 of 6); [b] friction sensitivity (BAM friction tester, method 1 of 6); [c] combined nitrogen and oxygen content; [d] oxygen balance toward carbon dioxide ($\Omega_{\text{CO}_2} = (n\text{O} - 2x\text{C} - y\text{H}/2)/(1600/M)$); [e] endothermic peak (DTA, $\beta = 5^\circ\text{C}\cdot\text{min}^{-1}$); [f] temperature of decomposition (DTA, $\beta = 5^\circ\text{C}\cdot\text{min}^{-1}$); [g] Densities measured by gas pycnometry; [h] standard molar enthalpy of formation; [i] detonation energy; [j] detonation temperature; [k] detonation pressure; [l] detonation velocity; [m] volume of detonation gases at standard temperature and pressure conditions

Table 6. Physical and energetic properties of compound 9–15.

	9	10 · H ₂ O	11	12	13 · H ₂ O	14	15
Formula	C ₆ H ₈ N ₁₀ O ₅	C ₆ H ₈ N ₁₀ O ₆ K ₂	C ₆ H ₁₄ N ₁₂ O ₅	C ₆ H ₁₆ N ₁₄ O ₅	C ₆ H ₈ N ₁₀ O ₆ Na ₂	C ₈ H ₁₈ N ₁₆ O ₅	C ₈ H ₂₀ N ₁₈ O ₅
<i>M</i> [g·mol ⁻¹]	300.20	394.39	334.25	364.29	362.17	418.34	448.37
<i>IS</i> ^[a] [J]	4	>40	10	10	10	>40	>40
<i>FS</i> ^[b] [N]	>360	>360	>360	>360	>360	>360	>360
<i>N+O</i> ^[c] [%]	73.31	59.86	74.22	75.79	56.17	72.69	74.07
Ω_{CO_2} ^[d] [%]	-59	-41	-67	-66	-44	-77	-75
<i>T</i> _{endo} ^[e] / <i>T</i> _{exo} ^[f] [°C]	-/187	143/195	181/225	-/196	155/208	-/268	-/220
ρ ^[g] [g·cm ⁻³]	1.73	1.90	1.72	1.68	1.82	1.54	1.50
$\Delta_f H^\circ$ ^[h] [kJ·mol ⁻¹]	266	403	695	1023	-378	722	961
EXPLO5 V6.05							
$-\Delta_E U^\circ$ ^[i] [kJ·kg ⁻¹]	5664	6887	7310	8029	4610	6003	6417
<i>T</i> _{C-J} ^[j] [K]	2987	3437	3260	3468	2686	2880	3011
$\rho_{\text{C-J}}$ ^[k] [GPa]	23.2	24.8	29.7	31.0	17.8	21.0	21.4
<i>D</i> _{C-J} ^[l] [m·s ⁻¹]	7818	7792	8877	9066	7063	7780	7865
<i>V</i> ₀ ^[m] [dm ³ ·kg ⁻¹]	767	525	860	885	531	862	884

[a] Impact sensitivity (BAM drophammer, method 1 of 6); [b] friction sensitivity (BAM friction tester, method 1 of 6); [c] combined nitrogen and oxygen content; [d] oxygen balance toward carbon dioxide ($\Omega_{\text{CO}_2} = (n\text{O} - 2x\text{C} - y\text{H}/2)/(1600/M)$); [e] endothermic peak (DTA, $\beta = 5^\circ\text{C}\cdot\text{min}^{-1}$); [f] temperature of decomposition (DTA, $\beta = 5^\circ\text{C}\cdot\text{min}^{-1}$); [g] Densities measured by gas pycnometry; [h] standard molar enthalpy of formation; [i] detonation energy; [j] detonation temperature; [k] detonation pressure; [l] detonation velocity; [m] volume of detonation gases at standard temperature and pressure conditions.

When looking at the energetic salts **2** to **5**, it was observed, that they show a high insensitivity towards friction, with values between 252 N for compound **3** and **5** and above 360 N for the potassium salt **2**. In case of the neutral bis-triazole **9** and its salts **10–15**, all compounds show no sensitivity towards friction. In regard to the impact

values of **9** and the salts **2–5** and **11–13** show quite high sensitivity. The ammonium salt **3** has the highest sensitivity of 2 J which is in the range of primary explosives. The hydroxylammonium salt **4**, the hydrazinium salt **5** as well as the neutral compound **9** are still more sensitive than RDX with values of 5 J and 3 J, respectively. The potassium salt **2**, the ammonium salt **11**, the hydrazinium salt **12** and the sodium hydrate salt **13** show a sensitivity value of 10 J, and therefore are these compounds less sensitive than RDX. Only the potassium hydrate salt **10**, the guanidinium **14** and aminoguanidinium salt **15** show no sensitivity towards impact.

The thermal properties of all compounds were determined by differential thermal analysis in the temperature range of 25–400 °C with a heating rate of 5 °C. For almost all compounds no endothermic event were observed, which could be assigned to melting points. Only the ammonium salt **11** and the sodium hydrate salt **13** show endothermic events at 181 °C for **11** and 155 °C for **13**. Regarding their decomposition temperatures, all compounds are quite in the range of RDX, which decomposes at 205 °C. The neutral compound **9** shows a decomposition temperature of 187 °C, which is a bit lower compared to RDX, but higher compared to the other bis-triazole **1**. In case of the salts, the lowest values were observed for ammonium salt **3** with 175 °C and hydroxylammonium salt **4** with 170 °C, followed by the hydrazinium salt **5**, the potassium salt **10** and the hydrazinium salt **12** with a decomposition temperature between 181–195 °C. The highest values can be observed for the ammonium salt **11** with a value of 225 °C.

All investigated compounds possess very high combined nitrogen and oxygen contents up to 80 % for compound **4**, except for the potassium salt **10** and the sodium salt **13** with a content below 60 %.

Based on the densities, obtained by gas pycnometry, and the heats of formation, obtained by CBS-4M calculations, the energetic properties were calculated with EXPLO5 (V6.05).^[22] The neutral compound **9** shows a density of 1.73 g cm⁻³, which is a bit lower compared to the other bis-triazole **1** and RDX. Regarding the salts **2–5** and **11–15** the densities range from 1.50 g cm⁻³ for compound **15** to 1.95 g cm⁻³ for compound **2**. Most of the compounds are in range of 1.70 and 1.80 g cm⁻³. In terms of detonation performance, the lowest values were obtained for the different alkali salts. The ammonium and hydrazinium salts show by far the highest values. Especially the hydrazinium salts **5** and **12** show both a value above 9000 m s⁻¹, which exceed RDX with a value of 8882 m s⁻¹. When looking at the detonation pressures, the values range from 17.4 GPa to 31.4 GPa, following the same trend as the detonation velocities, with the alkali salts having the lowest performance and the hydrazinium salts **5** and **12** the best.

5.3 Conclusion

In this work we present 10 new energetic salts (**2-5**, **10-15**), with promising properties based on triazoles bridged with two different bridging moieties the methylhydrazone (**1**) and the oxybismethylene (**9**) group. Both bridging moieties were compared in terms of physicochemical properties and detonation performance. The densities of the different compounds are all in the same range from 1.68 to 1.93 g cm⁻³, with the exception of compound **14**, which only has 1.54 g cm⁻³. The thermal stabilities of all measured compounds show good values ranging from 170 °C up to 268 °C. In terms of sensitivity all compounds show a very low friction sensitivity of above 252 N. In contrast, the impact sensitivity values are on the more sensitive end of the range for secondary explosives starting at 2 J up to 10 J for the methylhydrazone bridged compounds. For the oxybismethylene derivatives the impact sensitivities are much lower starting at 10 J up to over 40 J. The detonation velocities of the neutral compounds are 8654 m s⁻¹ for compound **1** and 7818 m s⁻¹ for compound **9**. The detonation performance of the energetic salts follows the usual trend, with the highest detonation velocities measured for the nitrogen rich salts (**4**, **5**, **11**, **12**) with excellent values ranging from 8701 m s⁻¹ to 9197 m s⁻¹. The remaining salts still show decent velocities between 7000 m s⁻¹ and 8000 m s⁻¹. When comparing both bridging moieties, the overall thermal stability is higher for the oxybismethylene bridge, additionally these compounds show lower sensitivity values regarding both impact and friction sensitivity. The compounds based on the methylhydrazone bridging moiety show the highest overall detonation performance, as well as higher combined nitrogen and oxygen contents. It also has to be mentioned, that due to the fixed double bond of the methylhydrazone, these molecules show asymmetry, which can be seen in the NMR measurements, which show twice the number of signals for the protons and carbon atoms of the triazoles. The synthesized compounds are valid candidates for more environmentally RDX replacements, but further testing like upscaling and toxicity measurements have to be conducted.

5.4 Experimental Section

All chemicals and solvents were purchased from Sigma Aldrich and used without further purification. The general information about analytical devices including NMR, X-ray crystallography, IR, DTA, as well as information about the calculation of the energetic properties can be found in the SI. Compound (1) and *N*-methyl-*N*-nitroso-*N*-nitroguanidine were synthesized according to literature procedures.^[X,27]

Caution: The investigated compounds are potentially toxic and explosive. Therefore, it is recommended to carry out all reactions in a small scale, in addition to using the proper safety equipment, including ear, hand and body protection.

Potassium bis(dinitramino-1,3,4-bistriazol-5-yl) methylhydrazone (2): Bis(dinitramino-1*H*-1,3,4-bistriazol-5-yl) methylhydrazone (1) (200 mg, 0.67 mmol, 1 eq) was dissolved in water (10 mL), potassium carbonate (92.7 mg, 0.67 mmol, 1.00 eq) was added and the mixture stirred for 1 h at 80 °C. The solvent was removed on air and the product was dried at 100 °C. Compound 2 was obtained as a yellow solid (177 mg, 0.47 mmol, 70 %). **¹H NMR** (400 MHz, DMSO-*d*₆): δ (ppm) = 11.15 (s, 2H), 8.58 (s, 2H); **¹³C NMR** (101 MHz, DMSO-*d*₆): δ (ppm) = 159.5, 158.7, 153.2, 150.4, 120.5; **IR** (ATR, rel. int.): $\tilde{\nu}$ (cm⁻¹) = 3338 (m), 1624 (w), 1533 (m), 1498 (w), 1451 (m), 1327 (s), 1229 (s), 1157 (s), 1076 (s), 934 (s), 854 (m), 767 (s), 495 (s), 453 (s); **Elemental analysis:** calcd. (%) for C₅H₄K₂N₁₂O₄·(374.36 g mol⁻¹): C 16.04, H 1.08, N 44.90; found: C 15.84, H 1.38, N 43.32; **Sensitivities** (grain size: 500–1000 μm): BAM impact: 10 J, BAM friction: >360 N; **DTA** (5 °C min⁻¹): T_{exo} = 205 °C.

Ammonium bis(dinitramino-1,3,4-bistriazol-5-yl) methylhydrazone (3): Bis(dinitramino-1*H*-1,3,4-bistriazol-5-yl) methylhydrazone (1) (233 mg 0.78 mmol, 1 eq) was dissolved in water (10 mL), ammonium carbonate (75.1 mg, 0.78 mmol, 1.00 eq) was added and the mixture stirred for 1 h at 80 °C. The solvent was removed on air and the product was dried at 50 °C. Compound 3 was obtained as a yellow solid (120 mg, 0.36 mmol, 46 %). **¹H NMR** (400 MHz, DMSO-*d*₆): δ (ppm) = 9.17, 7.29; **¹³C NMR** (101 MHz, DMSO-*d*₆): δ = 155.9, 155.3, 153.7, 151.4, 121.0; **IR** (ATR, rel. int.): $\tilde{\nu}$ (cm⁻¹) = 3182 (m), 3035 (m), 1532 (m), 1436 (m), 1314 (s), 1222 (s), 1157 (s), 1076 (s), 1003 (m), 934 (s), 854 (m), 667 (m), 620 (m), 497 (s); **Elemental analysis:** calcd. (%) for C₅H₁₂N₁₄O₄ (332.24 g mol⁻¹): C 18.08, H 3.64, N 59.02; found: C 17.78, H 3.60, N 54.68; **Sensitivities** (grain size: 500 - 1000 μm): BAM impact: 2 J, BAM friction: 252 N; **DTA** (5 °C min⁻¹): T_{exo} = 175 °C.

Hydroxylammonium bis(dinitramino-1,3,4-bistriazol-5-yl) methylhydrazone (4): Bis(dinitramino-1*H*-1,3,4-bistriazol-5-yl) methylhydrazone (1) (200 mg, 0.67 mmol, 1.00 eq) was dissolved in water (10 mL), hydroxylamine solution (50 % in water) (0.08 mL, 1.34 mmol, 2 eq) was added and the mixture stirred for 1 h at 80 °C. The solvent

was removed on air and the product was dried at 50 °C. Compound **4** was obtained as a yellow solid (167 mg, 0.46 mmol, 68 %). **¹H NMR** (400 MHz, DMSO-*d*₆): δ (ppm) = 14.00-7.00 (b, 5H), 9.31 (s, 2H), 6.00-3.80 (b, 5H); **¹³C NMR** (101 MHz, DMSO-*d*₆): δ (ppm) = 155.9, 154.3, 151.8, 151.6, 119.2; **IR** (ATR, rel. int.): $\tilde{\nu}$ (cm⁻¹) = 3143 (m), 2916 (m), 2708 (m), 1594 (w), 1513 (s), 1453 (m), 1315 (s), 1160 (s), 1082 (s), 996 (s), 937 (m), 858 (s), 771 (s), 628 (s), 446 (s); **Elemental analysis**: calcd. (%) for C₅H₁₂N₁₄O₆ (364.24 g mol⁻¹): C 16.49, H 3.32, N 53.85; found: C 16.41, H 3.33, N 51.71; **Sensitivities** (grain size: 100 – 500 μm): BAM impact: 5 J, BAM friction: 288 N; **DTA** (5 °C min⁻¹): T_{exo} = 177 °C.

Hydrazinium bis(dinitramino-1,3,4-bistriazol-5-yl) methylhydrazone (5): Bis(dinitramino-1*H*-1,3,4-bistriazol-5-yl) methylhydrazone (**1**) (200 mg, 0.67 mmol, 1.00 eq) was dissolved in water (10 mL), hydrazine hydrate (0.06 mL, 1.34 mmol, 2.00 eq) was added and the mixture stirred for 1 h at 80 °C. The solvent was removed on air and the product was dried at 50 °C. Compound **5** was obtained as a yellow solid (176 mg, 0.49 mmol, 72 %). **¹H NMR** (400 MHz, DMSO-*d*₆): δ (ppm) = 9.08 (b, 10H), 8.11 (b, 4H); **¹³C NMR** (101 MHz, DMSO-*d*₆): δ (ppm) = 156.8, 156.2, 156.0, 155.8, 122.7; **IR** (ATR, rel. int.): $\tilde{\nu}$ (cm⁻¹) = 3315 (w), 3079 (w), 1606 (w), 1506 (m), 1448 (w), 1320 (m), 1238 (m), 1159 (m), 1076 (s), 934 (s), 855 (m), 763 (m), 630 (m), 444 (s); **Elemental analysis**: calcd. (%) for C₅H₁₄N₁₆O₄ (362.27 g mol⁻¹): C 16.58, H 3.90, N 61.86; found: C 16.42, H 4.08, N 58.28; **Sensitivities** (grain size: 100 – 500 μm): BAM impact: 3 J, BAM friction: 252 N; **DTA** (5 °C min⁻¹): T_{exo} = 181 °C.

Diglycolic dihydrazide (7): Dimethyl 2,2'-oxydiacetate (**6**) (2.00 g, 12.3 mmol, 1 eq.) was dissolved in EtOH (50 mL) and hydrazine hydrate (1.50 mL, 30.8 mmol, 2.5 eq.) was added. The mixture was refluxed for 5 h, cooled to 0 °C, the precipitate filtered, washed with cold EtOH and dried at room temperature. Diglycolic dihydrazide **7** (1.80 g, 11.1 mmol, 90%) was afforded as a white solid. **¹H NMR** (400 MHz, DMSO-*d*₆): δ (ppm) = 9.35 (s, 2H, NH), 4.29 (s, 4H, NH₂), 3.94 (s, 4H, CH₂); **¹³C NMR** (101 MHz, DMSO-*d*₆): δ (ppm) = 167.3 (CO), 69.7 (CH₂); **IR** (ATR, rel. int.): $\tilde{\nu}$ (cm⁻¹) = 3269(m), 3223(m), 3211(m), 3190(m), 3184(m), 3124(w), 3080(w), 3048(m), 2931(w), 1661(m), 1615(s), 1542(s), 1532(s), 1404(m), 1367(m), 1351(m), 1333(s), 1312(m), 1292(m), 1263(m), 1175(m), 1116(s), 1045(s), 1045(s), 980(m), 963(s), 924(w), 769(s), 676(s), 588(vs), 566(s), 527(s).; **Elemental analysis**: calcd. (%) for C₄H₁₀N₄O₃ (165.15 g mol⁻¹): C 29.63; H 6.22; N 34.55, found: C 29.49; H 5.85; N 34.01; **DTA** (5 °C min⁻¹): T_{endo} = 166 °C, T_{exo} = 271 °C.

Diglycolic-di-N-amino-nitroguanidine (8): Diglycolic dihydrazide (**7**) (1.62 g, 10.0 mmol, 1 eq.) was dissolved in water (20 mL) and N methyl-N-nitroso-N'-nitroguanidine (2.94 g, 20.0 mmol, 2 eq.), suspended in water (50 mL) was added. The mixture was stirred for 3 h at 95 °C, cooled to 0 °C, the precipitate filtered and washed with cold

water and cold EtOH. After drying at room temperature, the product **8** (2.66 g, 7.91 mmol, 79 %) was afforded as a colorless solid. **¹H NMR** (400 MHz, DMSO-*d*₆): δ (ppm) = 10.03 (s, 2H, NH), 9.7 (bs, 2H, NH), 8.7 (bs, 2H, NH), 8.2 (bs, 2H, NH), 4.14 (s, 4H, CH₂).; **¹³C NMR** (101 MHz, DMSO-*d*₆): δ (ppm) = 168.8 (CO), 161.1 (C=N), 69.8 (CH₂); **IR** (ATR, rel. int.): $\tilde{\nu}$ (cm⁻¹) = 3387(m), 3351(w), 3332(w), 3301(m), 3255(w), 3182(m), 3176(m), 3062(m), 2970(w), 2930(w), 1738(w), 1699(s), 1642(s), 1587(s), 1564(m), 1507(m), 1423(m), 1378(s), 1352(s), 1318(vs), 1272(s), 1244(s), 1187(s), 1187(s), 1085(s), 1048(m), 1031(m), 990(w), 923(w), 784(w), 753(s), 616(vs), 564(m), 537(s), 507(m), 481(vs), 437(s).; **Elemental analysis**: calcd. (%) for C₆H₁₂N₁₀O₇ (336.23 g mol⁻¹): 21.43; H 3.60; N 40.80. Found: C 21.49; H 3.84; N 40.80; **DTA** (5 °C min⁻¹): T_{exo} = 193 °C.

Bis(3-nitramino-4*H*-1,2,4-triazole-5-yl) oxybis(methylene) (9): Diglycolic-di-N-amino-nitroguanidine (**8**) (1.00 g, 2.94 mmol, 1 eq.) was dissolved in water (20 mL) and KOH (500 mg, 8.93 mmol, 3.0 eq.), dissolved in water (15 mL), was added. The mixture was stirred overnight at 80 °C. The clear solution was cooled to 50 °C and acidified to pH 3 with HNO₃ (65 %). The resulting suspension was cooled to 0 °C, the precipitate filtered, washed with cold water and dried for two days at 100 °C to yield **9** (610 mg, 2.03 mmol, 68 %) as a beige solid. **¹H NMR** (400 MHz, DMSO-*d*₆): δ (ppm) = 14.2 (bs, 2H, ring-NH), 4.62 (s, 4H, CH₂); **¹³C NMR** (101 MHz, DMSO-*d*₆): δ (ppm) = 153.0 (C-CH₂), 147.5 (C-NNO₂), 62.4 (CH₂); **IR** (ATR, rel. int.): $\tilde{\nu}$ (cm⁻¹) = 3341(w), 3223(w), 2665(w), 2578(w), 1607(s), 1567(s), 1501(m), 1447(m), 1427(m), 1412(m), 1309(s), 1234(vs), 1210(s), 1127(s), 1098(s), 1015(m), 995(s), 951(m), 905(m), 870(m), 853(m), 803(w), 774(s), 774(s), 748(w), 713(s), 688(s), 665(m), 655(m), 603(m), 591(m), 575(m), 570(m), 545(m), 528(m), 484(m), 467(s), 444(s), 426(w), 420(w); **Elemental analysis**: calcd. (%) for C₆H₈N₁₀O₅ (300.20 g mol⁻¹): C 24.01; H 2.69; N 46.66; found: C 23.84; H 2.76; N 46.30; **Sensitivities** (grain size: 100–500 μm): BAM impact: 4 J, BAM friction: >360 N; **DTA** (5 °C min⁻¹): T_{exo} = 187 °C.

Potassium bis(3-nitramino-4*H*-1,2,4-triazole-5-yl) oxybis(methylene) hydrate (10·H₂O): Compound **9** (250 mg, 0.833 mmol, 1 eq.) was suspended in water (~ 3 mL), potassium hydroxide (0.93 g, 1.66 mmol, 2 eq.) was added and stirred until the mixture cleared up. The solution was then evaporated at 60 °C overnight. The potassium salt **10** · H₂O (240 mg, 0.608 mmol, 73 %) was obtained as colorless solid after drying for two days at 105 °C. **¹H NMR** (400 MHz, DMSO-*d*₆): δ (ppm) = 12.72 (s, 2H, NH), 4.36 (s, 4H, CH₂); **¹³C NMR** (101 MHz, DMSO-*d*₆): δ (ppm) = 157.6 (C-CH₂), 157.3 (C-N), 65.1 (CH₂); **IR** (ATR): $\tilde{\nu}$ = 3331(w), 3252(w), 3231(w), 1738(w), 1726(w), 1521(m), 1436(m), 1379(s), 1316(vs), 1274(m), 1251(s), 1237(s), 1229(s), 1141(m), 1131(m), 1087(s), 1061(s), 1035(m), 1017(m), 996(s), 859(m), 764(m), 728(m), 728(m), 713(m), 462(m), 453(m), 448(m); **Elemental analysis** : calcd. (%) for C₆H₆N₁₀O₅K₂ · H₂O

(394.39 g mol⁻¹): C 18.27; H 2.04; N 35.52 found: C 18.30; H 2.16; N 35.60; **Sensitivities** (grain size: 300–1000 μm): BAM impact: 40 J, BAM friction: >360 N; **DTA** (onset, 5 °C min⁻¹): T_{endo} = 143 °C, T_{exo} = 195 °C.

Ammonium bis(3-nitramino-4*H*-1,2,4-triazole-5-yl) oxybis(methylene) (11): Compound **9** (250 mg, 0.833 mmol, 1 eq.) was suspended in water (~ 3 mL), 2 M ammonia solution (0.83 mL, 1.66 mmol, 2 eq.) was added and stirred until the mixture cleared up. The solution was then evaporated at 60 °C overnight. The ammonia salt **11** (175 mg, 0.525 mmol, 63 %) was obtained as beige solid after drying for two days at 105 °C. **¹H NMR** (400 MHz, DMSO-*d*₆): δ (ppm) = 13.1 (bs, 2H, *NH*), 7.26 (s, 8H, *NH*₄⁺), 4.41 (s, 4H, *CH*₂); **¹³C NMR** (101 MHz, DMSO-*d*₆): δ (ppm) = 156.8 (*C-CH*₂), 155.5 (*C-NNO*₂), 64.7 (*CH*₂); **IR** (ATR): $\tilde{\nu}$ = 3141(m), 3026(m), 2863(m), 1739(w), 1618(w), 1505(m), 1461(m), 1421(s), 1371(s), 1312(vs), 1284(vs), 1229(vs), 1134(s), 1096(s), 1026(s), 1001(vs), 861(m), 764(m), 719(s), 655(m), 512(m), 471(m), 461(m), 461(m), 444(m); **Elemental analysis** : calcd. (%) for C₆H₁₄N₁₂O₅ (334.25 g mol⁻¹): C 21.56; H 4.22; N 50.29 found: C 21.66, H 4.10, N 50.05; **Sensitivities** (grain size: 300–1000 μm): BAM impact: 10 J, BAM friction: >360 N; **DTA** (onset, 5 °C min⁻¹): T_{endo} = 181 °C, T_{exo} = 225 °C.

Hydrazinium bis(3-nitramino-4*H*-1,2,4-triazole-5-yl) oxybis(methylene) (12): Compound **9** (250 mg, 0.833 mmol, 1 eq.) was suspended in water (~ 3 mL), hydrazine hydrate (0.08 mL, 1.66 mmol, 2 eq.) was added and stirred until the mixture cleared up. The solution was then evaporated at 60 °C overnight. The hydrazinium salt **12** (219 mg, 0.600 mmol, 72 %) was obtained as off-white solid after drying for two days at 105 °C. **¹H NMR** (400 MHz, DMSO-*d*₆): δ (ppm) = 12.7 (bs, 2H, *NH*), 6.5 (bs, 10H, *N*₂*H*₅⁺), 4.40 (s, 4H, *CH*₂); **¹³C NMR** (101 MHz, DMSO-*d*₆): δ (ppm) = 157.0 (*C-CH*₂), 156.0 (*C-NNO*₂), 64.8 (*CH*₂); **IR** (ATR): $\tilde{\nu}$ = 3385(m), 3366(m), 3316(m), 3255(w), 3210(w), 3191(w), 3121(m), 2971(m), 2941(m), 2870(m), 2763(m), 2687(m), 2634(m), 1739(w), 1726(w), 1613(w), 1529(s), 1473(m), 1454(m), 1387(s), 1326(vs), 1290(vs), 1229(s), 1229(s), 1147(s), 1126(s), 1091(vs), 1045(w), 1020(s), 1004(s), 968(s), 858(w), 763(w), 692(s), 621(m), 461(w); **Elemental analysis** : calcd. (%) for C₆H₁₆N₁₄O₅ (364.29 g mol⁻¹): C 19.78; H 4.43; N 53.83 found: C 19.93, H 4.33, N 53.54; **Sensitivities** (grain size: 300–1000 μm): BAM impact: 10 J, BAM friction: >360 N; **DTA** (onset, 5 °C min⁻¹): T_{exo} = 196 °C.

Sodium bis(3-nitramino-4*H*-1,2,4-triazole-5-yl) oxybis(methylene) hydrate (13·H₂O): Compound **9** (250 mg, 0.833 mmol, 1 eq.) was suspended in water (~ 3 mL), sodium hydroxide (0.67 g, 1.66 mmol, 2 eq.) was added and stirred until the mixture cleared up. The solution was then evaporated at 60 °C overnight. The sodium salt **13** · H₂O (259 mg, 0.716 mmol, 86 %) was obtained as colorless solid after drying for two days at 105 °C. **¹H NMR** (400 MHz, DMSO-*d*₆): δ (ppm) = 12.70 (s, 2H, *NH*), 4.36 (s,

4H, CH₂); ¹³C NMR (101 MHz, DMSO-*d*₆): δ (ppm) = 157.8 (C-CH₂), 157.4 (C-NNO₂), 65.2 (CH₂); IR (ATR): $\tilde{\nu}$ = 3224(m), 3190(m), 3173(m), 3140(m), 3124(m), 1738(m), 1727(w), 1526(m), 1453(m), 1350(vs), 1329(vs), 1264(s), 1231(m), 1218(m), 1141(m), 1085(s), 1032(w), 1005(s), 869(m), 760(m), 729(m), 673(m), 468(m), 468(m); **Elemental analysis** : calcd. (%) for C₆H₆N₁₀O₅Na₂ · H₂O (362.17 g mol⁻¹): C 19.90; H 2.23; N 38.67 found: C 19.82, H 2.36, N 38.47; **Sensitivities** (grain size: 300–1000 μm): BAM impact: 10 J, BAM friction: >360 N; **DTA** (onset, 5 °C min⁻¹): T_{endo} = 155 °C, T_{exo} = 208 °C.

Guanidinium bis(3-nitramino-4*H*-1,2,4-triazole-5-yl) oxybis(methylene) (14): Compound **9** (250 mg, 0.833 mmol, 1 eq.) was suspended in water (~ 3 mL), guanidinium carbonate (0.150 g, 0.833 mmol, 1 eq.) was added and the suspension was heated to 100 °C and stirred until the mixture cleared up. While cooling to room temperature, a precipitate formed, which was filtered and dried on air. The guanidinium salt **14** (310 mg, 0.741 mmol, 89 %) was obtained as cotton-wool-like colorless solid. ¹H NMR (400 MHz, DMSO-*d*₆): δ (ppm) = 12.82 (s, 2H, NH), 7.14 (s, 12H, guanidinium-NH₂), 4.37 (s, 4H, CH₂); ¹³C NMR (101 MHz, DMSO-*d*₆): δ (ppm) = 157.9, 157.3, 157.26, 65.3 (CH₂); IR (ATR): $\tilde{\nu}$ = 3386(m), 3351(m), 3141(m), 3123(m), 1650(m), 1523(m), 1504(m), 1455(m), 1443(m), 1379(m), 1350(m), 1327(vs), 1263(s), 1236(s), 1221(m), 1143(s), 1100(m), 1087(m), 1062(m), 1023(m), 1005(s), 994(m), 971(m), 971(m), 863(m), 767(w), 745(m), 740(w), 543(m), 481(m), 457(s); **Elemental analysis** : calcd. (%) for C₈H₁₈N₁₆O₅ (418.34 g mol⁻¹): C 22.97; H 4.34; N 53.57. Found: C 23.16; H 4.22; N 53.49; **Sensitivities** (grain size: 300–1000 μm): BAM impact: 40 J, BAM friction: >360 N; **DTA** (onset, 5 °C min⁻¹): T_{exo} = 268 °C.

Aminoguanidinium bis(3-nitramino-4*H*-1,2,4-triazole-5-yl) oxybis(methylene) (15): Compound **9** (250 mg, 0.833 mmol, 1 eq.) was suspended in water (~ 3 mL), aminoguanidinium bicarbonate (0.277 g, 1.66 mmol, 2 eq.) was added and the suspension was heated to 100 °C and stirred until the mixture cleared up. While cooling to room temperature, a precipitate formed, which was filtered and dried on air. The aminoguanidinium salt **15** (340 mg, 0.758 mmol, 91 %) was obtained as cotton-wool-like colorless solid. ¹H NMR (400 MHz, DMSO-*d*₆): δ (ppm) = 12.84 (s, 2H, NH), 8.83 (s, 2H, aminoguanidine-NH), 7.29 (m, 8H, aminoguanidine-NH₂), 4.70 (s, 4H, aminoguanidine-NH₂), 4.38 (s, 4H, CH₂); ¹³C NMR (101 MHz, DMSO-*d*₆): δ (ppm) = 158.9, 157.3, 157.3, 65.3 (CH₂); IR (ATR): $\tilde{\nu}$ = 3437(w), 3322(m), 3223(m), 3147(m), 3019(m), 2924(m), 2874(m), 2768(w), 1671(vs), 1666(s), 1523(m), 1509(s), 1459(m), 1442(s), 1351(s), 1333(s), 1300(vs), 1261(vs), 1235(s), 1147(s), 1103(m), 1079(s), 1005(vs), 1005(vs), 994(s), 863(m), 803(m), 766(m), 749(m), 734(m), 688(m), 673(w), 584(w), 498(m), 486(m), 483(m), 453(s); **Elemental analysis** : calcd. (%) for C₈H₂₀N₁₈O₅ (448.37 g mol⁻¹): C 21.43; H 4.50; N 56.23. Found: C 21.60; H 4.65; N

56.06; **Sensitivities** (grain size: 300–1000 μm): BAM impact: 40 J, BAM friction: >360 N; **DTA** (onset, 5 $^{\circ}\text{C min}^{-1}$): $T_{\text{exo}} = 220$ $^{\circ}\text{C}$.

Acknowledgements

For financial support of this work by the Ludwig-Maximilian University (LMU), the Office of Naval Research (ONR) under grant no. ONR N00014–19–1-2078 and the Strategic Environmental Research and Development Program (SERDP) under contract no. W912HQ19C0033 are gratefully acknowledged. The authors thank Stefan Huber for his help with the sensitivity measurement and Jasmin Lechner for graphical support.

5.5 References

- [1] D. Fournier, A. Halasz, J. Spain, R. J. Spanggord, J. C. Bottaro, J. Hawari, *Appl. Environ. Microbiol.*, **2004**, 70, 1123–1128.
- [2] J. S. Strehse, M. Brenner, M. Kisiela, et al., *Arch Toxicol*, **2020**, 94, 4043–4054.
- [3] P. F. Pagoria, G. S. Lee, A. R. Mitchell, R. D. Schmidt, *Thermochim. Acta*, **2002**, 384, 187–204.
- [4] K. Pu^a, L. Wang, J. Liu^b and K. Zhong, *RSC Adv.*, **2020**, 10, 13185–13195.
- [5] Q. Xue, F. Bi, J. Zhang, Z. Wang, L. Zhai, H. Huo, B. Wang, S. Zhang, *Front. Chem.*, **2020**, 7, 942.
- [6] S. Zhang, Z. Gao, D. Lan, Q. Jia, N. Liu, J. Zhang, K. Kou, *Molecules*, **2020**, 25 (15), 3475.
- [7] C. ZhaoXu, X. Heming, Y. Shulin, *Chem. Phys.*, **1999**, 250 (3), 243–248.
- [8] M. F. Bölter, A. Harter, T. M. Klapötke, J. Stierstorfer, *ChemPlusChem*, **2018**, 83, 804.
- [9] A. K. Chinnam, Q. Yu, G. H. Imler, D. A. Parrish, J. M. Shreeve, *Dalton Trans.*, **2020**, 49, 11498
- [10] M. F. Bölter, T. M. Klapötke, T. Kustermann, T. Lenz, J. Stierstorfer, *Eur. J. Inorg. Chem.*, **2018**, 4125–4132.
- [11] P. Yin, Q. Zhang, J. M. Shreeve, *Acc. Chem. Res.*, **2016**, 49 (1), 4–16.
- [12] A. Dippold, T. M. Klapötke, F. A. Martin, *Z. anorg. allg. Chem.*, **2011**, 637, 1181–1193.
- [13] L. Türker, *Def. Technol.*, **2016**, 12, 1–15.
- [14] D. Kumar, H. Imler, D. A. Parrish, J. M. Shreeve, *Chem. Eur. J.*, **2017**, 23, 7876.
- [15] Y. Joo, J. M. Shreeve, *J. Am. Chem. Soc.*, **2010**, 132, 42, 15081–15090.
- [16] Y. Joo, B. Twamley, J. M. Shreeve, *Chem. Eur. J.*, **2009**, 15, 9097–9104.
- [17] A. G. Harter, T. M. Klapötke, C. Riedelsheimer, J. Stierstorfer, S. M. Strobel, M. Voggenreiter, *Eur. J. Inorg. Chem.* **2022**, e202200100.
- [18] X. X. Sun, Y. C. Li, L. Li, Y. Hu, *Advanced Materials Research* **2012**, 430-432, 205-208.

- [19] B. D. Parthiban, S. Saxena, M. Chandran, P. S. Jonnalagadda, R. Yadav, R. R. Srilakshmi, Y. Perumal, S. Dharmarajan, *Chemical Biology & Drug Design* **2016**, *87*, 265-274.
- [19] Test methods according to the UN Recommendations on the Transport of Dangerous Goods., *Manual of Test and Criteria*, 4th revised ed., United Nations Publication: New York and Geneva, 2003, ISBN 92-1-139087-7, Sales No. E.03.VIII.2; 13.4.2 Test 3 a (ii) BAM Fallhammer.
- [20] M. Sućeska, *EXPLO5 V6.05 program*, Brodarski Institut: Zagreb, Croatia, **2020**.
- [21] M. Härtel, **2017**: Studies towards the gas-phase detection of hazardous materials by vapor pressure measurements with the transpiration method in combination with vacuum outlet GC/MS. Dissertation, LMU München: Fakultät für Chemie und Pharmazie.

5.6 Supplementary Information

5.6.1 NMR Spectroscopy

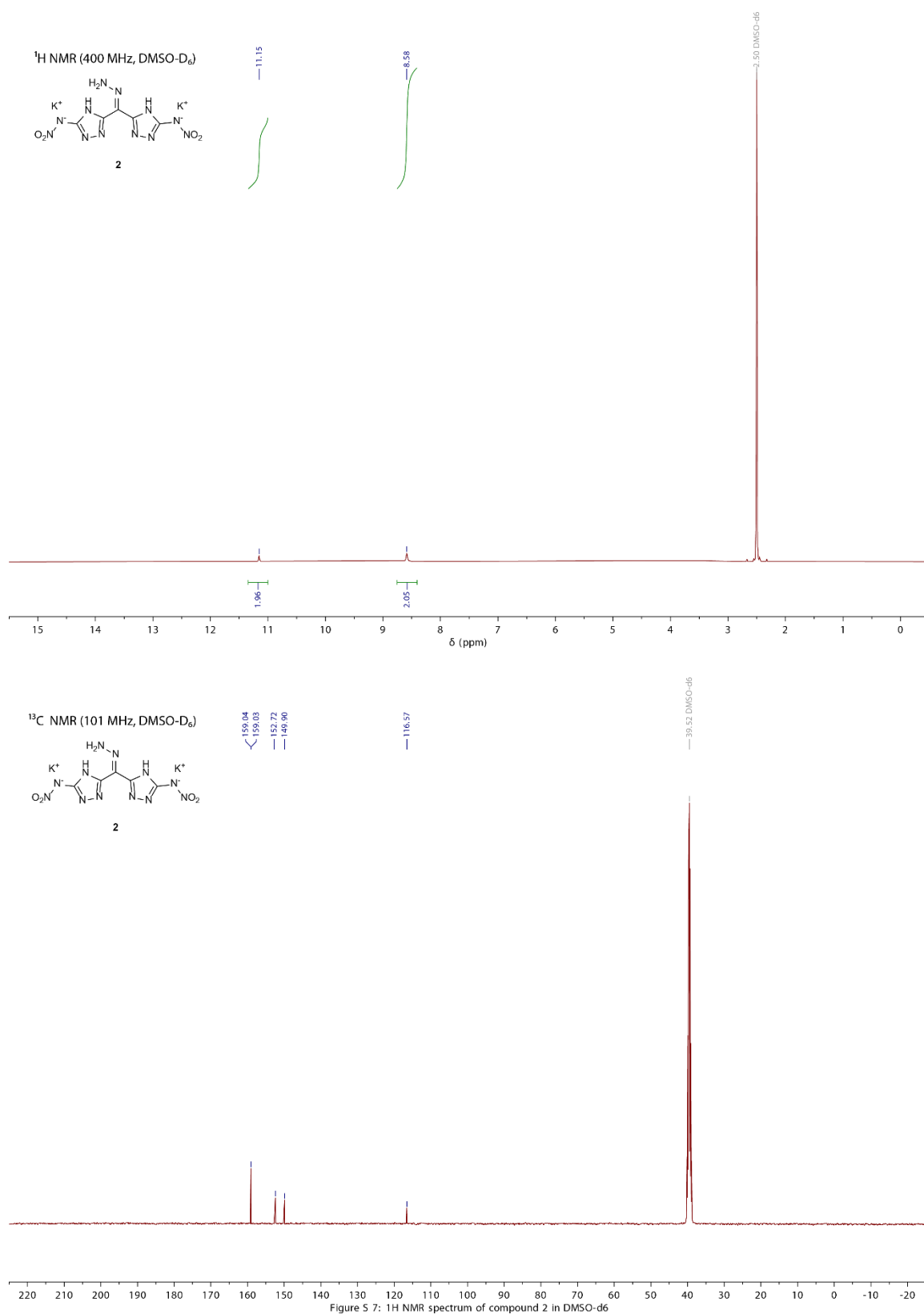


Figure S1. ¹H and ¹³C NMR spectra of compound 2.

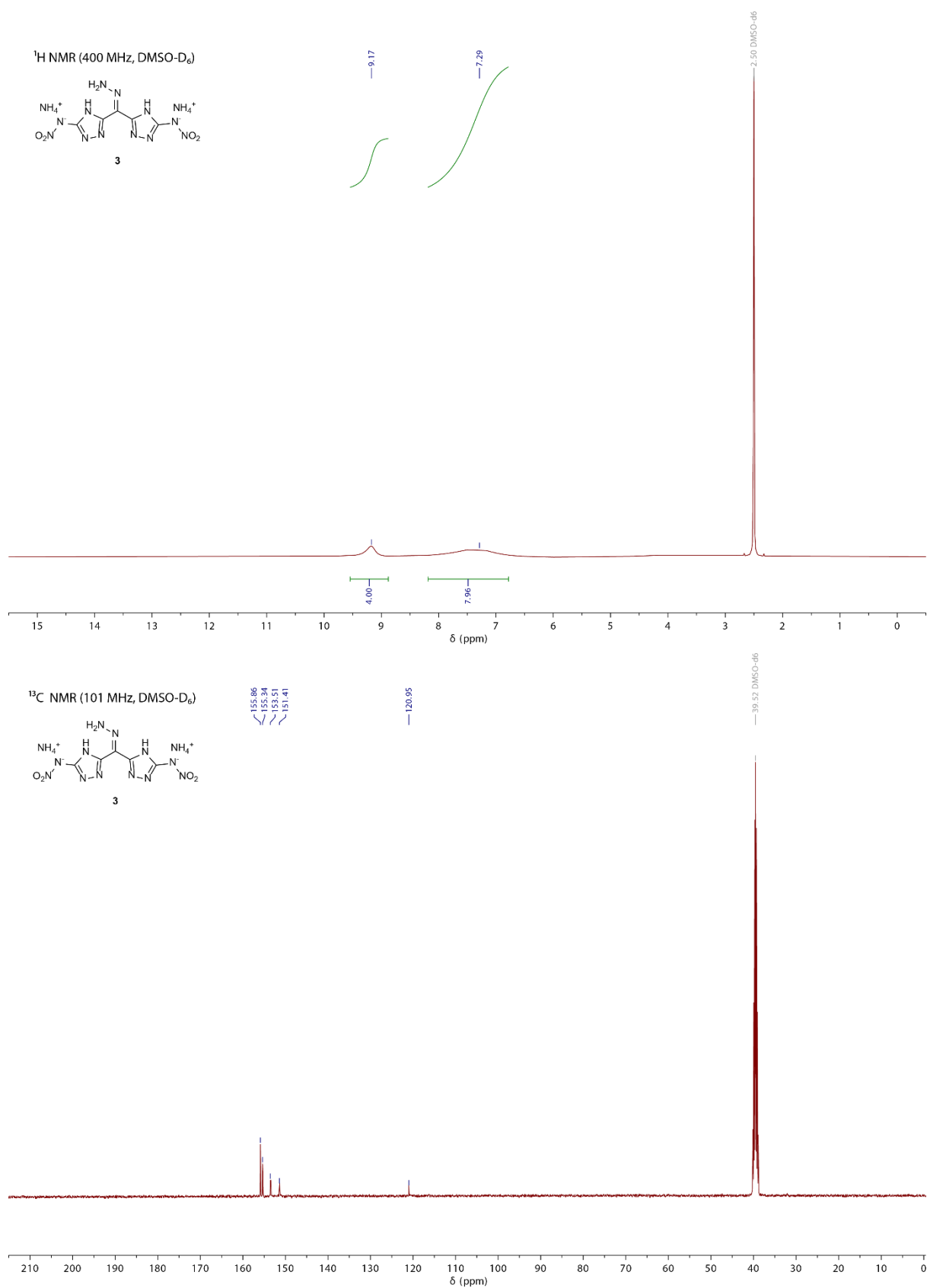


Figure S2. ¹H and ¹³C NMR spectra of compound 3.

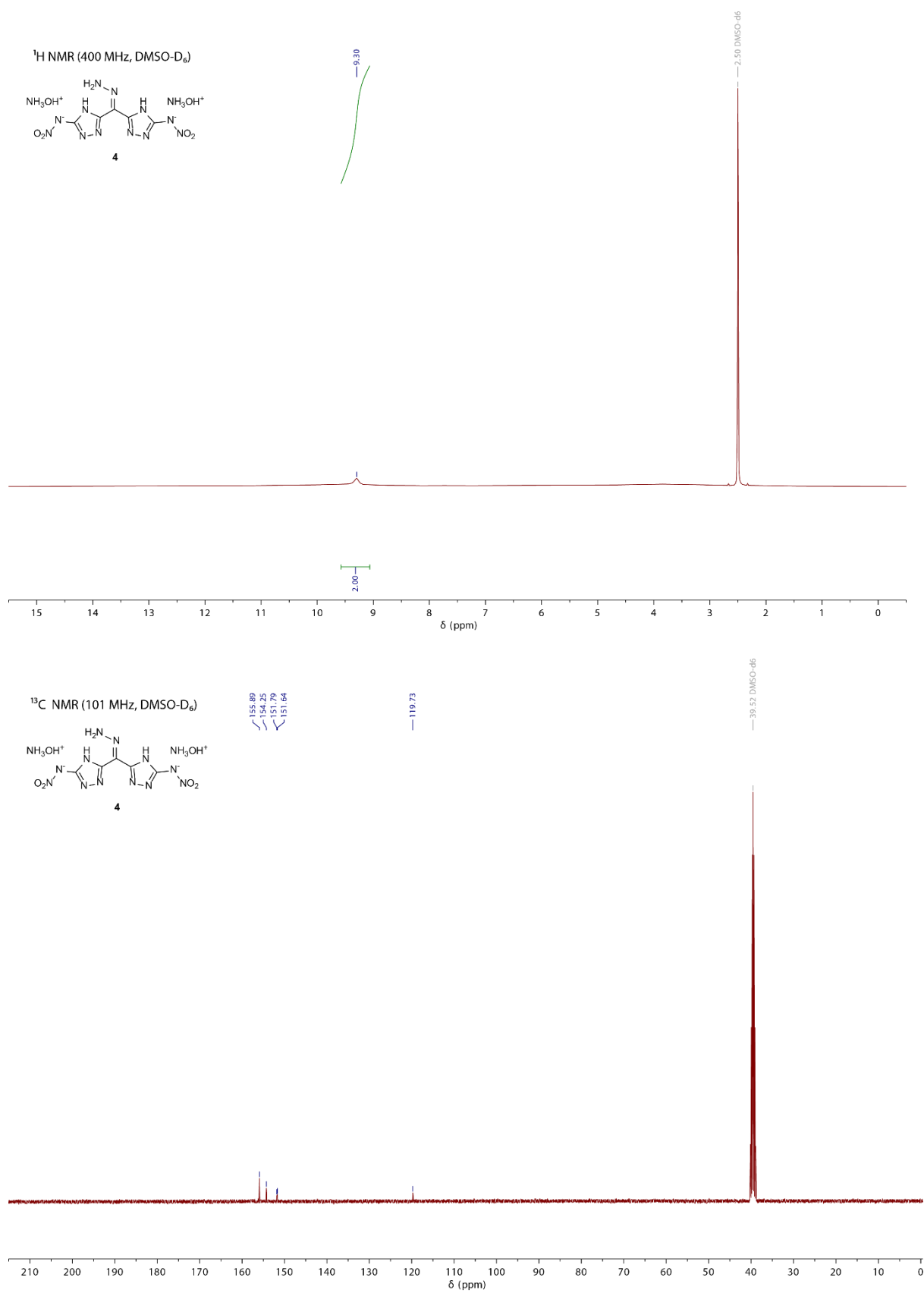


Figure S3. ¹H and ¹³C NMR spectra of compound 4.

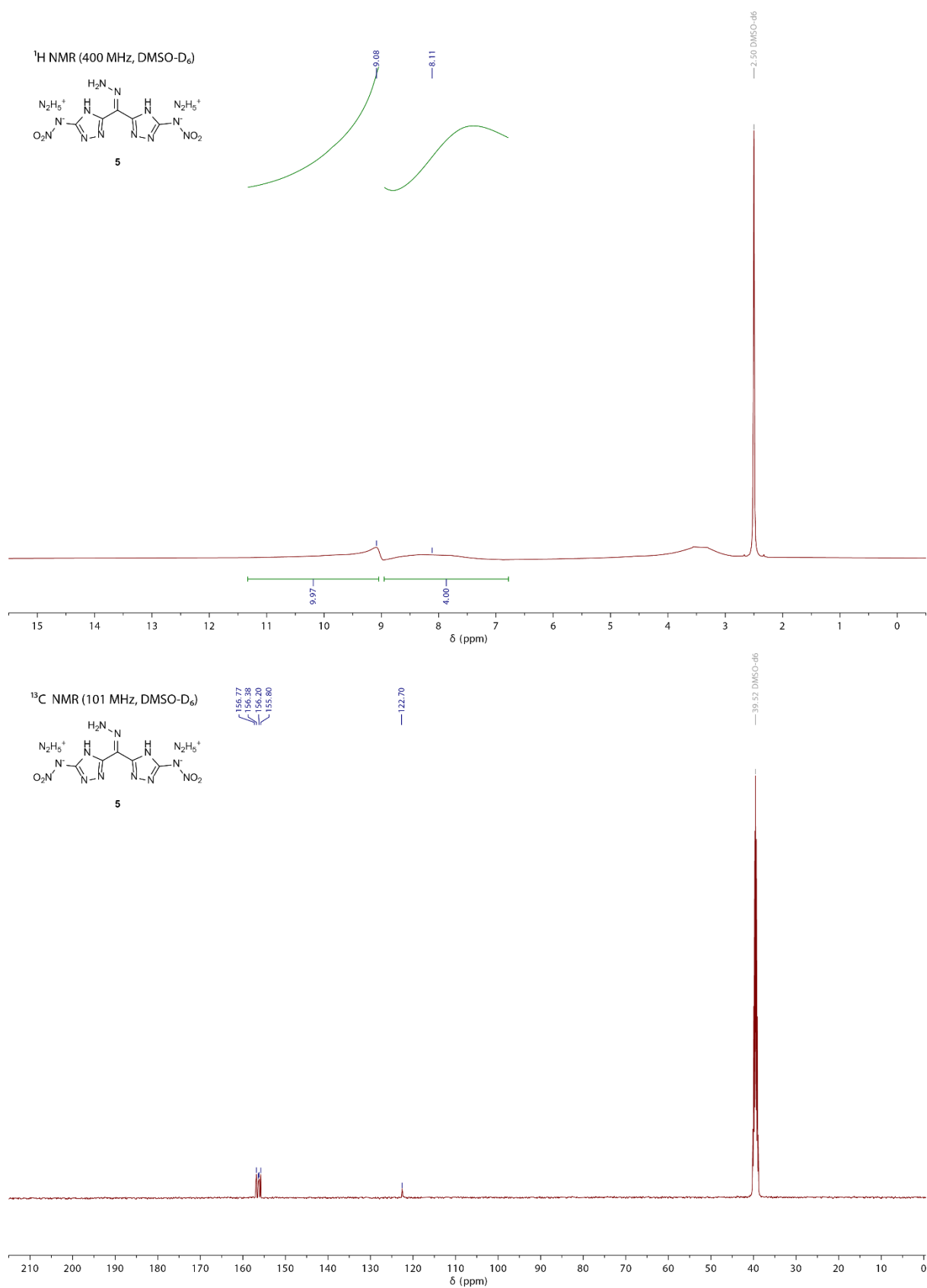


Figure S4. ¹H and ¹³C NMR spectra of compound 5.

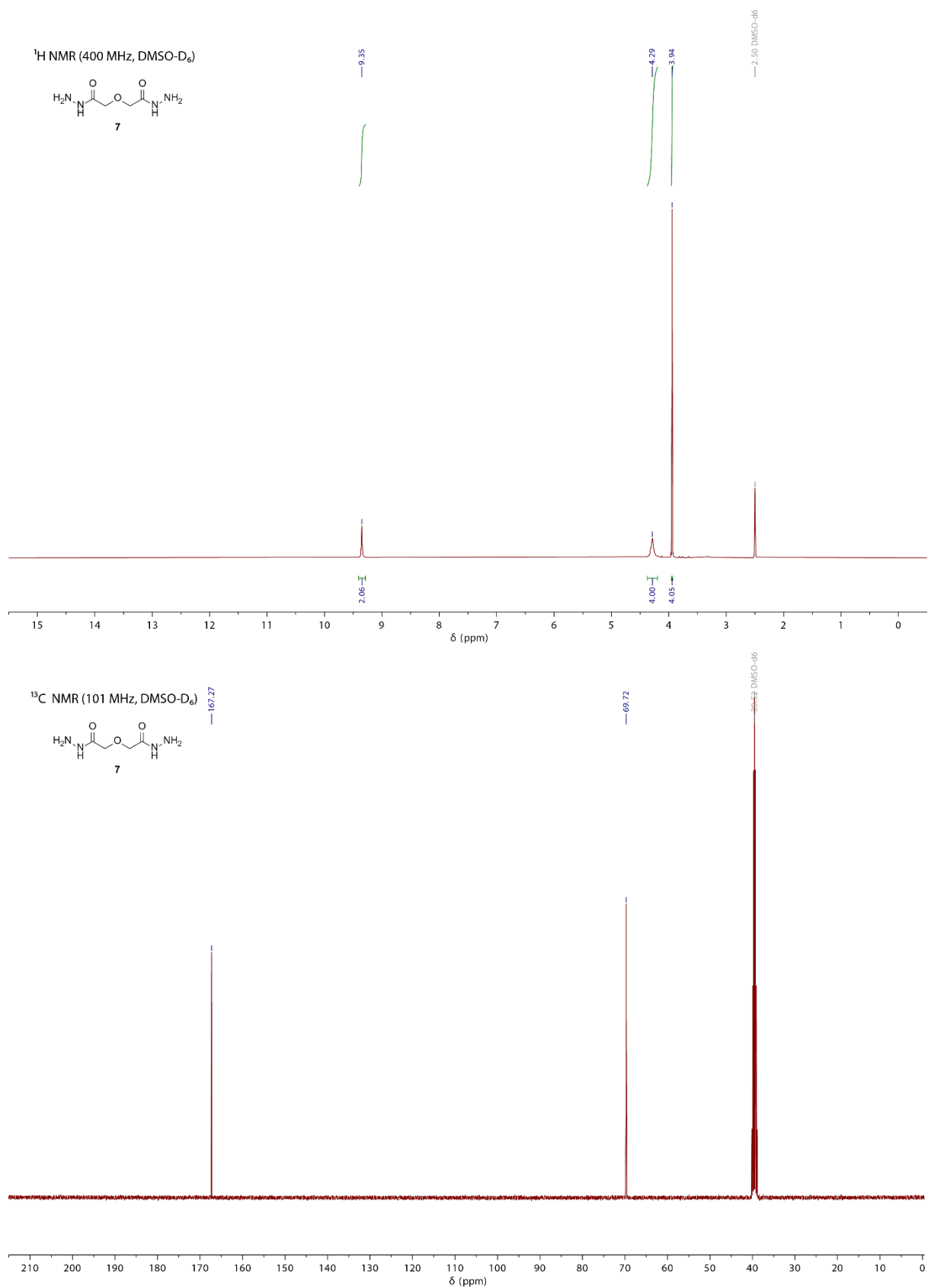


Figure S5. ¹H and ¹³C NMR spectra of compound **7**.

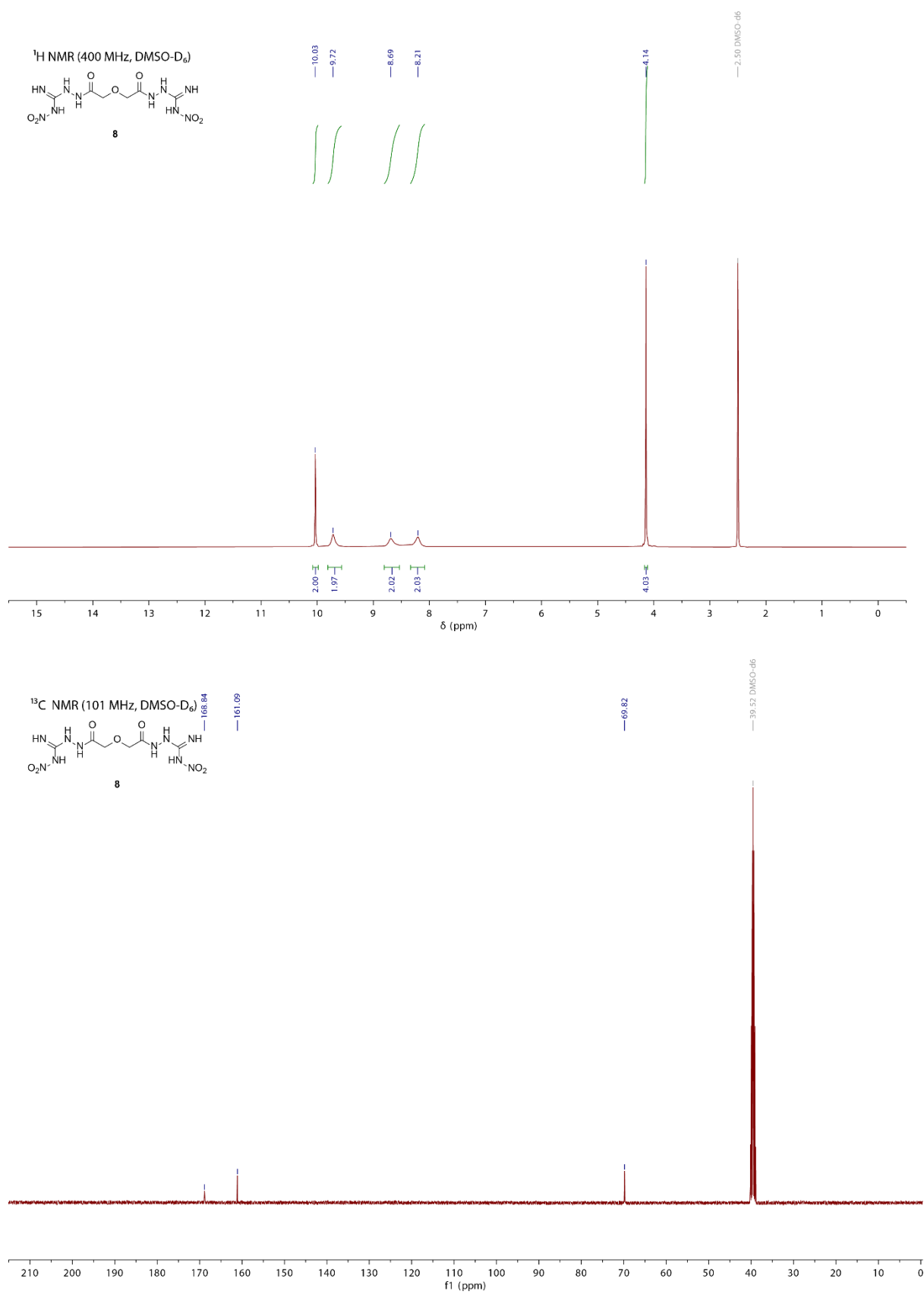


Figure S6. ¹H and ¹³C NMR spectra of compound 8

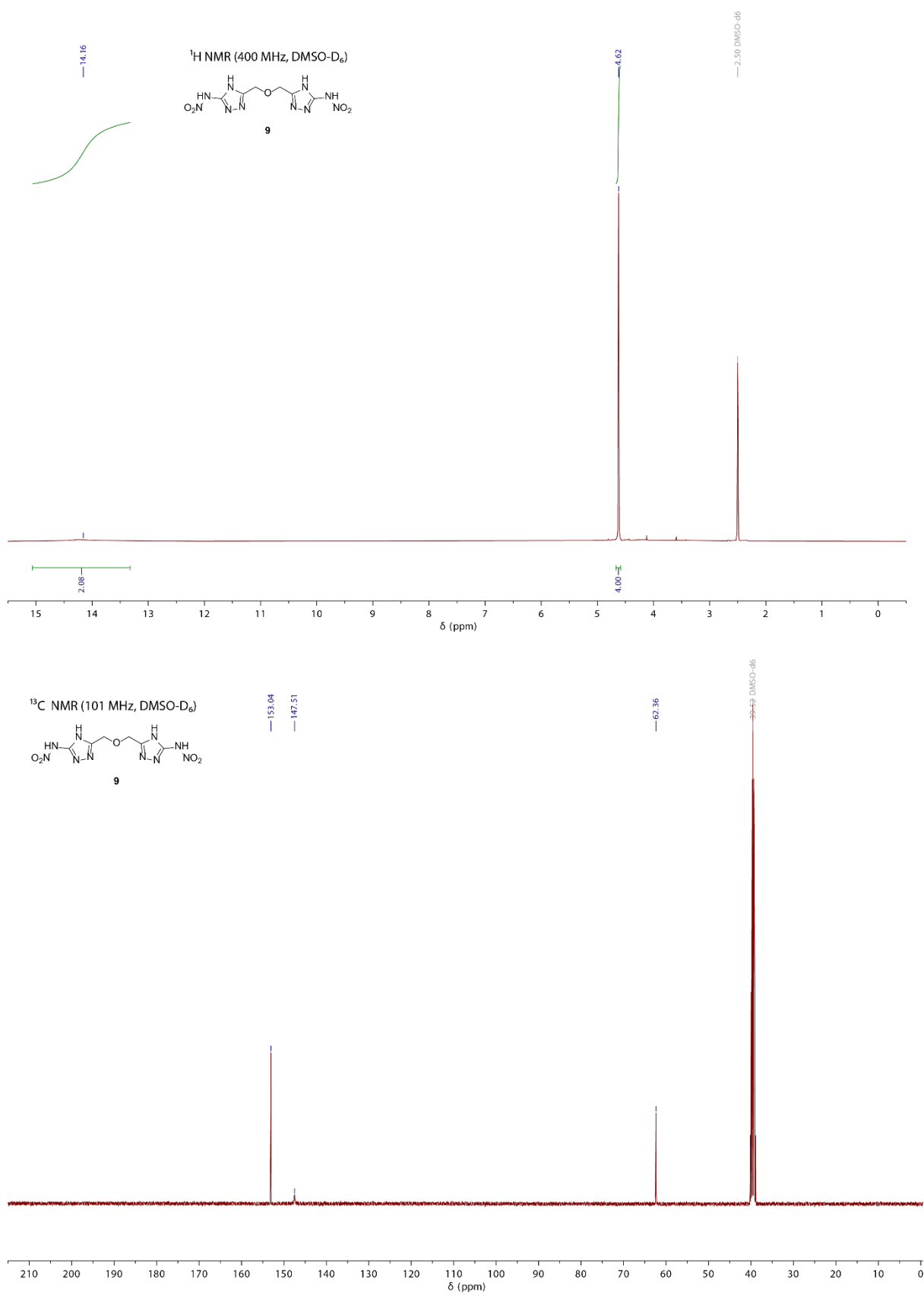


Figure S8. ¹H and ¹³C NMR spectra of compound **9**.

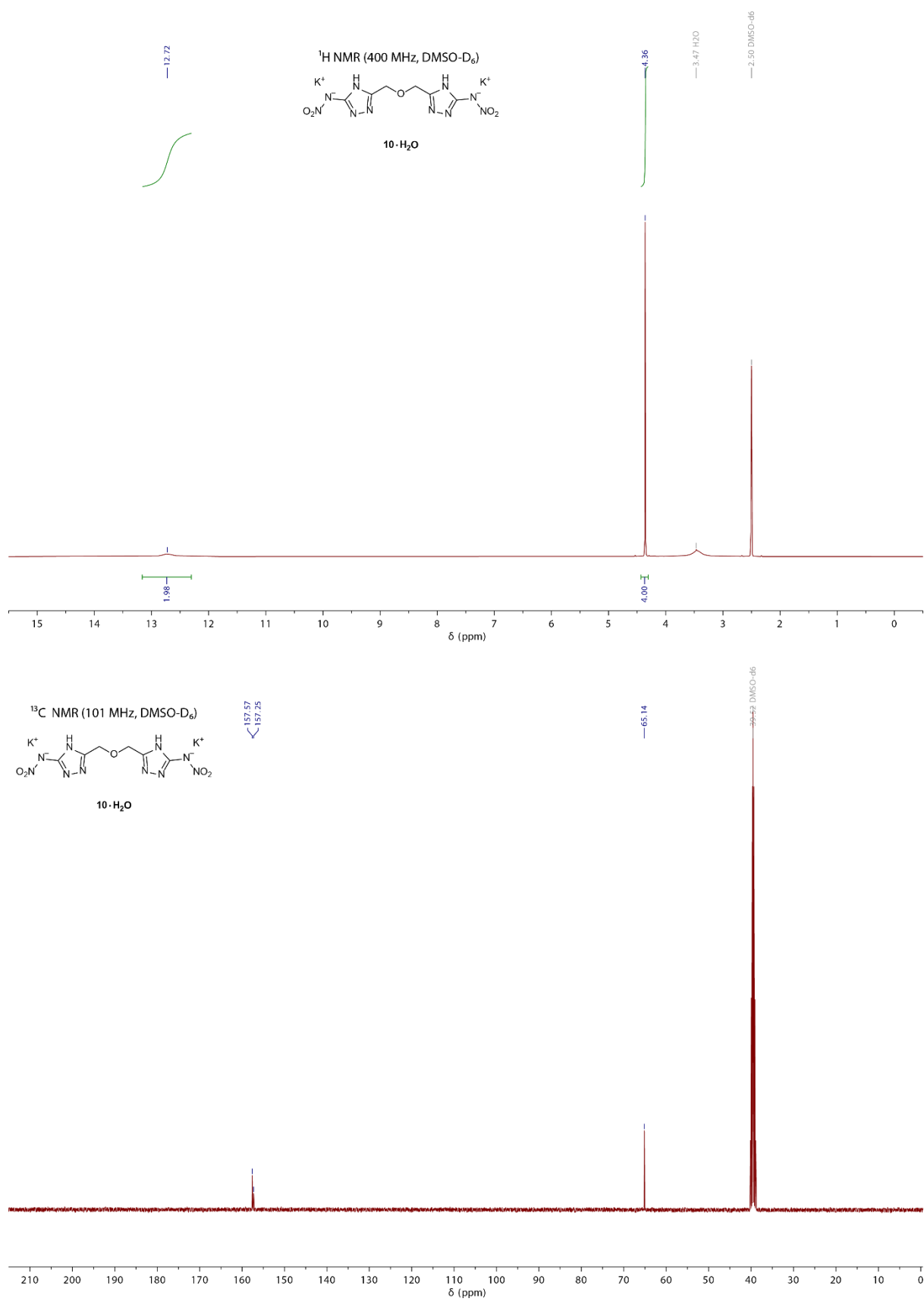


Figure S9. ¹H and ¹³C NMR spectra of compound 10 · H₂O.

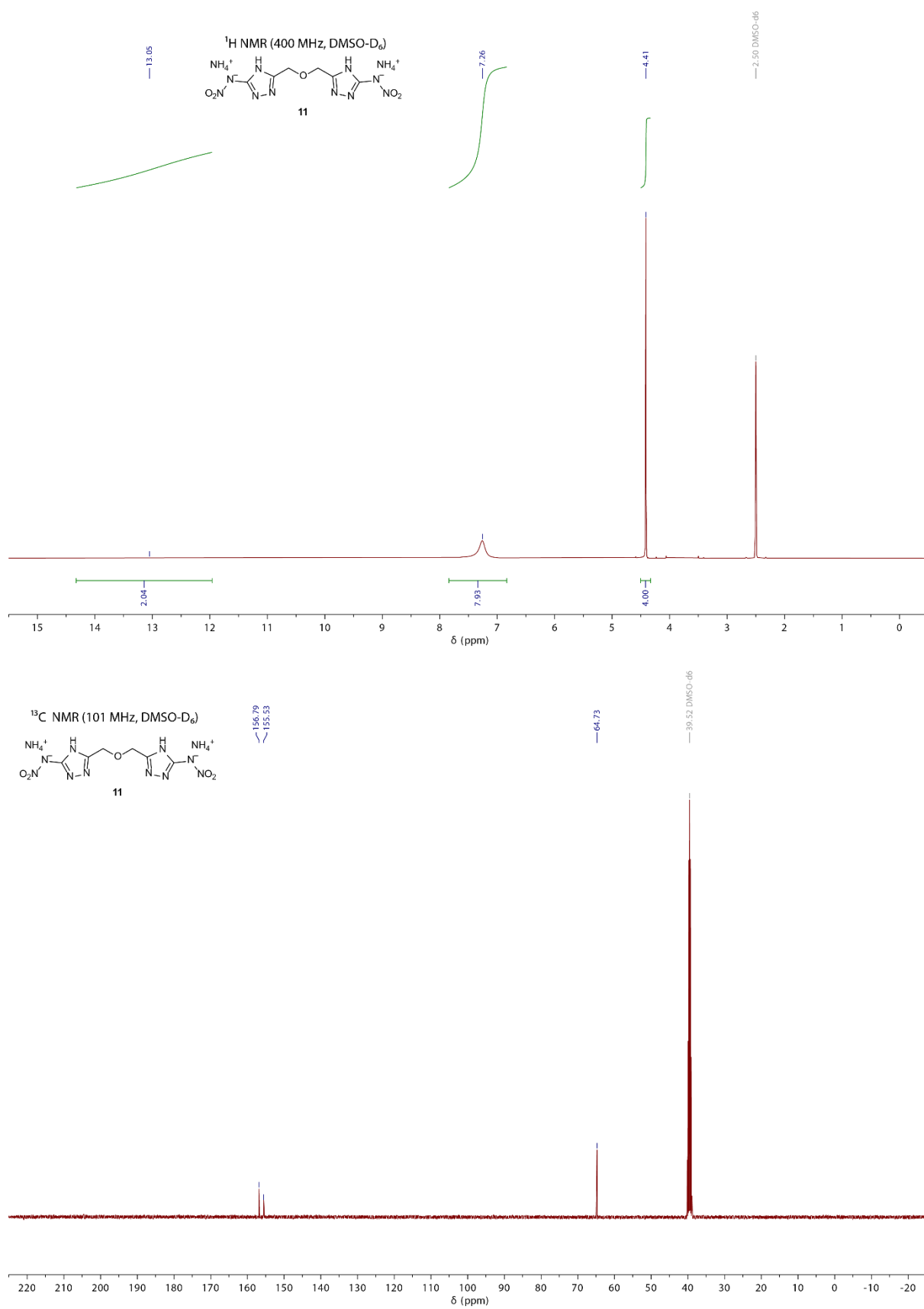


Figure S10. ¹H and ¹³C NMR spectra of compound **11**.

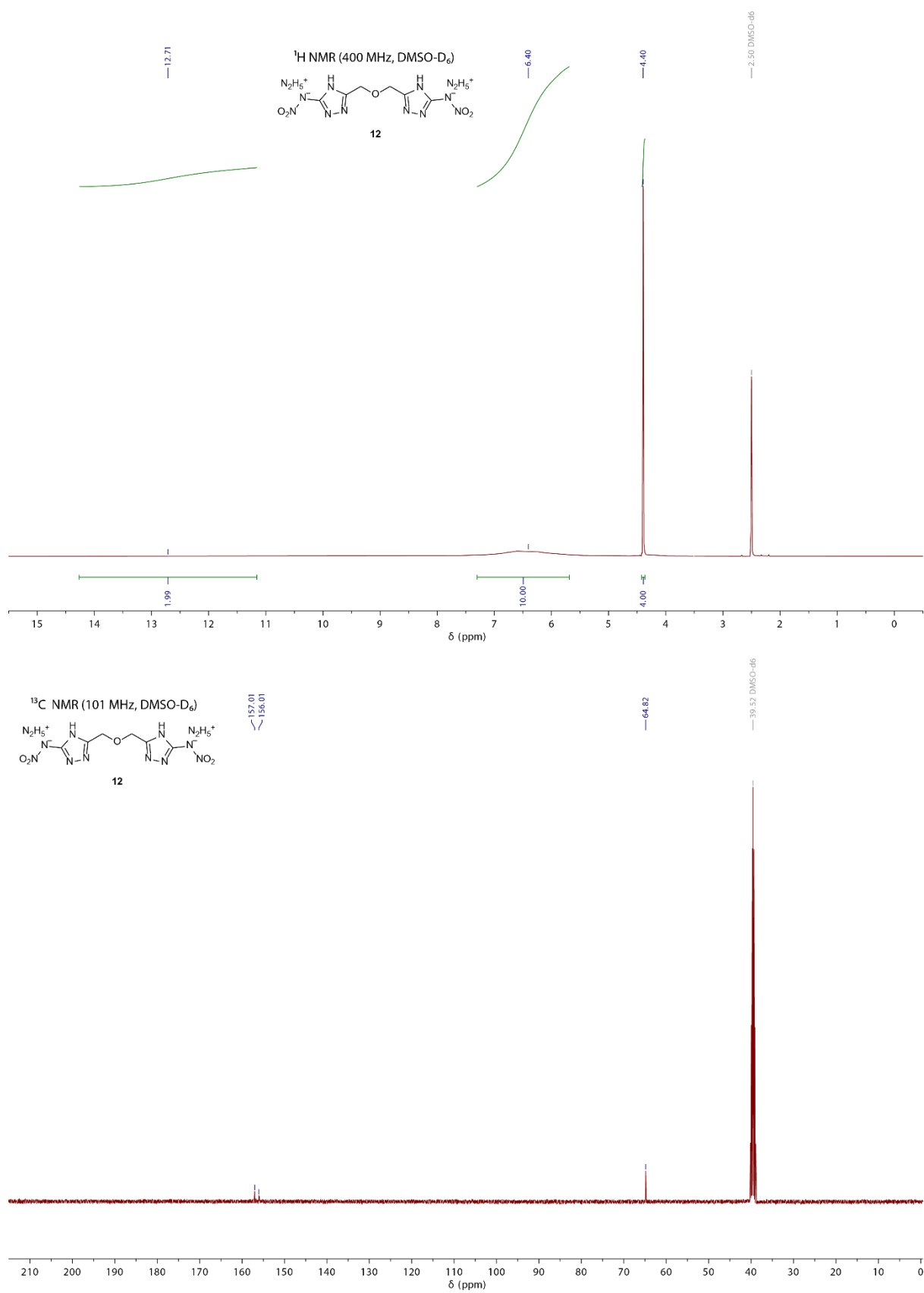


Figure S11. ¹H and ¹³C NMR spectra of compound 12.

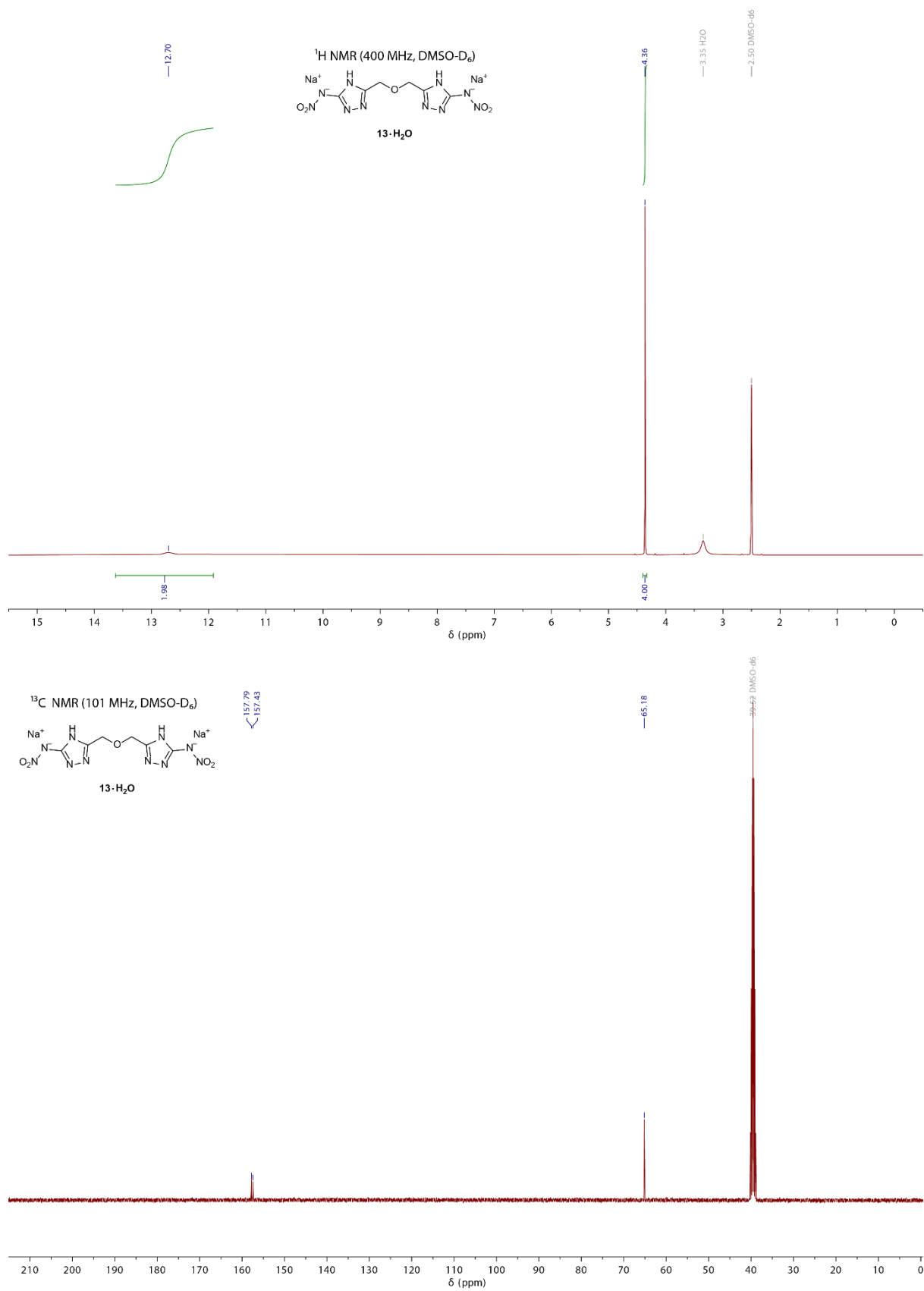


Figure S12. ¹H and ¹³C NMR spectra of compound **13** · H₂O.

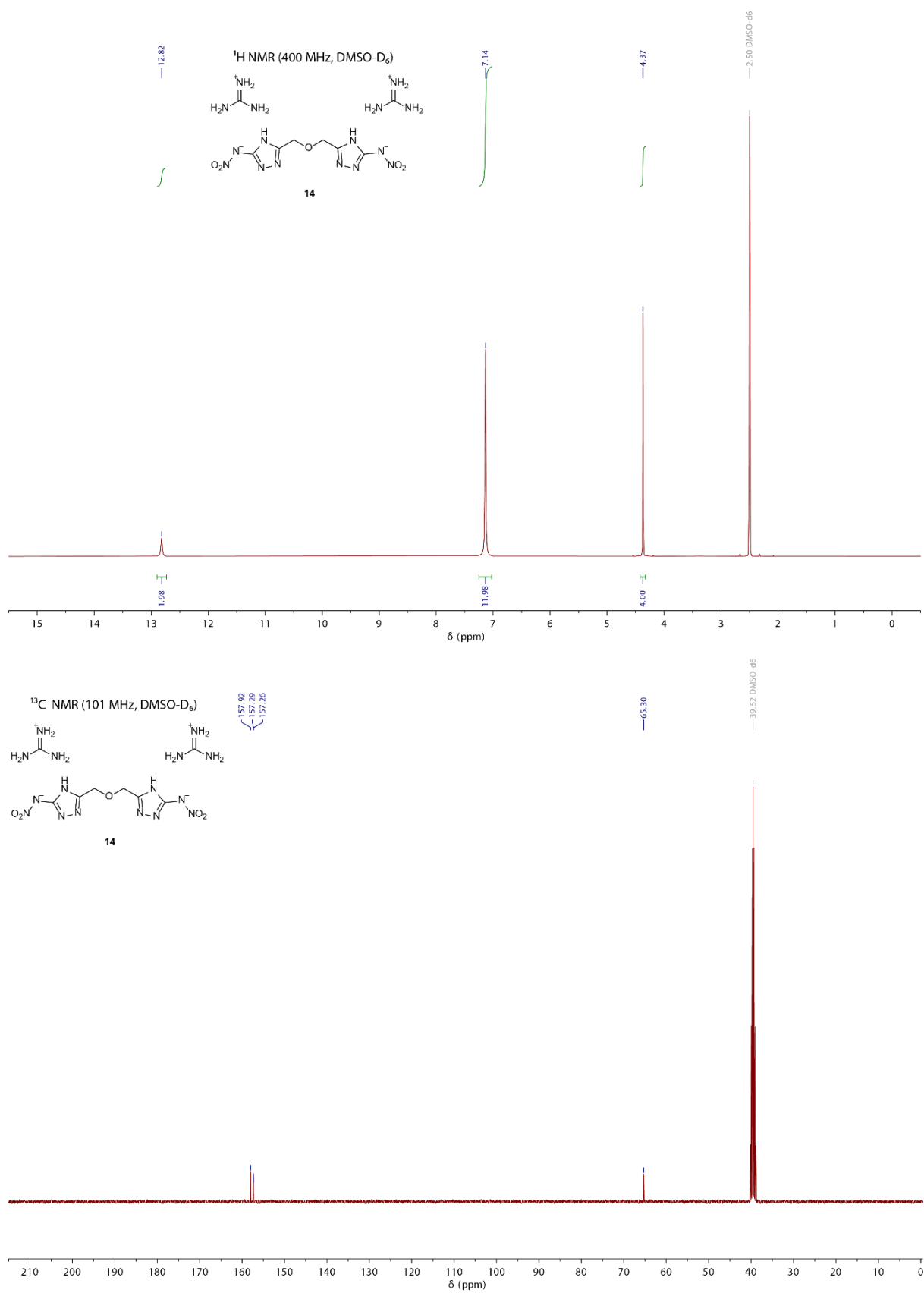


Figure S13. ¹H and ¹³C NMR spectra of compound 14.

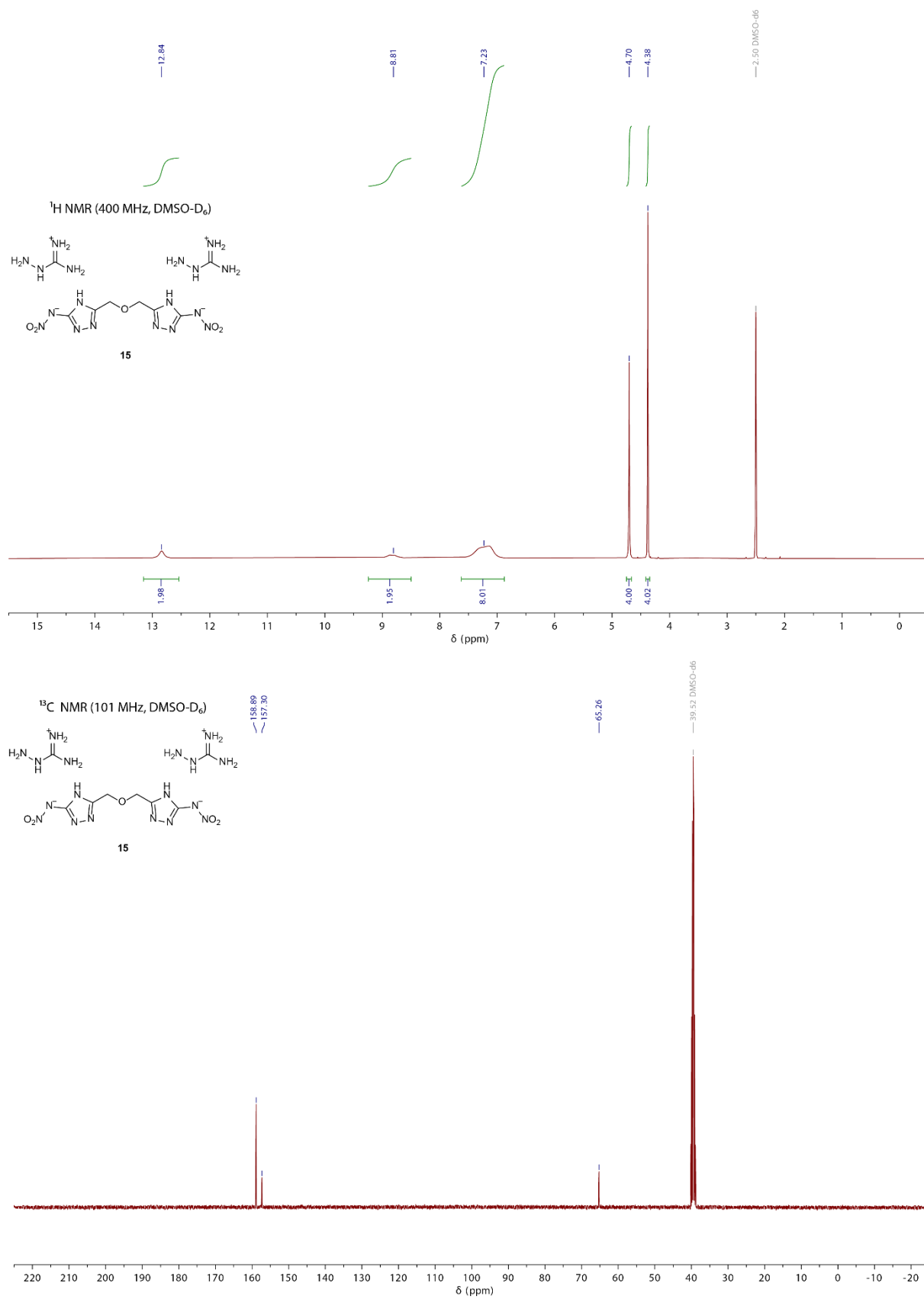


Figure S13. ¹H and ¹³C NMR spectra of compound **15**.

5.6.2 DTA measurements

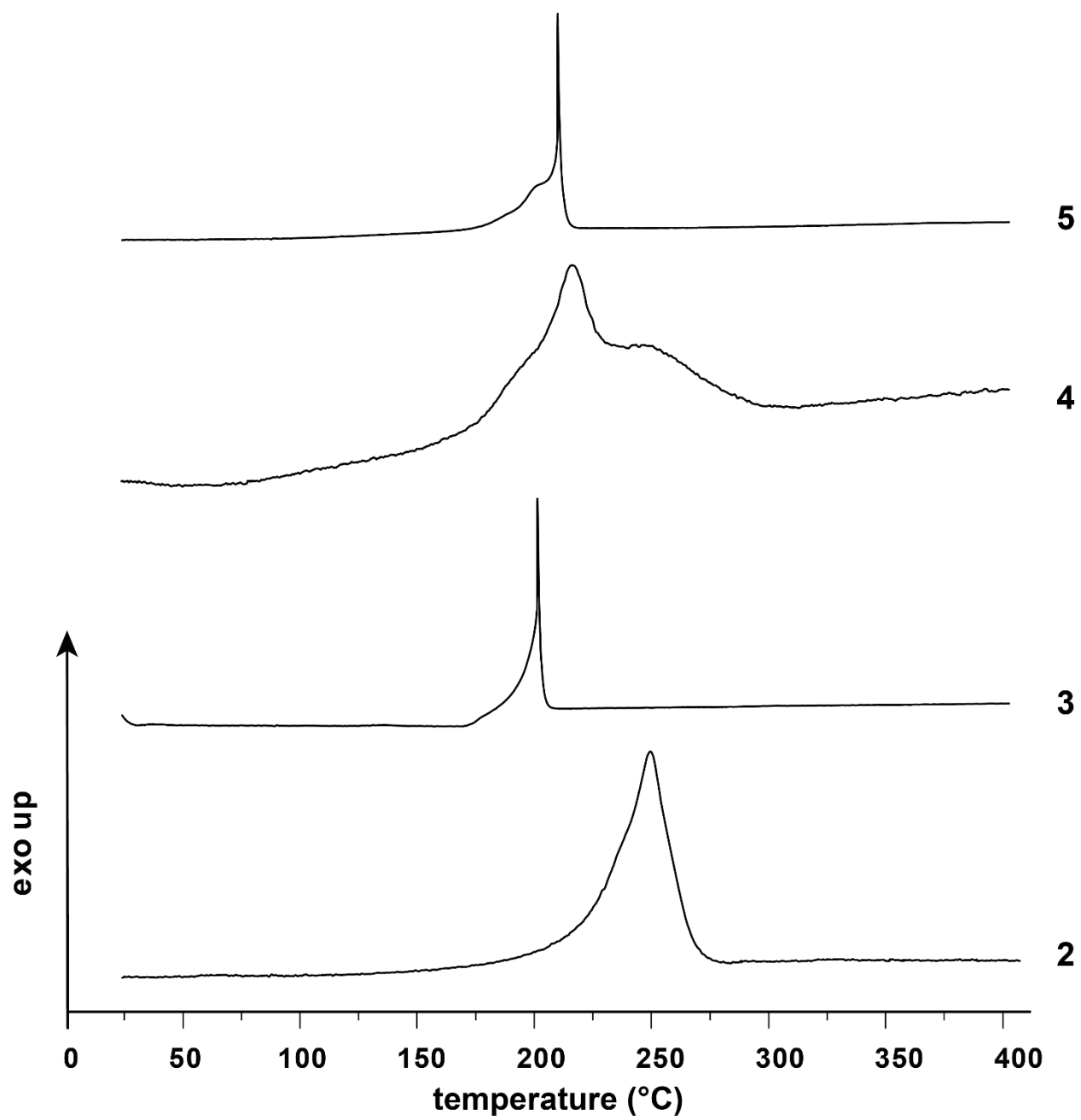


Figure S14. DTA measurements of compounds 2–5.

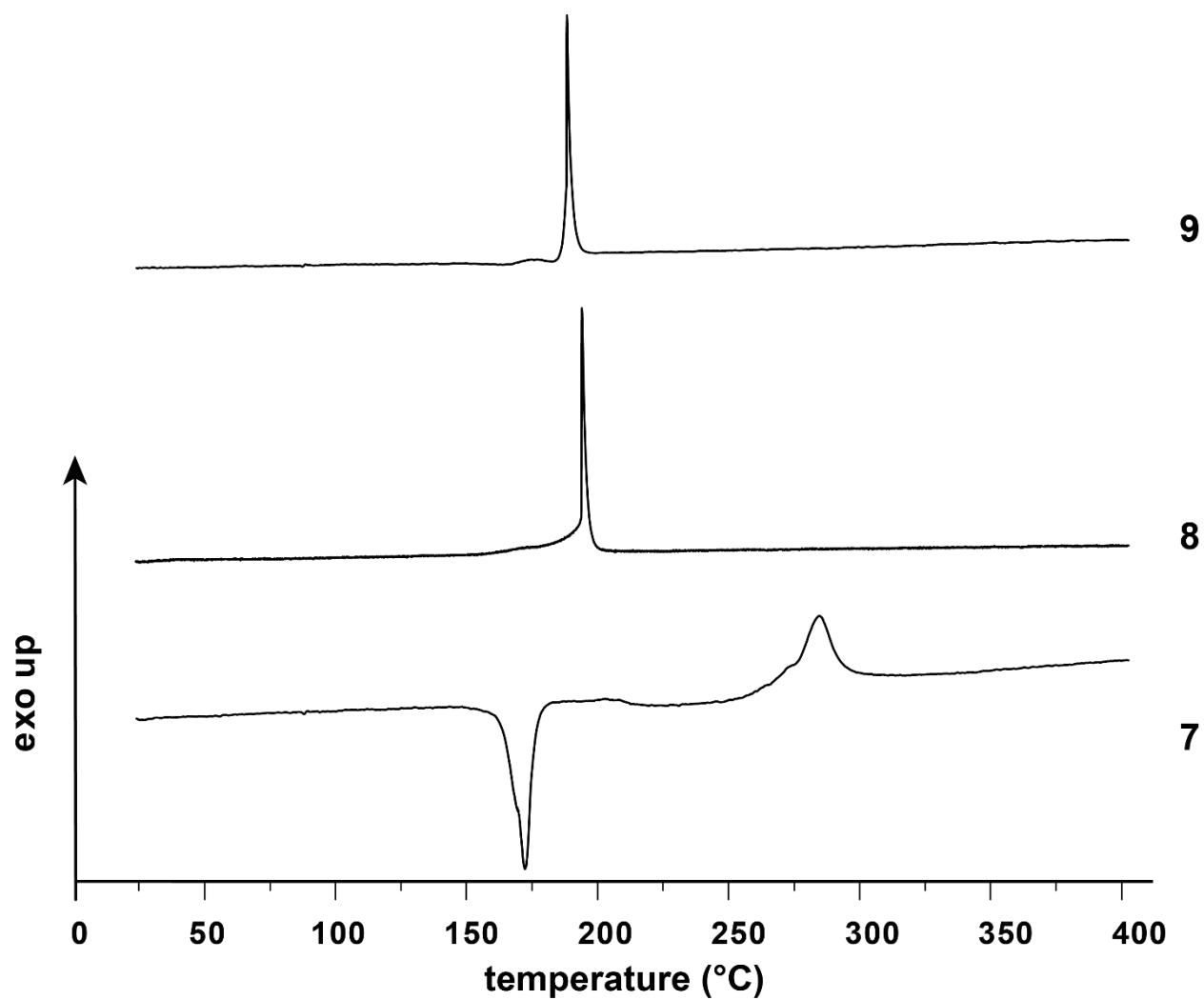


Figure S15. DTA measurements of compounds 7–9.

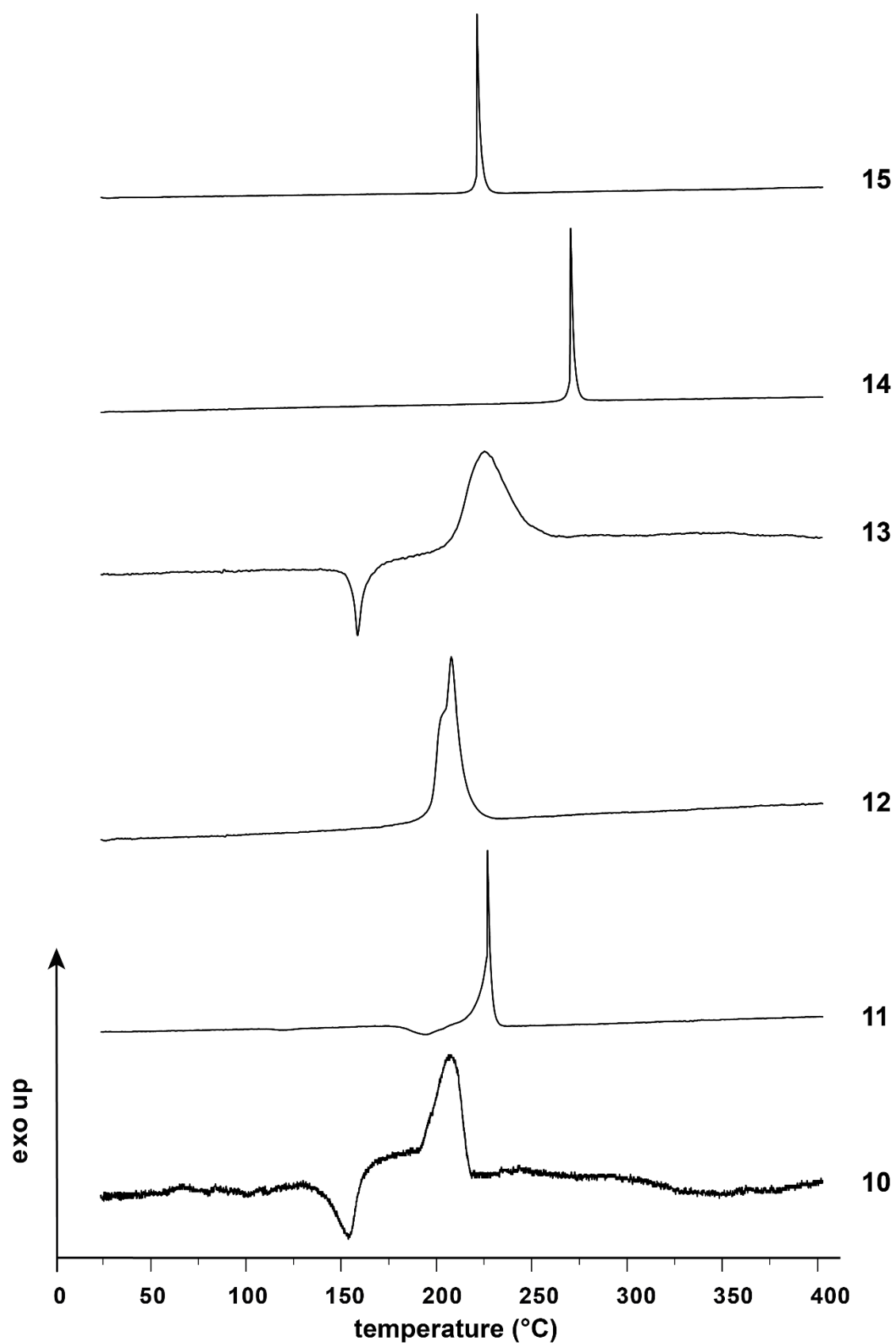


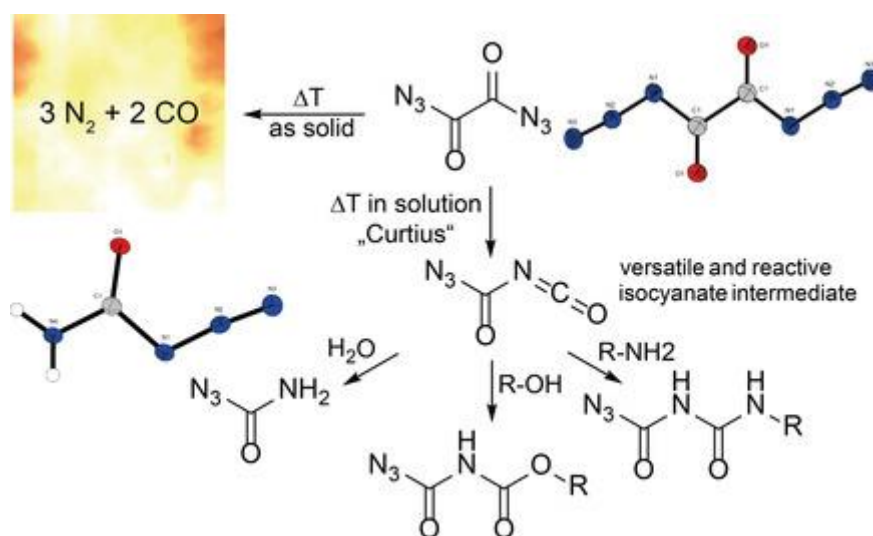
Figure S16. DTA measurements of compounds 10–15.

6. Synthesis, Characterization and Energetic Performance of Oxalyl Diazide, Carbamoyl Azide, and N,N'-Bis(azidocarbonyl)hydrazine

Alexander G. Harter, Prof. Dr. Thomas M. Klapötke*, Dr. Jörg Stierstorfer, Michael Voggenreiter, Prof. Dr. Xiaoqing Zeng

as published in ChemPlusChem **2021**, 6, 870–874

DOI: 10.1002/cplu.202100214



Key words: acyl azides, carbonyl azide, Curtius rearrangement, energetic materials, sensitivities, solid-state structure elucidation

Abstract: As pure compounds, small carbonyl azides enjoy a bad reputation, due to the high explosive sensitivity and instability they demonstrate. Consequently, most reported examples have only been poorly characterized. The compounds oxalyl diazide (**1**), carbamoyl azide (**2**), as well as *N,N*-bis(azidocarbonyl)hydrazine (**3**) were obtained by performing a diazotation reaction on the corresponding hydrazo precursor. Carbamoyl azide (**2**) could also be obtained from oxalyl diazide via Curtius rearrangement to the reactive isocyanate, followed by reaction with water. Further, different trapping reactions of the isocyanate with hydroxyl (methanol, oxetan-3-ol) and amino (2-amino-5*H*-tetrazole) functions are described. All products were extensively analyzed using IR, EA, DTA and multinuclear NMR spectroscopy, and the crystal structures elucidated using single crystal X-ray diffraction. In addition, the sensitivities toward friction and impact were determined and the energetic performances of the carbonyl azides were calculated using the EXPLO5 code.

6.1 Introduction

Carbonyl azides were first described more than a century ago by Curtius and Thiele in 1894.^{1, 2} Curtius was primarily interested in the explosive nature, as well as the decomposition of carbonyl azides. The low stability of acyl azides limits reports on the synthesis and the characterization of such compounds.³ Today, the Curtius rearrangement forming isocyanate intermediates and subsequent reaction with water, is a common method to convert carbonyl azides to amines.⁴⁻⁶ The number of carbonyl azides, which have been both spectroscopically and structurally characterized has slightly increased in recent years. In 1992, Willner and coworkers characterized fluorocarbonyl azide by gas electron diffraction.⁷ Zeng *et al.* published the crystal structure of carbonyl diazide in 2010. This was followed by the work of Banert *et al.* on formyl azide, which was later structurally characterized by Zeng.⁸⁻¹² Subsequently, Zeng *et al.* published the structures of *N*-methylcarbamoyl azide, as well as of aryl substituted carbonyl azides such as 1*H*-pyrrole carbonyl azide.^{13, 14} Recently, Benz *et al.* successfully synthesized and characterized nitrocarbamoyl azide, which shows remarkable stability.¹⁵ The publication by Benz mentioned the existence of two carbonyl azides, namely, oxalyl diazide and carbamoyl azide, however, neither were characterized (Figure 1).^{2, 16-18}

It is appropriate to include *N,N*-bis(azidocarbonyl)hydrazine, which has also been described in the literature, due to the structural relationship it has with both oxalyl diazide and carbamoyl azide.¹⁹ Not only does this work provide key information on

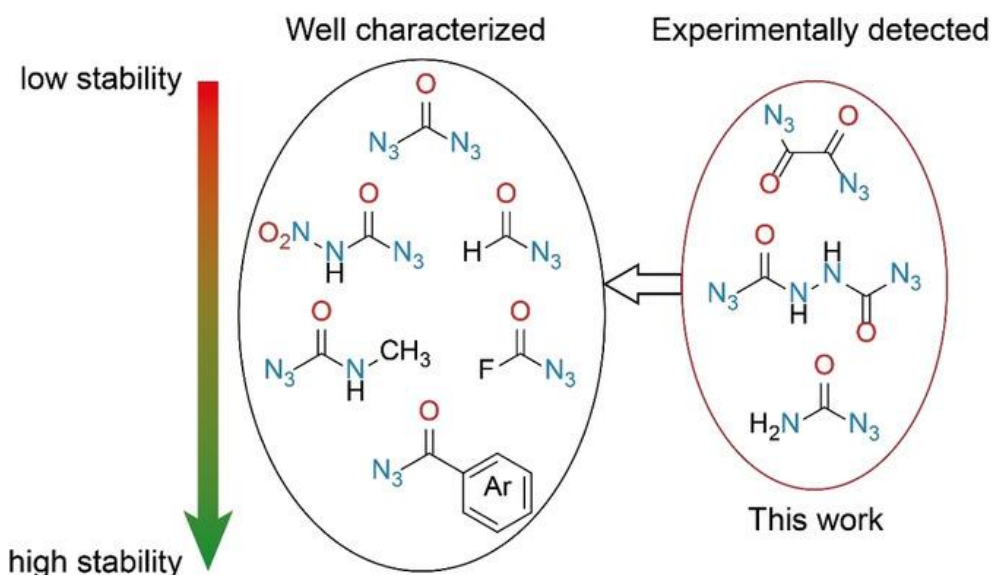


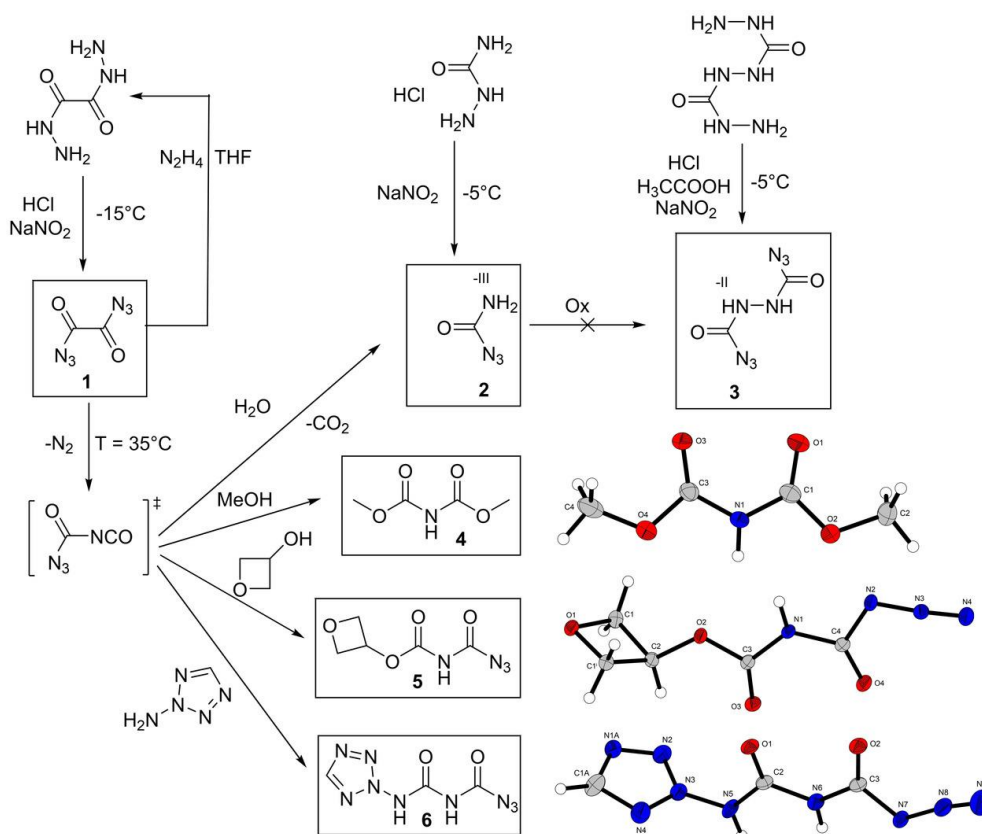
Figure 1. Well-characterized members of the carbonyl azide family arranged with respect to their stability towards heat and external stimuli. This work centers around the structural and physicochemical characterization of the carbonyl azides which have only been mentioned in the literature.

important missing and fundamental members of this class of compounds, namely, on oxalyl diazide (**1**), carbamoyl azide (**2**), and *N,N'*-bis(azidocarbonyl)hydrazine (**3**), it also demonstrates compounds **1–3** to be small, versatile, but very energetic members of the carbonyl azide family. In addition, the decomposition of oxalyl diazide via a Curtius rearrangement to form an isocyanate, as well as subsequent trapping reactions with hydroxyl and amino groups are reported.

6.2 Results and Discussion

6.2.1 Synthesis

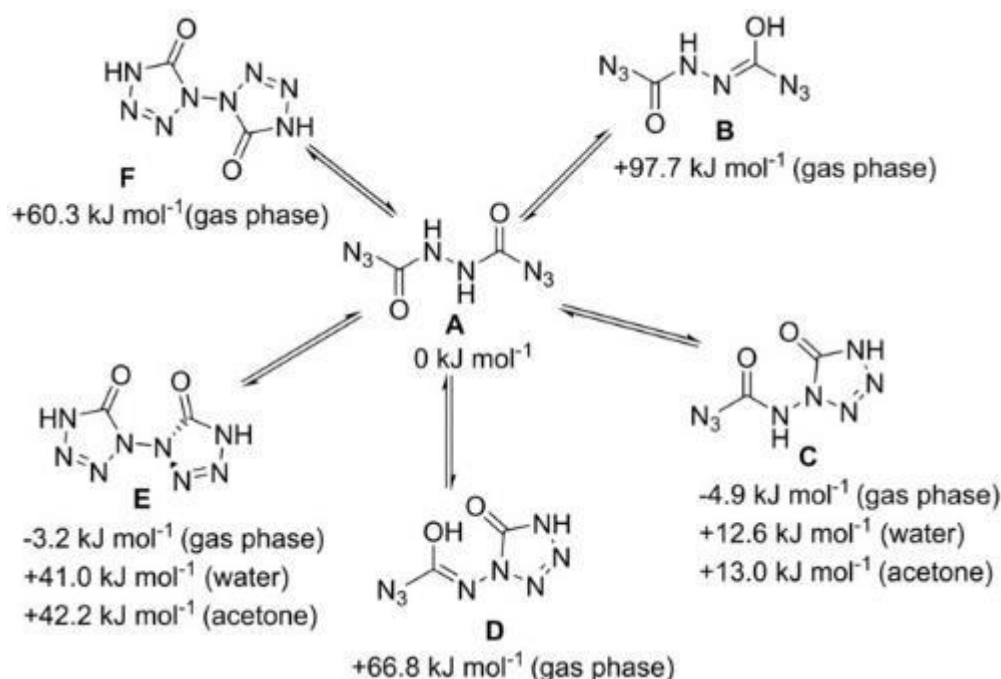
The hydrazino precursor compounds were synthesized according to literature procedures.^{16, 19} The carbonyl azides (**1–3**) can be synthesized by careful diazotation of the corresponding hydrazo- compounds (Scheme 1). The reactions have to be carried out at low temperature in order to achieve high yields: Pure **1** decomposes rapidly in protic solvents at room temperature forming the isocyanate intermediate and reacting with moist air or solvent. Another possible way to obtain **2** is by the Curtius rearrangement of **1**, followed by reaction with water. Furthermore, the reactive isocyanate intermediate can also be trapped with compounds containing a hydroxyl group, resulting in the formation of a carbamate-like carbonyl azide compound.¹⁷ This strategy also works well if a compound containing an amino functional group is used instead, which produces an acetamide-like carbonyl azide derivative.²⁰⁻²² In this work,



Scheme 1. Synthetic pathways used in this work to obtain the small carbonyl azide compounds **1–3**, and trapping reaction of the reactive isocyanate intermediate, which is used to obtain compounds **4–6** (CCDC deposition numbers 2077540, 2077535, 2077538). Thermal ellipsoids are drawn at the 50% probability level. Deposition Numbers 2077540, 2077535, and 2077538 contain the supplementary crystallographic data for this paper. These data are provided free of charge by the joint Cambridge Crystallographic Data Centre and Fachinformationszentrum Karlsruhe Access Structures service www.ccdc.cam.ac.uk/structures.

methanol was used which reacted with the isocyanate intermediate, and surprisingly, hydrazoic acid was eliminated by methanol and dimethyl iminodicarbonate (**4**) was formed. Furthermore, using oxetan-3-ol and 2-amino-2*H*-tetrazole as reagents, oxetan-3-yl-*N*-azidocarbonyl-carbamate (**5**) and *N*-azidocarbonyl-*N'*-(2*H*-tetrazol-2-yl)-urea (**6**) were obtained. Subsequently, several oxidative coupling reactions were attempted to convert **2** into **3**, using different oxidizing agents. However, despite these attempts, none of the oxidizing reagents successfully converted **2** into compound **3**, instead only decomposition or the starting material was observed. In this work, the molecular orbitals (MOs) of six different tautomers of *N,N'*-bis(azidocarbonyl)hydrazine (**3**) were calculated using the G09 W code (further details in the Supporting Information), and the gas phase energies were calculated at the CBS-4 M level. Surprisingly, the mono-tetrazolone tautomer (**C**), as well as the di-tetrazolone tautomer (**E**) are lower in energy than the open amide form (Scheme 2). However, all attempts to synthesize one of these tetrazolone forms (in polar, acidic or basic media) failed. To obtain more insight into which form is present in solution, the three tautomers **A**, **C** and

E were calculated with the solvents water and acetone at the MP2 level. In agreement with the experimental results in solution, **A** is calculated to be lower in energy in solution than either **C** or **E** (Scheme 2).



Scheme 2. Six different tautomers of *N,N'*-bis(azidocarbonyl)hydrazine (**3**): **A** amide form; **B** iminol form; **C** mono-tetrazolone form; **D** enol-tetrazolone form; **E** di-tetrazolone form (90° twist); **F** di-tetrazolone form (planar, transition state).

6.2.2 Crystal Structures

Compounds **1** and **2** crystallize in the space group number 14 (*P21/c* for **1** and *P21/n* for **2**) and **3** crystallizes in the monoclinic space group *C2/c* (No. 15). Compound **1** shows the highest density (1.701 g cm⁻³) followed by **3** (1.666 g cm⁻³) and **2** (1.565 g cm⁻³).

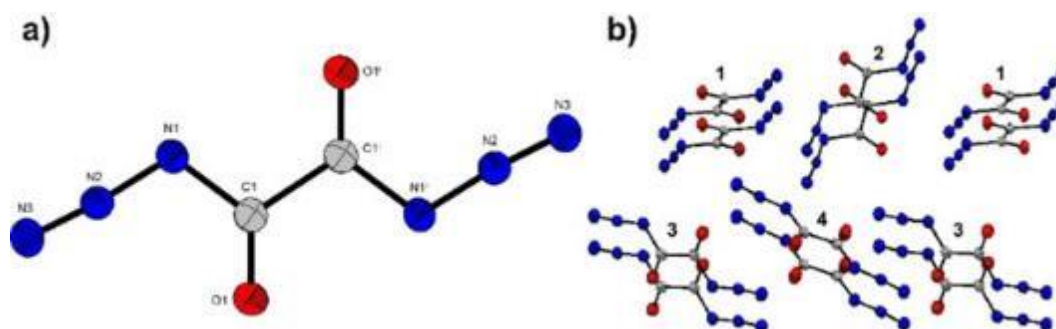


Figure 2. a) Crystal structure of oxalyl diazide (**1**). Thermal ellipsoids are drawn at the 50% probability level. b) Crystal packing of oxalyl diazide forming pairs. Ellipsoids are drawn at the 50% probability level. Deposition Number 2077536 (for **1**) contains the supplementary crystallographic data for this paper. These data are provided free of charge by the joint Cambridge Crystallographic Data Centre and Fachinformationszentrum Karlsruhe Access Structures service www.ccdc.cam.ac.uk/structures.

The angles of oxalyl diazide (**1**) around C1 are nearly trigonal planar, and the azide moiety has an angle of 174.4° at N1-N2-N3. As is the case in other carbonyl azides, the azido moiety is *syn* to the carbonyl group.^{8, 23, 24} In the crystal, oxalyl diazide forms pairs as shown above, in which the molecules are arranged alternately (Figure 2b). Oxalyl diazide has no stabilizing, intermolecular hydrogen bonds due to the absence of hydrogen atoms in the molecule, calculated from the Hirshfeld surface (further details in the Supporting Information).

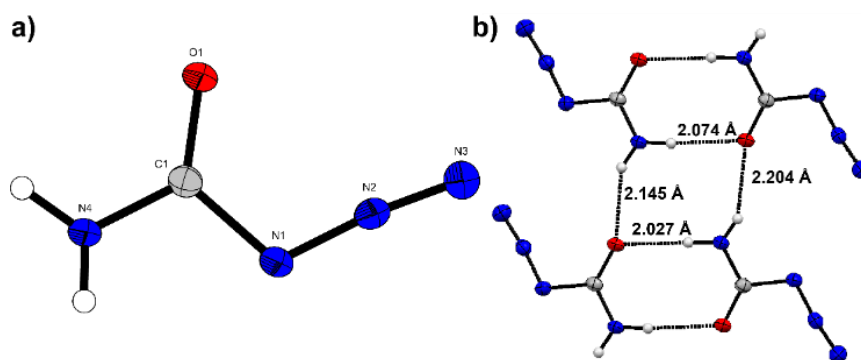


Figure 3. a) Molecular structure of carbamoyl azide (**2**). Thermal ellipsoids are drawn at the 50 % probability level. b) A network results from hydrogen bonds between the molecules with distance of about 2 Å. Deposition Number 2077537 (for **2**) contains the supplementary crystallographic data for this paper. These data are provided free of charge by the joint Cambridge Crystallographic Data Centre and Fachinformationszentrum Karlsruhe Access Structures service www.ccdc.cam.ac.uk/structures.

The N2–C1–N1 angle (111.2°) in carbamoyl azide (**2**) deviates from the expected 120° (Figure 3a). The azide moiety also has an angle of about 174° and is oriented *syn* with respect to the carbonyl group.^{8, 23, 24} The molecule is planar, and strong hydrogen bonds are present between the molecules (2.027 Å to 2.204 Å) (Figure 3b).

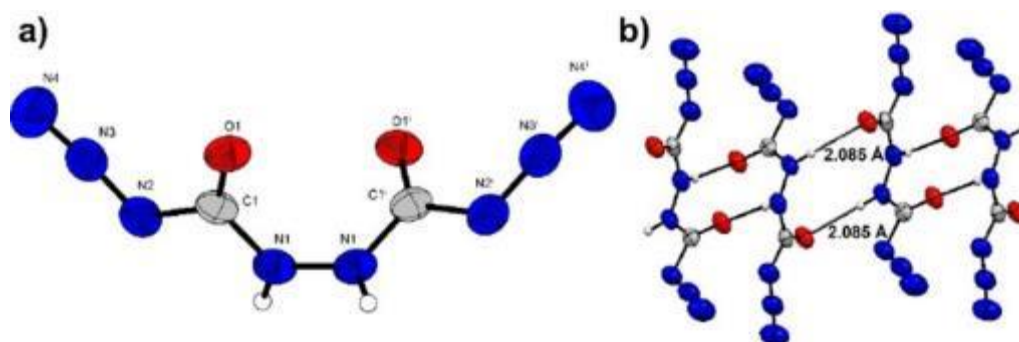


Figure 4. a) Crystal structure of *N,N*-bis(azidocarbonyl)hydrazine (**3**) (Deposition number 2077539). Thermal ellipsoids are drawn at the 50 % probability level. b) Hydrogen bond network of *N,N*-bis(azidocarbonyl)hydrazine with distances of 2.085 Å. Deposition Number 2077539 (for **3**) contains the supplementary crystallographic data for this paper. These data are provided free of charge by the joint Cambridge Crystallographic Data Centre and Fachinformationszentrum Karlsruhe Access Structures service www.ccdc.cam.ac.uk/structures.

The azide group of *N,N'*-bis(azidocarbonyl)hydrazine (**3**) azide group ($\angle(\text{NNN})=173.7^\circ$) is again oriented *syn* with respect to the carbonyl groups,^{8, 23, 24} and the molecule

possesses a center of symmetry between the hydrazino nitrogen atoms (N1, N1'). The molecule is twisted at the hydrazine bridge with a torsion angle of 72.2°. Compound **3** has strong intermolecular hydrogen bonds with a distance of 2.085 Å (Figure 4b) which results in the formation of a 3-dimensional network.

6.2.3 NMR and Vibrational spectroscopy

The azide and carbonyl moieties of **1** are identified by strong bands in the IR spectrum at 2178 cm⁻¹ and 1681 cm⁻¹ respectively. The FT-IR spectrum of solid **2** shows two medium bands at 3384 and 3247 cm⁻¹ corresponding to the amino group, and a strong band at 1674 cm⁻¹ for the carbonyl group. In the Ne-matrix and gas phase IR spectra, the bands corresponding to the amino group are observed at 3588 and 3470 cm⁻¹, which corresponds to a dramatic blue-shift from the pure solid (Figure 5). By contrast, the CO stretching mode which occurs at 1766 cm⁻¹ in the matrix IR spectrum and at 1750 cm⁻¹ in the gas phase, is significantly red-shifted to 1674 cm⁻¹ in the solid. Clearly, these large shifts are due to strong intermolecular hydrogen bonds between the amino and carbonyl groups in the solid state. The asymmetric stretching mode of the azido moiety in the IR (gas, solid, and Ne-matrix) and Raman (solid) spectra remains unchanged at around 2170 cm⁻¹. The IR spectrum of **3** showed weak bands at 3166 cm⁻¹ and 3004 cm⁻¹ corresponding to the hydrazine bridge, and bands for the azido moieties at 2170 cm⁻¹ (medium) and 2150 cm⁻¹ (strong).¹⁹ The carbonyl group in **3** was identified by bands at 1732 cm⁻¹ and 1683 cm⁻¹.

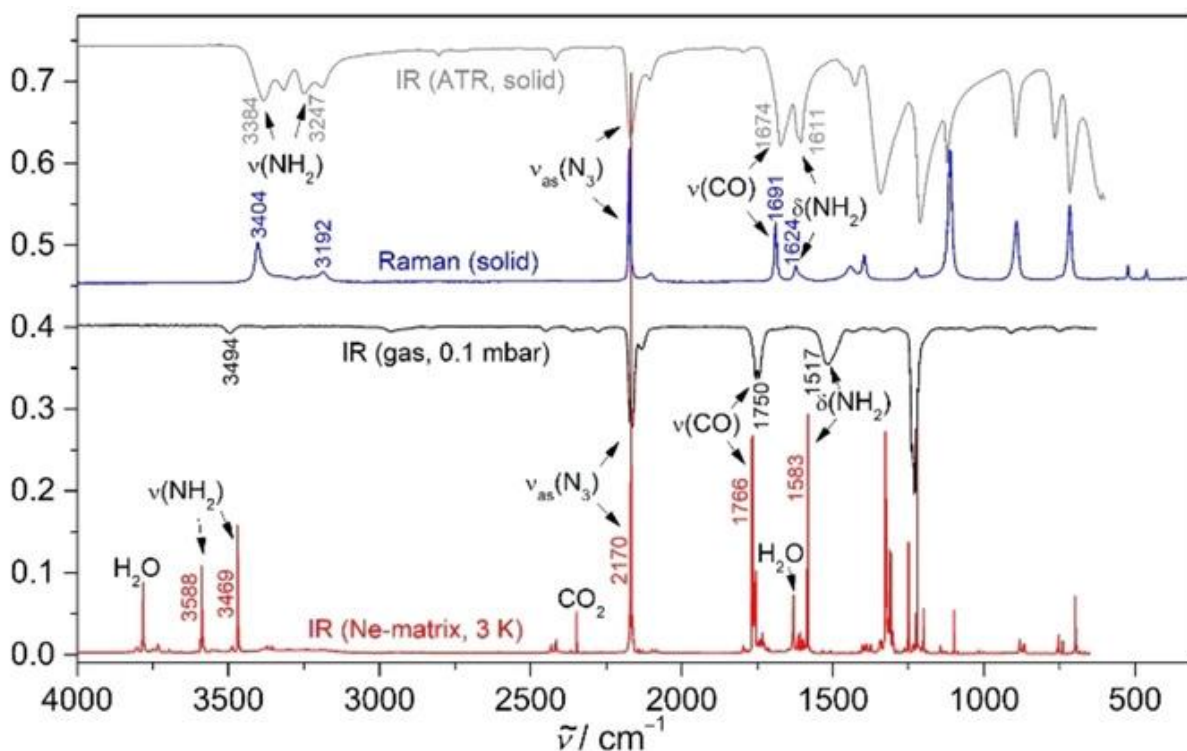


Figure 5. IR and Raman spectra of carbamoyl azide (**2**).

6.2.4 Physicochemical Properties

Oxalyl diazide explodes violently at 46 °C after melting. It is extremely sensitive towards external stimuli and was found to be too sensitive to be measured with the capabilities of our test setups (friction <0.1 N, impact <1 J). Micro-detonations of **1** occurred repeatedly without any obvious source of stimulus during handling. In contrast to compound **1**, carbamoyl azide (**2**) is insensitive (!) towards friction (>360 N) and shows only low sensitivity towards impact (20 J). Furthermore, **2** is quite thermally stable for a carbonyl azide, showing a melting point of 96 °C and a decomposition point of 133 °C (Table 1). *N,N'*-bis(azidocarbonyl)hydrazine (**3**) is thermally more stable than **1** or **2**, with a decomposition temperature of 154 °C without melting. The other two carbonyl azide compounds (**5** and **6**) show decomposition temperatures of 135 °C and 145 °C respectively. The detonation parameters were calculated using the EXPLO5 code and compared to the calculated detonation parameters of carbonyl diazide and nitrocarbamoyl azide.^{8, 11, 15} The calculated detonation velocities range from 6241 m s⁻¹ or the oxetane derivative (**5**) to 8236 m s⁻¹ for oxalyl diazide (**1**).

Table 1. Physicochemical properties of oxalyl diazide (1), carbamoyl azide (2), N,N'-bis(azidocarbonyl)hydrazine (3), oxetan-3-yl-N-azidocarbonyl-carbamate (5), N-azidocarbonyl-N'-(2H-tetrazol-2-yl)-urea (6), carbonyl diazide (CDA)^{8,11} and nitrocarbamoyl azide (HNCA).¹⁵

	1	2	3	5	6	CDA ^[8,11]	HNCA ^[15]
Formula	C ₂ N ₆ O ₂	CH ₂ N ₄ O	C ₂ H ₂ N ₈ O ₂	C ₅ H ₆ N ₄ O ₄	C ₃ H ₃ N ₉ O ₂	CN ₆ O	CHN ₅ O ₃
FW [g·mol ⁻¹]	140.06	86.05	170.09	186.13	197.12	112.05	131.05
I ^[a] [J]	<1	20	1–2	>40	4	<1*	<1
FS ^[b] [N]	<0.1	>360	0.1	>360	360	<0.1*	0.5
N / N+O ^[c] [%]	60.00 / 82.85	65.11 / 83.70	65.88 / 84.69	30.10 / 64.38	63.95 / 80.15	75.00 / 89.28	53.44 / 90.00
Ω _{CO} , Ω _{CO₂} ^[d] [%]	0, -22.8	-18.6, -37.2	-9.4, -28.2	-77.4, -34.4	-44.6, -20.3	0, -14.3	+18.3, +6.1
T _m ^[e] / T _{dec.} ^[f] [°C]	45/46	96/133	-/154	127/135	-/145	-/25–30*	72/83
ρ ^[g] [g·cm ⁻³]	1.701	1.565	1.666	1.604	1.678	1.676	1.708
Δ _f H ^[h] [kJ·mol ⁻¹]	329.7	41.7	309.3	-340.5	353.4	439.5	147.5
EXPLO5 V6.05							
-Δ _E U ^[i] [kJ·kg ⁻¹]	4626	2967	4015	2414	3682	5272	5066
T _{C-J} ^[j] [K]	4003	2536	3302	2051	2988	4507	4054
D _{C-J} ^[k] [m·s ⁻¹]	8236	7201	7907	6241	7645	8710	8333
p _{C-J} ^[l] [GPa]	26.5	18.0	23.7	13.8	21.6	29.7	27.0
V ₀ ^[m] [dm ³ ·kg ⁻¹]	768	852	805	715.9	780	825	794
I _{sp} ^[n] [s]	241	189	221	164	209	266	248

[a] Impact sensitivity (BAM drophammer, method 1 of 6); [b] friction sensitivity (BAM drophammer, method 1 of 6); [c] Nitrogen and oxygen content; [d] Oxygen balance toward carbon monoxide ($\Omega_{CO} = (nO - xC - yH/2)(1600/FW)$) and carbon dioxide ($\Omega_{CO_2} = (nO - 2xC - yH/2)(1600/FW)$); [e] melting point (DTA, $\beta = 5 \text{ }^\circ\text{C}\cdot\text{min}^{-1}$); [f] temperature of decomposition (DTA, $\beta = 5 \text{ }^\circ\text{C}\cdot\text{min}^{-1}$); [g] density at 298 K, from X-ray density: $\rho_{X\text{-ray}@100K}/1.0297$; [h] standard molar enthalpy of formation; [i] detonation energy; [j] detonation temperature; [k] detonation velocity; [l] detonation pressure [m] Volume of detonation products (assuming only gaseous products); [n] Specific impulse of neat compound (70.0 bar chamber pressure, isobaric combustion conditions (1 bar), equilibrium expansion); *estima

6.3 Conclusion

To conclude, oxalyl diazide (**1**), carbamoyl azide (**2**) and *N,N'*-bis(azidocarbonyl)hydrazine (**3**) were synthesized, comprehensively characterized and the solid state structures determined. All three compounds crystallize in the monoclinic space group 14 and have densities ranging from 1.565 g cm⁻³ for **2** to 1.701 g cm⁻³ for **1**. Oxalyl diazide is extremely sensitive towards external stimuli. Both carbamoyl azide and *N,N'*-bis(azidocarbonyl)hydrazine show multiple hydrogen bonds in the crystal structure, which contributes to their thermal stability, with decomposition points of 133 °C and 154 °C, respectively, and also to their lower sensitivities towards external stimuli. The Curtius rearrangement of **1** leads to a reactive isocyanate intermediate, which was trapped using water, methanol, oxetan-3-ol and 2-amino-2*H*-tetrazole. The crystal structures were elucidated for all trapping reaction products (**4–6**) and characterized by NMR spectroscopy. Based on the results, numerous new compounds should be accessible in analogous reactions. The ease of synthesis and handling in solution, as well as demonstration of the Curtius rearrangement of oxalyl diazide, together with the versatile capture reactions that were performed, will hopefully trigger further research in this field.

Acknowledgements

Financial support of this work by the Ludwig-Maximilian University of Munich (LMU), the Office of Naval Research (ONR) under grant no. ONR N00014-19-1-2078 (TMK) and the Strategic Environmental Research and Development Program (SERDP) grant WP19-1287 under contract no. W912HQ19C0033 (TMK) is gratefully acknowledged. X. Zeng thanks the National Natural Science Foundation of China (22025301) for financial support. Open access funding enabled and organized by Projekt DEAL.

6.4 References

- [1] T. Curtius, *Ber. Dtsch. Chem. Ges.* **1894**, 27, 778 – 781.
- [2] J. Thiele, O. Stange, *Liebigs Ann. Chem.* **1894**, 283, 1 – 46.
- [3] S. Bräse, C. Gil, *Angew. Chem., Int. Ed.* **2005**, 44, 5188 – 5240.
- [4] Q. J. Axthammer, T. M. Klapötke, B. Krumm, R. Scharf, C. C. Unger, *Dalton Trans.* **2016**, 45, 18909 – 18920.
- [5] Y. Ling, J. Guo, Q. Yang, P. Zhu, J. Miao, W. Hao, Y. Peng, J. Yang, K. Xu, B. Xiong, G. Liu, J. Tao, J. Luo, Q. Zhu, Y. Zhang, *Eur. J. Med. Chem.* **2018**, 144, 398 – 409.
- [6] R. Ikeda, T. Kimura, T. Tsutsumi, S. Tamura, N. Sakai, T. Konakahara, *Bioorg. Med. Chem. Lett.* **2012**, 22, 3506 – 3515.
- [7] H.-G. Mack, C. O. Della Védova, H. Willner, *J. Mol. Struct.* **1993**, 291, 197 – 209.
- [8] X. Zeng, M. Gerken, H. Beckers, H. Willner, *Inorg. Chem.* **2010**, 49, 9694 – 9699.
- [9] K. Banert, C. Berndt, M. Hagedorn, H. Liu, T. Anacker, J. Friedrich, G. Rauhut, *Angew. Chem., Int. Ed.* **2012**, 51, 4718 – 4721.
- [10] X. Zeng, E. Bernhardt, H. Beckers, K. Banert, M. Hagedorn, H. Liu, *Angew. Chem., Int. Ed.* **2013**, 52, 3503 – 3506.
- [11] T. Curtius, K. Heidenreich, *J. prakt. Chem.* **1895**, 52(1), 454 – 489.
- [12] X. Zeng, H. Beckers, H. Willner, J. F. Stanton, *Eur. J. Inorg. Chem.* **2012**, 21, 3403 – 3409.
- [13] H. Wan, H. Li, J. Xu, Z. Wu, Q. Liu, X. Chu, M. Abe, D. Bégué, X. Zeng, *Org. Chem. Front.* **2017**, 4, 1839 – 1848.
- [14] Q. Liu, H. Wan, Y. Lu, B. Lu, X. Zeng, *Eur. J. Org. Chem.* **2019**, 2 – 3, 401 – 411.
- [15] M. Benz, T. M. Klapötke, B. Krumm, M. Lommel, J. Stierstofer, *J. Am. Chem. Soc.* **2021**, 143, 1323 – 1327.
- [16] H. W. Roesky, O. Glemser, *Chem Ber.* **1964**, 97, 1710 – 1712.

- [17] T. M. Klapötke, B. Krumm, R. Scharf, *Eur. J. Inorg. Chem.* **2016**, 19, 3086 – 3093.
- [18] S. Mohan, K. S. P. Durairaj, S. P. Jose, *Spectrochim. Acta, Part A* **2003**, 59, 1697 – 1704.
- [19] J. M. Harris, R. McDonald, J. C. Vederas, *J. Chem. Soc., Perkin Trans. 1* **1996**, 2669 – 2674.
- [20] M. Figlus, A.C. Tarruella, A. Messer, S. L. Sollis, R. C. Hartley, *Chem. Comm.* **2010**, 46, 4405 – 4407.
- [21] I.-H. Kim, C. Morisseau, T. Watanabe, B. D. Hammock, *J. Med. Chem.* **2004**, 47, 2110 – 2122.
- [22] Z. Jaman, T. J. P. Sobreira, A. Mufti, C. R. Ferreira, R. G. Cooks, D. H. Thompson, *Org. Process Res. Dev.* **2019**, 23, 334 – 341.
- [23] L. A. Ramos, X. Zeng, S. E. Ulic, E. Beckers, H. Willner, C. O. Della Védona, *J. Org. Chem.* **2012**, 77, 6456 – 6462.
- [24] A. Baumann, A. Erbacher, C. Evangelisti, T. M. Klapötke, B. Krumm, S. F. Rest, M. Reynders, V. Sproll, *Chem. – Eur. J.* **2013**, 19, 15627 – 15638

6.5 Supplementary Information

6.5.1 Experimental Procedures

CAUTION! All described compounds are powerful energetic materials with high sensitivities towards shock and friction. Therefore, proper security precautions (safety glass, face shield, earthened equipment and shoes, Kevlar gloves and ear plugs) have to be applied all time while synthesizing and handling the described compounds. Especially oxalyl diazide (**1**) is extremely unstable and lead to several micro-detonations during the work.

Chemicals and solvents were employed as received (Sigma-Aldrich, Acros, TCI). ^1H , ^{13}C and ^{14}N spectra were recorded using a Bruker AMX 400 instrument. The chemical shifts quoted in ppm refer to tetramethylsilane (^1H , ^{13}C) and nitromethane (^{14}N). Decomposition temperatures were determined on an OZM Research DTA 552–Ex instrument with a heating rate of 5°C min^{-1} . Infrared (IR) spectra were recorded using a Perkin-Elmer Spektrum One FT–IR instrument. Elemental analyses were performed with an Elementar Vario el by pyrolysis of the sample and subsequent analysis of formed gases. The sensitivity data were collected using a BAM (Bundesanstalt für Materialforschung) drophammer^[1] according to STANAG 4489^[2] modified instruction^[3] and a BAM friction tester^[1] according to STANAG 4487^[4] modified instruction.^[5] The classification of the tested compounds results from the 'UN Recommendations on the Transport of Dangerous Goods'.^[6]

Oxalyl diazide (**1**)

Oxalyl dihydrazide was prepared according to the literature procedure.^[7,8] Oxalyl hydrazide (0.45 g, 3.81 mmol, 1.0 eq.) was suspended in concentrated hydrochloric acid (6 mL) and cooled to -15°C . The mixture was layered underneath with chloroform (20 mL). The stirrer speed was set to maximum and an ice-cold solution of sodium nitrite (0.63 g, 9.15 mmol, 2.4 eq.) in water (6 mL) was added dropwise to the mixture. The resulting yellow solution was stirred for 10 minutes and the layers were separated. The aqueous layer was extracted with cold chloroform (20 mL), the organic layers were combined and washed with ice-water (2 x 20 mL) prior to drying. The solvent was removed by slow evaporation leaving transparent crystals of oxalyl diazide (**1**, 0.43 g, 3.07 mmol, 81 %). **DTA** (T_{onset} , 5°C min^{-1}): 45°C (mp.) 46°C (dec.); **FT-IR** (ATR): $\tilde{\nu} = 3377$ (w), 2279 (w), 2178 (s), 1681 (s), 1155 (s), 970 (s), 823 (s), 574 (s), 506 (s), 463 (s) cm^{-1} ; **^{13}C NMR**{ **^1H** } (101 MHz, CDCl_3 , 25°C): $\delta = 163.9$ ppm; **^{14}N NMR** (27 MHz, CDCl_3 , 25°C): δ

= -130.9, -146.6, -252.4 ppm; **EA** (C₂N₆O₂) calcd.: C 17.15, H 0.00, N 60.00; found: C 17.18, H 0.27, N 59.41; **BAM drophammer** < 1 J (> 500 μm); **Friction test** < 0.1 N (> 500 μm).

Carbamoyl azide (2)

Carbamoyl azide was prepared according to Thiele.^[9] Semicarbazide hydrochloride (1.00 g, 8.966 mmol, 1.0 eq.) was dissolved in water (15mL) and cooled to -5 °C. An ice-cold solution of sodium nitrite (0.68 g, 9.862 mmol, 1.1 eq.) in water (7 mL) was added dropwise. After the addition, diethyl ether was added and the mixture stirred for 5 minutes. Ammonium sulfate (~9 g) was used to saturate the aqueous phase. The layers were separated and the aqueous phase was extracted with diethyl ether (3 x 20 mL) prior to drying. The solvent was removed by rotary evaporation, yielding 0.710 g (8.251 mmol, 92 %) of colorless carbamoyl azide. **DSC** (T_{onset}, 5 °C min⁻¹): 96 °C (mp.), 133 (dec.); **FT-IR** (ATR): $\tilde{\nu}$ = 3384 (m), 3247 (m), 2170 (s), 1674 (s), 1611 (s), 1420 (w), 1347 (s), 1212 (s), 888 (m), 760 (w), 713 (s), 509 (s) cm⁻¹; **¹H NMR** (400 MHz, CDCl₃, 25 °C): δ = 5.25 ppm; **¹³C NMR{¹H}** (101 MHz, CDCl₃, 25 °C): δ = 158.1 ppm; **¹⁴N NMR** (27 MHz, CDCl₃, 25 °C): δ = -144.7, -267.3, -302.5 ppm; **EA** (CH₂N₄O) calcd.: C 13.96, H 2.34, N 65.11; found: C 14.18, H 2.16, N 64.90; **BAM drophammer** 20 J (> 500 μm); **Friction test** >360 N (> 500 μm).

N,N'-bis(azidocarbonyl)hydrazine (3)

N,N'-Dicarbazoylhydrazine was synthesized according to the literature procedure.^[10] N,N'-Dicarbazoylhydrazine (0.207 g, 1.397 mmol, 1.0 eq.) was suspended in a mixture of acetic acid (6 mL), 2 M hydrochloric acid (2 mL) and water (2 mL) and cooled to 0 °C. Sodium nitrite (0.241 g, 3.493 mmol, 2.5 eq.) was dissolved in water (3 mL), cooled to 0°C and added dropwise to the previously described mixture. After the addition, diethyl ether was added and the mixture stirred for 10 minutes. The layers were separated and the aqueous phase was extracted with diethyl ether (2 x 20 mL). The combined organic layers were washed with ice-water (2 x 25 mL) and brine (20 mL) prior to drying. The solvent was removed by slow evaporation to yield 0.185 g (1.088 mmol, 78 %) of colorless N,N'-bis(azidocarbonyl)hydrazine (**3**). **DTA** (T_{onset}, 5 °C min⁻¹): 154 °C (dec.); **FT-IR** (ATR): $\tilde{\nu}$ = 3166 (w), 3004 (w), 2170 (m), 2150 (s), 1774 (m), 1732 (m), 1683 (m), 1521 (s), 1163 (s), 1143 (s), 919 (m), 747 (s), 644 (m), 590 (m), 555 (s), 503 (m), 493 (m) cm⁻¹; **¹H NMR** (400 MHz, acetone-d₆, 25 °C): δ = 9.16 ppm; **¹³C NMR{¹H}** (101 MHz, acetone-d₆ 25 °C): δ =

157.7 ppm; $^{14}\text{N NMR}$ (27 MHz, acetone- d_6 , 25 °C): $\delta = -144.6$ ppm; **EA** ($\text{C}_2\text{H}_2\text{N}_8\text{O}_2$) calcd.: C 14.12, H 1.19, N 65.88; found: C 14.39, H 1.46, N 65.36; **BAM drophammer** 1 – 2 J (> 500 μm); **Friction test** 0.1 N (> 500 μm).

Dimethyl Iminodicarbonate (4)

Oxalyl diazide (0.600 g, 4.28 mmol, 1.0 eq.) was dissolved in chloroform (15 mL) and methanol (5 mL) was added. The mixture was stirred at 35°C for 15 hours. The precipitate was filtered and recrystallized from ethyl acetate to yield 0.518 g (3.89 mmol, 91 %) of dimethyl iminodicarbonate (4). **FT-IR** (ATR): $\tilde{\nu} = 3205$ (m), 3036 (w), 2962 (w), 1805 (m), 1766 (m), 1711 (m), 1532 (s), 1454 (m), 1301 (m), 1209 (m), 1175 (s), 1101 (s), 1040 (s), 910 (w), 783 (m), 729 (m), 703 (m), 558 (w), 443 (m) cm^{-1} ; $^1\text{H NMR}$ (400 MHz, acetone- d_6 , 25 °C): $\delta = 9.21$ (s, 1H, NH), 3.69 (s, 6H, CH_3) ppm; $^{13}\text{C NMR}\{^1\text{H}\}$ (101 MHz, acetone- d_6 , 25 °C): $\delta = 152.4, 52.7$ ppm; **EA** ($\text{C}_4\text{H}_7\text{NO}_4$) calcd.: C 36.10, H 5.30, N 10.52; found: C 35.90 H 5.12 N 10.87.

Oxetan-3-yl-N-azidocarbonyl-carbamate (5)

Oxalyl diazide (0.625 g, 4.46mmol, 1.0 eq.) was dissolved in chloroform (15 mL) and oxetan-3-ol (0.330 g, 4.46 mmol, 1.0 eq.) was added and the mixture was stirred for 15 hours at 35°C. The solvent was removed by rotary evaporation to give 0.781 g (4.20 mmol, 94 %) of colorless oxetan-3-yl-N-azidocarbonyl-carbamate. **DTA** (T_{onset} , 5 °C min^{-1}): 127 °C (m.p.), 135 °C (dec.); **FT-IR** (ATR): $\tilde{\nu} = 3149$ (w), 2956 (m), 2160 (m), 1797 (s), 1722 (m), 1538 (s), 1373 (w), 1255 (m), 1164 (s), 1119 (s), 1092 (s), 978 (s), 957 (m), 916 (s), 871 (m), 758 (s), 695 (s), 560 (m), 506 (w), 456 (m) cm^{-1} ; $^1\text{H NMR}$ (400 MHz, CDCl_3 , 25 °C): $\delta = 7.44$ (br s, 1H, NH), 5.55 – 5.49 (m, 1H, $\text{CH}_{\text{oxetane}}$), 4.93 – 4.89 (m, 2H, $\text{CH}_2_{\text{oxetane}}$), 4.69 – 4.66 ($\text{CH}_2_{\text{oxetane}}$) ppm; $^{13}\text{C NMR}\{^1\text{H}\}$ (101 MHz, CDCl_3 , 25 °C): $\delta = 153.3, 149.1, 77.1, 69.9$ ppm; $^{14}\text{N NMR}$ (27 MHz, CDCl_3 , 25 °C): $\delta = -144.0, -146.8$ ppm; **EA** ($\text{C}_5\text{H}_6\text{N}_4\text{O}_4$) calcd.: C 32.27, H 3.25, N 30.10; found: C 32.42 H 3.00 N 29.98; **BAM drophammer** >40 J (> 500 μm); **Friction test** >360 N (> 500 μm).

N-Azidocarbonyl-N'-(2H-tetrazol-2-yl)-urea (6)

Oxalyl diazide (0.650 g, 4.64 mmol, 1.0 eq.) was dissolved in chloroform (15 mL) and 2H-tetrazole-2-amine (0.395 g, 4.64 mmol, 1.0 eq.) was added together with acetonitrile (2 mL). The mixture was heated to 35°C for 15 hours. The precipitate which formed was

filtered and dried to give 0.291 g (1.48 mmol, 32 %) of colorless N-azidocarbonyl-N'-(2H-tetrazol-2-yl)-urea. **DTA** (T_{onset} , 5 °C min⁻¹): 145 °C (dec.); **FT-IR** (ATR): $\tilde{\nu}$ = 3289 (m), 3228 (m), 3139 (m), 2191 (m), 2143 (m), 1747 (s), 1689 (w), 1539 (s), 1417 (m), 1280 (m), 1256 (s), 1235 (m), 1163 (s), 1125 (s), 1044 (m), 1015 (s), 994 (s), 903 (m), 876 (m), 732 (m), 709 (s), 667 (s), 654 (s), 592 (s), 546 (s), 504 (s) cm⁻¹; **¹H NMR** (400 MHz, DMSO-d₆, 25 °C): δ = 10.97 (s, 1H, NH), 8.99 (s, 1H, CH), 6.75 (s, 1H, NH) ppm; **¹³C NMR{¹H}** (101 MHz, DMSO-d₆, 25 °C): δ = 155.7, 152.3 ppm; **¹⁴N NMR** (27 MHz, DMSO-d₆, 25 °C): δ = -134.8, -146.5, -255.4 ppm; **EA** (C₃H₃N₉O₂) calcd.: C 18.28, H 1.53, N 63.95; found: C 18.54 H 1.87 N 63.58; **BAM drophammer** 4 J (> 500 μ m); **Friction test** 360 N (> 500 μ m).

NMR discussion of Compounds 1 – 3.

The ¹³C{¹H} NMR spectrum showed one signal at 164 ppm for compound **1** which is in accordance with the shifts reported for carbonyl azide compounds which are in between 150 to 160 ppm.^[11] The ¹³C NMR of carbamoyl azide (**2**) and N,N'-bis(azidocarbonyl)hydrazine (**3**) each show a signal at 158 ppm, which is due to the chemical similarity of both. N,N'-bis(azidocarbonyl)hydrazine (**3**) shows a signal at 9.16 ppm in the ¹H NMR spectrum. In addition to this signal, two smaller signals are also found in this region. These two signals indicate a species which is not symmetrical. Either it is a species formed by free rotation around the hydrazine bridge, or it is assumed that they belong to the mono-tetrazolone tautomer formed by free exchange in solution. The ¹⁴N NMR spectroscopy for **1** has shows resonance signals at -130.9 ppm for N_γ, -146.6 ppm (N_β) and -252.4 ppm (N_α). The signals for N_α as well as N_γ are shifted to lower field in relation to organic azides in the literature comparable to the carbonyl azides.^[11,12] Only three signals for **2** are found, -144.7 ppm (N_β), -267.3 ppm (N_α), as well as a signal at -302.5 ppm which can be assigned to the amino group. The signal of N_γ is possibly superimposed by the signal of N_β. For compound **3**, only one signal is found at -144.6 ppm which is assigned to N_β which possibly superimposed the N_γ resonance. No N_α signal was observed, however, it is known that for covalent azides, this signal is often very broad in ¹⁴N NMR spectra. The very broad resonance typical of the hydrazine bridge of **3** in ¹⁴N NMR was not observed.

6.5.2 NMR-Spectra

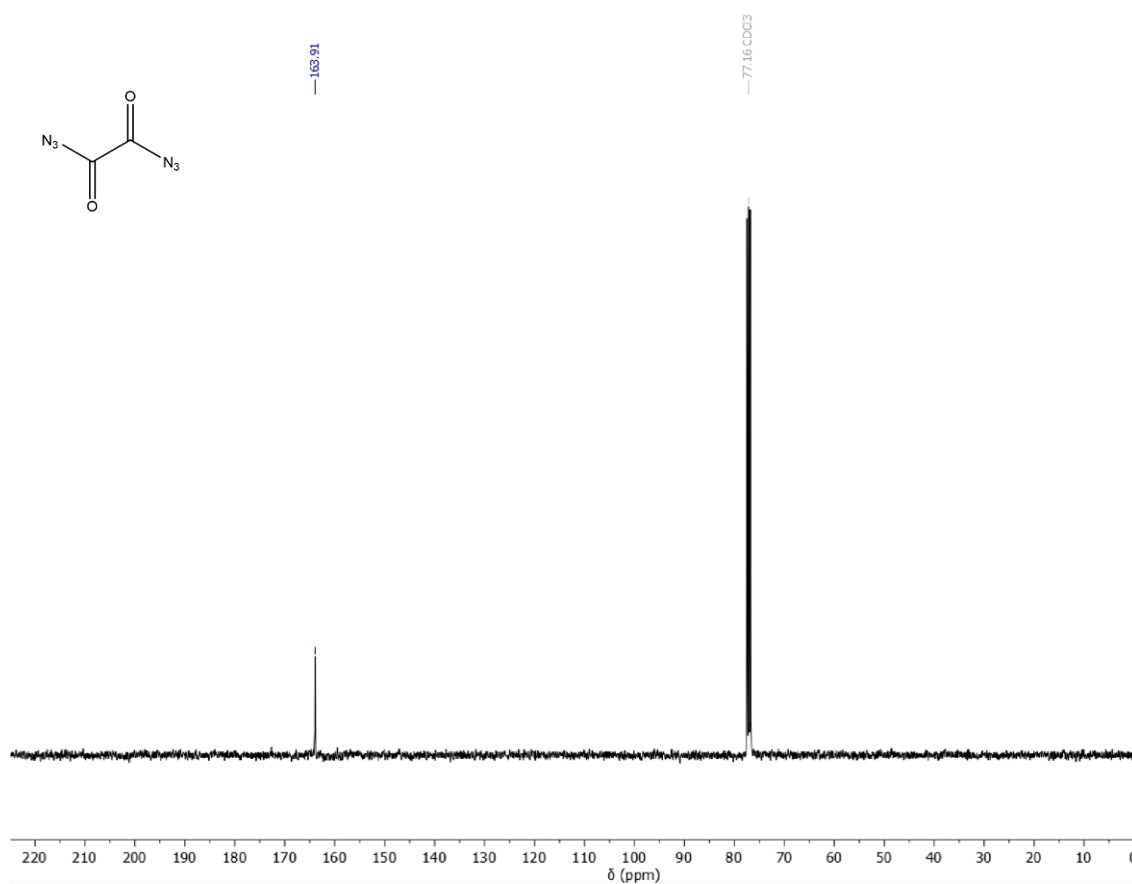


Figure S1. $^{13}\text{C}\{^1\text{H}\}$ NMR spectrum of oxalyl diazide (1).

Figure S2. ^{14}N NMR spectrum of oxalyl diazide (1).

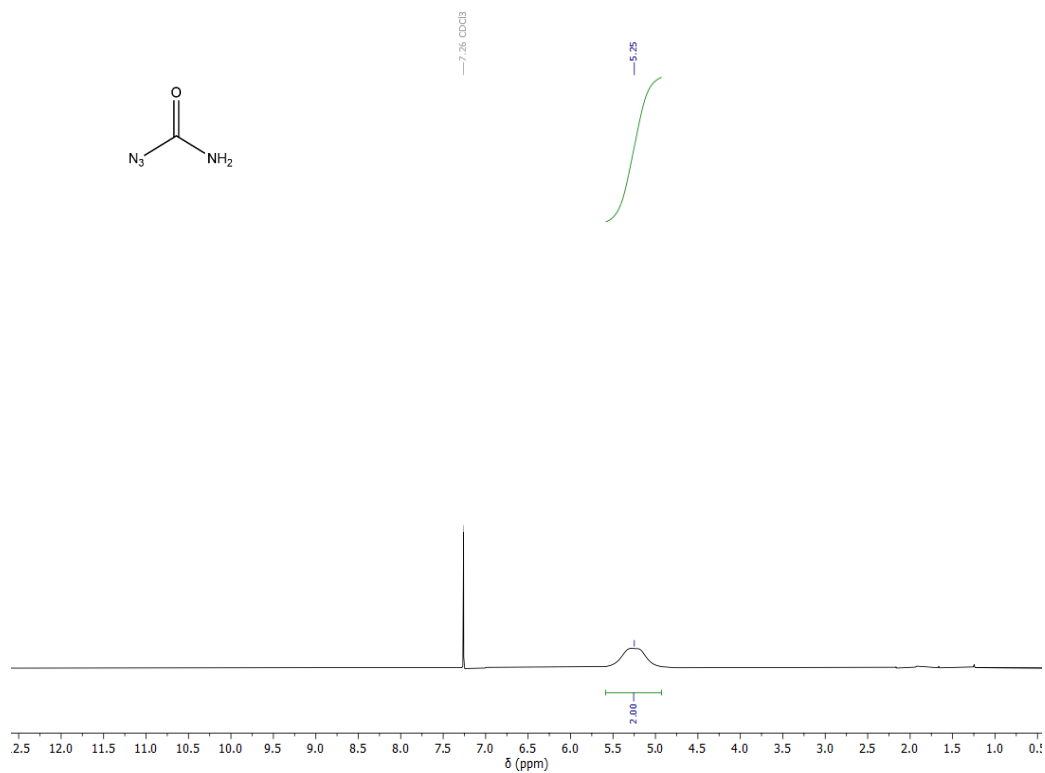


Figure S3. ^1H NMR spectrum of carbamoyl azide (2).

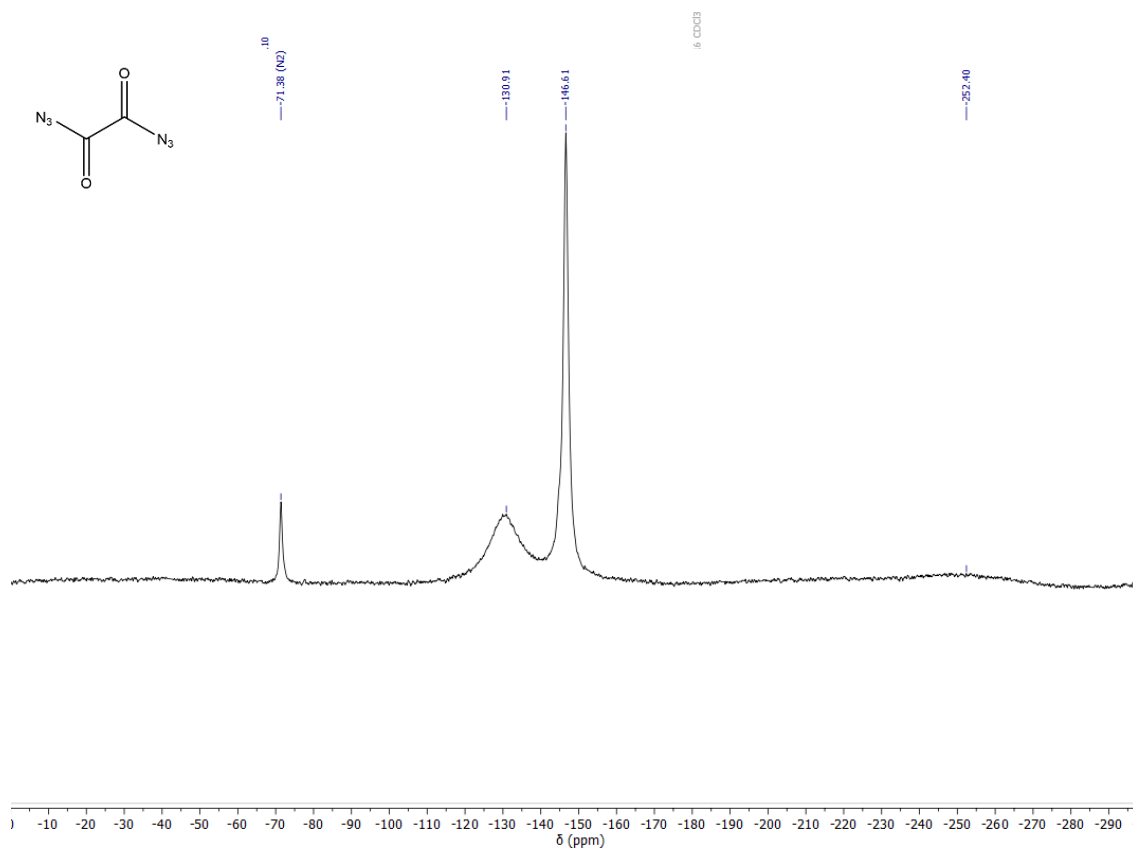


Figure S4. $^{13}\text{C}\{^1\text{H}\}$ NMR spectrum of carbamoyl azide (**2**).

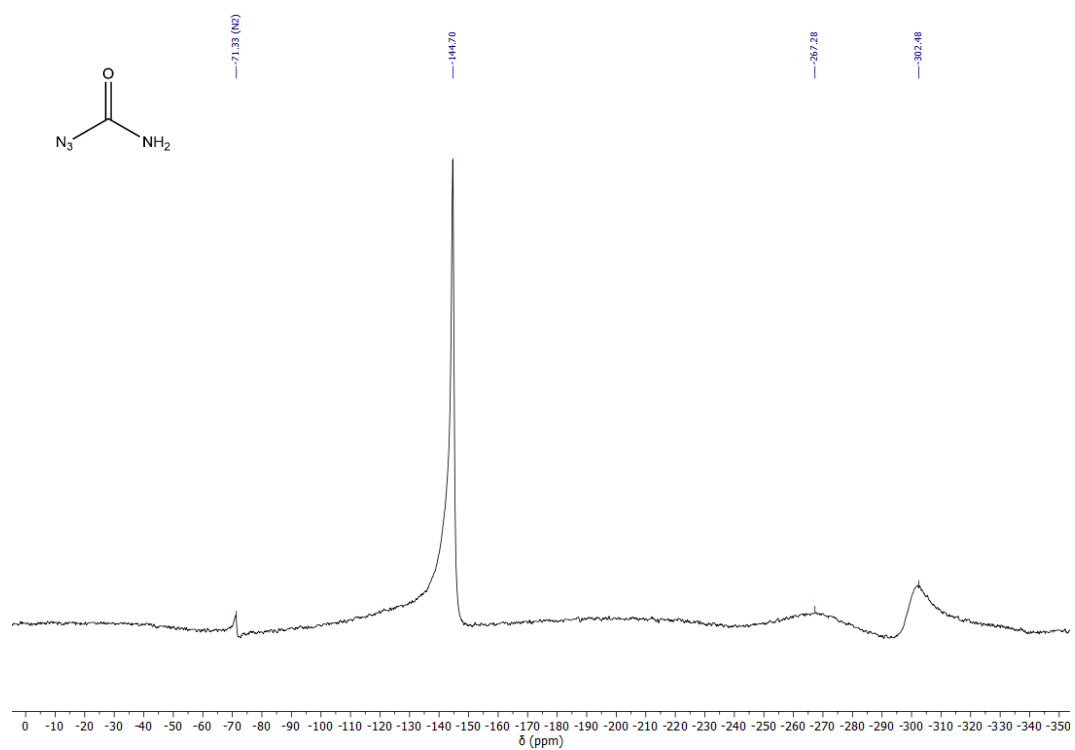


Figure S5. ^{14}N NMR spectrum of carbamoyl azide (**2**).

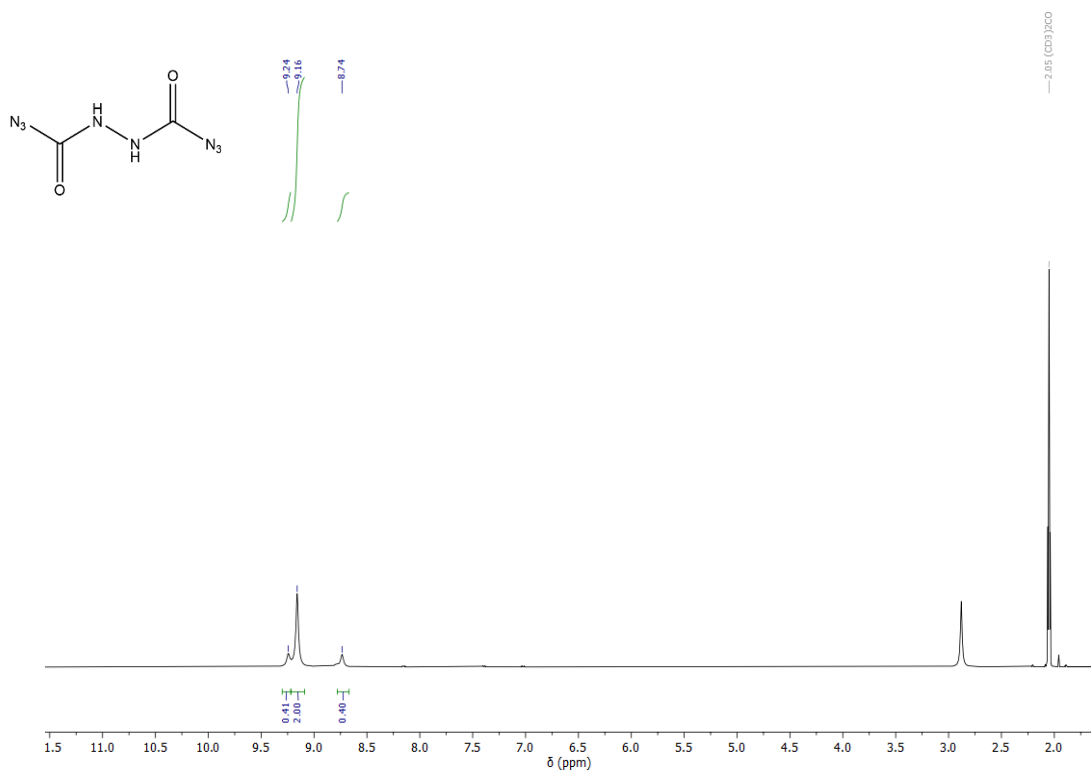


Figure S6. ^1H NMR spectrum of *N,N*-bis(azidocarbonyl)-hydrazine (**3**).

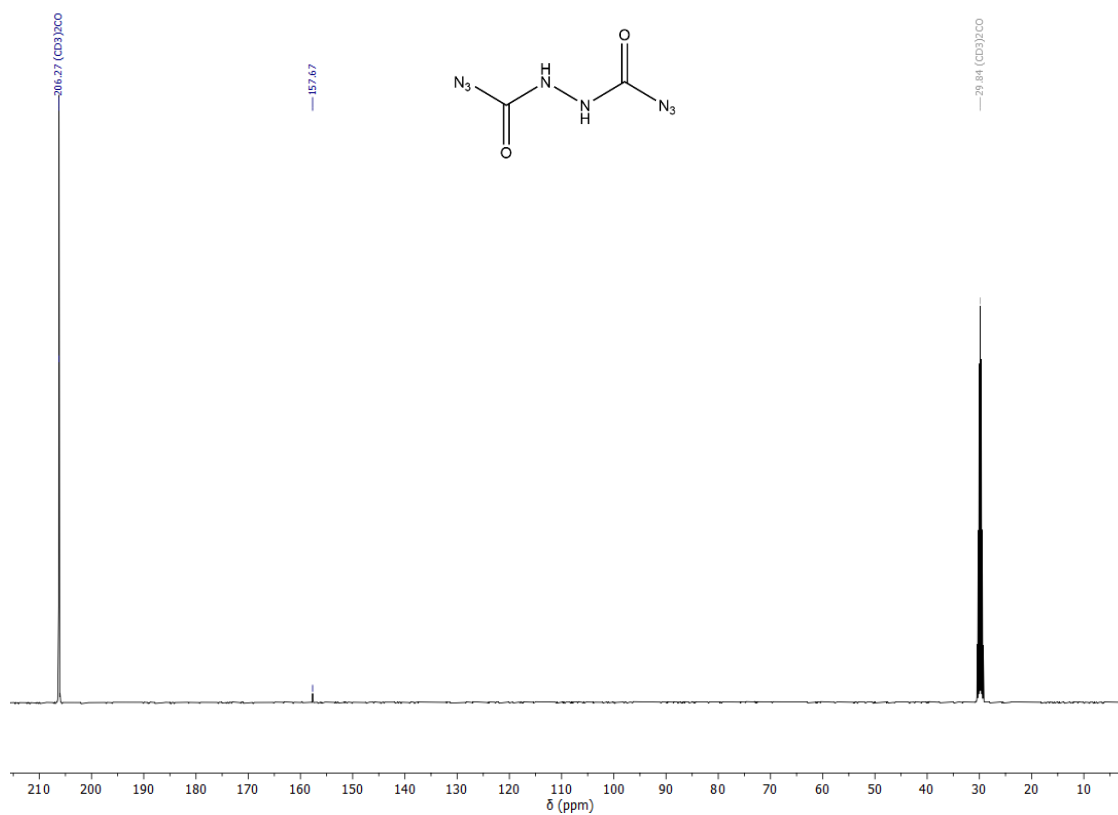


Figure S7. $^{13}\text{C}\{^1\text{H}\}$ NMR spectrum of *N,N*-bis(azidocarbonyl)-hydrazine (3).

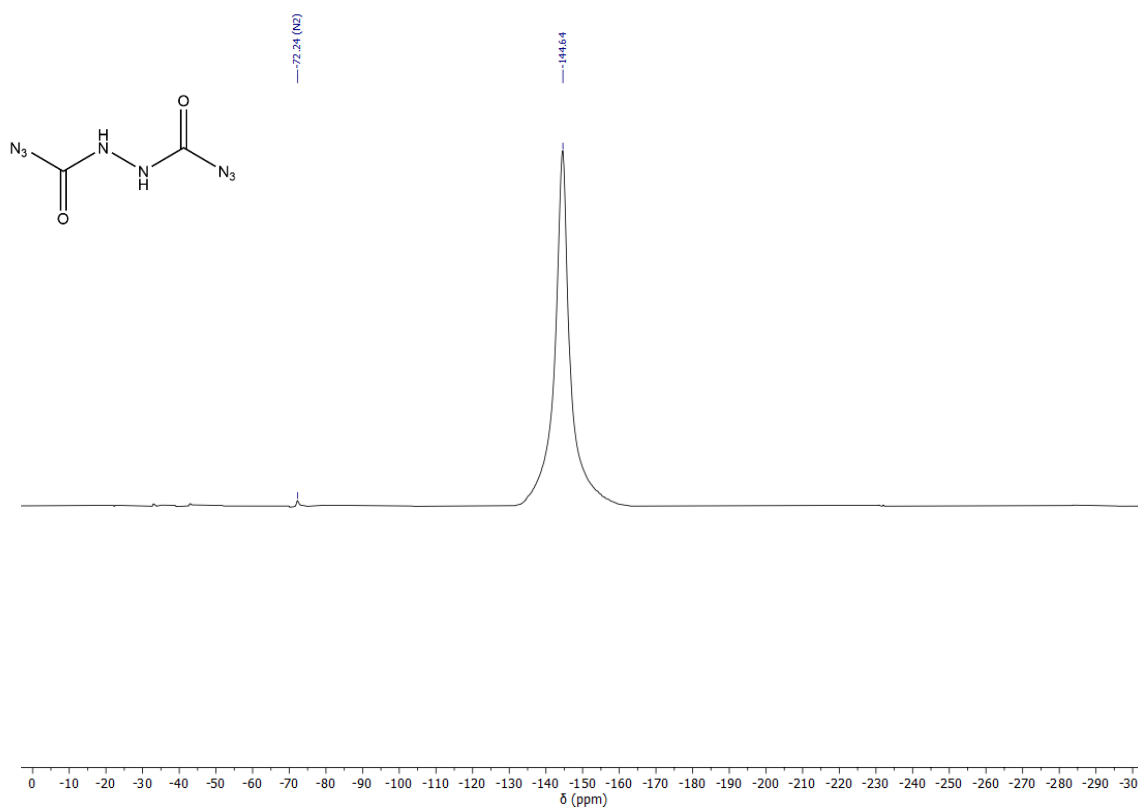


Figure S8. ^{14}N NMR spectrum of *N,N*-bis(azidocarbonyl)-hydrazine (3).

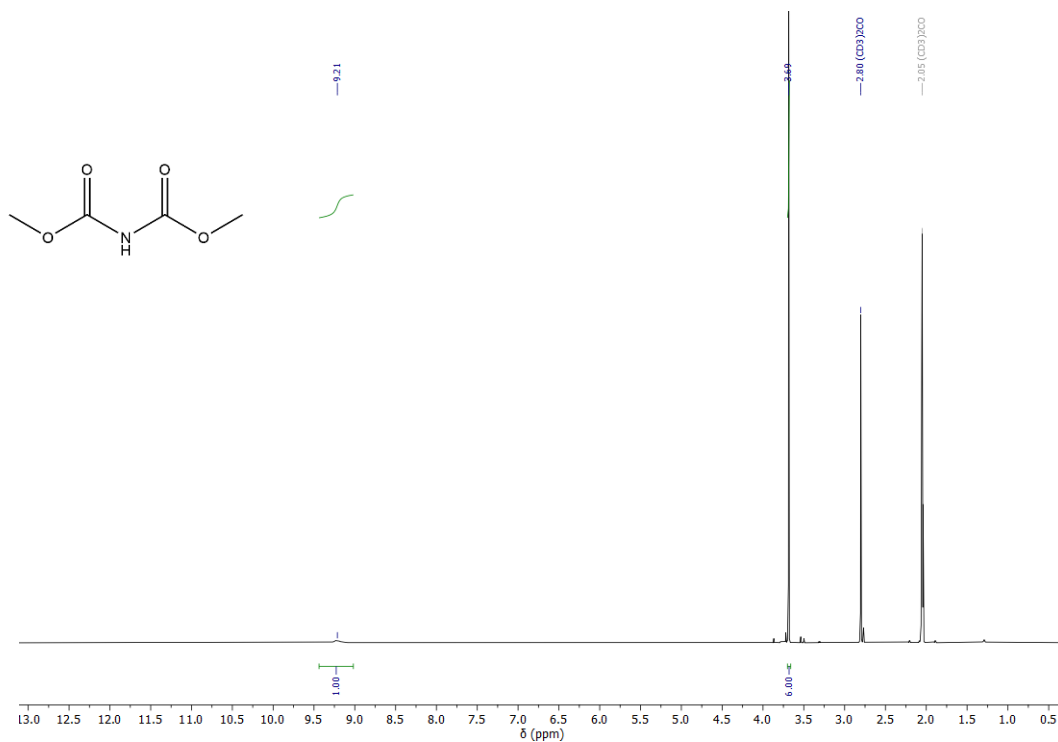


Figure S9. ^1H NMR spectrum of dimethyl iminodicarbonate (**4**).



Figure S10. $^{13}\text{C}\{^1\text{H}\}$ NMR spectrum of dimethyl iminodicarbonate (**4**).

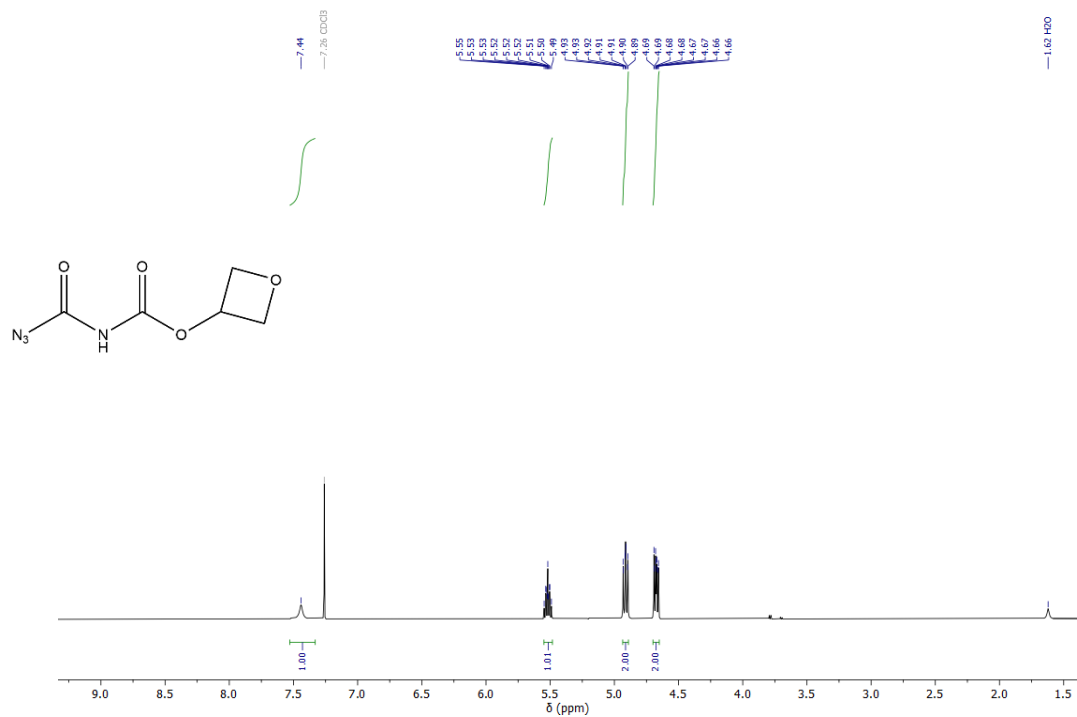


Figure S11. ¹H NMR spectrum of oxetan-3-yl-N-azidocarbonyl-carbamate (5).

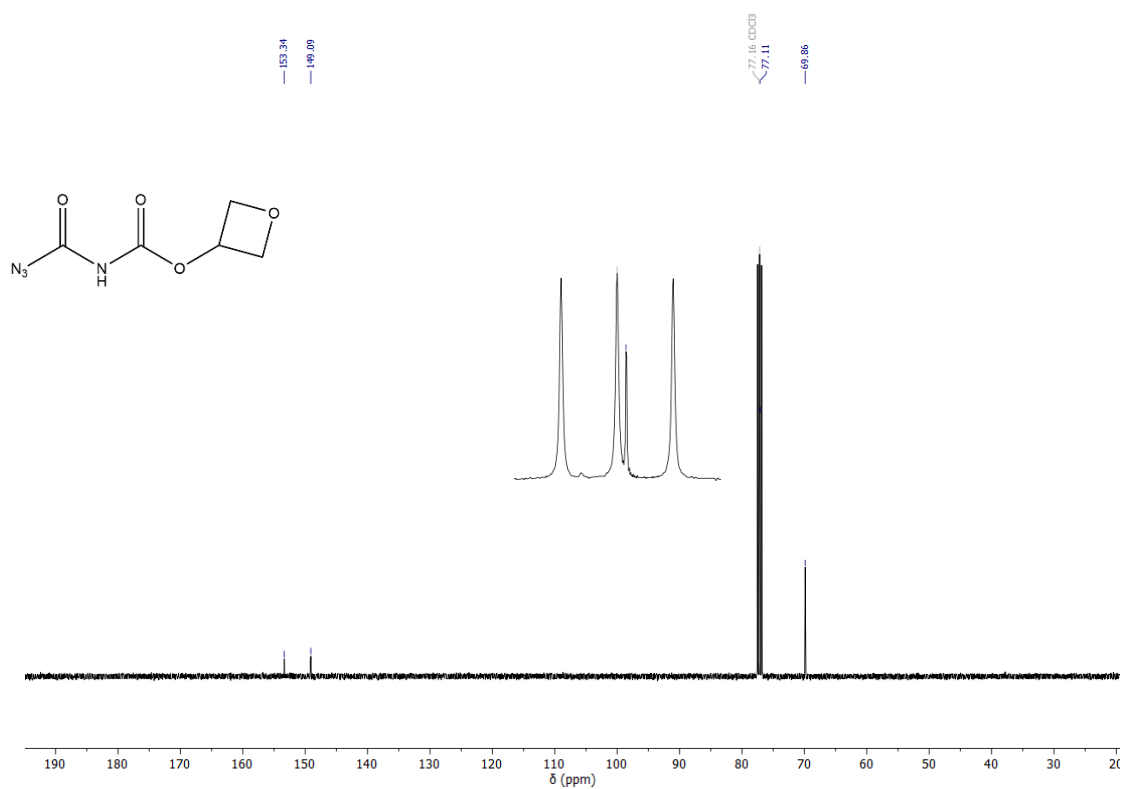


Figure S12. ¹³C{¹H} NMR spectrum of oxetan-3-yl-N-azidocarbonyl-carbamate (5).

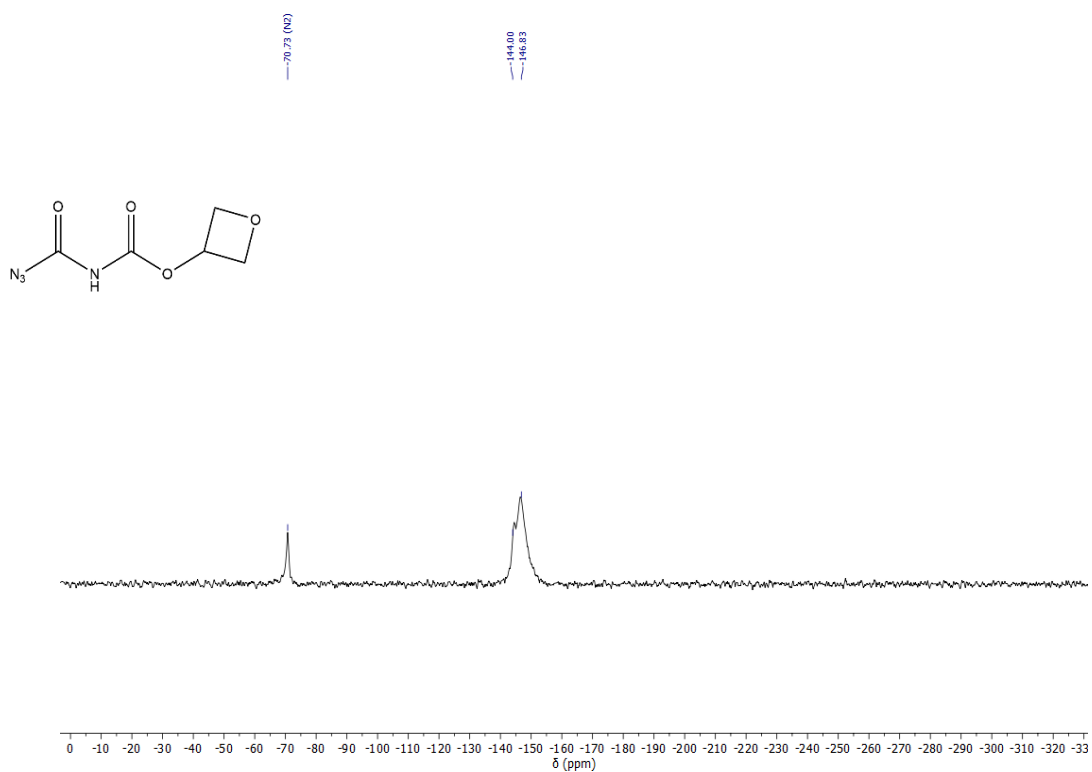


Figure S13. ¹⁴N NMR spectrum of oxetan-3-yl-*N*-azidocarbonyl-carbamate (5).

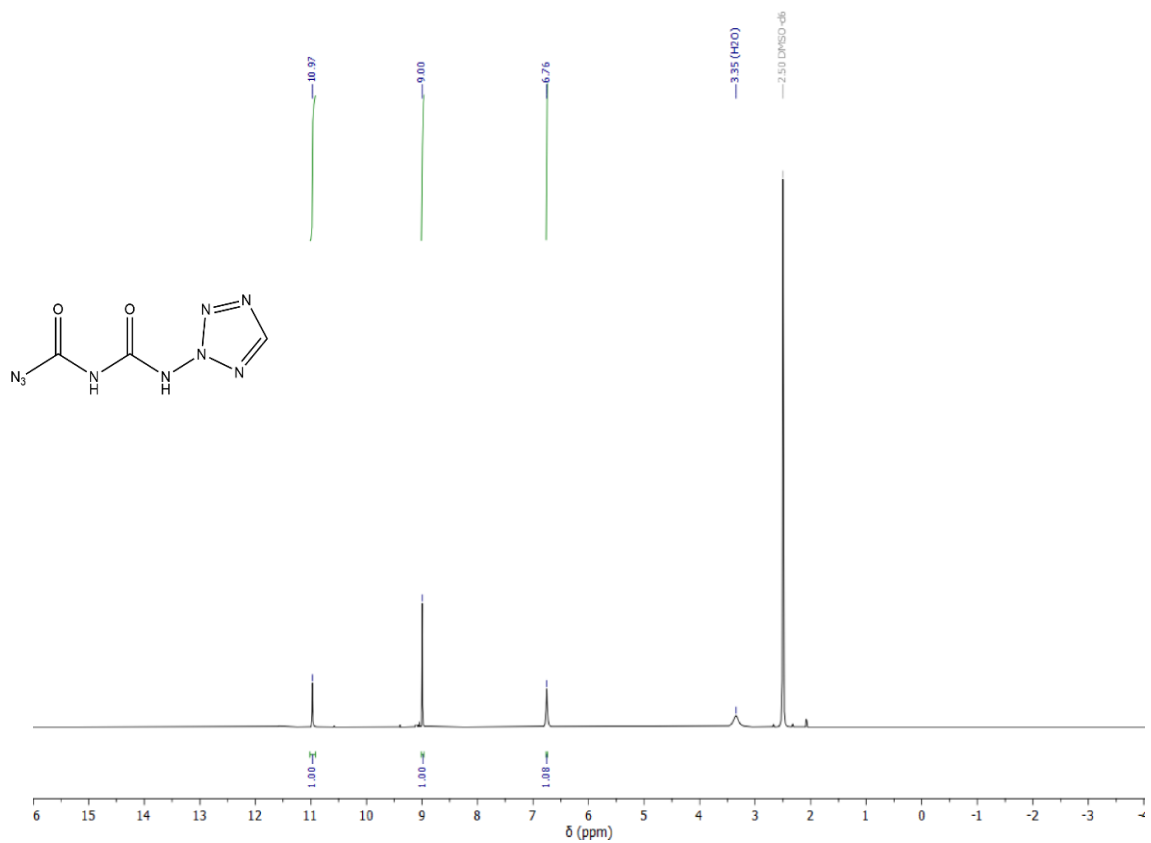


Figure S14. ¹H NMR spectrum of *N*-azidocarbonyl-*N*-(2*H*-tetrazol-2-yl)-urea (6).



Figure S15. $^{13}\text{C}\{^1\text{H}\}$ -NMR spectrum of *N*-azidocarbonyl-*N*-(2*H*-tetrazol-2-yl)-urea (6).

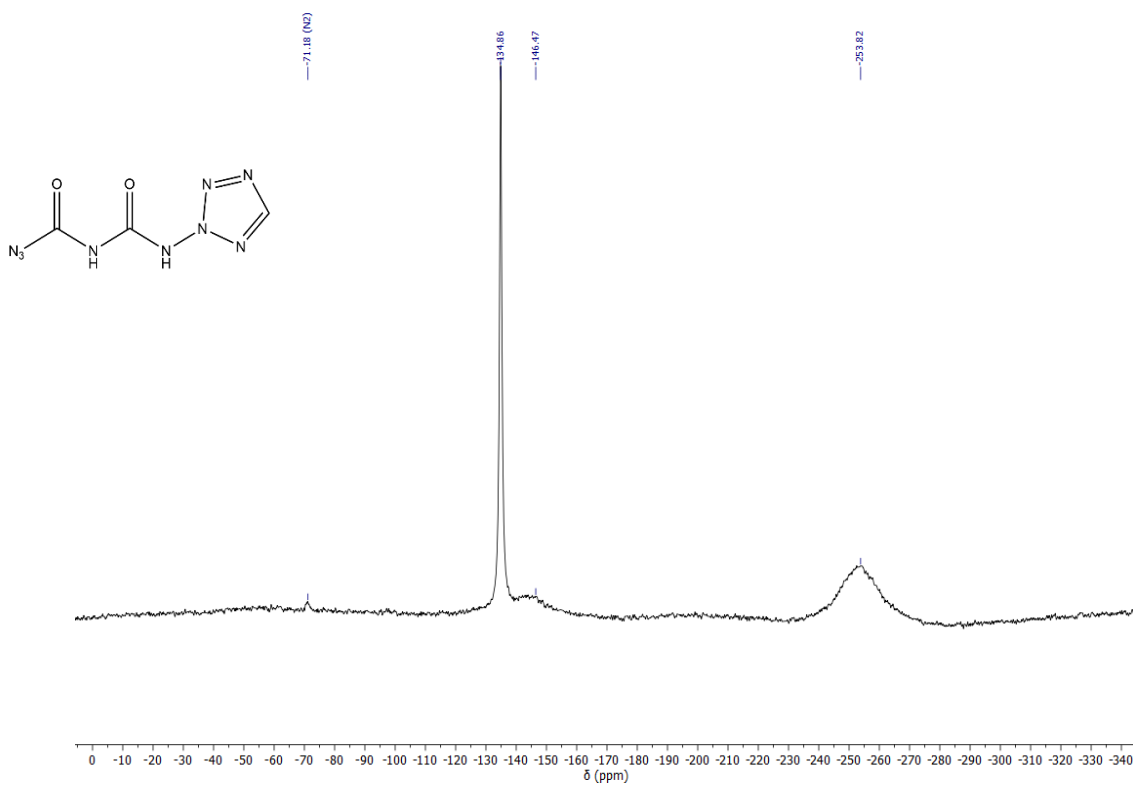


Figure S16. ^{14}N NMR spectrum of *N*-azidocarbonyl-*N*-(2*H*-tetrazol-2-yl)-urea (6).

6.5.3 IR Spectroscopy of Carbamoyl azide (**2**)

IR spectrum of solid carbamoyl azide (**2**) was recorded using an FTIR-ATR (attenuated total reflectance) Bruker 70V spectrometer at a resolution of 2 cm^{-1} . Gas-phase IR spectra were measured in a KBr gas cell on an INSA OPTICS FT-IR spectrometer (FOLI10-R) at a resolution of 2 cm^{-1} . Raman spectrum were recorded on a HR800 spectrometer at a resolution of 2 cm^{-1} . Matrix IR spectra were recorded on an FTIR Bruker 70V spectrometer in a reflectance mode using a transfer optic, and a KBr beam splitter and liquid nitrogen cooled mercury cadmium telluride (MCT) detector were used in the mid-IR region ($4000\text{--}500\text{ cm}^{-1}$) at a resolution of 0.5 cm^{-1} . The gaseous sample was mixed by passing a flow of Ne gas through a U-trap ($25\text{ }^\circ\text{C}$) containing ca. 10 mg of the azide. Then the mixture (sample/matrix gas $\approx 1 : 1000$ estimated) was deposited (2 mmol h^{-1}) onto the Rh-plated copper block matrix support (3 K) in a dynamic vacuum ($\sim 10^{-4}\text{ Pa}$).

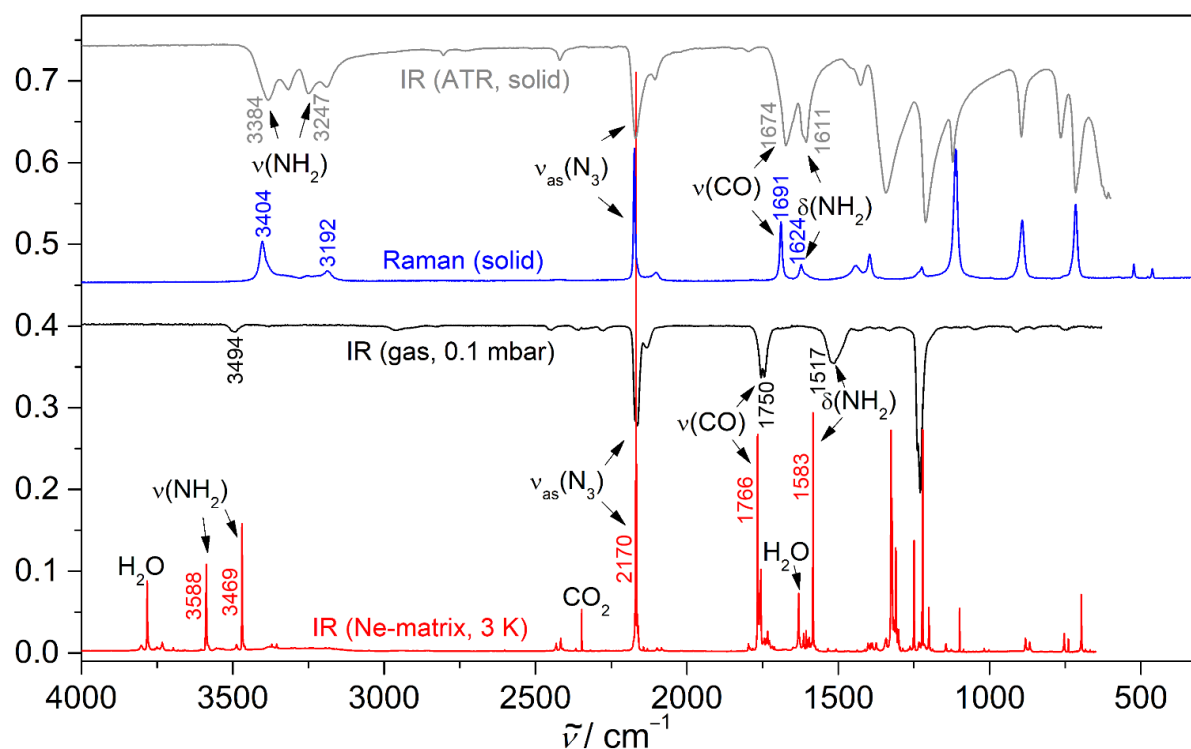


Figure S17. IR and Raman spectra of carbamoyl azide (**2**).

The FT-IR spectrum of pure, solid **2** shows two medium intensity bands at 3384 and 3247 cm^{-1} which correspond to the amino group, and a strong band at 1674 cm^{-1} for the carbonyl group. In the Ne-matrix and gas phase IR spectra, the stretching modes of the amino group are observed at 3588 and 3470 cm^{-1} , which are dramatically blue-shifted in relation to the IR spectrum of the pure solid. In contrast, the CO stretching mode occurs at 1766 cm^{-1} in the matrix IR spectrum, and at 1750 cm^{-1} in the gas phase spectrum, and is therefore significantly red-shifted in the solid state spectrum where it is observed at 1674 cm^{-1} . Clearly, these large shifts are due to strong intermolecular hydrogen bonds

between the amino and carbonyl groups in the solid state. In contrast, the bands for the asymmetric stretching mode of the azido moiety in the IR (gas, solid, and Ne-matrix) and Raman (solid) spectra remain almost unchanged at around 2170 cm^{-1} .

6.5.4 X-ray Diffraction and Hirshfeld Analysis

Crystal structure data were obtained from an Oxford Xcalibur3 diffractometer with a Spellman generator (voltage 50kV, current 40mA) and a Kappa CCD area for data collection using Mo-K α radiation ($\lambda=0.71073\text{\AA}$) or a Bruker D8 Venture TXS diffractometer equipped with a multilayer monochromator, a Photon 2 detector and a rotation-anode generator (Mo-K α radiation). The data collection was performed using the CRYSTALIS RED software.^[13] The solution of the structure was performed by direct methods and refined by full-matrix least-squares on F² (SHELXT)^[14] implemented in the OLEX2^[15] software suite. The non-hydrogen atoms were refined anisotropically and the hydrogen atoms were located and freely refined. The absorption correction was carried out by a SCALE3 ABSPACK multiscan method.^[16] The DIAMOND2 plots shown with thermal ellipsoids at the 50% probability level and hydrogen atoms are shown as small spheres of arbitrary radius. The SADABS program embedded in the Bruker APEX3 software was used for multi-scan absorption corrections in all structures.^[17]

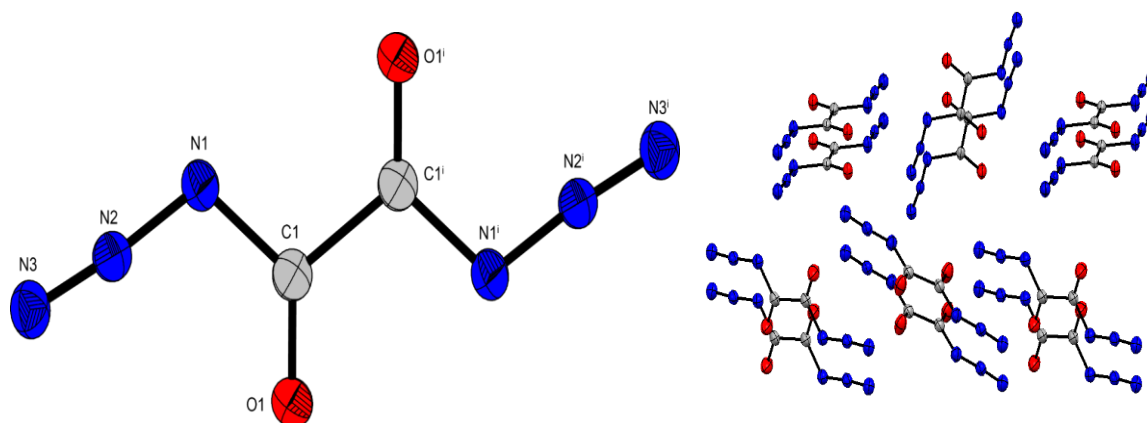


Figure S18. Crystal structure of oxalyl diazide (**1**). Thermal ellipsoids are drawn at the 50 % probability level. Oxalyl diazide forms alternating pairs in the crystal.

Oxalyl diazide (1) crystallizes in the monoclinic space group P21/c with 4 molecules in the unit cell and a density of 1.751 g cm⁻³ at 102 K. The bond lengths are in good accordance with the standard bond lengths expected. The C1 shows a nearly trigonal planar arrangement, also the azide moiety is slightly bent with an N1-N2-N3 angle of 174.4°. The molecule itself is planar. Oxalyl diazide forms pairs in the crystal and these pairs are arranged alternately. Hirshfeld analysis showed only the presence of destabilizing and repulsive short contacts in the molecule. The short contacts consist of N...O (45.6 %), N...N (31.9 %), C...N (15.3 %) and O...O (6.8 %) interactions. The distance for all contacts is large and at least 3.0 Å. The repulsive interactions cause the molecule to be highly rigid with respect to lattice deformation and mechanical stimuli.[18–20] Since there are no stabilizing interactions between the oxalyl diazide molecules, it can be assumed that the compound is extremely unstable, with very high sensitivity towards external stimuli, and very low thermal stability.

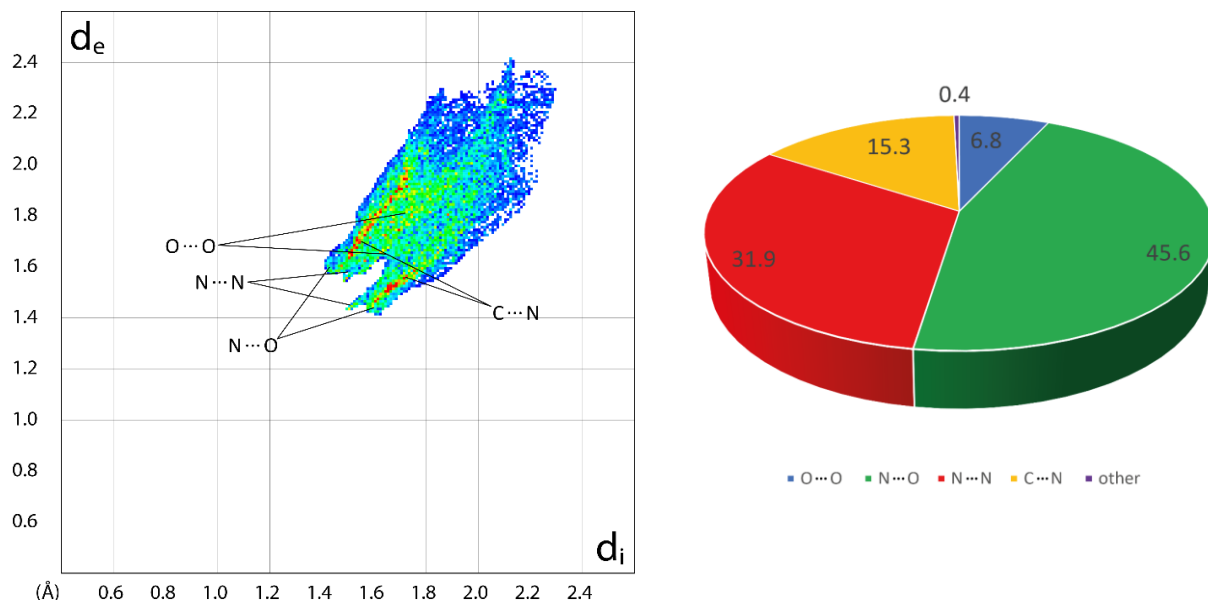


Figure S19. Two-dimensional Hirshfeld fingerprint plot of oxalyl diazide (1). Close contact distribution of compound 1.

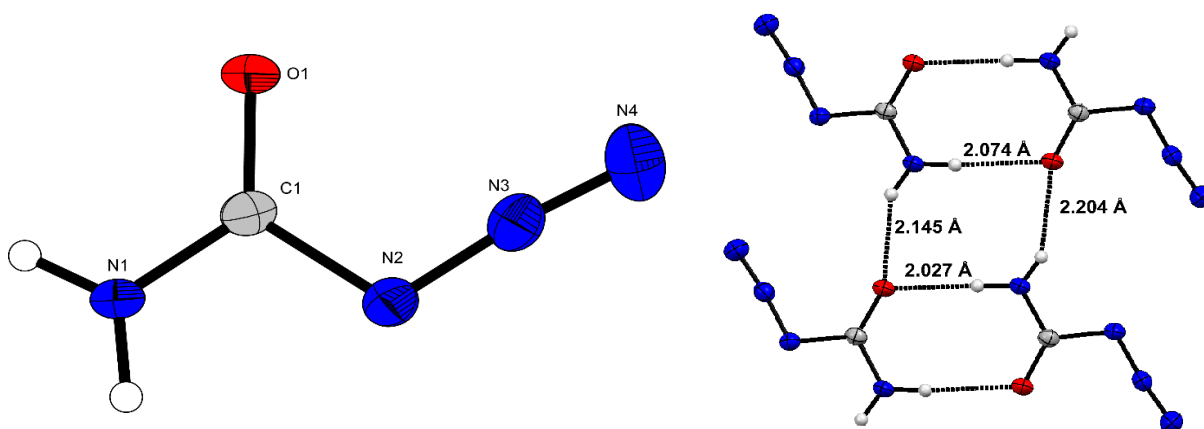


Figure S20. Crystal structure of carbamoyl azide (**2**). Thermal ellipsoids are drawn at the 50 % probability level. The carbamoyl azide (**2**) has strong hydrogen bonds with a distance of about 2 Å.

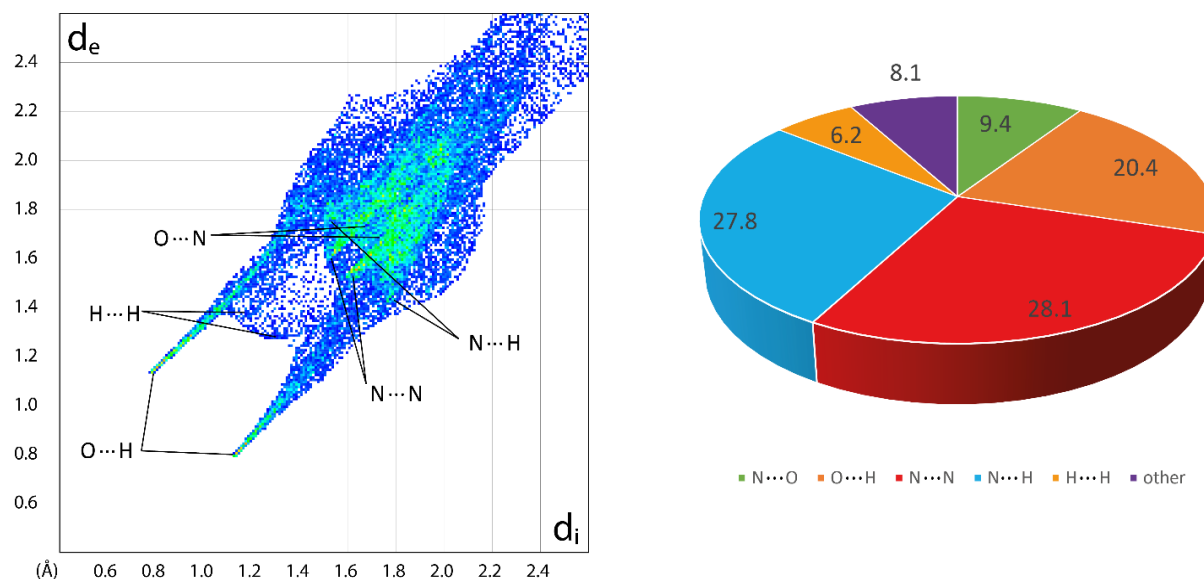


Figure S21. Two-dimensional Hirshfeld fingerprint plot of carbamoyl azide (**2**). Close contact distribution of compound **2**. Carbamoyl azide (**2**) crystallizes in the monoclinic space group $P2_1/n$ with eight formula units in the unit cell and a density of 1.611 g cm^{-3} at 101 K. All bond lengths were found to be in the range of those expected for standard bond lengths. The arrangement around the C1 should be trigonal planar, but the angle at N2-C1-N1 (111.2°) deviates considerably from the expected 120° . The azide moiety is only slightly bent (174.2°) and is oriented *syn* with respect to the carbonyl group. The molecule itself is planar. There are strong hydrogen bonds between the molecules with distances of 2.027 \AA to 2.204 \AA . A Hirshfeld analysis confirmed strong O...H (20.4 %) contacts with a distance of around 2 Å. Further, quite strong N...H (27.8 %) interactions are found with a distance of 3 Å. Some destabilizing interactions are also found, in particular, N...N (28.1 %), N...O (9.4 %) and H...H (6.2 %).^[18–20] A summary of the Hirshfeld analysis concludes that the destabilizing

close contacts are fairly well counterbalanced by the stabilizing interactions, and it is assumed that the molecule is quite thermally stable and not that sensitive towards external stimuli such as friction or impact.

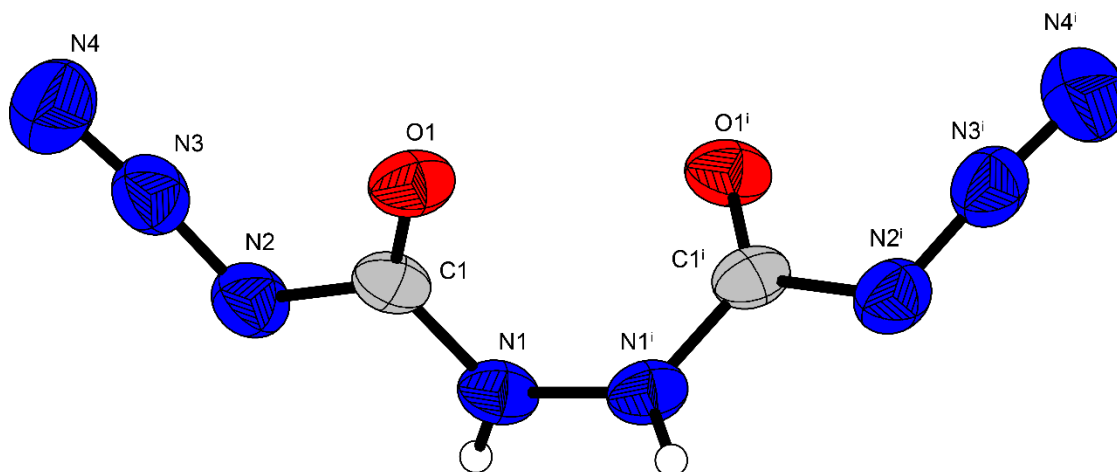


Figure S22. Crystal structure of *N,N*-bis(azidocarbonyl)hydrazine (**3**). Thermal ellipsoids are drawn at the 50 % probability level.

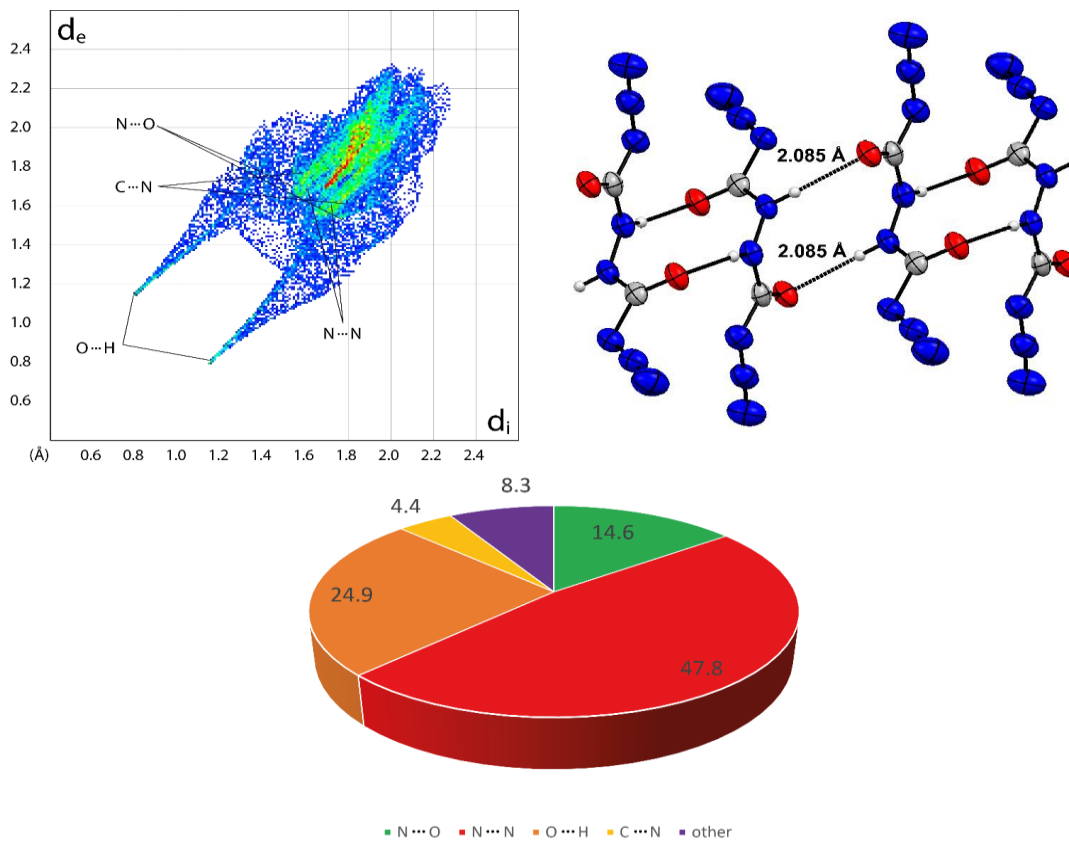


Figure S23. Two-dimensional Hirshfeld fingerprint plot of *N,N*-bis(azidocarbonyl)hydrazine (**3**). Network of hydrogen bonds in the crystal of **3** with a distance of about 2 Å. Close contact distribution of compound **3**.

N,N'-bis(azidocarbonyl)hydrazine (**3**) crystallizes in the monoclinic space group $C2/c$ with 4 molecules in the unit cell and a density of 1.697 g cm^{-3} at 173 K. The bond lengths correspond to those expected for standard bond lengths. The C1 atom shows distortion from a trigonal planar arrangement, since the O1-C1-N2 (125.8°) as well as at N1-C1-O1 (124.9°) angles are larger than 120° , while the N1-C1-N2 angle (109.2°) is smaller. The azido groups have an angle of 173.7° . As described before, the azide moiety is arranged *syn* relative to the carbonyl groups. The molecule possesses a center of symmetry between the nitrogen atoms of the hydrazine bridge with both sides of the symmetry point being planar. The molecule is twisted at the hydrazine bridge with a torsion angle of 72.2° . Compound **3** possesses very strong intermolecular hydrogen bonds with distances of 2.085 \AA , resulting in the formation of a network. A Hirshfeld analysis showed strong O...H (24.9 %) close contacts with a distance of around 2 \AA . A high percentage of N...N (47.8 %) contacts are found, which indicates compound **3** should show high sensitivity, due to the strong repulsive interactions which should occur upon crystal lattice deformation such those resulting from mechanical stimuli.^[18–20] Moreover, repulsive N...O (14.6 %) interactions are also found in the molecule. In summary, a lot of repulsive close contacts are found in **3**, but these are largely counterbalanced by the strong hydrogen bonds which are present. Compound **3** should be more sensitive towards mechanical stimuli than **2**, but less sensitive than **1**. *N,N'*-bis(azidocarbonyl)hydrazine (**3**) should show thermal stability similar to that as **2**.

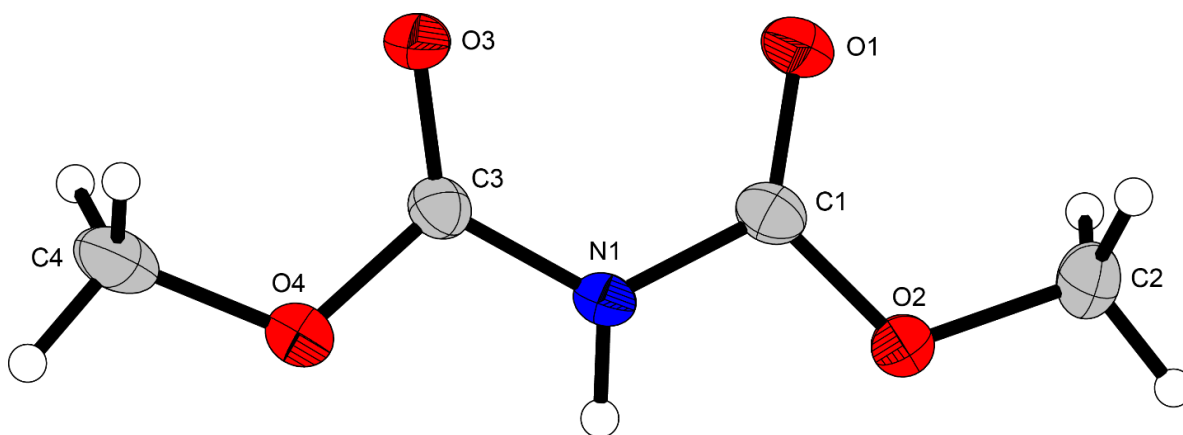


Figure S24. Crystal structure of dimethyl iminodicarbonate (**4**). Thermal ellipsoids are drawn at the 50 % probability level.

Dimethyl iminodicarbonate (**4**) crystallizes in the monoclinic space group $P2_1/c$ with four molecules in the unit cell and a density of 1.448 g cm^{-3} at 104 K. All bonds lengths correspond with those in the range of the expected standard bond lengths. The O1-C1-O2 and O1-C1-N1 angles are slightly larger (127.0° and 124.8° respectively) than those expected for a trigonal planar arrangement. The N1-C1-O2 angle (108.2°) is more similar

to that observed for a tetrahedral arrangement. The C1-N1-C3 angle is 124.9°. The same situation concerning the angles is on the other side of the symmetry axis of the molecule. Compound **4** is completely planar with no twists nor torsions. A strong hydrogen bond is found in this molecule with a distance of 2.037 Å from the H1 of N1 to O3.

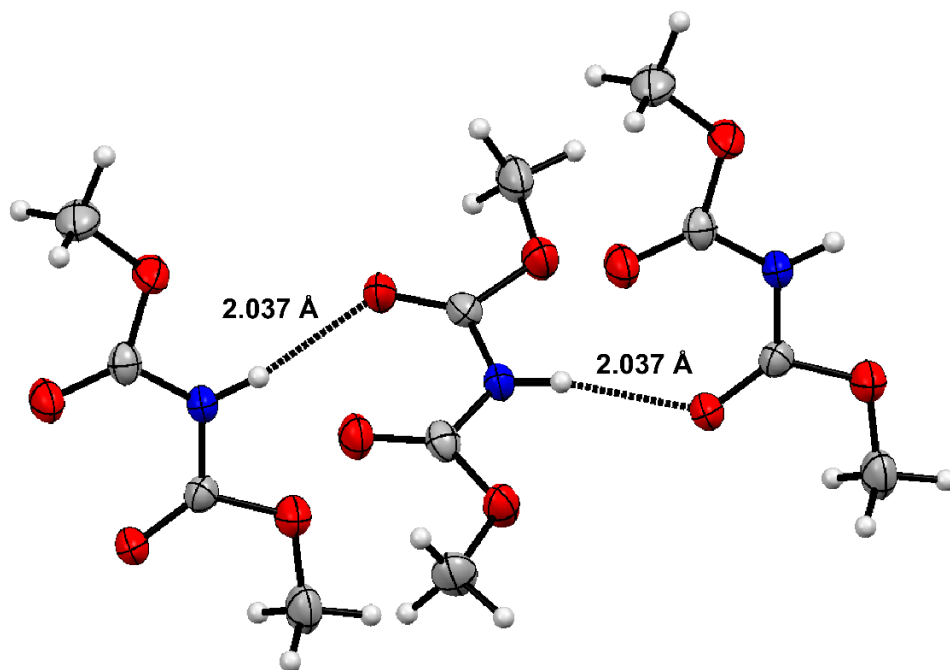


Figure S25. Dimethyl iminodicarbonate (**4**) forms a network in the crystal due to the formation of hydrogen bonds with a distance of 2.037 Å.

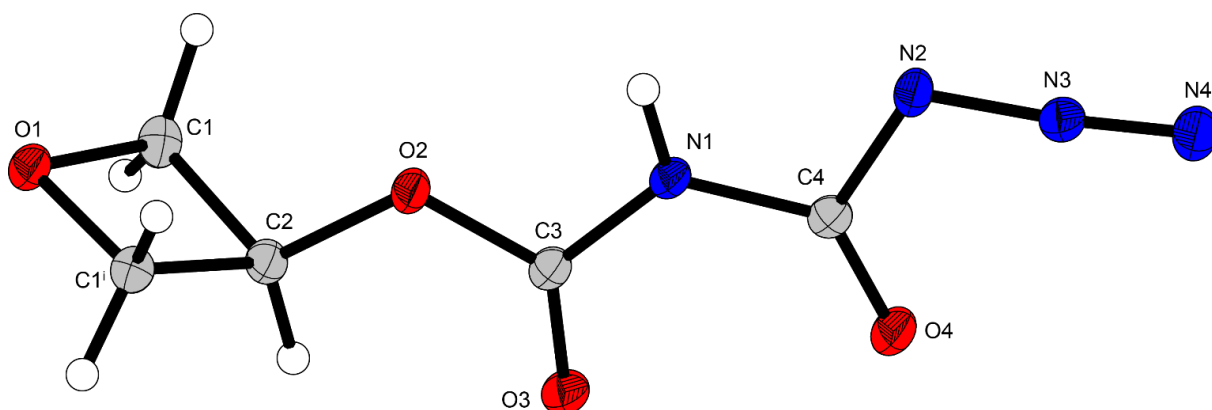


Figure S26. Crystal structure of oxetan-3-yl-*N*-azidocarbonyl-carbamate (**5**). Thermal ellipsoids are drawn at the 50 % probability level.

Oxetan-3-yl-*N*-azidocarbonyl-carbamate crystallizes in the monoclinic space group $C2/m$ with 4 formula units in the unit cell and a density of 1.651 g cm⁻³ at 101 K. All bond lengths are in the range expected for standard bond lengths. The angles in the oxetane ring are 90.9° (C1-O1-C1'), 91.3° (O1-C1-C2 and O1-C1'-C2), and 86.0° (C1-C2-C1'). Two angles centered at atoms C3 and C4 are slightly larger than the expected 120°, namely, O3-C3-

O2 is 126.1°, O3-C3-N1 is 127.2°, while O2-C3-N1 is 106.6°, which is significantly smaller than a trigonal planar angle and also smaller than a tetrahedral angle. Also, N1-C4-N2 (107.0°) is smaller than a trigonal planar angle and a tetrahedral angle. The other two are larger than a trigonal planar angle with 128.4° (N1-C4-O4) and 124.6° (O4-C4-N2). The azide moiety is only slightly bent with an angle of 174.9°. The usually planar oxetane group has a torsion angle of 5.3° and is twisted 132.2° with respect to the rest of the molecule which is planar. Compound **5** has strong intermolecular hydrogen bonds from H1 at N1 to O1 of the oxetane ring with a distance of 1.938 Å. Two molecules form pairs in the crystal through two symmetrical hydrogen bonds of the same distance.

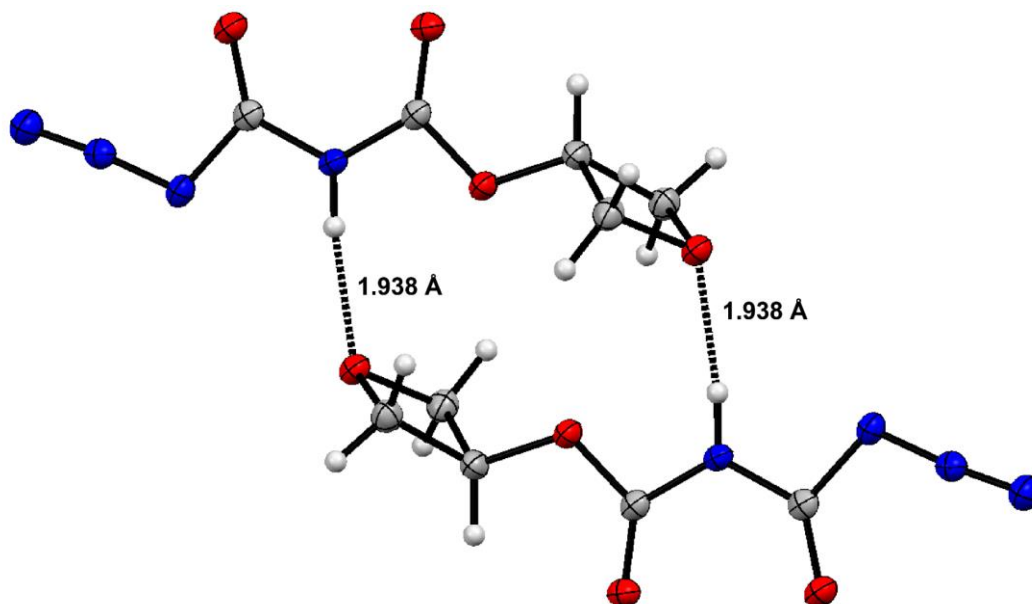


Figure S27. Two molecules of oxetan-3-yl-*N*-azidocarbonyl-carbamate (**5**) form pairs via two hydrogen bonds with a distance of 1.938 Å.

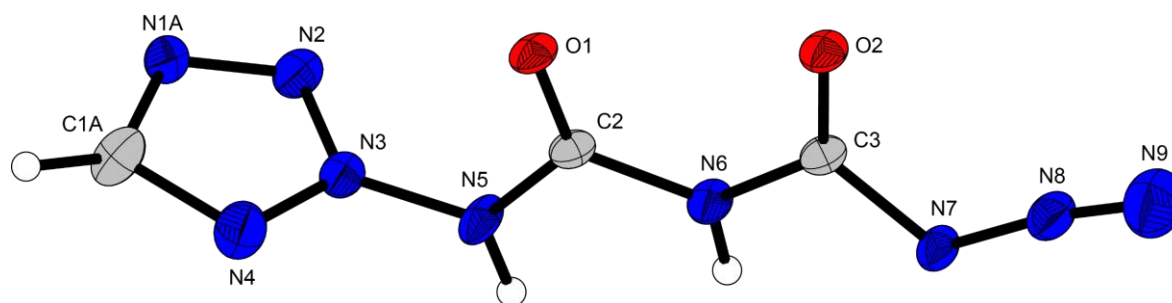


Figure S28. Crystal structure of *N*-azidocarbonyl-*N*-(2*H*-tetrazol-2-yl)-urea (**6**). Thermal ellipsoids are drawn at the 50 % probability level.

N-azidocarbonyl-*N*-(2*H*-tetrazol-2-yl)-urea (**6**) crystallizes in the monoclinic space group $P2_1/c$ with four molecules in the unit cell and a density of 1.727 g cm⁻³ at 102 K. The bond lengths are in good agreement with standard bond lengths. As described for the previous molecule (**5**), the N5-C2-O1 (123.0°) and O1-C2-N6 (125.0°) angles are slightly larger

than the expected values of 120° . The N5-C2-N6 (112.1°) angle is significantly smaller than a trigonal planar angle, but larger than a tetrahedral angle. The two angles, N6-C3-O2 and O2-C3-N7, are both 126.3° , which is also larger than that expected for a trigonal planar angle. The N6-C3-N7 angle is only 107.5° , which is smaller than both a trigonal planar and tetrahedral angle. The azido group N7-N8-N9 is bent with an angle of 171.7° . The usually planar tetrazole motif has a small torsion angle of about 4° , and is twisted by about 90° with respect to the rest of the molecule. The rest of the molecule is nearly planar, only O2-C3-N6-C2 is twisted by 9.8° . Compound **6** forms a network, in which one molecule forms three strong hydrogen bonds to the neighboring molecule. The H6.....O1 distance is 2.006 \AA , H5.....O1 is 2.099 \AA and H5.....O2 is 2.201 \AA .

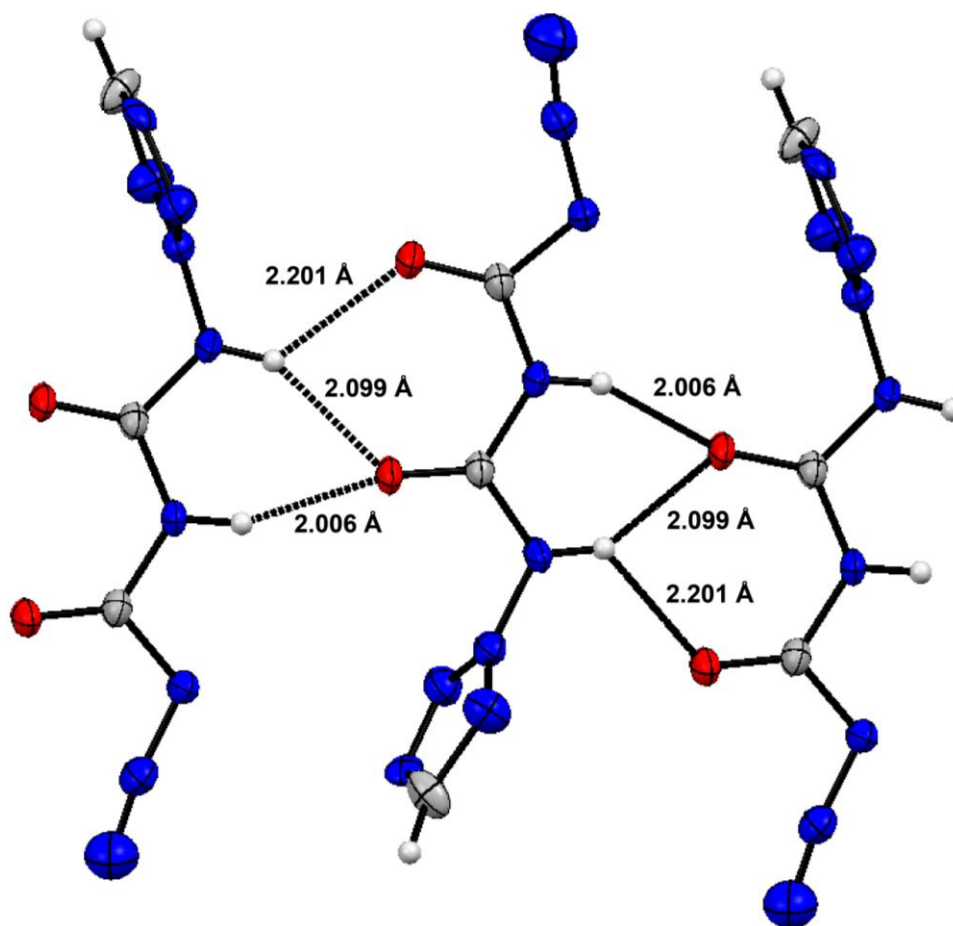


Figure S29. Network of *N*-azidocarbonyl-*N*-(2*H*-tetrazol-2-yl)-urea (**6**) forming three hydrogen bonds between the molecules with a distance of about 2 \AA .

Table S1. Crystallographic data and structure refinement details for the prepared compounds 1 – 6.

	Oxalyl diazide (1)	Carbamoyl azide	<i>N,N</i> -
Formula	C ₂ N ₆ O ₂	CH ₂ N ₄ O	C ₂ H ₂ N ₈ O ₂
FW [g mol ⁻¹]	140.08	86.07	170.12
Crystal system	monoclinic	monoclinic	monoclinic
Space group	<i>P</i> 2 ₁ / <i>c</i> (No. 14)	<i>P</i> 2 ₁ / <i>n</i> (No. 14)	<i>C</i> 2/ <i>c</i> (No. 15)
Color / Habit	colorless platelet	colorless rod	colorless platelet
Size [mm]	0.08 x 0.35 x 0.50	0.048 x 0.182 x	0.01 x 0.03 x 0.04
<i>a</i> [Å]	9.9766(15)	5.1411(6)	20.9800(14)
<i>b</i> [Å]	5.1435(5)	22.5003(19)	4.6103(3)
<i>c</i> [Å]	11.0086(15)	6.5540(10)	7.1227(4)
α [°]	90	90	90
β [°]	109.822(16)	110.632(14)	104.894(2)
γ [°]	90	90	90
<i>V</i> [Å ³]	531.43(13)	709.52(16)	665.79(7)
<i>Z</i>	4	8	4
ρ_{calc} [g cm ⁻³]	1.751	1.611	1.697
μ [mm ⁻¹]	0.155	0.139	0.148
<i>F</i> (000)	280	352	344
$\lambda_{\text{MoK}\alpha}$ [Å]	0.71073	0.71073	0.71073
<i>T</i> [K]	102	101	173
θ Min-Max [°]	2.2, 25.3	3.4, 26.4	4.0, 26.4
Dataset	-12: 10 ; -4: 6 ; -13:	-6: 6 ; -26: 28 ; -8:	-26: 26 ; -5: 5 ; -8: 8
Reflections	3015	5528	5226
Independent	975	1458	667
<i>R</i> _{int}	0.037	0.036	0.029
Observed	756	1135	580
Parameters	91	125	59
<i>R</i> ₁ (obs) ^[a]	0.0460	0.0352	0.0345
<i>wR</i> ₂ (all data) ^[b]	0.1314	0.0828	0.0841
<i>S</i> ^[c]	1.08	1.07	1.14
Resd. dens [e]	-0.31, 0.32	-0.18, 0.16	-0.11, 0.11
Device type	Oxford Xcalibur3	Oxford Xcalibur3	Bruker D8 Venture TXS
Solution	SHELXT	SHELXT	SHELXT
Refinement	SHELXL-2018	SHELXL-2018	SHELXL-2018
Absorption	multi-scan	multi-scan	multi-scan
CCDC	2077536	2077537	2077539

	Dimethyl	Oxetan-3-yl- <i>N</i> -	<i>N</i> -Azidocarbonyl- <i>N</i> -(2 <i>H</i> -
Formula	C ₄ H ₇ NO ₄	C ₅ H ₆ N ₄ O ₄	C ₃ H ₃ N ₉ O ₂
FW [g mol ⁻¹]	133.11	186.14	197.14
Crystal	monoclinic	monoclinic	monoclinic
Space	<i>P</i> 2 ₁ / <i>c</i> (No. 14)	<i>C</i> 2/ <i>m</i> (No. 12)	<i>P</i> 2 ₁ / <i>c</i> (No. 14)
Color / Habit	colorless needle	colorless prism	colorless platelet
Size [mm]	0.02 x 0.08 x 0.50	0.01 x 0.25 x 0.50	0.15 x 0.25 x 0.48
a [Å]	12.7890(18)	16.3279(17)	8.8833(12)
b [Å]	5.8869(7)	5.8786(7)	8.9823(7)
c [Å]	8.2990(9)	7.8026(7)	10.0444(12)
α [°]	90	90	90
β [°]	102.200(12)	90.113(8)	108.873(13)
γ [°]	90	90	90
V [Å ³]	610.70(13)	748.93(14)	758.38(16)
Z	4	4	4
ρ _{calc.} [g	1.448	1.651	1.727
μ [mm ⁻¹]	0.131	0.144	0.147
F(000)	280	384	400
λMoKα [Å]	0.71073	0.71073	0.71073
T [K]	104	101	102
θ Min-Max	1.6, 26.4	2.5, 26.4	2.4, 26.4
Dataset	-15: 15 ; -7: 7 ; -10:	-20: 15 ; -7: 7 ; -9: 8	-9: 11 ; -11: 11 ; -12: 11
Reflections	3774	2471	4769
Independent	1253	830	1546
R _{int}	0.049	0.022	0.031
Observed	787	731	1160
Parameters	88	90	146
R ₁ (obs) ^[a]	0.0664	0.0260	0.0451
wR ₂ (all	0.1769	0.0672	0.1297
S [c]	1.04	1.05	1.05
Resd. dens	-0.22, 0.89	-0.17, 0.21	-0.32, 0.23
Device type	Oxford Xcalibur3	Oxford Xcalibur3	Oxford Xcalibur3
Solution	SHELXT	SHELXT	SHELXT
Refinement	SHELXL-2018	SHELXL-2018	SHELXL-2018
Absorption	multi-scan	multi-scan	multi-scan
CCDC	2077540	2077535	2077538

[a] $R_1 = \frac{\sum ||F_0| - |F_c||}{\sum |F_0|}$; [b] $wR_2 = \frac{[\sum [w(F_0^2 - F_c^2)^2] / \sum [w(F_0^2)]]^{1/2}}{2}$; $w = [\sigma^2(F_0^2) + (xP)^2 + yP]^{-1}$ and $P = (F_0^2 + 2F_c^2)/3$; [c] $S = \{[\sum [w(F_0^2 - F_c^2)^2] / (n-p)]^{1/2}$ (n = number of reflections; p = total number of parameters).

6.5.5 Thermal analysis

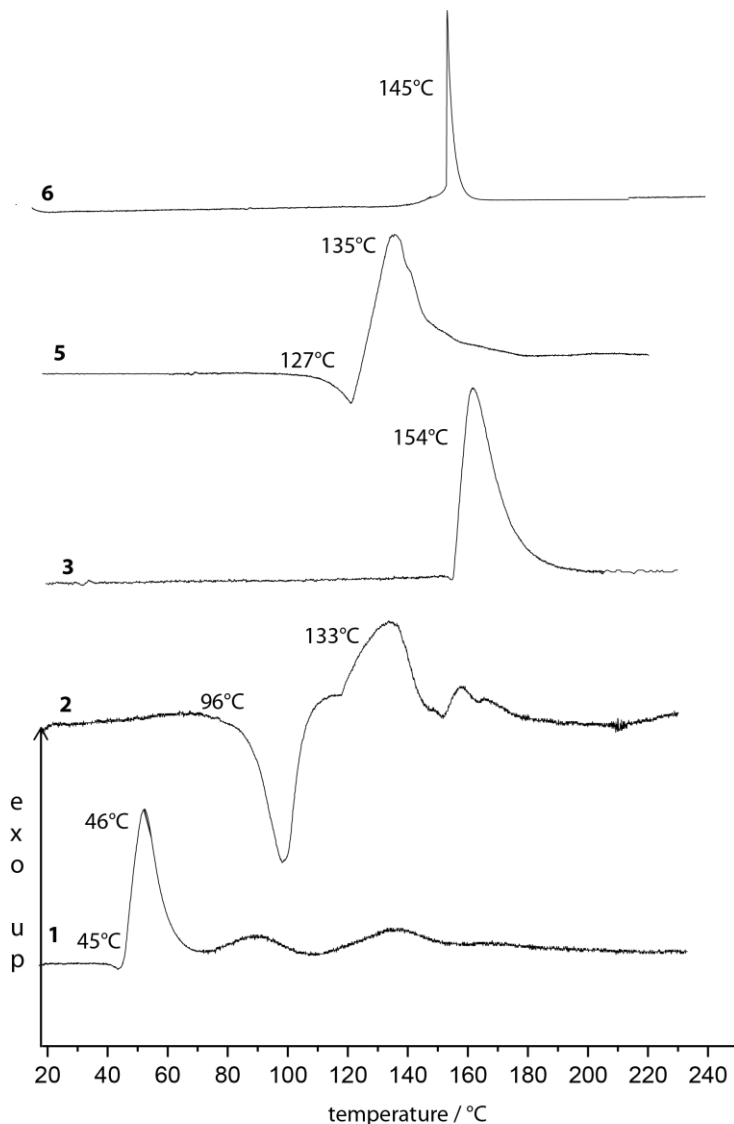


Figure S30. Differential thermal analysis plots of compound **1–3, 5** and **6**.

DTA plots of compounds **1, 2** and **5** showed melting point of 45°C, 96°C and 127°C for the respective compound. All synthesized carbonyl azide derivatives have a decomposition temperature of higher than 100°C, up to 154°C for **3**, except oxalyl diazide (**1**) which is rather unstable and decomposes at 46°C.

6.5.6 Computation

Heat of formation calculation

The atomization was used to determine the heat of formation of **1–3**, **5**, **6** using the atom energies in Table 2.

$$\Delta_f H^{\circ}(\text{g, M, 298}) = H_{(\text{molecule, 298})} - \sum H^{\circ}(\text{atoms, 298}) + \sum \Delta_f H^{\circ}(\text{atoms, 298})$$

Table S2. CBS-4M electronic enthalpies for atoms C, H, N and O and their literature values.

	$-H^{298} / \text{a.u.}$	$\Delta_f H^{\circ}_{\text{gas}} [^{21}]$
H	0.500991	217.998
C	37.786156	716.68
N	54.522462	472.68
O	74.991202	249.18

The Gaussian16 program package was used to calculate room temperature enthalpies on the CBS-4M level of theory.^[22] In order to obtain the energy of formation for the solid phase of **1**, the Trouton's Rule has to be applied ($\Delta H_{\text{sub}} = 188 \cdot T_m$).

Table S3. Heat of formation calculation results for compounds **1–3**, **5**, **6**.

M	$-H^{298}$ [a] [a.u.]	$\Delta_f H^{\circ}(\text{g, M})$ [b] [kJ mol ⁻¹]	$\Delta_{\text{sub}} H^{\circ}$ (M) [c] [kJ mol ⁻¹]	$\Delta_f H^{\circ}(\text{s})$ [d] [kJ mol ⁻¹]	Δn	$\Delta_f U(\text{s})$ [e] [kJ kg ⁻¹]
1	554.357072	389.6	59.8122	329.7	-4.0	2425.1
2	333.080962	-111.1	69.4002	41.7	-3.5	585.0
3	664.930052	389.7	80.3042	309.3	-6.0	1906.2
5	713.055212	-265.3	75.2282	-340.5	-7.0	-1736.1
6	758.261604	426.7	78.6122	348.1	-7.0	1854.0

[a] CBS-4M electronic enthalpy; [b] gas phase enthalpy of formation; [c] sublimation enthalpy; [d] standard solid state enthalpy of formation; [e] solid state energy of formation.

Molecular Orbital Calculation

To obtain insight into whether a closed tetrazolone or iminol form exist, we calculated six different possible tautomers using the G09W code.^[22] The energies were calculated at the CBS-4M level. The CBS-4M results suggested the presence of the mono- (**C**) and di-tetrazolone (**E**) forms relative to the amide (**A**). However, we were not able to experimentally verify the two more energetically favorable forms.

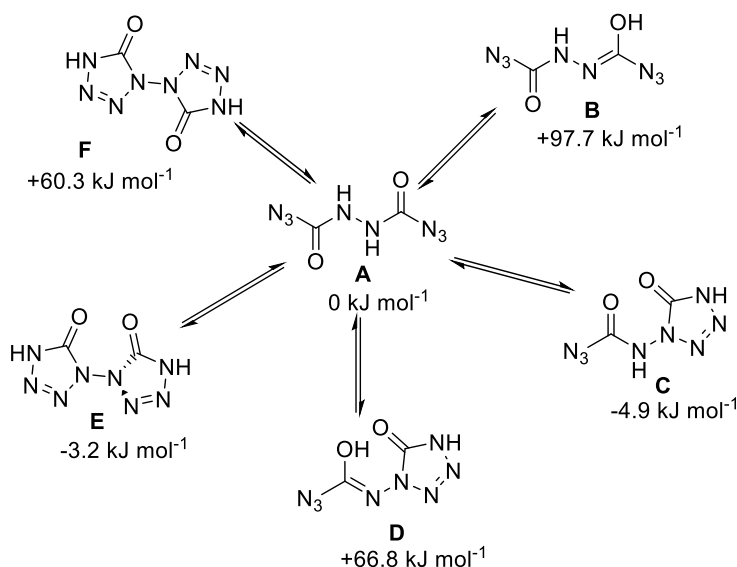


Figure S30. Six different tautomers of *N,N*-bis(azidocarbonyl)hydrazine (**3**) and their respective energies on the CBS-4M level relative to that of **A**.

In order to obtain more reliable energies for molecules **A**, **C** and **E** in solution, we carried out MP2 calculations with a cc-pVDZ basis set using the Polarizable Continuum Model. The Polarizable Continuum Model (PCM) is a widely used implicit solvation model. Implicit solvation models place the molecule of interest inside a cavity in a continuous homogenous dielectric medium that represents the solvent. As the solvent we used water and acetone with dielectric constants of $\epsilon(\text{H}_2\text{O}) = 78.39$ and $\epsilon(\text{acetone}) = 20.7$. The results are summarized in table 4. The results of the PCM model calculation indicate that the mono-tetrazolone (**C**) form is unfavored in relation to **A** in the solvents water and acetone with energies of +12.6 kJ mol⁻¹ and +13.0 kJ mol⁻¹, respectively. Furthermore, the di-tetrazolone (**E**) form is strongly unfavored relative to **A** with energies of +41.0 kJ mol⁻¹ in water and +42.3 kJ mol⁻¹ in acetone.

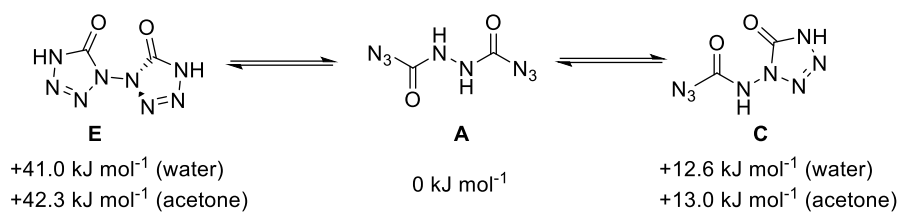


Figure S31. Three tautomers of *N,N*-bis(azidocarbonyl)hydrazine (**3**) and their respective energies on the MP2/cc-pVDZ level (PCM model) relative to **A** with water or acetone as the solvents.

Table S4. Energy differences for the six tautomers of compound **3** and additionally PCM calculations with solvents being water and acetone for **A**, **C**, **E**.

	A	B	C	D	E	F*
Symmetry	C ₂		C ₁		C ₂	
CBS-4M						
-E / a. u.	664.930052	664.892830	664.931926	664.904611	664.931271	664.907081
ΔH_f° (g) / kJ mol ⁻¹	+389.7	+487.4	+384.8	+465.5	+386.5	+450.0
ΔE / kJ mol ⁻¹	0.0	+97.7	-4.9	+66.8	-3.6	+60.3
MP2/cc-pVDZ solvent = water (PCM model)						
-E / a. u.	664.063131	-	664.058353	-	664.047450	-
ΔE / kJ mol ⁻¹	0.0	-	+12.5604	-	+41.03064	-
MP2/cc-pVDZ solvent = acetone (PCM model)						
-E / a. u.	664.062599	-	664.057531	-	664.046518	-
ΔE / kJ mol ⁻¹	0.0	-	+12.97908	-	+42.28668	-

* transition state

6.5.7 References

- [1] <http://www.bam.de>
- [2] NATO Standardization Agreement (STANAG) on Explosives, *Impact Sensitivity Tests*, no. 4489, 1st ed., September 17, **1999**.
- [3] WIWEB-Standardarbeitsanweisung 4-5.1.02, Ermittlung der Explosionsgefährlichkeit, hier der Schlagempfindlichkeit mit dem Fallhammer, November 8, **2002**.
- [4] NATO Standardization Agreement (STANAG) on Explosives, *Friction Sensitivity Tests*, no. 4487, 1st ed., August 22, **2002**.
- [5] WIWEB-Standardarbeitsanweisung 4-5.1.03, Ermittlung der Explosionsgefährlichkeit oder der Reibeempfindlichkeit mit dem Reibeapparat, November 8, **2002**.
- [6] Impact: Insensitive >40 J, less sensitive ≤35 J, sensitive ≤4 J, very sensitive ≤3 J; friction: Insensitive >360 N, less sensitive=360 N, sensitive 80 N, very sensitive ≤80 N, extreme sensitive ≤10 N; According to the UN Recommendations on the Transport of Dangerous Goods (+) indicates: not safe for transport.
- [7] H. W. Roesky, O. Glemser, *Chem Ber.* **1964**, 97, 1710 – 1712.
- [8] T. M. Klapötke, B. Krumm, R. Scharf, *Eur. J. Inorg. Chem.* **2016**, 19, 3086 – 3093.
- [9] J. Thiele, O. Stange, *Liebigs Ann. Chem.* **1894**, 283, 1 – 46.
- [10] J. M. Harris, R. McDonald, J. C. Vederas, *J. Chem. Soc., Perkin Trans. 1* **1996**, 2669 – 2674.
- [11] M. Benz, T. M. Klapötke, B. Krumm, M. Lommel, J. Stierstofer, *J. Am. Chem. Soc.* **2021**, 143, 1323 – 1327.
- [12] K. Banert, Y.-H. Joo, T. Ruffer, B. Walfort, H. Lang, *Angew. Chem., Int. Ed.* **2007**, 46, 1168 – 1171.
- [13] CrysAlisPro, Oxford Diffraction Ltd., *version 171.33.41*, **2009**.
- [14] G. M. Sheldrick, *Acta Cryst.* **2015**, A71, 3 – 8.
- [15] O. V. Dolomanov, L. J. Bourhis, R. J. Gildea, J. A. K. Howard, H. Puschmann, *J. Appl. Cryst.* **2009**, 42, 339 – 341.

- [16] *SCALE3 ABSPACK –An Oxford Diffraction program* (1.0.4, gui: 1.0.3), Oxford Diffraction Ltd., **2005**.
- [17] *APEX3*. Bruker AXS Inc., Madison, Wisconsin, USA.
- [18] D. E. Dosch, M. Reichel, M. Born, T. M. Klapötke, K. Karaghiosoff, *Cryst. Growth Des.* **2021**, *21(1)*, 243 – 248.
- [19] Y. Ma, A. Zhang, X. Xue, D. Jiang, Y. Zhu, C. Zhang, *Cryst. Growth Des.* **2014**, *14*, 6101 – 6114.
- [20] M. A. Spackman, D. Jayatilaka, *CrystEngComm* **2009**, *11*, 19 – 32.
- [21] M. W. Chase Jr., NIST-JANAF Thermochemical Tables, Fourth Edition, *J. Phys. Chem. Red. Data, Monograph 9* **1998**, 1 – 1951.
- [22] M. J. Frisch, G. W. Trucks, H. B. Schlegel, G. E. Scuseria, M. A. Robb, J. R. Cheeseman, G. Scalmani, V. Barone, G. A. Petersson, H. Nakatsuji, X. Li, M. Caricato, A. V. Marenich, J. Bloino, B. G. Janesko, R. Gomperts, B. Mennucci, H. P. Hratchian, J. V. Ortiz, A. F. Izmaylov, J. L. Sonnenberg, D. Williams-Young, F. Ding, F. Lipparini, F. Egidi, J. Goings, B. Peng, A. Petrone, T. Henderson, D. Ranasinghe, V. G. Zakrzewski, J. Gao, N. Rega, G. Zheng, W. Liang, M. Hada, M. Ehara, K. Toyota, R. Fukuda, J. Hasegawa, M. Ishida, T. Nakajima, Y. Honda, O. Kitao, H. Nakai, T. Vreven, K. Throssell, J. A. Montgomery, Jr., J. E. Peralta, F. Ogliaro, M. J. Bearpark, J. J. Heyd, E. N. Brothers, K. N. Kudin, V. N. Staroverov, T. A. Keith, R. Kobayashi, J. Normand, K. Raghavachari, A. P. Rendell, J. C. Burant, S. S. Iyengar, J. Tomasi, M. Cossi, J. M. Millam, M. Klene, C. Adamo, R. Cammi, J. W. Ochterski, R. L. Martin, K. Morokuma, O. Farkas, J. B. Foresman, D. J. Fox, *Gaussian16*, Gaussian, Inc., Wallingford, CT, USA, **2016**.

7. Thermodynamics of organic azides: experimental vapor pressures of organic polyazido compounds measured with the transpiration method

Greta Bikelytė, Alexander G. Harter, Martin A. C. Härtel, Stefanie B. Heimsch, Thomas M. Klapötke*

as published in *Fluid Phase Equilibria* **2021**, 549, 113222.

DOI: 10.1016/j.fluid.2021.113222

Key words: Vapor pressure, Organic azides, Gas-saturation, Vaporization enthalpy

Abstract: In this study experimental vapor pressures of several organic azides including 1,3-diazidopropan-2-ol (1,3-DAP, CAS: 57011-48-0), 2,3-diazidopropan-2-ol (2,3-DAP, CAS: 67880-10-8) and geminal diazido group containing 1,3-diethyl-2,2-diazidomalonate (DE-DAM, CAS: 168207-98-5) were measured for the first time using the transpiration method. The study provides p-T fitting equations and corresponding molar enthalpies of vaporization, adjusted to 298.15 K: (72.6±0.5) kJ mol⁻¹ for 1,3-DAP, (75.2±0.6) kJ mol⁻¹ for 2,3-DAP and (76.0±1.1) kJ mol⁻¹ for DE-DAM.

7.1 Introduction

The organic azides are useful as building blocks in “click” chemistry [1; 2], in pharmaceuticals [3], energetic materials [3; 4; 5] and many other applications [3]. In the field of energetic materials, the introduction of the azide functional group in the composition of potential energetic materials can result in “greener”, more environmentally friendly solutions since the combustion of the azide functional group containing materials is smokeless and produces environmentally harmless molecular nitrogen. However, the -N₃ group not only raises the energetic load of the compound, but often causes a significant increase in the sensitivity towards friction and impact [6]. The sensitivity of the compounds might hinder the determination of experimental thermodynamic parameters, such as molar enthalpies of phase transitions or molar enthalpy of formation, which are important for the assessment of the performance of potential high energy materials [7]. As a result, in recent years a considerable amount of effort was invested in the development of the computational methods to predict the thermochemical properties of the organic azides [6; 8; 9; 10; 11]. The development of the methods relies heavily on the availability of high-quality experimental thermodynamic data. Consequently, in the past decade several published studies aimed to provide new reliable data and to eliminate the existent disarray in experimental thermodynamic properties of organic azides [12; 13]. Moreover, the relatively “young” class of compounds containing geminal diazides have remained an uninvestigated area in terms of their thermodynamic behaviors [14].

Recently our research group executed investigations on the performance of several organic azides [15; 16]. Therefore, a group of relatively insensitive organic polyazido compounds, including two diazido propanols, 1,3-diazidopropan-2-ol (1,3-DAP) and 2,3-diazidopropan-2-ol (2,3-DAP), and a malonic ester with a geminal diazido group 1,3-diethyl-2,2-diazidomalonate (DE-DAM), were chosen for the determination of thermodynamic properties using the transpiration method (Fig. 1).

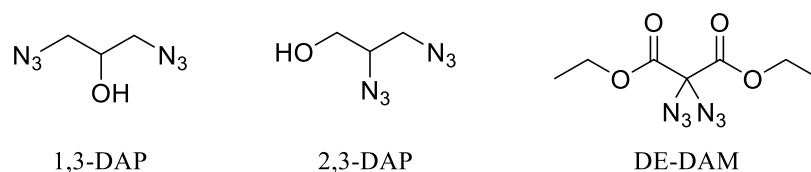


Figure 1. The compounds of interest, that were analyzed in this work: 1,3-DAP, 2,3-DAP and DE-DAM.

7.2 Materials and methods

7.2.1 Materials

CAUTION! 1,3-DAP, 2,3-DAP and DE-DAM are energetic materials with sensitivity to various stimuli. While we encountered no issues in the handling of these materials, we encourage to employ additional protective measures (Kevlar gloves, hearing protections, face shields, etc.) during the handling of all of the compounds at all times including vapor pressure measurements.

All of the compounds investigated in this study were synthesized by procedures, described previously in the literature. The 1,3-DAP and 2,3-DAP compounds were produced according to the methods described in *Farhanullah et al.* and *Samrin et al.*, respectively [17; 18]. Compound DE-DAM was prepared according to the synthetic path described in the study of *Erhart et al.* [19]. The purity of the compounds used in this study was investigated with the elemental analysis and ¹H-NMR spectroscopy and is reported in Table 1. Further information on purity assessment is provided in the Supporting Information.

Table 7. Origin and mass fraction purity P_{An} of the compounds investigated in this work.

Substance	IUPAC name	CAS #	P_{An} ^a
1,3-DAP	1,3-diazidopropan-2-ol	57011-48-0	>0.98
2,3-DAP	2,3-diazidopropan-1-ol ^b	67880-10-8	>0.95
DE-DAM	1,3-diethyl-2,2-diazidomalonate	168207-98-5	>0.98

^aPurity P_{An} of the samples as mass fraction, estimated from the ¹H-NMR, were clean spectra could be associated with the purity of >0.98 (m/m). The conservative estimations were backed up by elemental analyses. ^bee not determined.

Before the transpiration experiment took place, a sample conditioning step within the experimental setup was executed by subjecting the sample to the carrier gas stream at

ambient and elevated temperatures (315-320 K) for 2-3 hours each, in order to remove moisture and possible volatile impurities.

7.2.2 Transpiration Method

The measurements of the experimental vapor pressures were executed with the transpiration method described previously [20]. The method relies on the determination of the amount of the analyte in a saturated carrier gas stream. To facilitate the saturation conditions, a generous amount of the compound of interest (0.5-1 g) is homogeneously coated on the surface of the 1 mm diameter glass beads, which are placed in a temperature-regulated glass vessel, the so-called saturator. Given that the flow of the carrier gas is relatively slow (1-5 dm³·h⁻¹), the carrier gas stream enters the glass vessel and, upon the contact with the analyte, gets saturated. The saturation state is demonstrated by the independence of the analytical results and flow rate at the lowest experimental temperature. To determine the amount of the vapors of the analyte, present in the gas phase, the gas stream exits the saturator into a detachable glass tube, which is immersed in a cooling bath (isopropanol, 243 K). The vapors of the analyte condense on the glass walls and the amount of the analyte collected over a specific period of time is quantified by a chromatographic technique (HPLC-DAD, Shimadzu, Prominence® with LC-20AD pump module and SPDM20A Diode Array Detector). For the chromatographic methods please refer to the Supporting Information.

Experimental conditions including temperature of the saturator T (in K), ambient temperature T_{amb} (in K), volume of the carrier gas V_{N_2} (in m³) along with the amount of the analyte collected during the transpiration experiment m (in kg) are inserted into modified equation of the Ideal Gas Law (Eq. 1), which allows the calculation of absolute vapor pressure p_{sat} (in Pa).

$$p_{sat}(T) = \frac{mRT_{amb}}{MV_{N_2}} \quad (1)$$

Here R is universal gas constant 8.314462 [J·mol⁻¹·K⁻¹]; M : molecular weight [kg·mol⁻¹]. The validity of the Eq. 1 relies on the Dalton's law of partial pressures and the assumption that the volume of the vapors of the analyte is negligible in comparison to the volume of the carrier gas. The relationship between the absolute vapor pressures and the experimental temperature is described by a fitting equation:

$$\ln\left(\frac{p_{sat}}{p^\circ}\right) - \frac{\Delta_l^g C_{p,m}^\circ}{R} \ln \frac{T}{T_0} = A - \frac{B}{T} \quad (2)$$

Here p° is the reference pressure (in Pa), T_0 is the reference temperature (in K), A and B are fitting coefficients (A is unitless, B in K). Molar heat capacity differences between liquid

(l) and gaseous phase (g) at constant pressure $\Delta_l^g C_{p,m}^\circ$ for the compounds of interest were calculated using the procedure described by *Acree and Chickos* [21]. The molar heat capacities $C_{p,m}^\circ(l)$, required for this calculation were obtained via group contribution method by *Acree and Chickos* [22]. The values are detailed in Table 2.

Table 8. The estimated molar heat capacities $C_{p,m}^\circ$ and their differences of the organic azides, investigated in this work ($T = 298.15$ K).

Compound	$C_{p,m}^\circ(l)$ ^a	$-\Delta_l^g C_{p,m}^\circ$ ^b
	J·mol ⁻¹ ·K ⁻¹	J·mol ⁻¹ ·K ⁻¹
1,3-DAP	327.5	95.7
2,3-DAP	327.5	95.7
DE-DAM	458.0	129.7

^a Calculated according to the group contribution method by *Acree and Chickos* [22]. Group values for azide functional group were obtained from experimental heat capacity values by *Fagley and Myers* [23]. ^b Calculated by $-\Delta_l^g C_{p,m}^\circ = 10.58 + C_{p,m}^\circ(l) \times 0.26$ [21].

The determined p - T datasets allow the determination of the molar enthalpy of vaporization $\Delta_l^g H_m^\circ$ and molar entropy of vaporization $\Delta_l^g S_m^\circ$ at temperature T according to the equations

$$\Delta_l^g H_m^\circ(T) = RB + \Delta_l^g C_{p,m}^\circ T \quad (3)$$

$$\Delta_l^g S_m^\circ(T) = \frac{\Delta_l^g H_m^\circ(T)}{R} + R \ln \left(\frac{p_{sat}}{p^\circ} \right) \quad (4)$$

Here p° is the standard pressure (0.1 MPa).

For the evaluation of the uncertainties of molar enthalpies of vaporization $\Delta_l^g H_m^\circ(T)$, experimental vapor pressures were fitted to the linear equation $\ln p = f(T^{-1})$ using the method of least squares. The resulting enthalpies of vaporization, their corresponding uncertainties and the uncertainties introduced by the approximation were included in the calculations of the uncertainties of $\Delta_l^g H_m^\circ(T)$ (Eq. 2) [24].

7.3 Results and discussion

The results of the transpiration experiments performed as described above are reported in the Tables 3 – 5 together with the fitting functions according to Eq. 2 and molar enthalpies of vaporization, adjusted to 298.15K.

Table 3. 1,3-DAP (liq): experimental conditions and resulting absolute vapor pressures p_{sat} obtained by the transpiration method in this work.

$$\Delta_l^g H_m^\circ (298.15 \text{ K}) = (72.6 \pm 0.5) \text{ kJ mol}^{-1}$$

$$\ln \left(\frac{p_{sat}}{p^0} \right) = \frac{345.3}{R} - \frac{101171.93}{RT} - \frac{95.7}{R} \ln \frac{T}{298.15 \text{ K}}$$

T^a	m^b	$V_{N_2}^c$	T_{amb}^d	Gasflow	p_{sat}^e	$u(p_{sat})^f$
K	mg	dm ³	K	dm ³ ·h ⁻¹	Pa	Pa
274.5	0.13	14	295.9	3.6	0.161	0.009
274.6	0.26	28	299.8	1.6	0.160	0.009
274.6	0.12	14	295.9	4.8	0.153	0.009
278.4	0.41	28	295.6	1.6	0.251	0.011
283.4	0.15	5.6	295.5	4.8	0.445	0.016
288.3	0.12	2.8	296.0	4.8	0.753	0.024
293.3	0.09	1.2	296.0	4.8	1.23	0.04
298.2	0.17	1.4	295.8	4.8	2.10	0.06
303.2	0.24	1.2	295.3	4.9	3.38	0.09
303.2	0.24	1.2	295.2	4.8	3.37	0.09
303.2	0.24	1.2	295.3	4.8	3.41	0.09
303.2	0.24	1.2	298.8	4.9	3.34	0.09
308.2	0.38	1.2	296.6	4.8	5.43	0.14
313.2	0.55	1.2	302.0	4.9	7.77	0.20
318.2	0.45	0.6	299.9	2.4	12.7	0.3
323.1	0.51	0.5	295.5	1.8	19.0	0.5
328.1	0.75	0.5	297.1	1.8	28.2	0.7
333.1	0.99	0.4	298.5	1.6	41.2	1.0
333.1	1.09	0.5	298.8	1.6	41.3	1.0

333.1 0.99 0.4 300.0 1.7 41.2 1.0

^a Saturation temperature ($u(T) = 0.1$ K). ^b Mass of transferred sample condensed at 243 K. ^c Volume of nitrogen ($u(V) = 0.01$ dm³) used to transfer m ($u(m)/m = 0.015$) of the sample. ^d T_{amb} is the temperature of the soap film flowmeter used for measurement of the gas flow. ^e Vapor pressure at temperature T , obtained from the mass m and the residual vapor pressure at the condensation temperature, calculated by an iteration procedure; $p^\circ = 1$ Pa. ^f Standard uncertainties were calculated with $u(p/\text{Pa}) = 0.005 + 0.025(p/\text{Pa})$. The uncertainties for T , V and m are standard uncertainties. The determination of the $u(m)$ included the evaluation of the uncertainties associated with the preparation of internal standard solutions (caused by weighing and pycnometers), volumetric standard addition, chromatographic calibration and determination. The uncertainty of the molar enthalpy of vaporization (at 298.15 K) is the standard uncertainty with a confidence level of 0.68, calculated including uncertainties of vapor pressure, the uncertainties from the fitting equation and the uncertainty of temperature adjustment to $T = 298.15$ K. Detailed information on the methods of calculations was published previously [25; 26].

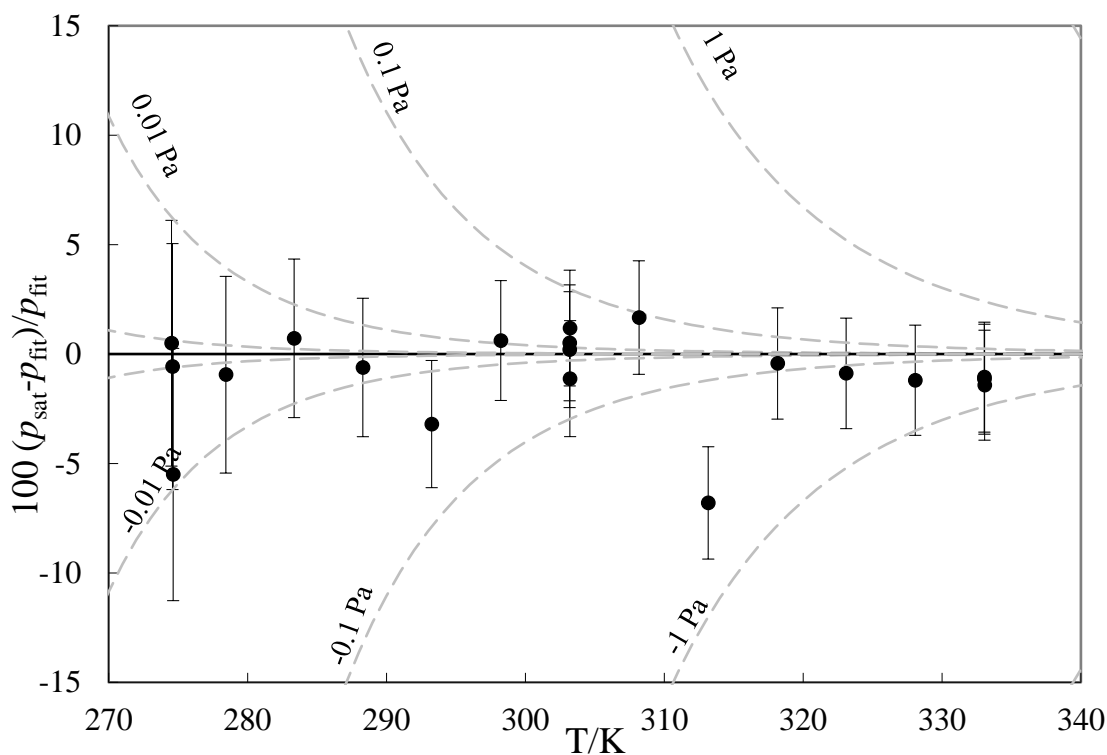


Figure 2. Experimental vapor pressure (●) deviations from the derived fitting equation for 1,3-DAP in Table 3. Dashed lines display the absolute deviation in pressure. Error bars are the standard uncertainties as reported in Table 3.

Table 4. 2,3-DAP (liq): experimental conditions and resulting absolute vapor pressures p_{sat} obtained by the transpiration method in this work.

$$\Delta_l^g H_m^\circ (298.15 \text{ K}) = (75.2 \pm 0.6) \text{ kJ mol}^{-1}$$

$$\ln \left(\frac{p_{sat}}{p^0} \right) = \frac{349.3}{R} - \frac{103721.26}{RT} - \frac{95.7}{R} \ln \frac{T}{298.15 \text{ K}}$$

T^a	m^b	$V_{N_2}^c$	T_{amb}^d	Gasflow	p_{sat}^e	$u(p_{sat})^f$
K	mg	dm ³	K	dm ³ ·h ⁻¹	Pa	Pa
274.2	0.07	14	297.7	4.8	0.082	0.007
274.2	0.32	66	296.2	3.6	0.081	0.007
274.2	0.15	32	296.6	2.0	0.081	0.007
274.2	0.21	42	298.0	2.4	0.084	0.007
278.1	0.07	8.7	297.2	4.8	0.133	0.008
283.1	0.06	4.4	297.1	4.8	0.226	0.011
288.1	0.06	2.3	296.4	4.8	0.410	0.015
293.1	0.07	1.6	296.3	4.8	0.680	0.022
298.1	0.09	1.2	296.2	4.8	1.17	0.03
303.1	0.14	1.2	296.0	4.8	1.94	0.05
303.1	0.14	1.2	296.2	4.8	1.91	0.05
303.1	0.14	1.2	295.9	4.8	1.94	0.05
303.1	0.14	1.2	297.1	4.8	1.91	0.05
308.1	0.22	1.2	295.4	4.8	3.07	0.08
313.0	0.35	1.2	296.8	4.8	4.87	0.13
318.0	0.54	1.2	296.5	4.8	7.49	0.19
323.0	0.87	1.2	297.0	4.8	12.0	0.3
328.0	0.80	0.7	295.2	2.8	18.6	0.5
328.0	0.79	0.7	295.3	2.8	18.6	0.5
332.9	1.14	0.7	295.4	2.8	26.7	0.7
333.0	1.14	0.7	295.3	2.8	26.7	0.7

333.0 1.12 0.7 295.2 2.8 26.3 0.7

For table legend please refer to Table 3.

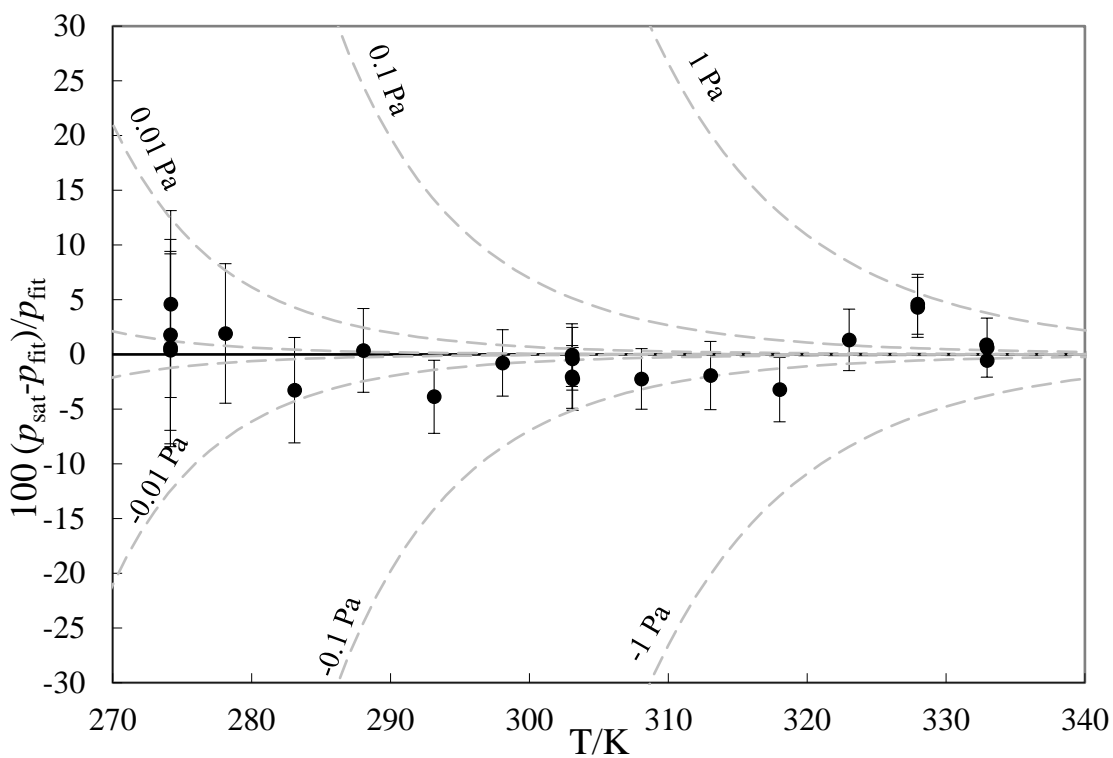


Figure 3. Experimental vapor pressure (●) deviations from the derived fitting equation for 2,3-DAP in Table 4. Dashed lines display the absolute deviation in pressure. Error bars are the standard uncertainties as reported in Table 4.

Table 5. DE-DAM (liq): experimental conditions and resulting absolute vapor pressures p_{sat} obtained by the transpiration method in this work.

$$\Delta_l^g H_m^\circ (298.15 \text{ K}) = (76.0 \pm 1.1) \text{ kJ mol}^{-1}$$

$$\ln \left(\frac{p_{sat}}{p^0} \right) = \frac{382.6}{R} - \frac{114672.99}{RT} - \frac{129.7}{R} \ln \frac{T}{298.15 \text{ K}}$$

T^a	m^b	$V_{N_2}^c$	T_{amb}^d	Gasflow	p_{sat}^e	$u(p_{sat})^f$
K	mg	dm ³	K	dm ³ ·h ⁻¹	Pa	Pa
278.5	0.67	78	296.3	4.8	0.09	0.01
283.4	0.50	30	296.4	4.8	0.17	0.02
288.3	0.52	18	296.2	4.8	0.30	0.02
293.3	0.51	12	297.1	4.8	0.44	0.03
298.2	0.51	6.4	296.8	4.8	0.80	0.05
303.2	0.45	3.6	297.1	4.8	1.25	0.07
308.1	0.50	2.4	297.7	4.8	2.08	0.11
313.1	0.47	1.5	297.4	4.8	3.26	0.17
313.1	0.50	1.6	296.4	4.8	3.13	0.17
313.1	0.51	1.6	296.3	4.8	3.20	0.17
318.1	0.58	1.2	296.5	4.8	4.83	0.25
323.0	1.00	1.2	297.5	4.8	8.40	0.43
328.0	1.49	1.2	297.0	4.8	12.5	0.6
333.0	2.22	1.2	296.5	4.8	18.5	0.9
338.0	3.09	1.2	297.5	4.8	25.8	1.3
342.9	7.15	1.9	297.2	4.8	38.9	2.0

^a Saturation temperature ($u(T) = 0.1 \text{ K}$). ^b Mass of transferred sample condensed at 243 K. ^c Volume of nitrogen ($u(V) = 0.01 \text{ dm}^3$) used to transfer m ($u(m)/m = 0.015$) of the sample. ^d T_{amb} is the temperature of the soap film flowmeter used for measurement of the gas flow. ^e Vapor pressure at temperature T obtained from the m and the residual vapor pressure at the condensation temperature, calculated by an iteration procedure; $p^0 = 1 \text{ Pa}$. ^f Standard uncertainties were calculated with $u(p/\text{Pa}) = 0.01 + 0.05(p/\text{Pa})$. The uncertainties for T , V and m are standard uncertainties. The determination of the $u(m)$ included the evaluation of the uncertainties associated with the preparation of internal standard solutions (caused by weighing and pycnometers), volumetric standard addition, chromatographic calibration and determination. The uncertainty of the molar enthalpy of vaporization (at 298.15 K) is the standard uncertainty with a confidence level of 0.68,

calculated including uncertainties of vapor pressure, the uncertainties from the fitting equation and the uncertainty of temperature adjustment to $T = 298.15\text{K}$. Detailed information on the methods of calculations was published previously [25, 26].

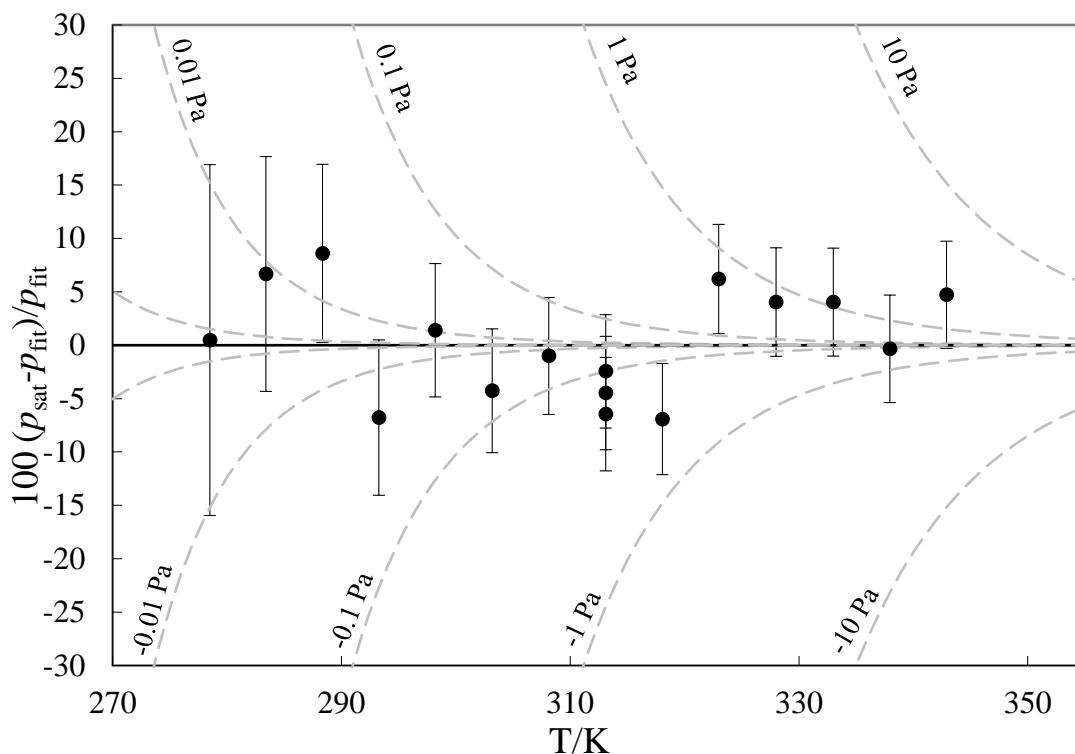


Figure 4. Experimental vapor pressure (\bullet) deviations from the derived fitting equation for DE-DAM in Table 5. Dashed lines display the absolute deviation in pressure. Error bars are the standard uncertainties as reported in Table 5.

Visualizations of the experimental vapor pressure deviations from fitting equations are provided in figures 2, 3, and 4. The experimental vapor pressures of DE-DAM exhibit significantly higher deviations from the fitting equation (Eq. 2) than for 1,3-DAP and 2,3-DAP and for this reason standard vapor pressure uncertainties for DE-DAM were increased by a factor of two.

If fitted to the *Clarke-Glew* equation [27] (Eq. 5), where vapor pressures are directly related to the thermodynamic functions of vaporization, the fitting equation yields a theoretically impossible positive $\Delta_l^g C_{p,m}^\circ$ value.

$$R \ln \left(\frac{p_{sat}}{p^\circ} \right) = \frac{-\Delta_l^g G_m^\circ(\theta)}{\theta} - \Delta_l^g H_m^\circ(\theta) \left(\frac{1}{\theta} - \frac{1}{T} \right) + \Delta_l^g C_{p,m}^\circ(\theta) \left(\frac{\theta}{T} - 1 + \ln \left(\frac{T}{\theta} \right) \right) \quad (5)$$

Here p_{sat} is the vapor pressure (in Pa) at the temperature T , p° is the standard pressure (0.1 MPa), θ is an arbitrary reference temperature (in this work $\theta = 298.15\text{K}$), $\Delta_l^g C_{p,m}^\circ$ is the difference in the isobaric molar heat capacities between gaseous and liquid states,

$\Delta_l^g H_m^\circ$ is the molar enthalpy of vaporization and $\Delta_l^g G_m^\circ$ is the difference in Gibbs energy between gaseous and liquid states.

Reduction of the experimental data-set at high and low temperatures eliminated this inconsistency and the remaining data points are presented in Table 5 and Figure 4. The full experimental vapor pressure data-set of DE-DAM is reported in table S4 and deviation plot is depicted in figure S4. The resulting molar enthalpies of vaporization at 298.15 K derived from reduced and full p - T -datasets ($76.0 \text{ kJ}\cdot\text{mol}^{-1}$ and $76.2 \text{ kJ}\cdot\text{mol}^{-1}$, respectively) agree within the experimental uncertainties.

Table 6. Compilation of the thermodynamic data on 1,3-DAP, 2,3-DAP and DE-DAM, derived from p - T -data obtained in this work.

Experiment	T -Range	T_{avg}	$\Delta_l^g H_m^\circ(T_{avg})^a$	$\Delta_l^g H_m^\circ(298.15 \text{ K})^b$	p_{sat}^c
	K	K	$\text{kJ}\cdot\text{mol}^{-1}$	$\text{kJ}\cdot\text{mol}^{-1}$	Pa
1,3-DAP	274.5 – 333.1	302.1	72.3 ± 0.5	72.6 ± 0.5	2.05
2,3-DAP	274.2 – 333.0	301.6	74.9 ± 0.6	75.2 ± 0.6	1.19
DE-DAM ^d	278.5 – 342.9	309.8	74.7 ± 1.0	76.0 ± 1.1	0.79

^a Molar enthalpies of vaporization at average temperature, derived by the linear data approximation $\ln p = f(T^{-1})$ and for the purpose of calculation of $u(\Delta_l^g H_m^\circ)$ from the equation 3. ^b Molar enthalpies of vaporization were adjusted according to *Acree and Chickos* [21] with values of $\Delta_l^g C_{p,m}^\circ$ and $C_{p,m}^\circ(l)$, stated in Table 2. The uncertainty of molar enthalpy of vaporization is expressed as standard uncertainty with the confidence level of 0.68. ^c The calculated vapor pressure at 298.15 K, according to the fitting equations reported in the Tables 3-5. ^d Results obtained from reduced data-set, as explained above.

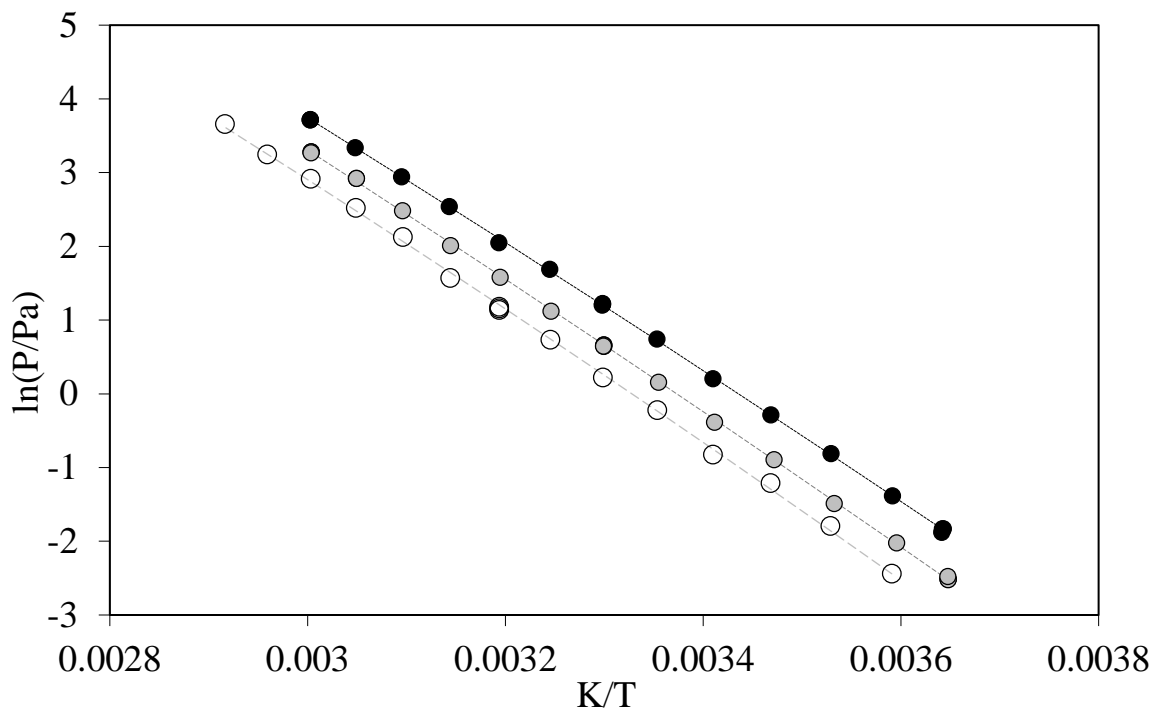


Figure 5. Comparison of the experimental vapor pressures of diazidopropanols: ● and dashed black line for 1,3 – DAP; ● and dashed dark grey line for 2,3- DAP; ○ and dashed light grey line for DE-DAM.

The thermodynamic properties, derived in this work for 1,3-DAP, 2,3-DAP and DE-DAM, are compiled in the Table 6. There are notable differences in the vaporization behavior of the diazidopropanols: the molar enthalpy of vaporization at 298.15 K of 1,3-DAP has a lower value ($72.6 \pm 0.5 \text{ kJ} \cdot \text{mol}^{-1}$) in comparison to the value of 2,3-DAP ($75.2 \pm 0.6 \text{ kJ} \cdot \text{mol}^{-1}$) and there is an obvious difference in absolute vapor pressures in the whole experimental temperature range, with the compound 1,3-DAP having higher vapor pressures. The reasoning behind these results could be that the compound 2,3-DAP is less symmetrical and, consequently, more polar than 1,3-DAP. Also, it is known that the hydrogen bond formation in the primary alcohol group (2,3-DAP) is less sterically hindered compared to the bond formation at the secondary alcohol group (1,3-DAP) [28]. With respect to that, more hydrogen bonds can be expected for 2,3-DAP. The increase of the molecule polarity and the hydrogen bonds lowers the vapor pressure of a compound. Similar behavior can be observed for analogous aliphatic compounds, where the molar enthalpy of vaporization for pentan-3-ol (CAS: 584-02-1, $53.2 \text{ kJ} \cdot \text{mol}^{-1}$ [22; 29]) is slightly lower than of 2-methyl-1-butanol (CAS: 137-32-6, $54.1 \text{ kJ} \cdot \text{mol}^{-1}$ [30; 31]).

As expected, the compound DE-DAM showed both lower vapor pressures and higher molar enthalpies of vaporization in comparison to the diazidopropanols, investigated in this work (Table 6).

Literature research revealed that only few studies discuss the vapor pressures of the compounds containing multiple azido groups [12; 32]. The work by *Lee et al.* [32] provides, as stated by the researchers, “approximate” results on the p - T -data for several aliphatic chains with terminal azido groups. In the work by *Verevkin et al.* [12] the results of *Lee et al.* were processed to yield the molar enthalpies of vaporization at 298.15 K and a correlation between the $\Delta_i^g H_m^\circ(298.15 \text{ K})$ and the carbon number in the aliphatic chain was derived. However, no experimental p - T -data are available for the -OH group containing aliphatic diazido- compounds, or, in fact, any of the compounds investigated in this work. One noteworthy datapoint available for 1,3-DAP is a boiling point, reported in the work of *Isaev et al.* [33] and it is depicted in the Figure S5 in the Supporting Information. The measured boiling point lies closely to the extrapolated fitting equation from the results achieved in this work (Table 3). Additionally, this is the first time that experimental vapor pressures and corresponding thermodynamic properties are reported for a geminal diazido- compound.

7.4 Conclusion

This study discusses the vaporization behavior of several compounds from a rarely thermodynamically investigated organic polyazido group: 1,3-diazidopropanol (1,3-DAP), 2,3-diazidopropanol (2,3-DAP) and 1,3-diethyl-2,2-diazidomalonate (DE-DAM). Their experimental vapor pressures were measured using the transpiration method. It is the first time the thermodynamic properties are reported for a compound, containing a geminal diazido- group (DE-DAM). The experimental p - T -datasets were obtained in the ambient temperature range and their corresponding p - T fitting equations were derived and reported. The achieved data allowed the determination of the molar enthalpies of vaporization and saturation vapor pressures at 298.15 K. The reported thermodynamic data could contribute to achieve a better understanding of the vaporization behavior of the azido- group containing organic compounds and improve the existent thermochemical parameter estimation methods for the compounds containing multiple azido groups.

Acknowledgements

For financial support of this work Ludwig-Maximilian University (LMU), the Office of Naval Research (ONR) [grant no. ONR N00014-19-1-2078], the Strategic Environmental Research and Development Program (SERDP) [contract no. W912HQ19C0033] and the DAAD (German Academic Exchange Service) [grant no. 57299294] are gratefully acknowledged. We would also like to thank Prof. Dr. Sergey P. Verevkin for the tremendous help establishing transpiration method in our group. Lastly, I would like to thank Andreas Neuer for his input during the time of his internship in our group.

List of symbols

p_{sat}	saturated vapor pressure, in Pa (Eq. 1)
p°	reference pressure, in Pa (Eq. 2)
m	mass of the analyte collected during the transpiration experiment, in kg (Eq.1)
T_{amb}	ambient temperature, in K (Eq. 1)
T	temperature, in K (Eq. 1)
T_0	Reference temperature, in K (Eq. 2)
V_{N_2}	volume of carrier gas at ambient conditions, in m ³ (Eq.1)
$C_{p,m}^\circ$	standard heat capacity at constant pressure, in J·mol ⁻¹ ·K ⁻¹ (Table 2)
$\Delta_l^g C_{p,m}^\circ$	difference of molar heat capacities at constant pressure, in J·mol ⁻¹ ·K ⁻¹ (Eq. 2)
$\Delta_l^g H_m^\circ$	standard molar enthalpy of vaporization, in J·mol ⁻¹ (Eq. 3)
$\Delta_l^g S_m^\circ$	standard molar entropy of vaporization, in J·mol ⁻¹ (Eq. 4)

7.5 References

- [1] M. Meldal, F. Diness, Recent Fascinating Aspects of the CuAAC Click Reaction, *Trends Chem.* 2 (2020) 569-584. <https://doi.org/10.1016/j.trechm.2020.03.007>.
- [2] Y. Takayama, K. Kusamori, M. Nishikawa, Click Chemistry as a Tool for Cell Engineering and Drug Delivery, *Molecules* 24 (2019) 172. <https://doi.org/10.3390/molecules24010172>.
- [3] S. Bräse, K. Banert, *Organic azides: syntheses and applications*, John Wiley & Sons (2010). <https://doi.org/10.1002/9780470682517>.
- [4] T.M. Klapötke, *Chemistry of high-energy materials*, Walter de Gruyter GmbH & Co KG, Berlin, 2019.
- [5] T. Lenz, T.M. Klapötke, M. Mühlemann, J. Stierstorfer, About the Azido Derivatives of Pentaerythritol Tetranitrate, *Prop., Explos., Pyrotech.* n/a. <https://doi.org/10.1002/prop.202000265>.
- [6] O.V. Dorofeeva, O.N. Ryzhova, M.A. Suntsova, Accurate prediction of enthalpies of formation of organic azides by combining G4 theory calculations with an isodesmic reaction scheme, *J. Phys. Chem. A* 117 (2013) 6835-6845. <https://doi.org/10.1021/jp404484q>.
- [7] M.H. Keshavarz, Improved prediction of heats of sublimation of energetic compounds using their molecular structure, *J. Hazard. Mater.* 177 (2010) 648-659. <https://doi.org/10.1016/j.jhazmat.2009.12.081>.
- [8] M.J. McQuaid, H. Sun, D. Rigby, Development and validation of COMPASS force field parameters for molecules with aliphatic azide chains, *J. Comput. Chem.* 25 (2004) 61-71. <https://doi.org/10.1002/jcc.10316>.
- [9] M. Jafari, M.H. Keshavarz, M.R. Noorbala, M. Kamalvand, A Reliable Method for Prediction of the Condensed Phase Enthalpy of Formation of High Nitrogen Content Materials through their Gas Phase Information, *ChemistrySelect* 1 (2016) 5286-5296. <https://doi.org/10.1002/slct.201601184>.
- [10] M.S. Elioff, J. Hoy, J.A. Bumpus, Calculating Heat of Formation Values of Energetic Compounds: A Comparative Study, *Adv. Phys. Chem.* 2016 (2016) 1-11. <https://doi.org/10.1155/2016/5082084>.
- [11] M.J. McQuaid, B.M. Rice, Report: Computational Chemistry-Based Enthalpy-of-Formation, Enthalpy-of-Vaporization, and Enthalpy-of-Sublimation Predictions for

Azide-Functionalized Compounds, ARMY RESEARCH LAB ABERDEEN PROVING GROUND MD WEAPONS AND MATERIALS RESEARCH DIRECTORATE (2006).

- [12] S.P. Verevkin, V.N. Emel'yanenko, M. Algarra, J.M. López-Romero, F. Aguiar, J.E. Rodriguez-Borges, J.C.E. da Silva, Vapor pressures and enthalpies of vaporization of azides, *J. Chem. Thermodyn.* 43 (2011) 1652-1659. <https://doi.org/10.1016/j.jct.2011.05.028>.
- [13] V.N. Emel'yanenko, M. Algarra, J.C.G. Esteves da Silva, J. Hierrezuelo, J.M. López-Romero, S.P. Verevkin, Thermochemistry of organic azides revisited, *Thermochim. Acta* 597 (2014) 78-84. <http://dx.doi.org/10.1016/j.tca.2014.10.015>.
- [14] A.P. Häring, S.F. Kirsch, Synthesis and Chemistry of Organic Geminal Di- and Triazides, *Molecules* 20 (2015) 20042-20062. <https://doi.org/10.3390/molecules201119675>.
- [15] M. Claßen, S.B. Heimsch, T.M. Klapötke, Synthesis and Characterization of New Azido Esters Derived from Malonic Acid, *Propellants Explos. Pyrotech.* 44 (2019) 1515-1520. <https://doi.org/10.1002/prop.201900285>.
- [16] S.B. Heimsch, Azido liquids as potential hydrazine replacements in a hypergolic bipropulsion system, Dissertation, LMU Munich, (2020). <https://doi.org/10.5282/edoc.26932>.
- [17] Farhanullah, T. Kang, E.-J. Yoon, E.-C. Choi, S. Kim, J. Lee, 2-[2-Substituted-3-(3,4-dichlorobenzylamino)propylamino]-1H-quinolin-4-ones as *Staphylococcus aureus* methionyl-tRNA synthetase inhibitors, *Eur. J. Med. Chem.* 44 (2009) 239-250. <https://doi.org/10.1016/j.ejmech.2008.02.021>.
- [18] F. Samrin, A. Sharma, I.A. Khan, S. Puri, Synthesis and Antibacterial Activity of New Diaryldiamines, *J. Heterocycl. Chem.* 49 (2012) 1391-1397. <https://doi.org/10.1002/jhet.1040>.
- [19] H. Erhardt, A.P. Häring, A. Kotthaus, M. Roggel, M.L. Tong, P. Biallas, M. Jübermann, F. Mohr, S.F. Kirsch, Geminal Diazides Derived from 1, 3-Dicarbonyls: A Protocol for Synthesis, *J. Org. Chem.* 80 (2015) 12460-12469. <https://doi.org/10.1021/acs.joc.5b02328>.
- [20] G. Bikelytė, M.A. Härtel, T.M. Klapötke, B. Krumm, A. Sadaunykas, Experimental thermochemical data of CWA simulants: Triethyl phosphate, diethyl

methylphosphonate, malathion and methyl salicylate, *J. Chem. Thermodyn.* 143 (2020) 106043. <https://doi.org/10.1016/j.jct.2019.106043>.

- [21] W. Acree, J.S. Chickos, Phase Transition Enthalpy Measurements of Organic and Organometallic Compounds. Sublimation, Vaporization and Fusion Enthalpies From 1880 to 2010, *J. Phys. Chem. Ref. Data* 39 (2010) 043101. <http://dx.doi.org/10.1063/1.3309507>.
- [22] W. Acree Jr, J.S. Chickos, Phase transition enthalpy measurements of organic and organometallic compounds. Sublimation, vaporization and fusion enthalpies from 1880 to 2015. Part 1. C1– C10, *J. Phys. Chem. Ref. Data* 45 (2016) 033101. <https://doi.org/10.1063/1.4948363>.
- [23] T.F. Fagley, H.W. Myers, The Heats of Combustion of Cyclopentyl and Cyclohexyl Azides, *Journal of the American Chemical Society* 76 (1954) 6001-6003. 10.1021/ja01652a031.
- [24] S.P. Verevkin, A.Y. Sazonova, V.N. Emel'yanenko, D.H. Zaitsau, M.A. Varfolomeev, B.N. Solomonov, K.V. Zherikova, Thermochemistry of Halogen-Substituted Methylbenzenes, *Journal of Chemical & Engineering Data* 60 (2015) 89-103. <https://doi.org/10.1021/je500784s>.
- [25] V.N. Emel'yanenko, S.P. Verevkin, Benchmark thermodynamic properties of 1,3-propanediol: Comprehensive experimental and theoretical study, *J. Chem. Thermodyn.* 85 (2015) 111-119. <http://dx.doi.org/10.1016/j.jct.2015.01.014>.
- [26] S.P. Verevkin, A.Y. Sazonova, V.N. Emel'yanenko, D.H. Zaitsau, M.A. Varfolomeev, B.N. Solomonov, K.V. Zherikova, Thermochemistry of halogen-substituted methylbenzenes, *J. Chem. Eng. Data* 60 (2014) 89-103. <https://doi.org/10.1021/je500784s>.
- [27] E.C.W. Clarke, D.N. Glew, Evaluation of thermodynamic functions from equilibrium constants, *Transactions of the Faraday Society* 62 (1966) 539-547. 10.1039/TF9666200539.
- [28] D. Kulikov, S.P. Verevkin, A. Heintz, Enthalpies of vaporization of a series of aliphatic alcohols: Experimental results and values predicted by the ERAS-model, *Fluid Ph. Equilibria* 192 (2001) 187-207. [https://doi.org/10.1016/S0378-3812\(01\)00633-1](https://doi.org/10.1016/S0378-3812(01)00633-1).
- [29] A.D. Peschenko, O.V. Shvaro, V.I. Zubkov, *Thermodyn. Org. Soedin. (Gorky)* 39 (1988) 41.

- [30] K.G. McCurdy, K.J. Laidler, HEATS OF VAPORIZATION OF A SERIES OF ALIPHATIC ALCOHOLS, *Can. J. Chem.* 41 (1963) 1867-1871. <https://doi.org/10.1139/v63-274>.
- [31] S.P. Verevkin, V.N. Emel'yanenko, V. Diky, C.D. Muzny, R.D. Chirico, M. Frenkel, New Group-Contribution Approach to Thermochemical Properties of Organic Compounds: Hydrocarbons and Oxygen-Containing Compounds, *J. Phys. Chem. Ref. Data* 42 (2013) 033102. <https://doi.org/10.1063/1.4815957>.
- [32] A. Lee, C.K. Law, A. Makino, Aerothermochemical studies of energetic liquid materials: 3. Approximate determination of some thermophysical and thermochemical properties of organic azides, *Combust. Flame* 78 (1989) 263-274. [https://doi.org/10.1016/0010-2180\(89\)90016-3](https://doi.org/10.1016/0010-2180(89)90016-3).
- [33] B. Isaev, S. Kanashin, M. Kozhukh, N. Tokarev, Combustion of some organic azides, *Chemical Physics of Combustion and Explosion. Chemical Reaction Kinetics, Proc. VI All-Union Symp. On Combustion and Explosion, Alma-Ata, 1980*, pp. 97-101.

7.6 Supplementary Information

7.6.1 Purity assessment

Elemental analysis (CHNS) of the liquid samples were performed with an *Elementar Vario El* instrument. $^1\text{H-NMR}$ spectra were measured with a *Bruker AVANCE* 400 MHz instrument and the processing was done with *MestReNova* v. 12.0.1-20560 software. Results of the purity assessment are presented in the following.

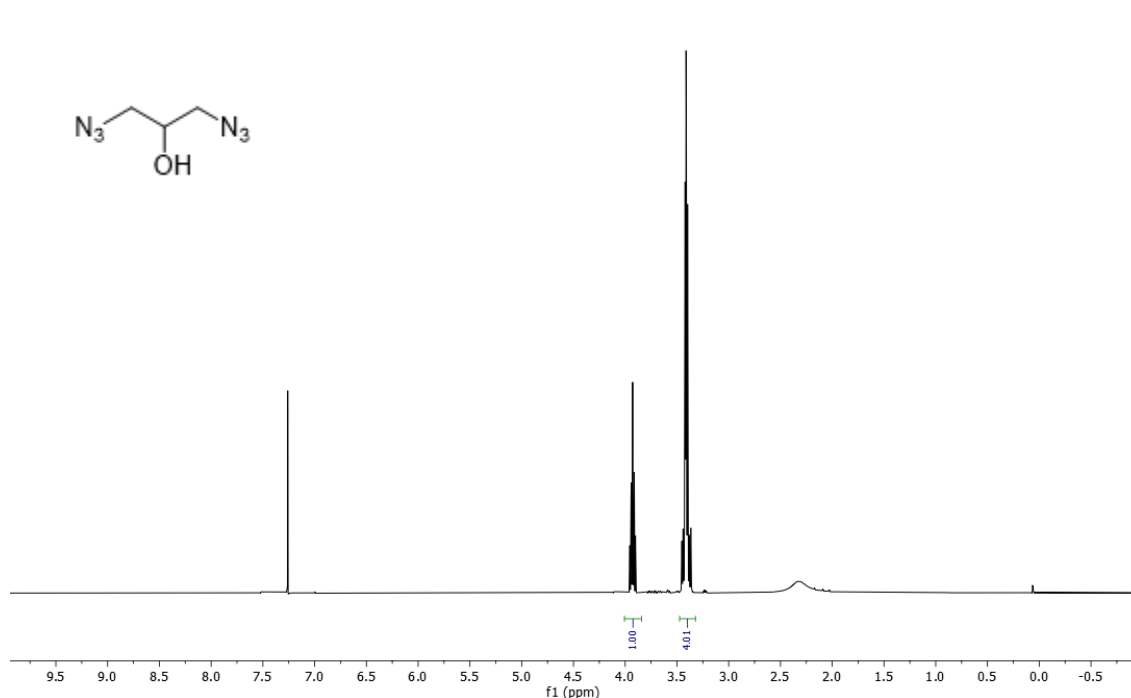


Figure S4. $^1\text{H-NMR}$ spectrum of 1,3-DAP.

1,3-DAP: $^1\text{H NMR}$ (CDCl_3 , 400 MHz): $\delta = 3.9$ (q, 1H, CH), 3.4-3.3 (m, 4H, CH_2), 2.3 (s, 1H, -OH) ppm. $^{13}\text{C NMR}$ (CDCl_3 , 101 MHz): $\delta = 69.7$ ($\text{CH}_2\text{-OH}$), 54.0 ($\text{CH}_2\text{-N}_3$) ppm. $^{14}\text{N NMR}$ (CDCl_3 , 29 MHz): $\delta = -134$ (N_β), -170 (N_α). **EA:** Calcd.: C 25.35, H 4.26, N 59.13 %; Found: C 25.05, H 3.99, N 59.04 %.

Table S9. Peak integrals for $^1\text{H-NMR}$ spectrum of 1,3-DAP in Fig. S1.

δ range	Integral (normalized)	Integral (absolute)
4.01 .. 3.84	1.00	286012.37
3.47 .. 3.32	4.01	1150154.36

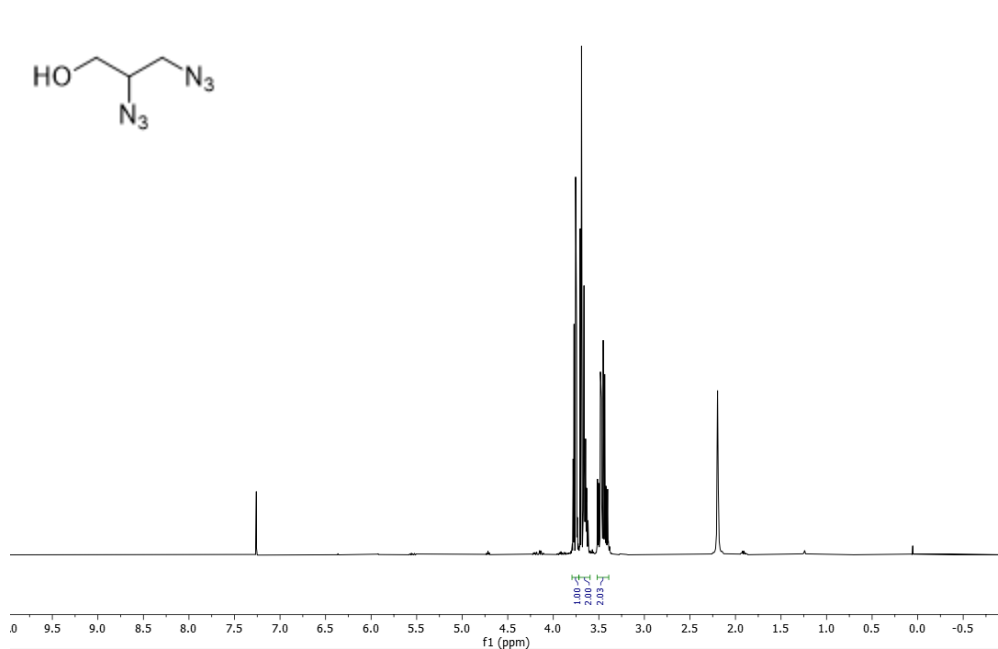


Figure S2. $^1\text{H-NMR}$ spectrum of enantiomeric mixture for compound **2,3-DAP**, ee not defined.

2,3-DAP: $^1\text{H NMR}$ (CDCl_3 , 400 MHz): $\delta = 3.82\text{-}3.72$ (m, 1H), 3.7-3.6 (m, 2H), 3.5-3.4 (m, 2H), 2.2 (s, 1H, $-\text{OH}$) ppm. $^{13}\text{C NMR}$ (CDCl_3 , 101 MHz): $\delta = 62.7$ ($\text{CH}_2\text{-OH}$), 62.7 (CH-N_3), 51.6 ($\text{CH}_2\text{-N}_3$) ppm. $^{14}\text{N NMR}$ (CDCl_3 , 29 MHz): $\delta = -134$ (N_β), -135 (N_β), -169 (N_γ) ppm. **EA:** Calcd.: C 59.13, H 4.26, N 25.35 %; Found: C 58.71, H 3.92, N 25.58 %.

Table S2. Peak integrals for $^1\text{H-NMR}$ spectrum of 2,3-DAP in Fig. S2.

δ range	Integral (normalized)	Integral (absolute)
3.79 .. 3.72	1.00	472590.20
3.72 .. 3.60	2.00	944603.83
3.52 .. 3.39	2.03	957175.81

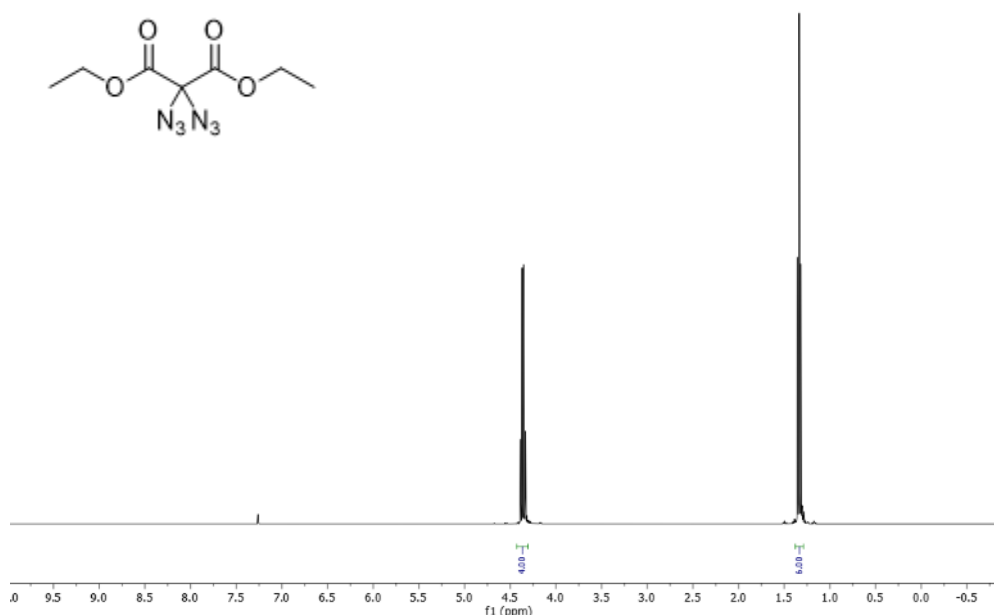


Figure S3. ^1H -NMR spectrum of DE-DAM.

DE-DAM: ^1H NMR (CDCl_3 , 400 MHz): $\delta = 4.4$ (q, 4H, CH_2CH_3), 1.3 (t, 6H, CH_3) ppm. ^{13}C NMR (CDCl_3 , 101 MHz): $\delta = 163.6$ (CO_2Et), 80.0 ($\text{C}(\text{N}_3)_2$), 64.2 (CH_2CH_3), 14.0 (OCH_2CH_3) ppm. ^{14}N NMR (CDCl_3 , 29 MHz): $\delta = -141$ (N_β), -156 (N_γ) ppm. **EA:** Calcd.: C 34.70, H 4.16, N 34.71 %; Found: C 34.97, H 3.75, N 33.01 %.

Table S3. Peak integrals for ^1H -NMR spectrum of DE-DAM in Fig. S3.

δ range	Integral (normalized)	Integral (absolute)
4.43 .. 3.30	4.00	1304431.14
1.38 .. 1.29	6.00	1958122.41

7.6.2 Experimental results of DE-DAM

Table S4. DE-DAM: experimental conditions and resulting absolute vapor pressures p_{sat} obtained by the transpiration method in this work.

$$\Delta_f^g H_m^\circ (298.15 \text{ K}) = (76.2 \pm 2.2) \text{ kJ mol}^{-1}$$

$$\ln \left(\frac{p_{\text{sat}}}{p^0} \right) = \frac{383.7}{R} - \frac{114870.37}{RT} - \frac{129.7}{R} \ln \frac{T}{298.15\text{K}}$$

T^a	m^b	$V_{N_2}^c$	T_{amb}^d	Gasflow	p_{sat}^e	$u(p_{sat})^f$
K	mg	dm ³	K	dm ³ ·h ⁻¹	Pa	Pa
274.6 ^g	0.41	69	297.4	4.8	0.06	0.01
274.6 ^g	0.46	79	296.7	4.8	0.06	0.01
274.6 ^g	0.42	72	298.0	4.0	0.06	0.01
274.7 ^g	0.44	70	297.6	3.0	0.06	0.01
278.5	0.67	78	296.3	4.8	0.09	0.01
283.4	0.50	30	296.4	4.8	0.17	0.02
288.3	0.52	18	296.2	4.8	0.30	0.02
293.3	0.51	12	297.1	4.8	0.44	0.03
298.2	0.51	6.4	296.8	4.8	0.80	0.05
303.2	0.45	3.6	297.1	4.8	1.25	0.07
308.1	0.50	2.4	297.7	4.8	2.08	0.11
313.1	0.47	1.5	297.4	4.8	3.26	0.17
313.1	0.50	1.6	296.4	4.8	3.13	0.17
313.1	0.51	1.6	296.3	4.8	3.20	0.17
318.1	0.58	1.2	296.5	4.8	4.83	0.25
323.0	1.00	1.2	297.5	4.8	8.40	0.43
328.0	1.49	1.2	297.0	4.8	12.5	0.6
333.0	2.22	1.2	296.5	4.8	18.5	0.9
338.0	3.09	1.2	297.5	4.8	25.8	1.3
342.9	7.15	1.9	297.2	4.8	38.9	2.0
347.7 ^g	5.86	1.0	296.2	3.0	59.0	3.0
347.7 ^g	4.43	0.8	296.2	3.0	59.5	3.0
347.7 ^g	4.43	0.8	296.2	3.0	59.3	3.0
347.8 ^g	4.47	0.7	296.5	3.0	60.2	3.0
347.9 ^g	4.38	0.7	296.4	3.0	59.1	3.0

352.9 ^g	9.40	1.1	296.8	4.5	83.4	4.2
353.1 ^g	6.11	0.7	296.5	2.4	84.7	4.2

^a Saturation temperature ($u(T) = 0.1$ K). ^b Mass of transferred sample condensed at 243 K. ^c Volume of nitrogen ($u(V) = 0.01$ dm³) used to transfer m ($u(m)/m = 0.015$) of the sample. ^d T_{amb} is the temperature of the soap film flowmeter used for measurement of the gas flow. ^e Vapor pressure at temperature T obtained from the m and the residual vapor pressure at the condensation temperature, calculated by an iteration procedure; $p^\circ = 1$ Pa. ^f Standard uncertainties were calculated with $u(p/\text{Pa}) = 0.01 + 0.05(p/\text{Pa})$. The uncertainties for T , V and m are standard uncertainties. The determination of the $u(m)$ included the evaluation of the uncertainties associated with the preparation of internal standard solutions (caused by weighing and pycnometers), volumetric standard addition, chromatographic calibration and determination. The uncertainty of the molar enthalpy of vaporization (at 298.15 K) is the standard uncertainty with a confidence level of 0.68, calculated including uncertainties of vapor pressure, uncertainties from the fitting equation and the uncertainty of temperature adjustment to $T = 298.15$ K. Detailed information on the methods of calculations was published previously [1; 2]. ^g Values not included for the determination of the fitting equation and molar enthalpies of vaporization.

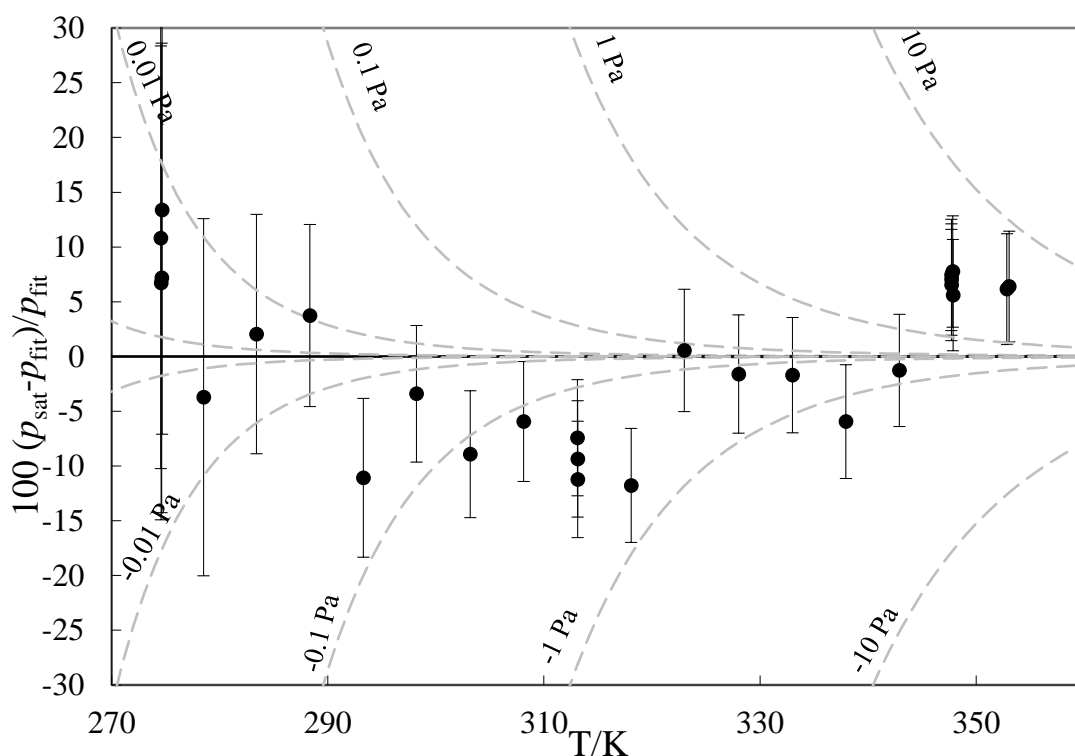


Figure S4. Experimental vapor pressure (●) deviations from the derived fitting equation for DE-DAM in Table S1. Dashed lines display the absolute deviation in pressure. Error bars are the standard uncertainties as reported in Table S1.

7.6.3 Comparison of literature data

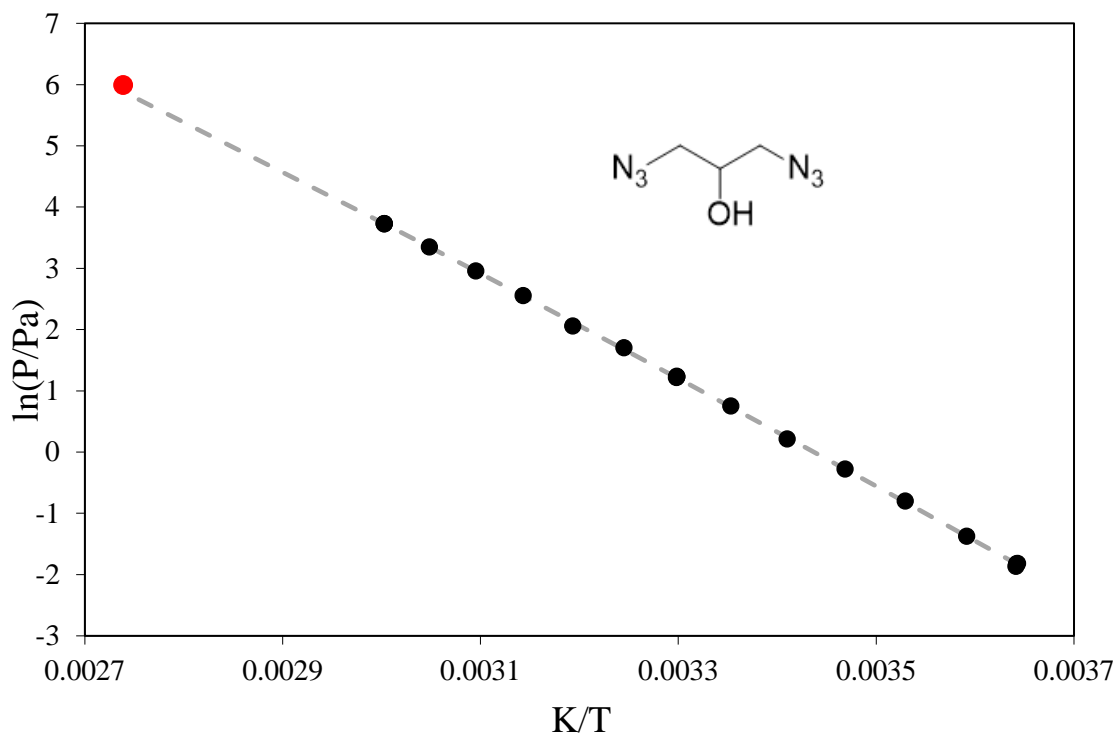


Figure S5. Experimental vapor pressures of 1,3-DAP from this work (●) and the derived fitting equation from the Table 3 (dashed line) in comparison with the boiling point (at reduced pressure of 3 mmHg) from the work of *Isaev et al.* [3] (●).

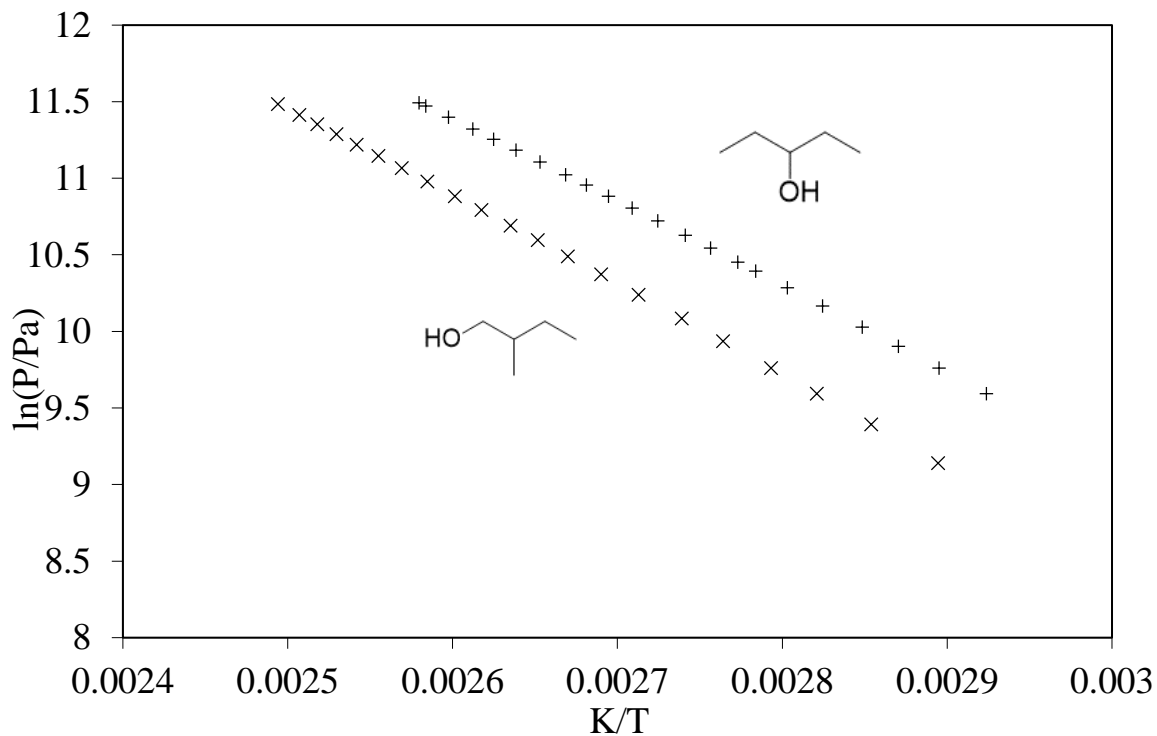


Figure S6. Experimental vapor pressures as of aliphatic analogues for diazidopropanols investigated in this work: 3-pentanol (+) and 2-methyl-1-butanol (x), as reported in the work by Čenský *et al.* [4].

7.6.4 HPLC-DAD parameters

HPLC	<i>Shimadzu Prominence</i> ® with LC-20AD pump module and SPD-M20A Diode Array Detector; software <i>LabSolutions v5.86</i>
Analytical column	<i>Phenomenex Kinetex</i> ® (2.6 μm Biphenyl, 100 Å, 150 × 4.6 mm)
Oven temperature:	40°C
Program	
1,3-DAP	Injection volume: 1 μL Total Flow: 0.75 mL/min Mobile phase: 25 % MeOH, 75 % Water Time: 15 min Channel 1 wavelength: 212 nm (1.3-DAP) Retention time: 6.0 min Channel 2 wavelength: 232 nm (standard, RDX) Retention time: 13.6 min

2,3-DAP

Injection volume: 1 μ L
Total Flow: 0.75 mL/min
Mobile phase: 25 % MeOH, 75 % Water
Time: 15 min
Channel 1 wavelength: 212 nm (2,3-DAP)
Retention time: 6.4 min
Channel 2 wavelength: 232 nm (standard, RDX)
Retention time: 13.5 min

DE-DAM

Injection volume: 1 μ L
Total Flow: 0.95 mL/min
Mobile phase: 60 % MeOH, 40 % Water
Time: 10 min
Channel 1 wavelength: 212 nm (DE-DAM)
Retention time: 8.4 min
Channel 2 wavelength: 280 nm (standard, 4-MNT)
Retention time: 6.2 min

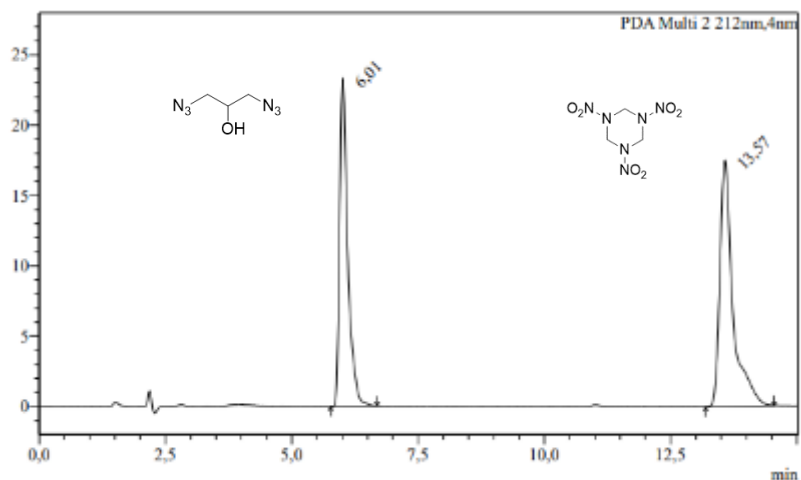


Figure S7. HPLC-DAD chromatogram of 1,3-DAP (retention time 6.01 min, integration wavelength $\lambda = 212$ nm) and standard RDX (retention time 13.57 min, integration wavelength $\lambda = 212$ nm), measured with a method, described in this section.

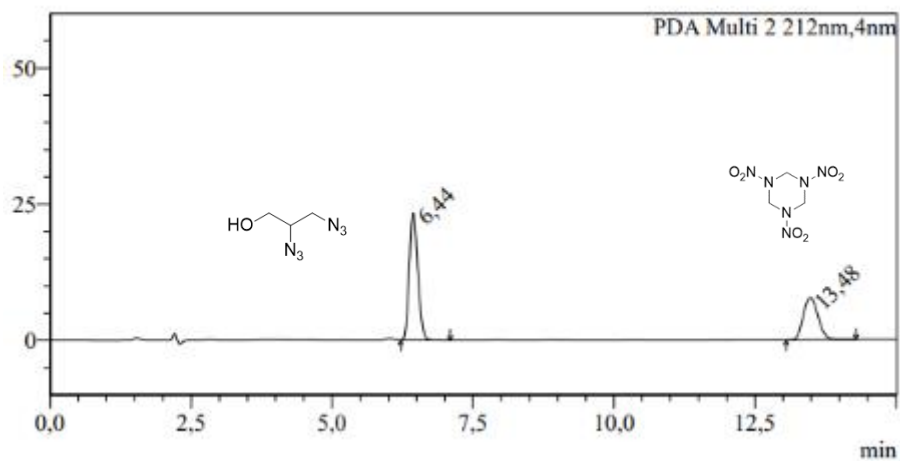


Figure S8. HPLC-DAD chromatogram of 2,3- DAP (retention time 6.44 min, integration wavelength $\lambda = 212$ nm) and standard RDX (retention time 13.48 min, integration wavelength $\lambda = 232$ nm), measured with a method, described in this section.

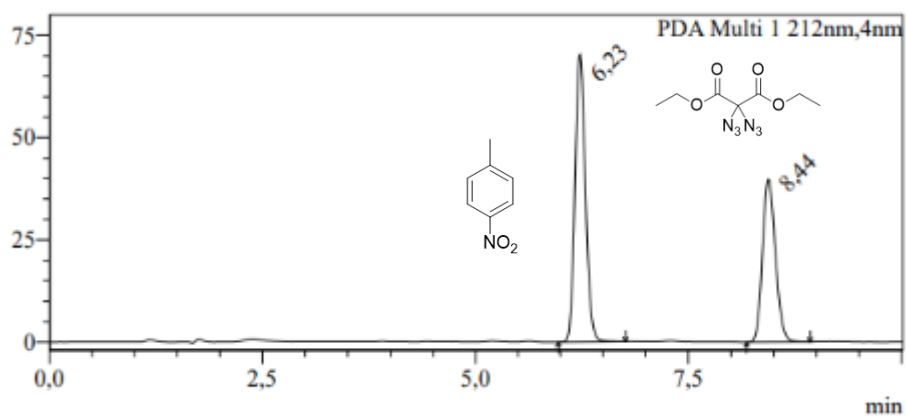


Figure S9. HPLC-DAD chromatogram of DE-DAM (retention time 8.40 min, integration wavelength $\lambda = 212$ nm) and standard 4-MNT (retention time 6.21 min, integration wavelength $\lambda = 280$ nm), measured with a method, described in this section.

7.6.5 References

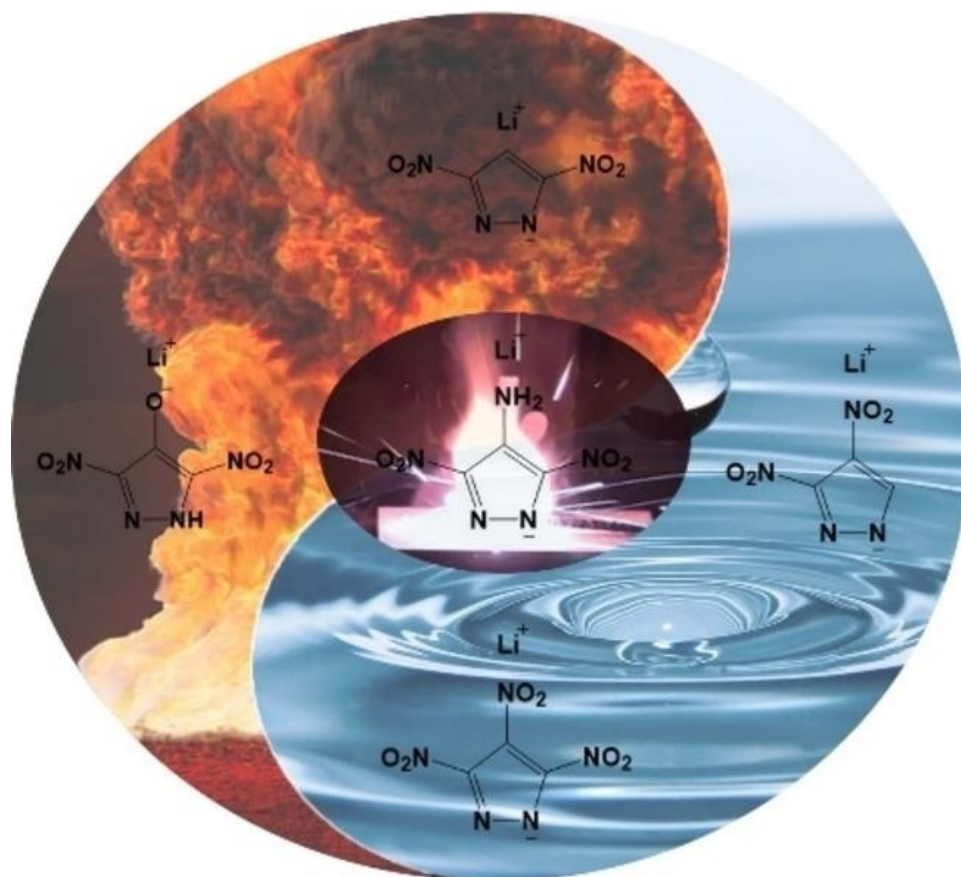
- [1] V.N. Emel'yanenko, S.P. Verevkin, Benchmark thermodynamic properties of 1,3-propanediol: Comprehensive experimental and theoretical study, *J. Chem. Thermodyn.* 85 (2015) 111-119. <http://dx.doi.org/10.1016/j.jct.2015.01.014>.
- [2] S.P. Verevkin, A.Y. Sazonova, V.N. Emel'yanenko, D.H. Zaitsau, M.A. Varfolomeev, B.N. Solomonov, K.V. Zherikova, Thermochemistry of halogen-substituted methylbenzenes, *J. Chem. Eng. Data* 60 (2014) 89-103. <https://doi.org/10.1021/je500784s>.
- [3] B. Isaev, S. Kanashin, M. Kozhukh, N. Tokarev, Combustion of some organic azides, *Chemical Physics of Combustion and Explosion. Chemical Reaction Kinetics, Proc. VI All-Union Symp. On Combustion and Explosion, Alma-Ata, 1980*, pp. 97-101.
- [4] M. Čenský, P. Vrbka, K. Růžička, M. Fulem, Vapor pressure of selected aliphatic alcohols by ebulliometry. Part 2, *Fluid Phase Equilibria* 298 (2010) 199-205. <https://doi.org/10.1016/j.fluid.2010.06.020>.

8. Lithium Nitropyrazolates as Potential Red Pyrotechnic Colorants

Alicia M. W. Dufter-Münster, Alexander G. Harter, Prof. Thomas M. Klapötke, Elena Reinhardt, Julia Römer, Dr. Jörg Stierstorfer

as published in European Journal of Inorganic Chemistry **2022**, 8.

DOI: 10.1002/ejic.202101048



Key words: Lithium salt, -nitration, -pyrazole, -pyrotechnic colorant, -stability

Abstract: Strontium-based red pyrotechnic colorants have fallen into disrepute due to the harmful influence of this alkaline earth metal on adolescents. In this context, the energetic character, safety, and combustion to benign nitrogen gas of nitropyrazoles are used for the design of the corresponding lithiated materials, which are investigated as potential replacements in the current work. For this purpose, the lithium salts of 3,4-dinitro-1*H*-pyrazole, 3,5-dinitro-1*H*-pyrazole, 4-amino-3,5-dinitro-1*H*-pyrazole, 3,4,5-trinitro-1*H*-pyrazole, and 4-hydroxy-3,5-dinitro-1*H*-pyrazole were extensively characterized by standard analytical methods, low-temperature single-crystal X-ray diffraction, studies of the thermo-chemical behavior, and sensitivity assessments. Our assumption that the high nitrogen contents and the low oxygen balances of these compounds would adjust a cool, reductive flame atmosphere essential for red emissions by lithium was put to the test.

8.1 Introduction

Nitropyrazoles have already found application in a wide range of pharmaceuticals and optics.¹ Lately, these compounds have also attracted interest among the energetic materials research community due to their balance between explosive performance and safety, while compared to high-energy density materials with a carbon backbone combusting to high volumes of environmentally benign nitrogen gas (see Figure 1).² The combustion of their numerous nitrogen atoms, especially that of neighboring ones, to triple-bonded dinitrogen leads to high heats of formation,^{2, 3} whereas the introduction of the explosophores forming dipolar interactions increases the density⁴ (3,4-dinitro-1*H*-pyrazole (**3**):⁵ $\rho=1.79 \text{ g cm}^{-3}$ at 298 K; 3,5-dinitro-1*H*-pyrazole (**5**):⁵ $\rho=1.78 \text{ g cm}^{-3}$ at 298 K; 3,4,5-trinitro-1*H*-pyrazole (**9**):⁶ $\rho=1.87 \text{ g cm}^{-3}$ at 293 K) and in combination with the substitution of carbon atoms in the ring by nitrogen contributes to positive oxygen balances (**3/5**: $\Omega_{\text{CO}}=0 \%$; **9**: $\Omega_{\text{CO}}=20 \%$). The aromaticity accounts for their thermal stabilities⁷ (**3**):⁵ $T_{\text{dec}}(\text{onset})=285 \text{ }^\circ\text{C}$; **5**):⁵ $T_{\text{dec}}(\text{onset})=299 \text{ }^\circ\text{C}$; **9**):⁶ $T_{\text{dec}}(\text{onset})=264 \text{ }^\circ\text{C}$) and their low sensitivities toward destructive stimuli further guarantee safe handling (**3**):⁵ FS=360 N, ESD=1.5 J; **5**):⁵ FS=360 N, ESD=1.0 J; **9**):⁶ FS=92 N, ESD>0.8 J). However, one decisive drawback of nitropyrazoles is the considerable acidity of the *N*-bonded proton resulting in a lack of compatibility and storage problems. There are three different possibilities to stabilize the nitropyrazole backbone: *N*-functionalization, amination or salt formation. While deprotonation by a base partially lowers the sensitivities toward ignition stimuli,⁸ hydrogen bonding between proton-donating amino groups and neighboring proton-accepting nitro functionalities⁹ additionally raises the density¹⁰ (4-amino-3,5-dinitro-1*H*-pyrazole (**8**): $pK_{\text{a}}=3.42$,¹¹ $\rho=1.90 \text{ g cm}^{-3}$ at 294 K,¹² $T_{\text{dec}}(\text{onset})=176 \text{ }^\circ\text{C}$,¹² FS>360 N,¹³ IS=12 J¹³). The same effect is expected for hydroxylation of nitropyrazoles

since the hydroxyl group also acts as proton donor (4-hydroxy-3,5-dinitro-1*H*-pyrazole (**10**) · 2/3 H₂O:⁶ $\rho=1.81 \text{ g cm}^{-3}$ at 293 K, $T_{\text{dec}}(\text{peak})=194 \text{ }^\circ\text{C}$).

Although pyrotechnic colorants should also contribute to the energetic character of a formulation, have low sensitivities toward destructive stimuli, and form environmentally acceptable combustion products, the literature provides hardly any information on the

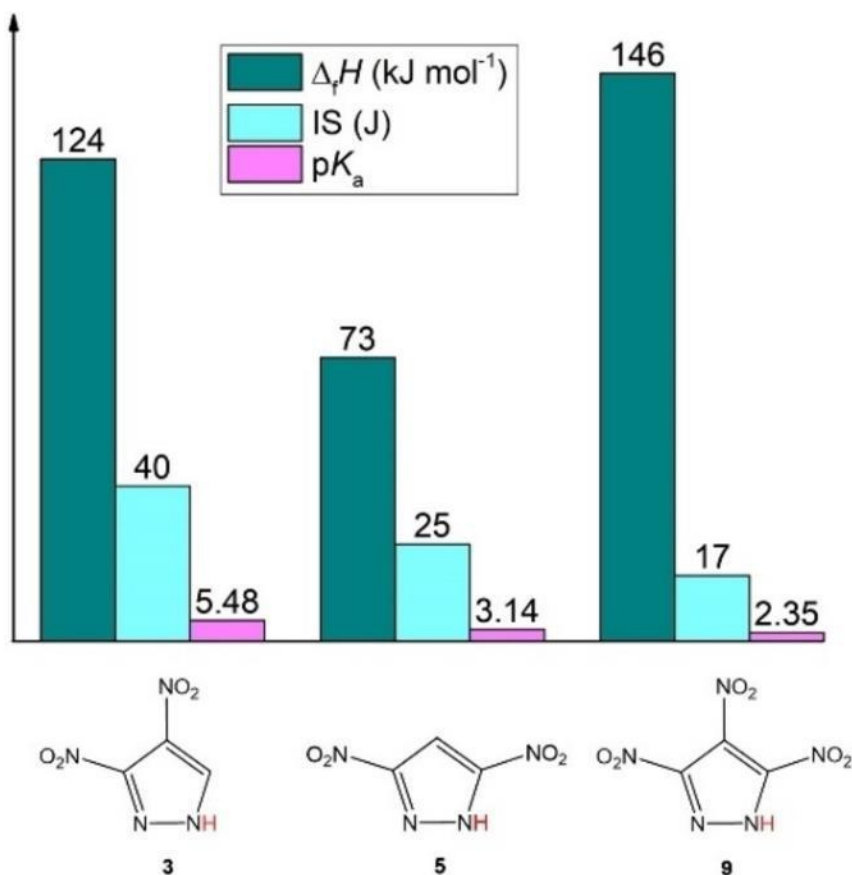


Figure 1. The combination of large energy content and low vulnerability in nitropyrazoles along with high acidity.

application of metal nitropyrazolates in this area.¹⁴ Especially in the case of red light-producing pyrotechnics based on lithium, which was recently proposed as strontium replacement after its proven adverse effect on the skeletal development,^{15, 16} the high nitrogen content of the nitropyrazoles should be advantageous. Lithium is bioactive, however, a total daily dose of roughly 200 to 1000 mg is required for the treatment of depression or bipolar disorder¹⁷ as opposed to the oral reference dose of 0.3 mg/kg/day for strontium.¹⁸ The red flame color of lithiated materials originates from the emissions of the metastable atomic species at 671 and 610 nm,^{15, 19} but high flame temperatures promote higher energetic electron transitions yielding orange light.²⁰ As a consequence, the flame needs to be cooled,²⁰ e. g. via the release of nitrogen gas.²¹ Another requirement

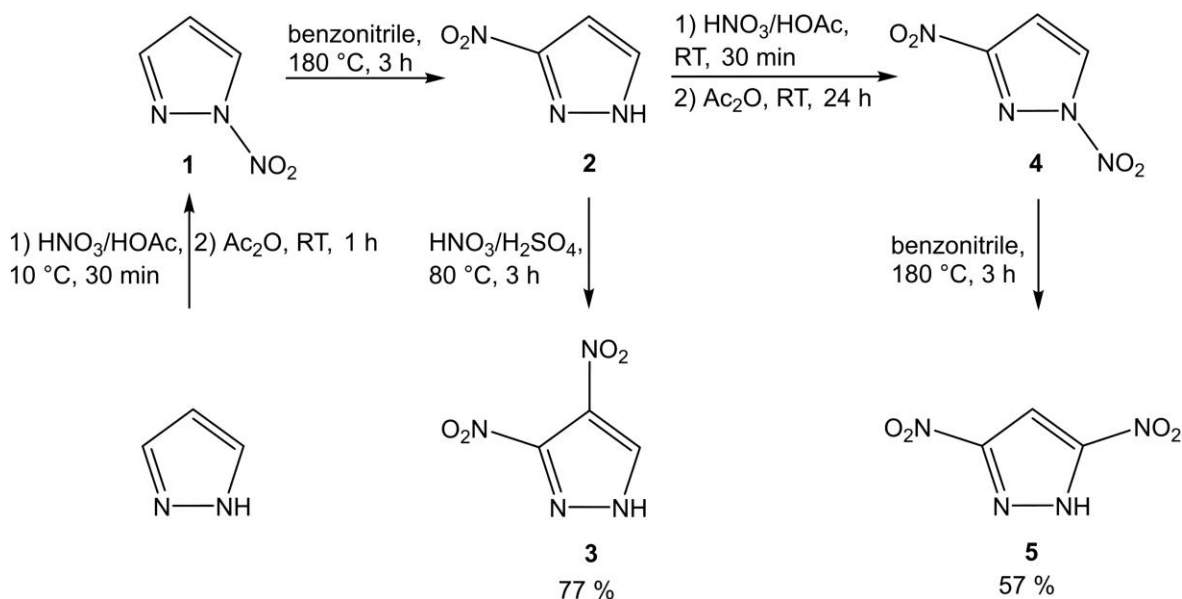
for a red signature by lithium is a reductive flame atmosphere,¹⁵ since otherwise incandescent reaction products are present covering the useful emission lines.²²

We herein present the lithium salts derived from 3,4-dinitro-1*H*-pyrazole, 3,5-dinitro-1*H*-pyrazole, 4-amino-3,5-dinitro-1*H*-pyrazole, 3,4,5-trinitro-1*H*-pyrazole, and 4-hydroxy-3,5-dinitro-1*H*-pyrazole that were extensively characterized by infrared spectroscopy, multinuclear magnetic resonance, elemental analysis, low-temperature single-crystal X-ray diffraction, differential thermal analysis, thermogravimetric analysis, and assessments of their sensitivities to friction, impact, and electrostatic discharge. Furthermore, their capability to serve as red coloring agents is evaluated.

8.2 Results and Discussion

8.2.1 Synthesis

Nitration of 1*H*-pyrazole using mixed acid takes place in 4-position.²³ In order to introduce a nitro group in the 3-position, an indirect route over *N*-functionalization with the use of nitric acid/acetic anhydride²⁴ and subsequent thermal rearrangement²⁵ needs to be taken (see Scheme 1). The migration of the nitro group is thereby assumed to proceed via a [1,5] sigmatropic shift and tautomerization of 3*H*-pyrazole.²⁶ *N*-nitropyrazoles are less stable than the *C*-substituted analogues²⁶ and their isomerization is sometimes accompanied by partial denitration.²³ Although a lot of effort has been put into finding synthesis strategies circumventing the unstable intermediate 1 *N*-nitropyrazole (**1**) and into establishing milder and more environmentally benign nitration systems,²⁷ the conventional method has been studied more comprehensively.^{23, 26} When **1** was rearranged according to our optimized procedure,²⁸ we did not encounter any problems concerning the isolation of the desired product, but with that of 1,3-dinitropyrazole (**4**). Commonly, after thermolysis **5** is separated from 3-nitro-1*H*-pyrazole (**2**) impurities by precipitation of a corresponding salt and subsequent neutralization^{5, 29} or by recrystallization from benzene.²³ This solvent is toxic, however, the high solubility of sodium 3,5-dinitropyrazolate in aqueous media makes its precipitation problematic, especially when working on a small scale. We found out that the use of a saturated sodium hydroxide solution ensures the formation of a solid.

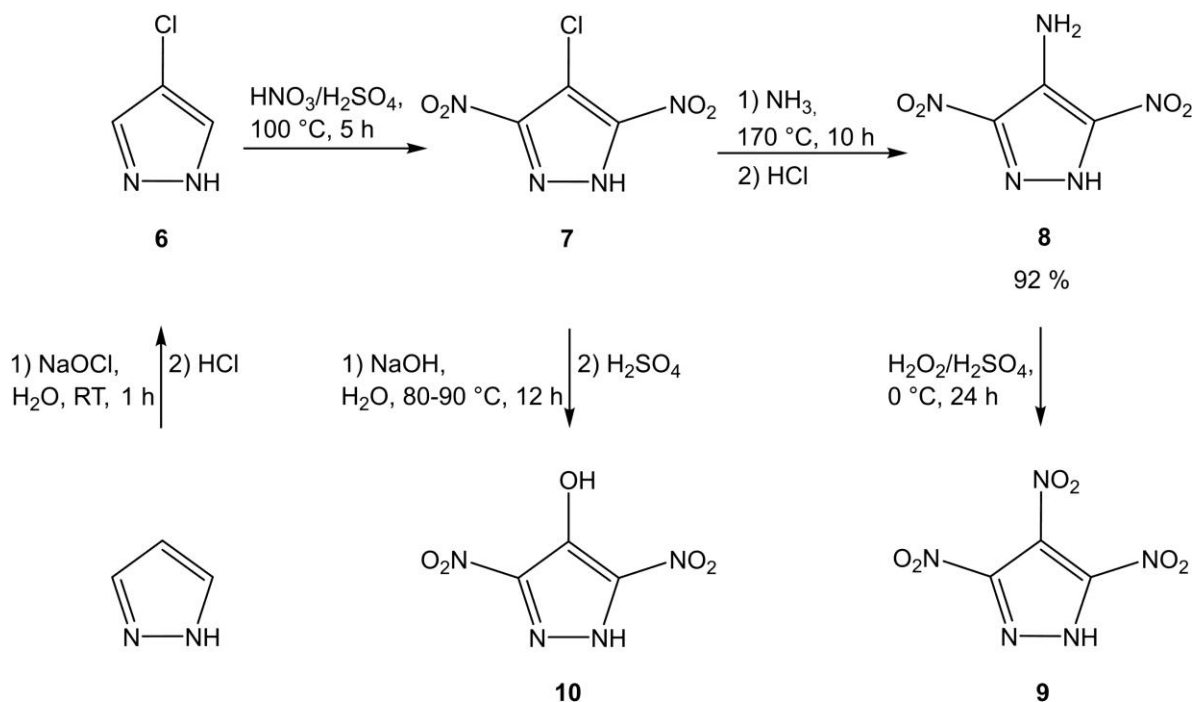


Scheme 1. Synthesis of 3,4-dinitro-1*H*-pyrazole (**3**) and 3,5-dinitro-1*H*-pyrazole (**5**).

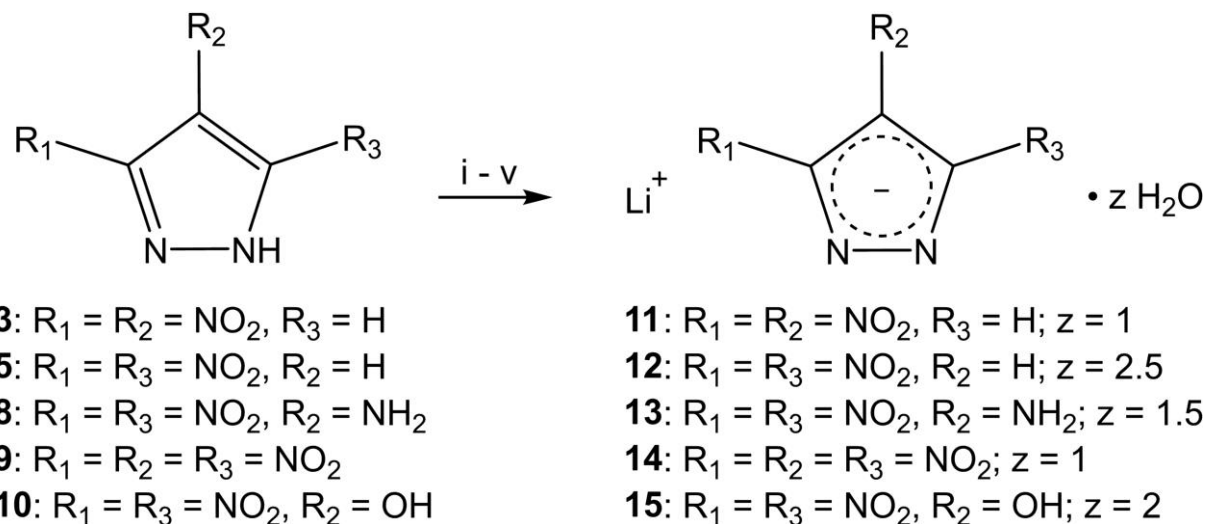
The literature provides three different synthetic pathways towards **8**: a) amination of **5** via vicarious nucleophilic substitution of hydrogen by 1,1,1-trimethylhydrazinium iodide or 4-

amino-1*H*-1,2,4-triazole in the presence of potassium *tert*-butoxide;^{12, 30} b) aromatic nucleophilic substitution of 4-chloro-3,5-dinitro-1*H*-pyrazole (**7**) or **9** by ammonia;^{6, 11, 30b} c) alkaline or acidic hydrolysis of the protective carbamate group of 4-carbomethoxyamino-3,5-dinitro-1*H*-pyrazole or 4-carbethoxyamino-3,5-dinitro-1*H*-pyrazole, respectively.^{11, 30b} Since among these synthetic routes the one starting from **7** is the most efficient and environmentally benign and can even be scaled up to small pilot plant scale,^{6, 11, 12, 30} it was chosen for synthesis of **8** (see Scheme 2). While **8** is readily oxidized to **9** by peroxydisulfuric acid,⁶ nucleophilic substitution of **7** by sodium hydroxide leads to **10**.³¹

Apart from **9**, which hydrolyses in alkaline water⁶ and was thus treated with lithium carbonate in ethanol, all other neutral compounds were reacted with stoichiometric amounts of lithium hydroxide in aqueous solution for at least one hour at room temperature or within a shorter period of time at elevated temperature to give the corresponding lithium salts (see Scheme 3). While lithium 4-oxo-3,5-dinitro-1*H*-pyrazolate · 2 H₂O (**15**) precipitated from the mother liquor upon reducing its volume, the other crude products were recrystallized from different solvents.



Scheme 2. Synthesis of 4-amino-3,5-dinitro-1*H*-pyrazole (**8**), 3,4,5-trinitro-1*H*-pyrazole (**9**), and 4-hydroxy-3,5-dinitro-1*H*-pyrazole (**10**).



Scheme 3. Synthesis of lithium 3,4-dinitropyrazolate $\cdot \text{H}_2\text{O}$ (**11**), lithium 3,5-dinitropyrazolate (**12**) $\cdot 2.5 \text{H}_2\text{O}$, lithium 4-amino-3,5-dinitropyrazolate $\cdot 1.5 \text{H}_2\text{O}$ (**13**), lithium 3,4,5-trinitropyrazolate $\cdot \text{H}_2\text{O}$ (**14**), and lithium 4-oxo-3,5-dinitropyrazolate $\cdot 2 \text{H}_2\text{O}$ (**15**). Reagents and conditions: (i) 1) LiOH, H_2O , RT, 1 h; 2) *i*-PrOH, 76%; (ii) 1) LiOH, H_2O , RT, 1 h; 2) EtOAc, 74%; (iii) 1) LiOH, H_2O , RT, 1 h; 2) EtOH, 53%; (iv) 1) Li_2CO_3 , EtOH, RT, 1 d; 2) EtOH; (v) LiOH, $\text{H}_2\text{O}/\text{MeOH}$ (1 : 1), 80 °C, 15 min, 86%.

8.2.2 Crystal Structures

While *Drukenmüller* et al. already refer to the difficulty of obtaining single crystals of 3,5-dinitropyrazolates, even fewer crystal structures of salts of **3** and **8** are deposited in The Cambridge Crystallographic Data Centre.^{5, 14, 32} The search for 4-oxo-3,5-dinitropyrazolates did not even return one hit. However, all salts included in this study were successfully crystallized from *iso*-propanol, ethyl acetate, ethanol, and a 1 : 1-mixture of water and methanol, respectively, before single-crystals were prepared and X-ray diffraction was conducted at temperatures ranging from 107 to 123 K. In contrast to elemental analysis, this analytical method indicates that **12** crystallizes as trihydrate. Furthermore, in **15** instead of the ring nitrogen atom the hydroxyl group is deprotonated due to the higher acidity of the latter functionality. **11**, **12** $\cdot 3 \text{H}_2\text{O}$, and **14** crystallize in monoclinic space groups (**11**: $P2_1/c$; **12** $\cdot 3 \text{H}_2\text{O}/$ **14**: $P2_1/n$), whereas **13** and **15** both crystallize in the triclinic space group $P\bar{1}$. Comparing the densities of the corresponding neutral compounds **3**, **5**, and **9**, those of **11** and **12** $\cdot 3 \text{H}_2\text{O}$ would be expected to be very similar and **14** should be packed closest, but **12** $\cdot 3 \text{H}_2\text{O}$ contains the most units of crystal water of all investigated lithiated materials and thus has the lowest density of 1.76 g cm^{-3} . The loose packing in **12** $\cdot 3 \text{H}_2\text{O}$ is also reflected by the remarkably low degree of cross-linking of this polymer. While in all other structures adjacent anions are connected by lithium cations and the latter mostly share water molecules, only the second motif is to be found in **12** $\cdot 3 \text{H}_2\text{O}$. The densities of **13** and **15** should both significantly exceed those of

the afore-mentioned lithium pyrazolates as on the one hand extensive hydrogen bonding is formed and on the other hand ring nitrogen atoms, nitro groups as well as the oxo group should act as electron donors to the lithium cation. Astonishingly, the density of **13** with a value of 1.78 g cm^{-3} is the second lowest, which might originate from a disordered water molecule.

In all investigated moieties, the pyrazole ring is planar and the intracyclic bonds match those of the parent compound ($1.33\text{--}1.38 \text{ \AA}^{33}$) taking into account that the bonds in anions are in general slightly elongated.⁶ The substituents are essentially coplanar, however, the nitro groups on C1 in **11** and on C2 in **14** with torsion angles of -23° and -79 to -86° , respectively, bend out of the ring plane due to steric hindrance. Additionally, to the ubiquitous classical O–H \cdots N/O hydrogen bonds as well as the N–H \cdots O contacts in **13** and **15** with lengths between 2.88 and 3.11 Å, non-classical C–H \cdots O interactions with bond lengths in the range of 3.04–3.39 Å can be found in the structures of **11** and **12** · 3 H₂O. While the classical hydrogen bonds in **12** · 3 H₂O, **13**, and **15** are partially slightly shortened, those in **14** are elongated. Furthermore, the number of different donor-acceptor combinations and the total of all contacts are the lowest for **11** and **14**.

None of the coordination spheres of lithium discussed herein match regular polyhedra. In **11**, each lithium atom is tetrahedrally coordinated by one ring nitrogen each of two 3,4-dinitropyrazolate units and by two water molecules, whereby the angle O5ⁱⁱ–Li1–N2ⁱ is considerably widened (see Figure 2).

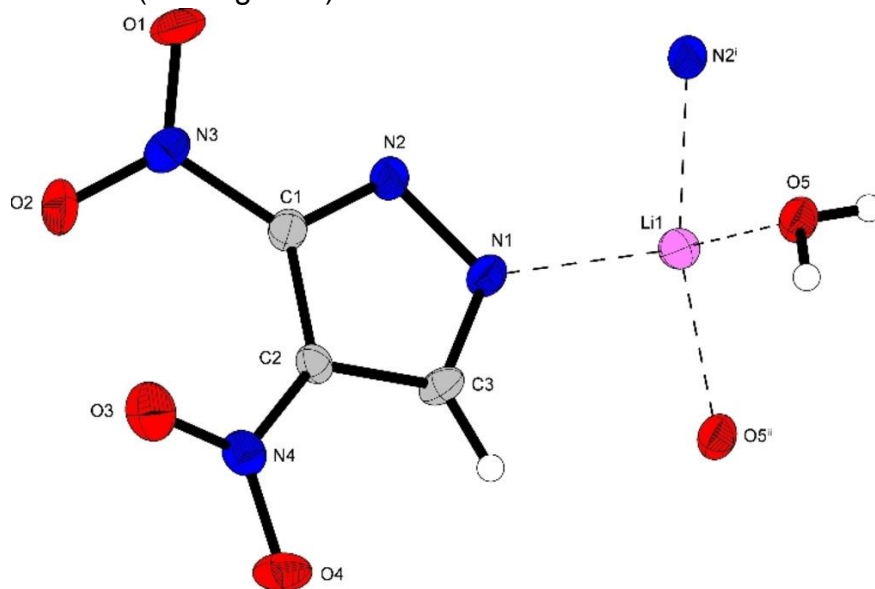


Figure 2. Advanced molecular unit of lithium 3,4-dinitropyrazolate · H₂O (**11**). Selected bond lengths (Å): N1–Li1 2.044(9), N2ⁱ–Li1 2.056(9), O5–Li1 2.101(11), O5ⁱⁱ–Li1 2.098(10); selected bond angles (°): N1–Li1–N2ⁱ 106.6(4), O5ⁱⁱ–Li1–N2ⁱ 130.8(5), O5–Li1–N2ⁱ 99.3(4), O5ⁱⁱ–Li1–N1 101.0(4), O5–Li1–O5ⁱⁱ 111.2(4), O5–Li1–N1 106.0(4); symmetry codes: (i) $-x, 2-y, -z$; (ii) $1+x, y, z$.

In contrast to that, the lithium cations in **12** · 3 H₂O have an octahedral coordination sphere consisting of the nitro group of a 3,5-dinitropyrazolate anion and five units of crystal water (see Figure 3). However, the remarkably long distances between Li1 and the nitro group O1 of 2.53 Å and especially between Li1 and the shared water molecule O6ⁱ of 2.61 Å should be noticed. The latter irregularities might also explain the fact that the crystal water content of the same sample determined by elemental analysis was only 2.5. The bridging aqua ligand might be slowly split off to reduce the amount of water included per unit cell. Even if repeated X-ray diffraction still gave the trihydrate, this analytical method is less representative of the statistical distribution within the sample.

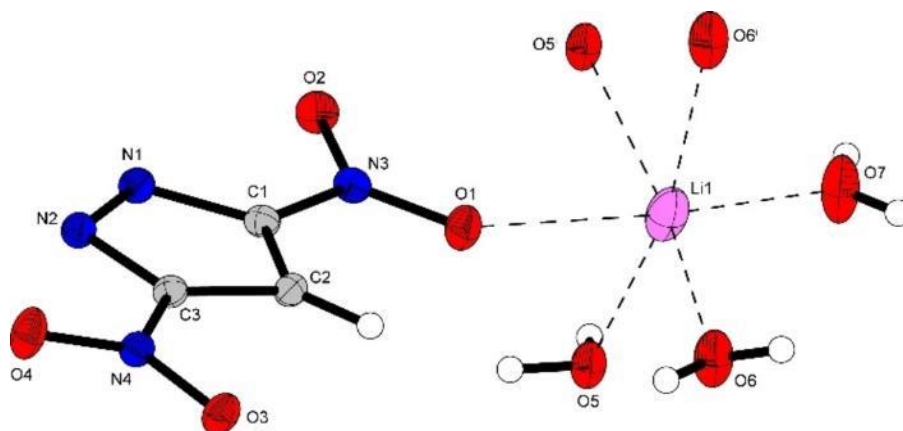


Figure 3. Advanced molecular unit of lithium 3,5-dinitropyrazolate (**12**) · 3 H₂O. Selected bond lengths (Å): O5ⁱ–Li1 2.064(3), O7–Li1 1.961(3), O6–Li1 2.005(3), O5–Li1 2.184(3); selected bond angles (°): O5–Li1–O6 85.35(11), O5–Li1–O5ⁱ 104.35(11), O5–Li1–O7 98.25(11), O6–Li1–O7 96.64(12), O5–Li1–O7 102.36(11); symmetry code: (i) $-1+x, y, z$.

In **13**, the coordination sphere of lithium is trigonal bipyramidal and it is built by one ring nitrogen atom each of two 4-amino-3,5-dinitropyrazolate anions, one nitro functionality, and two units of bridging crystal water (see Figure 4). The channels between the resulting chains of dimers are filled with an additional half-occupied water (see Figure 5).

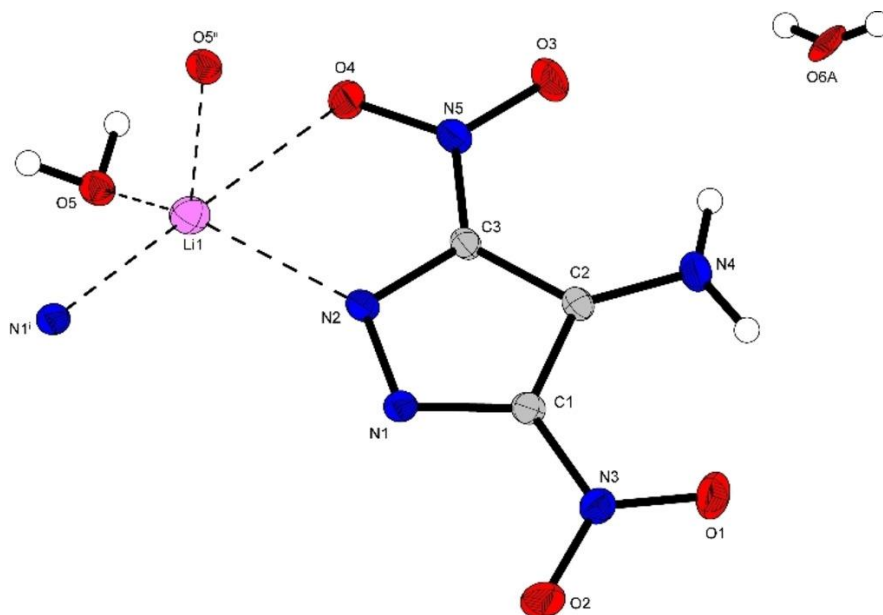


Figure 4. Advanced molecular unit of lithium 4-amino-3,5-dinitropyrazolate · 1.5 H₂O (**13**). Selected bond lengths (Å): O5–Li1 2.014(4), O5ⁱⁱ–Li1 1.997(4), O4–Li1 2.441(4), N2–Li1 2.100(4), N1ⁱ–Li1 2.116(4); selected bond angles (°): O4–Li1–O5 79.37(13), O4–Li1–O5ⁱⁱ 82.08(13), O4–Li1–N2 72.01(12), O5–Li1–O5ⁱ 116.23(19), O5ⁱⁱ–Li1–N2 102.99(15), O5–Li1–N2 127.01(18), O5–Li1–N1ⁱ 99.49(16), O5ⁱⁱ–Li1–N1ⁱ 99.73(16), N1ⁱ–Li1–N2 107.76(17), O4–Li1–N1ⁱ 178.17(17); symmetry codes: (i) 1–x, 2–y, 1–z; (ii) –1+x, y, z.

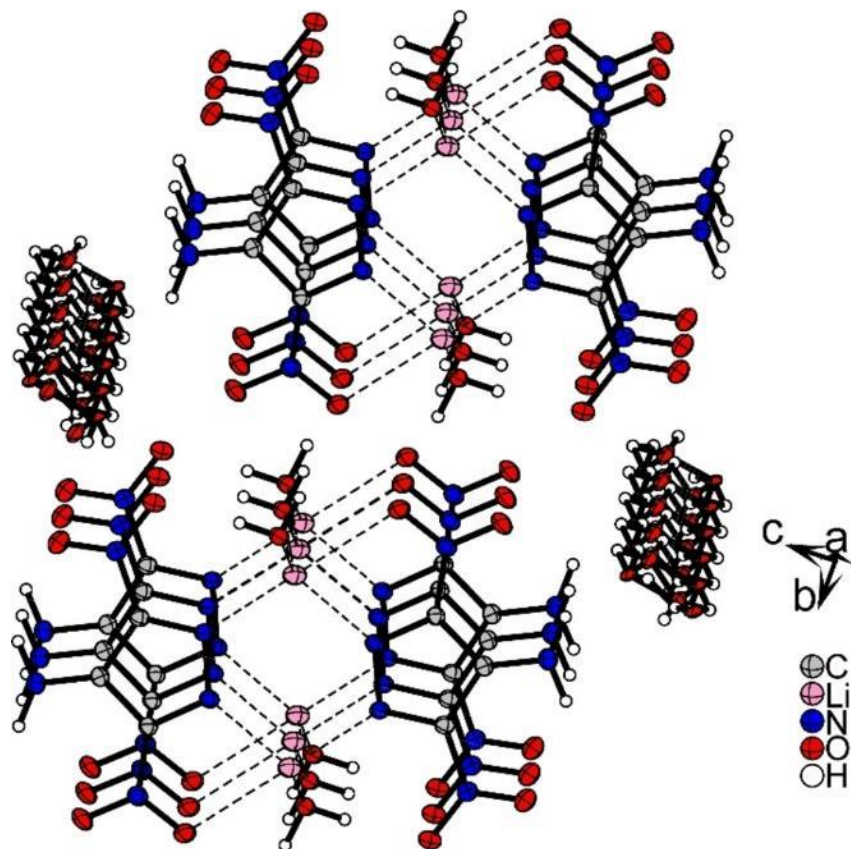


Figure 5. Macroscopic structure of lithium 4-amino-3,5-dinitropyrazolate · 1.5 H₂O (**13**).

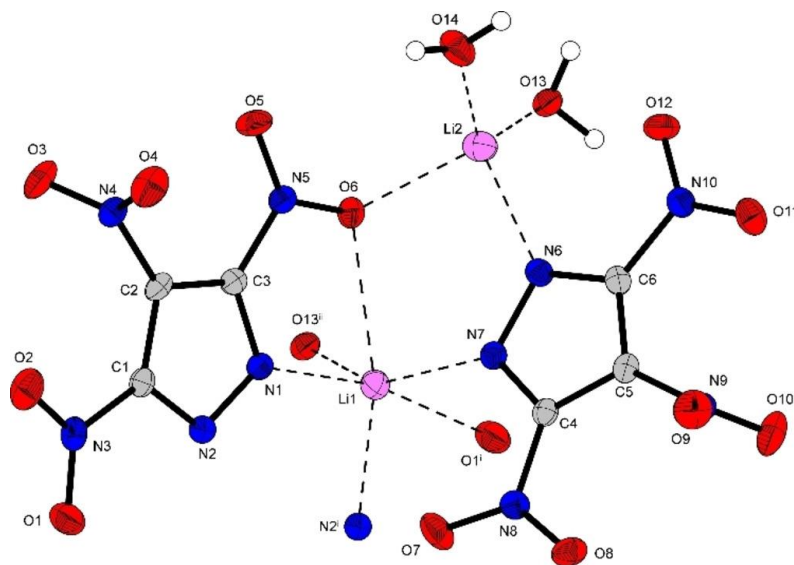


Figure 6. Advanced dimer of lithium 3,4,5-trinitropyrazolate · H₂O (**14**). Selected bond lengths (Å): N1–Li1 2.062(3), O13ⁱ–Li1 2.172(3), N7–Li1 2.169(3), N2ⁱ–Li1 2.095(3), O14–Li2 1.875(3), O13–Li2 1.965(3), N6–Li2 2.083(3), O6–Li2 2.066(3); selected bond angles (°): O13ⁱ–Li1–N1 96.58(11), N1–Li1–N7 103.63(11), N1–Li1–N2ⁱ 100.19(14), O13ⁱ–Li1–N2ⁱ 88.77(10), N2ⁱ–Li1–N7 114.98(13), O6–Li2–O14 103.27(13), O14–Li2–N6 120.65(14), O13–Li2–O14 111.95(16), O6–Li2–N6 89.14(13), O13–Li2–N6 109.02(13), O6–Li2–O13 121.75(13); symmetry codes: (i) 1–x, 1–y, 1–z; (ii) –x, 1–y, 1–z.

Interestingly, in **14** two different coordination spheres of lithium can be found: an octahedral structure motif with one ring nitrogen atom and one nitro group each of two 3,4,5-trinitropyrazolate moieties, one nitrogen of an additional anion, and an aqua ligand as well as a tetrahedral environment by one nitrogen and one nitro substituent of a nitropyrazolate unit and by two water molecules (see Figure 6). Nevertheless, similarly as with **12** · 3 H₂O the dative bonds of two of the ligands to the octahedrally coordinated lithium atom are highly elongated, but here it is the nitro groups (O6–Li1 2.51 Å, O1ⁱ–Li1 2.61 Å). Additionally, N1 and O6 as well as O1ⁱ and N2ⁱ are close together, since these ligands are bound to the same pyrazole ring, respectively. The angle N2ⁱ–Li1–N7 is remarkably widened. The tetrahedral coordination sphere is distorted in a way that the angle O6–Li2–N6 is very narrow. This is the only of the studied crystal structures in which adjacent lithium cations are not only connected by water bridges, but also by a nitro group.

The lithium cation in **15** is octahedrally coordinated by the oxo group and one nitro functionality of a 4-oxo-3,5-dinitropyrazolate unit, by one ring nitrogen atom and one nitro substituent of another anion, and by two aqua ligands (see Figure 7). The difference between the lengths of the bonds of the lithium atom to the two water molecules is the second greatest here. The coordination geometry is the most symmetric in this row and is only disturbed by the fact that the angle $O1^i-Li1-N2^i$ is narrow due to the common pyrazole ring of the ligands. The crystal structure of **15** is the only one lacking water bridges between the lithium cations.

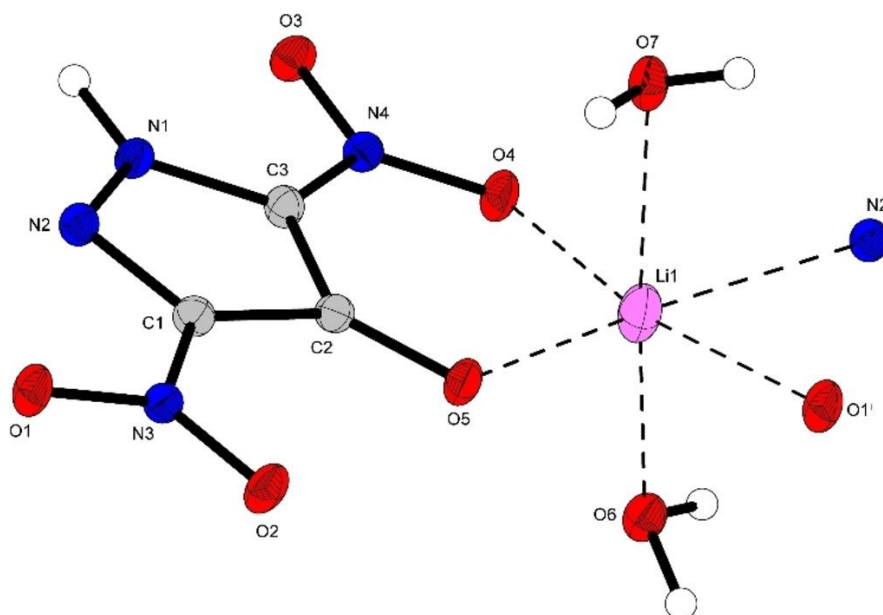


Figure 7. Advanced molecular unit of lithium-4-oxo-3,5-dinitropyrazolate · 2 H₂O (**15**). Selected bond lengths (Å): O4–Li1 2.051(3), O7–Li1 2.345(3), N2ⁱ–Li1 2.290(3), O1ⁱ–Li1 2.102(3), O6–Li1 2.136(3), O5–Li1 1.981(3); selected bond angles (°): O4–Li1–O7 87.77(11), O7–Li1–N2ⁱ 89.06(11), O1ⁱ–Li1–O7 89.65(12), O5–Li1–O7 87.74(12), O4–Li1–N2ⁱ 94.82(11), O1ⁱ–Li1–N2ⁱ 72.95(10), O1ⁱ–Li1–O5 97.92(12), O4–Li1–O5 94.15(13), O4–Li1–O6 92.23(13), O6–Li1–N2ⁱ 87.30(11), O1ⁱ–Li1–O6 89.58(12), O5–Li1–O6 95.90(13), O6–Li1–O7 176.35(15); symmetry code: (i) x, 1+y, z.

8.2.3 Physico-Chemical Properties

Even if next-generation pyrotechnic formulations should have a lower impact on health and environment, they must be at least as safe as current systems.³⁴ In order to evaluate the suitability of **11–15** as red colorants from this point of view, the thermal stabilities of these compounds were determined by DTA using a heating rate of 5 °C min⁻¹. In the case of **11**, DTA of a sample after storage at ambient conditions for one day revealed its hygroscopicity, whereas **14** already deliquesces within a shorter period of time (see Supporting Information). This behaviour matches our findings that in the crystal structures

of **11** and **14** the angles deviate the most from the expected values for the respective coordination spheres of lithium and that only weak hydrogen bonding is formed.

The large difference between the dehydration and the decomposition temperature of hydrated **12** allowed us to approach the problem of a non-homogeneous crystal water

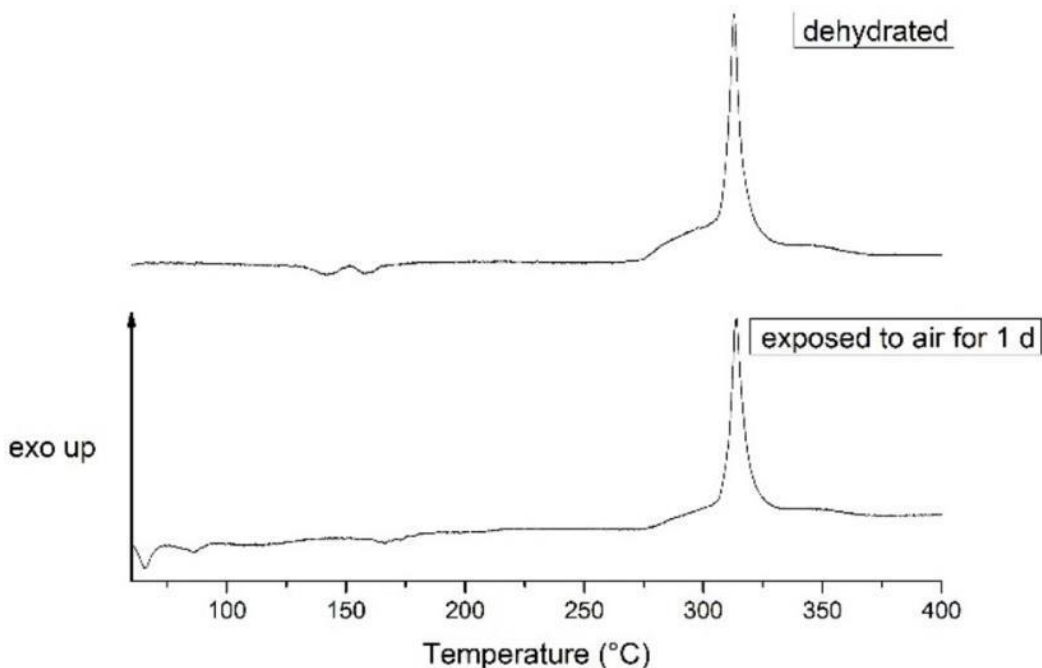


Figure 8. DTA plots of water-free lithium 3,5-dinitropyrazolate (**12**) from top to bottom after synthesis and exposure to air for one day.

content by heating this material at 100 °C overnight. Indeed, we obtained the water-free lithium salt in this way, but after exposure to air for one day the 2.5-hydrate was recovered as apparent from the reappearing endothermic signal at roughly 60 °C as well as from elemental analysis (see Figure 8).

Compounds **13** and **15**, which did not show any irregularities concerning hydration, were additionally studied by TGA. While in the case of **13** the weight reduction by 4 % at already 93 °C indicates the loss of the disordered hemihydrate followed by the splitting of another unit of crystal water at elevated temperature (see Figure 9), the weight decrease of **15** by almost 8 % at roughly 110 °C correlates well with the separation of the weakly bound water molecule O7 (see Figure 10). Interestingly, the leaving of the second aqua ligand takes place at remarkably high temperature and even releases heat. Our theory to explain this phenomenon is that after the loss of the second crystal water a rearrangement to an energetically more favorable lattice takes place.

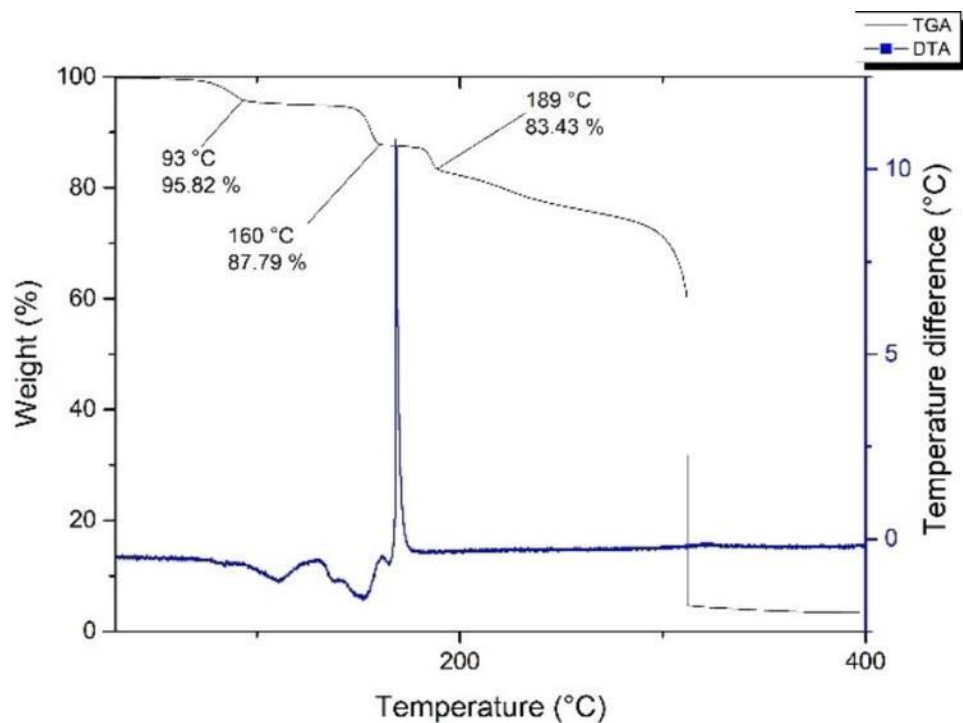


Figure 9. Combined DTA and TGA plots of lithium 4-amino-3,5-dinitropyrazolate · 1.5 H₂O (**13**).

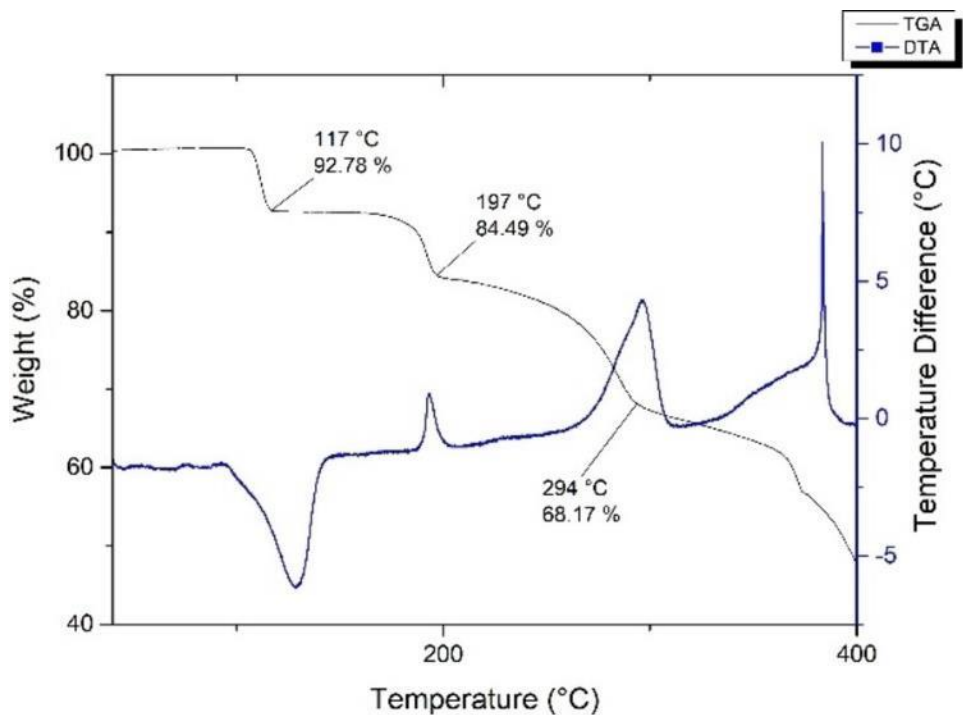


Figure 10. Combined DTA and TGA plots of lithium 4-oxo-3,5-dinitropyrazolate · 2 H₂O (**15**).

However, **12** · 2.5 H₂O is the most thermally stable among the investigated lithiated materials followed by **15** (see Table 1). The fact that **13** decomposes at significantly lower temperature coincides with the smaller coordination number of lithium in the respective structure. On the other hand, the latter compound is only less sensitive to friction, whereas

12 · 2.5 H₂O is sensitive to impact and like **15** also responds to electrostatic discharge. Regarding all determined sensitivity parameters, **13** seems to have the highest potential as pyrotechnic ingredient at this point and will function as both color imparter and fuel in a mixture due to its negative oxygen balance.

Table 1. Physico-chemical properties of lithium 3,5-dinitropyrazolate (**12**) · 2.5 H₂O, lithium 4-amino-3,5-dinitropyrazolate · 1.5 H₂O (**13**), and lithium 4-oxo-3,5-dinitropyrazolate · 2 H₂O (**15**).

	11	12 · 2.5 H₂O	13	14	15
Ω_{CO_2} [%] ^[a]	-22	-19	-23	0	-11
$T_{\text{dehydr}}(\text{onset})$ [°C] ^[b]	141	61	93, 132	111	109, 189
$T_{\text{dec}}(\text{onset})$ [°C] ^[c]	141	321	168	253	269
g.s. [μm] ^[d]	> 1000	< 100	100–500		< 100
FS [N] ^[e]	288	> 360	360		> 360
IS [J] ^[f]	15	35	> 40		> 40
ESD [J] ^[g]	0.2	0.2 ^[h]	1.5		0.2

[a] Oxygen balance with respect to formation of CO₂ and Li₂O. [b] Onset dehydration temperature. [c] Onset decomposition temperature. [d] Grain size. [e] Friction sensitivity. [f] Impact sensitivity. [g] Electrostatic discharge sensitivity. [h] The electrostatic discharge sensitivity of lithium 3,5-dinitropyrazolate · 2.5 H₂O was measured using a grain size of 100–500 μm .

8.2.4 Pyrotechnic Performance

A chlorine-free strontium-based composition²¹ was chosen as pyrotechnic matrix in order to test **13** for a red flame coloration. In the “drop-in” formulation, strontium nitrate was replaced by the ammonium oxidizer and 5-amino-1*H*-tetrazole serving as reducing agent was substituted by the new lithium salt (see Table 2). As metals unfavorably increase the flame temperature of such mixtures and the oxidation product of magnesium incandescences, the content of this fuel was reduced. The resistance of the resulting composition to moisture was attempted to be enhanced by using a higher amount of binder, still the test formulation is hygroscopic.

Table 2. Composition of a strontium-based chlorine-free reference and a test formulation containing lithium 4-amino-3,5-dinitropyrazolate · 1.5 H₂O (**13**).

	Reference	Test
Sr(NO ₃) ₂ [wt%]	48	
NH ₄ NO ₃ [wt%]		48
Mg [wt%] ^[a]	33	12
CH ₃ N ₅ [wt%]	12	
13 [wt%]		30
EPON 813/VERSAMID 140 [wt%] ^[b]	7	10

[a] Magnesium with a mesh size 50/100 (300 μm > grain size > 150 μm). [b] EPON 813 and VERSAMID 140 in a weight percent ratio of 80:20.

Figure 11 and Table 3 show that red light is emitted and the dominant wavelength almost reaches the minimum benchmark of 600 nm.²¹ While in comparison to the control the color purity of the investigated pyrotechnic mixture is still acceptable, its luminosity is by far lower. Spectral purity and luminous intensity are well-known antagonists in lithium flame chemistry: if the light output is improved by generating more condensed magnesium oxide in the flame, the color purity will suffer from that.¹⁹ Elsewhere, the use of magnesium with a smaller particle size turned out to enhance the luminosity without significantly impairing the spectral purity.²¹ Regarding safety, the test composition is thermally stable up to 173 °C and less sensitive to friction and electrostatic discharge than the reference

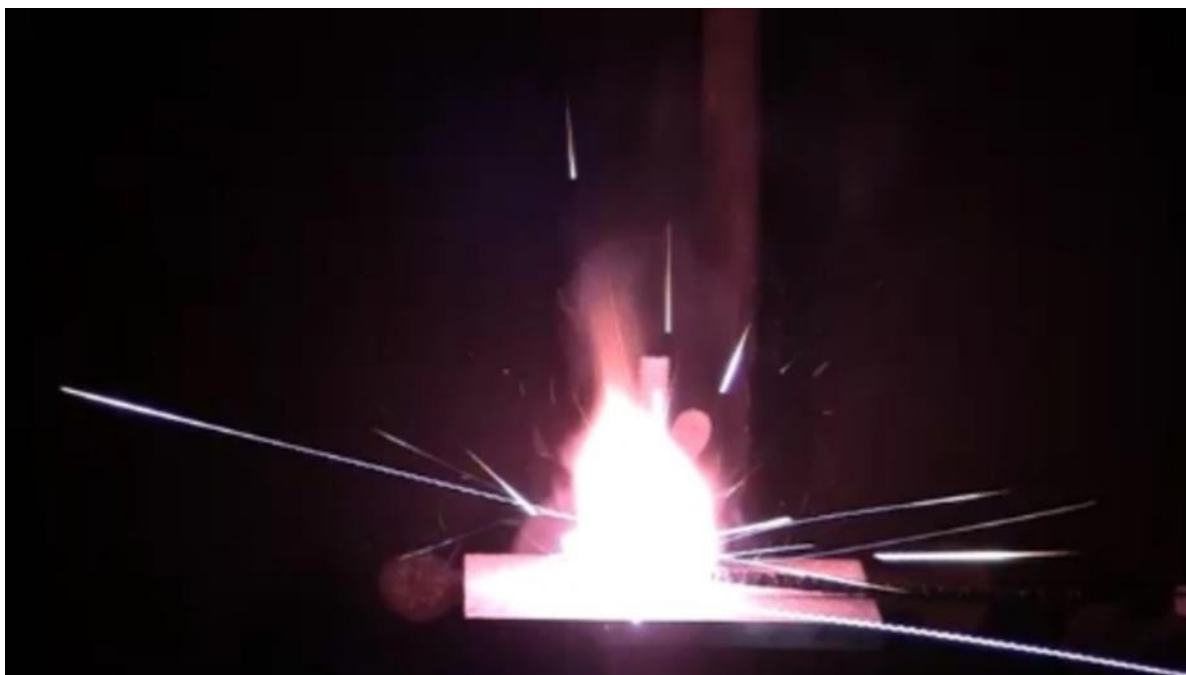


Figure 11. Combustion of the test formulation.

Table 3. Physico-chemical properties of reference and test formulation.

	Reference	Test
$T_{\text{dec}}(\text{onset})$ [°C] ^[a]	244	173
FS [N] ^[b]	192	> 360
IS [J] ^[c]	10	10
ESD [J] ^[d]	1.0	1.4
BT [s] ^[e]	3	15
λ_d [nm] ^[f]	606	599
Σ [%] ^[g]	75	64
LI [cd] ^[h]	14083	481

[a] Onset decomposition temperature. [b] Friction sensitivity. [c] Impact sensitivity. [d] Electrostatic discharge sensitivity. [e] Burn time. [f] Dominant wavelength. [g] Spectral purity. [h] Luminous intensity.

8.3 Conclusion

The hardly explored lithium salts of 3,4-dinitro-1*H*-pyrazole, 3,5-dinitro-1*H*-pyrazole, 4-amino-3,5-dinitro-1*H*-pyrazole, 3,4,5-trinitro-1*H*-pyrazole, and 4-hydroxy-3,5-dinitro-1*H*-pyrazole were investigated as potential replacements for strontium-based red pyrotechnic colorants. The neutral compounds were prepared applying common synthetic strategies, whereby the work-up of 3,5-dinitro-1*H*-pyrazole was improved, and were subsequently reacted with lithium bases. Thermal dehydration studies revealed lithium 3,4-dinitropyrazolate · H₂O and especially lithium 3,4,5-trinitropyrazolate · H₂O to be hygroscopic, whereas sensitivity assessments marked lithium 3,5-dinitropyrazolate · 2.5 H₂O and lithium 4-oxo-3,5-dinitropyrazolate · 2 H₂O as less useful for application in pyrotechnic items. Although the resistance of a test formulation containing lithium 4-amino-3,5-dinitropyrazolate · 1.5 H₂O to moisture and its luminosity should be enhanced in the future, the capability of this lithiated material to impart red color to a flame was demonstrated.

8.4 Experimental Section

CAUTION! The reactions of pyrazole described herein, especially the multiple nitrations, are partly exothermic and the respective products, their lithium salts, and the investigated pyrotechnic formulations are potentially explosive energetic materials, which are sensitive to various environmental stimuli (e.g. heat, friction, impact or electrostatic discharge). Therefore, proper safety precautions (safety glasses, face shield, leather coat, earthed equipment and shoes, KEVLAR gloves, KEVLAR sleeves, and ear protectors) have to be taken when synthesizing and manipulating these compounds.

3,4-Dinitro-1*H*-pyrazole (3):^[21] A suspension of 3-nitro-1*H*-pyrazole (2.00 g, 18 mmol, 1 eq.) in concentrated sulfuric acid (96 %, 3 mL, 56 mmol, 3 eq.) was cooled to approximately 0 °C and concentrated nitric acid (100 %, 2 mL, 48 mmol, 3 eq.) was added dropwise at a rate so that the temperature was below 10 °C. After the addition of further sulfuric acid (96 %, 7 mL, 131 mmol, 7 eq.), the nitration mixture was allowed to warm to room temperature and subsequently heated at 80 °C for three hours before it was quenched with ice/water (200 mL). The resulting solution was extracted with diethyl ether (3 x 50 mL) and the combined organic phases washed with bidistilled water (2 x 50 mL) and a saturated sodium chloride solution (50 mL). After the organic layers had been dried

over magnesium sulfate, the solvent was evaporated to give a yellowish crystalline material (2.16 g, 14 mmol, 77 %).

IR (ATR): $\tilde{\nu}$ = 3294 (m), 3260 (m), 3149 (m), 3135 (m), 2901 (w), 1768 (vw), 1541 (s), 1518 (vs), 1489 (s), 1477 (s), 1448 (m), 1426 (m), 1375 (s), 1341 (vs), 1273 (s), 1182 (w), 1154 (m), 1094 (s), 1065 (s), 935 (w), 888 (vw), 847 (m), 806 (vs), 796 (vs), 754 (s), 737 (vs), 608 (m), 575 (m), 470 (m), 445 (w) cm^{-1} . $^{14}\text{N}\{\text{H}\}$ NMR (DMSO- d_6 , 25 °C): δ = -25.5 (br s, NO_2) ppm. $^{13}\text{C}\{\text{H}\}$ NMR (DMSO- d_6 , 25 °C): δ = 148.1 (s, C- NO_2), 132.7 (s, CH), 126.3 (s, C- NO_2) ppm. $^1\text{H}\{\}$ NMR (DMSO- d_6 , 25 °C): δ = 14.90 (br s, 1H, NH), 9.13 (s, 1H, CH) ppm. EA ($\text{C}_3\text{H}_2\text{N}_4\text{O}_4$, 158.07): calcd. N 35.45, C 22.80, H 1.28 %; found N 34.95, C 22.95, H 1.56 %. DTA (5 °C min^{-1}): 72 (endothermic), 243 (exothermic) °C.

3,5-Dinitro-1H-pyrazole (5): 1,3-Dinitropyrazole (1.00 g, 6 mmol, 1 eq.) was thermally rearranged by heating a suspension in benzonitrile (28 mL) at 180 °C for roughly three hours. Upon addition of a saturated sodium hydroxide solution (22 mL) to the cool reaction mixture, sodium 3,5-dinitropyrazolate precipitated, which was filtered off, suspended in water (20 mL), and acidified to pH = 1 with hydrochloric acid. The resulting solution was extracted with diethyl ether (3 x 50 mL), dried over magnesium sulfate, and allowed to stand for crystallization. The title compound was obtained in the form of colorless crystals (0.57 g, 4 mmol, 57 %).

IR (ATR): $\tilde{\nu}$ = 3202 (m), 3165 (m), 3148 (m), 1693 (vw), 1566 (m), 1527 (s), 1477 (m), 1446 (m), 1399 (m), 1365 (s), 1331 (vs), 1271 (m), 1202 (s), 1083 (m), 1054 (w), 1012 (m), 983 (s), 846 (s), 829 (vs), 815 (s), 758 (m), 742 (vs), 686 (s), 628 (m), 604 (m), 572 (m), 512 (s) cm^{-1} . $^{14}\text{N}\{\text{H}\}$ NMR (DMSO- d_6 , 25 °C): δ = -25.2 (br s, NO_2) ppm. $^{13}\text{C}\{\text{H}\}$ NMR (DMSO- d_6 , 25 °C): δ = 151.4 (s, C- NO_2), 99.8 (s, CH) ppm. $^1\text{H}\{\}$ NMR (DMSO- d_6 , 25 °C): δ = 13.57 (br s, 1H, NH), 7.94 (s, 1H, CH) ppm. EA ($\text{C}_3\text{H}_2\text{N}_4\text{O}_4$, 158.07): calcd. N 35.45, C 22.80, H 1.28 %; found N 34.65, C 22.66, H 1.52 %. DTA (5 °C min^{-1}): 167 (endothermic), 284 (exothermic) °C.

4-Amino-3,5-dinitro-1H-pyrazole (8):^[5] A steel autoclave containing a suspension of 4-chloro-3,5-dinitro-1H-pyrazole (27.00 g, 140 mmol, 1 eq.) in concentrated ammonia solution (250 mL) was heated at 170 °C for ten hours. After the reaction mixture had cooled to room temperature, it was brought to pH = 1 using concentrated hydrochloric acid. Subsequently, the solution was extracted with ethyl acetate (4 x 200 mL), the

combined organic layers were dried over magnesium sulfate, and the solvent was removed on a rotary evaporator to yield a yellow powder (22.33 g, 129 mmol, 92 %).

IR (ATR): $\tilde{\nu}$ = 3432 (m), 3319 (s), 3151 (m), 2999 (m), 2929 (m), 1634 (vs), 1578 (m), 1510 (s), 1470 (s), 1430 (s), 1392 (w), 1340 (s), 1319 (s), 1297 (s), 1230 (s), 1208 (s), 1089 (m), 991 (m), 941 (m), 925 (m), 846 (s), 827 (s), 735 (m), 721 (s), 665 (m), 640 (w), 591 (w), 517 (vs), 494 (vs) cm^{-1} . $^{14}\text{N}\{\text{H}\}$ NMR (DMSO- d_6 , 25 °C): δ = -23.8 (br s, NO_2) ppm. $^{13}\text{C}\{\text{H}\}$ NMR (DMSO- d_6 , 25 °C): δ = 137.7 (s, C- NO_2), 128.7 (s, C- NH_2) ppm. $^1\text{H}\{\}$ NMR (DMSO- d_6 , 25 °C): δ = 11.00 (br s, 1H, NH), 7.11 (br s, 2H, NH_2) ppm. EA ($\text{C}_3\text{H}_3\text{N}_5\text{O}_4$, 173.09): calcd. N 40.46, C 20.82, H 1.75 %; found N 40.58, C 20.94, H 1.64 %. DTA (5 °C min^{-1}): 159 (endothermic, followed by exothermic signal) °C.

Lithium 3,4-dinitropyrazolate · H₂O (11): The acid base reaction of 3,4-dinitro-1*H*-pyrazole (0.50 g, 3 mmol, 1 eq.) with lithium hydroxide (78 mg, 3 mmol, 1 eq.) in water (5 mL) was allowed to proceed at room temperature for one hour before the reaction mixture was filtered and the solvent was removed from the filtrate in vacuo. The residue was recrystallized from 2-propanol (70 mL) to give a light brown solid (0.44 g, 2 mmol, 76 %).

IR (ATR): $\tilde{\nu}$ = 3615 (w), 3541 (m), 3416 (m), 3303 (w), 3140 (m), 1748 (vw), 1665 (m), 1531 (s), 1488 (vs), 1434 (s), 1396 (s), 1376 (s), 1337 (vs), 1286 (s), 1164 (s), 1118 (m), 1084 (s), 954 (m), 937 (w), 874 (w), 853 (s), 810 (s), 749 (s), 673 (w), 635 (m), 609 (m), 541 (s), 489 (s), 416 (m) cm^{-1} . $^7\text{Li}\{\text{H}\}$ NMR (DMSO- d_6 , 25 °C): δ = -1.0 (s, *Li*) ppm. $^{14}\text{N}\{\text{H}\}$ NMR (DMSO- d_6 , 25 °C): δ = -16.4 (br s, NO_2), -19.2 (br s, NO_2) ppm. $^{13}\text{C}\{\text{H}\}$ NMR (DMSO- d_6 , 25 °C): δ = 150.6 (s, C- NO_2), 137.3 (s, CH), 125.4 (s, C- NO_2) ppm. $^1\text{H}\{\}$ NMR (DMSO- d_6 , 25 °C): δ = 8.19 (s, 1H, *CH*), 4.11 (br s, 2H, H_2O) ppm. EA ($\text{LiC}_3\text{H}_3\text{N}_4\text{O}_5$, 182.02): calcd. N 30.78, C 19.80, H 1.66 %; found N 29.38, C 19.81, H 1.96 %. DTA (5 °C min^{-1}): 141 (endothermic, followed by exothermic signal) °C. FS (> 1000 μm): 288 N. IS (> 1000 μm): 15 J. ESD (> 1000 μm): 0.2 J.

Lithium 3,5-dinitropyrazolate (12) · 2.5 H₂O: The target salt was accessed by stirring a suspension of 3,5-dinitro-1*H*-pyrazole (0.50 g, 3 mmol, 1 eq.) and lithium hydroxide (77 mg, 3 mmol, 1 eq.) in water (5 mL) at room temperature for one hour. Afterwards, the reaction mixture was filtered and the solvent was removed from the filtrate on a rotary evaporator. Recrystallization of the resulting solid from ethyl acetate (27 mL) afforded colorless crystals (0.49 g, 2 mmol, 74 %).

IR (ATR): $\tilde{\nu}$ = 3599 (m), 3537 (m), 3211 (m), 3158 (m), 2808 (w), 2610 (w), 1640 (m), 1570 (m), 1531 (s), 1513 (s), 1473 (s), 1444 (s), 1351 (vs), 1318 (vs), 1274 (s), 1205 (m), 1172 (m), 1075 (w), 1016 (s), 998 (m), 834 (s), 822 (s), 749 (s), 667 (vw), 590 (m), 557 (m), 512 (w) cm^{-1} . $^7\text{Li}\{\text{H}\}$ NMR (DMSO- d_6 , 25 °C): δ = 1.7 (s, *Li*) ppm. $^{14}\text{N}\{\text{H}\}$ NMR (DMSO- d_6 , 25 °C): δ = -11.8 (br s, NO_2) ppm. $^{13}\text{C}\{\text{H}\}$ NMR (DMSO- d_6 , 25 °C): δ = 155.8 (s, C- NO_2), 98.6 (s, CH) ppm. $^1\text{H}\{\}$ NMR (DMSO- d_6 , 25 °C): δ = 7.37 (s, 1H, CH), 3.64 (br s, 5H, H_2O) ppm. EA ($\text{LiC}_3\text{H}_6\text{N}_4\text{O}_{6.5}$, 209.04): calcd. N 26.80, C 17.24, H 2.89 %; found N 26.07, C 17.02, H 2.90 %. DTA (5 °C min^{-1}): 61 (endothermic), 321 (exothermic) °C. FS (< 100 μm): > 360 N. IS (< 100 μm): 35 J. ESD (100–500 μm): 0.2 J.

Lithium 4-amino-3,5-dinitropyrazolate · 1.5 H₂O (13): After a reaction mixture consisting of 4-amino-3,5-dinitro-1*H*-pyrazole (0.50 g, 3 mmol, 1 eq.) and lithium hydroxide (68 mg, 3 mmol, 1 eq.) in water (5 mL) had been stirred at room temperature for one hour, it was filtered and the solvent was evaporated from the filtrate in vacuo. By recrystallization of the residue from ethanol (5 mL), orange crystals were obtained (0.31 g, 2 mmol, 53 %).

IR (ATR): $\tilde{\nu}$ = 3517 (w), 3436 (m), 3324 (s), 3182 (m), 1639 (s), 1578 (w), 1509 (w), 1466 (s), 1427 (s), 1303 (vs), 1287 (vs), 1257 (s), 1233 (s), 1208 (s), 1146 (m), 928 (m), 842 (m), 829 (s), 758 (m), 724 (w), 674 (w), 648 (w), 551 (w), 528 (m), 498 (m), 434 (m), 427 (m), 414 (m) cm^{-1} . $^7\text{Li}\{\text{H}\}$ NMR (DMSO- d_6 , 25 °C): δ = -1.0 (s, *Li*) ppm. $^{14}\text{N}\{\text{H}\}$ NMR (DMSO- d_6 , 25 °C): δ = -20.4 (br s, NO_2) ppm. $^{13}\text{C}\{\text{H}\}$ NMR (DMSO- d_6 , 25 °C): δ = 142.8 (s, C- NO_2), 131.5 (s, C- NH_2) ppm. $^1\text{H}\{\}$ NMR (DMSO- d_6 , 25 °C): δ = 6.68 (br s, 2H, NH_2), 3.64 (br s, 3H, H_2O) ppm. EA ($\text{LiC}_3\text{H}_5\text{N}_5\text{O}_{5.5}$, 206.04): calcd. N 33.99, C 17.49, H 2.45 %; found N 34.27, C 17.79, H 2.31 %. DTA (5 °C min^{-1}): 93 (endothermic), 132 (endothermic), 168 (exothermic) °C. FS (100–500 μm): 360 N. IS (100–500 μm): > 40 J. ESD (100–500 μm): 1.5 J.

Lithium 3,4,5-trinitropyrazolate · H₂O (14): 3,4,5-Trinitro-1*H*-pyrazole (0.25 g, 1 mmol, 2 eq.) was reacted with lithium carbonate (46 mg, 1 mmol, 1 eq.) in ethanol (10 mL) at room temperature overnight before the solvent was removed on a rotary evaporator. A yellow-brown solid was gained, which was recrystallized from ethanol (10 mL).

Lithium 4-oxo-3,5-dinitropyrazolate · 2 H₂O (15): 4-Hydroxy-3,5-dinitro-1*H*-pyrazole (0.60 g, 3 mmol, 1 eq.) and lithium hydroxide (83 mg, 3 mmol, 1 eq.) were dissolved in water/methanol (1:1, 10 mL) and the solution heated at 80 °C for 15 minutes. The mother

liquor was reduced in vacuo until yellow-orange crystals (0.64 g, 3 mmol, 86 %) precipitated from solution.

IR (ATR): $\tilde{\nu}$ = 3500 (w), 3400 (w), 3109 (m), 1680 (vw), 1617 (s), 1447 (m), 1389 (s), 1298 (vs), 1250 (s), 1207 (s), 982 (s), 855 (m), 835 (m), 799 (m), 761 (s), 738 (m), 603 (s), 546 (s), 531 (s), 519 (s), 467 (s) cm^{-1} . $^7\text{Li}\{\text{H}\}$ NMR (DMSO- d_6 , 25 °C): δ = 1.8 (s, *Li*) ppm. $^{14}\text{N}\{\text{H}\}$ NMR (DMSO- d_6 , 25 °C): δ = -23.2 (br s, *NO*₂) ppm. $^{13}\text{C}\{\text{H}\}$ NMR (DMSO- d_6 , 25 °C): δ = 142.1 (s, C-O), 140.7 (s, C-*NO*₂) ppm. $^1\text{H}\{\}$ NMR (DMSO- d_6 , 25 °C): δ = 5.06 (br s, 4H, *H*₂O) ppm. EA (LiC₃H₅N₄O₇, 216.03): calcd. N 25.94, C 16.68, H 2.33 %; found N 25.86, C 16.76, H 2.39 %. DTA (5 °C min⁻¹): 109 (endothermic), 189 (exothermic), 269 (exothermic) °C. FS (< 100 μm): > 360 N. IS (< 100 μm): > 40 J. ESD (< 100 μm): 0.2 J.

Acknowledgements

For financial support of this work by Ludwig-Maximilian University (LMU), the Office of Naval Research (ONR) under grant no. ONR N00014-19-1-2078 and the Strategic Environmental Research and Development Program (SERDP) under contract no. W912HQ19 C0033 are gratefully acknowledged. Open Access funding enabled and organized by Projekt DEAL.

8.5 References

- [1] A. A. Zaitsev, I. L. Dalinger, S. A. Shevelev, *Russ. Chem. Rev.* **2009**, *78*, 589–627.
- [2] H. Gao, J. M. Shreeve, *Chem. Rev.* **2011**, *111*, 7377–7436.
- [3] G. Steinhauser, G. Giester, N. Leopold, C. Wagner, M. Villa, A. Musilek, *Helv. Chim. Acta* **2010**, *93*, 183–202.
- [4] M. Göbel, T. M. Klapötke, *Acta Crystallogr. C* **2007**, *63*, o562–o564.
- [5] M. F. Bölter, A. Harter, T. M. Klapötke, J. Stierstorfer, *ChemPlusChem* **2018**, *83*, 804–811.
- [6] G. Herve, C. Roussel, H. Graindorge, *Angew. Chem.* **2010**, *122*, 3245–3249; *Angew. Chem. Int. Ed.* **2010**, *49*, 3177–3181.
- [7] Y.-C. Li, C. Qi, S.-H. Li, H.-J. Zhang, C.-H. Sun, Y.-Z. Yu, S.-P. Pang, *J. Am. Chem. Soc.* **2010**, *132*, 12172–12173.
- [8] Y. Zhang, Y. Guo, Y.-H. Joo, D. A. Parrish, J. M. Shreeve, *Chem. Eur. J.* **2010**, *16*, 10778–10784.
- [9] H. H. Cady, A. C. Larson, *Acta Crystallogr.* **1965**, *18*, 485–496.
- [10] P. Yin, D. A. Parrish, J. M. Shreeve, *J. Am. Chem. Soc.* **2015**, *137*, 4778–4786.
- [11] I. L. Dalinger, I. A. Vatsadze, T. K. Shkineva, G. P. Popova, S. A. Shevelev, Y. V. Nelyubina, *J. Heterocycl. Chem.* **2013**, *50*, 911–924.
- [12] R. D. Schmidt, G. S. Lee, P. F. Pagoria, A. R. Mitchell, *J. Heterocycl. Chem.* **2001**, *38*, 1227–1230.
- [13] T. M. Klapötke, T. G. Witkowski, *Propellants Explos. Pyrotech.* **2016**, *41*, 470–483.
- [14] I. E. Drukenmüller, T. M. Klapötke, Y. Morgenstern, M. Rusan, J. Stierstorfer, *Z. Anorg. Allg. Chem.* **2014**, *640*, 2139–2148.
- [15] E.-C. Koch, *J. Pyrotech.* **2001**, 1–8.
- [16] E. Storey, *J. Bone Jt. Surg.* **1965**, *47B*, 145–156.
- [17] J. Glück, T. M. Klapötke, M. Rusan, J. J. Sabatini, J. Stierstorfer, *Angew. Chem.* **2017**, *129*, 16733–16736; *Angew. Chem. Int. Ed.* **2017**, *56*, 16507–16509.
- [18] E.-C. Koch, C. Jennings-White in *Proceedings of the 36th International Pyrotechnics Seminar*, Rotterdam, **2009**, pp. 105–110.

- [19] J. J. Sabatini, E.-C. Koch, J. C. Poret, J. D. Moretti, S. M. Harbol, *Angew. Chem.* **2015**, *127*, 11118–11120; *Angew. Chem. Int. Ed.* **2015**, *54*, 10968–10970.
- [20] C. G. James, T. M. Sugden, *Proc. R. Soc. Lond.* **1958**, *248A*, 238–247.
- [21] J. W. A. M. Janssen, H. J. Koeners, C. G. Kruse, C. L. Habraken, *J. Org. Chem.* **1973**, *38*, 1777–1782.
- [22] R. Hüttel, F. Büchele, *Chem. Ber.* **1955**, *88*, 1586–1590.
- [23] J. W. A. M. Janssen, C. L. Habraken, *J. Org. Chem.* **1971**, *36*, 3081–3084.
- [24] J. W. A. M. Janssen, C. L. Habraken, R. Louw, *J. Org. Chem.* **1976**, *41*, 1758–1762.
- [25] a) A. R. Katritzky, E. F. V. Scriven, S. Majumder, R. G. Akhmedova, N. G. Akhmedov, A. V. Vakulenko, *Arkivoc* **2005**, 179–191. b) P. Ravi, C. K. Reddy, A. Saikia, G. M. Gore, A. K. Sikder, S. P. Tewari, *Propellants Explos. Pyrotech.* **2012**, *37*, 167–171. c) P. Ravi, G. M. Gore, A. K. Sikder, S. P. Tewari, *Synth. Commun.* **2012**, *42*, 3463–3471. d) P. Ravi, S. P. Tewari, *Catal. Commun.* **2013**, *42*, 35–39. e) P. Ravi, G. M. Gore, S. P. Tewari, A. K. Sikder, *J. Heterocycl. Chem.* **2013**, *50*, 1322–1327. f) P. Ravi, S. P. Tewari, *Catal. Commun.* **2012**, *19*, 37–41. g) P. Ravi, S. P. Tewari, *Propellants Explos. Pyrotech.* **2013**, *38*, 147–151.
- [26] A. M. W. Dufter, T. M. Klapötke, M. Rusan, A. Schweiger, J. Stierstorfer, *ChemPlusChem* **2020**, *85*, 2044–2050.
- [27] X. Zhao, C. Qi, L. Zhang, Y. Wang, S. Li, F. Zhao, S. Pang, *Molecules* **2014**, *19*, 896–910.
- [28] a) P. F. Pagoria, A. R. Mitchell, R. D. Schmidt, *J. Org. Chem.* **1996**, *61*, 2934–2935. b) S. Ek, N. V. Latypov, *J. Heterocycl. Chem.* **2014**, *51*, 1621–1627.
- [29] I. L. Dalinger, I. A. Vatsadze, T. K. Shkineva, G. P. Popova, S. A. Shevelev, *Synthesis* **2012**, *44*, 2058–2064.
- [30] a) L. TianLi, W. Jianlong, C. Lizhen, C. DuanLin, L. ZhiYan, W. NaNa, *Z. Kristallogr. NCS* **2019**, *234*, 933–934. b) B. Hu, Q. Shi, F. Lu, P. Zhang, P. Peng, C. Zhao, Y. Du, H. Su, S. Li, S. Pang, F. Nie, *Synlett* **2019**, *30*, 910–918. c) D. Fischer, J. L. Gottfried, T. M. Klapötke, K. Karaghiosoff, J. Stierstorfer, T. G. Witkowski, *Angew. Chem.* **2016**, *128*, 16366–16369; *Angew. Chem. Int. Ed.* **2016**, *55*, 16132–16135. d) Y.-L. Wang, F.-Q. Zhao, K.-Z. Xu, Y.-P. Ji, J.-H. Yi, B. Chen, T. An, *Inorg. Chim. Acta* **2013**, *405*, 505–510. e) Y. Zhang, Y. Huang, D. A. Parrish, J. M. Shreeve, *J.*

Mater. Chem. **2011**, *21*, 6891–6897. f) Y. V. Nelyubina, I. L. Dalinger, K. A. Lyssenko, *Russ. Chem. Bull.* **2013**, *62*, 1707–1719. g) P. Yin, L. A. Mitchell, D. A. Parrish, J. M. Shreeve, *Chem.: Asian J.* **2017**, *12*, 378–384. h) Y.-L. Wang, F.-Q. Zhao, Y.-P. Ji, J.-H. Yi, T. An, W.-X. Liu, *Chin. Chem. Lett.* **2014**, *25*, 902–906.

[31] J. Berthou, J. Elguero, C. Rerat, *Acta Crystallogr. B* **1970**, *26*, 1880–1881.

[32] J. J. Sabatini in *Green Energetic Materials* (Ed.: T. Brinck), Wiley, Chichester, **2014**, p. 64.

8.6 Supplementary Information

8.6.1 Synthesis Optimization

Partial *N*-denitration of 1,3-dinitro-*H*-pyrazole during its thermal rearrangement to 3,5-dinitro-1*H*-pyrazole has been a known problem for a long time.^[S1] The crude product can be purified either by crystallization from benzene^[S1] or by precipitation of the sodium salt and subsequent acidification.^[S2] Due to the toxicity of benzene, the second method was chosen. However, when working on a 1 g-scale sodium 3,5-dinitro-*H*-pyrazolate does not precipitate upon the addition of 2M sodium hydroxide solution and the aqueous phase then contains sodium 3-nitro-*H*-pyrazolate as well as the 3,5-dinitro-*H*-pyrazolate analogue. We assume that both sodium salts are well soluble in water and mainly their concentrations in aqueous media decide over precipitation. Using saturated sodium hydroxide solution ensures that a solid is formed and thus 3-nitro-1*H*-pyrazole is removed (see Figure S1).

is removed (see Figure S1).

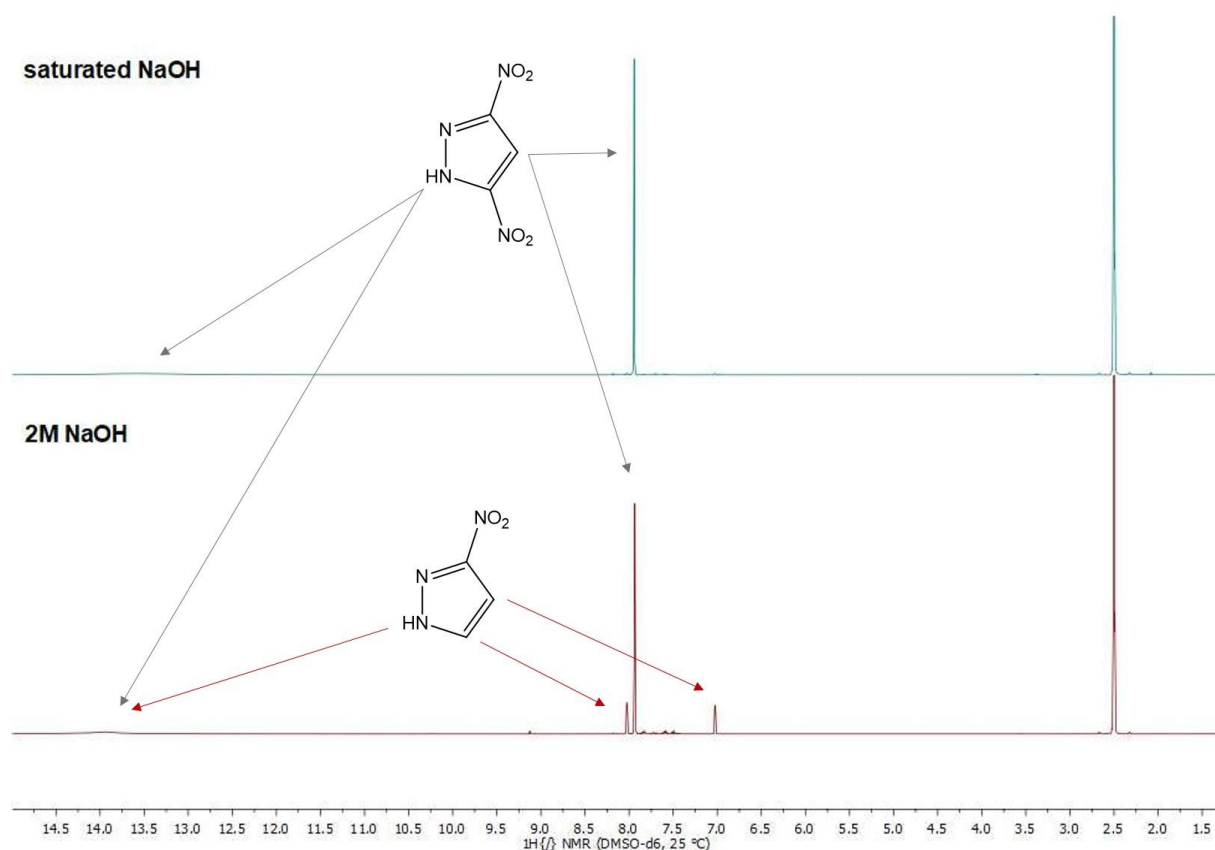


Figure S1. ¹H NMR spectra of 3,5-dinitro-1*H*-pyrazole (**5**) from bottom to top synthesized using 2M or saturated sodium hydroxide solution, respectively.

8.6.2 Thermal Dehydration Studies

Lithium 3,4-dinitropyrazolate · H₂O

After a sample of this salt had been stored at ambient conditions overnight, a broad endothermic signal above 100 °C occurred in the DTA curve (see Figure S2).

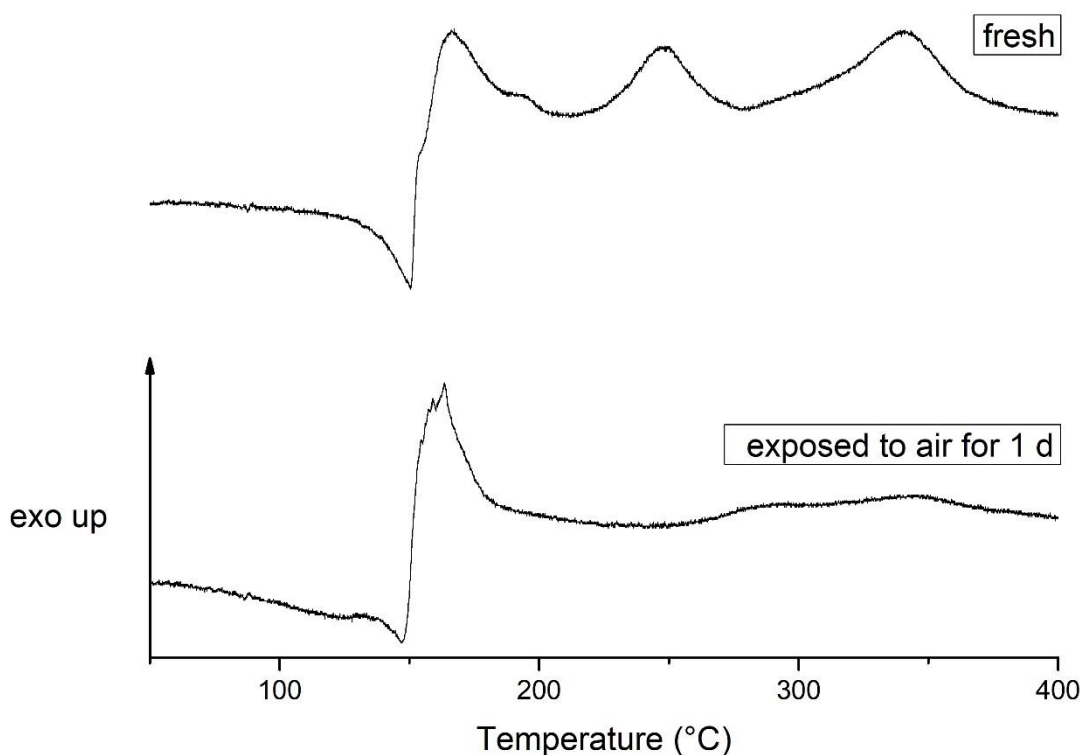


Figure S2. DTA plots of lithium 3,4-dinitropyrazolate · H₂O (**11**) from top to bottom before and after exposure to air for one day.

Lithium 3,5-dinitropyrazolate · 2.5 H₂O

While low-temperature single-crystal X-ray diffraction revealed lithium 3,5-dinitropyrazolate to crystallize as a trihydrate, elemental analysis of the same sample gave a crystal water content of 2.5. As a consequence, an uniform and reproducible form of the target compound was aimed at by dehydration of the recrystallized synthesis product in an oven at 100 °C overnight. However, after exposure of the water-free moiety to air for one day differential thermal analysis showed the endothermic signal at roughly 60 °C

indicating the loss of crystal water (see Figure S3) and according to elemental analysis the formula unit included 2.5 water molecules.

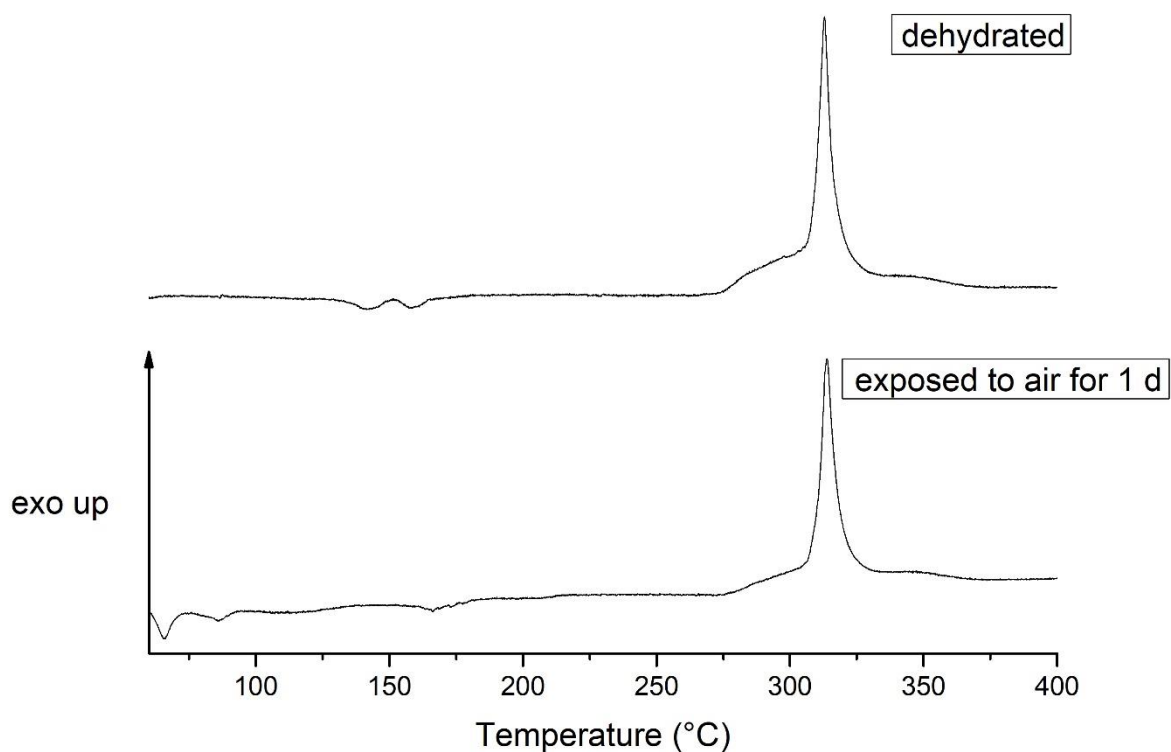


Figure S3. DTA plots of water-free lithium 3,5-dinitropyrazolate (**12**) from top to bottom before and after exposure to air for one day.

This hydrate seems to be stable, since no change in composition was detected after storage at ambient conditions overnight neither by DTA nor by elemental analysis.

Lithium 4-amino-3,5-dinitropyrazolate · 1.5 H₂O

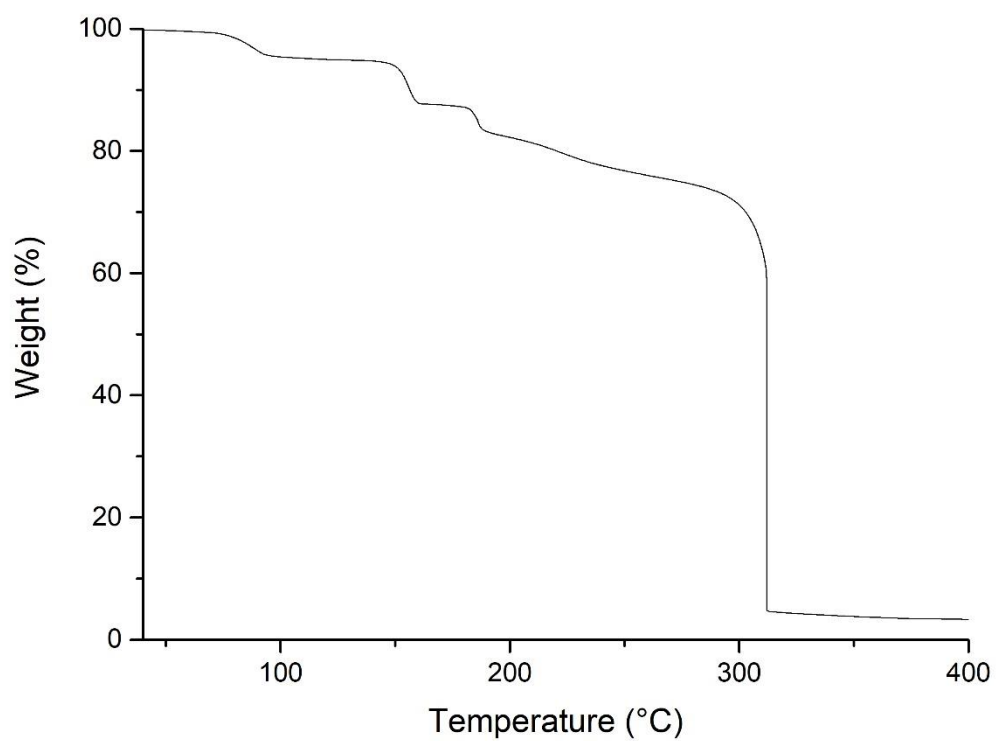


Figure S4. TGA plot of lithium 4-amino-3,5-dinitropyrazolate · 1.5 H₂O (13).

Lithium 3,4,5-trinitropyrazolate · H₂O

The strong hygroscopicity of the title compound shows in an endothermic signal at approximately 50 °C which appears in the DTA curve after exposure to air for one day (see Figure S5).

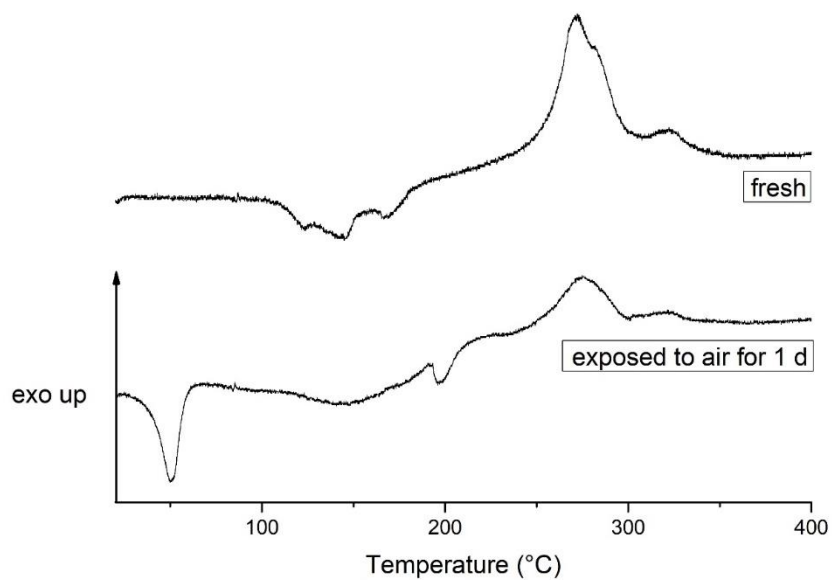


Figure S5. DTA plots of lithium 3,4,5-trinitropyrazolate · H₂O (**14**) from top to bottom before and after exposure to air for one day.

Lithium 4-oxo-3,5-dinitropyrazolate · 2 H₂O

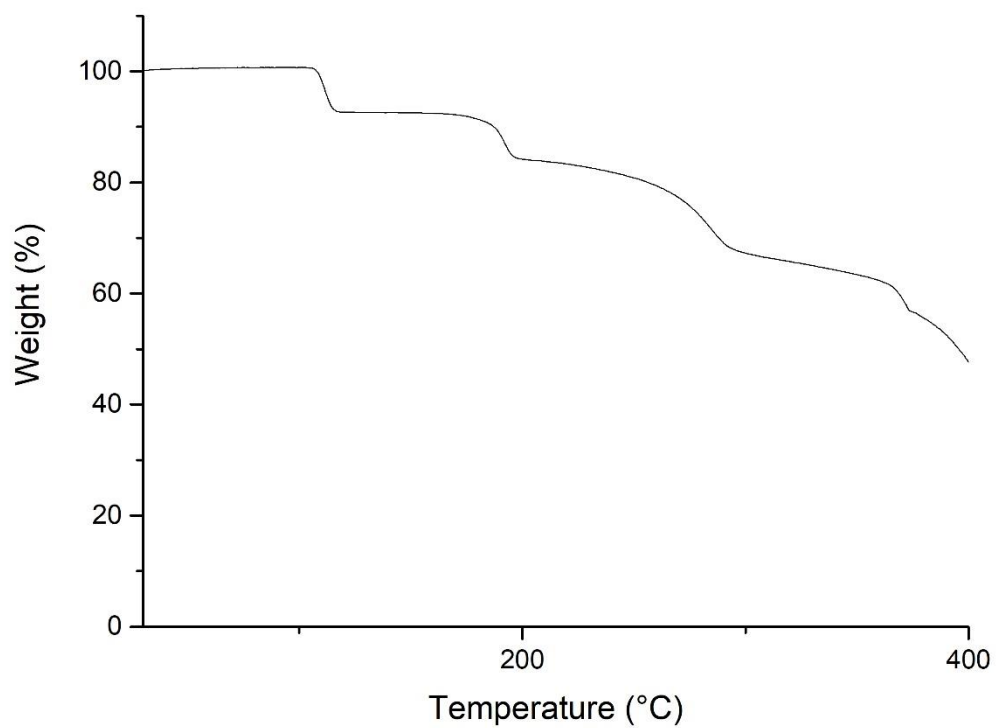


Figure S6. TGA plot of lithium 4-oxo-3,5-dinitropyrazolate · 2 H₂O (15).

8.6.3 General Methods

1*H*-pyrazole with a purity of 98 % was purchased from ABCR. Strontium nitrate with a purity of 98 % and ammonium nitrate with a purity of 99 % were received from GRÜSSING GMBH, magnesium with a purity of 98 % and grain sizes between 20 and 230 mesh from SIGMA-ALDRICH, 5-amino-1*H*-tetrazole with a purity of 98 % from ABCR, and EPON RESIN 813 and VERSAMID 140 from MILLER-STEPHENSON. Apart from magnesium, which was sieved, all chemicals were used as such. While 1-*N*-nitropyrazole^[S2], 3-nitro-1*H*-pyrazole^[S3], 3,4-dinitro-1*H*-pyrazole^[S2], 1,3-dinitropyrazole^[S2], 4-chloro-1*H*-pyrazole^[S4], 4-chloro-3,5-dinitro-1*H*-pyrazole^[S4], and 4-amino-3,5-dinitro-1*H*-pyrazole^[S4] were synthesized by our recently established procedures, 3,4,5-trinitro-1*H*-pyrazole^[S5] and 4-hydroxy-3,5-dinitro-1*H*-pyrazole^[S6] were prepared according to literature.

IR spectra of compounds **3**, **5**, **8**, **11**, **12** · 2.5 H₂O, **13**, and **15** were recorded by means of a PERKINELMER BXII FT-IR system provided with a SMITH DURASAMPLER IR II diamond ATR. NMR measurements were performed on a BRUKER 400, JEOL ECLIPSE 270, JEOL EX-400 or a JEOL ECLIPSE 400 instrument. The ¹H and ¹³C NMR shifts given in the Experimental Part relate to tetramethylsilane as internal standard, whereas the ¹⁴N NMR shifts are in relation to nitromethane and the ⁷Li NMR shifts to lithium chloride. All NMR samples were dissolved in DMSO-*d*₆. Elemental analysis was carried out on an ELEMENTAR VARIO EL or on a VARIO MICRO CUBE. The lithium salts **11**, **12** · 2.5 H₂O, and **13–15**, the crystal structures of which have not been published so far to the best of our knowledge, were additionally characterized by low-temperature single crystal X-ray diffraction using an OXFORD XCALIBUR3 diffractometer with a CCD area detector and a SPELLMAN HIGH VOLTAGE generator. The instrument applied Mo-*K*_α radiation with a wavelength of 0.71073 Å and the measuring temperatures varied between 107 and 123 K. The data collection and reduction were conducted with a CRYALISPRO software^[S7]. The crystal structures were solved by SIR92^[S8] and refined by full-matrix least-squares on *F*² (SHELXL^[S9]), whereby non-hydrogen atoms were refined anisotropically and the hydrogen atoms were located and freely refined. The structures thus obtained were checked using the PLATON software^[S10] integrated in the WINGX software suite^[S11] and the absorptions were corrected by a SCALE3 ABSPACK multiscan method^[S12]. Thermal ellipsoids in the DIAMOND2 plots represent the 50 % probability level and hydrogen atoms are depicted as small spheres of arbitrary radius. DTA of moieties **3**, **5**, **8**, **11**, **12** · 2.5 H₂O, **13**, and **15** was performed on an OZM DTA 552-Ex instrument in the temperature range of 25–400 °C at a heating rate of 5 °C min⁻¹. The onset temperatures of endothermic peaks indicating loss of water, melting or vaporization as well as of exothermic peaks implying decomposition are presented in the Experimental Section. In addition to that, **13**

and **15** were characterized by TGA in the temperature range of 30–400 °C at a heating rate of 5 °C min⁻¹ using a PERKINELMER TGA 4000 device. In order to further evaluate the suitability of the lithiated materials **11**, **12** · 2.5 H₂O, **13**, and **15** as red pyrotechnic colorants from a safety perspective, their sensitivities toward friction were determined by means of a BUNDESANSTALT FÜR MATERIALFORSCHUNG UND -PRÜFUNG (BAM) friction tester according to NATO Standardization Agreement (STANAG) 4487^[S13] with a modified instruction^[S14], impact sensitivities with the aid of a BAM drop hammer according to STANAG 4489^[S15] with a modified instruction^[S16], both using the 1-out-of-6 method, and the electrostatic discharge sensitivities by using an OZM X SPARK 10 instrument. The former were classified in regard of their friction and impact sensitivities according to the „UN Recommendations on the Transport of Dangerous Goods“: friction: insensitive > 360 N, less sensitive = 360 N, sensitive 360 N > FS > 80 N, very sensitive < 80 N, extremely sensitive < 10 N; impact: insensitive > 40 J, less sensitive > 35 J, sensitive > 4 J, very sensitive < 4 J.

All constituents of pyrotechnic formulations were weighed out according to their weight percentages with a deviation of 2 mg and hand-blended to homogeneous mixtures before solutions of EPON 813 and VERSAMID 140 in ethyl acetate with concentrations of roughly 20 or 10 g L⁻¹, respectively, were added in a weight percent ratio of 80:20. The resulting slurries were blended approximately every ten minutes until the solvent had completely evaporated. Subsequently, the compositions were cured at 60 °C over night and blended to fine powders. Portions of 500 mg were weighed out with a deviation of 2 mg and pressed in one increment at a consolidation dead load of 3 t with a dwell time of roughly 10 s by means of a tooling die to give cylindrically shaped pellets 12.9 mm in diameter and 466 to 500 mg in weight, respectively. The latter were ignited by the tip of a sparkler and their combustions recorded with the aid of a digital DCR-HC37E video camera from SONY. Dominant wavelengths, spectral purities, and luminous intensities of the formulations were measured by using an OCEAN INSIGHT HR2000+ES spectrometer with a SONY ILX511B linear silicon CCD array detector (range: 200–1100 nm) equipped with the SPECTRASUITE software at an acquisition time of 20 ms. The distance between the detector of the spectrometer and the sample was calibrated to 1.000 m. The dominant wavelengths as well as the color purities were processed based on the 1931 CIE method using illuminant C as the white reference point. All pyrotechnic performance parameters were determined taking the full burn of the pellets into account and were measured twice each. Additionally, thermal stability as well as sensitivity measurements of all formulations were carried out.

8.6.4 IR Spectra

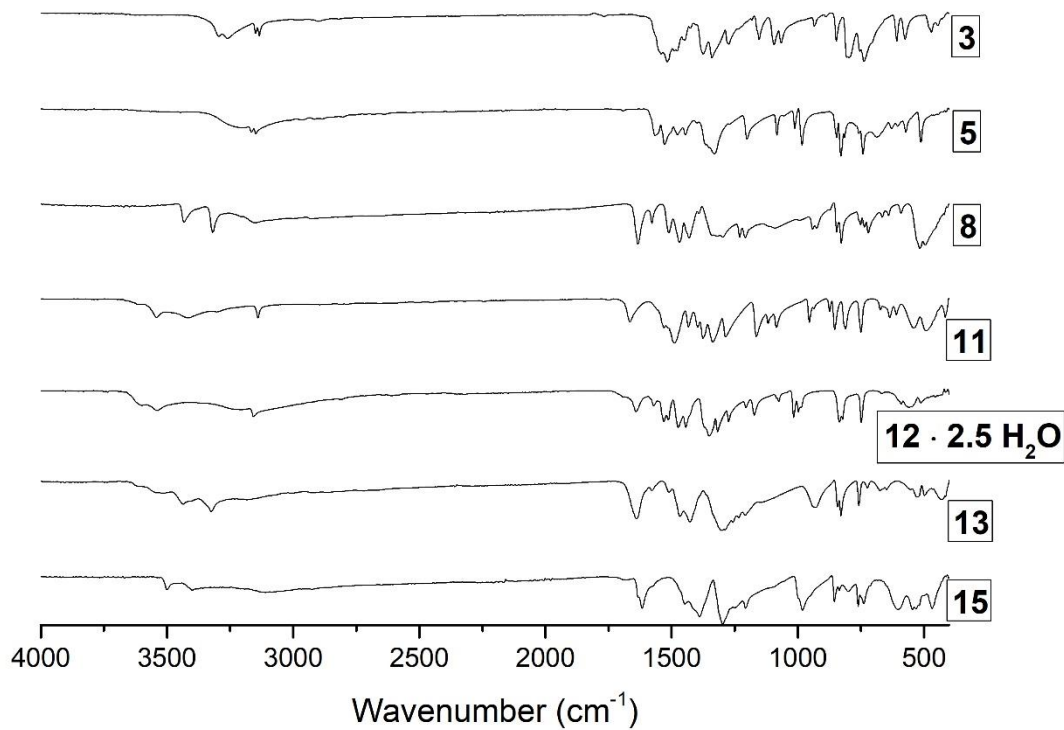


Figure S7. IR spectra from top to bottom of 3,4-dinitro-1*H*-pyrazole (**3**), 3,5-dinitro-1*H*-pyrazole (**5**), 4-amino-3,5-dinitro-1*H*-pyrazole (**8**), lithium 3,4-dinitropyrazolate · H₂O (**11**), lithium 3,5-dinitropyrazolate (**12**) · 2.5 H₂O, lithium 4-amino-3,5-dinitropyrazolate · 1.5 H₂O (**13**), and lithium 4-oxo-3,5-dinitropyrazolate · 2 H₂O (**15**).

8.6.5 NMR Spectra

^1H NMR Spectra

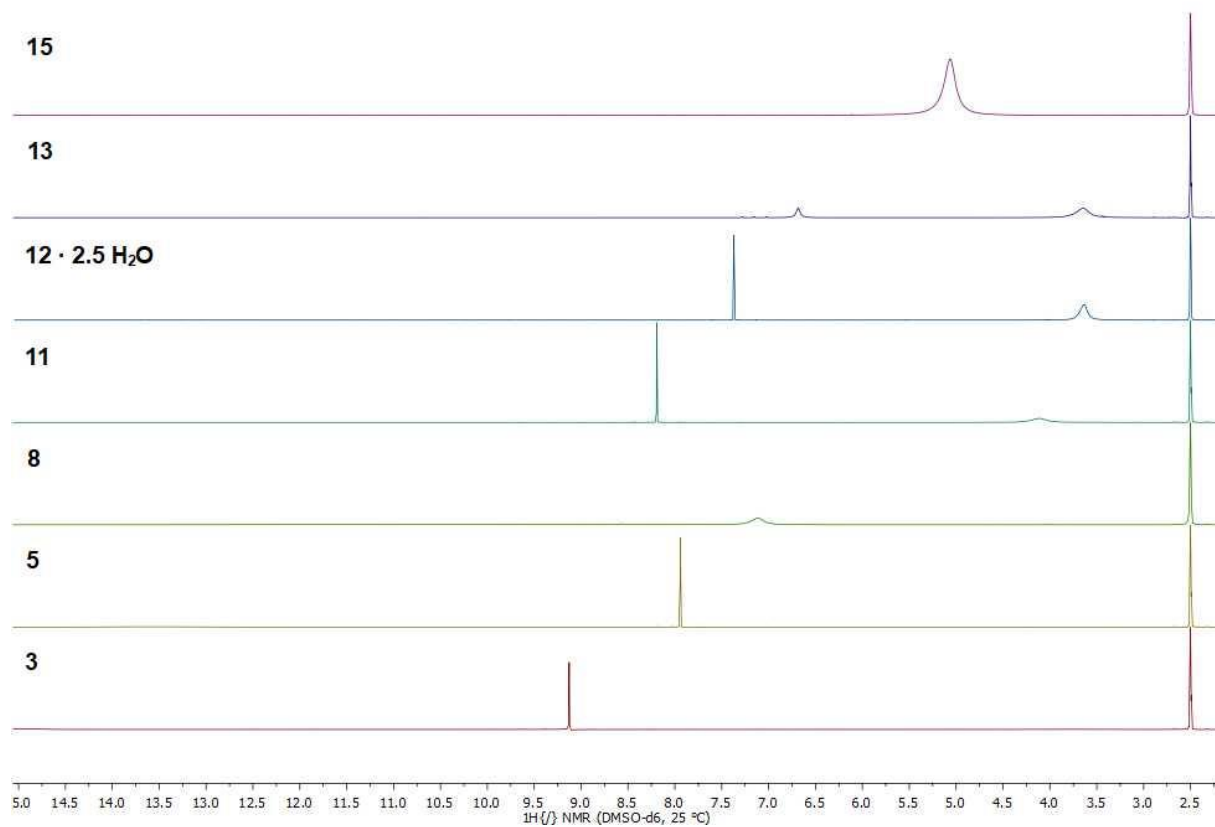


Figure S8. ^1H NMR spectra from bottom to top of 3,4-dinitro-1*H*-pyrazole (**3**), 3,5-dinitro-1*H*-pyrazole (**5**), 4-amino-3,5-dinitro-1*H*-pyrazole (**8**), lithium 3,4-dinitropyrazolate \cdot H_2O (**11**), lithium 3,5-dinitropyrazolate (**12**) \cdot $2.5 \text{H}_2\text{O}$, lithium 4-amino-3,5-dinitropyrazolate \cdot $1.5 \text{H}_2\text{O}$ (**13**), and lithium 4-oxo-3,5-dinitropyrazolate \cdot $2 \text{H}_2\text{O}$ (**15**).

^{13}C NMR Spectra

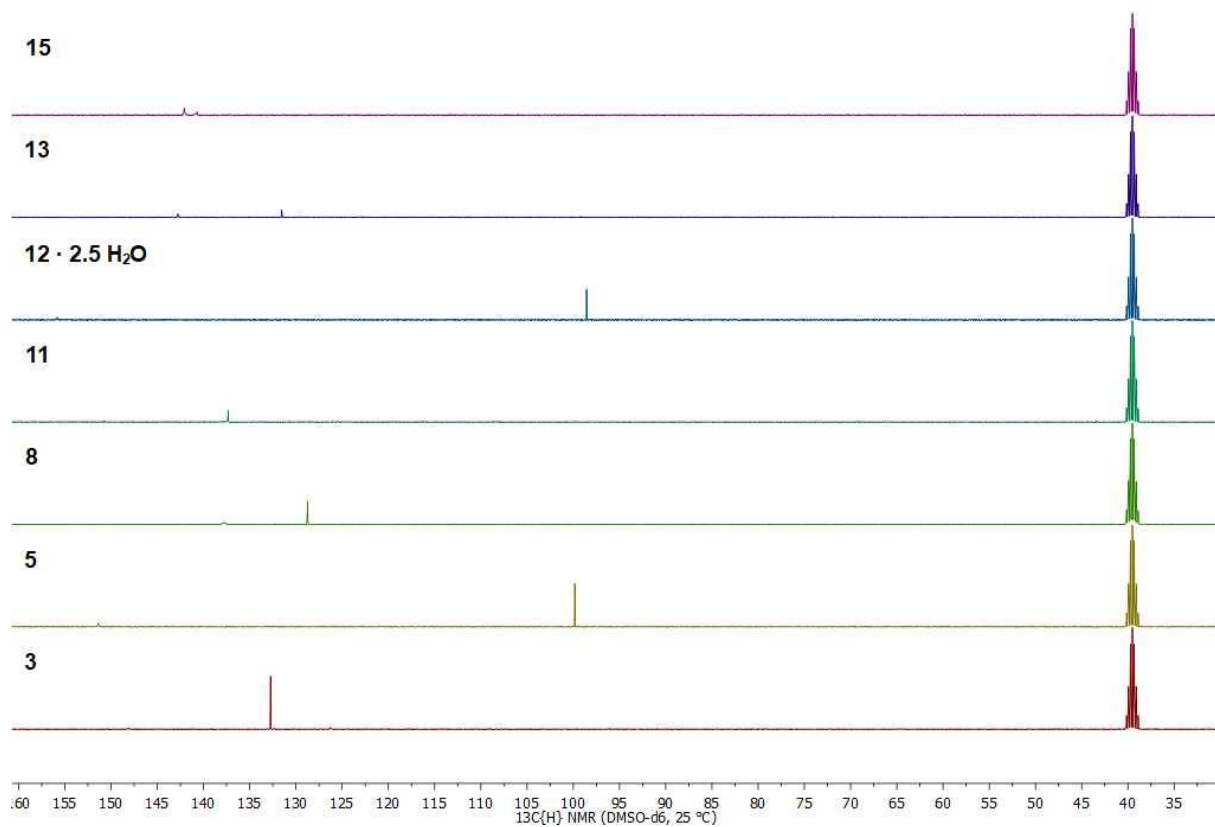


Figure S9. ^{13}C NMR spectra from bottom to top of 3,4-dinitro-1*H*-pyrazole (**3**), 3,5-dinitro-1*H*-pyrazole (**5**), 4-amino-3,5-dinitro-1*H*-pyrazole (**8**), lithium 3,4-dinitropyrazolate \cdot H_2O (**11**), lithium 3,5-dinitropyrazolate (**12**) \cdot $2.5 \text{ H}_2\text{O}$, lithium 4-amino-3,5-dinitropyrazolate \cdot $1.5 \text{ H}_2\text{O}$ (**13**), and lithium 4-oxo-3,5-dinitropyrazolate \cdot $2 \text{ H}_2\text{O}$ (**15**).

^{14}N NMR Spectra

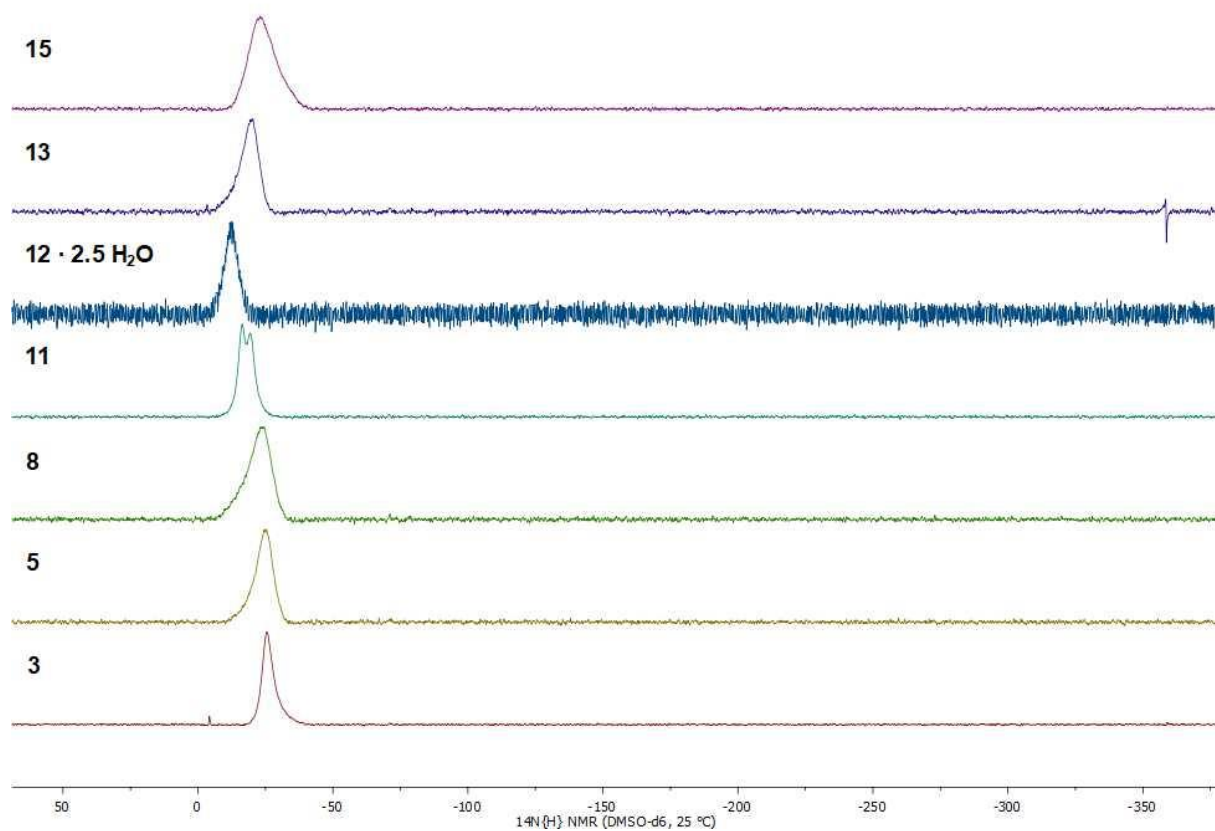


Figure S10. ^{14}N NMR spectra from bottom to top of 3,4-dinitro-1*H*-pyrazole (**3**), 3,5-dinitro-1*H*-pyrazole (**5**), 4-amino-3,5-dinitro-1*H*-pyrazole (**8**), lithium 3,4-dinitropyrazolate · H₂O (**11**), lithium 3,5-dinitropyrazolate (**12**) · 2.5 H₂O, lithium 4-amino-3,5-dinitropyrazolate · 1.5 H₂O (**13**), and lithium 4-oxo-3,5-dinitropyrazolate · 2 H₂O (**15**).

^7Li NMR Spectra

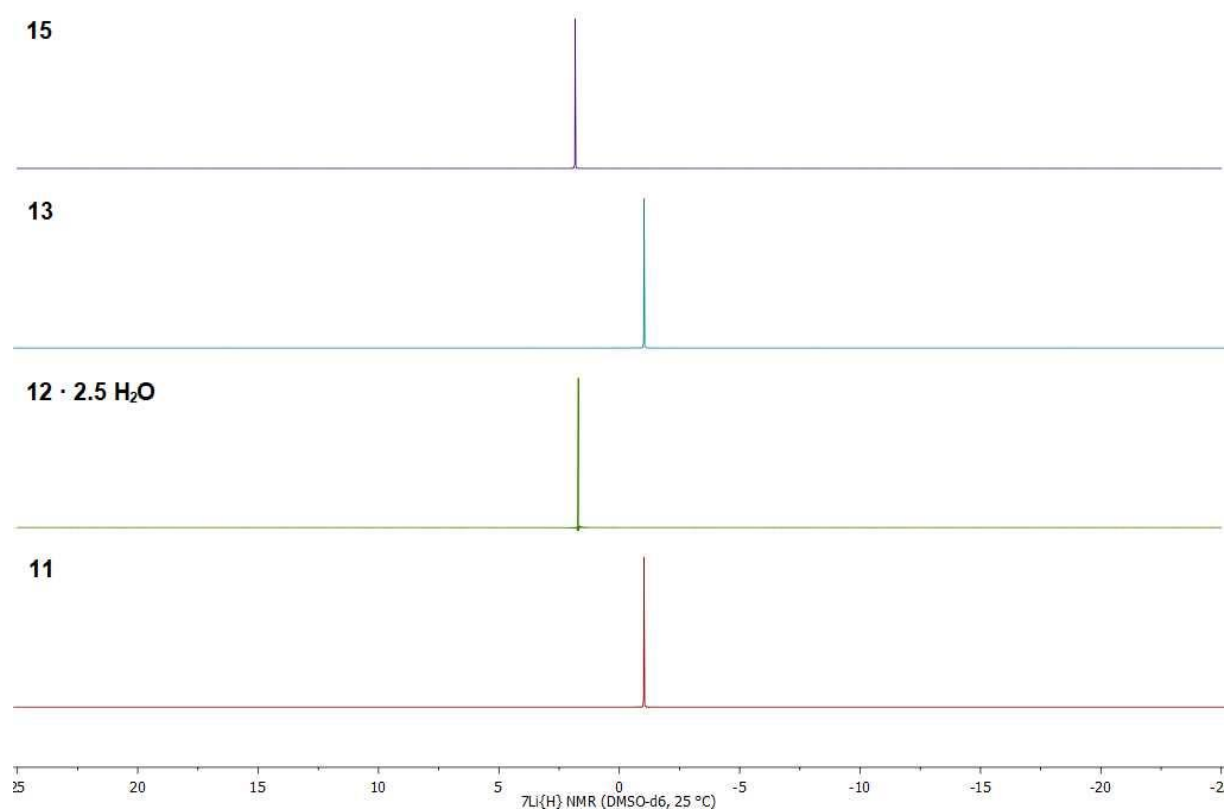


Figure S11. ^7Li NMR spectra from bottom to top of lithium 3,4-dinitropyrazolate · H₂O (**11**), lithium 3,5-dinitropyrazolate (**12**) · 2.5 H₂O, lithium 4-amino-3,5-dinitropyrazolate · 1.5 H₂O (**13**), and lithium 4-oxo-3,5-dinitropyrazolate · 2 H₂O (**15**).

8.6.6 Crystallographic Data

Table S1. Crystallographic data of lithium 3,4-dinitropyrazolate · H₂O (**11**), lithium 3,5-dinitropyrazolate (**12**) · 3 H₂O, lithium 4-amino-3,5-dinitropyrazolate · 1.5 H₂O (**13**), lithium 3,4,5-trinitropyrazolate · H₂O (**14**), and lithium 4-oxo-3,5-dinitropyrazolate · 2 H₂O (**15**).

	11	12 · 3 H₂O	13	14	15
Formula	LiC ₃ H ₃ N ₄ O ₅	LiC ₃ H ₇ N ₄ O ₇	LiC ₃ H ₅ N ₅ O _{5.5}	LiC ₃ H ₂ N ₅ O ₇	LiC ₃ H ₅ N ₄ O ₇
FW [g mol ⁻¹]	182.02	218.05	206.04	227.02	216.03
Crystal System	Monoclinic	Monoclinic	Triclinic	Monoclinic	Triclinic
Space Group	<i>P</i> 2 ₁ / <i>c</i>	<i>P</i> 2 ₁ / <i>n</i>	<i>P</i> -1	<i>P</i> 2 ₁ / <i>n</i>	<i>P</i> -1
Color/Habit	Yellowish block	Colorless rod	Yellow rod	Yellow block	Yellow block
Size [mm]	0.09 x 0.18 x 0.42	0.08 x 0.25 x 0.40	0.05 x 0.05 x 0.50	0.34 x 0.39 x 0.63	0.08 x 0.13 x 0.34
<i>a</i> [Å]	3.4643(3)	3.3560(2)	3.4057(2)	9.3009(4)	5.9627(4)
<i>b</i> [Å]	9.5834(6)	17.3695(9)	9.1857(5)	19.8282(6)	7.1520(4)
<i>c</i> [Å]	19.5933(14)	14.1549(9)	12.3747(7)	9.5957(4)	8.9760(6)
α [°]	90	90	87.979(4)	90	98.096(5)
β [°]	91.967(7)	91.900(6)	86.748(4)	114.836(5)	94.427(5)
γ [°]	90	90	85.699(4)	90	101.984(5)
<i>V</i> [Å ³]	650.11(8)	824.66(8)	385.23(4)	1605.97(13)	368.46(4)
<i>Z</i>	4	4	1	4	2
$\rho_{\text{calc.}}$ [g cm ⁻³]	1.860	1.756	1.776	1.878	1.947
μ [mm ⁻¹]	0.172	0.168	0.164	0.181	0.188
<i>F</i> (000)	368	448	210	912	220
$\lambda_{\text{MoK}\alpha}$ [Å]	0.71073	0.71073	0.71073	0.71073	0.71073
<i>T</i> [K]	108	123	110	108	107
$\theta_{\text{Min-Max}}$ [°]	2.1, 24.7	1.9, 32.3	2.2, 32.3	2.1, 26.4	2.3, 28.3
Dataset	-4:4; -11:11; -23:23	-5:5; -25:25; -21:20	-5:3; -13:10; -17:18	-8:11; -24:23; -11:11	-7:7; -9:9; -11:11
Reflections Collected	7776	16785	3811	8606	4293
Independent Refl.	1093	2786	2503	3278	1818
<i>R</i> _{int}	0.044	0.035	0.027	0.021	0.025

Observed Reflections	973	2204	1900	2813	1446
Parameters	126	160	162	303	156
R_1 (obs) ^[a]	0.0776	0.0380	0.0537	0.0305	0.0371
wR_2 (all data) ^[b]	0.1912	0.1070	0.1750	0.0749	0.0872
Goof ^[c]	1.17	1.05	1.13	1.04	1.05
Resd. Dens. [e Å ⁻³]	-0.33, 0.60	-0.22, 0.43	-0.42, 0.69	-0.25, 0.30	-0.24, 0.39
Absorption Correction	multi-scan	multi-scan	multi-scan	multi-scan	multi-scan
CCDC	2021636	2021637	1998248	2021635	2021634

[a] $R_1 = \sum ||F_o| - |F_c|| / \sum |F_o|$. [b] $wR_2 = [\sum [w(F_o^2 - F_c^2)^2] / \sum [w(F_o)^2]]^{1/2}$, $w = [\sigma^2(F_o^2) + (xP)^2 + yP]^{-1}$, and $P = (F_o^2 + 2F_c^2) / 3$. [c] $\text{Goof} = \{ \sum [w(F_o^2 - F_c^2)^2] / (n-p) \}^{1/2}$ (n = number of reflections, p = total number of parameters).

8.6.7 DTA Plots

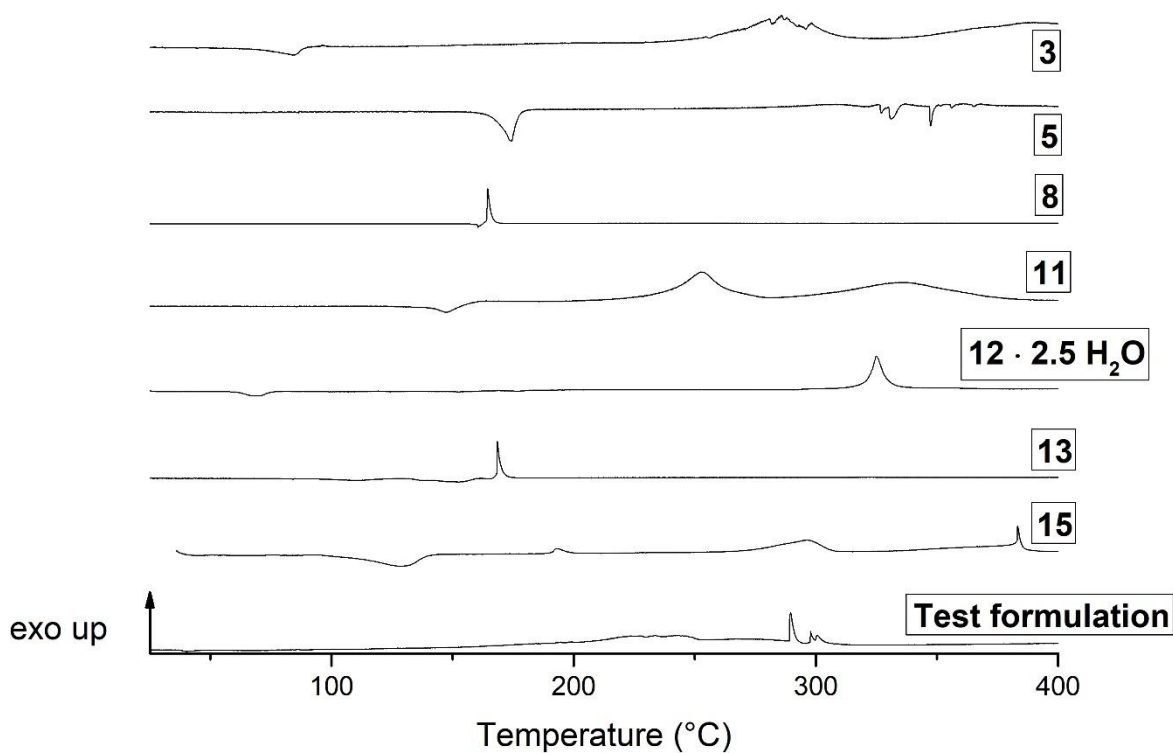


Figure S12. DTA curves from top to bottom of 3,4-dinitro-1*H*-pyrazole (**3**), 3,5-dinitro-1*H*-pyrazole (**5**), 4-amino-3,5-dinitro-1*H*-pyrazole (**8**), lithium 3,4-dinitropyrazolate · H₂O (**11**), lithium 3,5-dinitropyrazolate (**12**) · 2.5 H₂O, lithium 4-amino-3,5-dinitropyrazolate · 1.5 H₂O (**13**), lithium 4-oxo-3,5-dinitropyrazolate · 2 H₂O (**15**), and the test formulation.

8.6.8 Pyrotechnic Performance

Table S2. Composition of a test formulation containing lithium 4-amino-3,5-dinitropyrazolate · 1.5 H₂O (**13**).

NH ₄ NO ₃ [wt%]	Mg [wt%] ^[a]	13 [wt%]	EPON 813/VERSAMID 140 [wt%] ^[b]
48	12	30	10

[a] Magnesium with a mesh size 50/100 (300 μm > grain size > 150 μm). [b] EPON 813 and VERSAMID 140 in a weight percent ratio of 80:20.

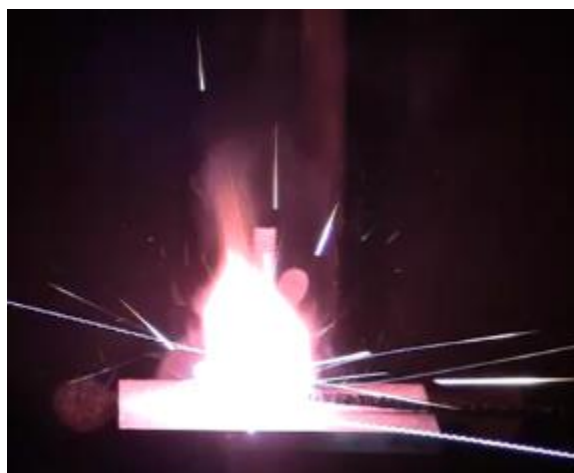


Figure S13. Combustion of the test formulation.

Table S3. Combustion parameters of the test formulation.

	BT [s] ^[a]	λ_d [nm] ^[b]	Σ [%] ^[c]	LI [cd] ^[d]
Sample 1	14.24	598.7	67.8	401
Sample 2	16.00	598.3	60.1	561
Average	15.12	598.5	64.0	481

[a] Burn time. [b] Dominant wavelength. [c] Spectral purity. [d] Luminous intensity.

8.6.9 References

- [S1] J. W. A. M. Janssen, H. J. Koeners, C. G. Kruse, C. L. Habraken, *J. Org. Chem.* **1973**, *38*, 1777–1782.
- [S2] M. F. Bölter, A. Harter, T. M. Klapötke, J. Stierstorfer, *ChemPlusChem* **2018**, *83*, 804–811.
- [S3] T. M. Klapötke, A. M. W. Dufter, M. Rusan, A. Schweiger, J. Stierstorfer, *ChemPlusChem* **2020**, *85*, 2044–2050.
- [S4] D. Fischer, J. L. Gottfried, T. M. Klapötke, K. Karaghiosoff, J. Stierstorfer, T. G. Witkowski, *Angew. Chem. Int. Ed.* **2016**, *55*, 16132–16135.
- [S5] Y. Zhang, Y. Guo, Y.-H. Joo, D. A. Parrish, J. M. Shreeve, *Chem. Eur. J.* **2010**, *16*, 10778–10784.
- [S6] I. L. Dalinger, I. A. Vatsadze, T. K. Shkineva, G. P. Popova, S. A. Shevelev, *Synthesis* **2012**, *44*, 2058–2064.
- [S7] *CrysAlisPro*, Version 171.33.41, Oxford Diffraction Ltd., **2009**.
- [S8] A. Altomare, G. Cascarano, C. Giacovazzo, A. Guagliardi, *J. Appl. Crystallogr.* **1992**, *26*, 343–350.
- [S9] a) G. M. Sheldrick, *SHELXL97, Program for the Refinement of Crystal Structures*, University of Göttingen, Germany, **1997**. b) G. M. Sheldrick, *Acta Crystallogr. A* **2008**, *64*, 112–122.
- [S10] A. L. Spek, *PLATON, A Multipurpose Crystallographic Tool*, Utrecht University, The Netherlands, **1999**.
- [S11] L. J. Farrugia, *J. Appl. Crystallogr.* **2012**, *45*, 849–854.
- [S12] Empirical absorption correction using spherical harmonics, implemented in SCALE3 ABSPACK scaling algorithm (CrysAlisPro, Version 171.33.41, Oxford Diffraction Ltd., 2009).
- [S13] NATO Standardization Agreement (STANAG) 4487, *Explosive, Friction Sensitivity Tests*, Aug. 22, **2002**.
- [S14] WIWEB-Standardarbeitsanweisung 4-5.1.03, *Ermittlung der Explosionsgefährlichkeit oder der Reibeempfindlichkeit mit dem Reibeapparat*, Nov. 8, **2002**.

[S15] NATO Standardization Agreement (STANAG) 4489, *Explosives, Impact Sensitivity Tests*, Sept. 17, **1999**.

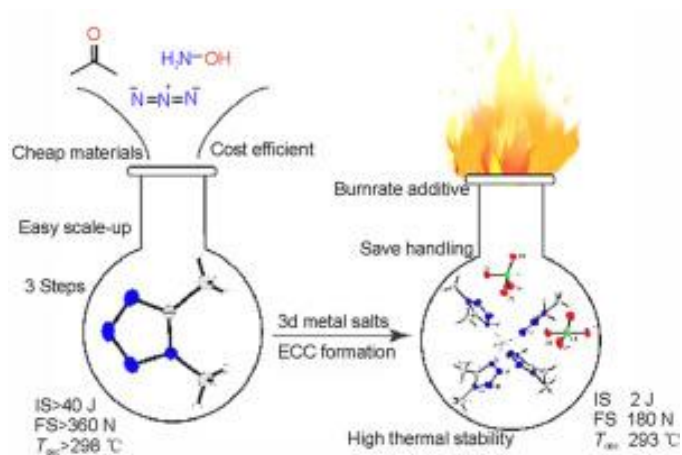
[S16] WIWEB-Standardarbeitsanweisung 4-5.1.02, *Ermittlung der Explosionsgefährlichkeit, hier der Schlagempfindlichkeit mit dem Fallhammer*, Nov. 8, **2002**.

9. 1,5-Dimethyltetrazole as a ligand in energetic 3d⁵ to 3d¹⁰-metal coordination compounds

Moritz Kofen, Alexander G. Harter, Thomas M. Klapötke, Jörg Stierstorfer*

as published in *Energetic Materials Frontiers* **2022**

DOI: 10.1016/j.enmf.2022.07.004



Key words: Transition metal; N-ligand; Energetic coordination compound; Tetrazole; Structure elucidation

Abstract: During the last decade, energetic coordination compounds gained considerable attention due to the simple adjustments in their physicochemical properties. By combining different metal cations, energetic anions, and ligands, those compounds can be adapted for their intended use. This study used 1,5-dimethyltetrazole (**3**) as a highly endothermic, easily accessible, and insensitive ligand. It is a structural isomer to 1-ethyl-5*H*-tetrazole (1-ETZ), which was recently described as a suitable ligand. 1,5-Dimethyltetrazole was synthesized using two different methods: (1) reaction of acetone with azido (trimethyl) silane and (2) reaction of acetoxime benzenesulfonate with sodium azide. Subsequently, 1,5-dimethyltetrazole was reacted with the perchlorate salts of different 3d metals (e.g., Mn, Fe, Co, Ni, Cu, Zn) to obtain new energetic coordination compounds (ECCs). In addition, copper (II) complexes with 2,4,6-trinitro-phenolate anions were synthesized. The resultant complexes were investigated through low-temperature, single crystal diffraction experiments complemented by elemental analysis, infrared spectroscopy, and differential thermal analysis. Moreover, sensitivities towards impact and friction were investigated. In this study, all ECCs exhibited impact sensitivities between 2–10 J, friction sensitivities between 128–360 N, and thermal stabilities of up to 360 °C.

9.1 Introduction

Owing to their physical and chemical properties, coordination compounds are critical to various applications, such as spin-crossover systems^{1,2}, metal-organic frameworks³, and energetic materials.⁴ Most specifically, metal-organic frameworks have recently gained significant attention as hypergolic solid fuels for aerospace applications.⁵⁻⁷ ECCs typically contain a 3d metal cation, are coordinated by a nitrogen-rich ligand, and gain charge balance with an oxidizing (e.g., ClO_4^- , ClO_3^-) or reducing (e.g., N_3^-) anion. Additionally, the concept of ECC formation expands many traditional synthetic approaches into new energetic materials, offering a broad range of further tuning the energetic properties towards their intended applications.^{8,9} Nevertheless, the synthesis of ligands themselves is subjected to the introduction of explosives¹⁰⁻¹¹, increasing enthalpy of formation by incorporating high amounts of nitrogen or oxygen in the molecule¹¹ or introducing a high strain.^{11,12} The use of azoles^{13,14} as ligands is highly desirable as they provide broad chemical diversity with high energy content due to their endothermic enthalpy of formation.¹¹ Furthermore, tetrazoles¹⁵⁻¹⁸ have been proven to be promising energetic compounds that are suitable to be applied as ligands in energetic coordination compounds.¹⁹⁻²⁰ Their energetic properties can be easily modified by altering their functional groups or substitution patterns, as shown in Fig. 1. 1,5-Dimethyltetrazole (DMT, **3**) is an easily accessible, small, neutral, and nitrogen-rich molecule, which makes it a potent candidate as an energetic ligand. Although the compound looks trivial, it has never

been used as a ligand; however, it offers a surprisingly high positive heat of formation. In this study, **3** was synthesized using different procedures from existing literature and further reacted with different 3d metal (e.g., Mn, Fe, Co, Ni, Cu, Zn) salts to form energetic coordination compounds. Besides their energetic properties, the change in the coordination of the ligand around the central metal was investigated. Finally, the influence of structural isomers was studied by comparing the ligands 1,5-dimethyltetrazole and 1-ethyl-5*H*-tetrazole.

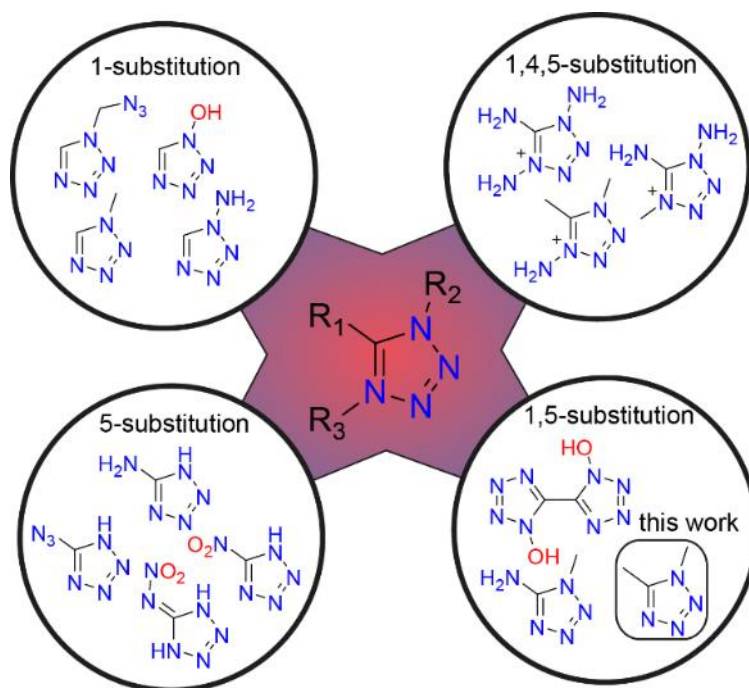


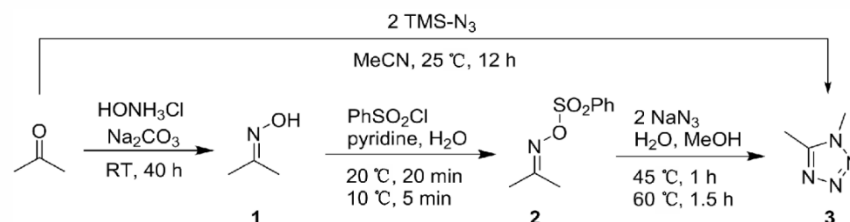
Figure 1. Possible substitution patterns of 1,2,3,4-tetrazole, which highlight the chemical diversity.^{17,18,21-26}

9.2 Results and Discussion

9.2.1 Synthesis

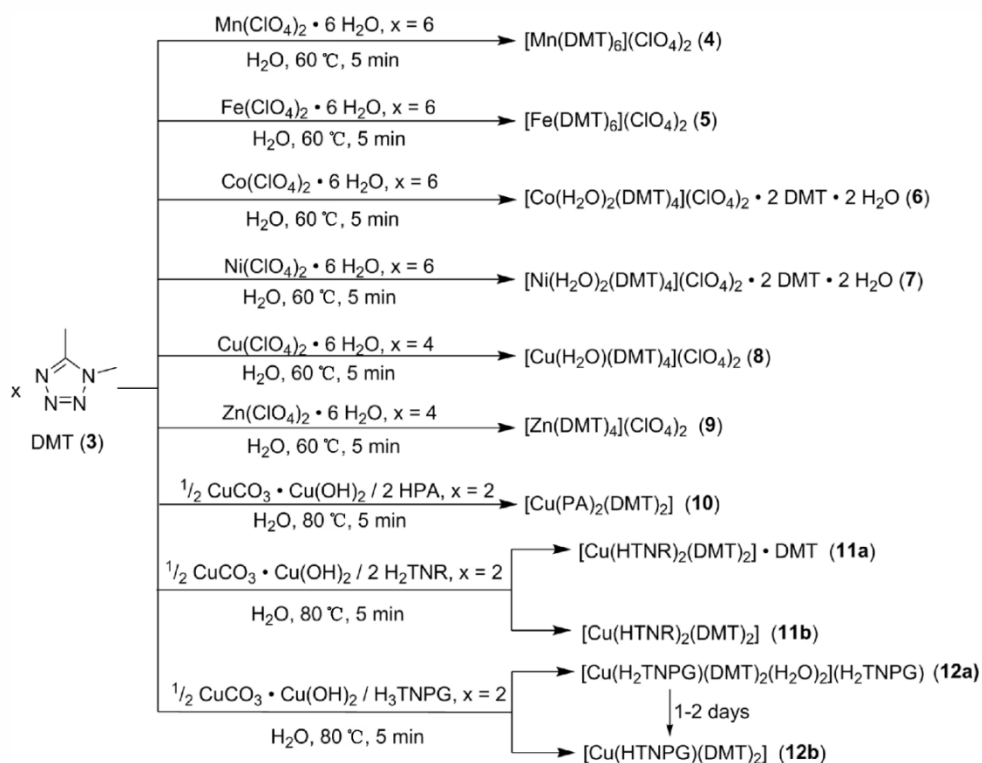
1,5-Dimethyltetrazole (DMT, **3**) can be synthesized by different routes according to relevant literature²⁷⁻²⁹ (Scheme 1). A straightforward method is the reaction of acetone with azidotrimethylsilane, which yields **3** in a one-step synthesis.³⁰ Another synthesis route starts with the reaction of acetone with hydroxylamine hydrochloride in water to form acetone oxime, followed by the reaction of acetone oxime with benzene sulfonyl chloride to form acetoxime benzenesulfonate, which acts as a leaving group in the final step of the reaction with sodium azide. The ring closure starts with a nucleophilic attack of the azide on the imine, accompanied by a [1,2]-rearrangement of one methyl group. Although the first synthesis procedure of applying trimethylsilylazide is more economical in terms of atoms, reaction time, and cost, the second procedure was preferred for the synthesis of **3**

on a 10–20 g scale since it has a slightly higher yield of 42% than the first one (34%). **3** can be obtained as a colorless solid in the form of blocky crystals through recrystallization from water.



Scheme 1. Synthetical routes of 1,5-DMT (**3**) starting with acetone.

ECCs **4–12** were synthesized by combining aqueous solutions of corresponding metal salts with stoichiometric amounts of **3** at elevated temperatures (60–80 °C; Scheme 2). Because of the unavailability of copper (II) nitroaromatic salts, their aqueous solutions were obtained by suspending basic copper (II) carbonate in water, adding corresponding free acid, and stirring at high temperatures until the solids dissolved. For compounds **4**, **8**, **9**, **10**, **11**, and **12**, crystals suitable for single crystal X-ray diffraction experiments were obtained. For compounds **5–7**, the evaporation of the solvent resulted in glass-like residues, from which single crystals started to grow under a high vacuum. After crystal structures of these compounds were obtained, further analysis was impossible – even by recrystallization from different solvents. When the aqueous solution of **3** was combined with that of copper (II) styphnate, solids began to precipitate immediately. This solid was insoluble and filtered off, and the resulting clear solution was left to crystallize. The growing crystals were collected and analyzed through single crystal X-ray diffraction as compound **11a**. Elemental analysis proved that the solid formed initially was compound **11b**, for which single crystals cannot be obtained. In the synthesis of compound **12**, needle-like (**12a**) and block-like (**12b**) crystals began to precipitate, and **12a** was consumed due to the formation of **12b** after several days. Therefore, **12b** was the main product. Complex **12a** contained deprotonated nitrophenol anions, one of which was coordinating and one was non-coordinating. The copper (II) cation in complex **12a** was further coordinated by two aqua ligands and two molecules of **3**. By contrast, the copper (II) cation in **12b** was coordinated by two double deprotonated anions, bridging different metal centers. Each center was also coordinated by two molecules of **3**, with no inclusion of water.



Scheme 2. Synthesis of energetic coordination compounds 4–12.

9.2.2 Crystal Structures

Compound **3** and all ECCs were characterized through low-temperature single-crystal X-ray diffraction. The crystal density of all structures was recalculated to values at room temperature (298 K) for the sake of comparison. The datasets of all compounds (except for **7**) were uploaded to the CSD database and can be accessed for free with CCDC 2169296 (**3**), 2163674 (**4**), 2163667 (**5**), 2163668 (**6**), 2163673 (**8**), 2163675 (**9**), 2163671 (**10**), 2163670 (**11a**), 2163672 (**12a**), and 2163669 (**12b**). The obtained crystals of **7** had poor quality, rendering proper measurement and refinement impossible. Nonetheless, an insight into the compound's composition and the coordination of the nickel (II) cation can be obtained. The depiction of the obtained structure is provided in the supporting information (Fig. S1). Compound **3** crystallizes in the orthorhombic space group *Pnma* with four formula units per cell and a density of 1.31 g·cm⁻³. While the bond lengths are in the same range as those of comparable 1- or 5-methyltetrazoles, **3** exhibits a mirror axis (σ_v) due to a C/N disorder (Fig. 2). This causes a difficult distinction between the C1 and N1 atoms, which is intensified by a simultaneous sharing of the atoms' positions. The crystal packing of **3** along the *b* axis (Fig. 2b) represents the stacking in sets of perpendicular but rotated against molecules of **3** (red/blue). The packing along the *c* axis

(Fig. 2b) shows that these sets exhibit an offset and are not face-on with each other, thereby presenting a screw-axis of 3 along the b axis.

Compounds **4** and **5** crystallize in the triclinic space group, $P\bar{3}$, and their calculated density is $1.53 \text{ g}\cdot\text{cm}^{-3}$ and $1.55 \text{ g}\cdot\text{cm}^{-3}$, respectively, with one formula unit per cell. The manganese (II) cation of **4** (Fig. 3, top) shows sixfold coordination by 1,5-DMT ligands,

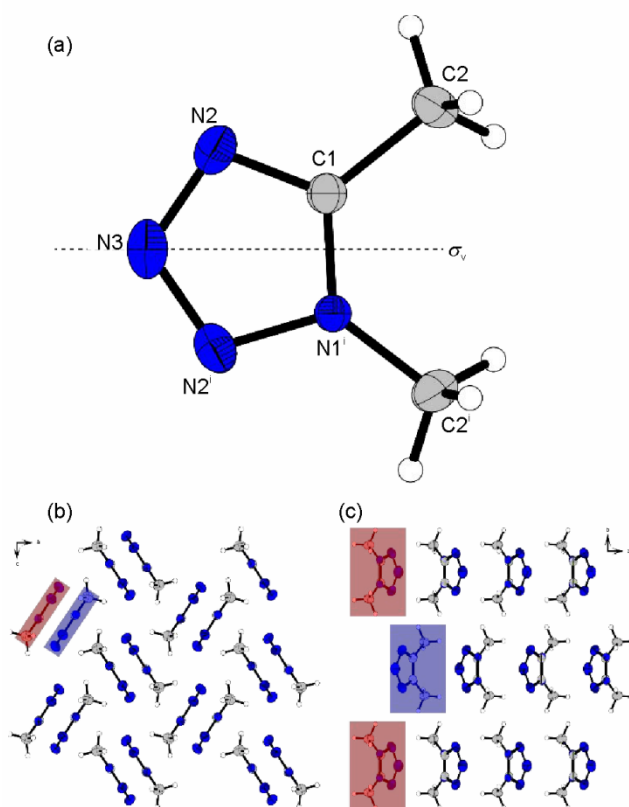


Figure 2. (a) Molecular structure of 1,5-dimethyltetrazole (**3**); (b) crystal packing of **3** along b -axis; (c) crystal packing of **3** along c -axis. Selected bond lengths [Å]: N1–N2 1.350(6), N1–C2 1.414(6), N2–N3 1.325(14), N2–C1 1.319(7), C1–C2 1.529(7); All ellipsoids are depicted with a probability of 50%. Symmetry codes: i) $+x, 3/2-y, +z$

forming a nearly perfect octahedron. Thus, only minor deviation angles of 0.06° from the perfect octahedron and M–L bond lengths of 2.303 Å for all six ligands can be observed. Accordingly, the manganese (II) cation with an electron configuration of $[\text{Ar}]3d^54s^0$ is in its high-spin state. Additionally, the iron cation of **5** (Fig. 3, bottom) also shows sixfold coordination by 1,5-DMT ligands, forming an octahedron with an angle deviation of only 0.65° from the perfect octahedron. The distortion is caused by the electron configuration of $[\text{Ar}]3d^6$ for a high-spin (hs) Fe (II) cation, leading to one fully filled t_{2g} orbital (Fig. 4). Since the t_{2g} orbitals do not participate in the building of σ -bonds and the π -back bonding is weak, the overall M–L bond lengths are not influenced by this distortion. Accordingly, a

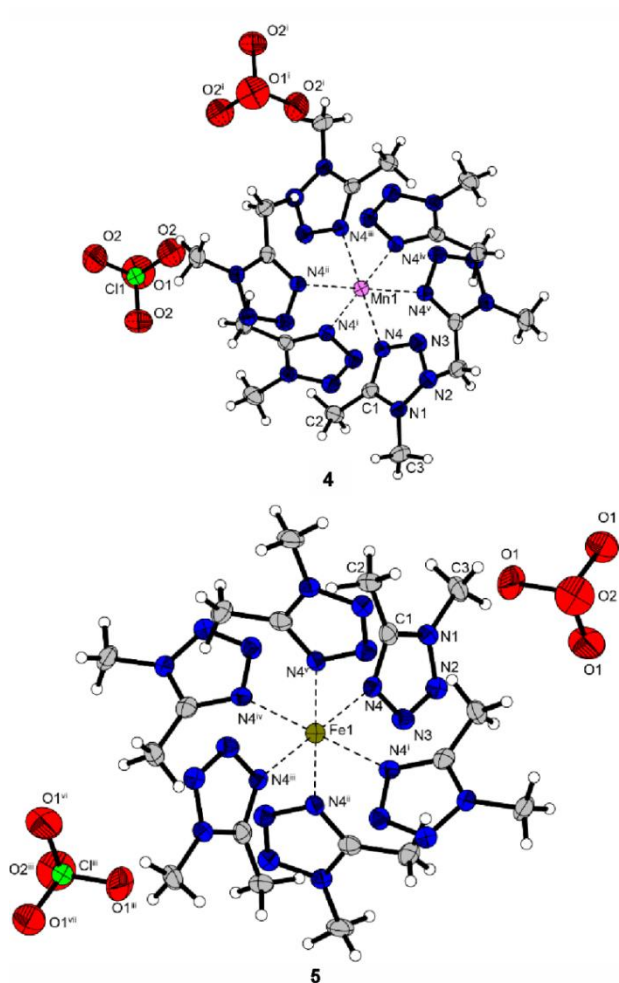


Figure 3. Molecular structures of ECCs **4** and **5** in the crystalline state, displaying the coordination of the metal cation centers by 1,5-DMT. Selected bond lengths [Å]: Mn1–N4 2.303(2), Fe1–N4: 2.238(5).

bond length of 2.238 Å is found in all six ligands, which is comparable to that of other hs-Fe (II) coordination compounds. By comparing the ion radii of hs-Mn (0.830 \AA^{31}) with hs-Fe (0.780 \AA^{31}) cations, the difference of 0.050 \AA is found to suit the observed change in

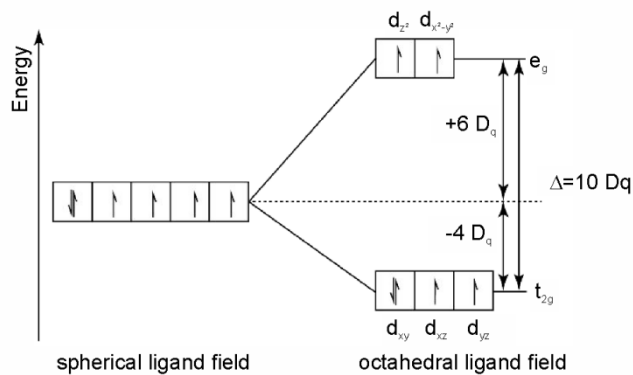


Figure 4. Electronic configuration of a Fe (II) cation and the splitting of *d*-orbitals due to an octahedral coordination.

M–L bond length of -0.065 \AA from Mn (II) to Fe (II), supporting the assumption of a *high spin* Fe (II) compound. Furthermore, unlike previously reported ECCs of iron (II) perchlorate³², compound **5** shows no thermochromic effect, which would derive from a change from hs-Fe (II) to low spin (ls)-Fe (II) when cooling crystals for low-temperature X-ray diffraction experiments. This effect is known for coordination compounds exhibiting sufficient ligand field splitting of *d*-orbitals. Cooling such coordination compounds results in an increase in ligand field splitting of the *d*-orbitals, ultimately enabling a spin-crossover from hs- to ls-state.³² Overall, this observation leads to the classification of 1,5-DMT as a weak field ligand. Compounds **6** (Fig. 5) and **7** (Fig. S1) crystallize in the monoclinic space group $P2_1/n$ and have calculated densities of $1.54 \text{ g}\cdot\text{cm}^{-3}$ and $1.55 \text{ g}\cdot\text{cm}^{-3}$, respectively. The cobalt cation in **6** is coordinated by four molecules of 1,5-DMT and two water molecules, forming a slightly distorted octahedron co-crystallized by one additional 1,5-DMT and one water molecule. The angle deviations from the perfect octahedron are smaller than those in **5** due to three different M–L bond lengths. Besides the M–O bond of the axial standing aqua ligands, there are two different M–N bonds built by two pairs of 1,5-DMT ligands. One pair of opposite standing ligands coordinate via N4 of the tetrazole ring, whereas the other pair coordinate via N3 of the tetrazole ring. Among all the ligands, the highest difference in bond length is found between Co1–O6 and Co1–N7, with a Δ of 0.12 \AA , which appears to be too small for *Jahn Teller*-like^[33] distortions. Since oxygen atoms have π -basic character due to their lone pair and thus do not increase the gap difference of the t_{2g} - and e_g -orbitals, the cobalt (II) cation is in its high spin state, where

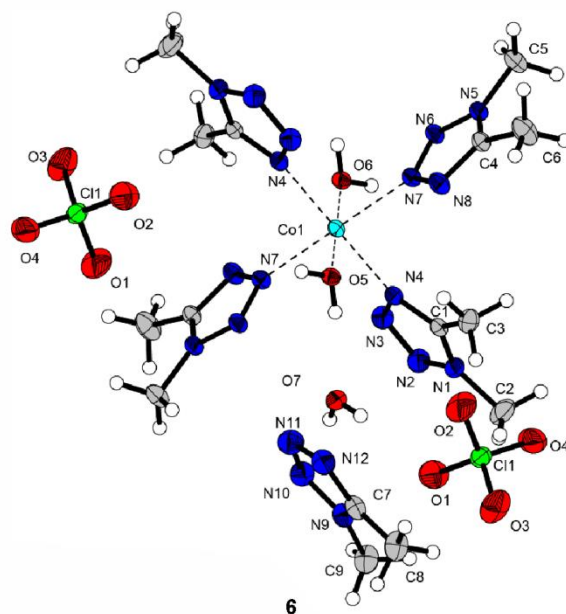


Figure 5. Crystal structures of ECC **6** representing the coordination of the cobalt cation by four molecules of 1,5-DMT and two aqua ligands. Selected bond lengths [\AA]: Co1 – N4 2.139(2), Co1 – N7 2.176(2).

significant *Jahn-Teller* effects are not expected. Consequently, steric effects between the DMT ligands and maintenance of a good π -orbital overlap cause the deviation from a perfect octahedron. Compound **7** shows the same coordination around the Ni (II) cation (Fig. S1) while being co-crystallized by two 1,5-DMT and two water molecules. Since the nickel cation has an electronic configuration of $[\text{Ar}]3d^8$ and the e_g orbital does not degrade, the slight deviations from the perfect octahedron are also caused by steric effects.

Like in compound **6**, the nickel cation of **7** is coordinated by two pairs of opposite standing DMT ligands and coordinates via N3 and N4 of the tetrazole rings, resulting in small differences in the M–L bond lengths. Compound **8** (Fig. 6, top) crystallizes in the orthorhombic space group *Pbca* and has a calculated density of $1.67 \text{ g}\cdot\text{cm}^{-3}$.

The copper (II) cation is coordinated and distorted pentagonal by four 1,5-DMT ligands and one aqua ligand. All four M–N bond lengths are equal within the error interval, with a value of around 2.00 \AA . The M–O bond length of 2.144 \AA can be explained by the degradation of the z^2 - over the x^2-y^2 -orbital for a d^9 -metal in a square-pyramidal ligand field. This structure perfectly aligns with a previously suggested square-pyramidal

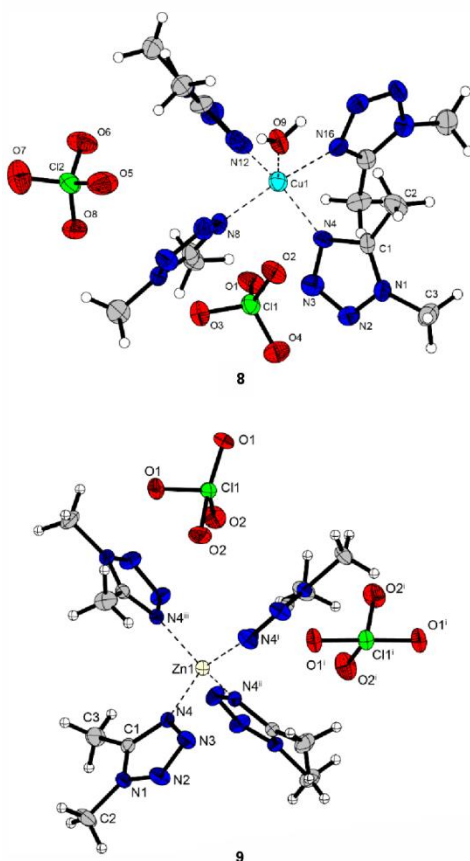


Figure 6. Crystal structures of ECCs **8** and **9**, showing the coordination of the metal cation centers by 1,5-DMT. Selected bond lengths [\AA]: Cu1–N4 1.995(7), Cu1–N8 2.016(7), Cu1–N12 1.991(6), Cu1–N16 2.010(7), Zn1–N4 1.990(2).

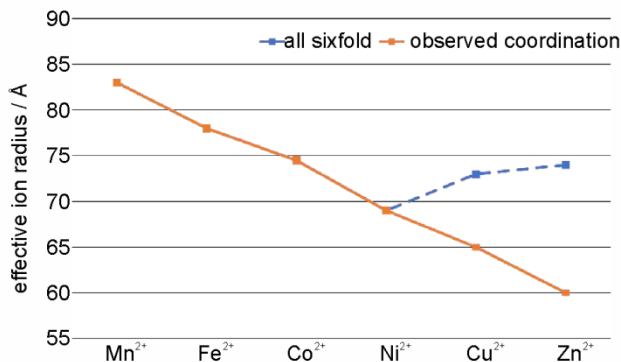
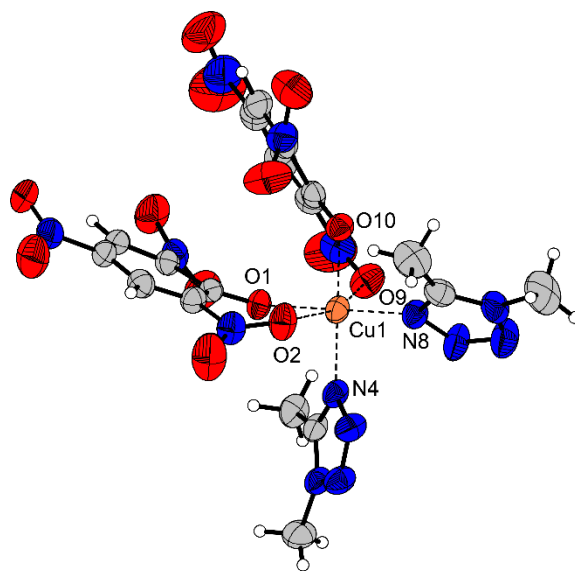


Figure 7. Effective ion radii of first row transition metals from Mn (II) to Zn (II). The dotted blue line shows the effective ion radii for all sixfold coordination of the metal cations. The orange line shows the effective ion radii while considering their coordination numbers.

coordination of Cu (II) cations in an aqueous solution^[34] rather than the more classical *Jahn-Teller* distorted octahedral sixfold coordination. Compound **9** (Fig. 6, bottom) crystallizes in the tetragonal space group $P4_12_12$ with a density of $1.63 \text{ g}\cdot\text{cm}^{-3}$. The zinc (II) cation is coordinated by four molecules of **3**, forming a nearly perfect tetrahedron with M–L bond lengths of 1.990 \AA for all four ligands. Throughout the series of first-row transition metals (**4–9**), a decrease in the metal-ligand bond length from $2.30(2) \text{ \AA}$ to $1.99(2) \text{ \AA}$ was observed, thus causing a strong contraction of the polyhedron and disfavoring the octahedral coordination of Cu (II) and Zn (II) cations by **3**. Additionally, the decreasing metal-ligand bond length indicates a decreasing radius of the corresponding metal cation. Fig. 7 shows the cation radii for first-row transition metals starting from manganese according to *Shannon & Prewitt*^{31, 35}. As shown in this figure, the radii of the cations, which have a coordination number (CN) of six, decrease from Mn (II) to Ni (II) and then increase (blue dotted line) for Cu (II) and Zn (II). However, this phenomenon was not observed in this study. Owing to the change in the coordination number for Cu (II) (CN = 5) and Zn (II) (CN = 4), the effective ion radii do not follow this trend. As concluded by *Shannon & Prewitt*, Cu (II) and Zn (II) cations exhibit a decreasing effective ion radius with a decrease in the coordination number. Therefore, the change in coordination, due to a decreased metal-ligand bond length, leads to a steady decrease in cation radii throughout the whole series of **4–9**.

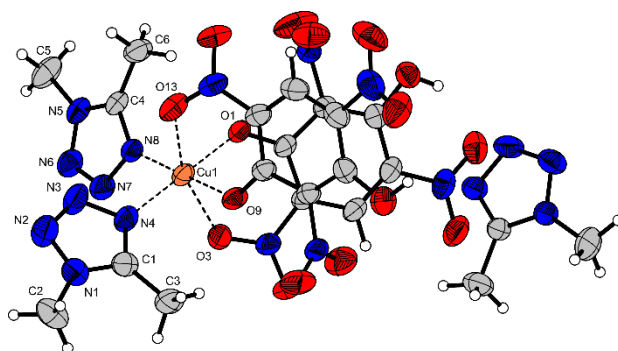
Compound **10** (Fig. 8) crystallizes in the monoclinic space group $P2_1/n$ with eight formula units per cell and a calculated density of $1.67 \text{ g}\cdot\text{cm}^{-3}$. Like in comparable ECCs⁹, the picrate anions coordinate. Therefore, the copper (II) cation in compound **10** is sixfold coordinated by two picrate anions and two molecules of **3**, forming a highly distorted square bipyramid. Ultimately, the deprotonated hydroxy groups and the 1,5-DMT ligands are positioned in the equatorial plane with bond lengths between $1.935(3) \text{ \AA}$ (Cu1–O1)



10

Fig. 8. Crystal structure of $[\text{Cu}(\text{PA})_2(\text{DMT})_2]$ (**10**), showing two coordination picrate anions and two 1,5-DMT ligands.

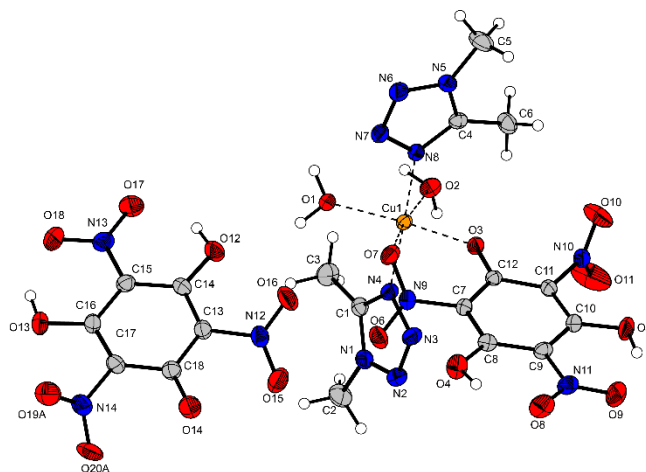
and 1.995(3) Å (Cu1–N8). Additionally, the oxygen atoms of the two coordinating nitro groups are in axial position with bonds Cu1–O9 and Cu1–O8 with lengths of 2.372(3) Å and 2.420(3), respectively. While the angles within the equatorial plane differ only marginally (0.781°) from a perfect 90°, the axial positions are bent by 17.015° from the perfect 180° due to the rigidity of the anions. Compound **11a** (Fig. 9) crystallizes in the triclinic space group $P\bar{1}$ with one formula unit per unit cell and a density of 1.65 g·cm⁻³. Like in **10**, the copper (II) cation in compound **11a** is also sixfold coordinated. The deprotonated hydroxy groups and the nitrogen atoms of the 1,5-DMT ligands are positioned in an equatorial plane, and the oxygen atoms of the coordinating nitro groups are axially positioned. Like those in **10**, the bond lengths and angles of compound **11a** range between 1.941 Å (Cu1–O9) and 2.014 Å (Cu1–N4) within the equatorial plane and 2.286 Å (Cu1–O13) and 2.301 Å (Cu1–O3) at axial positions. Additionally, the axial positions are strongly bent by 17.5° from the perfect 180° also due to the high rigidity of the anions. Compound **12a** (Fig. 10) crystallizes in the monoclinic space group $P2_1/c$ with four formula units per cell and a calculated density of 1.77 g·cm⁻³—the highest among all investigated compounds. Like in **10** and **11a**, the copper (II) cation in **12a** is sixfold coordinated by two molecules of **3**, two aqua ligands, and one deprotonated trinitro phloroglucinolate anion. Owing to the rigidity of the anion occupying two coordination sites, a strongly distorted square bipyramid is formed. Meanwhile, an equatorial plane is formed by the deprotonated hydroxy group, the two 1,5-DMT ligands, and one aqua ligand with bond lengths between 1.983(1) Å (Cu1–O3) and 2.025(1) Å (Cu1–O1). Unlike to **10** and **11a**, the bond lengths of the axially positioned atoms of **12a** are 2.210(1) Å (Cu1–O2) and 2.433(1) Å (Cu1–O7), ultimately



11a

Figure 9. Crystal structure of $[\text{Cu}(\text{HTNR})_2(\text{DMT})_2] \cdot \text{DMT}$ (**11a**), showing two coordination picrate styphnate and two 1,5-DMT ligands with one co-crystallized 1,5-DMT molecule.

distorting the bipyramid in its axial expansion. Interestingly, **12a** is the only nitroaromatic compound in which the 1,5-DMT ligands are in a *trans* position towards each other, while they are in a *cis* position in **10** and **11a**. Additionally, the axis O1–Cu1–O7 in **12a** is strongly bent to an angle of 168.65° , which is comparable to that of axes in **10** and **11a**. Compound **12b** (Fig. 11) crystallizes in the monoclinic space group $P2_1/n$ with four formula units per cell and a calculated density of $1.72 \text{ g}\cdot\text{cm}^{-3}$. The copper (II) cation in **12b** is sixfold coordinated by two 1,5-DMT molecules and two deprotonated trinitro phloroglucinolate anions, which bridge two copper centers. While compound **12b** is free of water, the ligands form a distorted square bipyramid like in **12a**. Like all other nitroaromatic compounds (**10**, **11a**, and **12a**), the equatorial plane of **12b** is formed by the deprotonated hydroxy groups together with the 1,5-DMT ligands, with bond lengths between $1.922(2) \text{ \AA}$ (Cu1–O1) and $2.007(2) \text{ \AA}$ (Cu1–N4) and minor angle deviations ($<2.5^\circ$) from the ideal 90° . The axial positions of **12b** are also coordinated by the nitro groups of the anions, with different bond lengths (2.249 \AA (Cu1–O4) and $2.407(3) \text{ \AA}$ (Cu1–



12a

Fig. 10. Crystal structure of $[\text{Cu}(\text{H}_2\text{TNPg})(\text{DMT})_2(\text{H}_2\text{O})_2](\text{H}_2\text{TNPg})$ (**12a**), showing one coordinating trinitro-phloroglucinolate anion, two 1,5-DMT, and two aqua ligands coordinating the copper(II) cation.

O9B)) and an angle deviation of 18.5° from the perfect 180°—the highest distortion of the ideal axis observed in this study.

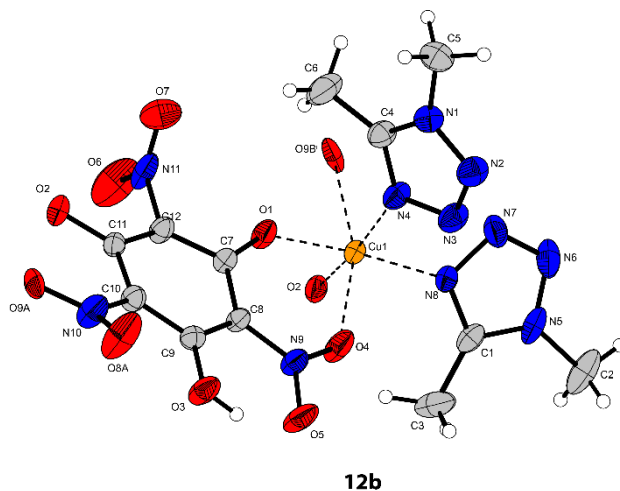


Fig. 11. Crystal structure of $[\text{Cu}(\text{HTNPG})_2(\text{DMT})_2]$ (**12b**), showing two coordination trinitro-phloroglucinolate anions and two 1,5-DMT ligands. The anions bridge two copper (II) centers.

9.2.3 Infrared spectroscopy

The infrared spectra of compounds obtained as single crystals are depicted in Fig. 12 (**3**), Fig 13 (**4**, **8**, and **9**), and S7 (**10**, **11b**, and **12b**). The spectra of the obtained ECCs pure samples were recorded according to the initially conducted elemental analysis. The IR spectra of batches produced later were compared to those of the pure batch. They were used without further purification if consensus was above 98 %. The spectrum of pure compound **3** shows asymmetric stretching vibration of the methyl groups at 2960 cm^{-1} . The broad range of $3500\text{--}3000\text{ cm}^{-1}$ was derived from small amounts of residual water. Additionally, strong bands at 1097 , 728 cm^{-1} and 657 cm^{-1} can be attributed to the deformation vibrations of the tetrazole ring.

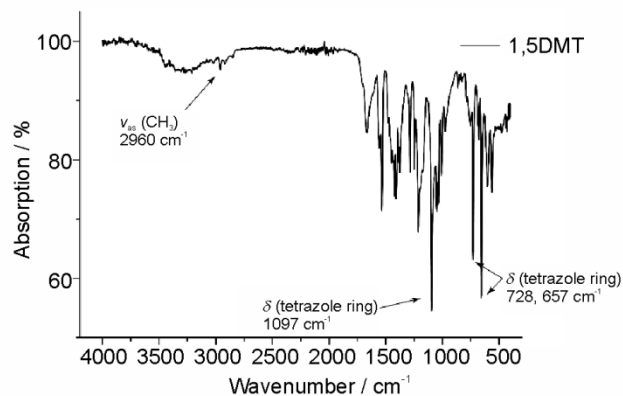


Fig. 12. IR spectrum of pure 1,5-dimethyltetrazole (**3**).

Fig. 13 depicts the IR spectra of the obtained perchlorate containing ECCs **4**, **8**, and **9**. Compound **4** shows a weak band at 2968 cm^{-1} , attributing to the asymmetric stretching vibration of the methyl groups that are slightly shifted due to coordination compared to pure **3**. The deformation vibrations of the tetrazole rings are represented by the IR bands at 729 cm^{-1} and 663 cm^{-1} . The characteristic bands of the perchlorate anions are observed at 1079 cm^{-1} and 622 cm^{-1} , which greatly agrees with the published values of non-coordinating perchlorate anions (1100 cm^{-1} and $600\text{--}700\text{ cm}^{-1}$)³⁶. These bands are slightly split, indicating weak hydrogen bonds between the anions and the 1,5-DMT ligands. Compounds **8** and **9** have no characteristic bands of methyl groups due to a very weak IR activity, as was already observed in pure compound **3**. Both compounds exhibit strong bands for the deformation vibrations of the tetrazole rings and the perchlorate anions, with the same range as **4**. Additionally, ECC **8** shows a broadened band with a maximum of 3421 cm^{-1} , corresponding to the vibration of the aqua ligand. Owing to the

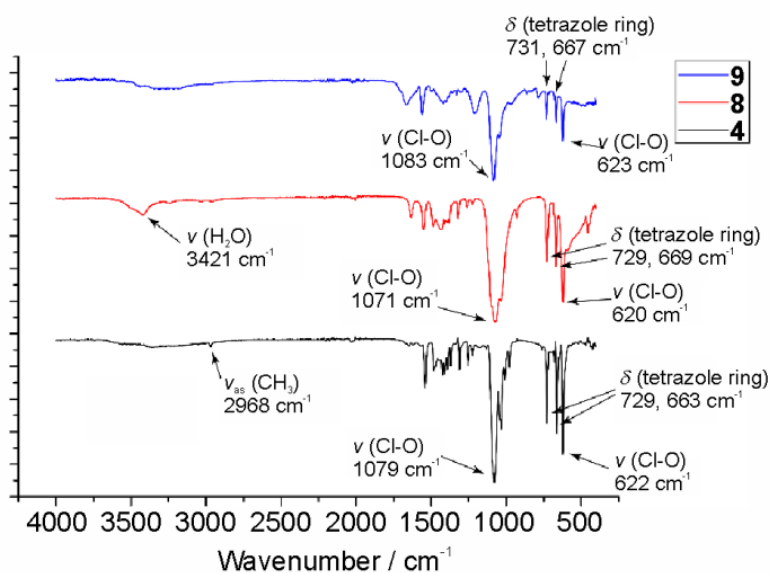


Fig. 13. IR spectra of ECCs **4**, **8**, and **9**.

substantial overlap of bands between the ligands and the nitroaromatic anions (Fig. S7) in the fingerprint regions below 1500 cm^{-1} for compounds **10**, **11b**, and **12b**, the assignment of characteristic vibrations is quite elaborate and is not necessary for this study.

9.2.4 Thermal behavior and sensitivities

The physicochemical properties of **3** and the complexes obtained as bulk materials are summarized in Table 1. The reported melting point of **3** at 73°C ³⁷ was confirmed through DTA measurements. A second endothermic event occurred at 298°C , which was identified as the boiling point of **3** (Fig. 14). The conducted TGA measurement showed a mass loss of 96.8 % between $100\text{--}214^\circ\text{C}$, which is related to the slow evaporation of **3** already starting at 100°C , suggesting high vapor pressure of **3** when melting. An exothermic decomposition was not observed in **3**. Therefore, the thermal stability of 1,5-DMT is

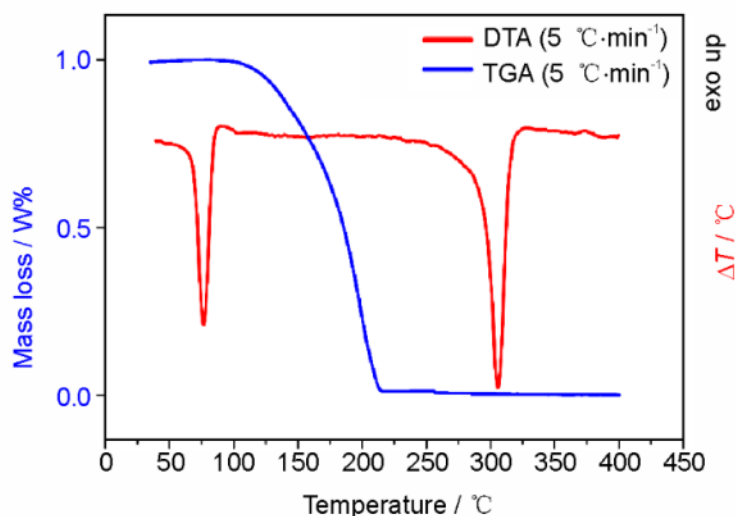


Fig. 14. DTA (red) and TGA (blue) analyses of 1,5-DMT (**3**) at a heating rate of $5^\circ\text{C}\cdot\text{min}^{-1}$.

presumably above 293°C .

The thermal behavior of ECCs **4**, **8**, **9**, **10**, **11b**, and **12b** were investigated through DTA measurements at a heating rate of $\beta=5^\circ\text{C}\cdot\text{min}^{-1}$ (Fig. 15). As shown by DTA and TGA measurements, an endothermic event was observed in compound **4** at 171°C as a loss of ligands (weight loss: 38.8 wt%; Fig. 15), while an endothermic event was observed in **8** at 106°C , corresponding to a loss of aqua ligands (weight loss: 2.68 wt%). Moreover, compound **9** showed an endothermic event at 292°C , shortly followed by an exothermic event starting at 321°C , exhibiting the highest stability observed in this study. The conducted TGA measurement (Fig. 15) did not show weight loss until 293°C . Therefore,

the endothermic peak of the DTA measurement corresponded to the decomposition temperature of **9**, which is extraordinarily high for ECCs.³⁸⁻⁴¹ As the same behavior of an endothermic event immediately evolved into an exothermic event during the DTA measurements of **10** and **11b**, no further TGA measurement was conducted for these two compounds. Additionally, since no thermal event was observed prior to the exothermic decomposition of compound **12b**, no TGA analysis was conducted. Generally, compound **10** showed a very high thermal stability of 250°C, while **11b** and **12b** showed drastically lower yet adequate thermal stabilities of 184°C (**11b**) and 192°C (**12b**). Although the direct influence of anions on thermal stability cannot be deduced, the perchlorate containing ECCs (**4**, **8**, and **9**) exhibited their exothermic decomposition reaction at higher temperatures than those containing nitroaromatic anions. Indeed, it must be kept in mind that compounds **4** and **8** exhibited endothermic decompositions due to the loss of ligands before any exothermic event happened. Furthermore, the measured thermal stabilities of nitroaromatic ECCs **10–12b** do not allow the deduction of the direct influence of nitroaromatic anions compared to each other. Nonetheless, they agree well with previously reported ECCs⁹, which also have no direct influence of anions on thermal stabilities. According to BAM standards, the sensitivities of the compounds to impact and friction have been determined and classified according to the UN recommendations on the transport of dangerous goods⁴². Accordingly, it was determined that **3** was completely insensitive to mechanical stimuli (> 40 J, > 360 N), ECCs **4**, **10**, **11b**, and **12b** were not sensitive to friction, while **5** and **6** were slightly sensitive to friction, with friction sensitivity (FS) of 128 N and 180 N, respectively. All compounds were sensitive to impact, with **4** (10 J) and **10** (8 J) showing lower impact sensitivities than **8** (3 J), **9** (3 J), **11b** (2 J), and **12b** (2 J). Therefore, ECCs **8**, **9**, **11b**, and **12b** exhibited impact sensitivities in the range of a primary explosive, whereas **4** and **10** exhibited sensitivities as typical secondary explosives, such as hexogen.²⁴ Although the direct influence of anions on thermal stability could not be previously deduced, their influence can be determined by comparing sensitivities. Even though the differences in sensitivities between nitroaromatic compounds are not as prominent as those between other ligand systems^{8, 33}, compound **10**, which incorporated the picrate anions, exhibited the lowest sensitivities, followed by compounds **11b** and **12b**. Generally, the increasing number of hydroxy functionalities from picrate to trinitrophenylroglucinate also increases the sensitivities to impact and friction. Furthermore, the sensitivities of the perchlorate-containing ECCs (**4**, **8**, and **9**) are higher than those of the nitroaromatic compounds, yet they are still moderately sensitive at least to friction. Owing to their poor crystallizability, enough compounds **5**, **6**, and **7** could not be obtained. Therefore, their thermal and energetic behavior was not explored. To further investigate the energetic properties, hot plate (HP) and hot needle (HN) tests of

compounds **4** and **9** were performed (Fig. 16). HP tests were conducted to determine the performance of the samples under fast heating on a copper plate, during which both compounds showed deflagration without detonation. While HP tests do not necessarily allow any conclusions on the compound's capability as a primary explosive, the HN tests can be used to correlate deflagration with the detonation transition (DDT) capability of a compound. Therefore, HN tests were performed by fixing the sample underneath adhesive tape on a copper plate, followed by penetration with a red heated needle. A compound possesses rapid DDT if detonation occurs, which was not the case for the tested compounds.

Table 1 Sensitivities and thermal behavior of compounds **4**, **8**, **9**, and **10–12**.

Compound	IS ^a /J	FS ^b /N	$T_{\text{endo.}}^{\text{c}}$ /°C	$T_{\text{exo.}}^{\text{d}}$ /°C
3	>40	>360	73	>293
4	10	> 360	171	307
8	3	128	106	226
9	2	180	293	321
10	8	>360	–	250
11b	2	>360	–	184
12b	2	360	–	192

^a Impact sensitivity according to the BAM drop hammer^[43] (method 1 of 6). ^b Friction sensitivity according to the BAM friction tester^[43] (method 1 of 6). ^c Temperature of endothermic events (onset temperatures at a heating rate of 5 °C·min⁻¹) ^d Temperature of decomposition indicated by exothermic event according to DTA (onset temperatures at a heating rate of 5 °C·min⁻¹).

Interestingly, there is a reported energetic coordination compound based on copper (II) perchlorate with 1-ethyl-5-tetrazole (1-ETZ) as ligand⁴. Given that 1,5-DMT and 1-ETZ are structural isomers and have the same empirical formula of C₃H₆N₄, it seems reasonable to compare both compounds as ligands. This, unfortunately, was impossible in this study since no isomeric complexes were obtained. All reported coordination compounds with 1-ETZ as ligand exhibit octahedral coordination of the copper (II) cation, whereas the obtained copper(II) complex displayed different coordination in this study. This results from higher steric demand of **3** compared to 1-ETZ. Specifically, the ethyl functionalization can easily minimize steric repulsion by rotation of the C-C bond for **3**, which is impossible for 1,5-DMT. Besides their coordinative behavior, the major difference between both compounds is their thermal behavior. 1-ETZ is a liquid at room temperature with thermal stability of up to 208°C. Therefore, it is by far inferior to **3** in terms of thermal stability. This is also accompanied by a slight decrease in enthalpy of formation of **3** (184.1

$\text{kJ}\cdot\text{mol}^{-1}$) compared to 1-ETZ ($224.1 \text{ kJ}\cdot\text{mol}^{-1}$). Thereby, higher stability of the resulting ECCs can be assumed.

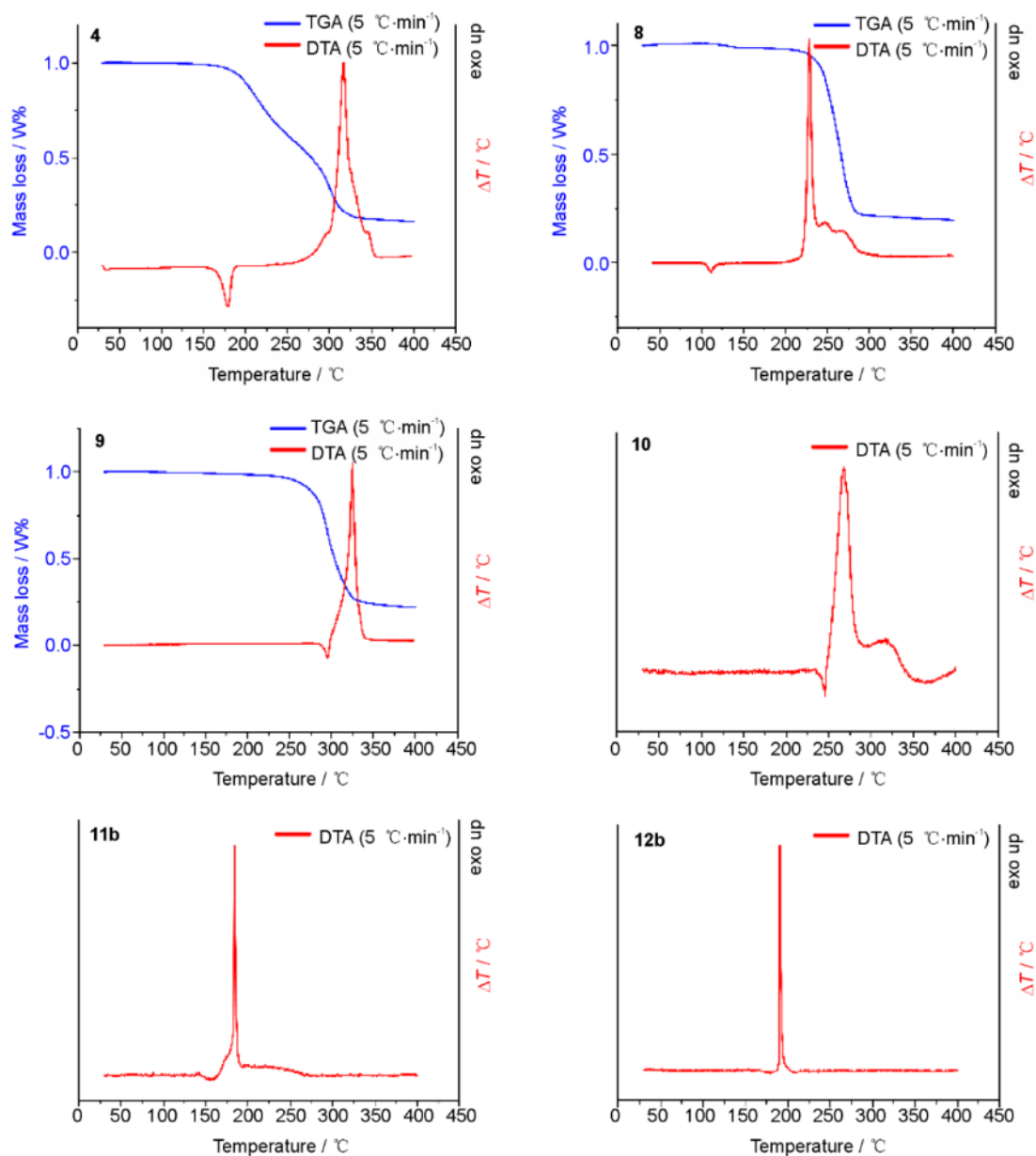


Fig. 15. Combined DTA and TGA measurements of ECCs **4**, **8**, and **9** and DTA of ECCs **10**, **11b**, and **12b** at a heating rate of $5 \text{ }^\circ\text{C}\cdot\text{min}^{-1}$.

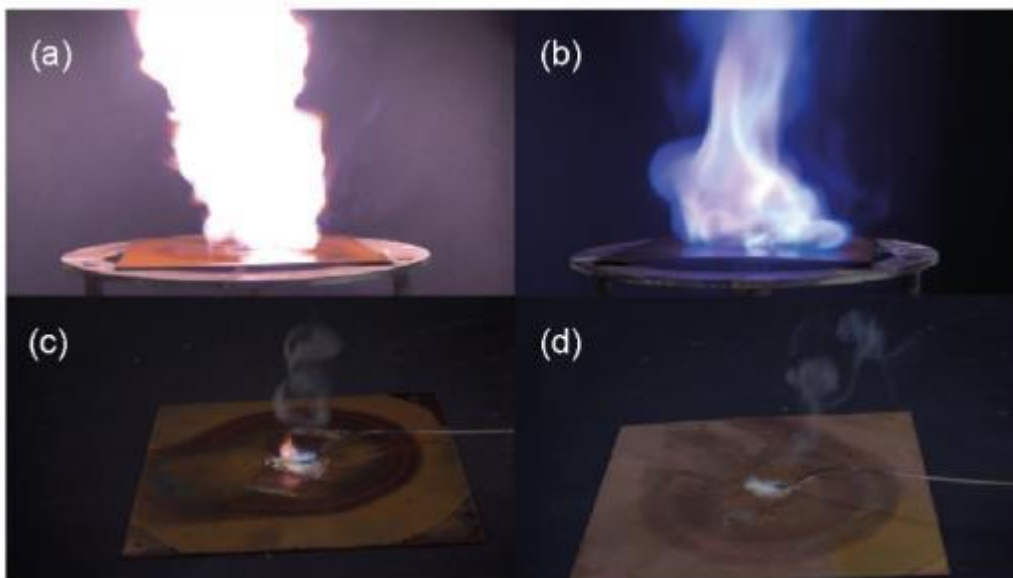


Fig. 16. HP and HN tests of compounds **4** and **9**. **a:** HP test of **4**; **b:** HP test of **9**; **c:** HN test of **1**; **d:** HN test of **9**.

9.3 Conclusion

1,5-DMT (**3**) was synthesized using a three-step procedure starting with acetone and hydroxylamine. This route was observed to be more economical than the one-step synthesis using TMS-N₃. 1,5-DMT (**3**) was fully characterized as a completely insensitive (> 360 N, > 40 J) and highly thermally stable (> 293°C) compound with an astonishing high positive HOF of 184.1 kJ mol⁻¹. Therefore, **3** was applied as a nitrogen-rich (N = 57.1%) ligand to 11 new energetic coordination compounds of the 3d⁵–3d¹⁰ metal (e.g., Mn, Fe, Co, Ni, Cu, Zn) perchlorate salts. The change from a sixfold (**4**, **5**) to a fourfold (**9**) coordination of the central metal cation was observed. This change was caused by a decreasing metal-ligand bond length throughout the first-row transition metals, which decreased the coordination number and ultimately led to steadily decreasing cation radii. The additional increase in steric repulsion of the ligands favors the decrease in the coordination number, supporting the change in coordination. All measured ECCs exhibited exothermic decomposition events above 184°C (**11b**). For compound **9**, an extraordinarily high decomposition temperature of 293°C was measured, representing the highest thermal stability investigated in this study. Hot plate tests of the most promising compounds showed a complete decomposition without detonation, while the hot needle tests indicated that none of the compounds can be classified as applicable primary explosives since no rapid DDT was observed. However, the compounds are ideal candidates for burning rate catalysts in propellant charges due to their simple and cheap syntheses and great stability.

9.4 Experimental Section

Acetone Oxime (1): Sodium carbonate (28.6 g, 0.27 mol) was added to a solution of hydroxyl ammonium chloride (15.6 g, 0.23 mol) and acetone (8.7 g, 0.15 mol) in water (300 mL). The mixture was stirred for 40 h at room temperature, and the residue was extracted with diethyl ether (4 × 100 mL). After washing with a saturated sodium chloride solution and drying over sodium sulfate, the solvent was removed under reduced pressure, and acetone oxime (7.7 g, 0.11 mol, 70 %) was obtained as a colorless solid.

¹H NMR (400 MHz, CDCl₃): δ = 1.89 (3H, CH₃), 1.90 (3H, CH₃), 7.77 (1H, OH); **¹³C NMR** (101 MHz, CDCl₃): δ = 14.8, 21.9, 155.9.

Acetoxime Benzenesulfonate (2): Acetone oxime (6 g, 0.08 mol) was dissolved in pyridine (6.5 mL, 0.08 mol), and water (16 mL) and benzene sulfonyl chloride (10.2 mL, 0.08 mol) was added dropwise with the temperature kept at 15–20°C. A colorless solid precipitated, and the suspension was cooled to 10°C. After filtration and washing with cold water, the solid was dried, yielding acetoxime benzenesulfonate in quantitative amounts.

¹H NMR (400 MHz, CDCl₃): δ = 1.93 (3H, CH₃), 1.98 (3H, CH₃), 7.54 (2H, CH(3, 5)), 7.65 (1H, CH(4)), 7.97 (2H, CH(2, 6)); **¹³C NMR** (101 MHz, CDCl₃): δ = 17.1 (CH₃), 21.8 (CH₃), 128.9 (2 CH), 129.0 (2 CH), 133.9 (CH), 165.2 (H₃CC(N)CH₃).

1,5-Dimethyltetrazole (3): Sodium azide (4.6 g, 0.07 mol) was dissolved in water (15 mL) and was added to a solution of acetoxime benzenesulfonate (15 g, 0.07 mol) in methanol (60 mL). The mixture was stirred for 1 h at 45°C and later for 1.5 h at 60°C. The solvent was removed under reduced pressure and the residue was extracted with hot benzene (4 × 30 mL). After evaporation of the solvent, 1,5-dimethyltetrazole (3.3 g, 0.033 mol, 48 %) was obtained as a colorless solid. Recrystallization from water yields **3** as colorless block-shaped crystals.

DTA (5 °C·min⁻¹) onset: 73°C (*T*_{endo}), 298°C (*T*_{endo}); **¹H NMR** (400 MHz, DMSO-d₆): δ = 2.49 (3H, CH₃), 3.96 (3H, CH₃) ppm; **¹³C NMR** (101 MHz, DMSO-d₆): δ = 8.1 (CCH₃), 33.2 (NCH₃), 152.4 ppm (N₄C); **IR:** (ν /cm⁻¹) (rel. int.) = 2961 (w), 1655 (w), 1533 (s), 1481 (m), 1451 (m), 1436 (m), 1423 (m), 1409 (m), 1386 (m), 1380 (m), 1374 (m), 1285 (m), 1248 (m), 1212 (m), 1097 (s), 1048 (m), 1034 (m), 1008 (m), 976 (w), 728 (s), 678 (w), 657 (vs), 605 (w), 565 (w).

Alternatively, acetone (1 g, 17 mmol, 1 eq.) was mixed with trimethylsilyl azide (5.87 g, 51 mmol, 3 eq.) and tin (II)chloride (0.322 g, 1.7 mmol, 0.1 eq.) and were stirred at 55°C for 20 h. Extraction with benzene followed by evaporation yielded 1,5-dimethyltetrazole (0.66 g, 7.14 mmol, 42 %) as a white solid.

$^1\text{H NMR}$ (400 MHz, $\text{DMSO-}d_6$): $\delta = 2.49$ (3H, CH_3), 3.96 (3H, CH_3); $^{13}\text{C NMR}$ (101 MHz, $\text{DMSO-}d_6$): $\delta = 8.1$ (CCH_3), 33.3 (NCH_3), 152.4 (N_4C).

General procedure for the preparation of complexes 4–9:

Stoichiometric amounts of the corresponding metal (II) perchlorate and **3** were individually dissolved in water, combined, and stirred for a short period at elevated temperatures. The product was obtained after crystallization at ambient conditions.

[Mn(DMT)₆](ClO₄)₂ (4): Compound **4** was isolated as a colorless crystalline precipitate.

DTA (5 °C min⁻¹) onset: 171°C (T_{endo}), 307°C (T_{exo}); **IR** (ATR, $\tilde{\nu}$ /cm⁻¹): 3346 (vw), 1540 (m), 1481 (w), 1408 (w), 1390 (m), 1370 (m), 1311 (w), 1254 (w), 1224 (w), 1079 (s), 1033 (s), 1009 (m), 979 (w), 729 (m), 678 (s), 663 (s), 622 (s); **Elemental Analysis** calcd. [%] for $\text{C}_{18}\text{H}_{36}\text{Cl}_2\text{MnN}_{24}\text{O}_8$ (842.48): C 25.66, H 4.31, N 39.90; found: C 25.31, H 4.09, N 38.93; BAM drop hammer: 10 J; BAM friction tester: >360 N.

[Fe(DMT)₆](ClO₄)₂ (5): Compound **5** was obtained as a brown glass-like solid. Crystals suitable for X-ray determination were obtained by subjecting a small amount to a high vacuum for several days.

[Co(H₂O)₂(DMT)₄](DMT)(H₂O)(ClO₄)₂ (6): Out of the oily red product, crystals suitable for X-ray determination of complex **6** were obtained. Owing to its consistency, only X-ray determination was possible.

[Ni(DMT)₄(H₂O)₂](DMT)₂(H₂O)₂(ClO₄)₂ (7):

Inhomogeneous solids were formed after evaporation of the solvent. From these inhomogeneous solids, small crystals of **7** suitable for X-ray determination were picked using a light microscope.

[Cu(H₂O)(DMT)₄](ClO₄)₂ (8): Complex **8** crystallized as deep blue needles suitable for X-ray determination.

DTA (5 °C min⁻¹) onset: 106°C (loss of water), 226°C (*T*_{exo}); **IR** (ATR, $\tilde{\nu}$ /cm⁻¹): 3425 (w), 1554 (w), 1434 (w), 1070 (s), 727 (m), 668 (m), 619 (s); **Elemental Analysis** calcd. [%] for C₁₂H₂₆Cl₂CuN₁₆O₁₀ (672.89): C 21.42, H 3.69, N 33.31; found: C 21.50, H 3.74, N 33.32; BAM drop hammer: 3 J; friction tester: 128 N.

[Zn(DMT)₄](ClO₄)₂ (9): Complex **9** was obtained as colorless crystals suitable for X-ray determination.

DTA (5 °C min⁻¹) onset: 293°C (*T*_{endo}), 321°C (*T*_{exo}); **IR** (ATR, $\tilde{\nu}$ /cm⁻¹): 1561 (w), 1500 (w), 1331 (w), 1265 (w), 1084 (s), 1042 (m), 731 (m), 678 (w), 666 (m), 623 (s); **Elemental Analysis** calcd. [%] for C₁₂H₂₄Cl₂ZnN₁₆O₈ (656.71): C 21.95, H 3.68, N 34.13; found: C 21.84, H 3.46, N 33.88; BAM drop hammer: 2 J; friction tester: 180 N).

[Cu(PA)₂(DMT)₂] (10): Basic copper(II) carbonate (50 mg, 226 μmol) was suspended in water (10 mL), and picric acid (104 mg, 452 μmol) was added. The mixture was stirred until all solids were dissolved and **3** (44 mg, 452 μmol) was added. After stirring for 5 min at 80°C, the solution was left to crystallize. Compound **10** was obtained as green needles with a high yield (268 mg, 375 μmol, 83%).

DTA (5 °C min⁻¹) onset: 250°C (*T*_{exo.}); **IR** (ATR, $\tilde{\nu}$ /cm⁻¹): 3087 (w), 1741 (w), 1616 (s), 1612 (s), 1576 (s), 1533 (s), 1507 (s), 1480 (s), 1418 (s), 1361 (s), 1326 (vs), 1269 (vs), 1168 (s), 1110 (m), 1083 (m), 1047 (m), 941 (m), 916 (s), 846 (w), 824 (w), 785 (m), 743 (m), 728 (m), 704 (vs), 679 (m), 666 (s), 551 (m), 517 (m), 455 (w), 428 (w), 416 (w); **Elemental Analysis** calcd. [%] for C₁₈H₁₆CuN₁₄O₁₄ (715.96): C 30.20, H 2.25, N 27.39; found: C 30.31, H 2.25, N 27.58; BAM drop hammer: 8 J; BAM friction tester: >360 N.

[Cu(HTNR)₂(DMT)₂] (11b): Basic copper(II) carbonate (50 mg, 226 mmol) was suspended in water (10 mL), and trinitro resorcinol (110 mg, 452 mmol) was added. The solution was heated to 80°C and **3** (44 mg, 452 mmol) was added. After stirring for 5 min at 80°C, the formed precipitate of **11b** was filtered out with a high yield (267 mg, 357 mmol, 79%). The remaining solution was left to crystallize for several days, from which a few crystals of **11a** were obtained.

DTA (5 °C min⁻¹) onset: 184°C (*T*_{exo}); **IR** (ATR, $\tilde{\nu}/\text{cm}^{-1}$): 3096 (w), 1628 (s), 1561 (s), 1535 (s), 1528 (s), 1476 (s), 1453 (s), 1377 (s), 1353 (s), 1319 (s), 1284 (vs), 1194 (s), 1175 (s), 1088 (s), 1049 (s), 930 (s), 828 (w), 781 (m), 762 (m), 727 (s), 713 (s), 698 (s), 681 (s), 666 (s), 641 (m), 543 (m), 462 (w), 427 (m), 417 (m); **Elemental Analysis** calcd. [%] for C₁₈H₁₆CuN₁₄O₁₆ (747.95): C 28.91, H 2.16, N 26.22; found: C 28.79, H 2.27, N 28.76; BAM drop hammer: 2 J; BAM friction tester: >360 N.

[Cu(HTNPG)(DMT)₂] (12b): Basic copper(II) carbonate (50 mg, 226 mmol) was suspended in water (10 mL), and trinitro phloroglucinol (118 mg, 452 mmol) were added. The solution was heated to 80°C and **3** (44 mg, 452 mmol) was added. After stirring for 5 min at 80°C, the solution was left standing to crystallize. After 1–2 d, crystals in the form of needles (**12a**) and blocks (**12b**) started to form. The initially formed **12a** started to be consumed as blocks of **12b** continued to grow. After 3–4 d, crystals of **12b** were the main product of crystallization and then were filtered out and dried. **12b** was obtained as dark blocks with a high yield (197 mg, 379 mmol, 84%).

DTA (5 °C min⁻¹) onset: 192°C (*T*_{exo}); **IR** (ATR, $\tilde{\nu}/\text{cm}^{-1}$): 1736 (w), 1588 (s), 1538 (s), 1520 (vs), 1486 (s), 1455 (s), 1399 (s), 1345 (s), 1284 (vs), 1255 (vs), 1192 (s), 1175 (s), 1158 (s), 1134 (vs), 1109 (s), 1048 (s), 1027 (m), 929 (s), 837 (m), 825 (m), 806 (m), 792 (s), 708 (vs), 681 (s), 665 (vs), 642 (s), 456 (m), 434 (s), 413 (s), 408 (s); **Elemental Analysis** calcd. [%] for C₁₂H₁₃CuN₁₁O₉ (518.85): C 27.78, H 2.53, N 29.70; found: C 27.47, H 2.53, N 28.42; BAM drop hammer: 2 J; BAM friction tester: 360 N.

Acknowledgements

This work was funded by the Ludwig-Maximilian University of Munich (LMU), the Office of Naval Research (ONR) under Grant No. ONR.N00014-16-1-2062. The authors would like to thank Stefan Huber for sensitivity measurements.

9.5 References

- [1] Pritchard R, Kilner CA, Barrett SA, Halcrow MA. Two new 4,4' -disubstituted dipyrazolylpyridine derivatives, and the structures and spin states of their iron(II) complexes. *Inorg. Chim. Acta* 2009;362:4365–4371.
- [2] Mohammed R, Chastanet G, Tuna F, Malkin TL, Barrett SA, Kilner CA, Létard JF, Halcrow MA. Synthesis of 2,6-Di(pyrazol-1-yl)pyrazine Derivatives and the Spin-State Behavior of Their Iron(II) Complexes. *Eur. J. Inorg. Chem.* 2013;2013:819–831.
- [3] Cook TR, Zheng YR, Stang PJ. Metal–Organic Frameworks and Self-Assembled Supramolecular Coordination Complexes: Comparing and Contrasting the Design, Synthesis, and Functionality of Metal–Organic Materials. *Chem. Rev.* 2013;113:734–777.
- [4] Wurzenberger MHH, Gruhne MS, Lommel M, Szimhardt N, Klapötke TM, Stierstorfer J. Comparison of 1-Ethyl-5*H*-tetrazole and 1-Azidoethyl-5*H*-tetrazole as Ligands in Energetic Transition Metal Complexes. *Chem. Asian J.* 2019;14:2018–2028.
- [5] Titi HM, Marrett JM, Dayaker G, Arhangelskis M, Mottillo C, Morris AJ, Rachiero GP, Friščić T, Rogers RD. Hypergolic zeolitic imidazolate frameworks (ZIFs) as next-generation solid fuels: Unlocking the latent energetic behavior of ZIFs. *Sci. Adv.* 2019;5:eaav9044.
- [6] Wang QY, Wang J, Wang S, Wang ZY, Cao M, He CL, Yang JQ, Zang SQ, Mak TCW. *o*-Carborane-Based and Atomically Precise Metal Clusters as Hypergolic Materials. *J. Am. Chem. Soc.* 2020;142:12010–12014.
- [7] Wang C, Wang YJ, He CL, Wang QY, Zang SQ. Assembling Silver Cluster-Based Organic Frameworks for Higher-Performance Hypergolic Properties. *JACS Au* 2021;1:2202–2207.
- [8] Wurzenberger MHH, Gruhne MS, Lommel M, Braun V, Szimhardt N, Stierstorfer J. Taming the Dragon: Complexation of Silver Fulminate with Nitrogen-Rich Azole Ligands. *Inorg. Chem.* 2020; 59:17875–17879.
- [9] Wurzenberger MHH, Bissinger BRG, Lommel M, Gruhne MS, Szimhardt N, Stierstorfer J. Synthesis and comparison of copper(ii) complexes with various N-aminotetrazole ligands involving trinitrophenol anions. *New J. Chem.* 2019;43:18193–18202.

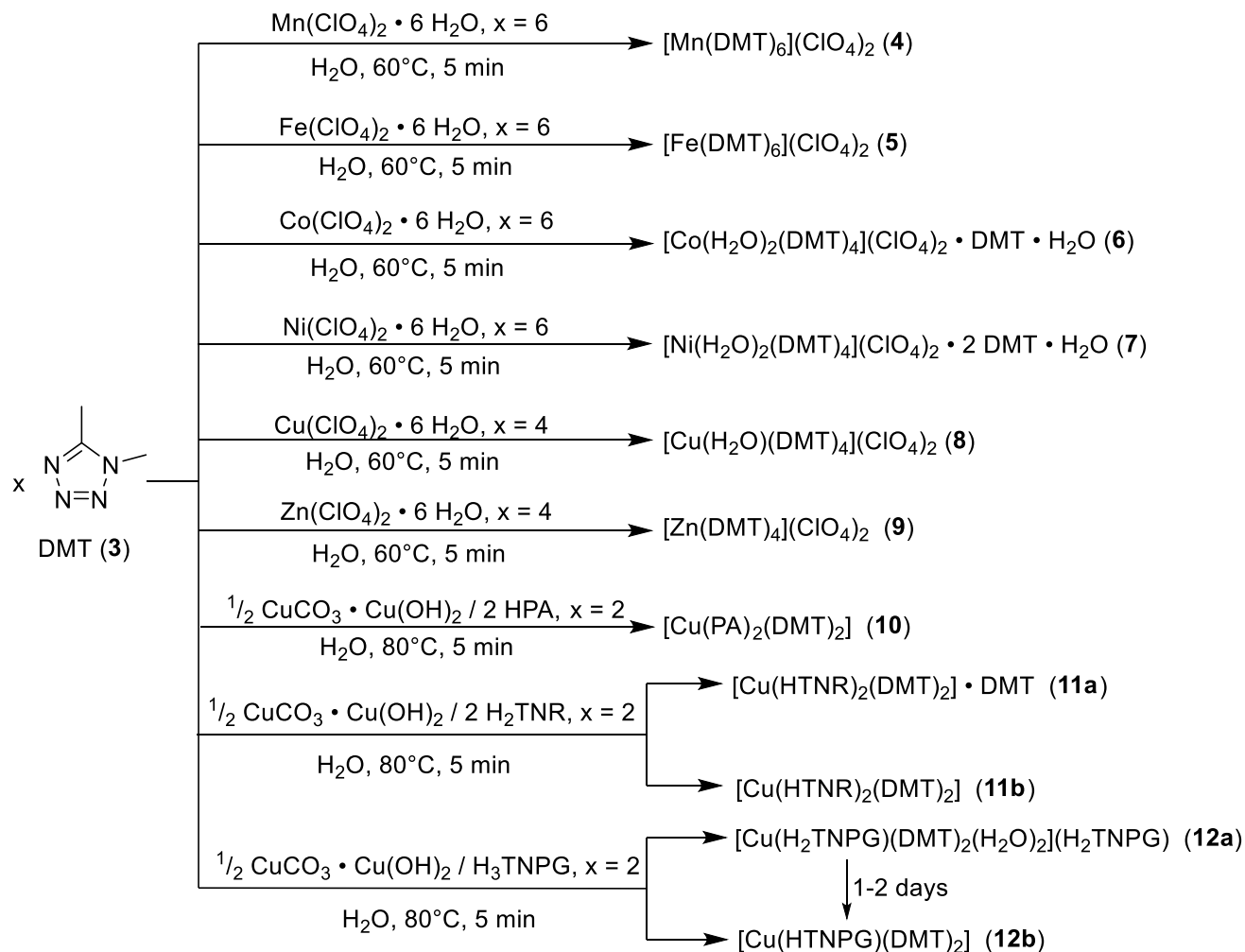
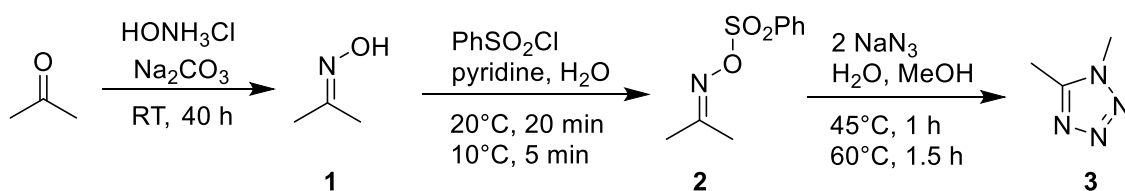
- [10] Wilbrand J. Notiz über Trinitrotoluol. *Justus Liebigs Annalen der Chemie* 1863;128: 178–179.
- [11] Klapötke TM, Chemistry of High-Energy Materials. 5th ed. Berlin/Boston: De Gruyter, 2019.
- [12] Simpson RL, Urtiew PA, Ornellas DL, Moody GL, Scribner KJ, Hoffman DM. CL-20 performance exceeds that of HMX and its sensitivity is moderate. *Propellants Explos. Pyrotech.* 1997; 22:249–255.
- [13] Verkhovina ON, Kizhnyaev VN, Vereshchagin LI, Rokhin AV, Smirnov AI. Synthesis of Polynuclear Nonfused Azoles. *Russ. J. Org. Chem.* 2003;39:1792–1796.
- [14] Kumar D, Tang Y, He C, Imler GH, Parrish DA, Shreeve JnM. Multipurpose Energetic Materials by Shuffling Nitro Groups on a 3,3'-Bipyrazole Moiety. *Chem. Eur. J.* 2018;24:17220–17224.
- [15] Gettings ML, Thoenen MT, Byrd EFC, Sabatini JJ, Zeller M, Piercey DG. Tetrazole Azasydnone (C₂N₇O₂H) And Its Salts: High-Performing Zwitterionic Energetic Materials Containing A Unique Explosophore. *Chem. Eur. J.* 2020;26:14530–14535.
- [16] Wozniak DR, Zeller M, Byrd EC, Piercey DG. An Improved Synthesis of Bromotetrazole. *Z. Anorg. Allg. Chem.* 2022;648:e202100333.
- [17] Szimhardt N, Wurzenberger MHH, Zeisel L, Gruhne MS, Lommel M, Stierstorfer J. Maximization of the energy capability level in transition metal complexes through application of 1-amino- and 2-amino-5*H*-tetrazole ligands. *J. Mater. Chem. A* 2018;6:16257–16272.
- [18] Klapötke TM, Kofen M, Schmidt L, Stierstorfer J, Wurzenberger MHH. Selective Synthesis and Characterization of the Highly Energetic Materials 1-Hydroxy-5*H*-tetrazole (CHN₄O), its Anion 1-Oxido-5*H*-tetrazolate (CN₄O⁻) and Bis(1-hydroxytetrazol-5-yl)triazene. *Chem. Asian J.* 2021;16:3001–3012.
- [19] Wurzenberger MHH, Endraß SMJ, Lommel M, Klapötke TM, Stierstorfer J. Comparison of 1-Propyl-5*H*-tetrazole and 1-Azidopropyl-5*H*-tetrazole as Ligands for Laser Ignitable Energetic Materials. *ACS Appl. Energy Mater.* 2020;3:3798–3806.

- [20] Fronabarger J, Schuman A, Chapman R, Fleming W, Sanborn W, Massis T. Chemistry and development of BNCP, a novel DDT explosive (deflagration-to-detonation). *31st Joint Propulsion Conference and Exhibit*, AIAA, July, 1995.
- [21] Moderhack D, Noreiks M. Tetrazolium N-Aminides. *Heterocycles*, 2004;63:2605–2614.
- [22] Klapötke TM, Piercey DG, Stierstorfer J. The 1,4,5-Triaminotetrazolium Cation (CN₇H₆⁺): A Highly Nitrogen-Rich Moiety. *Eur. J. Inorg. Chem.* 2012;2012:5694–5700.
- [23] Sharon P, Afri M, Mitlin S, Gottlieb L, Schmerling B, Grinstein D, Welner S, Frimer AA. Preparation and characterization of bis(guanidinium) and bis(aminotetrazolium)dodecahydroborate salts: Green high energy nitrogen and boron rich compounds. *Polyhedron* 2019;157:71–89.
- [24] Klapötke TM, *Energetic Materials Encyclopedia*. 2nd ed. Berlin/Boston: De Gruyter, 2021.
- [25] Fischer N, Fischer D, Klapötke TM, Piercey DG, Stierstorfer J. Pushing the limits of energetic materials - the synthesis and characterization of dihydroxylammonium 5,5'-bistetrazole-1,1'-diolate. *J. Mater. Chem.* 2012;22:20418–20422.
- [26] Klapötke TM, Stierstorfer J. The CN₇⁻ Anion. *J. Am. Chem. Soc.* 2009;131:1122–1134.
- [27] Langhals H, Range G, Wistuba E, Rüdhardt C. Alkylwanderungen bei Sextettumlagerungen. *Chem. Ber.* 1981;114:3813–3830.
- [28] Kamuf M, Rominger F, Trapp O. Investigation of the Rearrangement in Alkyl-Bridged Bis(carbamoyldiaziridine) Derivatives. *Eur. J. Org. Chem.* 2012;2012:4733–4739.
- [29] KNOLL AG, Deutsches Reich, Verfahren zur Darstellung von Tetrazolen, 1926.
- [30] El-Ahl AAS, Elmorsy SS, Soliman H, Amer FA. A facile and convenient synthesis of substituted tetrazole derivatives from ketones or α,β -unsaturated ketones. *Tetrahedron Lett.* 1995;36:7337–7340.
- [31] Shannon R. Revised effective ionic radii and systematic studies of interatomic distances in halides and chalcogenides. *Acta Crystallogr. A* 1976;32:751–767.

- [32] Braun V, Wurzenberger MHH, Weippert V, Stierstorfer J. Tailoring the properties of 3d transition metal complexes with different N-cycloalkyl-substituted tetrazoles. *New J. Chem.* 2021;45:11042–11050.
- [33] Kofen M, Lommel M, Wurzenberger MHH, Klapötke TM, Stierstorfer J. 1-(Azidomethyl)-5*H*-tetrazole – a Powerful New Ligand for Highly Energetic Coordination Compounds. *Chem. Eur. J.* 2022:e202200492.
- [34] Frank P, Benfatto M, Szilagyi RK, D'Angelo P, Della Longa S, Hodgson KO. The Solution Structure of [Cu(aq)]²⁺ and Its Implications for Rack-Induced Bonding I n Blue Copper Protein Active Sites. *Inorg. Chem.* 2005;44:1922–1933.
- [35] Shannon RD, Prewitt CT. Effective ionic radii in oxides and fluorides. *Acta Crystallogr. B* 1969;25:925–946.
- [36] Lewis DL, Estes ED, Hodgson DJ. The infrared spectra of coordinated perchlorates. *J. Mol. Struct.* 1975;5:67–74.
- [37] Xie A, Zhang Q, Liu Y, Feng L, Hu X, Dong W. An Environmentally Friendly Method for N-Methylation of 5-Substituted 1*H*-Tetrazoles with a Green Methylating Reagent: Dimethyl Carbonate. *J. Heterocycl. Chem.* 2015;52:1483–1487.
- [38] Szimhardt N, Gruhne MS, Lommel M, Hess A, Wurzenberger MHH, Klapötke TM, Stierstorfer J. 2,2-Bis(5-tetrazolyl)propane as Ligand in Energetic 3d Transition Metal Complexes. *Z. Anorg. Allg. Chem.* 2019;645:354–361.
- [39] Szimhardt N, Stierstorfer J. Methylsemicarbazide as a Ligand in Late 3d Transition Metal Complexes. *Chem. Eur. J.* 2018;24:2687–2698.
- [40] Szimhardt N, Wurzenberger MHH, Klapötke TM, Lechner JT, Reichherzer H, Unger CC, Stierstorfer J. Highly functional energetic complexes: stability tuning through coordination diversity of isomeric propyl-linked ditetrazoles. *J. Mater. Chem. A* 2018;6:6565–6577.
- [41] Joas M, Klapötke TM, Szimhardt N. Photosensitive Metal(II) Perchlorates with 1,2-Bis[5-(1-methylhydrazinyl)tetrazol-1-yl]ethane as Ligand: Synthesis, Characterization and Laser Ignition. *Eur. J. Inorg. Chem.* 2014;2014:493–498.
- [42] UN, in *Recommendations on the Transport of Dangerous Goods: Model Regulations 19th ed.*, New York, 2015.
- [43] BAM, <http://www.bam.de>, (accessed April 2022).

9.6 Supplementary Information

9.6.1 Overview of compounds



9.6.2 Single Crystal X-Ray Diffraction

For all crystalline compounds an Oxford Xcalibur3 diffractometer with a CCD area detector or Bruker D8 Venture TXS diffractometer equipped with a multilayer monochromator, a Photon 2 detector, and a rotating-anode generator were employed for data collection using Mo- K_{α} radiation ($\lambda = 0.7107 \text{ \AA}$). On the Oxford device, data collection and reduction were carried out using the CrysAlisPRO software.^{S1} On the Bruker diffractometer, the data were collected with the Bruker Instrument Service v3.0.21, the data reduction was performed using the SAINT V8.18C software (Bruker AXS Inc., 2011). The structures were solved by direct methods (SIR-92,^{S2} SIR-97,^{S3,S4} SHELXS-97^{S5,S6} or SHELXT^{S7}), refined by full-matrix least-squares on F^2 (SHELXL^{S5,S6}) and finally checked using the PLATON software^{S8} integrated in the WinGX^{S7,S9} or Olex2^{S8} software suite. The non-hydrogen atoms were refined anisotropically and the hydrogen atoms were located and freely refined. The absorptions were corrected by a SCALE3 ABSPACK or SADABS Bruker APEX3 multi-scan method.^{S11,S12} All DIAMOND2 plots are shown with thermal ellipsoids at the 50% probability level and hydrogen atoms are shown as small spheres of arbitrary radius.

Table S1. Crystallographic data and structure refinement details for compounds 3, 4, and 9.

	3	4	5
Formula	C ₃ H ₆ N ₄	C ₁₈ H ₃₆ MnN ₂₄ Cl ₂ O ₈	C ₁₈ H ₃₆ FeN ₂₄ Cl ₂ O ₄
FW [g mol ⁻¹]	98.12	842.55	843.46
Crystal system	orthorhombic	trigonal	trigonal
Space group	<i>Pnma</i> (No. 62)	<i>P</i> -3 (No.147)	<i>P</i> -3 (No.147)
Color / Habit	colorless block	colorless platelet	colorless needles
Size [mm]	0.05 x 0.10 x 0.18	0.07 x 0.13 x 0.57	0.06 x 0.08 x 0.35
a [Å]	7.9923(5)	12.0103(8)	11.9258(17)
b [Å]	11.3058(7)	12.0103(8)	11.9258(17)
c [Å]	5.3980(3)	7.2015(6)	7.1630(12)
α [°]	90	90	90
β [°]	90	90	90
γ [°]	90	120	120
V [Å ³]	487.76(5)	899.63(16)	882.3(3)
Z	4	1	1
ρ _{calc.} [g cm ⁻³]	1.336	1.555	1.587
μ [mm ⁻¹]	0.096	0.593	0.658
F(000)	208	435	436
λ _{MoKα} [Å]	0.71073	0.71073	0.71073
T [K]	173	153	133
θ Min-Max [°]	4.2, 27.1	3.4, 26.4	3.5, 26.3
Dataset	-10: 10 ; -14: 14 ; -6: 6	-15: 15 ; -13: 15 ; -9: 7	-14: 14; -14: 14; -8: 8
Reflections collected	7550	5923	6811
Independent refl.	563	1225	1205
R _{int}	0.036	0.061	0.171
Observed reflections	507	896	708
Parameters	45	83	83
R ₁ (obs) ^[a]	0.0361	0.0466	0.0708
wR ₂ (all data) ^[b]	0.0995	0.1160	0.1801
S ^[c]	1.18	1.09	1.00
Resd. dens [e Å ⁻³]	-0.15, 0.22	-0.34, 0.48	-0.48, 0.99
Device type	Bruker D8 Venture TXS	Oxford Xcalibur3	Oxford Xcalibur3
Solution	SHELXT	SHELXT	SHELXT
Refinement	SHELXL-2018	SHELXL-2018	SHELXL-2018
Absorption correction	multi-scan	multi-scan	multi-scan

^[a]R₁ = Σ||F_o|-|F_c||/Σ|F_o|; ^[b]wR₂ = [Σ[w(F_o²-F_c²)²]/Σ[w(F_o)²]^{1/2}; w = [σ²(F_o²)+(xP)²+yP]⁻¹ and P=(F_o²+2F_c²)/3; ^[c]S = {Σ[w(F_o²-F_c²)²]/(n-p)}^{1/2} (n = number of reflections; p = total number of parameters).

Table S2. Crystallographic data and structure refinement details for compounds 3, 4, and 9.

	6	8	9
Formula	C ₁₈ H ₄₄ CoN ₂₄ O ₁₂ Cl ₂	C ₁₂ H ₂₆ CuN ₁₆ O ₉ Cl ₂	C ₁₂ H ₂₄ N ₁₆ ZnCl ₂ O ₈
FW [g mol ⁻¹]	918.60	672.93	656.74
Crystal system	monoclinic	orthorhombic	tetragonal
Space group	<i>P2₁/n</i> (No. 14)	<i>Pbca</i> (No. 61)	<i>P4₂2₁2</i> (No. 94)
Color / Habit	rose block	blue platelet	colorless platelet
Size [mm]	0.14 x 0.24 x 0.57	0.06 x 0.12 x 0.75	0.12 x 0.18 x 0.38
a [Å]	11.6339(4)	18.761(6)	11.3468(2)
b [Å]	7.0276(3)	14.286(4)	11.3468(2)
c [Å]	24.2339(10)	19.482(5)	10.0931(3)
α [°]	90	90	90
β [°]	93.894(4)	90	90
γ [°]	90	90	90
V [Å ³]	1976.75(14)	5222(3)	1299.49(6)
Z	2	8	2
ρ _{calc.} [g cm ⁻³]	1.543	1.712	1.679
μ [mm ⁻¹]	0.654	1.118	1.222
F(000)	954	2760	672
λ _{MoKα} [Å]	0.71073	0.71073	0.71073
T [K]	124	130	118
θ Min-Max [°]	2.0, 30.5	3.3, 26.4	3.2, 26.4
Dataset	-14: 16 ; -6: 9 ; -33: 32	-13: 23 ; -15: 17 ; -24: 12	-14: 14 ; -14: 14 ; -12: 12
Reflections collected	14030	14591	10299
Independent refl.	5386	5331	1328
R _{int}	0.040	0.166	0.043
Observed reflections	3996	2210	1234
Parameters	265	377	112
R ₁ (obs) ^[a]	0.0462	0.0814	0.0238
wR ₂ (all data) ^[b]	0.1060	0.1820	0.0594
S ^[c]	1.05	0.95	1.06
Resd. dens [e Å ⁻³]	-0.34, 0.41	-0.79, 0.82	-0.20, 0.28
Device type	Oxford Xcalibur3	Oxford Xcalibur3	Oxford Xcalibur3
Solution	SHELXT	SHELXT	SHELXT
Refinement	SHELXL-2018	SHELXL-2018	SHELXL-2018
Absorption correction	multi-scan	multi-scan	multi-scan

^[a]R₁ = $\sum ||F_o| - |F_c|| / \sum |F_o|$; ^[b]wR₂ = $[\sum [w(F_o^2 - F_c^2)^2] / \sum [w(F_o^2)]]^{1/2}$; $w = [\sigma^2(F_o^2) + (xP)^2 + yP]^{-1}$ and $P = (F_o^2 + 2F_c^2) / 3$; ^[c]S = $\{\sum [w(F_o^2 - F_c^2)^2] / (n-p)\}^{1/2}$ (n = number of reflections; p = total number of parameters).

Table S3. Crystallographic data and structure refinement details for compounds 3, 4, and 9.

	10	11a
Formula	C ₁₈ H ₁₆ CuN ₁₄ O ₁₄	C ₆₀ H ₆₀ Cu ₃ N ₅₀ O ₄₈
FW [g mol ⁻¹]	715.99	2440.20
Crystal system	monoclinic	triclinic
Space group	<i>P2₁/n</i> (No. 14)	<i>P</i> -1 (No. 2)
Color / Habit	green rod	green block
Size [mm]	0.03 x 0.03 x 0.10	0.05 x 0.06 x 0.07
a [Å]	17.6292(9)	10.3830(7)
b [Å]	11.2830(5)	15.8679(12)
c [Å]	28.5934(13)	16.3150(11)
α [°]	90	116.042(2)
β [°]	90.412(2)	90.788(2)
γ [°]	90	90.416(3)
V [Å ³]	5687.4(5)	2414.6(3)
Z	8	1
ρ _{calc.} [g cm ⁻³]	1.672	1.678
μ [mm ⁻¹]	0.862	0.779
F(000)	2904	1241
λ _{MoKα} [Å]	0.71073	0.71073
T [K]	304	173
θ Min-Max [°]	2.3, 25.4	2.4, 26.4
Dataset	-21: 21 ; -13: 13 ; -34: 34	-12: 12 ; -19: 19 ; -20: 20
Reflections collected	93558	40595
Independent refl.	10411	9841
R _{int}	0.060	0.047
Observed reflections	7562	7902
Parameters	855	738
R ₁ (obs) ^[a]	0.0505	0.0395
wR ₂ (all data) ^[b]	0.1300	0.1084
S ^[c]	1.05	1.04
Resd. dens [e Å ⁻³]	-0.33, 0.43	-0.39, 0.90
Device type	Bruker D8 Venture TXS	Bruker D8 Venture TXS
Solution	SHELXT	SHELXT
Refinement	SHELXL-2018	SHELXL-2018
Absorption correction	multi-scan	multi-scan

^[a]R₁ = $\sum ||F_o| - |F_c|| / \sum |F_o|$; ^[b]wR₂ = $[\sum [w(F_o^2 - F_c^2)^2] / \sum [w(F_o^2)]]^{1/2}$; $w = [\sigma^2(F_o^2) + (xP)^2 + yP]^{-1}$ and $P = (F_o^2 + 2F_c^2) / 3$; ^[c]S = $\{\sum [w(F_o^2 - F_c^2)^2] / (n - p)\}^{1/2}$ (n = number of reflections; p = total number of parameters).

Table S4. Crystallographic data and structure refinement details for compounds 3, 4, and 9.

	12a	12b
Formula	C ₁₈ H ₂₀ CuN ₁₄ O ₂₀	C ₁₂ H ₁₃ CuN ₁₁ O ₉
FW [g mol ⁻¹]	816.02	518.87
Crystal system	monoclinic	monoclinic
Space group	<i>P2₁/c</i> (No. 14)	<i>P2₁/n</i> (No. 14)
Color / Habit	green block	green plate
Size [mm]	0.05 x 0.06 x 0.08	0.03 x 0.09 x 0.13
a [Å]	21.4502(18)	13.6964(12)
b [Å]	7.8186(7)	8.7538(8)
c [Å]	18.0115(18)	16.7837(15)
α [°]	90	90
β [°]	94.679(3)	102.646(3)
γ [°]	90	90
V [Å ³]	3010.7(5)	1963.5(3)
Z	4	4
ρ _{calc.} [g cm ⁻³]	1.800	1.755
μ [mm ⁻¹]	0.840	1.189
F(000)	1660	1052
λ _{MoKα} [Å]	0.71073	0.71073
T [K]	173	173
θ Min-Max [°]	1.9, 26.4	2.8, 26.4
Dataset	-25: 26 ; -9: 9 ; -22: 22	-17: 17 ; -10: 10 ; -20: 20
Reflections collected	53283	39911
Independent refl.	6161	3993
R _{int}	0.054	0.057
Observed reflections	5454	3638
Parameters	509	323
R ₁ (obs) ^[a]	0.0302	0.0312
wR ₂ (all data) ^[b]	0.0814	0.0859
S ^[c]	1.07	1.07
Resd. dens [e Å ⁻³]	-0.41, 0.33	-0.32, 0.65
Device type	Bruker D8 Venture TXS	Bruker D8 Venture TXS
Solution	SHELXT	SHELXT
Refinement	SHELXL-2018	SHELXL-2018
Absorption correction	multi-scan	multi-scan

^[a]R₁ = $\sum ||F_o| - |F_c|| / \sum |F_o|$; ^[b]wR₂ = $[\sum [w(F_o^2 - F_c^2)^2] / \sum [w(F_o^2)]]^{1/2}$; $w = [\sigma^2(F_o^2) + (xP)^2 + yP]^{-1}$ and $P = (F_o^2 + 2F_c^2) / 3$; ^[c]S = $\{\sum [w(F_o^2 - F_c^2)^2] / (n - p)\}^{1/2}$ (n = number of reflections; p = total number of parameters).

9.6.3 Single Crystal X-Ray Diffraction

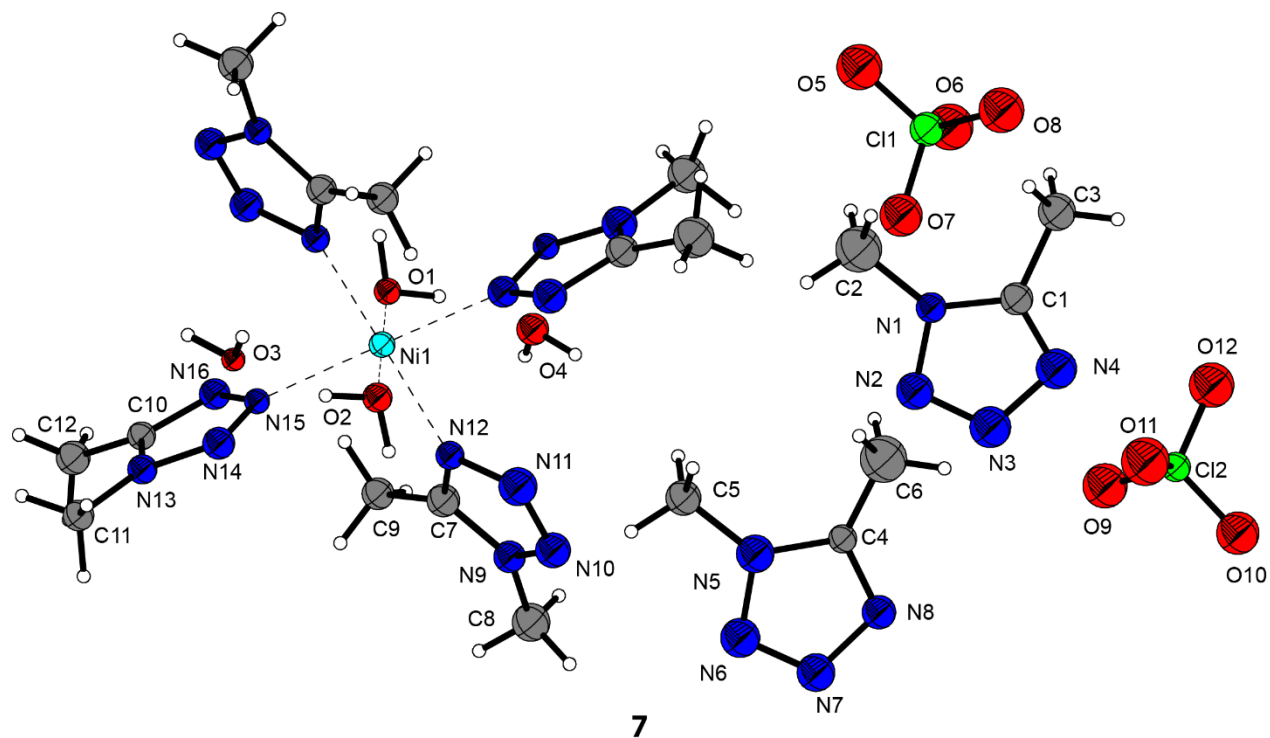
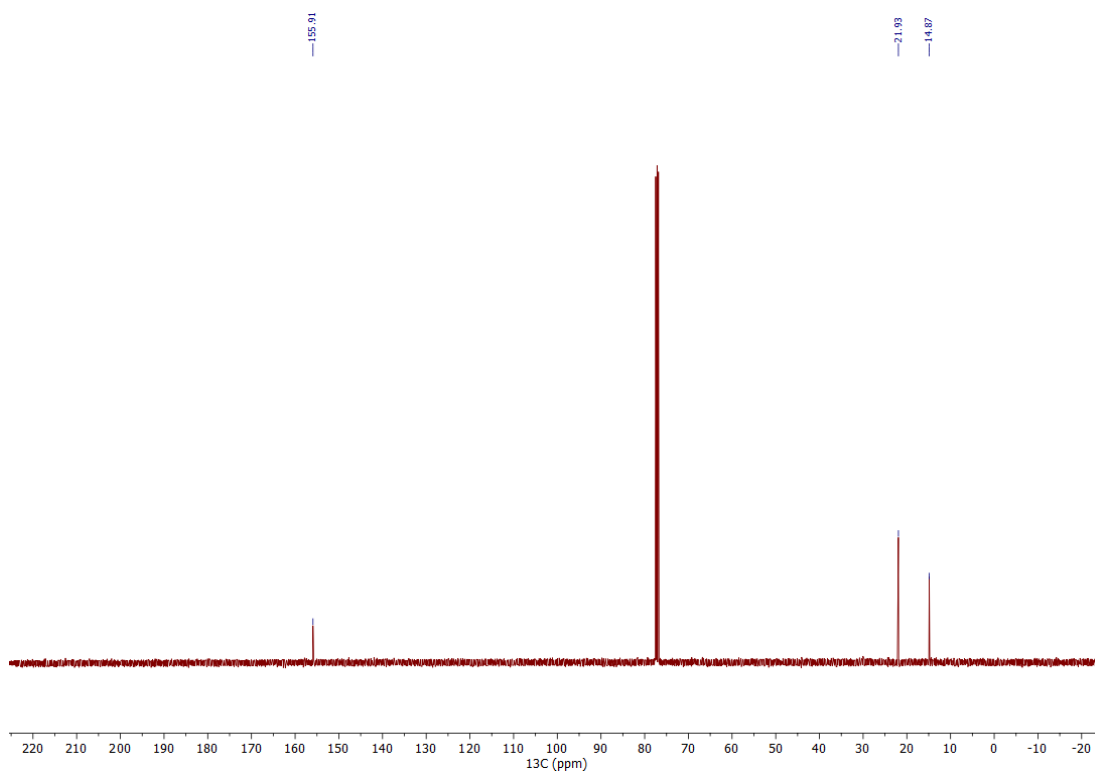
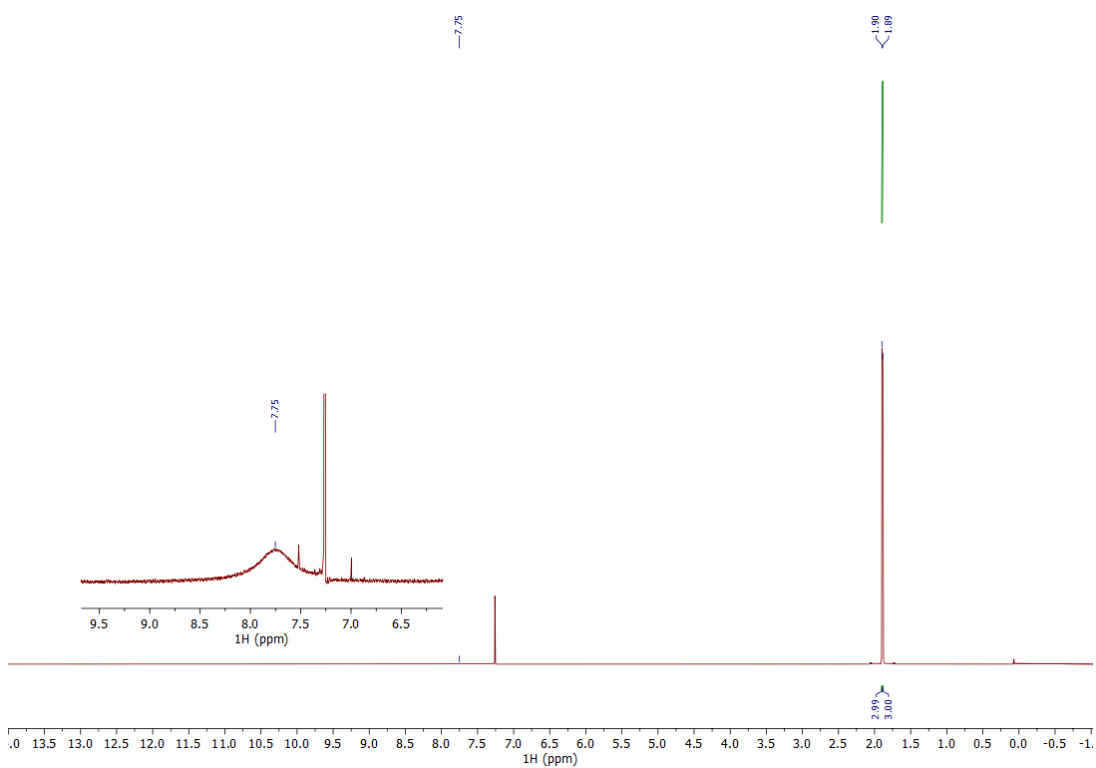


Figure S1. Depiction of obtained structure of compound 7.

9.6.4 NMR spectroscopy of 1-3



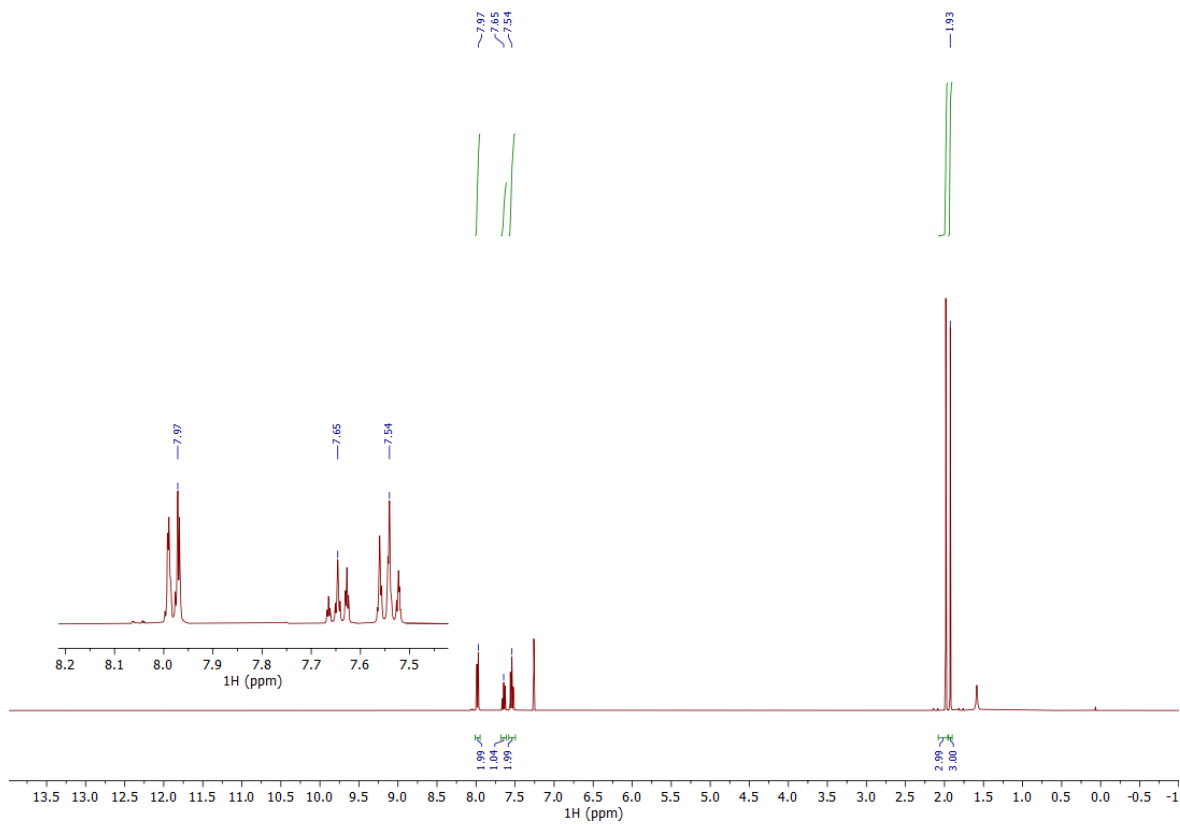


Figure S3. ¹H NMR of compound 2 in CDCl₃.

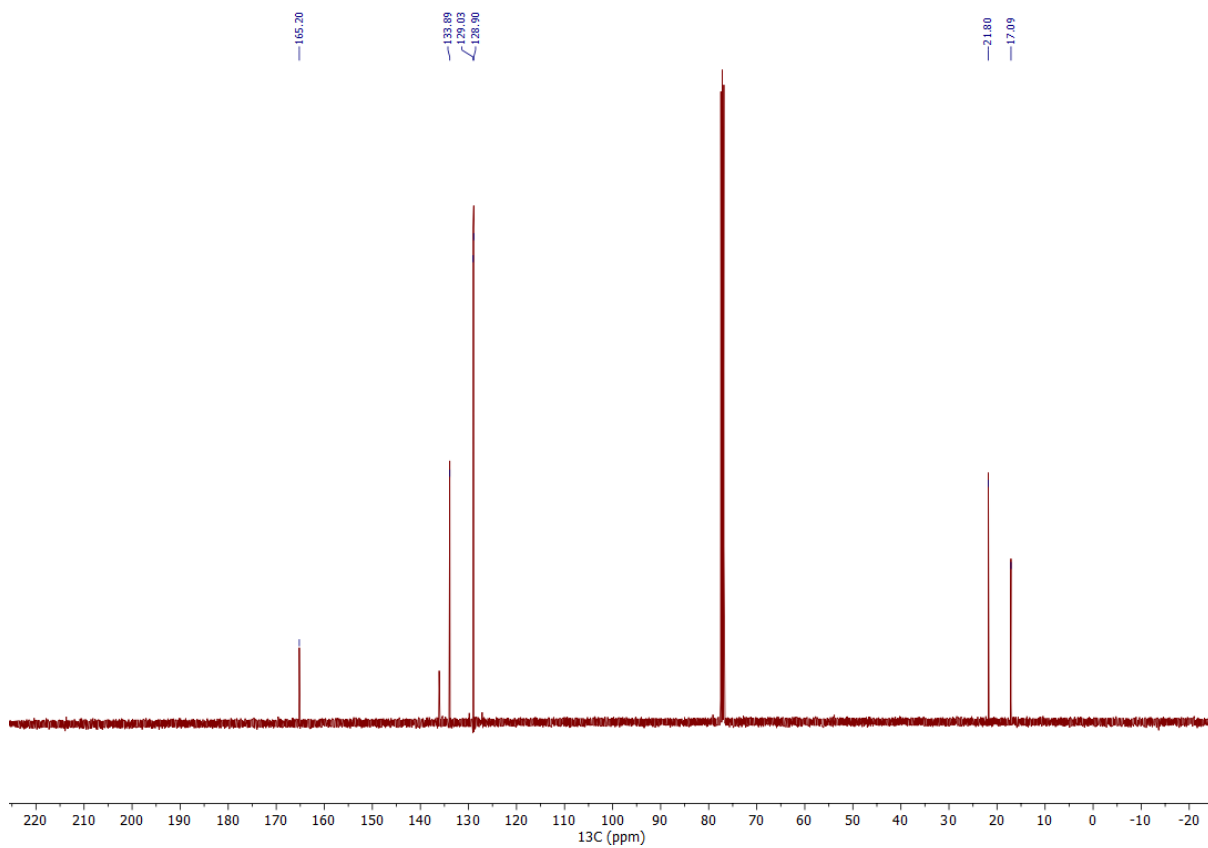


Figure S4. ^{13}C NMR of compound **2** in CDCl_3

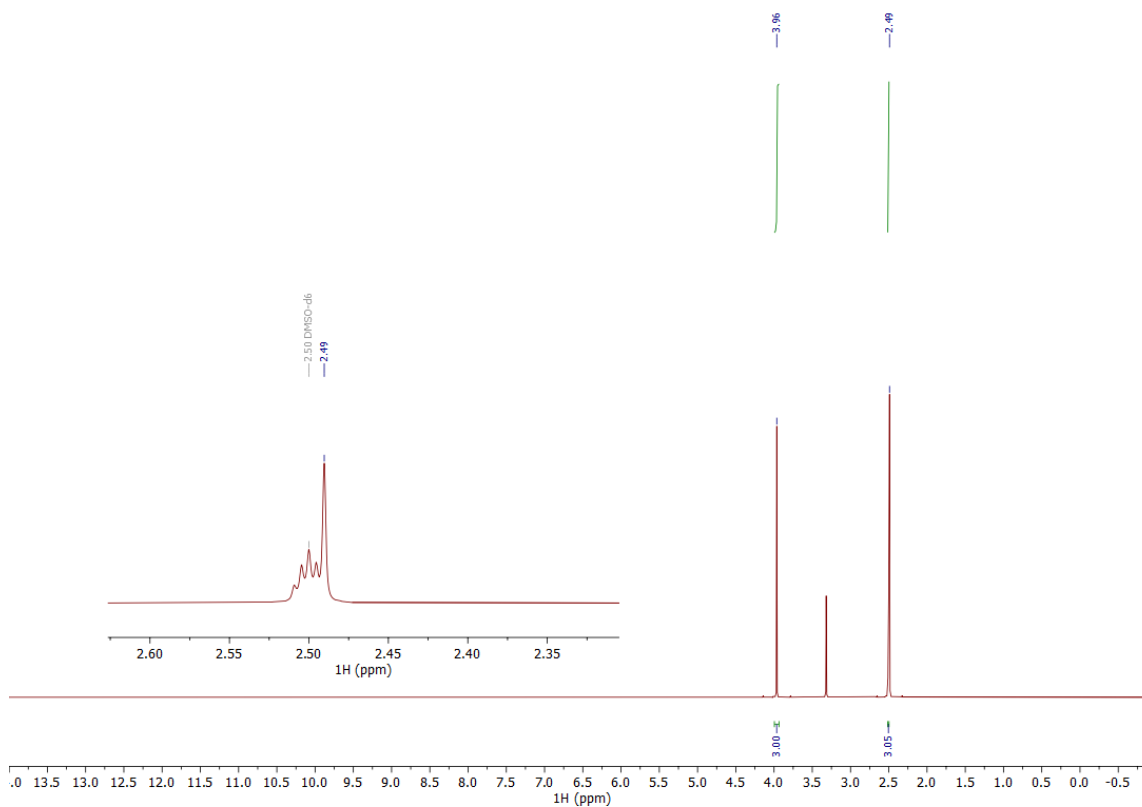


Figure S5. ^1H NMR of compound **3** in DMSO-d_6 .

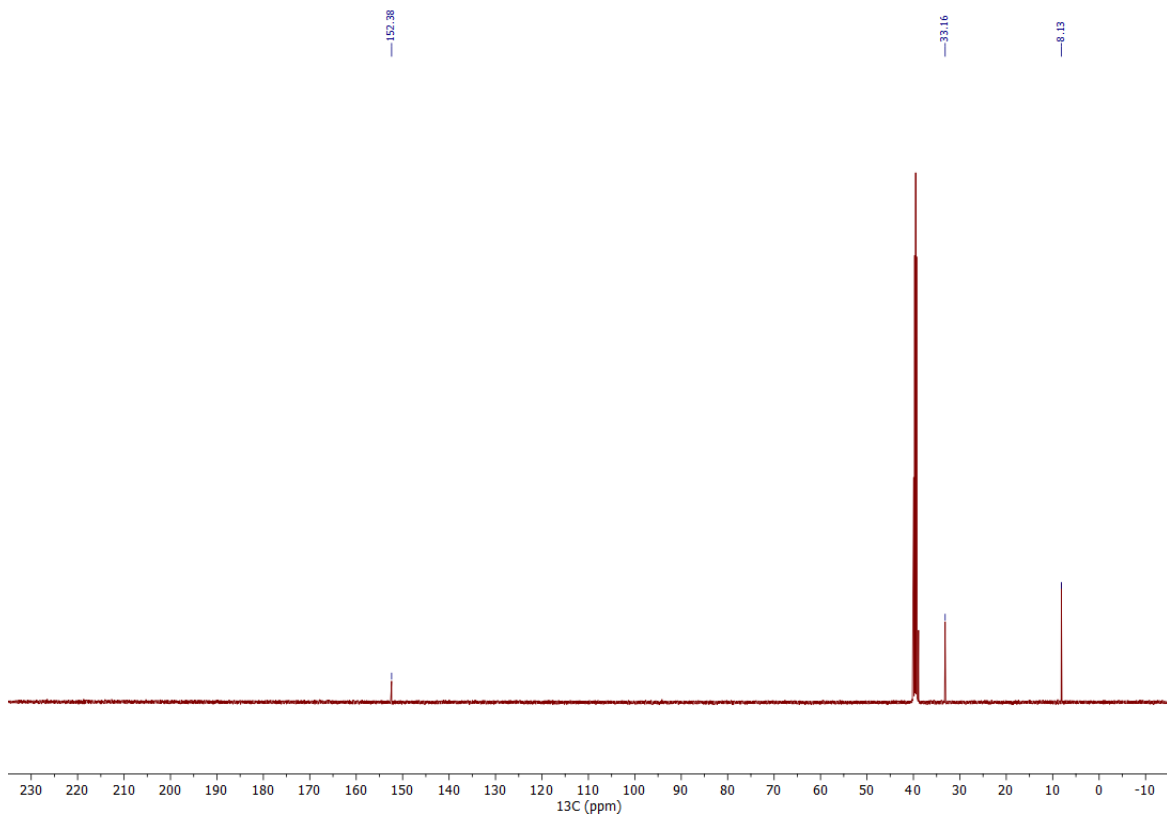


Figure S6. ^{13}C NMR of compound **3** in DMSO-d_6 .

9.6.5 General Methods

All chemicals and solvents were employed as received (Sigma-Aldrich, Fluka, Acros, ABCR). ^1H , $^{13}\text{C}\{^1\text{H}\}$, ^{14}N , $^{15}\text{N}\{^1\text{H}\}$ spectra were recorded at ambient temperature using a JEOL Bruker 27400, Eclipse 270, JEOL EX 400 or a JEOL Eclipse 400 instrument. The chemical shifts quoted in ppm in the text refer to typical standards such as tetramethylsilane (^1H , ^{13}C) nitromethane (^{14}N , ^{15}N) in DMSO- d_6 , D₂O or acetone- d_6 as the solvent. Endothermic and exothermic events of the described compounds, which indicate melting, loss of crystal water or decomposition, are given as the extrapolated onset temperatures. The samples were measured in a range of 25–400 °C at a heating rate of 5 °C min⁻¹ through differential thermal analysis (DTA) with an OZM Research DTA 552-Ex instrument. Infrared spectra were measured with pure samples on a Perkin-Elmer BXII FT-IR system with a Smith DuraSampler IR II diamond ATR. Determination of the carbon, hydrogen, and nitrogen contents was carried out by combustion analysis using an Elementar Vario EI (nitrogen values determined are often lower than the calculated ones' due to their explosive behavior). Impact sensitivity tests were carried out according to STANAG 4489^{S13} with a modified instruction^{S14} using a BAM (Bundesanstalt für Materialforschung) drophammer.^{S15} Friction sensitivity tests were carried out according to STANAG 4487^{S17} with a modified instruction^{S18} using the BAM friction tester.^{S15,16} The classification of the tested compounds results from the "UN Recommendations on the Transport of Dangerous Goods".^{S19,20}

9.6.6 References

- S1 CrysAlisPRO (Version 171.33.41), Oxford Diffraction Ltd., 2009.
- S2 A. Altomare, G. Cascarano, C. Giacovazzo, and A. Guagliardi, *J. Appl. Crystallogr.*, 1992, **26**, 343.
- S3 A. Altomare, G. Cascarano, C. Giacovazzo, A. Guagliardi, A. G. G. Moliterni, M. C. Burla, G. Polidori, M. Camalli and R. Spagna, SIR97, 2003.
- S4 A. Altomare, M. C. Burla, M. Camalli, G. L. Cascarano, C. Giacovazzo, A. Guagliardi, A. G. G. Moliterni, G. Polidori and R. Spagna, *J. Appl. Crystallogr.*, 1999, **32**, 115.
- S5 G. M. Sheldrick, SHELXL-97, University of Göttingen, Germany, 1997.
- S6 G. M. Sheldrick, *Acta Crystallogr. Sect. A*, 2008, **64**, 112.
- S7 G. M. Sheldrick, *Acta Cryst. A*, 2015, **71**, 3–8.
- S8 A. L. Spek, PLATON, Utrecht University, The Netherlands, 1999.
- S9 L.J. Farrugia, *J. Appl. Cryst.*, 2012, **45**, 849.
- S10 O. V. Dolomanov, L. J. Bourhis, R. J. Gildea, J. A. K. Howard and H. Puschmann, *J. Appl. Cryst.*, 2009, **42**, 339–341.
- S11 Empirical absorption correction using spherical harmonics, implemented in SCALE3 ABSPACK scaling algorithm (CrysAlisPro Oxford Diffraction Ltd., Version 171.33.41, 2009).
- S12 APEX3, Bruker AXS Inc., Madison, Wisconsin, USA.
- S13 NATO standardization agreement (STANAG) on explosives, impact sensitivity tests, no. 4489, 1st ed., Sept. 17, 1999.
- S14 WIWEB-Standardarbeitsanweisung 4-5.1.02, Ermittlung der Explosionsgefährlichkeit, hier der Schlagempfindlichkeit mit dem Fallhammer, Nov. 8, 2002.
- S15 BAM, <http://www.bam.de>, (accessed April 2022).
- S16 OZM, <http://www.ozm.cz>, (accessed April 2022).
- S17 NATO standardization agreement (STANAG) on explosive, friction sensitivity tests, no. 4487, 1st ed., Aug. 22, 2002.
- S18 WIWEB-Standardarbeitsanweisung 4-5.1.03, Ermittlung der Explosionsgefährlichkeit oder der Reibeempfindlichkeit mit dem Reibeapparat, Nov. 8, 2002.

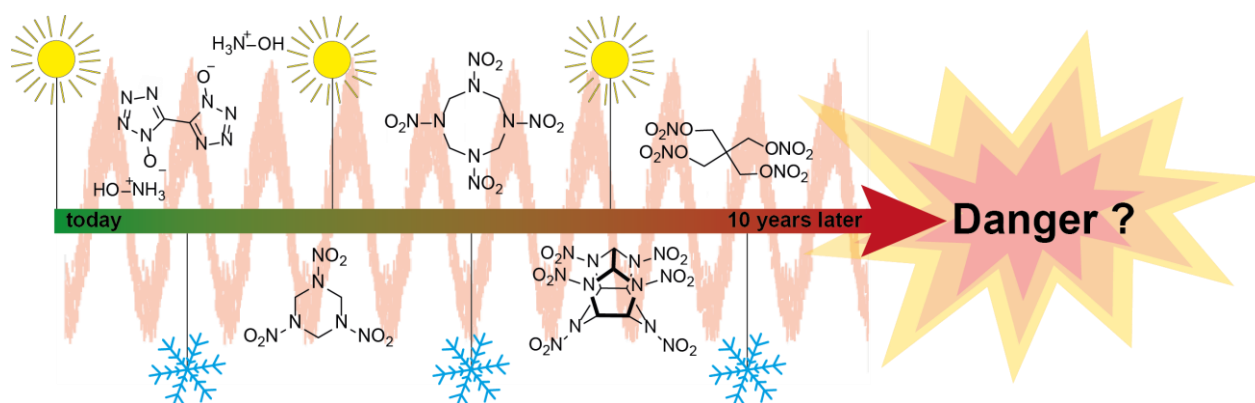
- S19 UN Model Regulation: Recommendations on the Transport of Dangerous Goods – Manual of Tests and Criteria, section 13.4.2.3.3, 2015.
- S20 Impact: insensitive > 40 J, less sensitive ≥ 35 J, sensitive ≥ 4 J, very sensitive ≤ 3 J; Friction: insensitive > 360 N, less sensitive = 360 N, sensitive < 360 N and > 80 N, very sensitive ≤ 80 N, extremely sensitive ≤ 10 N. According to the UN Recommendations on the Transport of Dangerous Goods, 5th ed., 2009.

10. Kinetic Predictions Concerning the Long-Term Stability of TKX-50 and Other Common Explosives Using the NETZSCH Kinetics Neo Software

Alexander G. Harter, Thomas M. Klapötke, Jasmin T. Lechner, Jörg Stierstorfer

as published in *Propellants, Explosives, Pyrotechnics* **2022**, 7.

DOI: 10.1002/prop.202200031



Key words: Activation Energy, Energetic Materials, Kinetic Studies, Long-term Stability, Storage Safety

Abstract: Explosives are used in both military and civilian applications all over the world. Sufficient longevity and good thermal stability are therefore essential for safe handling and safe storage of energetic materials. In this work, five well-known compounds, TKX-50, RDX, HMX, CL-20 and PETN, were investigated by means of different kinetic models, in order to make predictions about their long-term stability. For this purpose, the compounds were synthesized according to literature-known procedures and thermogravimetric (TG) measurements were performed. The TG plots were analyzed using the Ozawa-Flynn-Wall, Friedman and ASTM E698 kinetic models with the NETZSCH Kinetics Neo software and the activation energy and isothermal long-term stability were determined. Moreover, various climatic predictions of different countries were made.

10.1 Introduction

In order to be used in an industrial scale an energetic compound has to meet certain criteria 1, 2, some of them are shown in Figure 1.

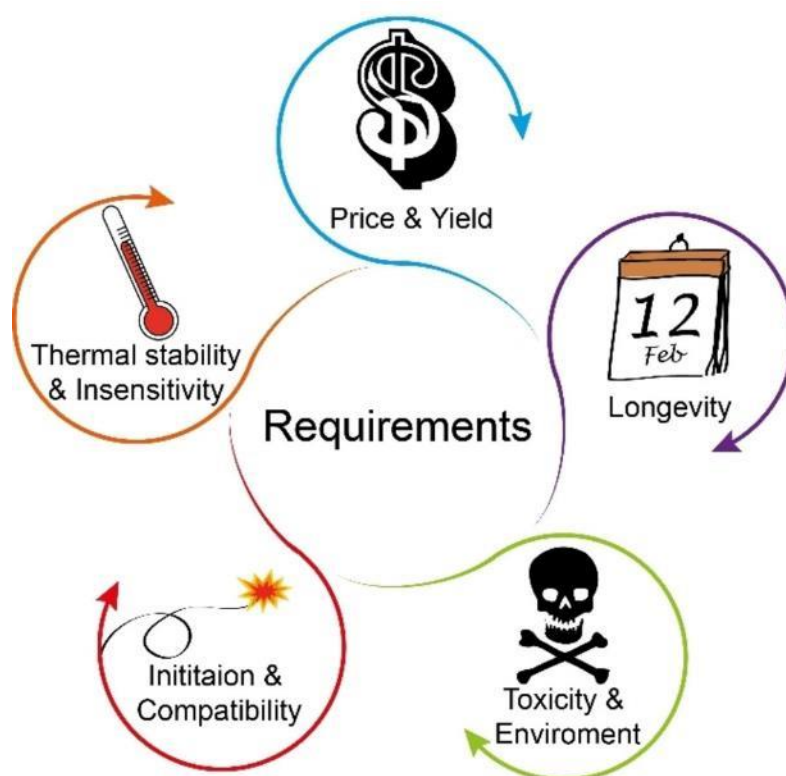


Figure 1. Main requirements of a commercial explosive like TKX-50.

Of course, economic aspects like price and yield play a major role during the development of energetic materials. The synthesis should follow a simple route, with a minimal amount of reaction steps, and should ideally start from cheap chemicals, which are potentially recyclable. In addition, the yield of the product should be as high as possible and both reactants and products, should be neither toxic nor harmful to the environment 3.

In addition, the initiation properties and the compatibility 4 of energetic compounds are of high importance, since they are commonly used in mixtures or compositions. Those mixtures usually contain common secondary explosives such as hexogen (RDX), octogen (HMX) or pentaerythritol tetranitrate (PETN) 5-8.

In terms of safe handling the sensitivities of high explosives towards impact, friction and electrostatic discharge (ESD) are important parameters 9. Those can easily be determined accurately by standardized measurements according to BAM 10. However, energetic compounds are not only sensitive towards the previously named stimuli but also towards thermal influences. Most energetic compounds are potentially able to undergo self-accelerated decomposition, when exposed to higher temperatures 11. This process also takes place at room temperature, if the compound is stored for very long periods of time. In order to guarantee safe long-term storage, the explosive compounds must be stable at low and especially at high temperatures. This longevity is important to prevent catastrophic accidents, such as the ammonium nitrate detonation, which recently occurred in Beirut 12.

In order to better forecast the long-term stability, in this work, kinetic predictions were performed using the example of the widely used secondary explosives TKX-50, RDX, HMX, CL-20 and PETN. The structures of these compounds are shown in Figure 2. Since energetic materials are used all over the world and for a wide variety of applications, this work also investigates the stability of named compounds in regard to different climatic profiles like Munich, Washington D.C. and Cairo.

In the following, the long-term stability predictions and calculations for TKX-50 are discussed in detail, and compared to the other commonly known energetic materials. The in-depth results of the other compounds can be found in the Supplementary Information.

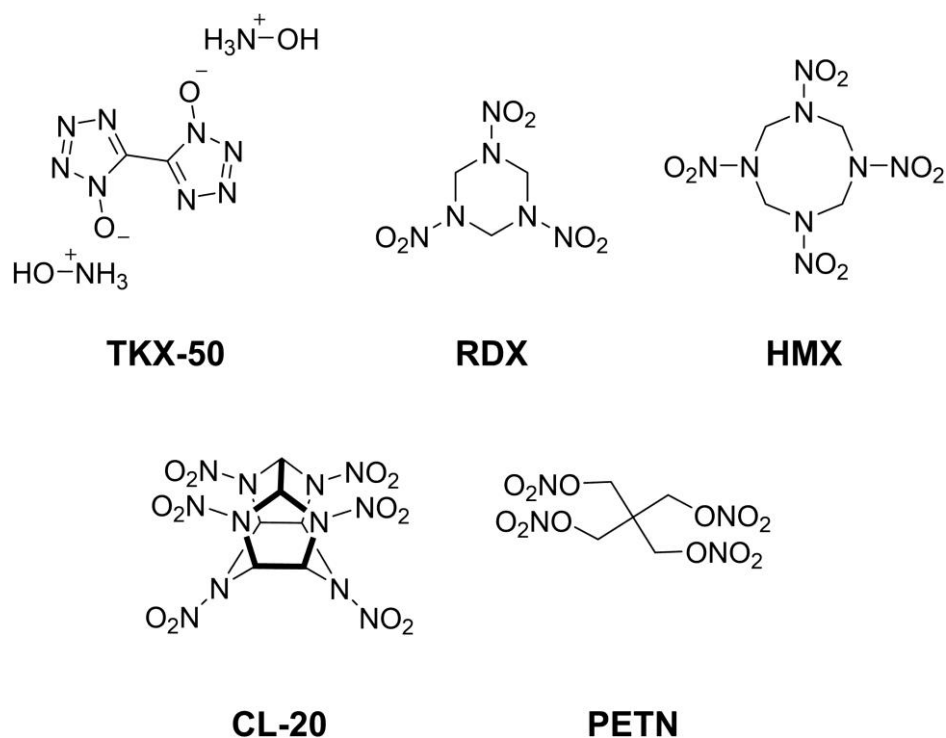


Figure 2. Molecular structures of TKX-50, RDX, HMX, CL-20 and PETN.

10.2 Experimental Section

All compounds were prepared according to literature-known syntheses.[13,14] They were checked for purity by NMR and elemental analysis.

To evaluate the samples with the NETZSCH Kinetics Neo software[15], thermal gravimetric analysis (TGA) measurements with a PerkinElmer TGA4000 were performed. In order to provide a consistent set of measurements, the samples were dried and sieved to keep them solvent free and within a uniform range of particle size. The measurements were performed at heating rates of 1 K min^{-1} ($m= 2.071 \text{ mg}$), 2 K min^{-1} ($m= 1.879 \text{ mg}$), 5 K min^{-1} ($m= 2.285 \text{ mg}$) and 10 K min^{-1} ($m= 2.105 \text{ mg}$) within a temperature range of 303 K to 673 K.

The sample weights of the verification experiment can be found in the SI.

10.3 Results and Discussion

10.3.1 Theoretical Background

In order to do predictions of the long-term stabilities, the kinetics of the decomposition processes have to be studied. Based on the data provided by the TGA measurements at different heating rates, kinetic models can be developed to accurately describe the decomposition process.[11,16] Different established theoretical methods like ASTM E698, Ozawa-Flynn-Wall and Friedman have been investigated, to find the model, which best fits the experimental data. All three of those methods are model free approaches, which allow to determine the necessary parameters like activation energies and pre-exponential factors, without assumption of the reaction type. Therefore, a set of several TGA measurements is required.[17]

The ASTM method is based on first order kinetics, determining the activation energy using peak maxima points of the temperature T_p . [18] With the assumption that the extent of the reaction rate at T_p is constant, a set of heating rates β is used to plot $\ln(\beta)$ against $1/T_p$, resulting in a straight line. The slope of this line is proportional to the activation energy. Since decomposition reactions are usually multistep and not first order reactions, in most cases this approach is not suitable for a decent description of the kinetic behavior of decomposing energetic materials.

Therefore, the Ozawa-Flynn-Wall and Friedman approaches, which are both isoconversional methods and suitable for multiple-step reactions, were investigated.[16] In order to apply those methods, two assumptions are made. The first assumption of model free analysis is that the reaction can always be described by eq. 1. It is based on the dependence of the activation energy E_a and the pre-exponential factor A on the reaction progress α .

$$\frac{d\alpha}{dt} = A(\alpha)f(\alpha) \exp\left(-\frac{E(\alpha)}{RT}\right) \quad (1)$$

Secondly it is assumed that the reaction rate at a constant conversion value can be described as a function, which is only dependent on the temperature.

The Ozawa-Flynn-Wall method is an integral isoconversional approach, solving eq. 1 by integration, which results in eq. 2.[19]

$$g(\alpha) = \int_0^1 \frac{d\alpha}{f(\alpha)} = \frac{A(\alpha)}{\beta} \int_{T_0}^T \exp\left(-\frac{E(\alpha)}{RT}\right) dT \quad (2)$$

This equation is transformed into eq. 3 by the approximation according to Doyle [20].

$$\log(\beta) = \log\left(\frac{AE_a}{R}\right) - 2.315 - 0.4567 \frac{E_a}{RT} \quad (3)$$

The graphic logarithm of the heating rate is applied to the inverse temperatures of the points with the same conversion for different heating rates, resulting in straight lines connecting points of same conversion. From the slope of these lines the activation energy and the preexponential factor can be determined.[21]

The Friedman approach relies on a differential solution of eq. 1, resulting in eq. 4, where R is the universal gas constant and T is the temperature.[22] The activation energy and the preexponential factor are determined analog to the previous method, by the slope and intersect of the straight lines, connecting points of same conversion, when plotting the logarithm of the conversion rate against the inverse temperatures.[23]

$$\ln\left(\frac{d\alpha}{dt}\right) = \ln(A f(\alpha)) - \frac{E_a}{RT} \quad (4)$$

In addition to these model free methods, a model-based approach was investigated for TKX-50. Therefore, again several assumptions were made. The reaction has to consist of a number of reaction steps, and for each of these steps the reaction rate can be described by the kinetic equation 5, depending on the concentration of the initial reactant e_j , the concentration of the product p_j , the preexponential factor A_j and the activation energy E_j . This equation is specific for the reaction step j and the reaction type of each step can be described by the function f_j . [24]

$$\alpha = A_j f_j(e_j, p_j) \exp\left[\frac{-E_j}{RT}\right] \quad (5)$$

The second assumption is that the relevant factors including activation energy, preexponential factor, order of reaction and reaction type for each step are considered constant. Lastly it is assumed that the thermoanalytical signal equals the sum of the signals of the single reaction steps, while the effect of each step is calculated by multiplying the reaction rate with the mass loss of this step.

In case of TKX-50 a three-step decomposition process was observed from the TGA measurements. The best fit to the analytical data was achieved by assuming the first

step to be an auto-catalytic reaction of first order and the following two steps reactions of n^{th} order. All investigated models were compared in terms of their fit to the measured data and the results are summarized in Table 1 for the example of TKX-50.

Table 10 Comparison of the kinetic models in regard to their fit to the measured data of TKX-50.

Method	R^2 [a]	Sum of dev. squares	Mean Residual
OzawaFlynnWall	0.98085	99829	2.758
ASTM E698	0.98200	93910	4.117
Model based	0.99964	1913	0.607
Friedman	0.99971	1543	0.493

[a] correlation coefficient.

The best fit was achieved using the Friedman method, with an excellent R^2 value of 0.99971. The model-based approach was only slightly lower with an R^2 of 0.99964. In order to calculate long term stabilities, the R^2 value should be around 0.999 to give decent predictions. Therefore, the Friedman method was chosen for all investigated compounds, since it provided the best fit values over all.

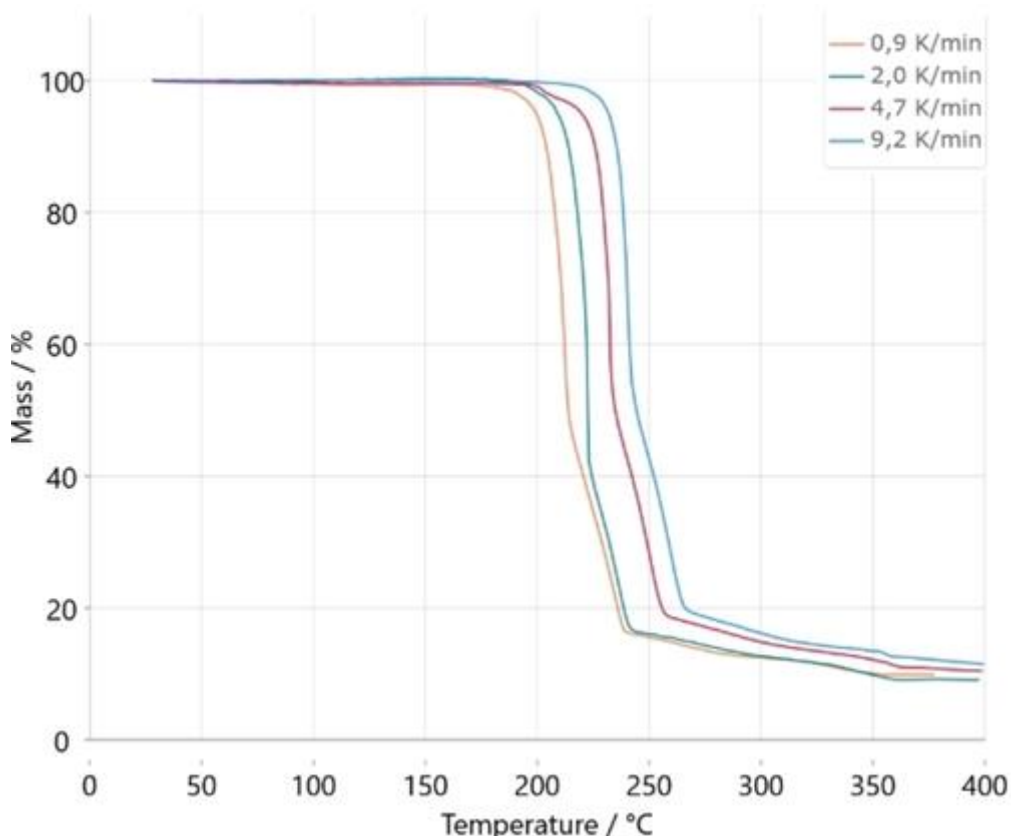
10.3.2 Method Evaluation

In order to obtain a solid set of data, TGA measurements were performed at four different heating rates, shown in Figure 3, for the example of TKX-50. A three-step decomposition process with a sudden mass loss between 180 and 220 °C, depending on the heating rate, can be observed. During the first step a mass loss of about 50 % takes place, followed by a slightly flattened second step, which leads to a mass loss of over 80 %. The third step is much slower in comparison to the first two, resulting in an overall mass loss of about 90 %, when heating to 400 °C.

Following the same method, the remaining four compounds were analyzed. RDX starts decomposing between 160 and 180 °C in a much more unsteady manner compared to TKX-50. This can be explained by partial melting and decomposition showing a mass loss of about 20 %. A second step can be observed between 200 and 250 °C, showing a clean decomposition leading to a mass loss of over 95 %. In case of HMX the TGA measurements show a one-step decomposition process starting between 230 and 260 °C and ending at 260 to 280 °C with a mass loss of 95 %. CL-20 has a first decomposition step starting at 200 – 240 °C and leading to a mass loss of about 90 %.

A second very slow step takes place between 250 and 400 °C with an additional minor mass loss of 5 %. When looking at the measurement of PETN a mass loss of 95 – 98 %, starting at 140 – 170 °C, depending on the heating rate, can be observed.

Here it has to be mentioned, that in order to improve the accuracy of determining the stability it might be necessary to take the individual characteristics like melting point,



vapor pressure and exact decomposition reactions into account. In order to not **Figure 3.** TGA measurements of TKX-50.

overcomplicate the analysis and comparison we decided to not take these variables into account.

The measured datasets were now evaluated with the Netsch kinetics Neo software. In order to make long term stability predictions the previously established Friedman method was used to describe the decomposition process of all five compounds. These fits of the calculated values compared to the measured data is shown on Figure 4 for the example of TKX-50.

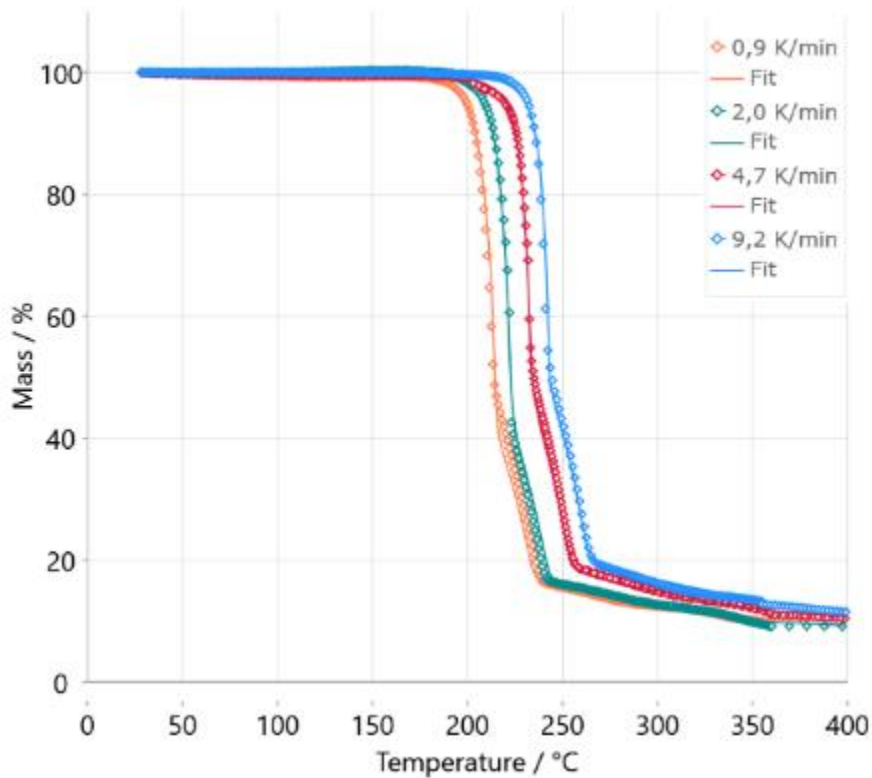


Figure 4. Friedman conversion-fit of TKX-50.

In case of TKX-50, RDX and PETN the Friedman method produced a fit with excellent R^2 values of above 0.999. Due to their very sudden decomposition, HMX and CL-20 showed slightly lower R^2 values of 0.99768 (HMX) and 0.99776 (CL-20), but in order to get a good comparison and full dataset the samples were evaluated even though they did not reach the ideal R^2 value.

10.3.3 Activation Energy

With the analysis by the Friedman method, the activation energy throughout the decomposition process was determined and depicted against the conversion in Figure 5 for the example of TKX-50.[25,26]

The determined activation energy accurately describes the three-step decomposition

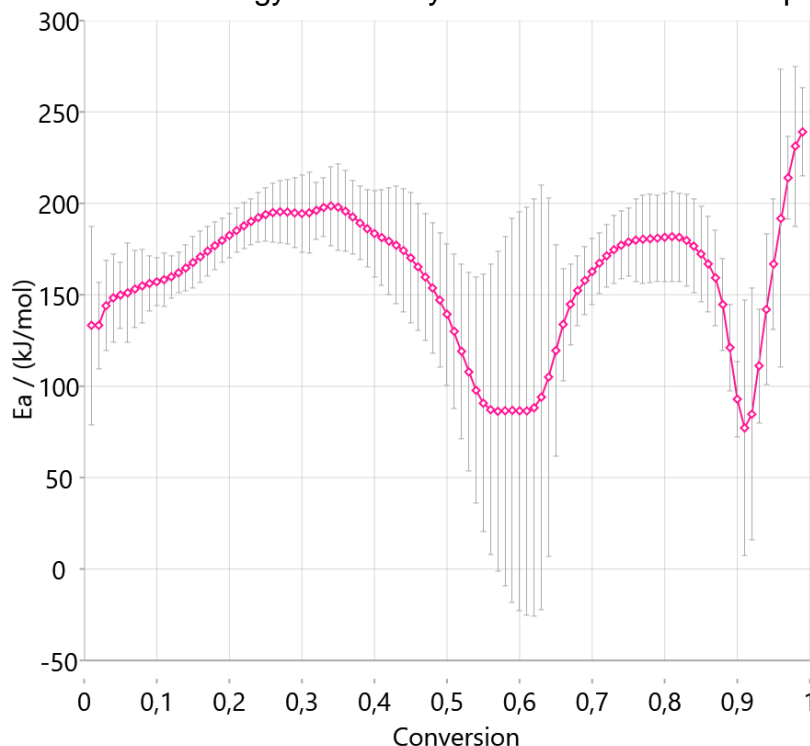


Figure 5. Activation energy applied against the conversion for the decomposition of TKX-50 determined by the Friedman method.

process of TKX-50 with three peak maxima. It starts at 133 kJ mol^{-1} and reaches a maximum of 198 kJ mol^{-1} during the first decomposition step which ends with a minimum of 86 kJ mol^{-1} at a conversion of 50 %. Afterwards, it rises to a local maximum of 181 kJ mol^{-1} during the second step, followed by a minimum of 77 kJ mol^{-1} . The last decomposition step is characterized by a sudden increase to a peak maximum of 239 kJ mol^{-1} . According to literature the activation energy of TKX-50 was already determined using different methods. Values between 112 kJ mol^{-1} and 176 kJ mol^{-1} were reported, so our predicted value of 133 kJ mol^{-1} fits well to previous calculations.[25]

The activation energy plot of RDX also meets the expectations, starting at 170 kJ mol^{-1} . Followed by the first unsteady decomposition step, which is represented by a peak maximum of 238 kJ mol^{-1} : After that a sharp drop to 60 kJ mol^{-1} at a conversion of around 15 % could be seen. With the start of the second decomposition step the activation energy rises to 213 kJ mol^{-1} at 30 % conversion and then steadily drops down to 40 kJ mol^{-1} at the end of the reaction. In case of HMX the activation energy starts at 95 kJ mol^{-1} and increases to 387 kJ mol^{-1} at a conversion of 20 %. From that

point it rises slowly to an overall maximum of 428 kJ mol^{-1} at a conversion of about 70 % followed by a minor drop to 360 kJ mol^{-1} at the end of the decomposition. The plot for CL-20 shows an initial activation energy of 163 kJ mol^{-1} , which increases to 383 kJ mol^{-1} at a conversion value of about 0.1. The energy value then slowly decreases to 230 kJ mol^{-1} until 85 % of the reaction has taken place, where it drops suddenly to 3 kJ mol^{-1} , rises to 143 kJ mol^{-1} and finally decreases again to -354 kJ mol^{-1} , indicating a barrier free reaction during the final part of the decomposition process. The reaction of PETN start at an activation energy of 132 kJ mol^{-1} and immediately drops to 44 kJ mol^{-1} at a conversion of 10 %. It then slowly increases to a maximum value of 83 kJ mol^{-1} at a conversion of 90 %, followed by a final sharp drop to -31 kJ mol^{-1} .

10.3.4 Isothermal predictions and long-term stability

In order to evaluate all compounds in regard to their long-term stability, isothermal predictions at different temperatures were calculated over a time period of 10 years. Starting at $0 \text{ }^{\circ}\text{C}$ we calculated mass loss in $20 \text{ }^{\circ}\text{C}$ steps, up to $100 \text{ }^{\circ}\text{C}$, which gives a comprehensive insight into the thermal stabilities of the investigated compounds, ranging from a frozen storage to high temperature stress. The isothermal prediction for TKX-50 is depicted in Figure 6.

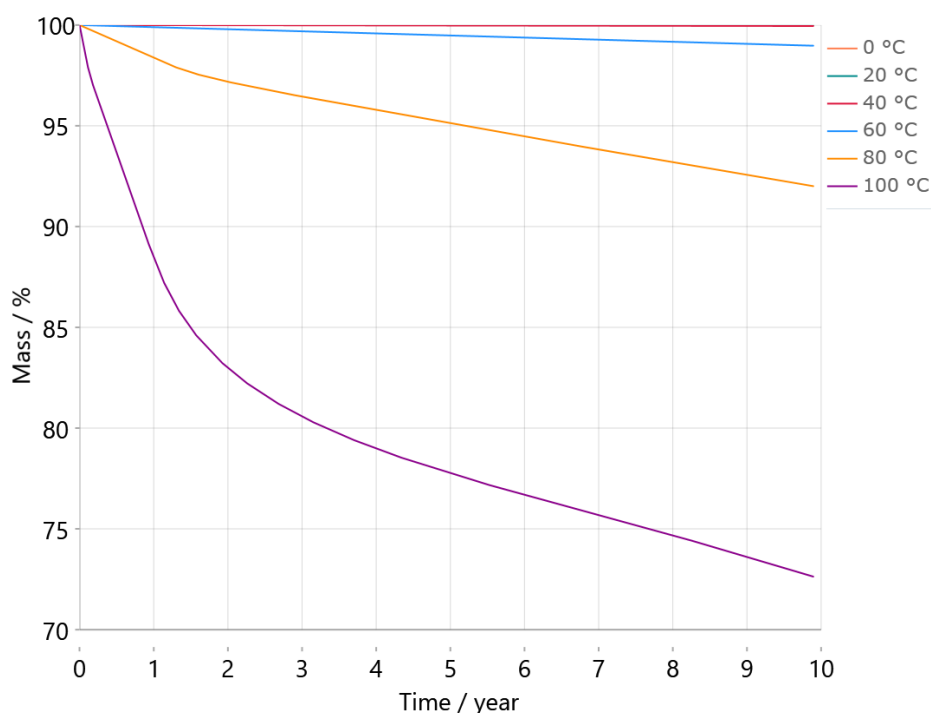


Figure 6. Isothermal predictions of TKX-50 at different temperatures for 10 years.

TKX-50 shows excellent thermal stabilities between 0 °C and 40 °C, with no notable mass loss over the predicted time period. Even when stored at 60 °C, which has been measured as a maximum temperature for sea shipping container, the predicted mass loss of TKX-50 is below 2 % over 10 years [27]. If TKX-50 is exposed to high temperature stress of 100 °C the prediction shows a steep mass loss of about 20 % during the first 3 years, and a total mass loss of 27 % over the entire 10 years.

RDX performs quite similar to TKX-50, with no notable mass loss between 0 °C and 40 °C, but it shows a slightly higher mass loss of about 35 % when stored under 100 °C. When looking at HMX, a surprisingly low mass loss of only 5 % can be observed, when stored at 100 °C over 10 years, with the majority taking place during the first year. In addition, HMX already has a notable mass loss of 1.5 % at 40 °C, which makes it less stable than RDX and TKX-50 at lower temperatures. CL-20 possesses the best overall stability at all measured temperatures. No notable mass loss can be detected up to 60 °C and even at 100 °C the mass loss over ten years barely reaches the 4 % mark. In contrast to this, PETN exhibits the lowest long-term stability of the tested compounds. In this case the prediction does not reflect the actual behavior of PETN in storage, since PETN has a low melting point and an overall higher vapor pressure, which leads to a slight, but constant mass loss up to the decomposition during the TGA measurement. This mass loss process is interpreted by the software as a decomposition and therefore the prediction shows a lower stability than PETN exhibits in reality. Nonetheless the overall trend fits the expectations of PETN being the least stable of the investigated compound. According to the prediction it is stable without mass loss between 0 °C and 20 °C, but already decomposes entirely after 3 years, when stored at 40 °C. Above 60 °C the decomposition takes place in under 3 months.

In order to verify the calculated data, samples of the investigated compounds were placed in an oven at 100 °C for four weeks. The mass loss of each individual compound was measured after 4, 14 and 28 days, respectively and summarized in Table 2.

Table 2 Mass loss of common explosives at 100 °C over 4 weeks.

Time ^a	TKX-50	RDX	HMX	CL-20	PETN
[d]	[mass%]	[mass%]	[mass%]	[mass%]	[mass%]
4	0.078	0.070	0.043	0.052	0.083
14	0.080	0.224	0.118	0.027	0.775
28	0.298	0.451	0.792	0.207	1.358

^a Time of storage at 100 °C in days.

For a correct interpretation of the experimental values the samples were dried for 2 days in advance to eliminate unwanted mass loss due to moisture. When taking this into consideration, the experimental values certify the calculated stabilities exceptionally well. The mass loss of RDX and TKX-50 is comparable, with TKX-50 showing a slightly better performance when comparing the values of 4 to 28 days. The prediction of HMX showed a higher mass loss during the first months, which is also the case for the experimental data. As expected, CL-20 shows the lowest, and PETN the highest overall mass loss. To provide a better overview, the experimental results are visualized in Figure 7.

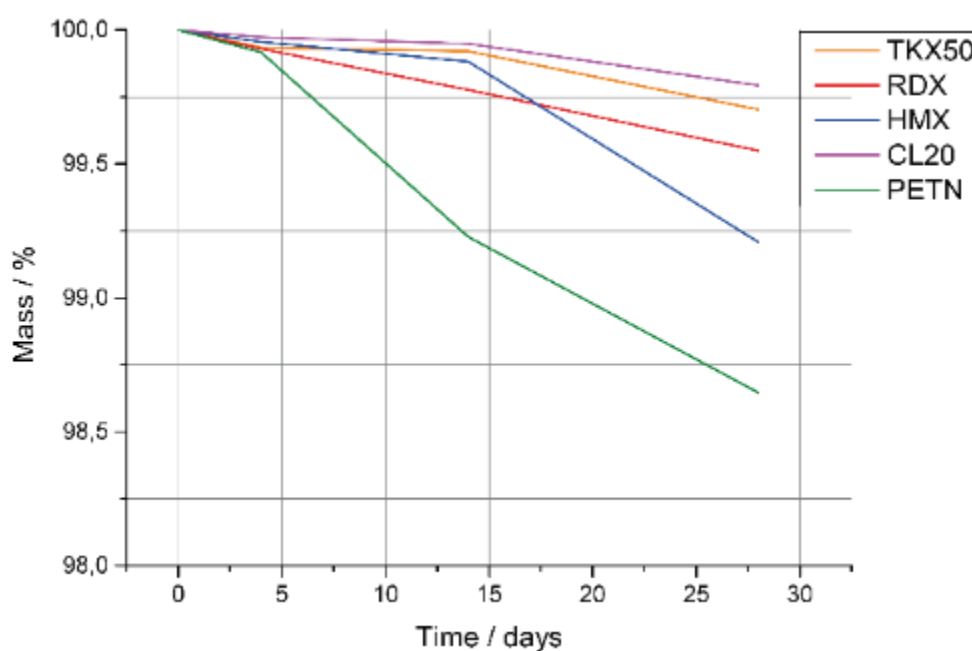


Figure 7. Mass loss of common explosives at 100 °C over 4 weeks.

10.3.5 Climatic predictions

In addition to isothermal temperature predictions, it was also possible to calculate long term stabilities in dependency of climatic data. Therefore the climatic data of different cities was averaged over the last 30 years and used to predict long term stabilities for the investigated energetic materials, when stored under those conditions. The goal was to include a broad spectrum of different climatic conditions, while still using locations of high international importance. Our final selection included six cities on four different continents, including Munich, Moscow, Washington D.C., Brasilia, Cairo and Beijing, representing Europe, North America, South America, Africa and Asia, respectively.

The climatic predictions for TKX-50 over 10 years are depicted in Figure 8. Similar to the isothermal predictions, TKX-50 shows excellent stabilities under all climatic conditions with a mass loss of below 0.01 mass % during the chosen time period. Even under harsh conditions like the hot summers in Cairo and the tropical climate in Brasilia, TKX-50 only loses around 0.003 % of its mass. But it has to be mentioned, that the humidity is not included in these predictions, as it is assumed that secondary explosives are stored under dry conditions. As expected the milder regions like Europe and North America show even better stabilities, with Moscow having the best values, due to its cold winters. For the other compounds, the observed trend for the isothermal predictions is validated by the climatic predictions. RDX has a comparable performance to TKX-50, while PETN shows the highest mass loss and CL-20 the overall best stability. HMX also fits the isothermal data well, showing a high mass loss at low temperatures in comparison to the other compounds.

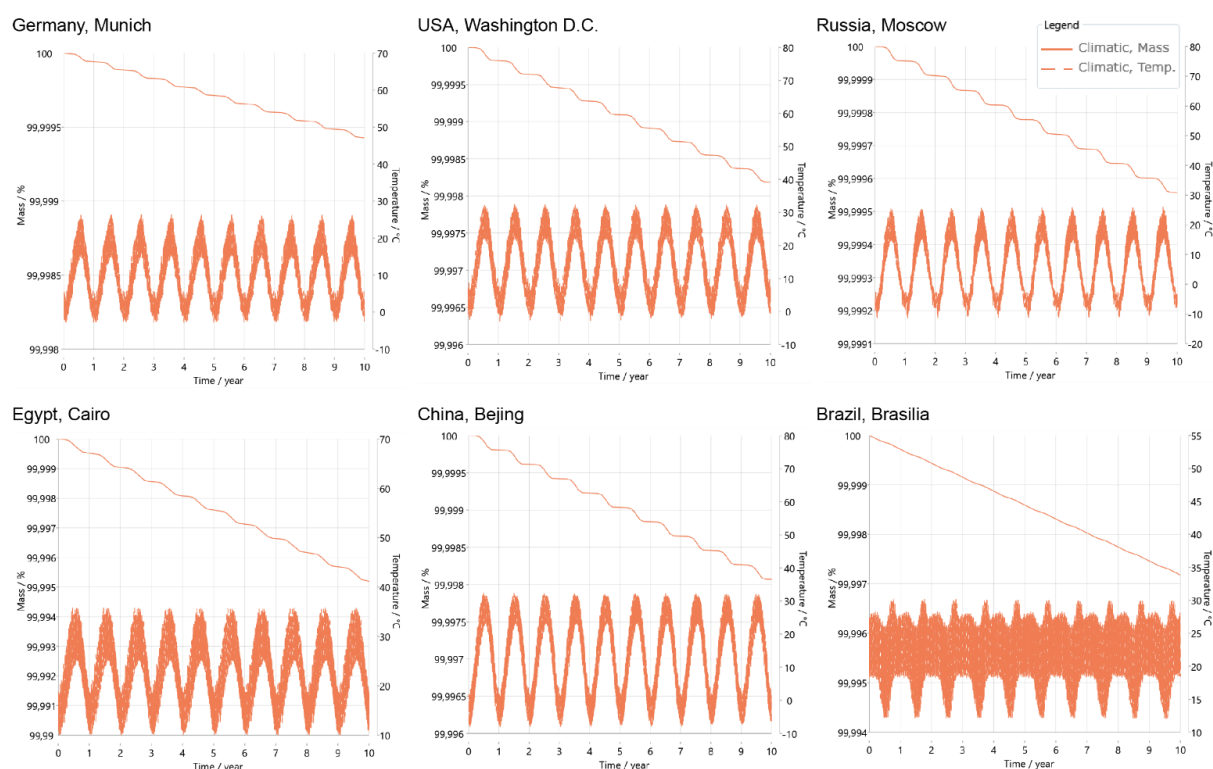


Figure 8. Climatic prediction of TKX-50 for 10 years using the average temperature data of the last 30 years in various different climate zones.

10.3.6 Conclusion

In order to establish a reliable database about the long-term stability of energetic materials, five commonly known secondary explosives, TKX-50, RDX HMX, CL-20 and PETN, were investigated in this work. Based on TGA measurements, three kinetic models, the Ozawa-Flynn-Wall method, the ASTM E698 and the Friedman method were evaluated regarding their fit to the experimental data. In all cases, the best results were obtained with the Friedman method, which was used to predict long term stabilities for the named compounds over 10 years. In summary, the highest long-term stability can be predicted for CL-20 and the lowest for PETN. TKX-50 shows excellent longevity, with a slightly better behavior than RDX. In addition, the long term stability of TKX-50 was investigated in regard to various different climatic conditions.

In order to validate the calculated results, the five compounds were stored at 100°C for 4 weeks and their mass loss was investigated during this time. The obtained data was consistent to the kinetic predictions.

Acknowledgements

For financial support of this work by Ludwig Maximilian University (LMU), the Office of Naval Research (ONR) under grant no. ONR N00014-19-1-2078 and the Strategic Environmental Research and Development Program (SERDP) under contract no. W912HQ19C0033 are gratefully acknowledged.

10.4 References

- [1] T. M. Klapötke, *Chemistry of High-Energy Materials*, 5th ed., DE GRUYTER, Berlin/Boston **2019**.
- [2] P. Ying, D. A. Parrish, J. M. Shreeve, Bis(nitroamino-1,2,4-triazolates): N-Bridging Strategy Toward Insensitive Energetic Materials, *Angew. Chem. Int. Ed.* **2014**, *53*, 1288–12892.
- [3] L. E. Fried, M. R. Manaa, P. F. Pagoria, R. L. Simpson, Design and Synthesis of Energetic Materials, *Annu. Rev. Mater. Sci.* **2001**, *31*, 291–321.
- [4] F. G. J. May, Australian test procedures for determination of compatibility and stability of military explosives, *J. Hazard. Mater.* **2077**, *2*, 127–135.
- [5] J.-S. Lee, C.-K. Hsu, The thermal behaviors and safety characteristics of composition B explosive, *Thermochimica Acta* **2001**, *367–368*, 371–374.
- [6] S. H. Kim, B. W. Nyande, H. S. Kim, J. s. Park, W. J. Lee, M. Oh, Numerical analysis of thermal decomposition for RDX, TNT, and Composition B, *J. Hazard. Mater.* **2016**, *308*, 120–130.
- [7] E. G. Mahadevan, *Ammonium Nitrate Explosives for Civil Applications*, Wiley-VCH., Weinheim, **2013**.
- [8] J. Köhler, R. Meyer, A. Homburg, *Explosivstoffe*, 10th ed., Wiley-VCH, Weinheim **2008**.
- [9] a) NATO standardization agreement (STANAG) on explosives, impact sensitivity tests, no. 4489, 1st ed., Sept. 17, 1999; b) NATO standardization agreement (STANAG) on explosive, friction sensitivity tests, no. 4487, 1st ed., Aug. 22, 2002.
- [10] <http://www.bam.de>, Accessed October 2021.
- [11] C. C. Unger, M. Holler, B. Krumm, T. M. Klapötke, Oxygen-Rich Bis(trinitroethyl esters): Suitable Oxidizers as Potential Ammonium Perchlorate Replacements, *Energy Fuels* **2020**, *34*, 16469–16475.
- [12] T. M. Klapötke, Ammoniumnitrat – Dünger, Sprengstoff, Gasgenerator, *Chem. Unserer Zeit* **2021**, *55*, 256–263.
- [13] N. Fischer, D. Fischer, T. M. Klapötke, D. G. Piercy, J. Stierstorfer, Pushing the limits of energetic materials – the synthesis and characterization of dihydroxylammonium 5,50-bistetrazole-1,10-diolate, *J.Mater.Chem.* **2012**, *22*, 20418–20422.

- [14] M. A. C. Härtel, Studies Towards the Gas-Phase Detection of Hazardous Materials by Vapor Pressure Measurements with the Transpiration Method in Combination with Vacuum Outlet GC/MS, dissertation LMU Munich, **2017**.
- [15] NETZSCH Kinetics Neo software, version 2.5.0.1, 2021.
- [16] P. Ravi, Model free isoconversional procedure for evaluating the effective activation energy values of thermally stimulated processes in dinitroimidazoles, *J. Chem. Phys.* **2014**, *140*, 204201.
- [17] S. Vyazovkin, Model-free kinetics, *J. Therm. Anal. Calorim.* **2006**, *83*, 45–51.
- [18] P. Stolarek; S. Ledakowicz, Evaluation of the ASTM E 698 Method for Determination of Kinetic Parameters of Thermal Decomposition Processes, *Chem. Process Eng.* **2003**, *24*, 701–715.
- [19] T. Ozawa, A New Method of Analyzing Thermogravimetric Data, *Bull. Chem. Soc. Jpn.* **1965**, *38 (11)*, 1881–1886.
- [20] C. Doyle, Series Approximations to the Equation of Thermogravimetric Data, *Nature* **1965**, *207*, 290–291.
- [21] H. Flynn and L. A. Wall, General Treatment of the Thermogravimetry of Polymers, *J. Res. Nat. Bur. Standards* **1966**, *70A*, 487.
- [22] H. L. Friedman, Kinetics of Thermal Degradation of Char-Forming Plastics from Thermogravimetry. Application to a Phenolic Plastic, *J. polym. sci.* **1964**, *6*: 183–195.
- [23] M. Venkatesh, P. Ravi, S. P. Tewari, Isoconversional Kinetic Analysis of Decomposition of Nitroimidazoles: Friedman method vs Flynn–Wall–Ozawa Method, *Phys. Chem. A* **2013**, *117*, 40, 10162–10169.
- [24] A. S. Portnyagin, A. P. Golikolov, V. A. Drozd, V. A. Avramenko, An alternative approach to kinetic analysis of temperature-programmed reaction data, *RSC Adv.* **2018**, *8*, 3286-3295.
- [25] N. V. Muravyev, K. A. Monogarov, A. F. Asachenko, M. S. Nechaev, I. V. Ananyev, I. V. Fomenkov, V. G. Kiselev, A. N. Pivkina, Pursuing Reliable Thermal Analysis Techniques for Energetic Materials: Decomposition Kinetics and Thermal Stability of Dihydroxylammonium 5,5'- Bistetrazole-1,1'-Diolate (TKX-50), *Phys. Chem. Chem. Phys.* **2017**, *19*, 436–449.
- [26] Y. Yu, S. Chen, T. Li, S. Jin, G. Zhang, M. Chen, L. Li, Study on a novel high energetic and insensitive munitions formulation: TKX-50 based melt cast high explosive, *RSC Adv.* **2017**, *7*, 31485–31492.

- [27] S. P. Singh, K. Saha, J. Singh, A. P. S. Sandhu, Measurement and Analysis of Vibration and Temperature Levels in Global Intermodal Container Shipments on Truck, Rail and Ship, *Packag. Technol. Sci.* **2012**, 25, 149–160.

10.5 Supplementary Information

10.5.1 Method evaluation

RDX

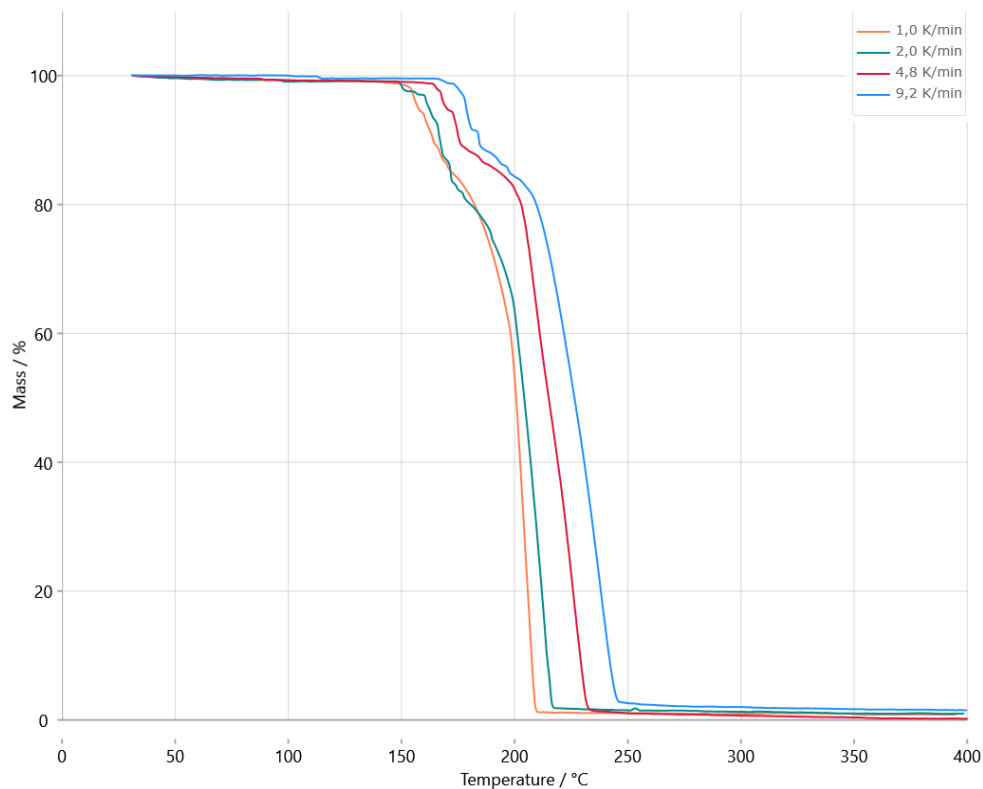


Figure S1. TGA measurements of RDX.

Table S1. Sample weights of the different TGA measurements of RDX.

TGA heating rate	Sample weight [mg]
1 K min ⁻¹	2.649
2 K min ⁻¹	2.325
5 K min ⁻¹	2.651
10 K min ⁻¹	2.436

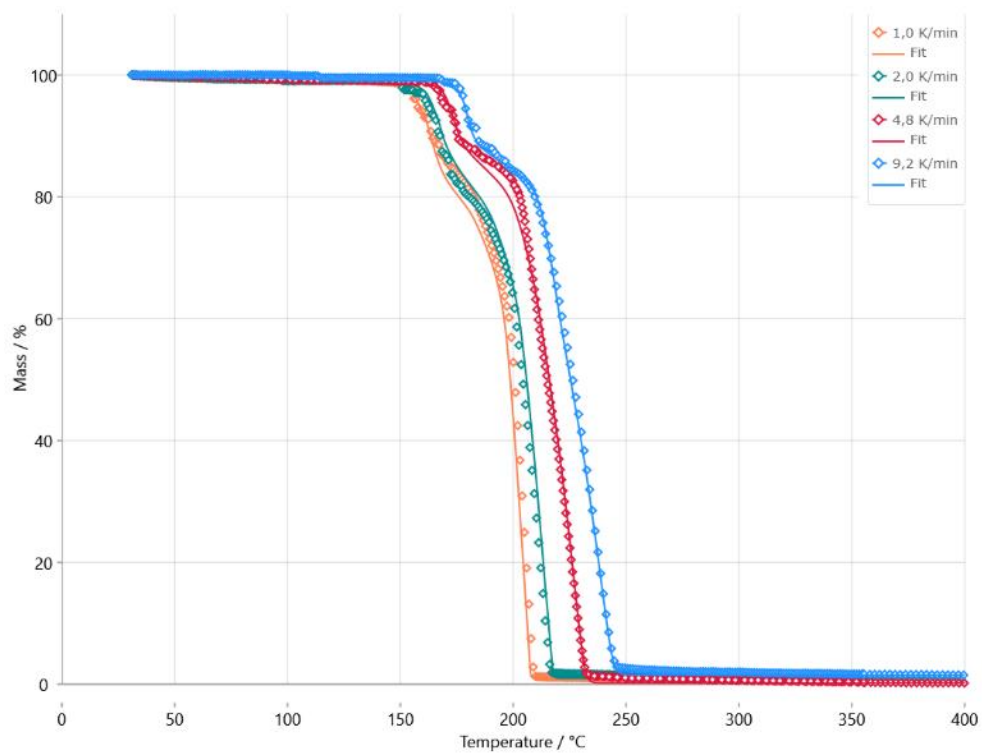


Figure S2. Friedman conversion-fit of RDX.

HMX

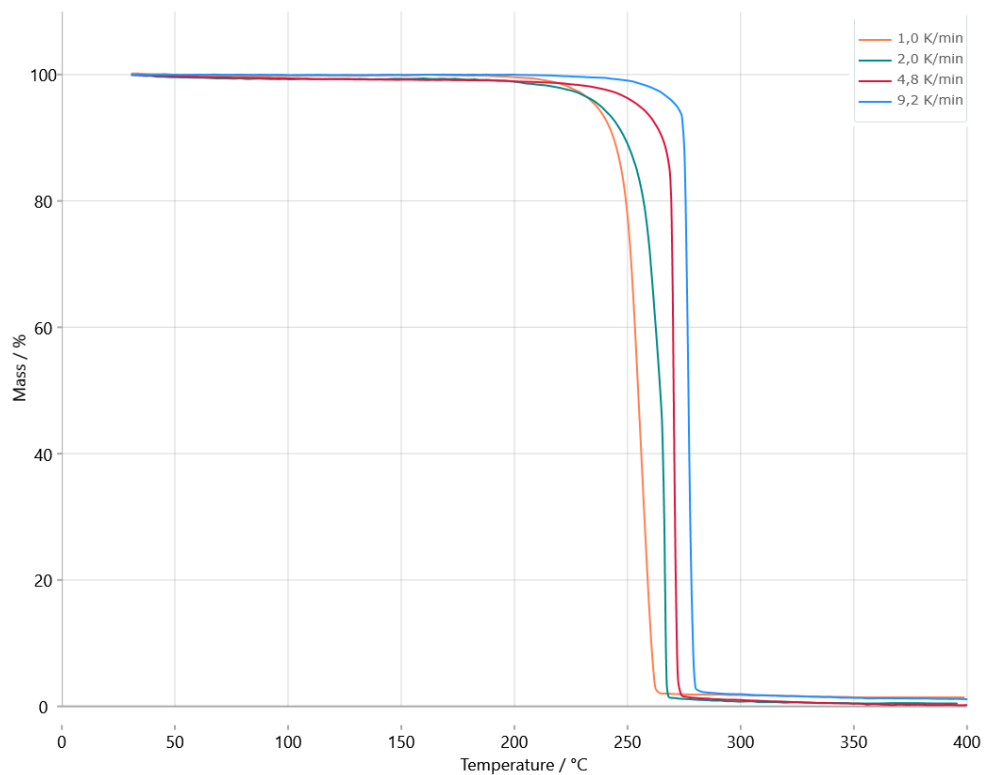


Figure S3. TGA measurements of HMX.

Table S2. Sample weights of the different TGA measurements of HMX.

TGA heating rate	Sample weight [mg]
1 K min ⁻¹	2.920
2 K min ⁻¹	1.920
5 K min ⁻¹	3.144
10 K min ⁻¹	2.993

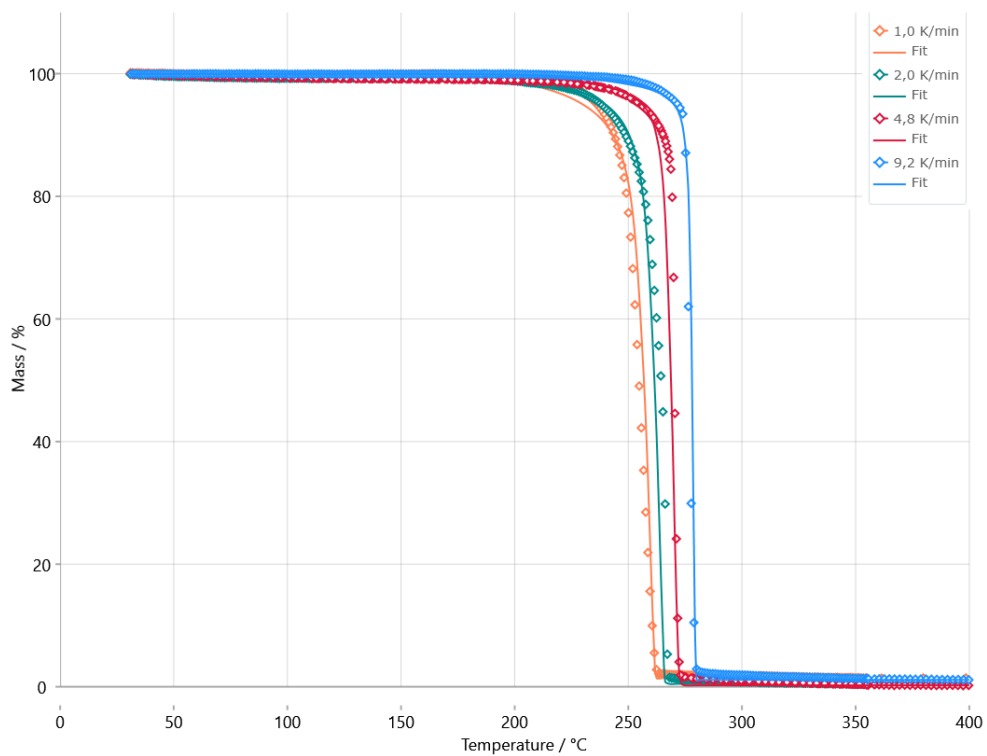


Figure S4. Friedman conversion-fit of HMX.

CL-20

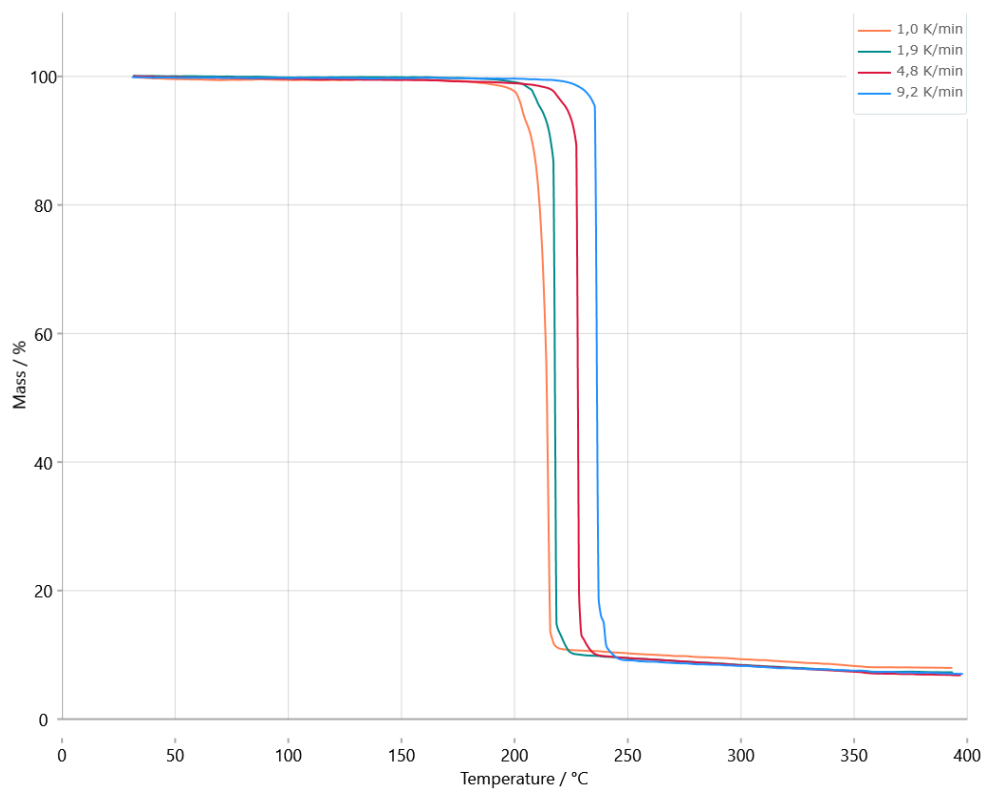


Figure S5. TGA measurements of CL-20.

Table S3. Sample weights of the different TGA measurements of CL-20.

TGA heating rate	Sample weight [mg]
1 K min ⁻¹	3.985
2 K min ⁻¹	3.665
5 K min ⁻¹	3.638
10 K min ⁻¹	2.097

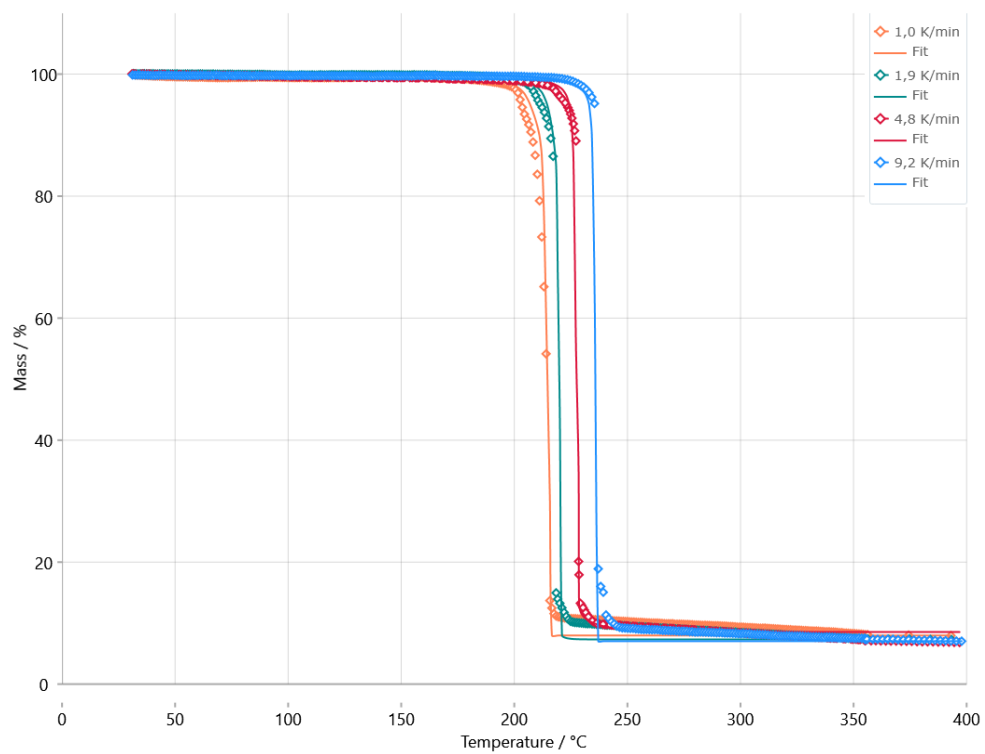


Figure S6. Friedman conversion-fit of CL-20.

PETN

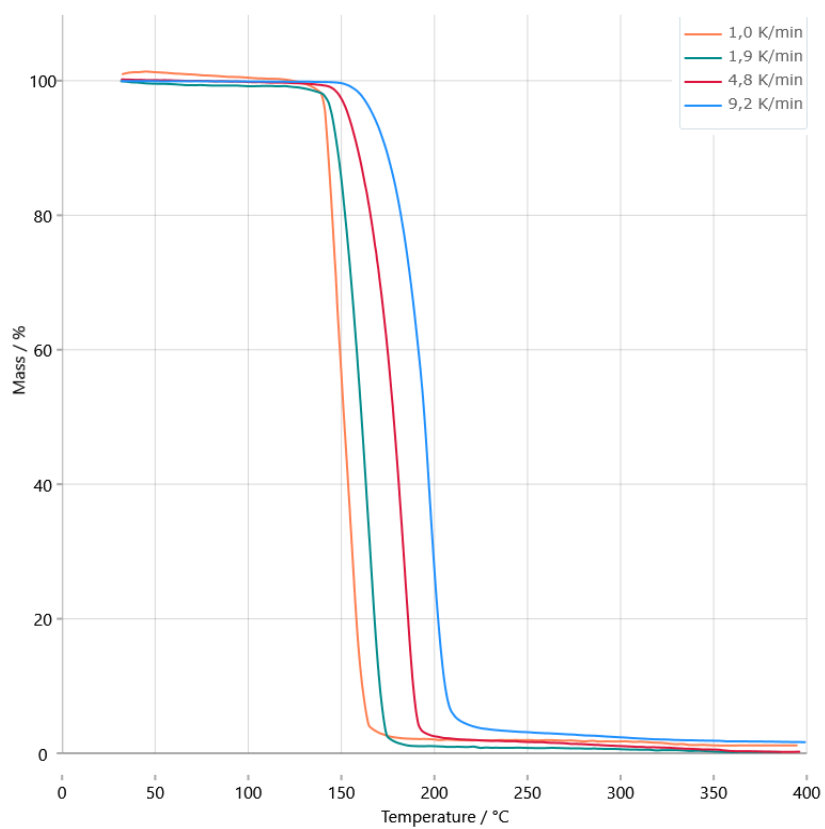


Figure S7. TGA measurements of PETN.

Table S4. Sample weights of the different TGA measurements of PETN.

TGA heating rate	Sample weight [mg]
1 K min ⁻¹	2.481
2 K min ⁻¹	2.141
5 K min ⁻¹	2.384
10 K min ⁻¹	5.308

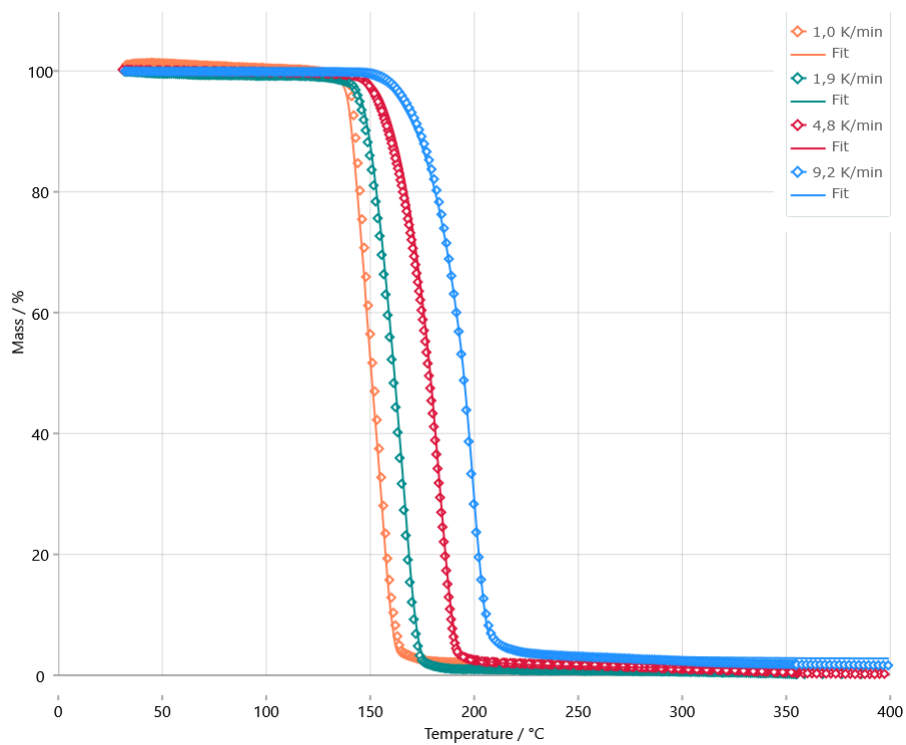


Figure S8. Friedman conversion-fit of PETN.

10.5.2 Activation energy

RDX

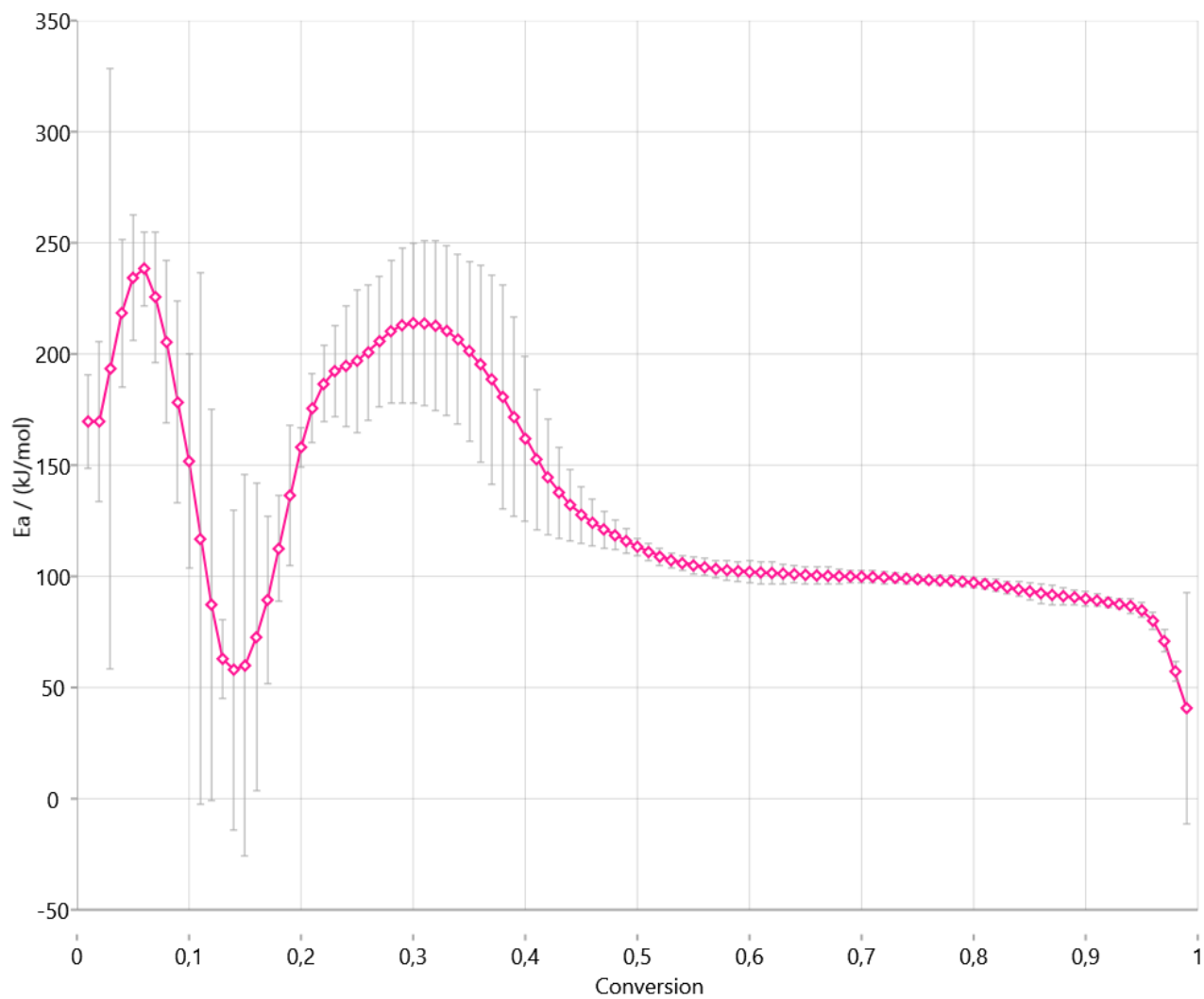


Figure S9. Apparent activation energy of RDX determined by the Friedman method.

HMX

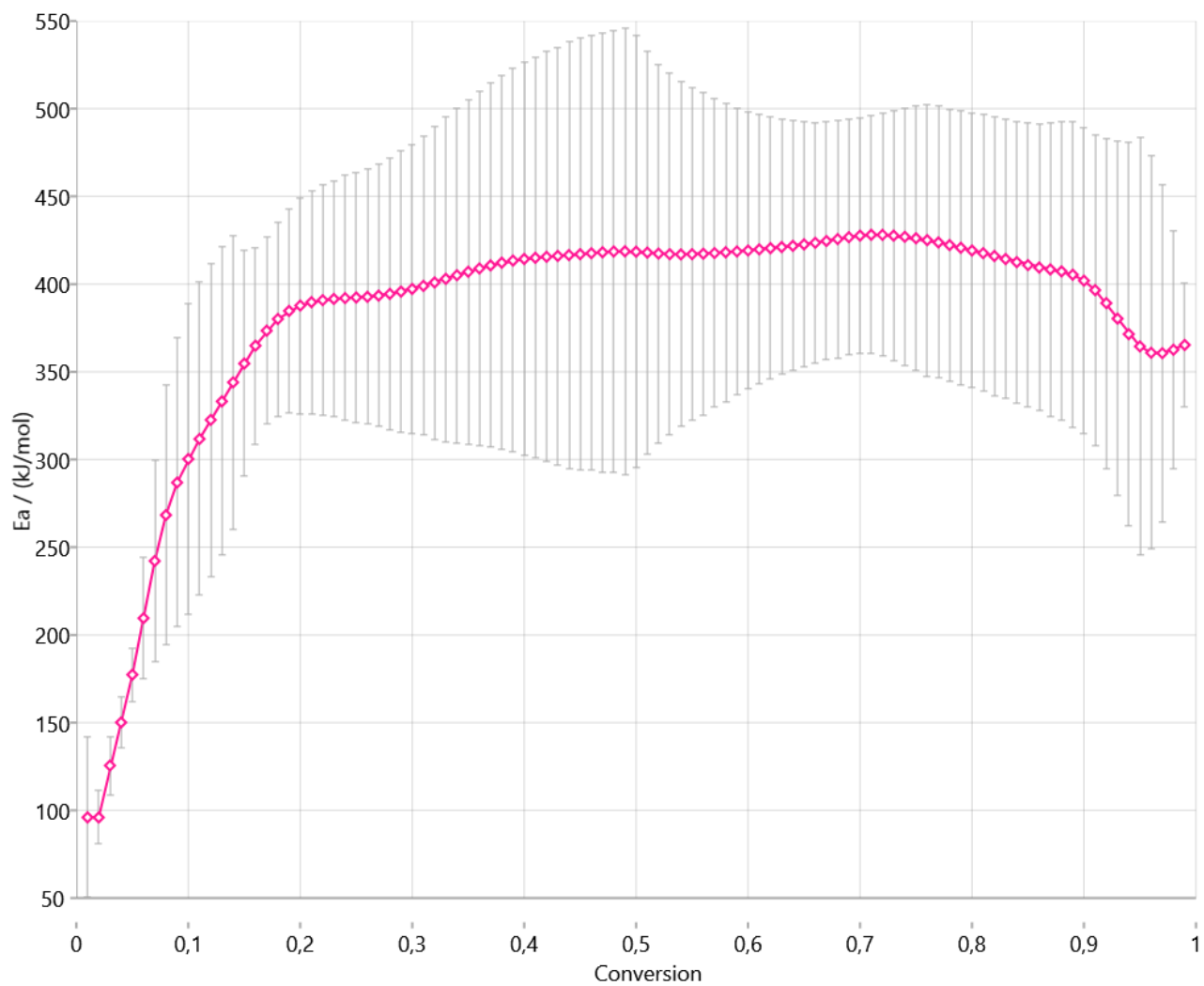


Figure S10. Apparent activation energy of HMX determined by the Friedman method.

CL-20

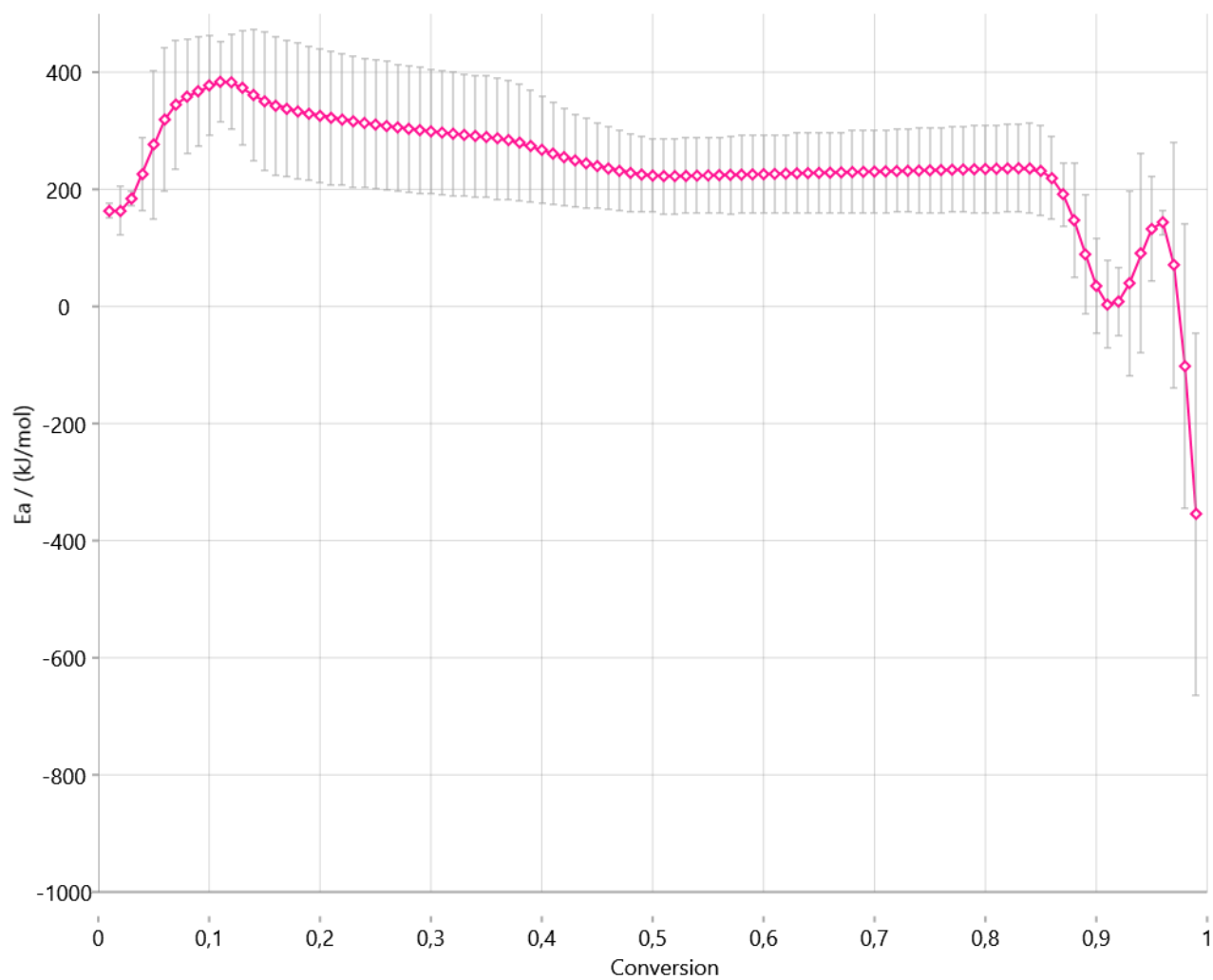


Figure S11. Apparent activation energy of CL-20 determined by the Friedman method.

PETN

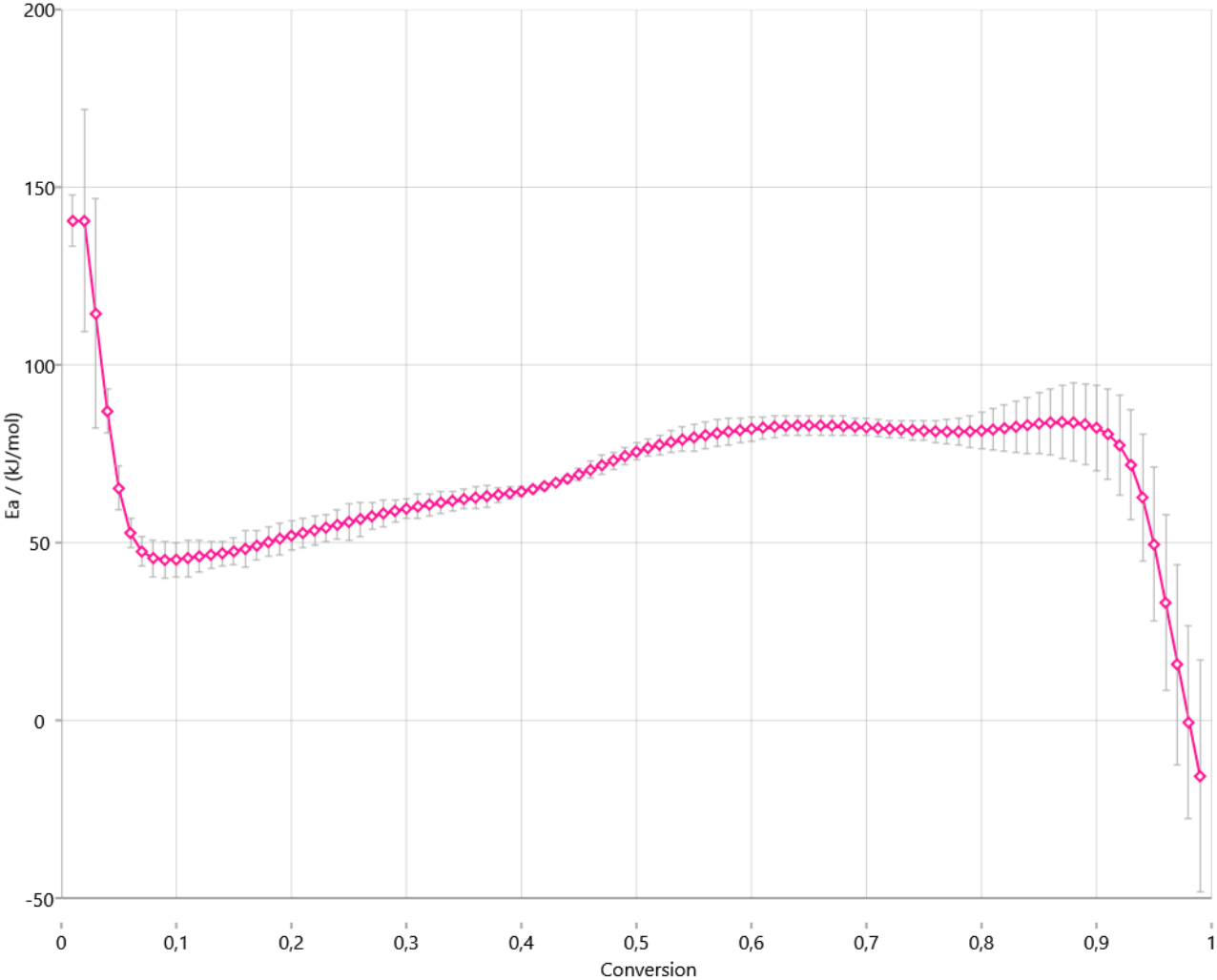


Figure S12. Apparent activation energy of PETN determined by the Friedman method.

10.5.3 Isothermal predictions and long-term stability

RDX

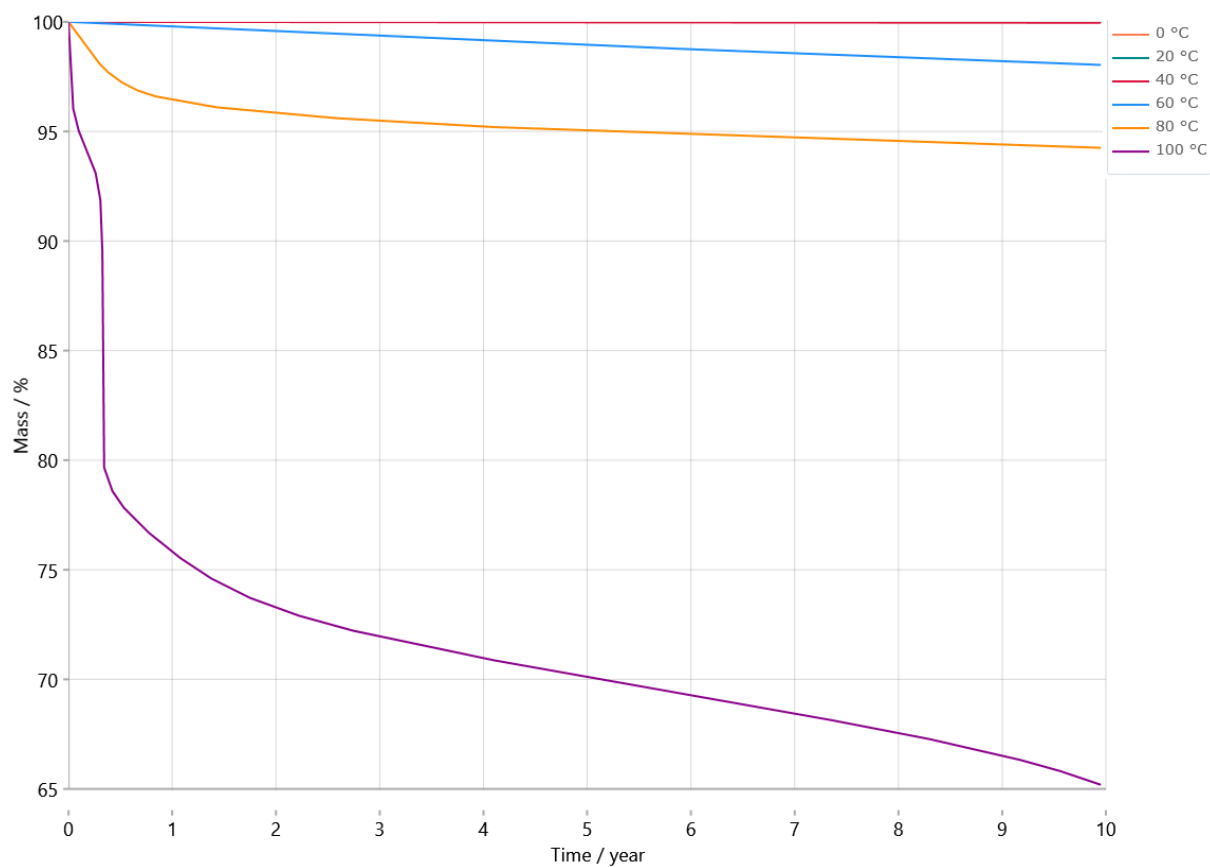


Figure S13. Isothermal predictions of RDX at different temperatures for 10 years.

HMX

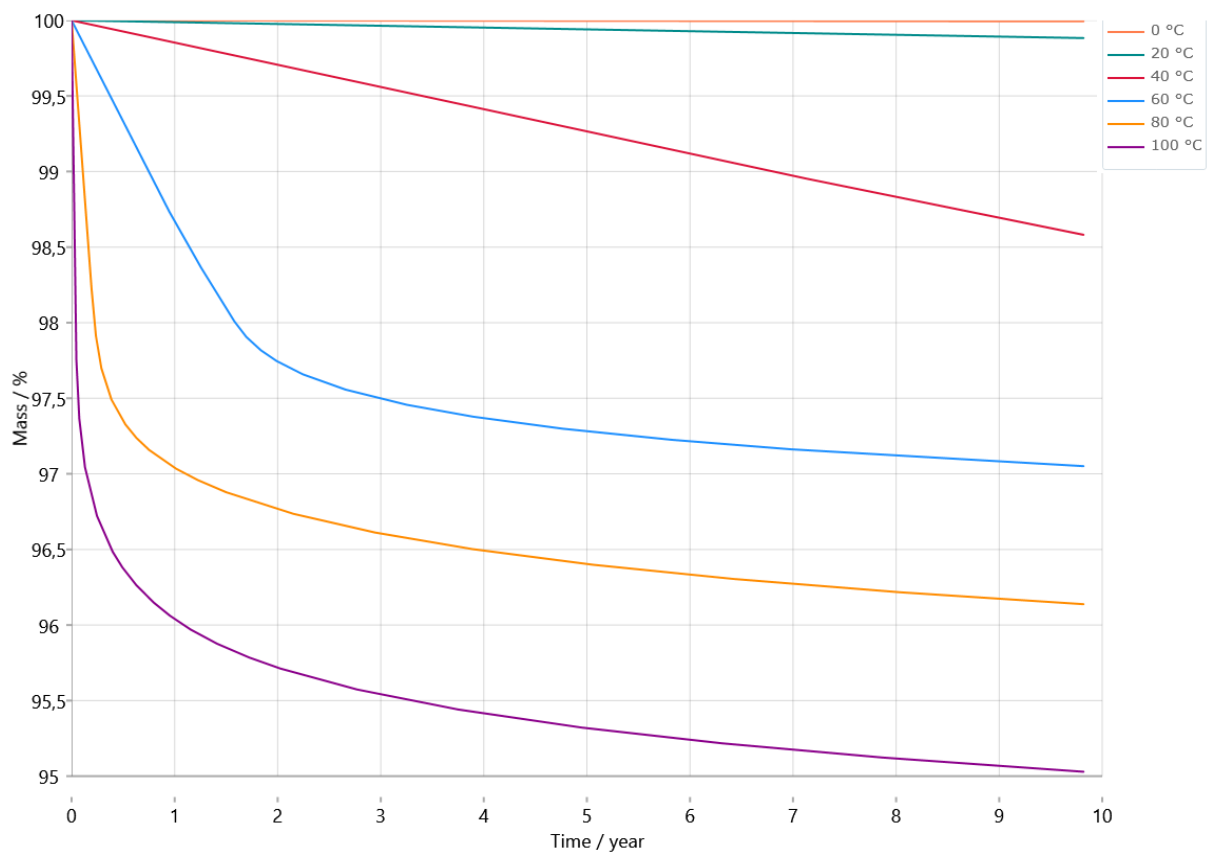


Figure S14. Isothermal predictions of HMX at different temperatures for 10 years.

CL-20

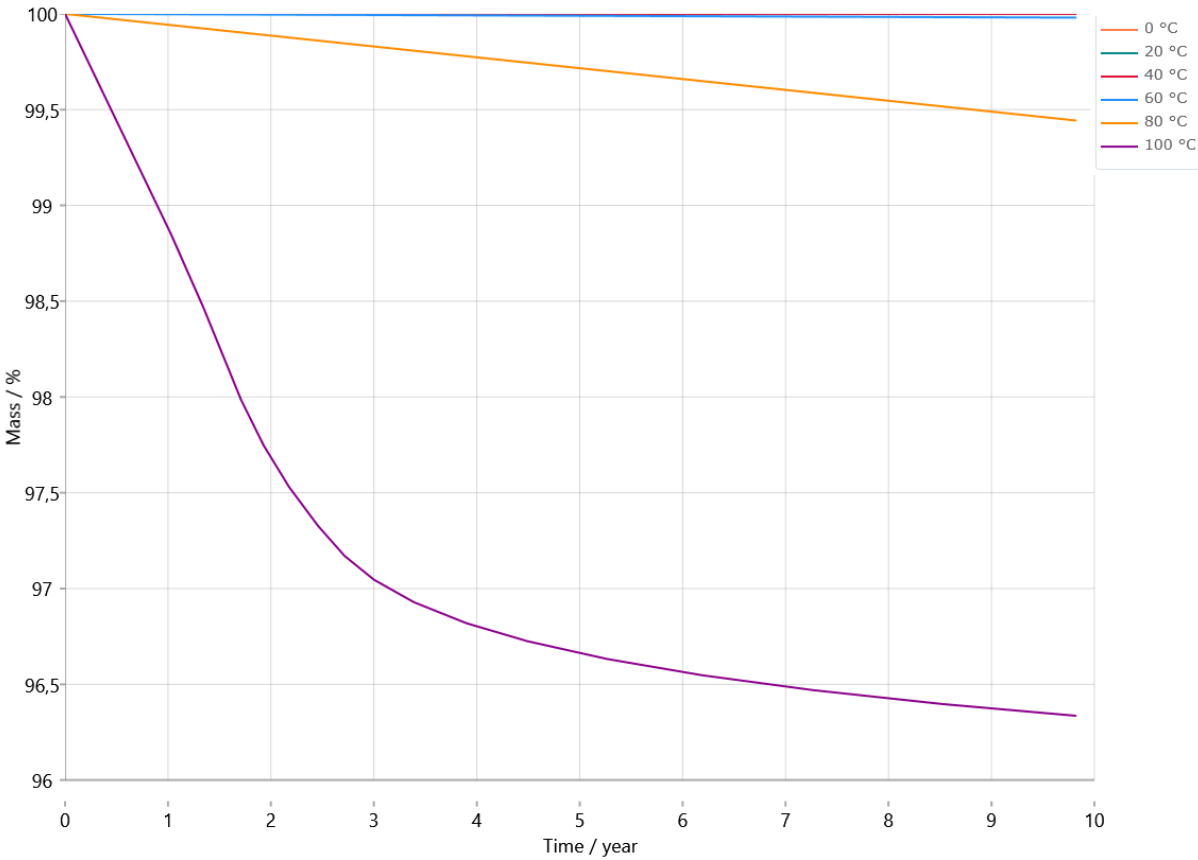


Figure S15. Isothermal predictions of CL-20 at different temperatures for 10 years.

PETN

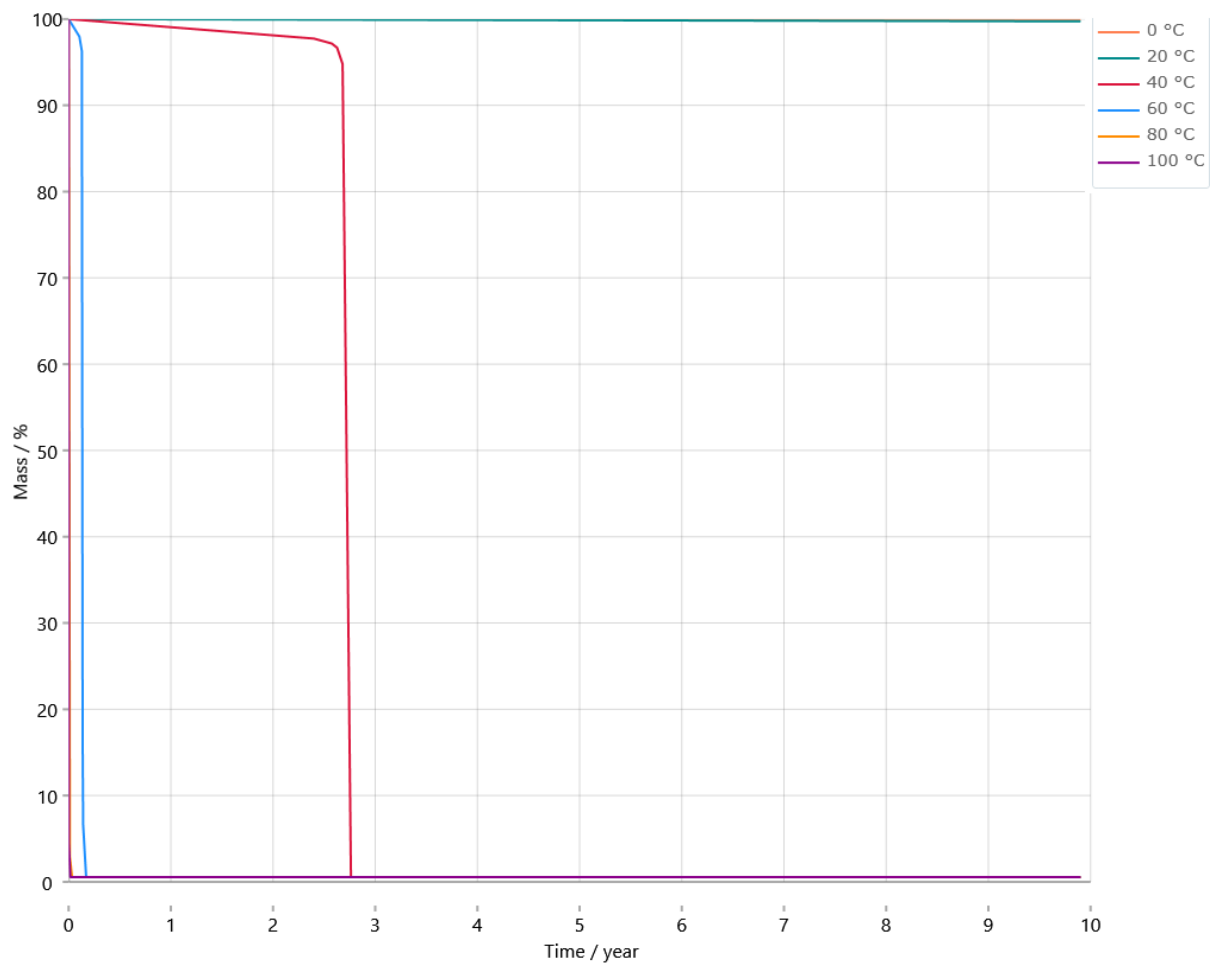


Figure S16. Isothermal predictions of PETN at different temperatures for 10 years.

10.5.4 Climatic predictions

RDX

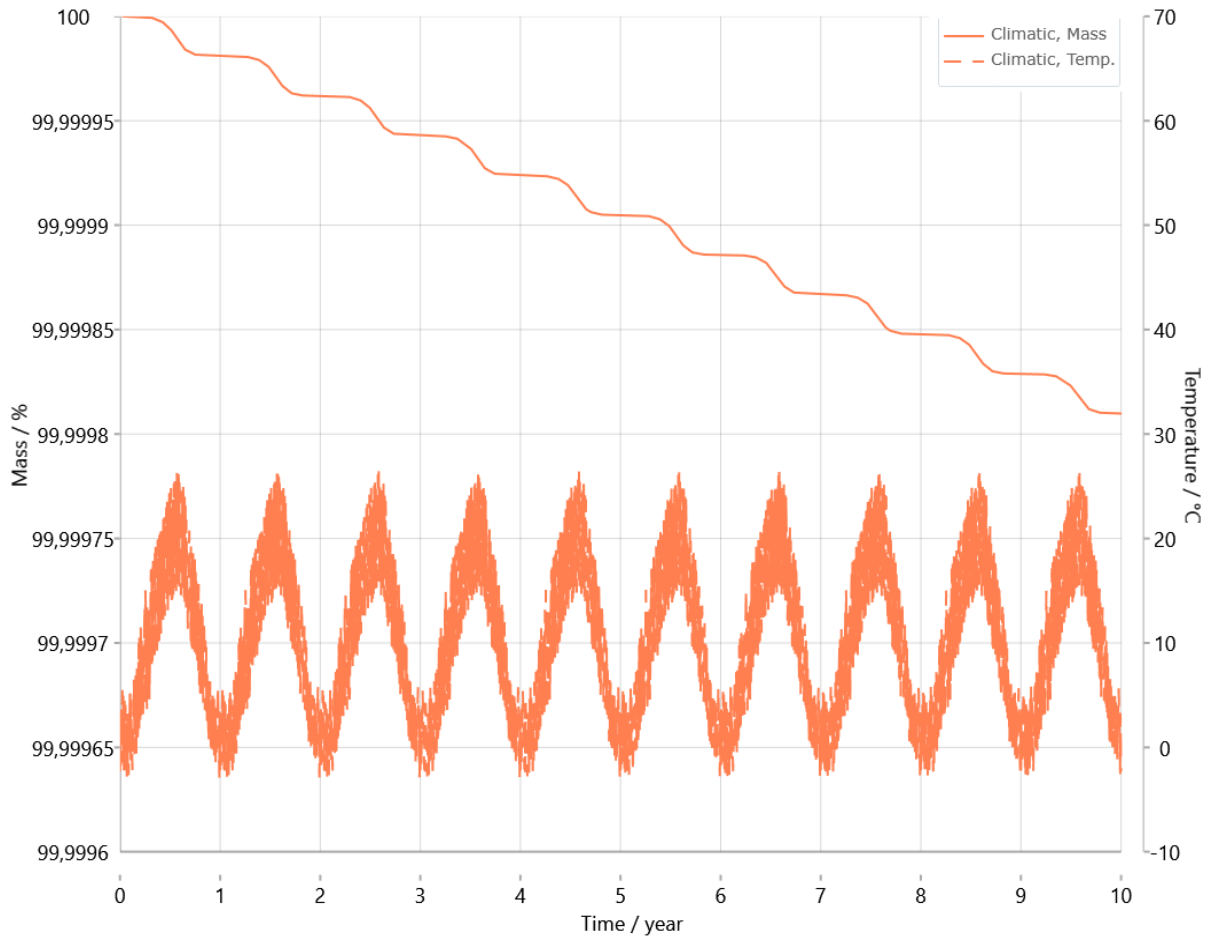


Figure S17. Climatic prediction of RDX for 10 years using the averaged temperature data of the last 30 years in munich.

HMX

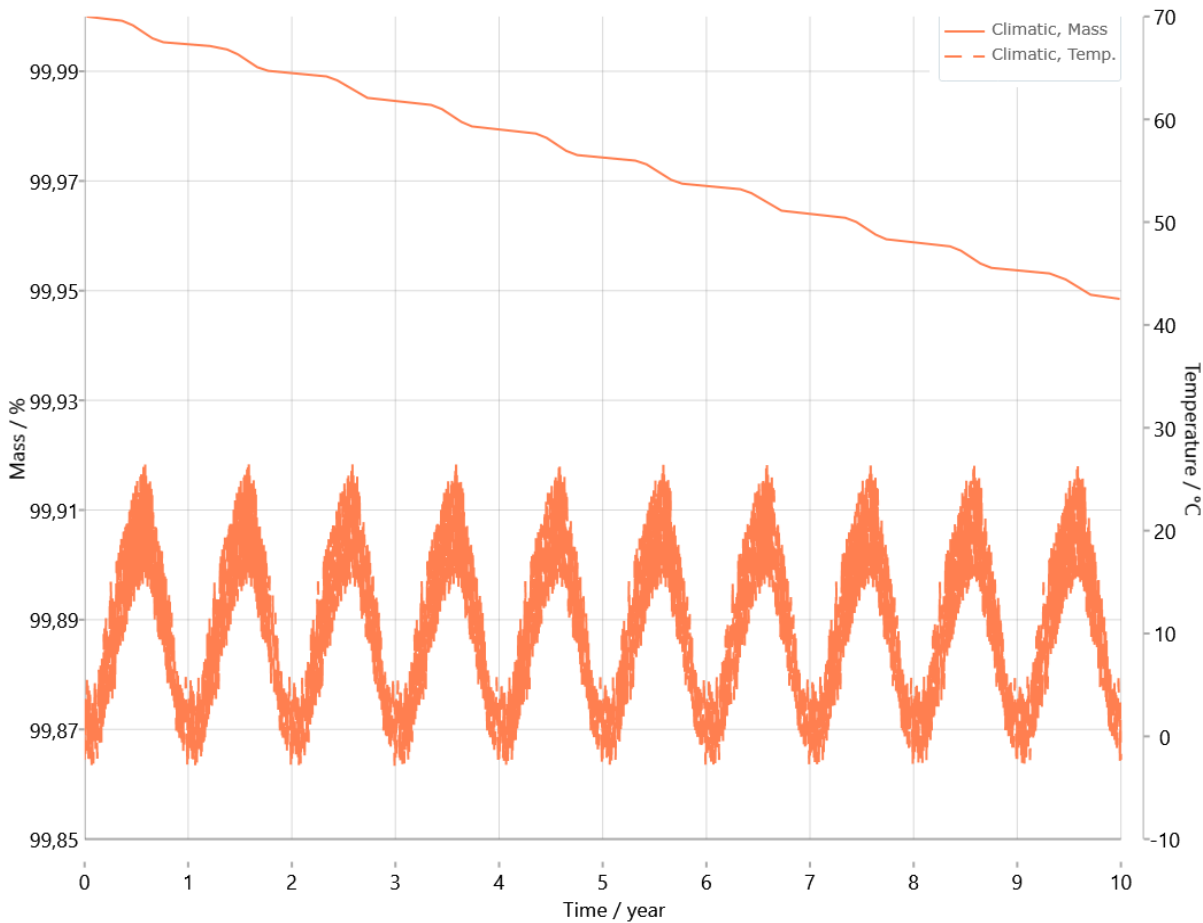


Figure S18. Climatic prediction of HMX for 10 years using the averaged temperature data of the last 30 years in munich.

CL-20

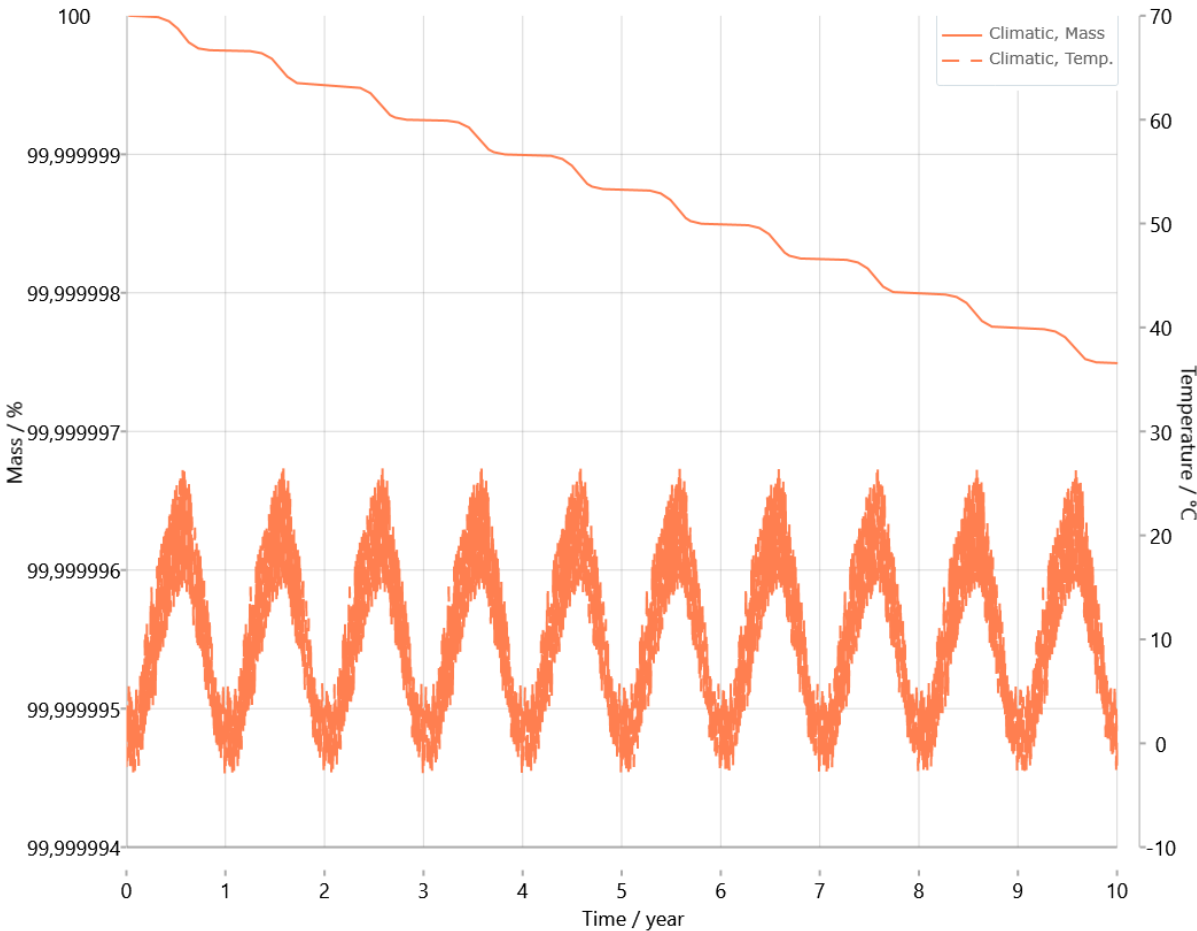


Figure S19. Climatic prediction of CL-20 for 10 years using the averaged temperature data of the last 30 years in munich.

PETN

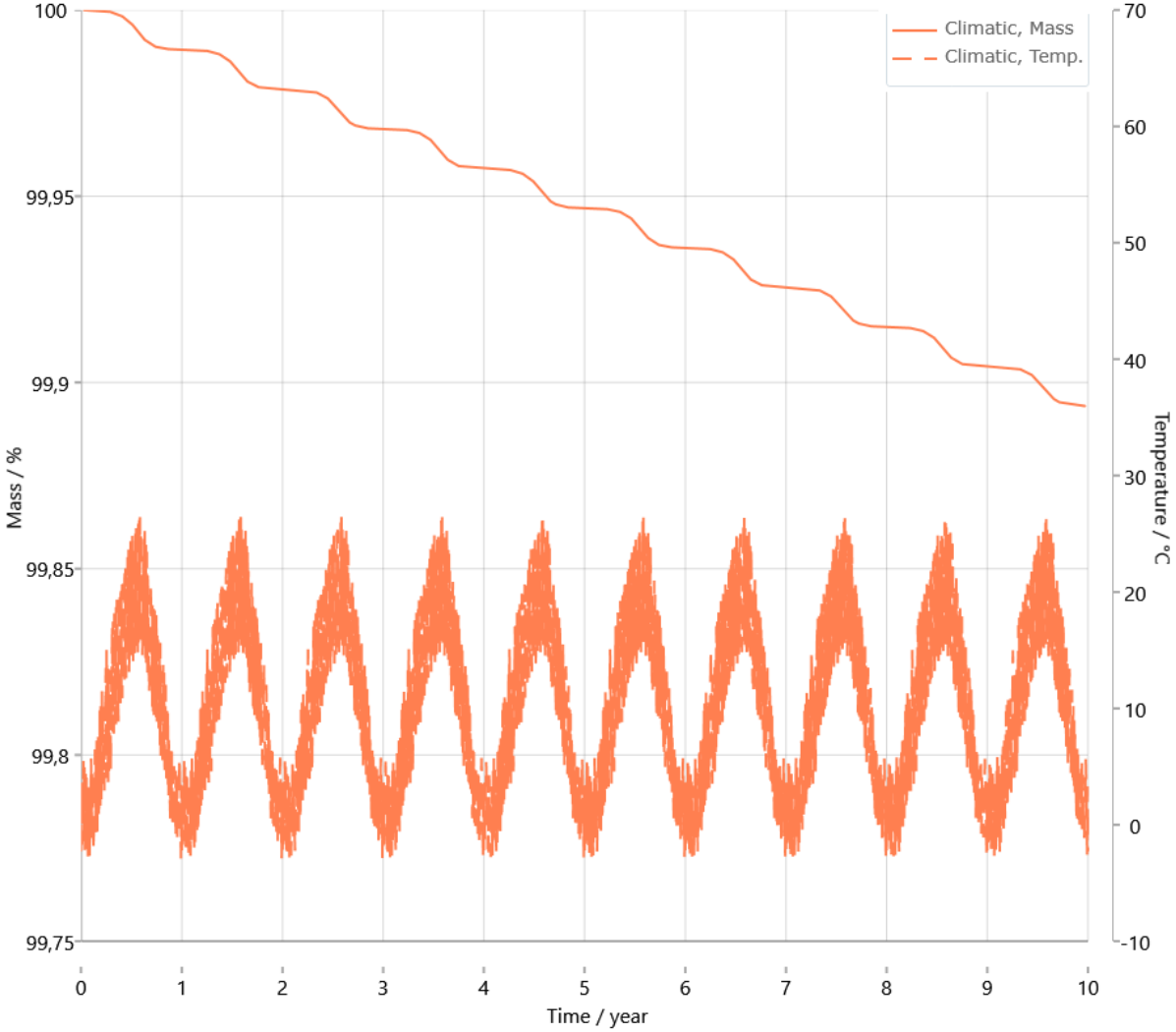


Figure S20. Climatic prediction of PETN for 10 years using the averaged temperature data of the last 30 years in munich.

10.5.5 Verification Experiment

The different samples were stored in open glass vessels in a ventilated oven at 100°C.

Table S5. Sample weights of the verification experiment.

	TKX-50	RDX	HMX	CL-20	PETN
Zeroweight of the vessel [mg]	12473.88	12540.28	12483.42	12432.81	12427.33
Weight after 48 h drying at 100°C [mg] (Start weight)	13472.63	13545.66	12644.95	13320.37	13435.50
Weight after 96 h at 100°C [mg]	13471.85	13544.96	12644.88	13319.91	13434.66
Weight after 2 weeks at 100°C [mg]	13471.83	13543.41	12644.76	13320.13	13427.69
Weight after 4 weeks at 100°C [mg]	13469.65	13541.13	12643.67	13318.53	13421.81

Table S6. Sample weights after 96 h.

Mass loss after 96 h at 100°C [mg]	0.78	0.70	0.07	0.46	0.84
Mass loss after 96 h at 100°C [mg]	0.078	0.070	0.043	0.052	0.083

Table S7. Sample weights after 2 weeks.

Mass loss after 2 weeks at 100°C [mg]	0.80	2.25	0.19	0.24	7.81
Mass loss after 2 weeks at 100°C [mg]	0.080	0.224	0.118	0.027	0.775

Table S8. Sample weights after 4 weeks.

Mass loss after 4 weeks at 100°C [mg]	2.98	4.53	1.28	1.84	13.69
Mass loss after 4 weeks at 100°C [mg]	0.298	0.451	0.792	0.207	1.358